Title
Recent advances in continuum plasticity: phenomenological modeling and experimentation using X-ray diffraction.

Author
Edmiston, John K.

Publication Date
2012

Peer reviewed|Thesis/dissertation

Recent advances in continuum plasticity: phenomenological modeling and experimentation using X-ray diffraction.

by

John Kearney Edmiston

A dissertation submitted in partial satisfaction of the
requirements for the degree of
Doctor of Philosophy

in

Engineering - Mechanical Engineering

in the

Graduate Division

of the

University of California, Berkeley

Committee in charge:

Professor David J. Steigmann, Co-chair
Professor George C. Johnson, Co-chair
Professor Tarek I. Zohdi
Professor John W. Morris
Dr. Nathan R. Barton

Spring 2012

Recent advances in continuum plasticity: phenomenological modeling and experimentation using X-ray diffraction.

Abstract

Recent advances in continuum plasticity: phenomenological modeling and experimentation using X-ray diffraction.

by

John Kearney Edmiston

Doctor of Philosophy in Engineering - Mechanical Engineering

University of California, Berkeley

Professor David J. Steigmann, Co-chair
Professor George C. Johnson, Co-chair

This work explores the field of continuum plasticity from two fronts. On the theory side, we establish a complete specification of a phenomenological theory of plasticity for single crystals. The model serves as an alternative to the popular crystal plasticity formulation. Such a model has been previously proposed in the literature; the new contribution made here is the constitutive framework and resulting simulations. We calibrate the model to available data and use a simple numerical method to explore resulting predictions in plane strain boundary value problems. Results show promise for further investigation of the plasticity model. Conveniently, this theory comes with a corresponding experimental tool in X-ray diffraction. Recent advances in hardware technology at synchrotron sources have led to an increased use of the technique for studies of plasticity in the bulk of materials. The method has been successful in qualitative observations of material behavior, but its use in quantitative studies seeking to extract material properties is open for investigation. Therefore in the second component of the thesis several contributions are made to synchrotron X-ray diffraction experiments, in terms of method development as well as the quantitative reporting of constitutive parameters. In the area of method development, analytical tools are developed to determine the available precision of this type of experiment - a crucial aspect to determine if the method is to be used for quantitative studies. We also extract kinematic information relating to intragranular inhomogeneity which is not accessible with traditional methods of data analysis. In the area of constitutive parameter identification, we use the method to extract parameters corresponding to the proposed formulation of plasticity for a titanium alloy (HCP) which is continuously sampled by X-ray diffraction during uniaxial extension. These results and the lessons learned from the efforts constitute early reporting of the quantitative profitability of undertaking such a line of experimentation for the study of plastic deformation processes.

Dedicated to my family. And to Tyke.

Contents

Acknowledgments

First off, I would like to thank the Mechanical Engineering department at UC-Berkeley for giving me a chance to succeed in their program by accepting me as a PhD student. I am grateful that I was able to come into contact with Professor Johnson in my first term. Working with him as a GSI gave me my first financial foundation in the department, which gave stability to my otherwise uncertain beginnings here. The periodic course corrections offered by Professor Johnson were helpful in focusing my research, and I appreciated his attentiveness to my personal goals and state of mind throughout the PhD process. I am grateful that I met Professor Steigmann towards the end of my first term, at the nudging of Professor Zohdi, for which I also give thanks. The concise clarity Professor Steigmann brings to the presentation of mechanics was highly influential in my development. I also owe a debt to Nathan Barton at Lawrence Livermore National Lab, who gave me a chance by taking me on as a summer student. This eventually led to a fellowship, letting me focus further attention on research. He introduced me to the wonderful world of Emacs, which greatly increased my computational productivity. He also provided alternate perspectives on many problems of discussion, which kept me well rounded. I would also like to thank Joel Bernier at LLNL for taking me on several beamline excursions. These experiences further enriched my understanding of applied X-ray diffraction. On a related note, I'd like to thank Ulrich Leinert (Argonne National Lab), Matt Brandes (Ohio State), and Matt Miller (Cornell) for letting me examine their X-ray data as part of the thesis. Finally on personal note, I'd like to thank my fellow graduate, best friend, and future wife Lindsay for cheering me up when frustration would inevitably set in. I don't know if I'd be where I am without your support.

Between the three persons I had the most discussions, Professors Johnson and Steigmann, and Nathan, they each brought different sets of skills and points of view to the table, ranging from theoretical abstraction to experimental expertise. The set of capabilities I am exiting Berkeley with is probably in part a manifestation of the intersection of these perspectives. During the difficult times encountered by most PhD students at some point, I pictured a Venn diagram, and wondered if this intersection was in fact the null set. But in the end I am happy with the work contained in this thesis, and I hope an upcoming student gets some use out of it. The student is the target audience I had in mind while writing.

Chapter 1

Introduction

On the profession of structural engineering: '... modeling materials we do not really understand, into shapes we cannot really analyze, so as to withstand forces we cannot really assess, in such a way that the public does not really suspect' in Winds on High Rise Buildings, (Parmelee, 1970)

The subject of this thesis falls under the weathered and tattered banner of continuum plasticity[1]. In this introductory chapter we explain why such a classical subject still warrants attention and give an overview of the thesis content. In §1.1 we begin by discussing the general issues that remain in theoretical and experimental plasticity, as we see them. In §1.2, the essential source of these issues is diagnosed as being difficulties in experimental and constitutive frameworks for plasticity; a description of these difficulties is given. Finally in §1.3 a summary of the rest of the thesis content is given.

1.1 Why plasticity?

Plasticity has been the subject of academic research for over 100 years (Reusch, 1867; Andrade, 1914; Taylor, 1938; Schmid and Boas, 1950). Over that time, many models of plasticity have been suggested. Many have been successful for their target application. Given its long history it follows that one might ask why further study of plasticity is warranted. To this question we respond with the following two observations from the field:

1. Lack of experimental techniques. Apart from simple tests such as uniaxial tension, experimental capabilities for the quantitative comparison of plasticity models to physical data simply have not been developed and/or are not widely available. More details of these issues will be explained in §1.2. A modern, promising answer to this challenge are

[1] To set terminology, in this document the term plasticity always refers to plasticity of continuous media.

X-ray diffraction experiments, particularly from synchrotron sources (Poulsen et al., 1997)[2]. Therefore, as one component of this work we provide detailed information about the ability of X-ray diffraction experiments to investigate plasticity phenomena. This type of X-ray diffraction experiment is referred to in the literature as High Energy Diffraction Microscopy (HEDM) or Three Dimensional X-ray Diffraction (3DXRD) (Poulsen, 2004; Lienert et al., 2011). Application of the method in several experiments is used to demonstrate how this method can provide previously unquantified data. In particular, we are interested in using the technique for constitutive investigation. Furthermore, we would like to determine which properties and characteristics of single crystals can be obtained by experimentation using polycrystals.

2. Unexplored gap in theoretical development. These days, the framework most often used to model the plasticity of single crystals is crystal plasticity (Asaro, 1983). Details of this model will be given later on in this chapter. For now it suffices to characterize the model as being physically motivated, based on experimental observations of dislocations moving through a crystal at the atomic scale.

In contrast, the plasticity of polycrystalline materials has historically been approached using phenomenological considerations which have few inherent restrictions apart from material symmetry or other fundamental relations such as frame-invariance. For example, many macroscopic polycrystals are reasonably successfully characterized by isotropic material symmetry; the well known J_2 theory arises from the application of this phenomenological approach (Malvern, 1969, p. 347). This type of modeling has also been used to describe certain types of anisotropic polycrystals: the deformation processes required in the production of sheet metal result in materials which have been profitably modeled as transversely isotropic or orthotropic (Barlat et al., 1991; Cleja-Tigoiu and Iancu, 2011).

In summary, researchers of single crystals use crystal plasticity, and researchers of polycrystals use classical phenomenology. Although these may each be assessed as phenomenological theories, a distinguishing feature is that the latter imposes minimal restrictions apart from material symmetry, whereas the former is constrained to slip system activity. For the most part, these two similar yet distinct approaches characterize the modern plasticity literature to date.

Between these two approaches there is a modeling possibility which, at present, remains unexplored apart from theoretical suggestions: a classically motivated phenomenological theory for single crystals. Certain aspects of this approach may be considered similar to the formulations used to model polycrystals. However the material symmetries characterizing single crystals are much more challenging to deal both theoretically and experimentally, than, e.g., transverse isotropy. Given the widely accepted successes of crystal plasticity, such a phenomenological theory might seem out of date. On the other hand, in terms of arriving at answers of practical interest, phenomenological modeling is typically (historically speaking)

[2]Although synchrotrons are not widely available!

excellent. After all, phenomenological relations such as Hooke's law seem to have turned out fairly well in terms of guiding structural design. Many similar examples exist, such as Fick's law of diffusion for chemical engineering problems. Such formulations exhibit a degree of elegance in the acceptance of our modeling ignorance, and recognition that detailed interactions of individual atoms will in the end not be important to the goals of a particular macroscopic application. More precisely stated, these models simply express that complicated physics can at times be captured better by using a model which is flexible enough to accommodate the complexity while remaining true to the most fundamental considerations. Therefore, while physically motivated models like crystal plasticity are clearly attractive, we should keep in mind the community's experience from other applications of continuum physics, where the ability of physical models to describe experimental data at continuum length scales is often wanting. For example, strain energy functions for rubber materials derived from statistical thermodynamics considerations prove to be inadequate in comparison to phenomenological approaches (Treloar, 1974; Ogden, 1982). Furthermore in plasticity itself, there are still phenomenological observations which have not been well answered, such as the Hall-Petch effect (Lim et al., 2011).

In conclusion, given the unexplored nature of the modeling framework, along with possible benefits in certain applications, the second aspect of this thesis is the development of a classically justified phenomenological model of plasticity for crystalline materials. Constitutive equations are suggested, and numerical predictions of the resulting theory are reported. The hope is that this work at least gives the proposed approach to plasticity the opportunity to show itself to be useful. Whether or not it is of course, can be judged upon the basis of the model's ability to explain experimental observations.

In the next section, we see that these points are really two aspects of the same fundamental problem - the lack of validated constitutive frameworks for plasticity. We share some general thoughts on the importance of constitutive functions in continuum mechanics, and explain why the constitutive problem is singularly difficult to establish for theories of plasticity.

1.2 Challenges in constitutive equations for elastic-plastic materials

In theories describing the motion of continuum material bodies, constitutive functions relating the motion of the material to the forces generated by the material are required to make predictions. These functions can only be deduced from experimental observations at some stage, a theoretical model is not sufficient (even for molecular-level modeling, particle masses must be known from experiment). With these constitutive functions in hand, numerical simulations can be utilized to make predictions about material behavior under various situations of practical engineering interest.

The specification of constitutive functions is usually reducible to the determination of certain constants which characterize the material behavior. That is, for the same family of constitutive functions, the numerical values of the constants generally differ from material to material. Such constants quantify the distinction in physical behavior between dropping a block of steel from a given height onto the ground from that of water under the same conditions. Intuitively, the vastly different outcomes expected from this scenario underlines the importance of determining these material dependent functions and parameters in order to make predictions. It is noteworthy to point out that in this steel/water example, the core theoretical framework (balance equations) in both cases are identical - therefore the determination of the material parameters is crucial in order to make meaningful physical predictions of material behavior in different conditions.

The experiments required to obtain values for these constitutive parameters are not always straightforward to execute. For solid elastic bodies, the experimental prescription is well established, at least for materials which are available as large single crystals. To date, however, the situation remains challenging for the constitutive specification of functions involved with elastic-plastic deformation. This is the case for several reasons, which we now describe.

(1) First, the mathematical description of elastic-plastic deformation requires some notion of a decomposition of the total material deformation into elastic and plastic parts.[3] The task of measuring both elastic and plastic portions of the deformation immediately causes severe experimental challenges compared with considering elastic strains alone, challenges which to date have not been adequately put to rest.

Currently, measuring elastic and plastic strain has the most hope for crystalline materials, where techniques such as X-ray diffraction give a unique definition of elastic strain. The total material strain is also measurable at the surface on the same length scale as the X-ray diffraction measurement with modern techniques such as Digital Image Correlation or DIC, (Sutton et al., 1986; Vendroux and Knauss, 1998). A proposed experiment would use both techniques at the same time, thereby enabling the measurement of both elastic and plastic strain by deducing plastic strain from the independently measured total strain and elastic strain.

Interestingly, in Taylor's original experiments on the plasticity of single crystals in the 1920s (Taylor and Elam, 1923), he was essentially able to measure both elastic strain (at least lattice orientation) and total material strain by using a combination of X-ray diffraction and the geometric measurement of a set of lines scribed into the material, see Figure 1.1. Even now, we really haven't improved experimental techniques for the study of plasticity to a great degree over the methods of Taylor almost 100 years ago. Digital Image Correlation is simply a more refined method of measuring total material strain than Taylor used: essentially

[3]More formal definitions of what is meant by elastic strain vs. plastic strain in this study will be provided in the next section

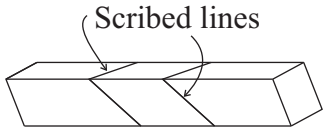

Figure 1.1: Scribed lines on the single crystals used in Taylor's experiments, translated from (Taylor and Elam, 1923). Taylor's careful measurements of these lines gave an estimate of the total material deformation. At the same time, X-ray diffraction measurements were performed, giving an estimate for the lattice strain (orientation). This complex experimental technique is required for constitutive validation of elastic-plastic constitutive equations, but executing such a program with modern technology is still not easily achieved.

taking a ruler to measure the evolving lengths of material lines. X-ray diffraction technology has also improved, so that full elastic strain tensor can be estimated instead of only the orientation component. However the basic method for X-ray analysis is the same as for Taylor. Only the data collection hardware and the quality of X-rays have changed.

(2) The second reason constitutive specification for elastic-plastic deformation is challenging is that there are simply many constitutive functions to determine, many more than for elasticity for instance. In the theory developed here, we will see that at a bare minimum, we require the specification of a plastic flow rule, which describes the time evolution of the plastic strain. The flow rule might simply be a function of, say, a stress measure. Based on the experimental challenges mentioned in the previous paragraph, however, the task of determining this 'simple' function is difficult enough to accomplish. The situation becomes progressively more complicated as arguments which are necessary to capture phenomenology associated with plasticity are added to the constitutive functions. For example, incorporating hardening behavior into the model necessitates additional functional arguments, hence additional experimental measurements, and therefore a greatly complicated experimental picture.

Summary. Clearly, the experimental undertaking required in obtaining constitutive functions for elastic plastic deformation of single crystals is challenging. The challenges to producing a constitutive framework validated by experimental data for elastic plastic deformation have not been significantly reduced since Taylor's time. This is probably one reason continuum plasticity is still subjected to new theoretical formulations. The lack of constitutive information and experimental validation enables such a proliferation of formulations. Admittedly, in this work we further muddle this state of affairs, by adding another formulation of plasticity to the mix. However, we also describe how this theory may be investigated experimentally, and establish calibration of constitutive functions to available data. That is, we pay our debt, so to speak.

1.3 Overview of thesis content

The primary contributions in this work present progress in plasticity by developing an extension of phenomenological plasticity to single crystals, as well as a detailed analysis of a modern class of synchrotron X-ray diffraction experiments. These topics are naturally synergistic since X-ray diffraction is required to execute an experimental investigation of the proposed theory. They also share a clean commonality of formulation. We now describe a more detailed summary of the thesis. What are felt as novel contributions to the field are pointed out as they are addressed, in order to draw experienced readers' attention.

In Chapter 2, we develop the phenomenological formulation of single crystal plasticity and give numerical predictions. The theoretical development is in the family of work by Fox (1968); Naghdi and Srinivasa (1993a); Gupta et al. (2011). The present contribution is made distinct from these previous works by developing these models to the level of detail needed to make numerical predictions, then coding and executing the simulations. For the first time, therefore, the validity of the previously proposed phenomenological frameworks for single crystals can be critically examined against experimental observations.

Of primary importance, this task requires the construction and validation of constitutive functions. One may be tempted to consider the problem of writing down constitutive function representations for crystals trivial, upon recognition of the presence the review article by Zheng (1994). These methods use the elegant structural tensor approach to generate constitutive functions in a systematic fashion (Liu, 1982). However, for higher symmetry crystals such as cubics, the representation problem is not as easy as with low crystal symmetries like monoclinic, for instance. If high symmetry crystals were of little use in applications, this may not pose a problem, but high symmetry crystals include the practically important structural metals such as iron (BCC), aluminum (FCC), and titanium (HCP). Furthermore, the structural tensor approach becomes rapidly less favorable when considering multiple tensor arguments (Xiao, 1996), as we will require.

We found that producing appropriate constitutive functions for the symmetry groups characterizing crystals requires a certain willingness to tolerate relatively lengthy mathematical procedures needed to reduce the constitutive equations. In fact, the tedious nature of generating these functions may be one cause of the previously mentioned gap between J_2 phenomenological plasticity and slip system based crystal plasticity[4]. We give examples which should be sufficient to develop constitutive functions for each of the 32 crystal point groups, for functions of several arguments. In particular the maximal cubic symmetry and maximum hexagonal symmetry groups are investigated. This contribution is further emboldened by providing a calibration of the constitutive framework against available data. These efforts open up this line of modeling to further application-based study by the community, and is a useful outcome of the modeling component of this thesis.

[4]As we will see, the formulation of slip system based crystal plasticity cleverly avoids these computations.

A second contribution is that the numerical framework has the capability to compute the geometrically necessary dislocations as a quantity derived from the spatial gradients in plastic deformation. The role of geometrically necessary dislocations in theories of plasticity is not a new notion (Acharya and Bassani, 2000; Gupta et al., 2007), however incorporating such quantities into simulations is more recent (Lele and Anand, 2009). Therefore we examine the predictions resulting from several proposed constitutive functions which incorporate hardening due to geometrically necessary dislocations.

Next we examine experimental aspects of the theory. In Chapter 3, we discuss modern synchrotron X-ray diffraction techniques from the HEDM and 3DXRD family in detail. To date, the method has been successful in terms of discovery type research, which is important but is of a qualitative nature. It remains to be determined what else the experiment can be used for. Here, we are interested in using it to investigate constitutive behavior of single crystals. Several early studies along these lines are reported in the literature (Bernier et al., 2008; Efstathiou et al., 2010) but further research is needed. We recast the kinematic theory of X-ray diffraction from a mechanics, as opposed to crystallographic, perspective. This imbues a natural synergy between single crystal plasticity and X-ray diffraction which is hopefully appealing to non-crystallographers, and highlights the natural relation between X-ray diffraction and the theory developed in Chapter 2. These background sections should then serve as a good one-stop reference for other crossover researchers from mechanics to applied crystallography, although they are also needed as the foundation for modeling efforts in later sections of the chapter.

Following this background, we examine two novel methods of analyzing the data from this type of experiment. The first method is targeted at investigating the attainable precision from the measurements, i.e. uncertainty analysis. Such uncertainty analysis determines the strength of the conclusions which can be made from a given experiment, and is particularly important to consider in the constitutive context (Zohdi, 2001). The second method develops the theory for numerical implementation of a novel approach to lattice refinement which can quantify the intragranular texture development in single crystal grains by forward modeling individual diffraction peak intensities. It should be emphasized that the deductions from these approaches to the analysis of X-ray diffraction data are not accessible with conventional methods. Finally, the model and experiment are brought into direct alignment when we extract constitutive parameters from the plasticity theory by analyzing the data from a titanium alloy loaded in tension with *in situ* X-ray experimentation.

Chapter 2

Phenomenological Plasticity

Chapter overview. In this chapter we develop the theoretical foundations of the proposed model for single crystal plasticity. An attractive goal of the theory is for it to be amenable to investigating using a prescribed experimental approach. In light of this all quantities presented in the theory are directly measurable using X-ray diffraction experiments[1].

The theoretical basis for the plasticity model is similar in thinking to those previously proposed in the literature (Fox, 1968; Naghdi and Srinivasa, 1993a,b; Gupta et al., 2011). The basic idea in these theories is that, in addition to the standard mathematical structure of a continuum, a triad of inertia-less directors is defined at each material point. The directors characterize the stress response of the material, which in turn couples to the overall material motion through balance laws. Importantly, during plastic deformation the directors evolve independently of the material. In the present theory, these directors are interpreted as the (direct) lattice vectors of the crystal. Since the direct lattice is isomorphic with the reciprocal lattice, and X-ray diffraction measures the reciprocal lattice, we can therefore obtain experimental measurements of the directors.

At a minimum, this theory requires constitutive functions for the stress response and the evolution of the directors during plastic flow. The main contribution in this chapter is that we develop these constitutive functions for various classes of crystal symmetries, e.g. cubic, hexagonal (Green and Adkins, 1970). These functions are the missing ingredient in, for instance, previous papers (Fox, 1968; Naghdi and Srinivasa, 1993a,b; Gupta et al., 2011), which has limited the investigation and subsequent judgment of the viability of the formulation until this point. Based on the importance of cubic crystals in engineering (e.g. aluminum (FCC), iron (BCC)), we calibrate several proposed constitutive functions for cubic crystals against available data. This data is generated through simulations of crystal plasticity models from the literature. In Chapter 3 we also calibrate a hexagonal crystal model directly against X-ray diffraction data. Together, the proposed constitutive functions for several crystal symmetries with calibrated parameters constitute the one outcome from

[1] X-ray diffraction theory and application is discussed in Chapter 3.

this chapter.

We then implement the model in numerical plane strain simulations to test its predictions in illustrative boundary value problems. A benefit of the numerical framework we use is that it enables the computation of geometrically necessary dislocations from gradients in the plastic deformation field. Several authors have proposed incorporating such information into the plastic constitutive equations (Acharya and Bassani, 2000; Gupta et al., 2007), but only recently has this been reported on numerically (Lele and Anand, 2009). In the work of Lele and Anand (2009), it is not clear how to relate their definition of geometrically necessary dislocations to ours, since their material is isotropic, which we do not restrict ourselves to here. Therefore, the numerical predictions of geometrically necessary dislocations and their incorporation into constitutive functions for cubic crystals are a second contribution from this chapter.

Content of chapter. In §2.1, a historical review of plasticity research is given. We explain the fundamental discoveries resulting from G.I. Taylor's influential experiments, and summarize the largely independent evolutions of crystal plasticity and phenomenological plasticity. We also discuss objections that have been leveled toward these two approaches to plasticity. In §2.2, we develop the advertised theory of phenomenological plasticity for single crystals. Relevant thermodynamics and balance laws are recorded, along with the general constitutive framework. We describe a rate independent model, as well as the rate dependent, viscoplastic extension. In §2.3, more precise constitutive functions are posed by accepting additional hypotheses such as maximum plastic dissipation. Phenomenological constitutive equations for single crystals are difficult to determine, particularly for high symmetry crystals such as cubics. This difficulty may be one reason previous researchers have not attempted the present approach to modeling single crystal plasticity. In an attempt to make the framework more appealing for future investigation, in §2.3 we provide detailed examples of the generation of constitutive equations for several crystal types. The hope is that these examples serve as points of reference should other researchers utilize this model for any of the 32 crystallographic point groups. In §2.4 the theory and constitutive framework from the previous sections are implemented into numerical simulations. The phenomenological constitutive model is calibrated against data by using material point simulations constructed to approximate experimental techniques. The data is obtained through simulation, using calibrated crystal plasticity models from the literature in the same material point simulation. Finally, plane strain boundary value problems are executed. The results are assessed for qualitative properties such as the localization of plastic flow and development of geometrically necessary dislocations. A lack of experimental data restricts the investigation beyond this level of detail. Since the constitutive framework is basically open, several parameter studies are performed. In particular, implications of hardening and plastic flow viscosity are examined.

2.1 Background

The goal of this section is to review aspects of the history of plasticity. In this way we can see a zoomed out view of plasticity theories, in hopes that the gap in development mentioned in §1.1 becomes evident. We begin by reviewing G.I. Taylor's experimental work (Taylor and Elam, 1923), which eventually led to modern crystal plasticity. We then discuss the simultaneous but independent developments of crystal plasticity and classically motivated phenomenological plasticity. Finally we discuss objections which have been leveled at both approaches to plasticity. It is important to note that all objections made carry admittedly little weight until the experimental challenges to investigating plasticity phenomena noted in §1.2 are answered.

2.1.1 Historical review of continuum plasticity

In this section we give a brief history of continuum plasticity. We first give an account of Taylor's contributions to plasticity. Then we describe the subsequent development of the current gold standard modeling framework, crystal plasticity. We also review the development of phenomenological theories similar to the one we will be employing later in the chapter. We begin with a brief exposition on an atomistic view of plasticity in crystals, the main ideas of which are commonly seen in undergraduate texts of materials science.

Review: crystal slip. In materials science, the description of the mechanics of plastic deformation of single crystals is dominated by the notion of slip. Kinematically, slip is a simple shear deformation on particular crystallographic lattice planes in particular crystallographic directions. Recall that the deformation gradient for a simple shear motion is written as

$$\mathbf{F} = \mathbf{I} + \gamma \mathbf{s} \otimes \mathbf{n}, \tag{2.1}$$

where $\mathbf{F}$ is the deformation gradient, $\mathbf{I}$ is the identity, $\mathbf{n}$ is the normal to the plane of shear, $\mathbf{s}$ is the direction of the shearing motion, and γ is the magnitude of the shear. For later use, the velocity gradient corresponding to time evolution of γ in (2.1) is given by

$$\dot{\mathbf{F}}\mathbf{F}^{-1} = \dot{\gamma} \mathbf{s} \otimes \mathbf{n}, \tag{2.2}$$

where $\dot{\gamma} = \gamma_{,t}$ is the rate of shear on the slip system.

According to experimental studies near the atomic scale, plastic deformation is accommodated by the motion of dislocations on certain planes in the material. The motion of a large number of dislocations on the same family of lattice planes approximates the shearing motion given by Equation (2.1). This shear deformation mechanism becomes active when the resolved shear stress on the dislocation reaches a certain critical level. Given an appropriate stress measure $\mathbf{T}$ (say, the Cauchy stress), the traction vector, $\mathbf{t}$, on the shear plane with normal $\mathbf{n}$ is given by $\mathbf{t} = \mathbf{T}\mathbf{n}$. The resolved shear stress conjugate to the shearing

motion (2.1) is then given by projecting the traction vector $\mathbf{t}$ on the shear direction, giving the quantity $\tau = \mathbf{T}\mathbf{n} \cdot \mathbf{s}$, where τ is the resolved shear stress. Typically, we impose that for $\tau < \tau_c$, where τ_c is a certain critical stress level, there is no slip. For resolved stresses at or above τ_c, the shear rate $\dot{\gamma}$ is non zero, and a shearing motion of the form (2.1) is manifested in the material over time.

These notions of plastic deformation, which are accepted as obvious to modern students of engineering or materials science, were not given an experimental foundation until the work of G.I. Taylor in the 1920s-1930s (Taylor and Elam, 1923; Taylor, 1938). His experiments showed that simple shear, (2.1), was indeed the deformation mode present in crystals. This was deduced by loading specially prepared samples in tension, and simultaneously using X-ray and visual measurements of the lattice and material, respectively. Although simple shear was suggested as the deformation mode of crystals based on previous observations of glide bands in single crystals, see for instance Schmid and Boas (1950, p. 57), Taylor examined the problem without accepting this notion a priori.

In many respects, the experiments of Taylor have not been surpassed - since in his work both material deformation, $\mathbf{F}$, and lattice deformation, denoted $\mathbf{H}$, were measured independently. Due to the importance of Taylor's contribution to the mechanics of crystals, and as an interesting point of historical discussion, we review his experimental method and subsequent deductions in the next section.

2.1.2 Contributions of G.I. Taylor

The advent of many concepts in modern plasticity are generally attributed to G.I. Taylor's experiments in the 1920s. In this section we give a short overview of Taylor's methods and findings. We focus on the experiment reported by Taylor and Elam (1923). In these experiments, large single crystals of aluminum, machined into a parallelepiped geometry, were scribed with a set of lines, see Figure 1.1. These samples were loaded in axial tension, until plastic flow commenced. At various points during this process, the scribed lines were used to measure the total material deformation in the sample, by measuring angles and lengths with microscopes and micrometers (Taylor and Elam, 1923). Simultaneously, X-ray diffraction measurements were made, monitoring the rotation of the crystal. They extended the crystal up to 78% total strain, measuring the material deformation at various times during the test.

Analysis of their data resulted in the following deductions. From the X-ray observations, they found that during the extension, the material remained of the same crystal symmetry. From the total deformation, they found that the material density was essentially constant. Based on these findings, and perhaps some hints from glide band geometry, they decided to examine what they call the unstretched cones in the material. The term cone is somewhat laden with connotation; here the unstretched cones are the sheets of material that remain of the same Euclidean length at various stages of deformation. They are not necessarily a cone shape in normal usage of the term.

For a visualization of the unstretched cone upon different deformations in a two dimensional schematic, see Figures 2.1(a) and 2.1(b), which depict simple shear and axial extension, respectively. In these figures, an initial array of material points is traced by a circle. Upon deformation, these points map to become elliptical shapes. The unstretched cone is defined instantaneously by the line segments which may have rotated but do not change in length. Using the constant length attribute, the unstretched cone can be plotted geometrically by finding the points of intersection between the deformed ellipse and the initial circle, as shown in Figures 2.1(a), 2.1(b). In the book by Havner (1992), Taylor's expressions for determin-

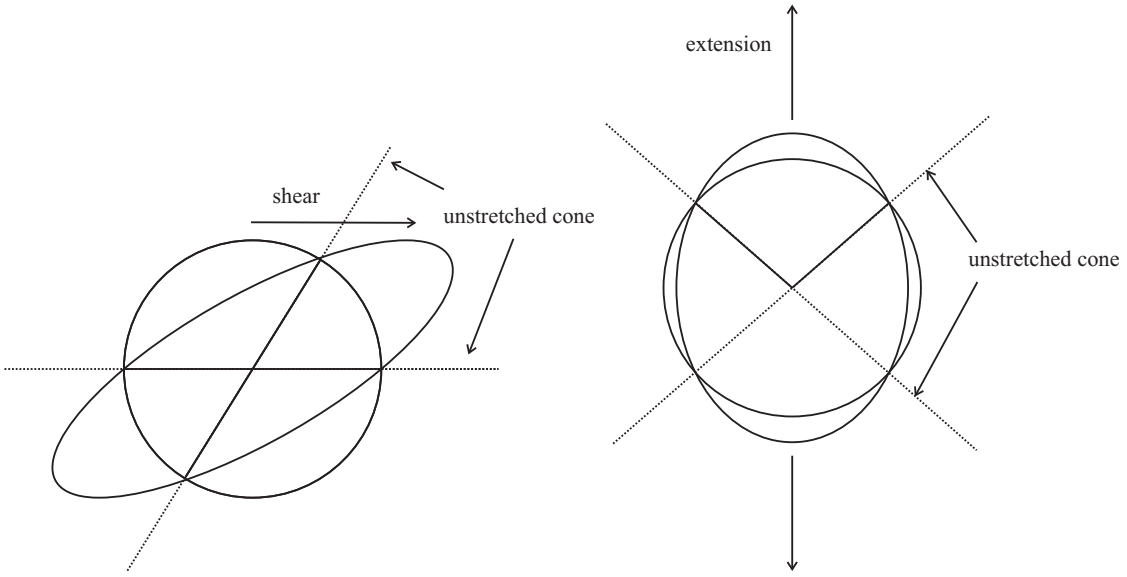

(a) Simple shear. (b) Uniaxial extension.

Figure 2.1: Two-dimensional depiction of the unstretched cone, in a homogeneous simple shearing deformation on the left and uniaxial extension on the right. The initial material points traced by the circle are deformed into an ellipse. The line elements in the material with the same length at the deformed and undeformed state constitutive the unstretched cone. This cone is defined at the intersection between the initial circle and the ellipse.

ing the unstretched cone are simplified mathematically; they are concisely expressed as the directions $\mathbf{v}$, such that

$$\mathbf{v} \cdot \mathbf{F}^{\mathrm{T}}\mathbf{F}\mathbf{v} = 1, \tag{2.3}$$

where $\mathbf{F}$ is the material deformation gradient, and $\mathbf{v}$ is the unit vector of unextended direction.

Taylor's original published results of the unstretched cones are reproduced in Figures 2.2 and 2.3. In these figures, the unit directions $\mathbf{v}$ satisfying Equation (2.3) are projected onto the stereographic net, which is shown in Figure 2.4. To make sense of the symbols in Figures 2.2 and 2.3, assign a standard spherical polar coordinate map to $\mathbf{v}$. Then the crosses

in the figures represent material directions for which $\theta \geq \pi/2$, where θ is the polar angle, and the solid dots represent material directions for which $\theta < \pi/2$. Figure 2.2 represents the unstretched cone data up to 40% axial strain, while Figure 2.3 represents the same data from 40 - 78% axial strain. There are clearly some qualitative differences between the two levels of deformation, which we explain next.

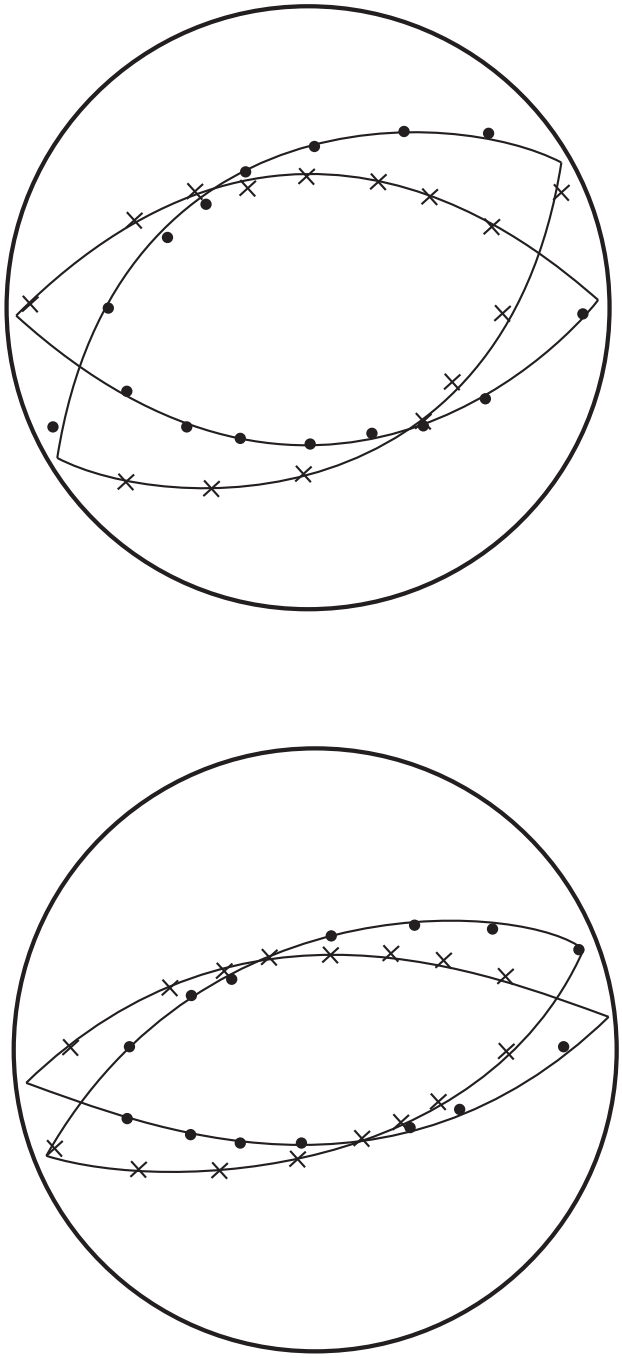

Figure 2.2: Experimental data of the unstretched cones from (Taylor and Elam, 1923). The crosses indicate projected points which have spherical polar angle $\theta \geq \pi/2$ dots are at $\theta < \pi/2$. This data is similar to what would be expected upon a simple shear deformation, see Figures 2.1(a), 2.5(a).

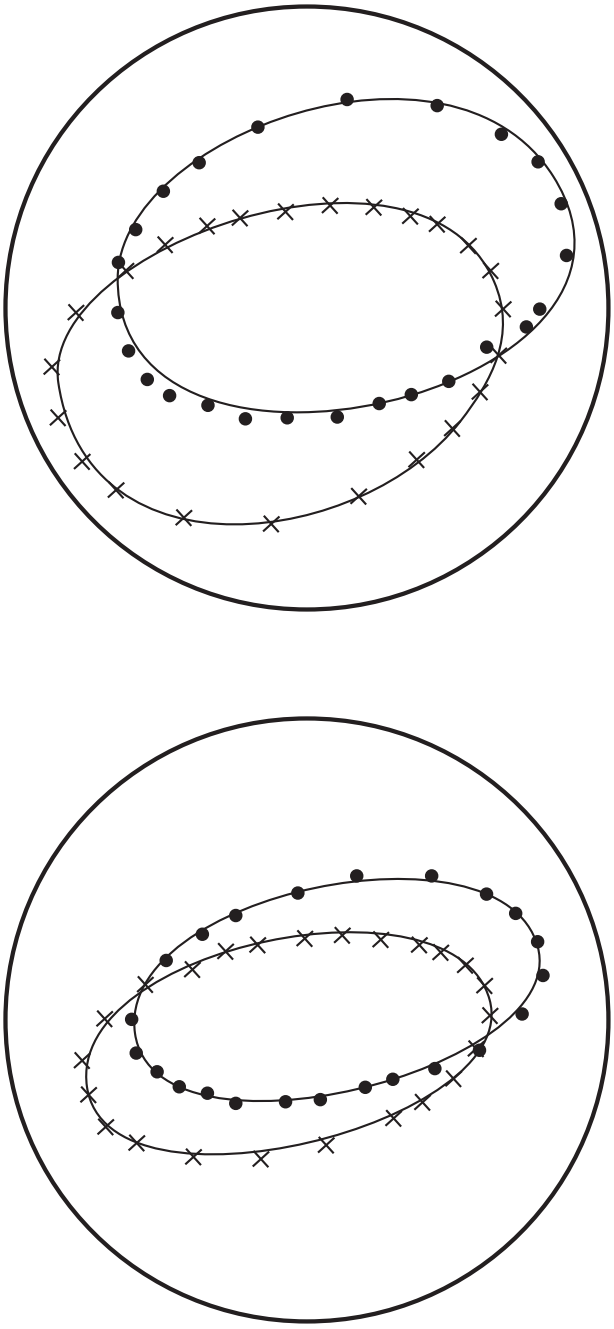

Figure 2.3: Experimental data of the unstretched cones from (Taylor and Elam, 1923). The crosses indicate projected points which have spherical polar angle $\theta \geq \pi/2$ dots are at $\theta < \pi/2$. This data is similar to what would be expected upon a uniaxial deformation, see Figures 2.1(b), 2.5(b).

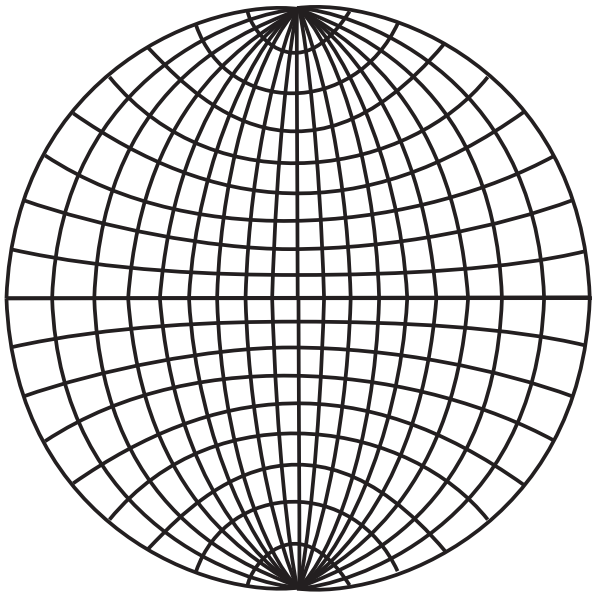

Figure 2.4: Stereographic net used to visualize the projection of unit vectors onto a two dimensional plane, from (Taylor and Elam, 1923). To relate this to a familiar object, the vertical lines meeting at the poles represent longitude, the corresponding orthogonal set of lines represent latitude.

Analysis of Taylor's results. The low strain result of Figure 2.2 has an unstretched cone consisting of what are apparently two planes, cutting through the initial material ellipsoid (a sphere in three dimensions). Taylor deduced that this indicates that simple shear deformation is indeed prevalent during plastic deformation. To see this, we first generalize the two dimensional schematics in Figures 2.1(a) and 2.1(b) to three dimensional deformation in Figures 2.5(a) and 2.5(b). In three dimensions, these figures show how a simple shear deformation has two unextended planes, while uniaxial extension produces a conical section which projects to a circle on the stereographic projection.

Comparing the simple shear deformation depicted in Figure 2.5(a) to the data in Figure 2.2 shows that the simple shear hypothesis appears valid up to moderate extensions. For higher strains, the data in Figure 2.3 compares more favorably to Figure 2.5(b), which depicts an axial extension. This latter case can probably be explained by a history of multiple slip, that is, that two slip systems eventually became activated.

In summary, Taylor's experimental measurements indicated that simple shear kinematics of plastic deformation of single crystals is experimentally observed. As a secondary observation, they found that multiple slip occurs at higher extensions, in which case the unstretched cone looks more like that of a volume preserving uniaxial deformation.

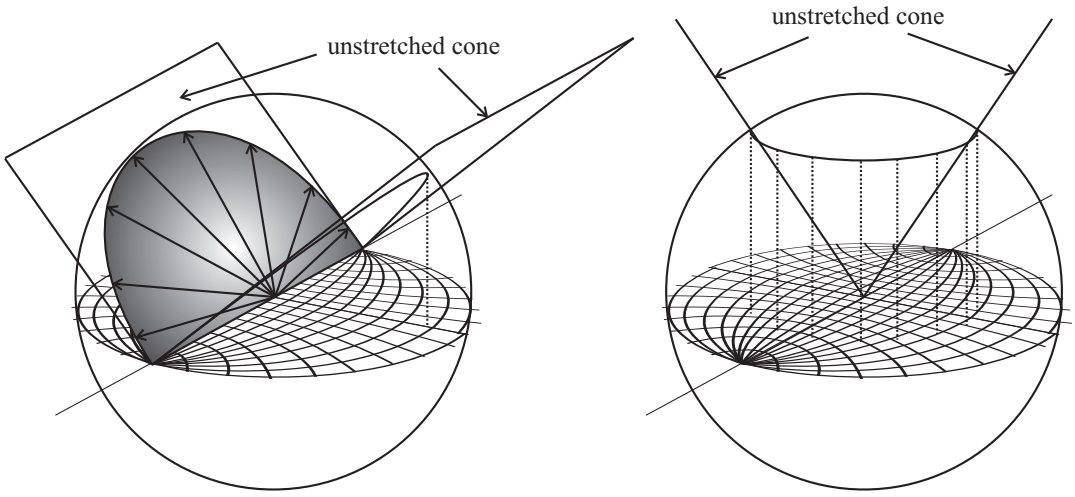

(a) Simple shear. (b) Uniaxial extension.

Figure 2.5: Three dimensional illustration of the unstretched cones for simple shear on the left and axial extension deformation on the right. The projection of the unstretched cone on a stereographic net for simple shear more closely represents the data in Figure 2.2 than Figure 2.3, and vice versa.

Subsequent developments in plasticity. Taylor's conclusive deductions of simple shear slip kinematics led to a long history of experimental and theoretical development of single crystal slip, in the years leading up to roughly 1970. See (Bell and Green, 1967) for a critical review of many studies of the deformation of single crystal wires in tension up to that point in time. This quantitative experimental work set the foundations for the development of crystal plasticity in the 1980s.

Meanwhile, during this activity of investigating slip in single crystals in the years 1920-1970, the modern theory of continuum mechanics was under development. These theories were concerned with determining the most fundamental aspects of general continuum theory. After considering thermodynamic restrictions, the only impositions on constitutive functions were due to material symmetry requirements and observer invariance. Constitutive hypotheses such as equipresence[2]are probably open for debate from practical grounds. Typically, the form of these constitutive functions was in the form of polynomials, due to convenience. For an arbitrary constitutive function, there is no physical reason polynomials should be preferred. Nevertheless, there are many examples of successes with simple polynomial constitutive functions. For the strain energy function, a quadratic order polynomial in the strain tensor leads to a linear elastic stress response for instance.

With regard to plasticity theory in particular, applied studies from the phenomenological/continuum school were largely concerned with polycrystalline materials. J_2 plasticity is probably the best known example. J_2 theory arises as a phenomenological formulation by considering isotropic material symmetry, which is a reasonable approximation for polycrystals at sufficiently large length scales. The application of similar phenomenological formulations to single crystal plasticity was apparently overlooked however, at least with regard to developing constitutive equations and examining applications. Instead of this seemingly natural evolution, crossover between the experimental foundations of single crystal slip and continuum mechanics theory began to overlap with the works of Rice (1971), Hill and Rice (1972), Hill and Havner (1982), and Asaro (1983). These important combinations eventually culminated in modern computational crystal plasticity (Peirce et al., 1983; Asaro and Needleman, 1984), which is an up-scaling of Taylor's experimental findings based on (2.2) to model a phenomenological combination of deformation modes due to the presence of different slip systems. The basic framework of crystal plasticity hasn't changed much in structure since these foundations were laid, nearly 30 years ago.

We now examine some of the details of modern crystal plasticity models. Havner (1992) suggests that the advent of crystal plasticity is an outgrowth of the constitutive equation for

[2]The principle of equipresence states that if a constitutive function is presumed to have certain dependencies, say $\mathbf{T} = \hat{\mathbf{T}}(\mathbf{A}, \mathbf{B}, \mathbf{C}, ...)$, then any other constitutive function should have the same set of dependencies as long as such a form does not violate a more fundamental physical relationship.

slip plane flow apparently first suggested by Hutchinson (1976)

$$\dot{\gamma}^{\alpha} = \dot{\eta}_0 \frac{\tau^{(\alpha)}}{\tau_0^{(\alpha)}} \left| \frac{\tau^{(\alpha)}}{\tau_0^{(\alpha)}} \right|^{n-1}, \qquad \dot{\gamma}_0 > 0, \tag{2.4}$$

where $\tau^{(\alpha)} = \mathbf{T} \cdot (\text{sym } (\mathbf{s}^{(\alpha)} \otimes \mathbf{n}^{(\alpha)})$ is the resolved shear stress on the α^{th} slip system, $\mathbf{s}^{(\alpha)}, \mathbf{n}^{(\alpha)}$ are the current slip direction and slip plane normal, respectively, and $\tau_0^{(\alpha)}, \dot{\eta}_0, n$ are material parameters representing physics akin to a stress scale, reference shear rate, and rate sensitivity, respectively (Havner, 1992). The parameter n falls between 3 and 8 for most metals, according to Hutchinson (1976). The shear rates $\dot{\gamma}_\alpha$ are then incorporated into slip kinematics of the form (2.2). In modern crystal plasticity theories, the constitutive equation for plastic flow has been refined and improved to the most often used form

$$\dot{\mathbf{F}}^{\text{p}} (\mathbf{F}^{\text{p}})^{-1} = \sum_{\alpha} \dot{\gamma}^{\alpha} \mathbf{s}_0^{\alpha} \otimes \mathbf{n}_0^{\alpha}, \tag{2.5}$$

where $\mathbf{F}^{\text{p}} \in \text{GL}(3, \mathbb{R})$ is the plastic deformation. Here $\mathbf{s}_0^{\alpha}, \mathbf{n}_0^{\alpha}$ are the slip direction and normal in a fixed intermediate configuration of the lattice (Asaro, 1983). The shear rate $\dot{\gamma}^{\alpha}$ is typically given by, (see Anand et al. (1997); Barton et al. (2005), among others)

$$\dot{\gamma}^{\alpha} = \dot{\gamma}_0 \left(\frac{|\tau^{\alpha}|}{s^{\alpha}} \right)^{1/m} \text{sign}(\tau^{\alpha}), \tag{2.6}$$

where $\tau^{\alpha} = \mathbf{S} \cdot \mathbf{s}_0^{\alpha} \otimes \mathbf{n}_0^{\alpha}$ is the resolved shear stress on the slip system, $\mathbf{S}$ is the symmetric Piola-Kirchoff stress in the intermediate configuration of the lattice, s^{α} is the flow resistance for the slip system, $\dot{\gamma}_0$ represents a reference shear rate, and m is a rate sensitivity parameter. The total material deformation is constructed using the multiplicative decomposition

$$\mathbf{F} = \mathbf{F}^{\text{e}} \mathbf{F}^{\text{p}}, \tag{2.7}$$

where $\mathbf{F}^{\text{e}}$ is the elastic deformation. Some familiarity with crystal plasticity is assumed in this section and we do not go into further details. Comments on the intermediate configuration of the lattice, and other quantities are given in a later section; here the goals are to introduce the historical development.

The original application for Equation (2.4) was to model plasticity at elevated temperatures Hutchinson (1976). Although authors such as Havner (1992, p. 201) suggest that applying equations similar to (2.4), (2.5), (2.6) to analyze mechanics at ordinary temperatures are 'computational expedients', he acknowledges that macroscopic texture predictions have been successful with the method. The reduction of plastic flow to the form (2.5) along with the Taylor hypothesis for polycrystals also gave rise to alternate views of analyzing deformation textures which effectively avoid the solution of solving the full boundary value problem (Mathur and Dawson, 1989; Bohlke et al., 2006).

In contrast to this history of robust work based on crystal plasticity hypotheses, applications of classically motivated phenomenological theories of plasticity have generally been relegated to polycrystalline materials. Although theoretical development of these phenomenological theories has continued (Gupta et al., 2011; Cleja-Tijoiu, 2003), most modern work, and certainly most incorporation of experimental information, appears to be in the sheet metal community. For example, deformation-induced anisotropy from the rolling process requires phenomenologically derived anisotropic yield functions (Barlat and Lian, 1989; Barlat et al., 1991, 2005) which are measured by punching out tensile specimens from the sheet and performing uniaxial tension tests.

Of late, there has been renewed interest in refinements to phenomenological theories of anisotropic materials due to the elegant mathematical structures available (Cleja-Tijoiu, 2003; Gupta et al., 2011; Steigmann and Gupta, 2011). However apart from a few studies of related formulations (Papadopoulos and Lu, 2001), analysis of these phenomenological theories remains of a theoretical nature. It bears repeating that one large obstacle to testing the capabilities of the phenomenological modeling regime is the lack of experimental data (Papadopoulos and Lu, 2001, section 5). Crystal plasticity does not suffer from this obstacle as much, since the vast assortment of single crystal experiments done in the decades after Taylor's experiments (Bell and Green, 1967) can be directly implemented into constitutive equations of the form (2.6).

It might be thought possible to calibrate a phenomenological model based on the same data used to inform crystal plasticity. However, as noted by Bell and Green (1967), most if not all of the data from these tests are presented in such a way that it is not possible to re-deduce phenomenological constitutive behavior. For example, the classical crystal plasticity experiment of the time (1920-1970) was uniaxial tension tests on single crystal wires. The data from these tests are presented in the literature by resolving the shear stress on the active slip plane (Bell and Green, 1967). In hindsight, it would have been more useful to have the uniaxial stress-strain data, along with the associated lattice orientation. Such data could then be used to calibrate a phenomenological model, which by nature does not suppose the simple slip shear mode a priori.

Lack of usable data aside, the present work attempts to breathe some life into a phenomenological theory which is amenable to investigating using an experimental methods such as X-ray diffraction. We calibrate the model against a crystal plasticity prediction from the literature. Although not as good as data, it will have to suffice. Of note, in Chapter 3, we calibrate directly against X-ray data for a titanium alloy.

In the next sections, we highlight potential objections which have been made in the literature against both crystal plasticity and classical phenomenological approaches. For single crystals in prescribed orientations and under quasistatic conditions, models which reduce to single slip, such as (2.5), make for an excellent model, as Taylor's experiments showed. The question of behavior in more complicated situations, such as a single crystal embedded in a polycrystal, the influence of rate dependence, and the presence of large elastic strains and/or hardening, is more open experimentally. We should keep in mind

that experimental investigations of crystal behavior in these sort of practical but complex situations has been limited, to date. Until this state of affairs improves, a degree of open-mindedness should be kept toward alternate modeling approaches which are backed up by experimental observations.

2.1.3 Deficiencies of crystal plasticity

Although crystal plasticity has been dominant in the computational plasticity community over the last 30 years, it is not without detractors. Recall that the characteristic hypothesis of crystal plasticity is form of the flow rule, written in Equation (2.5). An important thing to note in regard to (2.5) is that, although physically motivated, it is still phenomenological since slips are assumed to occur simultaneously, and not sequentially. When viewed as a phenomenological theory, however, the form of the plastic flow is restricted by the supposed physics of the material behavior, which may leave deformation modes exhibited in true materials difficult or even impossible to manifest in the theory (consider how to model plastic volumetric flow in the context of crystal plasticity, for instance). In essence, as the physics and true slip behavior becomes more complicated, it is possible that an approach following the structure of Equation (2.5) may detectably differ from experimental observations. The point we are trying to make is that the form of the flow rule *potentially* limits the flexibility of the theory to be predictive for the macroscopic quantities which are typically of interest for engineering purposes, e.g. the macroscopic phenomenology.

One objection to the model from the point of view of mathematical elegance is because the classically considered rate independent limit is not possible to achieve in crystal plasticity. This is due to the non-uniqueness of slip systems required to accommodate a particular plastic deformation (Havner, 1992). Therefore, in computations, either serious modifications of the update algorithm are needed, or crystal plasticity must assume that all slip systems are active simultaneously, hence the use of (2.6).

Thirdly, although constitutive parameters can be refined to match macroscopic experimental data, it's also not clear from literature reports if those constitutive parameters for the same material work in other experimental configurations. Calibration of the plasticity model (say, s^α, $\dot{\gamma}_0$, m of (2.6)) is done according to one experiment, but frequently the resulting parameters are not checked against other situations. The limited scope of experimentation available is of course a general deficiency of most studies of material behavior, and is not an objection at crystal plasticity per se. Therefore this is a general criticism that can be leveled at most theories of material behavior. The point is that being of restricted phenomenology, following Equation (2.5) may be less flexible than other phenomenological formulations.

Lastly, as in any plasticity theory, there is no overwhelming experimental evidence that the theory of crystal plasticity describes experimental data, apart from achieving the undoubtedly important single slip limit. This is particularly true for modeling polycrystals where the mechanics of individual grains is of interest. Although we showed that Taylor's experiments clearly support the notion of simple shear and slip, the material length scales at

which this notion is a good one are not clear. Applying the Taylor hypothesis to single crystal grains embedded in polycrystals has been shown experimentally to be possibly suspect (Winther et al., 2004).

As noted in the introduction, plasticity experiments do not yet have the widely available capability needed to fully investigate these questions, but there have been a few attempts. For example, in a recent study by Kalidindi et al. (2004), finite element simulations of a polycrystal were compared to X-ray diffraction data. Although the macroscopic texture predictions agreed with the data, the behavior of individual grains was not as positive. This only underscores the motivation for having improved experimental techniques to critically examine crystal plasticity models' ability to capture physics in complicated loading situations.

The goal behind listing these objections is only that we should leave the door open to other modeling frameworks until experiments can catch up to supporting the model development. It is not to refute the viability of crystal plasticity, which is clearly a thoughtfully constructed model which has attractive features and which has shown itself to be useful in applications. In this current work we accept crystal plasticity models as the current gold standard. Our goals are simply to offer a potentially viable alternative, by adopting a phenomenological viewpoint with fewer assumptions from the start, and to see how far this vantage point takes us.

2.1.4 Deficiencies of phenomenological modeling

Of course, phenomenological theories also have deficiencies which have been described in the literature. To illuminate these, it is useful to explicitly record a discussion by Yang and Lee (1993, section 2), where an excellent review of phenomenological plasticity theories up to that time is given. Although the notion of a phenomenological plasticity theory for single crystals (i.e. the present work) had not been considered in their review, they list some limitations of what they call 'macroscopic plasticity'. Macroscopic plasticity is interpreted to be synonymous with phenomenological plasticity. The framework they promote is called 'mesoplasticity', which for the purposes of comparison can be understood as following the hypotheses of slip-system based crystal plasticity. We list their issues with phenomenological plasticity here, since they serve as useful points of discussion. Direct quotations from their book are enclosed in ' '.

From Yang and Lee (1993, p. 60): 'At present moment [...] the painful practices [sic] on displaying the major limitations of macroplasticity has to be exercised as follows:'

1. 'Detached from actual plastic deformation mechanisms. The source of plastic deformation in a macroplasticity formulation is either assumed devoid of physical explanation or observed phenomenologically through macroscopic data. In macroplasticity, plastic deformation is defined by concept rather than through actual physical image. [...] A related consequence of macroplasticity [...] is the lack of any direct (mechanical

and experimental) means to detect current plastic deformation without the help of a hypothetical (and sometimes unjustified) process of elastic unloading. '

2. 'Empirical assumptions on material responses. The basic practice in continuum mechanics approach relies on a priori, empirical assumptions for different material responses, under the help of the general guidelines deduced axiomatically from the basic postulates and limited empirical testing data. Whereas a mesoplasticity analysis is lined with detailed material specification and microstructural parameters of the material system under consideration. The significance of this distinction is highlighted by the ability (for mesoplasticity approach) or limited ability (for macroplasticity) to get material insights into constitutive formulation.'

3. ' Ambiguities in the essential structures of macroscopic plasticity framework. Although new results on the essential structures of plasticity formulation have been constantly emerged [sic] from study on macroplasticity aspect, several vitally important issues are still elusive and probably cannot be fully resolved from macroplasticity knowledge alone. Those issues include the basic physical postulate which gives rise to the structure of the flow rule, the selection of the co-rotational rate, the cause and evolution of anisotropic hardening in accompany with material texture development, the resolution (both physical and mathematical) of elastic and plastic deformation at large strain, the geometry of yield surface especially the vertex formulation, etc.'

4. 'Difficulties in the description of microstructural sensitive phenomena. Phenomena such as phase transformation, flow localization, ductile fracture and material damage are extremely sensitive to the microstructural details, especially the inhomogeneities scattered inside the material systems. The homogeneous continuum devoid of any internal structures is assumed as the corner stone in macroplasticity. However, it would undoubtedly cause barriers in the characterization of microstructural sensitive phenomena, rendering their accurate description intrinsically difficult if approached from macroplasticity methodology alone.'

5. 'Unable to handle applications of microplastic nature. [...] there are some practical applications which are intrinsically mesoplastic. Examples for these applications include ultra-precision machining, texture control of superconductive alloys, surface finishing improvement of mechanical processing, superplastic manufacturing, etc., not to mention the applications related to the material failures. These applications are closely related to the evolution of microstructures and the stress-strain history recorded by individual grains'

We now respond, one by one, to these criticisms of phenomenological formulations of plasticity with the current framework of anisotropic phenomenological plasticity in mind.

1. This objection, while probably valid for polycrystalline plasticity theories where definitions of elastic and plastic strain are difficult to measure experimentally, does not apply to the current study. In the next section, we will see that plastic deformation here is defined by the time evolution from an initial state in space-time. The material state can be measured using standard methods. Given a source of X-rays, the lattice state can also be measured. Therefore we have direct experimental means to detect plastic deformation since the theory relates the two through a multiplicative decomposition like (2.7). It should be noted that Yang and Lee (1993) suggest that in the crystal plasticity approach experimental capabilities for their target variables (such as dislocation flow) are well established. This might be the case for certain quantities like $\mathbf{F}^{\mathrm{e}}$, but if they are supposing their theory to be based on experimentally measuring dislocation densities, this would require destructive evaluation of the material and therefore cannot be used for direct validation of elastic-plastic deformation even in the mesoplasticity case. At least in our model, we directly describe the experimental program needed to investigate the theory.

2. This objection seems to suggest that phenomenological constitutive equations are not adequate to serve as macroscopic predictors. I would again point to isotropic Hooke's law, which seems to have served engineers well for a long time. Their statement is largely a manifestation of the fact that experimental plasticity of single crystals has been historically inadequate for phenomenological models to develop detailed constitutive equations; therefore it is supposed that focusing on smaller length scale phenomena gives rise to better macroscopic constitutive behavior. We have yet to see irrefutable evidence that microscale mechanics gives macroscopic predictions which can not be reproduced with a phenomenological approach applied at the micro-scale. We must keep in mind the type of information we are hoping to obtain from implementing our theories in simulations for the purposes of solving engineering applications, which is usually of a macroscopic nature. See Treloar (1974) for a related debate from another field, rubber elasticity.

3. By using the anisotropy of the single crystal in constitutive equations, phenomenological parameters will naturally be demanded by the theory. These parameters have the capability to model the features mentioned. Therefore this objection is really a symptom of not attempting to apply anisotropic phenomenology to the mechanics of single crystals.

4. We will see that the model presented here naturally leads to predictions of plastic localization in plane strain tension. This comment is evident again, of the lack of attempt at an anisotropic plasticity model. The comment may be true for isotropic/polycrystalline plasticity, but it is not true for our model, at least for the question of strain localization.

5. Historically speaking, phenomenological models have had superior performance in

terms of predicting macroscopic information: the force required to achieve a certain level of deformation in a material processing plant is one example of were phenomenological approaches shine. These authors acknowledge this. But it's not evident that their cited applications have in fact benefited from mesoplasticity apart from qualitative understanding and observation of certain phenomena. Again, no one has tried a single crystal phenomenological approach, so it's not fair to say that such a framework cannot be useful for the analysis of these applications.

Summary. Setting argued benefits or deficiencies of differing approaches to plasticity aside, review of the literature has indicated that there is room for a contribution of classical continuum mechanics phenomenology applied to single crystals. Crystal plasticity is a proven framework, but experiments may potentially show that it has deficiencies which might be better addressed with a flexible phenomenological approach. The lack of good constitutive information required to implement a phenomenological model should not make such a theory irrelevant to consider.

In the next section, we develop the phenomenological theory of plasticity which has been referred to in these introductory sections. We then move on to describe philosophies of constitutive behavior, and present numerical simulations. We also calibrate several proposed constitutive models against crystal plasticity models reported in the literature; this being the closest connection to experimental data we can find. Finally we give examples of implementing the calibrated model into plane strain simulations, and report several qualitative and quantitative observations from them. Throughout, we assume a certain familiarity with standard mechanics formulations and mathematical manipulations.

2.2 Theoretical development

As stated in the introduction, plasticity is a phenomenon which has been studied for over 100 years but is one which still receives attention and suggested modeling frameworks. These theories share many of the same basic ingredients. Commonalities include notions of elastic and plastic strain, the specification of a plastic evolution equation (flow rule), the concept of a yield function, and phenomenology to account for hardening.Ideally, each proposed theory must be evaluated against data in order to provide a proven measure of the usefulness of the model. However, quantitative experimental validation of plasticity models is prohibitively difficult; in fact only recently has technology advanced to the degree where such studies can realistically be attempted[3](Winther et al., 2004; Kalidindi et al., 2004; Quey et al., 2010). Therefore, these experimental obstacles have led to the current state of affairs in plasticity, which we feel still has open questions with regard to settling on a modeling approach which gives verified physical predictions. Until the experimental challenge is answered, these

[3]Reasons for this difficulty were noted in §1.2.

questions will surely linger.

In this section we develop the theoretical framework for the proposed formulation of plasticity of single crystals. An appealing characteristic of the theory is that it can be quantitatively investigated using X-ray diffraction experiments, and, at this stage, does not appeal to any so-called hidden or internal variables which are a hallmark of many theories of plasticity including crystal plasticity (Rice, 1971; de Souza Neto et al., 2008). In Chapter 3 practical application of the experimental method is described in detail. The content of the section is as follows. First, in §2.2.1 we define our decomposition of elastic plastic strain, and describe how X-ray diffraction enables this decomposition to be measured experimentally. Then in §2.2.2, a brief overview of the thermodynamic structure is given, along with the equations of motion. In §2.2.3 the general constitutive problem is described.

Almost all of the content of this section is standard based on previous literature, for a review see Gupta et al. (2007) and references therein. This development is required in order to implement the numerical simulations, which represent the new material. Throughout the section, a familiarity with notions of continuum mechanics is understood.

2.2.1 Definition of elastic and plastic strain

To begin, we describe in general how the mathematical description of elastic-plastic deformation differs from the description of purely elastic bodies. It is useful to give a review of classical elastic bodies in continuum mechanics in order to underscore how plasticity differs.

Review of elasticity. In elasticity material bodies are considered to be differentiable manifolds, covered by a single coordinate chart. Material coordinates on the manifold are denoted by $\mathbf{X}$. The motion of the body is described by the function $\boldsymbol{\chi}(\mathbf{X}, t)$, which satisfies differential equations representing the balance of forces, obtained from Newton's laws. For instance, the balance of linear momentum equation reads

$$\rho_0 \frac{\mathrm{d}^2 \boldsymbol{\chi}}{\mathrm{d}t^2} = \mathrm{grad} \cdot \mathbf{T} + \rho \mathbf{b}, \tag{2.8}$$

where $\mathbf{T}$ is the (Cauchy) stress response of the material, ρ is the material density, t is the time, and $\mathbf{b}$ is the body-force vector, representing gravitational forces for example, and grad is the gradient operator in the spatial configuration. In elasticity theory, the stress response of the material, $\mathbf{T}$ is given by constitutive functions $\hat{\mathbf{T}}(\mathbf{F})$, where $\mathbf{F} = \nabla \boldsymbol{\chi}(\mathbf{X}, t)$ is called the deformation gradient, where ∇ is the gradient operator in the reference configuration. The balance of angular momentum equation requires that the Cauchy stress is symmetric, $\mathbf{T} = \mathbf{T}^{\mathrm{T}}$. This requirement is typically incorporated in the constitutive specification of the stress response $\hat{\mathbf{T}}(\mathbf{F})$.

The principal unknown in elasticity theory is therefore the field $\boldsymbol{\chi}(\mathbf{X}, t)$ which completely specifies the state of the body. In contrast, in plasticity theory the unknowns are the motion

of the material, $\boldsymbol{\chi}(\mathbf{X}, t)$, along with a field representing plastic deformation. Here we denote this field as $\mathbf{K}(\mathbf{X}, t)$. Furthermore, the stress response is not a function of $\mathbf{F}$, but instead a function of elastic deformation. We denote this field as $\mathbf{H}(\mathbf{X}, t)$. Since notions of elastic vs plastic strain has been a historically contentious issue (Naghdi, 1990; Yang and Lee, 1993) we spend some effort explicitly describing our formulation for this to avoid misinterpretation of what we are advocating.

Geometric notion of elastic and plastic deformation

Much of the difficulty in defining elastic vs. plastic strain arises when the concept of a local unloading process after straining is required to define the elastic strain, as noted in §2.1.4, item 1. In this notion it is supposed that the unloading process removes any elastic strain and the remaining strain is deemed plastic. The current proposed formulation does not define elastic and plastic strain via an unloading process, but instead uses a geometrically motivated definition that is supported experimentally by X-ray diffraction measurements. To see this, first note that this formulation of elastic-plastic deformation is closely tied with the beautiful director theory of Fox (1968). In that theory, along with the motion of the material $\boldsymbol{\chi}(\mathbf{X}, t)$, Fox (1968) describes the motion of a microstructural component, characterized by three linearly independent vectors, $\mathbf{d}_i, i = 1, 2, 3$, which can rotate and distort relative to the material itself, but carry no inertia. The stress response function is determined by the rotation and distortion of these microstructural directors, $\hat{\mathbf{T}}(\mathbf{d}_1, \mathbf{d}_2, \mathbf{d}_3)$.

To see why that theory is relevant to mention, recall that our model is meant to apply to single crystals, which are characterized by a lattice of atoms. The description of a crystal lattice requires knowledge of only three linearly independent lattice vectors, $\mathbf{l}_i, i = 1, 2, 3$. Furthermore, the distortion of the lattice is coupled to the stress response through constitutive relations, $\hat{\mathbf{T}}(\mathbf{l}_1, \mathbf{l}_2, \mathbf{l}_3)$. Therefore the lattice vectors (or their duals) play the role of the directors in the theory of Fox (1968).

The directors are experimentally measurable for crystals, since the structure of single crystals can be probed in detail using X-ray diffraction (Cullity, 1978). To explain, in X-ray diffraction, the definition of lattice distortion comes from characterizing linear transformations from a fixed lattice configuration $\boldsymbol{\kappa}$ to the current configuration where the diffraction measurement is made.[4] The configuration $\boldsymbol{\kappa}$ is constructed based on an assigned reference state of the lattice. Usually it can be thought of as a stress free configuration, since $\boldsymbol{\kappa}$ is generated by unit cell parameters obtained from a powder sample under ambient conditions. In such a case, the tensor $\mathbf{H}$ can be used in a normal interpretation of constitutive equations for stress, e.g. $\mathbf{T} = \hat{\mathbf{T}}(\mathbf{H})$ and $\hat{\mathbf{T}}(\mathbf{H} = \mathbf{I}) = \mathbf{0}$. The physics of this measurement and further details are developed in Chapter 3, for now it suffices to accept that such a measurement is possible. This transformation is denoted by $\mathbf{H}$, and this tensor defines what we call the

[4] In addition to the fixed lattice configuration $\boldsymbol{\kappa}$, there is a material reference configuration which has the normal definition from traditional elasticity. That is, the motion of the material, $\boldsymbol{\chi}$ is defined over the points of this material reference configuration, $\boldsymbol{\chi}(\mathbf{X}, t)$.

lattice deformation. To relate this transformation to lattice vectors, $\mathbf{H}$ can be written in terms of its action on the lattice vectors in the fixed lattice configuration, by

$$\mathbf{l}_i \equiv \mathbf{H}\mathbf{L}_i, \tag{2.9}$$

where $\mathbf{L}_i, i = 1, 2, 3$ are the lattice vectors in the configuration $\boldsymbol{\kappa}$, and $\mathbf{l}_i$ are the lattice vectors in the physical configuration. Define the reciprocal lattice vectors by $\mathbf{L}^i$. These have the basic property

$$\mathbf{L}_i \cdot \mathbf{L}^j = \delta_i^j. \tag{2.10}$$

By inspection of (2.10) and (2.9), $\mathbf{H}$ has the representation

$$\mathbf{H} = \mathbf{l}_i \otimes \mathbf{L}^i, \tag{2.11}$$

so that $\mathbf{H}$ is defined in terms of the lattice vectors $\mathbf{L}_i$ and the transformed $\mathbf{l}_i$.

Comparing this framework with the theory of Fox (1968), we see the same structure in both cases - inertia-less directors ($\mathbf{H}\mathbf{L}_i$) which determine the elastic response $\hat{\mathbf{T}}(\mathbf{H})$. Therefore, in this work, statements referring to (1) lattice vectors (2) directors (3) $\mathbf{H}$, are all synonymous through the construction used in developing (2.11). To summarize, the lattice distortion $\mathbf{H}$, or equivalently, the directors $\mathbf{l}_i$ are well defined quantities which can be measured experimentally. Next the measurement of plastic strain is described.

In the context of crystal lattices, in the presence of plastic deformation the local lattice deformation $\mathbf{H}$ evolves independently of the local material deformation $\mathbf{F}$. Therefore the field $\mathbf{H}(\mathbf{X}, t)$ is not compatible with the overall motion, for instance $\mathbf{H} \neq \nabla\boldsymbol{\chi}$ in general. However the material deformation $\mathbf{F} = \nabla\boldsymbol{\chi}$ is by definition compatible. Therefore the plastic deformation $\mathbf{K}$ restores compatibility by the relation

$$\mathbf{F} = \mathbf{H}\mathbf{K}^{-1}. \tag{2.12}$$

As a motivating illustration, consider Figure 2.6, which shows the construction of the reference lattice configuration $\boldsymbol{\kappa}$, and subsequent mappings into the material reference configuration and physical configuration through $\mathbf{K}, \mathbf{H}$. In the figure the subscript $\boldsymbol{\kappa}$ is used to emphasize the dependence of $\mathbf{H}, \mathbf{K}$ on the construction of the fixed lattice configuration.

Consider Figure 2.6, which shows a reference cube with edges $\mathbf{e}_1, \mathbf{e}_2, \mathbf{e}_3$. Under a structural map $\mathbf{H}_\mathrm{s}$ using the unit cell parameters $a_0, b_0, c_0, \alpha_0, \beta_0, \gamma_0$, the configuration $\boldsymbol{\kappa}$ is defined and fixed. Lattice vectors in $\boldsymbol{\kappa}$ are denoted $\mathbf{L}_i$. These reference lattice vectors can be thought of as originating from the cube edges $\mathbf{e}_i$ through the relationship, $\mathbf{L}_i = \mathbf{H}_\mathrm{s}\mathbf{e}_u$. In the current configuration, the lattice vectors are mapped to $\mathbf{l}_i = \mathbf{H}\mathbf{L}_i$, see the lower right of the figure. The material vectors $\mathbf{G}_i$ are defined in the material reference configuration, in the lower left of Figure 2.6. There is no explicit connection between $\mathbf{G}_i$ and $\mathbf{L}_i$. However, the material vectors $\mathbf{G}_i$ may be conveniently defined based on the lattice vectors at the initial time, so that $\mathbf{G}_i(\mathbf{X}) = \mathbf{K}(\mathbf{X}, 0)\mathbf{L}_i$. In the definition of $\mathbf{G}_i$ based on initial lattice vectors, it becomes easy to see that a non-zero plastic deformation implies that the resulting lattice deformation

differs from the material deformation, as indicated in the lower right image of Figure 2.6. More is said on the construction of unit cells, the structural map, and the configuration $\boldsymbol{\kappa}$ in §3.3.5.

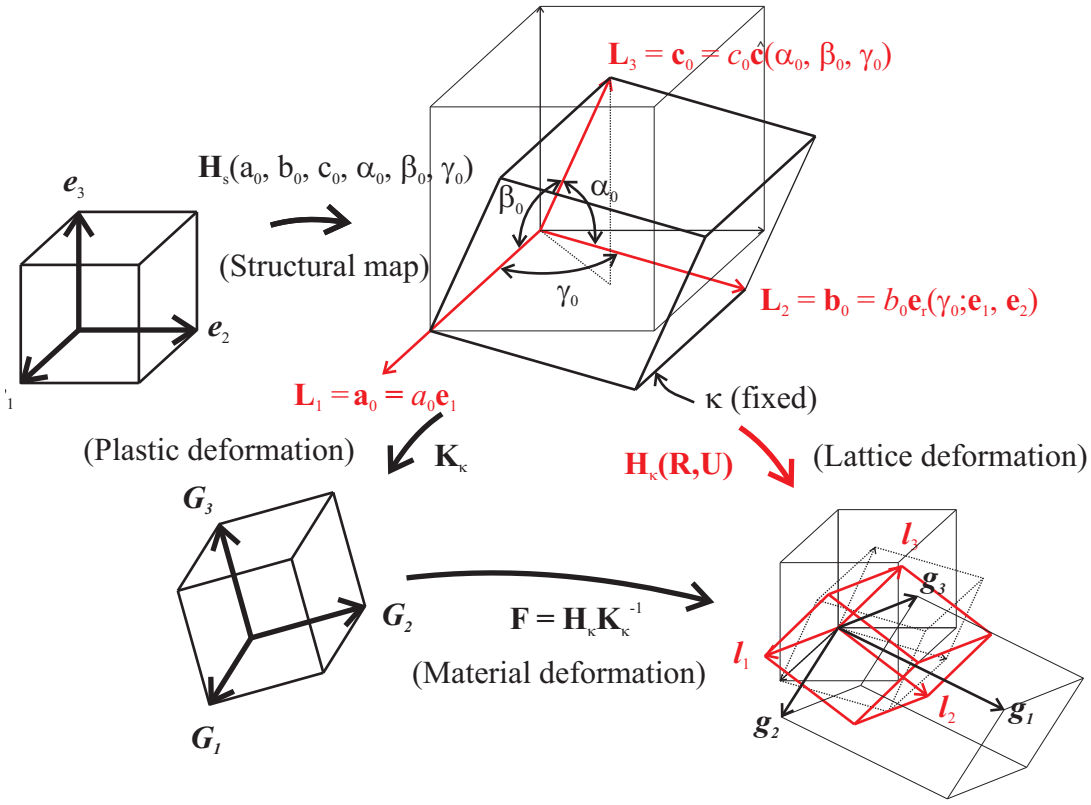

Figure 2.6: Illustration of elastic plastic deformation, resp. $\mathbf{H}, \mathbf{K}$ making up total material deformation, $\mathbf{F}$. Constructing the reference configuration $\boldsymbol{\kappa}$ requires a structural map $\mathbf{H}_s$, which acts on a fictitious reference cube to generate the reference lattice configuration. More details on this construction are provided in §3.3.5, see also (Edmiston et al., 2012). The red lines track the mappings of lattice vectors $\mathbf{L}_i$ in the fixed reference configuration $\boldsymbol{\kappa}$, whose construction is introduced later, in §3.3.5. The lattice vectors in the physical configuration are denoted $\mathbf{l}_i$.

Dislocations

Materials science observations suggest that dislocations are fundamental to plasticity behavior. In the present framework, incompatibility in the $\mathbf{H}, \mathbf{K}$ fields can be interpreted to represent the geometrically necessary dislocation density in the crystal. For example, integration of the plastic deformation around a closed contour $\partial\Omega$ of the area Ω gives the net Burgers vector of all dislocation lines passing through Ω,

$$\mathbf{d} = \int_{\partial\Omega} \mathbf{K}^{-1} \cdot \mathrm{d}\mathbf{X}. \tag{2.13}$$

We can rearrange this equation using Stokes' theorem, written as

$$\int_A \mathbf{n} \cdot \nabla \times \mathbf{v} = \int_l \mathbf{v} \cdot \mathrm{d}\mathbf{l}, \tag{2.14}$$

and substituting $\mathbf{v} = \mathbf{K}^{\mathrm{T}}\mathbf{a}$, in (2.14) for $\mathbf{a}$ an arbitrary constant vector. After simplifications we obtain the equivalent result

$$\mathbf{d} = \int_\Omega (\mathrm{Curl}\, \mathbf{K}^{-1})\mathbf{N}\mathrm{d}A, \tag{2.15}$$

so that $\mathrm{Curl}\, \mathbf{K}^{-1}$ is related to the dislocation content. Gupta et al. (2007) define what they call the true dislocation content,

$$\boldsymbol{\xi} = J_K \mathbf{K}^{-1} \mathrm{Curl}\, \mathbf{K}^{-1}, \tag{2.16}$$

which has convenient properties under changes of reference frame. We investigate the effect of adding the dislocation measure $\boldsymbol{\xi}$ to constitutive functions in a subsequent section.

Summary remarks.

It is important to establish some limitations of this approach to describing plastic evolution. With respect to applications, we determine the $\mathbf{K}$ field at an initial time t_0. Time evolutions of the plastic deformation, $\mathbf{K}$, from this initial state can then be modeled effectively in our given framework. The initial $\mathbf{K}$-field can be calculated indirectly from X-ray diffraction measurements, which give direct measurements of $\mathbf{H}(\mathbf{X}, t)$. To see this, in the initial measurement state, per normal usage define the material reference configuration such that $\mathbf{F} = \mathbf{I}$ and so from (2.12), $\mathbf{K}_0 = \mathbf{H}_0$. This history dependence could only be overcome by using an experimental technique and theory which can obtain the positions of all atoms in the material. Such a technique is not available, and if it were continuum mechanics would be relegated to ancient history. Until then, users of either this model or crystal plasticity must understand that evolutions are what the model is predicting. In any case, this is sufficient

for a most engineering applications. See Barton et al. (2011) for an example of the evolution toward using atomic information in a continuum level simulation.

In the next section we develop the thermodynamic framework for this theory of elastic plastic deformation, including balance laws and constitutive equations. Familiarity with basic continuum mechanics is assumed, see (Liu, 2002) for a good modern treatment.

2.2.2 Thermodynamics and balance equations.

Continuum field theories define quantities of interest over differentiable manifolds which are diffeomorphisms of a reference configuration of the material body. In the thermoelastoplastic case, we seek the fields $\boldsymbol{\chi}(\mathbf{X},t), \theta(\mathbf{X},t), \mathbf{K}(\mathbf{X},t)$, where $\theta(\mathbf{X},t)$ is the temperature field. The other fields have been defined previously. We do not make explicit use of temperature in this thesis, but, in following with standard presentations, retain it for this section. We now derive the balance equations and thermodynamic restrictions for such a mathematical body. Using the material reference configuration the equation of motion is (Liu, 2002)

$$\rho_0 \ddot{\boldsymbol{\chi}} = \operatorname{Div} \mathbf{P}(\mathbf{F},\mathbf{K}) + \rho_0 \mathbf{b}, \tag{2.17}$$

where $\ddot{\boldsymbol{\chi}} = \boldsymbol{\chi}_{,tt}$, ρ_0 is the reference material density, Div is the divergence operator in the material reference configuration, $\mathbf{b}$ is the body force, and $\mathbf{P}$ is the Piola stress in the material reference configuration. $\mathbf{P}$ is given by a constitutive function of $\mathbf{F}, \mathbf{K}$. It is related to the Cauchy stress, $\mathbf{T}$, by

$$\mathbf{P} = J\mathbf{T}\mathbf{F}^{-\mathrm{T}}, \tag{2.18}$$

where $J = \det \mathbf{F}$. So far this is no different than elasticity, (2.8). The difference is that we have a time evolution of the plastic deformation, described by a flow rule

$$\dot{\mathbf{K}} = \hat{\dot{\mathbf{K}}}(\mathbf{F},\mathbf{K}), \tag{2.19}$$

where, for now, we have used the same functional dependence in the flow rule as for the Piola stress. This can be thought of as a result of the principle of equipresence, which states we should at least have the same dependence in all constitutive functions unless precluded by more fundamental information. Experimental evidence, while limited, appears to suggest that equipresence is not a good practical assumption for plasticity, due to observations of rate dependence and dislocation content, $\boldsymbol{\xi}$, on plastic flow, which are not strongly manifested in the elastic response. Incorporating these entities into the plastic flow rule (2.19) will be considered later.

Next, we postulate the energy balance,

$$\int_V \rho_0 \dot{u} \mathrm{d}V = \int_V \mathbf{P} \cdot \nabla \dot{\boldsymbol{\chi}} \mathrm{d}V + \int_A \mathbf{q} \mathrm{d}A + \int_V r \mathrm{d}V, \tag{2.20}$$

where V is the material volume, A is the associated bounding area, u is the internal energy function, $\mathbf{q}$ is the energy flux vector, and r is the volumetric energy generation. Using the divergence theorems and localization gives the local form

$$\rho_0 \dot{u} = \mathbf{P} \cdot \nabla \dot{\chi} - \nabla \cdot \mathbf{q} + \rho_0 r. \tag{2.21}$$

Equation (2.21) is needed if the temperature field $\theta(\mathbf{X}, t)$ is desired.

Coleman-Noll procedure. We now follow the classical Coleman-Noll procedure to restrict constitutive equations (Coleman and Noll, 1963; Coleman and Gurtin, 1967). The second law of thermodynamics requires

$$\frac{\mathrm{d}}{\mathrm{d}t} \int_V \rho \eta \mathrm{d}V \geq - \int_A \frac{1}{\theta} \mathbf{q} \cdot \mathbf{n} \mathrm{d}A + \int_V \frac{\rho_0 r}{\theta} \mathrm{d}V, \tag{2.22}$$

where η is the entropy, which localizes to

$$\rho_0 \dot{\eta} \geq -\nabla \cdot \frac{\mathbf{q}}{\theta} + \frac{\rho_0 r}{\theta}. \tag{2.23}$$

Multiplying (2.23) by θ gives

$$\theta \rho_0 \dot{\eta} \geq -\nabla \cdot \mathbf{q} + \frac{1}{\theta} \mathbf{q} \cdot \nabla \theta + \rho_0 r. \tag{2.24}$$

Next, define the Helmholtz energy function Ψ by

$$\Psi = u - \theta \eta, \tag{2.25}$$

so that

$$u = \Psi + \theta \eta. \tag{2.26}$$

Using (2.26) in (2.21) gives

$$\rho_0 (\Psi + \theta \eta) = \rho_0 (\dot{\Psi} + \dot{\theta} \eta + \theta \dot{\eta}) = \mathbf{P} \cdot \nabla \dot{\chi} - \nabla \cdot \mathbf{q} + \rho_0 r. \tag{2.27}$$

Rearranging (2.27) gives

$$\rho_0 (\dot{\Psi} - \dot{\theta} \eta) - \mathbf{P} \cdot \nabla \dot{\chi} + \nabla \cdot \mathbf{q} = \rho_0 \theta \dot{\eta}. \tag{2.28}$$

Implementing this in (2.24) gives

$$\theta \rho_0 \dot{\eta} \geq \frac{1}{\theta} \mathbf{q} \cdot \nabla \theta + \rho_0 (\dot{\Psi} + \dot{\theta} \eta + \theta \dot{\eta}) - \mathbf{P} \cdot \nabla \dot{\chi}, \tag{2.29}$$

or

$$0 > \frac{1}{\theta} \mathbf{q} \cdot \nabla \theta + \rho_0 \dot{\Psi} + \rho_0 \dot{\theta} \eta - \mathbf{P} \cdot \nabla \dot{\chi}. \tag{2.30}$$

For elastic-plastic bodies, the material energy function Ψ is assumed to be related to the strain energy of the lattice configuration $W(\mathbf{H})$ by

$$\Psi(\mathbf{F},\mathbf{K}) = \frac{1}{J_K} W(\mathbf{F}\mathbf{K}). \tag{2.31}$$

The material energy rate $\dot{\Psi}$ has the following chain rule representation in terms of the lattice energy W: (taking derivative of (2.31))

$$\dot{\Psi} = -\frac{1}{J_K} W \mathbf{K}^{-\mathrm{T}} \cdot \dot{\mathbf{K}} + \frac{1}{J_K}\left(\frac{\partial W}{\partial \mathbf{F}} \cdot \dot{\mathbf{F}} + \frac{\partial W}{\partial \mathbf{K}} \cdot \dot{\mathbf{K}} + \frac{\partial W}{\partial \theta}\dot{\theta}\right). \tag{2.32}$$

Substitution of (2.32) in (2.30) gives

$$0 \geq \frac{1}{\theta}\mathbf{q}\cdot\nabla\theta + \rho_0 \frac{1}{J_K}\left(-W\mathbf{K}^{-\mathrm{T}}\cdot\dot{\mathbf{K}} + \frac{\partial W}{\partial \mathbf{F}}\cdot\dot{\mathbf{F}} + \frac{\partial W}{\partial \mathbf{K}}\cdot\dot{\mathbf{K}}\right) + \rho_0\left(\frac{1}{J_K}\frac{\partial W}{\partial\theta} + \eta\right)\dot{\theta} - \mathbf{P}\cdot\nabla\dot{\chi}. \tag{2.33}$$

Rearranging (2.12) gives

$$\mathbf{H} = \mathbf{F}\mathbf{K}. \tag{2.34}$$

Next, using (2.34) the partial derivatives in (2.33) are given by

$$\frac{\partial W}{\partial \mathbf{F}}\cdot\dot{\mathbf{F}} = \frac{\partial W}{\partial \mathbf{H}}\frac{\partial \mathbf{H}}{\partial \mathbf{F}}\cdot\dot{\mathbf{F}} = \frac{\partial W}{\partial \mathbf{H}}\mathbf{K}^{\mathrm{T}}\cdot\dot{\mathbf{F}} \tag{2.35}$$

and

$$\frac{\partial W}{\partial \mathbf{K}}\cdot\dot{\mathbf{K}} = \frac{\partial W}{\partial \mathbf{H}}\frac{\partial \mathbf{H}}{\partial \mathbf{K}}\cdot\dot{\mathbf{K}} = \mathbf{F}^{\mathrm{T}}\frac{\partial W}{\partial \mathbf{H}}\cdot\dot{\mathbf{K}}. \tag{2.36}$$

Then using (2.35) and (2.36) in (2.33) we have

$$0 > \frac{1}{\theta}\mathbf{q}\cdot\nabla\theta + \rho_0\left(\frac{1}{J_K}\frac{\partial W}{\partial \mathbf{H}}\mathbf{K}^{\mathrm{T}}\cdot\dot{\mathbf{F}} + \frac{1}{J_K}\left(\mathbf{F}^{\mathrm{T}}\frac{\partial W}{\partial \mathbf{H}} - W\mathbf{K}^{-\mathrm{T}}\right)\cdot\dot{\mathbf{K}}\right) + \rho_0\left(\frac{1}{J_K}\frac{\partial W}{\partial\theta} + \eta\right)\dot{\theta} - \mathbf{P}\cdot\nabla\dot{\chi}. \tag{2.37}$$

Using $\nabla\dot{\chi} \equiv \dot{\mathbf{F}}$ and rearranging gives

$$0 \geq \frac{1}{\theta}\mathbf{q}\cdot\nabla\theta + \left(\rho_0\frac{1}{J_K}\frac{\partial W}{\partial \mathbf{H}}\mathbf{K}^{\mathrm{T}} - \mathbf{P}\right)\cdot\dot{\mathbf{F}} + \rho_0\frac{1}{J_K}\left(\mathbf{F}^{\mathrm{T}}\frac{\partial W}{\partial \mathbf{H}} - W\mathbf{K}^{-\mathrm{T}}\right)\cdot\dot{\mathbf{K}} + \rho_0\left(\frac{1}{J_K}\frac{\partial W}{\partial\theta} + \eta\right)\dot{\theta}. \tag{2.38}$$

Assuming no temperature gradients, and taking arbitrary independent variations of the kinematic fields $\dot{\mathbf{F}}, \dot{\mathbf{K}}, \dot{\theta}$ shows that (2.38) requires

$$\mathbf{P} = \frac{1}{J_K}\mathbf{P}_{\mathbf{H}}\mathbf{K}^{\mathrm{T}}, \tag{2.39}$$

where

$$\mathbf{P}_{\mathbf{H}} \equiv \frac{\partial W}{\partial \mathbf{H}} \tag{2.40}$$

is the Piola stress in the fixed reference lattice configuration. The stress measure $\mathbf{P}$ in (2.39) can also be obtained by matching Cauchy stresses in the current configuration, so that

$$\frac{1}{J}\mathbf{P}\mathbf{F}^{\mathrm{T}} = \frac{1}{J_{\mathbf{H}}}\mathbf{P}_{\mathbf{H}}\mathbf{H}^{\mathrm{T}}, \tag{2.41}$$

and solving (2.41) for $\mathbf{P}$ gives (2.39). We also will see that

$$\mathbf{P}_{\mathbf{H}} = \frac{J_H}{J}\mathbf{P}\mathbf{K}^{-\mathrm{T}} = J_K\mathbf{P}\mathbf{K}^{-\mathrm{T}}. \tag{2.42}$$

Similarly, the entropy is given by

$$\eta = -\frac{1}{J_K}\frac{\partial W}{\partial \theta}. \tag{2.43}$$

Next we examine the plastic evolution, $\dot{\mathbf{K}}$. Rearranging the conjugate stress to $\dot{\mathbf{K}}$ in (2.38), we have the condition

$$0 \geq \left(\mathbf{F}^{\mathrm{T}}\mathbf{P} - \frac{1}{J_K}W\mathbf{I}\right)\mathbf{K}^{-\mathrm{T}} \cdot \dot{\mathbf{K}}, \tag{2.44}$$

where we have used (2.42). Rearranging (2.44), we have the requirement

$$\left(\frac{1}{J_K}W\mathbf{I} - \mathbf{F}^{\mathrm{T}}\mathbf{P}\right) \cdot \dot{\mathbf{K}}\mathbf{K}^{-1} \geq 0, \tag{2.45}$$

which represents positive dissipation due to plastic flow. In (2.45), the quantity in parenthesis is the Eshelby stress, defined by

$$\mathcal{E} = \Psi(\mathbf{F}, \mathbf{K})\mathbf{I} - \mathbf{F}^{\mathrm{T}}\mathbf{P}. \tag{2.46}$$

where we have used (2.31) in obtaining (2.46).

In summary the second law of thermodynamics through the Coleman Noll procedure shows that the dissipation, D is positive,

$$D = \mathcal{E} \cdot \dot{\mathbf{K}}\mathbf{K}^{-1} \geq 0. \tag{2.47}$$

Another form of the dissipation based on (2.46) is useful to expose the intrinsic sources of the phenomena. Define

$$\mathcal{E}' = W\mathbf{I} - \mathbf{H}^{\mathrm{T}}\mathbf{P}_{\mathbf{H}} \tag{2.48}$$

as the Eshelby stress in the lattice configuration, so that we can rewrite (2.47) as

$$D = \frac{1}{J_K}\mathbf{K}^{-\mathrm{T}}\mathcal{E}'\mathbf{K}^{\mathrm{T}} \cdot \dot{\mathbf{K}}\mathbf{K}^{-1} \geq 0 \tag{2.49}$$

$$= \frac{1}{J_K}\mathcal{E}' \cdot \mathbf{K}^{-1}\dot{\mathbf{K}} \geq 0. \tag{2.50}$$

We now examine (2.50) to get an intuitive picture of what the dissipation equation indicates physically.

Physical interpretation of dissipation inequality. This section provides a physical interpretation of the dissipation inequality (2.50) in the form

$$\mathcal{E}' \cdot \mathbf{K}^{-1}\dot{\mathbf{K}} \geq 0. \tag{2.51}$$

Recall that the decomposition of elastic and plastic deformation is given by

$$\mathbf{F} = \mathbf{H}\mathbf{K}^{-1}. \tag{2.52}$$

In recognition of experimental facts we regard the primitive quantities to be $\mathbf{F}$ and $\mathbf{H}$, in that $\mathbf{F}$ is derived from the motion of the material relative to the assigned material reference configuration, and $\mathbf{H}$ tracks the evolution of lattice vectors (measurable from X-ray data). Using convected coordinates (material coordinates), any linear transformation from a material reference configuration to a material deformed configuration is specified by the deformation of three material tangent vectors, $\mathbf{G}_i, i = 1, 2, 3$, in the reference configuration to the current configuration, $\mathbf{g}_i \equiv \mathbf{F}\mathbf{G}_i$. Using this with the property $\mathbf{G}_i \cdot \mathbf{G}^j = \delta_i^j$ gives the representation

$$\mathbf{F} = \mathbf{g}_i \otimes \mathbf{G}^i, \tag{2.53}$$

where $\mathbf{G}^i$ are the material reciprocal vectors. Similarly, we have

$$\mathbf{H} = \mathbf{l}_i \otimes \mathbf{L}^i, \tag{2.54}$$

where $\mathbf{L}^i$ is a reference reciprocal lattice vector in the crystal, and $\mathbf{l}_i$ is a lattice vector in the physical configuration. From (2.53) we have

$$\mathbf{F}^{-1} = \mathbf{G}_i \otimes \mathbf{g}^i \tag{2.55}$$

by inspection. Next, from $\mathbf{K} = \mathbf{F}^{-1}\mathbf{H}$, we compute

$$\begin{aligned} \mathbf{K} &= \left(\mathbf{G}_i \otimes \mathbf{g}^i\right)\left(\mathbf{l}_j \otimes \mathbf{L}^j\right) \\ &= \left(\mathbf{g}^i \cdot \mathbf{l}_j\right)\mathbf{G}_i \otimes \mathbf{L}^j. \end{aligned} \tag{2.56}$$

Then, define

$$\mathbf{r}_j = \left(\mathbf{g}^i \cdot \mathbf{l}_j\right)\mathbf{G}_i. \tag{2.57}$$

so that (2.56) becomes

$$\mathbf{K} = \mathbf{r}_i \otimes \mathbf{L}^i. \tag{2.58}$$

This leads to

$$\dot{\mathbf{K}} = \dot{\mathbf{r}}_i \otimes \mathbf{L}^i \tag{2.59}$$

and

$$\mathbf{K}^{-1} = \mathbf{L}_j \otimes \mathbf{r}^j, \tag{2.60}$$

so that

$$\mathbf{K}^{-1}\dot{\mathbf{K}} = \left(\mathbf{r}^j \cdot \dot{\mathbf{r}}_i\right) \mathbf{L}_j \otimes \mathbf{L}^i. \tag{2.61}$$

To simplify things, considering the first instant of plastic flow, where say $\dot{\mathbf{l}}_j = 0$, $\dot{\mathbf{g}}_j \neq 0$. Therefore

$$\dot{\mathbf{r}}_j = \overline{(\mathbf{g}^i \cdot \dot{\mathbf{l}}_j)\, \mathbf{G}_i} = \left(\dot{\mathbf{g}}^i \cdot \mathbf{l}_j\right) \mathbf{G}_i. \tag{2.62}$$

To continue from this result, the reciprocal material vectors $\mathbf{g}^i$ are not convenient for interpretation. Instead, we would like to use the direct material vectors, $\mathbf{g}_i$, since these have a more intuitive behavior under deformations (e.g. they grow in size and rotate along with deformation). Then, we have the results

$$0 = \dot{\delta}^i_j = \dot{\overline{(\mathbf{g}_i \cdot \mathbf{g}^j)}} = \dot{\mathbf{g}}_i \cdot \mathbf{g}^j + \mathbf{g}_i \cdot \dot{\mathbf{g}}^j \implies \dot{\mathbf{g}}_i \cdot \mathbf{g}^j = -\mathbf{g}_i \cdot \dot{\mathbf{g}}^j. \tag{2.63}$$

Resolving $\dot{\mathbf{g}}^i$ on the reciprocal material basis gives

$$\dot{\mathbf{g}}^j = \left(\dot{\mathbf{g}}^j \cdot \mathbf{g}_i\right) \mathbf{g}^i. \tag{2.64}$$

Then using (2.63) in (2.64) gives

$$\dot{\mathbf{g}}^j = (-\dot{\mathbf{g}}_i \cdot \mathbf{g}^j)\mathbf{g}^i. \tag{2.65}$$

Substitution of (2.65) into (2.62) gives

$$\dot{\mathbf{r}}_k = (-\dot{\mathbf{g}}_i \cdot \mathbf{g}^j) \left(\mathbf{g}^i \cdot \mathbf{l}_k\right) \mathbf{G}_j. \tag{2.66}$$

Taking $\mathbf{K}^{-1} = \mathbf{H}^{-1}\mathbf{F}$ gives

$$\mathbf{K}^{-1} = (\mathbf{L}_j \otimes \mathbf{l}^j)(\mathbf{g}_i \otimes \mathbf{G}^i) \tag{2.67}$$

$$= (\mathbf{l}^j \cdot \mathbf{g}_i)\mathbf{L}_j \otimes \mathbf{G}^i, \tag{2.68}$$

so that by comparing with (2.60) we see that

$$\mathbf{r}^j = (\mathbf{l}^j \cdot \mathbf{g}_i)\mathbf{G}^i. \tag{2.69}$$

Then using (2.69) and (2.66) in (2.61) we have

$$\mathbf{r}^l \cdot \dot{\mathbf{r}}_k = (\mathbf{l}^l \cdot \mathbf{g}_m)(\mathbf{G}^m \cdot \mathbf{G}_j)(-\dot{\mathbf{g}}_i \cdot \mathbf{g}^j) \left(\mathbf{g}^i \cdot \mathbf{l}_k\right) \tag{2.70}$$

$$= -(\mathbf{l}^l \cdot \mathbf{g}_j)(\dot{\mathbf{g}}_i \cdot \mathbf{g}^j) \left(\mathbf{g}^i \cdot \mathbf{l}_k\right) \tag{2.71}$$

$$= -(\dot{\mathbf{g}}_i \otimes \mathbf{l}^l) \cdot (\mathbf{g}_j \otimes \mathbf{g}^j) \left(\mathbf{g}^i \cdot \mathbf{l}_k\right) \tag{2.72}$$

$$= -(\dot{\mathbf{g}}_i \cdot \mathbf{l}^l) \left(\mathbf{g}^i \cdot \mathbf{l}_k\right). \tag{2.73}$$

Next we consider the stress. Using (2.48), (2.54), and $\mathbf{P_H} = \mathbf{P_H I} = \mathbf{P_H L}^i \otimes \mathbf{L}_i$ the Mandel component of the Eshelby stress is expressed as

$$\mathbf{H}^{\mathrm{T}}\mathbf{P_H} = (\mathbf{L}^i \otimes \mathbf{L}_m)(\mathbf{l}_i \cdot \mathbf{P_H L}^m). \tag{2.74}$$

Use of (2.74) and (2.61) in the dissipation term (2.51) gives

$$\begin{aligned}
\mathbf{H}^{\mathrm{T}}\mathbf{P_H} \cdot \mathbf{K}^{-1}\dot{\mathbf{K}} &= (\mathbf{r}^j \cdot \dot{\mathbf{r}}_i)(\mathbf{l}_j \cdot \mathbf{P_H L}^i) && (2.75)\\
&= -(\dot{\mathbf{g}}_m \cdot \mathbf{l}^j)\,(\mathbf{g}^m \cdot \mathbf{l}_i)\,(\mathbf{l}_j \cdot \mathbf{P_H L}^i) && (2.76)\\
&= -(\mathbf{P_H L}^i \otimes \dot{\mathbf{g}}_m) \cdot (\mathbf{l}_j \otimes \mathbf{l}^j)(\mathbf{g}^m \cdot \mathbf{l}_i) && (2.77)\\
&= -(\mathbf{P_H L}^i \cdot \dot{\mathbf{g}}_m)(\mathbf{g}^m \cdot \mathbf{l}_i). && (2.78)
\end{aligned}$$

Finally, let the reference material vectors $\mathbf{G}_i$ be defined by the images of the lattice vectors under the plastic deformation field $\mathbf{K}$, so that $\mathbf{G}_i = \mathbf{K L}_i$. Standard kinematic relations also give

$$\mathbf{G}^m = \mathbf{K}^{-\mathrm{T}}\mathbf{L}^m \tag{2.79}$$

and

$$\begin{aligned}
\mathbf{g}^m &= \mathbf{F}^{-\mathrm{T}}\mathbf{G}^m && (2.80)\\
&= \mathbf{F}^{-\mathrm{T}}\mathbf{K}^{-\mathrm{T}}\mathbf{L}^m. && (2.81)
\end{aligned}$$

Then with $\mathbf{l}_i = \mathbf{H L}_i = \mathbf{F K L}_i$ we have

$$\begin{aligned}
\mathbf{g}^m \cdot \mathbf{l}_i &= (\mathbf{F}^{-\mathrm{T}}\mathbf{K}^{-\mathrm{T}}\mathbf{L}^m) \cdot (\mathbf{F K L}_i)\\
&= \mathbf{L}^m \cdot \mathbf{L}_i\\
&= \delta_i^m, && (2.82)
\end{aligned}$$

and substitution of (2.82) into (2.78) gives

$$\begin{aligned}
D &= -\mathbf{H}^{\mathrm{T}}\mathbf{P_H} \cdot \mathbf{K}^{-1}\dot{\mathbf{K}} && (2.83)\\
&= (\mathbf{P_H L}^i \cdot \dot{\mathbf{g}}_i) \geq 0. && (2.84)
\end{aligned}$$

Equation (2.84) has a nice physical interpretation. Note that $\mathbf{P_H L}^j$ is the resolved stress on the $\mathbf{L}^j$ plane in the lattice reference configuration ($\mathbf{L}^j$ is the crystallographic plane normal). The positivity of dissipation in Equation (2.84) states that the resolved traction vector $\mathbf{P_H L}^i$, and the direction of instantaneous material motion $\dot{\mathbf{g}}_i$, during plastic flow, must not be in opposite directions. By the construction of the $\mathbf{G}_i$ using $\mathbf{G}_i = \mathbf{K L}_i$, this relation holds for any value of plastic deformation $\mathbf{K}$.

This section should not be thought of as a fanciful exercise in vector operations. The notion of plastic flow as the independant evolution of the material configuration with respect to the lattice configuration, used in motivating (2.62), is used in §3.5 for the determination of constitutive equations for yield from X-ray diffraction experiments. Next we consider the constitutive functions requested by the theory developed so far.

2.2.3 Constitutive development: general considerations

The formulation of plasticity thus far presented is general; no constitutive equations have been introduced, so no predictions of material behavior can be made. This is the point at which earlier incarnations of the theory have stopped (Fox, 1968; Naghdi and Srinivasa, 1993a,b; Gupta et al., 2011). In this section we develop a constitutive theory to complete the modeling framework. This will enable us to examine numerical predictions of the theory which is presented in §2.4. The minimum requirements for the constitutive theory are that we need (1) the strain energy function $W(\mathbf{H})$ and (2) the flow rule $\hat{\dot{\mathbf{K}}}(\mathbf{H})$. In this section we will also introduce a yield function, $y(\mathbf{H})$, which, with the maximum dissipation postulate, gives an appealing mathematical structure in which to model rate independent plasticity. We can modify the rate independent theory slightly to allow for rate dependence, and then describe the rate independent theory as the limit of the rate dependent theory as the plastic flow viscosity tends to 0^+.

For each of the required constitutive quantities, we will first consider only general considerations, primarily the core requirements of material symmetry and observer invariance. We then introduce the maximum dissipation postulate and rate independent flow rule. Next, additional conditions on constitutive relations motivated from experimental observations will also be given. Then, in the next section, we will describe the general specific representation problem, and carry out the calculations for crystals of engineering interest.

2.2.3.1 Strain energy function

We require the specification of a strain energy function to determine the elastic stress (2.39) and complete the equation of motion (2.17). In the current formulation, we see no reason to adopt entities such as geometrically necessary dislocations into the strain energy function, as some authors propose (Kuroda and Tvergaard, 2008). Therefore in this model there is nothing different from the strain energy functions of standard elasticity. We employ strain energy functions of the form

$$W(\mathbf{H}) = \frac{1}{2} C_{ijkl} E_{ij} E_{kl} + ..., \tag{2.85}$$

where $E_{ij} = \mathbf{E} \cdot \mathbf{e}_i \otimes \mathbf{e}_j$, $\mathbf{E} \equiv (1/2)(\mathbf{H}^{\mathrm{T}}\mathbf{H} - \mathbf{I})$, and C_{ijkl} are the elastic constants. The reduced form $W(\mathbf{H}) = W(\mathbf{E})$ comes from the requirement of observer invariance. For any $\mathbf{Q} \in O(3, \mathbb{R})$ we must have $W(\mathbf{H}) = W(\mathbf{QH})$. Therefore taking $\mathbf{Q} = \mathbf{R}^{\mathrm{T}}$ where $\mathbf{H} = \mathbf{RU}$ is the polar decomposition gives that $W(\mathbf{H}) = W(\mathbf{U}) = W(\mathbf{C}) = W(\mathbf{E})$. where $\mathbf{C} = \mathbf{H}^{\mathrm{T}}\mathbf{H}$ is the lattice metric. The function (2.85) can be expanded in an arbitrary number of terms, with an associated increased experimental cost. Truncating at quadratic order in strain as depicted in (2.85) gives the familiar linear elastic stress response,

$$S_{ij} = C_{ijkl} E_{kl}, \tag{2.86}$$

where $S_{ij} = \mathbf{S} \cdot \mathbf{e}_i \otimes \mathbf{e}_j$ and $\mathbf{S} = \mathbf{H}^{-1}\mathbf{P}_\mathbf{H}$ is the second Piola Kirchoff stress in the lattice configuration. It should be noted that other proposed strain energies can be employed for crystals, see Schroeder et al. (2008); Ebbing (2010); Schroeder et al. (2010) for some recent examples.

2.2.3.2 Flow rule

In (2.19) we require the specification of the evolution of the plastic deformation, the $\mathbf{K}$-field. For reasons of the thermodynamic interpretation of Equation (2.50) it will be convenient to write the constitutive function for plastic flow in the form

$$\mathbf{K}^{-1}\dot{\mathbf{K}} = \mathbf{L}_\mathrm{p}(\mathbf{F}, \mathbf{K}). \tag{2.87}$$

where $\mathbf{L}_\mathrm{p}$ is called the plastic velocity gradient. We expect plastic flow to occur due to intrinsic lattice distortion, so we collapse the functional dependence to simply

$$\mathbf{K}^{-1}\dot{\mathbf{K}} = \mathbf{L}_\mathrm{p}(\mathbf{H}). \tag{2.88}$$

Using the basic formulation of (2.88), invariance under change of physical observer then requires that we have

$$\mathbf{K}^{-1}\dot{\mathbf{K}} = \mathbf{L}_\mathrm{p}(\mathbf{H}) = \mathbf{L}_\mathrm{p}(\mathbf{Q}\mathbf{H}) \qquad \forall \mathbf{Q} \in O(3, \mathbb{R}). \tag{2.89}$$

To see this, note that the plastic velocity gradient is invariant under change of observer by the construction of $\mathbf{K}$, so that $\mathbf{K}^+ = \mathbf{K}$ and $\dot{\mathbf{K}}^+ = \dot{\mathbf{K}}$. These taken together give $(\mathbf{K}^{-1}\dot{\mathbf{K}})^+ = \mathbf{K}^{-1}\dot{\mathbf{K}}$. Next in (2.89) take the particular choice $\mathbf{Q} = \mathbf{R}^\mathrm{T}$, where $\mathbf{H} = \mathbf{R}\mathbf{U}$ is the polar decomposition of $\mathbf{H}$. This shows that we must have the reduced form

$$\mathbf{K}^{-1}\dot{\mathbf{K}} = \mathbf{L}_\mathrm{p}(\mathbf{U}) = \mathbf{L}_\mathrm{p}(\mathbf{C}) = \mathbf{L}_\mathrm{p}(\mathbf{E}). \tag{2.90}$$

In the rest of this section, each of the kinematic quantities $\mathbf{U}, \mathbf{C}, \mathbf{E}$ as defined here can be used as arguments in the plastic flow function, $\mathbf{L}_\mathrm{p}$, and we do not assign any special interpretation to any of them due to the bijections between them. Furthermore, under the assumption of small elastic strains, the second Piola Kirchoff stress is given by $\mathbf{S} = \mathcal{C}[\mathbf{E}]$, where $\mathcal{C} : \mathrm{sym} \to \mathrm{sym}$ are the elastic moduli, with representation $\mathcal{C} = C_{ijkl}\mathbf{e}_i \otimes \mathbf{e}_j \otimes \mathbf{e}_k \otimes \mathbf{e}_l$. This is a bijective relation since the moduli are invertible for convex strain energies, a characteristic which can be imbued to the value of the constants C_{ijkl} of (2.85). Using the bijection between $\mathbf{S}$ and $\mathbf{E}$ we can also use flow rules of the form $\mathbf{L}_\mathrm{p}(\mathbf{S})$. In the rest of the section we use the symbol $\mathbf{C}$, but again, either of $\mathbf{U}, \mathbf{E}$, or $\mathbf{S}$ for the small elastic strain formulation can be substituted.

Rate independent flow function. A classically considered problem in phenomenological plasticity is the rate independent limit, which effectively means that the material's plastic

response is instantaneous. In this limit, we must have the flow function invariant under change in time scale, so that under $t \to \lambda t$ we have

$$\mathbf{K}^{-1}\dot{\mathbf{K}} = \mathbf{L}_{\mathrm{p}}(\mathbf{C}, \dot{\mathbf{C}}) \to \lambda \mathbf{K}^{-1}\dot{\mathbf{K}} = \mathbf{L}_{\mathrm{p}}(\mathbf{C}, \lambda\dot{\mathbf{C}}) \implies \mathbf{L}_{\mathrm{p}}(\mathbf{C}, \lambda\dot{\mathbf{C}}) = \lambda \mathbf{L}_{\mathrm{p}}(\mathbf{C}, \dot{\mathbf{C}}). \tag{2.91}$$

Therefore for rate independence, $\mathbf{L}_{\mathrm{p}}(\mathbf{C}, \dot{\mathbf{C}})$ is linear in $\dot{\mathbf{C}}$. The constitutive function for plastic flow can then be written as

$$\mathbf{L}_{\mathrm{p}}(\mathbf{C}, \dot{\mathbf{C}}) = \boldsymbol{\Gamma}(\mathbf{C}) \cdot \dot{\mathbf{C}}. \tag{2.92}$$

for a fourth order tensor $\boldsymbol{\Gamma}(\mathbf{C}) : \mathrm{sym} \ \to \mathbb{R}^9$. Thus far we have considered the restrictions due to observer invariance and rate independence. Next we consider the effect of material symmetry.

Material symmetry restrictions Denote the symmetry group of the material by g_κ. Coarsely speaking, g_κ is a collection of elements of $O(3, \mathbb{R})$, whose operation does not affect constitutive functions. For the flow rule, invariance under the symmetry group of the material gives the necessary conditions

$$\mathbf{L}_{\mathrm{p}}(\mathbf{Q}_{(i)}\mathbf{C}\mathbf{Q}_{(i)}^{\mathrm{T}}, \mathbf{Q}_{(i)}\dot{\mathbf{C}}\mathbf{Q}_{(i)}^{\mathrm{T}}) = \mathbf{Q}_{(i)}\mathbf{L}_{\mathrm{p}}(\mathbf{C}, \dot{\mathbf{C}})\mathbf{Q}_{(i)}^{\mathrm{T}} \qquad \forall \mathbf{Q}_{(i)} \in g_\kappa. \tag{2.93}$$

Here we have used $\mathbf{K}^{-} = \mathbf{Q}\mathbf{K}$ and $\dot{\mathbf{K}}^{-} = \mathbf{Q}\dot{\mathbf{K}}$. $\dot{\mathbf{Q}} = 0$ since $\mathbf{Q}$ is a fixed element of the symmetry group in this analysis. Note that these transformations differ from those in (2.90), since the rotations $\mathbf{Q}_{(i)}$ operate on the lattice configuration, not the spatial configuration as for the change of observer.

The hypotheses we have accepted to this point can get us no further in suggesting a form for $\mathbf{L}_{\mathrm{p}}(\mathbf{C}, \dot{\mathbf{C}})$. Any constitutive function which satisfies the necessary conditions of material symmetry (2.93) is admissible in this framework; experimental data is required to inform a particular functional form. With this in mind, one approach which is certainly admissible under the given framework is to simply consider polynomial functions

$$\mathbf{L}_{\mathrm{p}}(\mathbf{C}, \dot{(\mathbf{C})})_{ij} = (D_{ijklmn}C_{mn} + D'_{ijklmnop}C_{mn}C_{op} + ...)\dot{C}_{kl} \tag{2.94}$$

for the rate independent formulation, where the arrays $D_{ijklmn}, D'_{ijklmnop}$ represent material constants which have appropriate symmetries. We could also have

$$\mathbf{L}_{\mathrm{p}}(\mathbf{C})_{ij} = E_{ijmn}C_{mn} + E'_{ijmnop}C_{mn}C_{op} + ... \tag{2.95}$$

where E_{ijmn}, E'_{ijmnop} are material constants with dimensions of $[t]^{-1}$, where $[t]$ are time units, for an alternative approach which is not rate independent. In recognition of similar constitutive formulations in the historical development of elasticity, the equations (2.94) and (2.95) might be considered 'hypoplastic' constitutive functions, since we have not made appeal to any notion of a flow potential. See Xiao et al. (2006, p. 21) for critical comments on flow functions of the form (2.94), (2.95).

2.2.3.2.1 Yield function, maximum dissipation. A primitive observation of the behavior of crystals under load is that below a certain level of lattice distortion, the material returns to its original configuration upon unloading, with no plastic flow. The region in stress or strain coordinates where no plastic flow occurs is called the elastic region or elastic range in the literature. It makes physical sense, then, to conceive of a material function which delineates between elastic and plastic behavior. Therefore, introduce the yield function, $y(\mathbf{C})$, which is designed to induce the basic property

$$\begin{aligned} y(\mathbf{C}) \leq 0 &\implies \mathbf{L}_{\mathrm{p}}(\mathbf{C}) = 0 \\ y(\mathbf{C}) > 0 &\implies \mathbf{L}_{\mathrm{p}}(\mathbf{C}) \neq 0. \end{aligned}$$

That is, below some level of critical lattice distortion, there is no plastic flow. Going back to the text after (2.2), recall that this notion is encoded in the critical shear stress level needed to move a dislocation. Constitutively, the yield function may be a scalar valued function of the lattice distortion measure, e.g. $y = y(\mathbf{C})$. Other functional dependencies can be incorporated into the yield function, such as the dislocation density, $\boldsymbol{\xi}$.

We may propose simple polynomials to describe y as done for the flow rule. However, here we introduce an additional feature, that the function be an even function of lattice distortion such that $y(\mathbf{C}) = y(-\mathbf{C})$, (Hill, 1950). That is, in the polynomial representation, we'd have expansions of the form

$$y(\mathbf{C}) = C_{ijkl}C_{ij}C_{kl} + C''_{ijklmnop}C_{ij}C_{kl}C_{mn}C_{op} + ... \tag{2.96}$$

for constants $C_{ijkl}, C''_{ijklmnop}$. This requirement is due to experimental observations that yield stresses in tension and compression are usually of equal magnitude. If materials are studies which do not exhibit this behavior, the requirement can be relaxed. The constants $C_{ijkl}, C''_{ijklmnop}$ satisfy the necessary conditions for material symmetry, written as

$$y(\mathbf{C}) = y(\mathbf{Q}_{(i)}\mathbf{C}\mathbf{Q}_{(i)}^{\mathrm{T}}) \qquad \forall \mathbf{Q}_{(i)} \in g_{\kappa}. \tag{2.97}$$

The yield concept can be incorporated into the flow rules developed thus far by postulating flow functions of the form

$$\mathbf{L}_{\mathrm{p}}(\mathbf{C}) = \begin{cases} \gamma(\mathbf{C})\mathbf{f}(\mathbf{C}) \text{ if } y(\mathbf{C}) > 0 \\ 0, \text{ if } y(\mathbf{C}) \leq 0 \end{cases} \tag{2.98}$$

for a flow function $\mathbf{f} : \mathrm{sym} \to \mathrm{Lin}$, and where $\gamma : \mathrm{sym} \to \mathbb{R}^+$ may embed effects of material viscosity in the flow rate, for instance. Note that the structure of (2.98) is similar to the overstress models of Perzyna (1966); Nath (1998), typically used with isotropic material models.

Eshelby stress formulation. Finally, in recognition of the role of the Eshelby stress as the work conjugate quantity to plastic flow from (2.47), it seems reasonable to postulate that the flow rule be of the form

$$\mathbf{K}^{-1}\dot{\mathbf{K}} = \mathbf{L}_{\mathrm{p}}(\mathcal{E}') = \mathbf{L}_{\mathrm{p}}(\mathcal{E}'_{\mathrm{S}}, \mathcal{E}'_{\Omega}), \tag{2.99}$$

where $\mathcal{E}'_{\mathrm{S}} = \operatorname{sym} \mathcal{E}'$ and $\mathcal{E}'_{\Omega} = \operatorname{skw} \mathcal{E}'$. Based on (2.99), invariance requirements are automatically satisfied by the intrinsic nature of $\mathcal{E}'$. That is,

$$\mathcal{E}'^{+} = \frac{1}{J_K^+}\left(W^+(\mathbf{C})\mathbf{I}^+ - (\mathbf{H}^+)^{\mathrm{T}}\mathbf{P}^+_{\mathbf{H}}\right) = \frac{1}{J_K}\left(W(\mathbf{C})\mathbf{I} - \mathbf{H}^{\mathrm{T}}\mathbf{P}_{\mathbf{H}}\right) = \mathcal{E}'. \tag{2.100}$$

Similarly, in this framework it is reasonable to postulate that the yield function be formed directly over the Eshelby stress space, so that

$$\begin{aligned} y(\mathcal{E}') \leq 0 &\implies \mathbf{L}_{\mathrm{p}}(\mathcal{E}') = 0 \\ y(\mathcal{E}') > 0 &\implies \mathbf{L}_{\mathrm{p}}(\mathcal{E}') \neq 0. \end{aligned}$$

Next, we refine the hypoplastic flow rules in (2.94),(2.95) by taking advantage of the yield function along with the maximum dissipation postulate.

Maximum dissipation postulate Not satisfied with the arbitrariness of the flow rules (2.94),(2.95), we now improve the situation to a degree. The principle of maximum dissipation is a widely used constitutive hypothesis in modern continuum plasticity. The postulate follows from Drucker's postulate, or the weaker version, Ilyushin's postulate (Gupta et al., 2011).

In isotropic plasticity, the maximum dissipation postulate requires only the scalar valued yield function y be specified; the flow rule $\mathbf{L}_{\mathrm{p}}$ is then given by appropriate derivatives of the yield function. This capability clearly simplifies the constitutive description of the plastic flow process, since we need only consider a scalar function rather than a arbitrary tensor function. However the current model is constructed with recognition that the lattice deformation $\mathbf{H}$ is directly measurable from X-ray diffraction experiments. We will see that the classical version of the maximum dissipation postulate is not sufficient to describe the behavior of the materials we are trying to model, and we require an extra constitutive relation to capture lattice reorientation (Lubliner, 1986). We now work out the details.

Given the following: (1) an elastic-plastic body, with (2) a strain energy function, W, and (3) a yield function y, we can solve for the form of the flow rule satisfying the principle of maximum dissipation. The dissipation D is given by (2.50), see also Gupta et al. (2007, 2011)

$$D = \mathcal{E}' \cdot \mathbf{K}^{-1}\dot{\mathbf{K}}, \tag{2.101}$$

where $\mathcal{E}' = J_K^{-1}\mathbf{K}^{\mathrm{T}}\mathcal{E}\mathbf{K}^{-\mathrm{T}}$, is the Eshelby stress in the fixed lattice configuration, and $\mathcal{E} = W\mathbf{I} - \mathbf{F}^{\mathrm{T}}\mathbf{P}_{\mathbf{F}}$ is the Eshelby stress in the material reference configuration. The Eshelby stress

in the fixed lattice configuration may then be written as

$$J_K\mathcal{E}' = W\mathbf{I} - \mathbf{H}^{\mathrm{T}}\mathbf{P}_{\mathbf{H}} = W\mathbf{I} - \mathbf{CS}. \tag{2.102}$$

The implementation of the maximum dissipation postulate is phrased as an optimization problem on the permissible states of stress: The energy dissipation D, (2.101) is maximized, subject to the constraints $y(\mathcal{E}') \leq 0$. That is, that the elastic stress is at or below the yield surface. Additionally, we have equality constraints on the stress state, $\mathcal{E}'\mathbf{C} \in$ sym. The optimization problem is then written as

$$\begin{array}{l} \text{maximize } D \\ \text{subject to the inequality constraints } y(\mathcal{E}') \leq 0 \\ \text{and the equality constraints } \mathcal{E}'\mathbf{C} \in \text{sym}. \end{array} \tag{2.103}$$

We can then solve for the form of the flow rule once and for all by satisfying the Kuhn Tucker conditions of the optimization problem (2.103), see Greig (1980). The Kuhn-Tucker conditions applied to (2.103) then give (Steigmann and Gupta, 2011)

$$\mathbf{K}^{-1}\dot{\mathbf{K}} = \lambda\frac{\partial y}{\partial \mathcal{E}'} + \mathbf{\Omega C}, \tag{2.104}$$

where $\lambda \geq 0$ is a Lagrange multiplier associated with the inequality constraint and $\mathbf{\Omega} \in$ skw are Lagrange multipliers associated with the equality constraint. The Lagrange multipliers $\mathbf{\Omega}$ appear from taking the equality constraint in the form

$$\mathcal{E}'\mathbf{C} \in \text{sym} \implies \text{skw } \mathcal{E}'\mathbf{C} = \mathbf{0}. \tag{2.105}$$

For an arbitrary $\mathbf{A}$, $(\text{skw } \mathbf{A})_{ij} = \epsilon_{ikj}a_k$, for a_k the axial vector of skw $\mathbf{A}$, and so $a_k = (1/2)\epsilon_{ikj}(\text{skw } \mathbf{A})_{ij}$. The Kuhn-Tucker conditions for the optimal solution to the system (2.103) require calculation of

$$\frac{\partial \mu_k \epsilon_{ikj}\mathcal{E}'_{im}\mathbf{C}_{mj}}{\partial \mathcal{E}'_{rp}} = \mu_k\epsilon_{ikj}\delta^i_r\delta^m_p\mathbf{C}_{mj} = \mu_k\epsilon_{rkj}\mathbf{C}_{pj} = 2\mathbf{\Omega}'_{rj}\mathbf{C}_{pj}, \tag{2.106}$$

where μ_i are the Lagrange multipliers associated with the three constraint equations

$$\langle \text{skw } \mathcal{E}'\mathbf{C}\rangle = \mathbf{0},$$

and $2\langle\mathbf{\Omega}'\rangle = \mu_k\mathbf{e}_k$. Here $\langle\cdot\rangle$ denotes the map from skew tensors to axial vectors, see (A.16), (A.17). Finally, redefining (2.106) through $\mathbf{\Omega} = 2\mathbf{\Omega}'$ gives the result (2.104).

Small elastic strain. We now consider the small elastic strain reduction of the flow rule (2.104). That is, strains at which linear elasticity is thought to be valid. To order $O(\mathbf{E})$ we have the Eshelby stress as

$$\mathcal{E}' = W\mathbf{I} - \mathbf{CS} \approx -\mathbf{S}. \tag{2.107}$$

The yield function $y(\mathcal{E}')$ is then expressed as a function of the symmetric Piola Kirchoff stress,

$$y = y(\mathbf{S}). \tag{2.108}$$

The maximum dissipation postulate with the constraints $y(\mathbf{S}) \leq 0$ and $\mathbf{S} = \mathbf{S}^{\mathrm{T}}$ gives the flow rule (2.104) as

$$\mathbf{K}^{-1}\dot{\mathbf{K}} = -\lambda\frac{\partial y}{\partial \mathbf{S}} + \mathbf{\Omega}. \tag{2.109}$$

Furthermore, rate independence requires that the flow rule be linear in $\dot{\mathbf{S}}$, (Gupta et al., 2007), so that we consider flow rules (2.109) of the form

$$\mathbf{K}^{-1}\dot{\mathbf{K}} = -\lambda\frac{\partial y}{\partial \mathbf{S}} + \mathbf{\Omega}(\mathbf{S}, \dot{\mathbf{S}}), \tag{2.110}$$

where the spin $\mathbf{\Omega}(\mathbf{S}, \dot{\mathbf{S}})$ is linear in $\dot{\mathbf{S}}$ (see (2.92)). In a later section, we also use flow functions of the form

$$\mathbf{K}^{-1}\dot{\mathbf{K}} = -\lambda\left(\frac{\partial y}{\partial \mathbf{S}} + \mathbf{\Omega}(\mathbf{S})\right). \tag{2.111}$$

As a final point, in the small strain limit, the dissipation (2.50) is written

$$D = \mathbf{K}^{-1}\dot{\mathbf{K}} \cdot -\mathbf{S} = \lambda\frac{\partial y}{\partial \mathbf{S}} \cdot \mathbf{S} \geq 0, \tag{2.112}$$

since the inner-product with $\mathbf{S} \in \mathrm{sym}$ eliminates the contribution from the spin. Regarding $\mathbf{S}$ as coordinates of a six-dimensional space, this inequality implies that the yield function $y(\mathbf{S})$ is a convex function. Therefore convexity of the yield function will be another important property which the theory implies. Convex yield functions have a rich literature in the sheet metal community (Soare and Barlat, 2010). We describe the imposition of convexity into y for cubic crystals later in this chapter, and again for hexagonal crystals in §3.5.1.2.

This completes the treatment of the theoretical implications on the constitutive framework. We now consider aspects which should be taken into consideration based on experimental observations.

2.2.3.3 Additional observations from experimental plasticity

We began this section with the simplest complete constitutive formulation for elastic plastic bodies: a strain energy function and a flow rule. We refined these results by deriving a rate independent flow rule. We then introduced the yield function concept, and incorporated it into flow functions of the over stress/Perzyna type. Accepting the maximum dissipation postulate gave us further use from the yield function, although we were not able to completely characterize the plastic flow from the consequences of the postulate (Lubliner, 1986) since lattice reorientation is a fundamental experimental observable. The functional forms for the constitutive relations are basic polynomial expansions consistent with the point group

symmetry of the material. We have only required that the yield function be an even function of the distortion, (2.96).

As noted several times previously, conclusive experimental observations of plasticity have been historically elusive (Bell and Green, 1967). Nevertheless, we now consider further refinements to the constitutive framework developed thus far, by considering what is known to be observed from what experiments are available. Incorporating these observations into the constitutive functions will make the theory of greater practical use.

Lattice reorientation - requirement for plastic spin The basic experimental observation which motivates the inclusion of the spin is that the lattice of a single crystal, pulled in uniaxial tension, rotates, while the material does not. Equivalently, the lattice of a single crystal in simple shear on a slip plane, does not rotate, while the material does. In crystal plasticity, the reorientation effect comes out naturally from the assumed form of the flow rule

$$\dot{\mathbf{F}}^{\mathrm{p}}(\mathbf{F}^{\mathrm{p}})^{-1} = \sum_{\alpha} \dot{\gamma}^{\alpha} \mathbf{s}_0^{\alpha} \otimes \mathbf{n}_0^{\alpha}. \tag{2.113}$$

The skew part of (2.113) is naturally nonzero, in general, by the presumed form of the plastic flow function on slip dyads $\mathbf{s}_0^{\alpha} \otimes \mathbf{n}_0^{\alpha}$. Directly computing, we have

$$\mathbf{W}_{\mathrm{p}} = \mathrm{skw}\ \dot{\mathbf{F}}^{\mathrm{p}}(\mathbf{F}^{\mathrm{p}})^{-1} = \sum_{\alpha} \dot{\gamma}^{\alpha} (\mathbf{s}_0^{\alpha} \otimes \mathbf{n}_0^{\alpha} - \mathbf{n}_0^{\alpha} \otimes \mathbf{s}_0^{\alpha}). \tag{2.114}$$

In a precursor to this work, Gupta et al. (2007) construct a model of plasticity which defines $\mathbf{K}$ so that the plastic flow $\mathbf{K}^{-1}\dot{\mathbf{K}}$ is restricted to be symmetric. However with this restriction $\mathbf{H}$ loses its interpretation in terms of the transformation of lattice vectors from a fixed reference state, as in Figure 2.6. This removes the ability of X-ray diffraction experiments to be used to evaluate the predictions of the theory, since in uniaxial extension there would be no lattice rotation predicted by such a theory, apart from elastic rotations which would be small. To see this, consider the symmetric axial material deformation

$$\mathbf{F}(s) = s\mathbf{e}_1 \otimes \mathbf{e}_1 + \frac{1}{\sqrt{s}}(\mathbf{e}_2 \otimes \mathbf{e}_2 + \mathbf{e}_3 \otimes \mathbf{e}_3), \tag{2.115}$$

where $s \in \mathbb{R}^+$ is the extension parameter. This implies that $\dot{\mathbf{F}}\mathbf{F}^{-1} \in \mathrm{sym}$. Using the decomposition $\mathbf{F} = \mathbf{H}\mathbf{K}^{-1}$ and $\mathbf{K}^{-1}\dot{\mathbf{K}} = -\dot{\mathbf{K}}^{-1}\mathbf{K}$ we have

$$\dot{\mathbf{F}}\mathbf{F}^{-1} = \dot{\mathbf{H}}\mathbf{H}^{-1} - \mathbf{H}\mathbf{K}^{-1}\dot{\mathbf{K}}\mathbf{H}^{-1}. \tag{2.116}$$

To cut through this equation, consider large plastic strains, so that $\|\mathbf{K}^{-1}\| > \|\mathbf{H}\|$. Then $\mathbf{H} \approx \mathbf{R}$, where $\mathbf{H} = \mathbf{R}\mathbf{U}$ is the polar decomposition of $\mathbf{H}$. With this, (2.116) becomes

$$\dot{\mathbf{F}}\mathbf{F}^{-1} = \dot{\mathbf{R}}\mathbf{R}^{-1} - \mathbf{R}\mathbf{K}^{-1}\dot{\mathbf{K}}\mathbf{R}^{-1}. \tag{2.117}$$

Next, recall that $\dot{\mathbf{R}}\mathbf{R}^{-1} \in$ skw , since $\mathbf{R} \in O(3,\mathbb{R})$. Taking the skew part of (2.117), for the extension (2.115) gives

$$\text{skw } \dot{\mathbf{F}}\mathbf{F}^{-1} = 0 = \dot{\mathbf{R}}\mathbf{R}^{-1} - \text{skw } (\mathbf{R}\mathbf{K}^{-1}\dot{\mathbf{K}}\mathbf{R}^{-1}). \tag{2.118}$$

But, skw $(\mathbf{R}\mathbf{K}^{-1}\dot{\mathbf{K}}\mathbf{R}^{-1}) = \mathbf{R}\mathbf{K}^{-1}\dot{\mathbf{K}}\mathbf{R}^{-1} - \mathbf{R}^{-\mathrm{T}}\mathbf{K}^{-1}\dot{\mathbf{K}}^{\mathrm{T}}\mathbf{R}^{\mathrm{T}}$. Therefore

$$\text{skw } (\mathbf{R}\mathbf{K}^{-1}\dot{\mathbf{K}}\mathbf{R}^{-1}) = \mathbf{R}(\text{skw } \mathbf{K}^{-1}\dot{\mathbf{K}})\mathbf{R}^{-1}.$$

Substituting this in Equation (2.118) shows that for axial material deformations,

$$\dot{\mathbf{R}}\mathbf{R}^{-1} = \mathbf{R}(\text{skw } \mathbf{K}^{-1}\dot{\mathbf{K}})\mathbf{R}^{-1}. \tag{2.119}$$

Now, if $\mathbf{K}^{-1}\dot{\mathbf{K}} \in$ sym as supposed in Gupta et al. (2007), then (2.119) indicates that $\dot{\mathbf{R}}\mathbf{R}^{-1} = 0$, hence $\dot{\mathbf{R}} = 0$, and there is no lattice reorientation due to plastic flow. Therefore in the present theory we cannot make the supposition $\mathbf{K}^{-1}\dot{\mathbf{K}} \in$ sym . This discussion is necessary to include since this present theory closely resembles that in Gupta et al. (2007), however this proves the model presented here is clearly distinct. From another perspective, the spin factor $\boldsymbol{\Omega}$ is a necessary ingredient of the theory in order to utilize the experimental method coupled to the theory, X-ray diffraction. Should further justification be needed, in the previous section we showed that a non zero spin is permissible under thermodynamic restrictions of the maximum dissipation postulate. Hence there is no thermodynamic reason why a spin should not exist, although we find the argument based on experimental observations more convincing to appeal to.

Next, we consider another experimentally observed phenomena which crystal plasticity encodes naturally but which we must consider as a separate hypothesis: lattice spin reversal under load reversal.

Lattice reorientation reversal Consider the spin to be written as a function of a single argument, say

$$\boldsymbol{\Omega} = \boldsymbol{\Omega}(\mathbf{S}). \tag{2.120}$$

If the spin were of even order in $\mathbf{S}$, then the lattice reorientation would not change directions upon reversal of the load, $\mathbf{S} \to -\mathbf{S}$. For example consider tension and compression experiments on single crystals. Note that this reorientation reversal is naturally encoded in the crystal plasticity model (2.5), (2.6), through the use of $\dot{\gamma}^{\alpha} \propto \text{sign}(\tau)$. In terms of polynomial expansions, we therefore require $\boldsymbol{\Omega}$ to be an odd function of $\mathbf{S}$. It is not clear how lattice reorientation reversal would be encoded a priori in the rate independent functions of the form $\boldsymbol{\Omega} = \boldsymbol{\Omega}(\mathbf{S}, \dot{\mathbf{S}})$. This is a critical point to highlight, and makes such constitutive formulations based on bilinear dependence on the stress or strain-rate dubious in our opinion. Although such a formulation may capture data in certain scenarios, there could also be some non-physical predictions in different experimental situations. That is, if the constitutive law is calibrated in one test, it may not give acceptable predictions in a second experimental test. In summary, we have much more confidence in predictions based on (2.120) than on $\boldsymbol{\Omega} = \boldsymbol{\Omega}(\mathbf{S}, \dot{\mathbf{S}})$, although both cases are investigated in a later section.

2.3 Constitutive functions: detail

Thus far, we have developed the theory behind the current model of elastic-plastic deformation of single crystals and given an outline of the proposed constitutive framework. In this section we develop the precise constitutive equations required to complete the model, and make numerical predictions. We focus on the version of constitutive model for plastic flow which makes use of the maximum dissipation postulate. To review, the entities we require are

1. $W(\mathbf{E})$, the strain energy function
2. $y(\mathbf{E})$ or $y(\mathcal{E}')$, the yield function
3. $\boldsymbol{\Omega}(\mathbf{S})$, $\boldsymbol{\Omega}(\mathbf{S}, \dot{\mathbf{S}})$ or $\boldsymbol{\Omega}(\mathcal{E}', \dot{\mathcal{E}}')$, the lattice spin

We will also consider the effect of incorporating geometrically necessary dislocations $\boldsymbol{\xi}$, in (2.16). Therefore, we also would like to determine

2a. $y(\mathbf{E}, \boldsymbol{\xi})$ or $y(\mathcal{E}', \boldsymbol{\xi})$

3a. $\boldsymbol{\Omega}(\mathbf{S}, \dot{\mathbf{S}}, \boldsymbol{\xi})$ or $\boldsymbol{\Omega}(\mathcal{E}', \dot{\mathcal{E}}', \boldsymbol{\xi})$

First, some preliminary comments on the generation of phenomenological constitutive equations respecting material symmetry requirements. For constitutive functions of one variable, it is straightforward to compute the representation problem by a variety of methods (Green and Adkins, 1970; Liu, 1982; Zheng, 1994). However for functions of several variables and higher order polynomials, it gets more complicated, (Xiao, 1996). Each of these techniques for the representation problem can be thought of as reporting a functional basis for the constitutive equation. For an idea, isotropic materials (e.g. no material symmetry requirements) would have the smallest functional basis, while highly anisotropic crystals would have a larger basis. According to a given material symmetry, the smallest integrity basis is desired. Rigorously showing a particular functional basis is the smallest representation is difficult, especially for multiple tensor argument, no matter which method in Green and Adkins (1970); Liu (1982); Zheng (1994) is used.

Although generating constitutive functions using any representation procedure is somewhat of a crank-turning procedure, it is not really a process which can be automated. For example, detecting redundant basis element using symbolic tools like Mathematica is not straight-forward. In this section we examine the use of both method: anisotropic structural tensors and integrity bases for polynomial functions. We generate several of the constitutive functions enumerated in the above list. We focus on cubic symmetry, this being an example of a symmetry which is both difficult to generate reduced constitutive functions for, as well as being relevant to the target application of the theory. Furthermore, cubic crystals are common in structural metals of interest (Fe(BCC), Al(FCC), Cu(FCC)).

We now consider many of the functions we are required to compute in order to complete the model. In Table 2.1, we list the functional expansions we require for the theory of §2.2. Here $\mathbf{A}, \mathbf{B}, \mathbf{C}$ represent arbitrary symmetric second order tensors, and $\mathbf{v}, \mathbf{w}, \mathbf{u}, \mathbf{t}$ represent axial vectors of skew symmetric tensors. Note that for functions incorporating arbitrary second order tensors, such as $\mathcal{E}', \boldsymbol{\xi}$, in the representation formula the symmetric and skew-symmetric factors are split off and handled independently. For example, for a scalar function, f, depending on the geometrically necessary dislocation content, we have $f(\boldsymbol{\xi}) = f(\text{sym } \boldsymbol{\xi}, \text{skw } \boldsymbol{\xi}) = f(\mathbf{A}, \mathbf{v})$, where $\mathbf{A} \equiv \text{sym } \boldsymbol{\xi}$ and $\mathbf{v} \equiv \langle \text{skw } \boldsymbol{\xi} \rangle$. Note that in this study, only the first three function classes in Table 2.1 will be examined in detail.

Table 2.1: Constitutive equations required for phenomenological plasticity. These functions must be constructed to be invariant under the point group symmetry of the material.

Scalar valued function $\rightarrow$ Target constitutive entity
$F(\mathbf{A}) \rightarrow W(\mathbf{E}), y(\mathbf{E})$
$F(\mathbf{A}, \mathbf{v}) \rightarrow \boldsymbol{\Omega}(\mathbf{S}),\ y(\mathcal{E}')$
$F(\mathbf{A}, \mathbf{B}, \mathbf{v}) \rightarrow \boldsymbol{\Omega}(\mathbf{S}, \dot{\mathbf{S}}),\ y(\mathbf{E}, \boldsymbol{\xi})$
$F(\mathbf{A}, \mathbf{B}, \mathbf{v}, \mathbf{w}) \rightarrow y(\mathcal{E}', \boldsymbol{\xi})$
$F(\mathbf{A}, \mathbf{B}, \mathbf{v}, \mathbf{w}, \mathbf{u}) \rightarrow \boldsymbol{\Omega}(\mathcal{E}', \dot{\mathcal{E}}')$
$F(\mathbf{A}, \mathbf{B}, \mathbf{C}, \mathbf{v}, \mathbf{w}) \rightarrow \boldsymbol{\Omega}(\mathbf{S}, \dot{\mathbf{S}}, \boldsymbol{\xi})$
$F(\mathbf{A}, \mathbf{B}, \mathbf{C}, \mathbf{v}, \mathbf{w}, \mathbf{u}, \mathbf{t}) \rightarrow \boldsymbol{\Omega}(\mathcal{E}', \dot{\mathcal{E}}', \boldsymbol{\xi})$

2.3.1 Structural tensor methods

In the continuum mechanics literature, constitutive representation theory is typically concerned at its core with the representation of isotropic functions (Spencer, 1971), that is, functions for which

$$\mathbf{Q} * f(\mathbf{A}) = f(\mathbf{Q} * \mathbf{A}) \qquad \forall \mathbf{Q} \in O(3, \mathbb{R}), \tag{2.121}$$

where * is an operator to denote the rotation operation on arbitrary tensor quantities. This notation is also used in the representation literature (Zheng, 1994; Xiao, 1996). As an example, for a second order tensor $\mathbf{T}$, $\mathbf{Q} * \mathbf{T} \equiv \mathbf{Q}\mathbf{T}\mathbf{Q}^{\mathrm{T}}$. For a given constitutive function $f(\mathbf{A})$, it has been shown (Liu, 1982) that by adding a functional dependence on tensors which characterize the anisotropy, in the sense that they are invariant under action of elements of the symmetry group, that an isotropic function of the original agencies along with the structural tensor has the desired functional properties (Zheng, 1994). Therefore, by using structural tensors, classical results from isotropic function representations (Spencer, 1971) can be applied to anisotropic materials. For background literature on the structural tensor approach, see Liu (1982); Zheng (1994); Xiao (1996).

The structural tensor method works brilliantly for material symmetries commonly encountered in applications of non-linear elasticity. For example composites or biological materials are often treated assuming transversely isotropic symmetry or orthotropic symmetry. For crystals, the method also works well for low symmetry materials, such as monoclinic. But for higher symmetry materials, such as cubic or hexagonal, higher order structural tensors (fourth order for cubics, sixth order for hexagonals) need to be incorporated. Generation methods then create an assortment of complete yet redundant function basis elements (Xiao, 1996), from which it can be difficult to decipher the complete basis. For simple constitutive functions like the strain energy function, the structural tensor approach is manageable for crystals, but we would like to be able to consider functions with multiple tensorial arguments. Therefore we consider an alternative method.

2.3.2 Polynomial generation

An older framework to obtaining constitutive equations is the method described in Green and Adkins (1970); Spencer (1971). In this method, polynomial scalar valued constitutive functions are considered, and algebraic theorems are applied to find the integrity basis of the function by examining the symmetries in the arguments under the symmetry transformations $\mathbf{Q} \in g_\kappa$.

This method can be extended to obtain tensor functions and not just scalar valued functions. To show this, consider a tensor function $\mathbf{A} : \text{sym} \rightarrow \text{sym}\ , \mathbf{A} = \mathbf{A}(\mathbf{E})$. The necessary condition for invariance under symmetry transformations is given by

$$\mathbf{A}(\mathbf{Q}\mathbf{E}\mathbf{Q}^{\mathrm{T}}) = \mathbf{Q}\mathbf{A}(\mathbf{E})\mathbf{Q}^{\mathrm{T}}, \forall \mathbf{Q} \in g_\kappa, \tag{2.122}$$

where g_κ is the symmetry group for the material relative to the configuration κ. Now, using (2.122), form the inner product with an arbitrary tensor $\mathbf{D}$, which has the transformation $\bar{\mathbf{D}} = \mathbf{Q}\mathbf{D}\mathbf{Q}^{\mathrm{T}}$. Then

$$A_{ij}(\bar{\mathbf{E}})\bar{D}_{ij} = Q_{ik}A_{kl}(\mathbf{E})Q_{jl}\bar{D}_{ij}, \tag{2.123}$$

where $\bar{\mathbf{E}} = \mathbf{Q}\mathbf{E}\mathbf{Q}^{\mathrm{T}}$, and similarly for $\bar{\mathbf{D}}$, for $\mathbf{Q} \in g_\kappa$. Next, the result $\bar{D}_{ij} = Q_{ik}D_{kl}Q_{jl}$ substituted into (2.123) and simplifying gives

$$A_{ij}(\bar{\mathbf{E}})\bar{D}_{ij} = A_{kl}(\mathbf{E})D_{kl}, \tag{2.124}$$

so that the scalar valued function

$$F = A_{ij}(\mathbf{E})D_{ij} \tag{2.125}$$

is invariant under the symmetry group of the material, g_κ. The constitutive equation for $A_{ij}(\mathbf{E})$ is then given by computing the derivative of the scalar function F through

$$A_{ij} = \left.\frac{\partial F}{\partial D_{ij}}\right|_{\mathbf{D}=\mathbf{0}}. \tag{2.126}$$

Using this approach we can generate tensor valued functions by applying the methods in Green and Adkins (1970); Spencer (1971). The examples in these references are helpful but not sufficient for our purposes, since we require the incorporation of multiple arguments. As a side note, we highly recommend reviewing these examples, in order to better digest the rest of this section.

Now we examine the functions we must consider in order to complete the quantities shown in Table 2.1. The scalar valued strain energy W and yield function y are straightforward to determine. The generation of the lattice spin, however, deserves emphasis. We first repeat the derivation leading to (2.126). Since $\mathbf{\Omega} \in$ skw , the inner product

$$F = \Omega_{ij} D_{ij} \tag{2.127}$$

only depends on the antisymmetric part of D_{ij}. Therefore we can obtain

$$F = \Omega_{ij} D_{ij} = D^a_{ij} \Omega_{ij} = \epsilon_{ikj} d_k \epsilon_{ilj} w_l = \delta_{kl} d_k \omega_l = d_k \omega_k, \tag{2.128}$$

where ω_k, d_k are the axial vectors of Ω_{ij}, D^a_{ij}, respectively. The axial vector of $\mathbf{\Omega}$ is then obtained via

$$\omega_k = \left. \frac{\partial F}{\partial d_k} \right|_{\mathbf{d}=\mathbf{0}} . \tag{2.129}$$

For example, for item 3, in Table 2.1, the rate independent spin, we require the representation for the anisotropic scalar function

$$F = F(\mathbf{S}, \dot{\mathbf{S}}, \mathbf{v}), \tag{2.130}$$

where $\mathbf{v}$ is the axial vector of a skew symmetric tensor.

Similar arguments hold if the desired constitutive function is a symmetric tensor. Taking the product

$$F = A_{ij} D_{ij}$$

for a symmetric $\mathbf{A}$, $A_{ij} = A_{ji}$, only depends on the symmetric component of D_{ij}, and the constitutive function is obtained by computing

$$A_{ij} = \left. \frac{\partial F}{\partial D^{\mathrm{s}}_{ij}} \right|_{D^{\mathrm{s}}_{ij}=0} . \tag{2.131}$$

where D^{s}_{ij} is the symmetric part of D_{ij}.

2.3.3 Constitutive functions for plasticity - integrity basis.

We now develop several constitutive equations from Table 2.1. For the functions not covered explicitly, the general plan of attack should be evident. The procedure utilizes the prescription in Green and Adkins (1970); Spencer (1971) which is based on mathematical theorems of polynomials. In overview, we apply the elements of the symmetry group one at a time, and apply one of several theorems, as they are required, in order to ensure invariance of the polynomial integrity basis. Specifically, we will make use of the following theorems:

Theorem 1 (Green, 1970)**.** *A polynomial basis for polynomials which are symmetric in the two sets of variables* $(y_1, y_2, ..., y_n)$ *and* $(z_1, z_2, ..., z_n)$ *is formed from the quantities*

$$K_j = \frac{1}{2}(y_j + z_j) \qquad (j = 1, 2, ..., n) \tag{2.132}$$

$$K_{jk} = \frac{1}{2}(y_j z_k + y_k z_j) \qquad (j, k = 1, 2, ..., n) \tag{2.133}$$

Theorem 2 (Green, 1970)**.** *A polynomial basis for polynomials which are symmetric in the three pairs of variables* (y_1, z_1)*,* (y_2, z_2)*, and* (y_3, z_3) *is formed by the quantities*

$$\begin{aligned}
&L_1 = y_1 + y_2 + y_3 && L_2 = y_2y_3 + y_3y_1 + y_1y_2\\
&L_3 = y_1y_2y_3 && L_4 = z_1 + z_2 + z_3\\
&L_5 = z_2z_3 + z_3z_1 + z_1z_2 && L_6 = z_1z_2z_3\\
&L_7 = y_2z_3 + y_3z_1 + y_1z_2 + z_2y_3 + z_3y_1 + z_1y_2 && L_8 = y_1z_2z_3 + y_2z_3z_1 + y_3z_1z_2\\
&L_9 = z_1y_2y_3 + z_2y_3y_1 + z_3y_1y_2
\end{aligned}$$

Theorem 3 (Green, 1970)**.** *A polynomial basis for polynomials which are symmetric in variables* $(y_1, y_2, y_3, z_1, z_2, z_3)$ *which are form-invariant under cyclic rotation of the subscripts 1,2,3 is formed by the quantities*

$$\begin{aligned}
&M_1 = y_1 + y_2 + y_3 && M_2 = y_2y_3 + y_3y_1 + y_1y_2\\
&M_3 = y_1y_2y_3 && M_4 = z_1 + z_2 + z_3\\
&M_5 = z_2z_3 + z_3z_1 + z_1z_2 && M_6 = z_1z_2z_3\\
&M_7 = y_2z_3 + y_3z_1 + y_1z_2 && M_8 = z_2y_3 + z_3y_1 + z_1y_2\\
&M_9 = y_3y_2^2 + y_1y_3^2 + y_2y_1^2 && M_{10} = z_3z_2^2 + z_1z_3^2 + z_2z_1^2\\
&M_{11} = y_1z_2z_3 + y_2z_3z_1 + y_3z_1z_2 && M_{12} = z_1y_2y_3 + z_2y_3y_1 + z_3y_1y_2\\
&M_{13} = y_1y_2z_2 + y_2y_3z_3 + y_3y_1z_1 && M_{14} = z_1z_2y_2 + z_2z_3y_3 + z_3z_1y_1
\end{aligned}$$

Theorem 4 (Green, 1970)**.** *A polynomial basis for a polynomial in the variables*

$$y_1, y_2, ..., z_n, N_1, N_2, ..., N_k,$$

which is form-invariant under a group of transformations under which $N_1, N_2, ..., N_k$ *are invariant is formed by adjoining to the quantities* $N_1, N_2, ..., N_k$ *the polynomial basis for polynomials in the variables* $y_1, y_2, ..., z_n$ *which are form-invariant under the given group of transformations.*

Theorem 5 (Spencer, 1971)**.** *An integrity basis for polynomials which are symmetric in the three sets of variables* $(u_1, v_1, w_1, ..., z_1)$*,* $(u_2, v_2, w_2, ..., z_2)$*,* $(u_3, v_3, w_3, ..., z_3)$ *is formed by*

$$u_1 + u_2 + u_3, \qquad u_2u_3 + u_3u_1 + u_1u_2 \qquad u_1u_2u_3 \tag{2.134}$$

together with the expressions obtained by substituting $v_i, w_i, ..., z_i$ *for* u_i*;*

$$u_1v_1 + u_2v_2 + u_3v_3, \qquad u_2u_3v_1 + u_3u_1v_2 + u_1u_2v_3 \qquad u_1v_2v_3 + u_2v_3v_1 + u_3v_1v_2 \tag{2.135}$$

together with the expressions obtained by substituting for u_i and v_i all distinct combinations of two different symbols formed from $u_i, v_i, ..., z_i$;

$$u_1 v_1 w_1 + u_2 v_2 w_2 + u_3 v_3 w_3$$

together with the expressions obtained by substituting for u_i, v_i, w_i all distinct combinations of three different symbols formed from $u_i, v_i, ..., z_i$.

Theorem 6 (Spencer, 1971)**.** *An integrity basis for polynomials in the three sets of variables $(u_1, v_1, w_1, ..., z_1)$, $(u_2, v_2, w_2, ..., z_2)$, $(u_3, v_3, w_3, ..., z_3)$ which are invariant under cyclic permutations of the suffixes 1,2, and 3 consists of the integrity basis for polynomials which are symmetric in the variables given by Theorem 5;*

$$u_2 u_3 (u_2 - u_3) + u_3 u_1 (u_3 - u_1) + u_1 u_2 (u_1 - u_2) \tag{2.136}$$

together with the expressions obtained by substituting $v_i, w_i, ..., z_i$ for u_i;

$$\begin{gathered} u_1 (v_2 - v_3) + u_2 (v_3 - v_1) + u_3 (v_1 - v_2) \\ u_2 u_3 (v_2 - v_3) + u_3 u_1 (v_3 - v_1) + u_1 u_2 (v_1 - v_2) \\ v_2 v_3 (u_2 - u_3) - v_3 v_1 (u_3 - u_1) - v_1 v_2 (u_1 - u_2) \end{gathered} \tag{2.137}$$

together with the expressions obtained by substituting for u_i and v_i all distinct combinations of two different symbols formed from $u_i, v_i, ..., z_i$;

$$u_1 v_1 (w_2 - w_3) + u_2 v_2 (w_3 - w_1) + u_3 v_3 (w_1 - w_2)$$

together with the expressions obtained by substituting for u_i, v_i, w_i all distinct combinations of three different symbols formed from $u_i, v_i, ..., z_i$.

After applying the one or more of the above theorems, depending on the case under consideration, we will arrive at an integrity basis for the polynomial $F = F(\mathbf{A}, \mathbf{B}, \mathbf{v}, ...)$, written in the form

$$F = F(\mathbf{A}) = F(x_1, x_2, ..., y_1, y_2, ..., z_1, z_2, ...) \tag{2.138}$$

where, in this case $x_i, y_i, z_i : \mathbf{A} \to \mathbb{R}$ are the integrity basis elements based on the argument $\mathbf{A}$. Here only, let the symbols x, y, z carry additional meaning: they refer to the order of the integrity element. Therefore $x_i, i = 1, 2, ..., N_x$ are of, say order 1, $y_i, i = 1, 2, ..., N_y$ are of order 2, and $z_i, i = 1, 2, ..., N_z$ are of order 3. Depending on the symmetry group, higher order terms may be required. The polynomial representation (to order 3) is then given by the expansion

$$\begin{aligned} F(\mathbf{A}) = b + \sum_i c_i x_i + \sum_i \sum_j d_{ij} x_i x_j + \sum_i e_i y_i + \sum_i \sum_j \sum_k f_{ijk} x_i x_j x_k \\ + \sum_i \sum_j g_{ij} x_i y_j + \sum_i h_i z_i, \end{aligned} \tag{2.139}$$

where the arrays $b, c_i, d_{ij}, e_i, f_{ijk}, g_{ij}, h_i$ are material constants which have certain symmetries like $d_{ij} = d_{ji}$, $f_{ijk} = f_{jik}$, etc. Of course, cross order terms have $g_{ij} \neq g_{ji}$, in general. The expansion (2.139) is more complicated for multiple arguments in the function F, but the same idea holds; take all possible combinations of the integrity elements up to a certain specified order of expansion. We now proceed to apply the above tools to generate the constitutive equations for specific crystal types.

2.3.3.1 Cubic crystals

In this section we generate constitutive functions for cubic crystals. These are an important case to consider, both as a point of practical relevance (iron is BCC, aluminum is FCC), and of theoretical interest, since constitutive functions are more difficult for cubic crystals than for monoclinic, for example. There are several groups in the cubic class (Green and Adkins, 1970). The group of maximum order is the hexoctahedral point group, which characterizes many elemental metals. The hexoctahedral group consists of the following elements of $O(3, \mathbb{R})$

$$\begin{array}{l} \mathbf{I}, \mathbf{C}, \mathbf{R}_1, \mathbf{R}_2, \mathbf{R}_3, \mathbf{D}_1, \mathbf{D}_2, \mathbf{D}_3, \mathbf{T}_1, \mathbf{C}\mathbf{T}_1, \mathbf{R}_1\mathbf{T}_1, \mathbf{R}_2\mathbf{T}_1, \mathbf{R}_3\mathbf{T}_1, \mathbf{D}_1\mathbf{T}_1, \mathbf{D}_2\mathbf{T}_1, \mathbf{D}_3\mathbf{T}_1, \\ \mathbf{T}_2, \mathbf{C}\mathbf{T}_2, \mathbf{R}_1\mathbf{T}_2, \mathbf{R}_2\mathbf{T}_2, \mathbf{R}_3\mathbf{T}_2, \mathbf{D}_1\mathbf{T}_2, \mathbf{D}_2\mathbf{T}_2, \mathbf{D}_3\mathbf{T}_2, \mathbf{T}_3, \mathbf{C}\mathbf{T}_3, \mathbf{R}_1\mathbf{T}_3, \mathbf{R}_2\mathbf{T}_3, \mathbf{R}_3\mathbf{T}_3, \\ \mathbf{D}_1\mathbf{T}_3, \mathbf{D}_2\mathbf{T}_3, \mathbf{D}_3\mathbf{T}_3, \mathbf{M}_1, \mathbf{C}\mathbf{M}_1, \mathbf{R}_1\mathbf{M}_1, \mathbf{R}_2\mathbf{M}_1, \mathbf{R}_3\mathbf{M}_1, \mathbf{D}_1\mathbf{M}_1, \mathbf{D}_2\mathbf{M}_1, \mathbf{D}_3\mathbf{M}_1, \\ \mathbf{M}_2, \mathbf{C}\mathbf{M}_2, \mathbf{R}_1\mathbf{M}_2, \mathbf{R}_2\mathbf{M}_2, \mathbf{R}_3\mathbf{M}_2, \mathbf{D}_1\mathbf{M}_2, \mathbf{D}_2\mathbf{M}_2, \mathbf{D}_3\mathbf{M}_2, \end{array} \tag{2.140}$$

where $\mathbf{C} = -\mathbf{I}$ is central inversion, $\mathbf{R}_i$ are reflections though planes normal to $\mathbf{e}_i$, $\mathbf{D}_i$ are π rotations about $\mathbf{e}_i$, $\mathbf{T}_1$ is reflection in the plane through the $\mathbf{e}_1$ axis bisecting the angle between $\mathbf{e}_2$ and $\mathbf{e}_3$, $\mathbf{T}_2$ is reflection in the plane through the $\mathbf{e}_2$ axis bisecting the angle between $\mathbf{e}_3$ and $\mathbf{e}_1$, $\mathbf{T}_3$ is reflection in the plane through the $\mathbf{e}_3$ axis bisecting the angle between $\mathbf{e}_1$ and $\mathbf{e}_2$. $\mathbf{M}_1, \mathbf{M}_2$ are rotations of $2\pi/3, 4\pi/3$ respectively about the axis $\mathbf{e}_1+\mathbf{e}_2+\mathbf{e}_3$. These elements are introduced in the book by Green and Adkins (1970).

We will carry out the general procedure for functions $F(\mathbf{A}, \mathbf{B}, \mathbf{v})$ under the elements of the symmetry group given in (2.140). As seen in Table 2.1 this will give us access to $W(\mathbf{E})$, $y(\mathbf{E})$, $\boldsymbol{\Omega}(\mathbf{S})$, $y(\mathcal{E}')$, $\boldsymbol{\Omega}(\mathbf{S}, \dot{\mathbf{S}})$, $y(\mathbf{E}, \boldsymbol{\xi})$. The requirements for each of these functions will be different, that is, we have previously established that $y(\mathbf{E})$ will be even in $\mathbf{E}$ where $\boldsymbol{\Omega}(\mathbf{S})$ will be odd in $\mathbf{S}$. During the derivation we highlight when relevant constitutive equations can be picked out for lower symmetry crystals. For example, note that the elements in (2.140) include the subgroups

$$\mathbf{I}, \mathbf{C}, \mathbf{R}_1, \mathbf{D}_1 \tag{2.141}$$

and

$$\mathbf{I}, \mathbf{C}, \mathbf{R}_1, \mathbf{R}_2, \mathbf{R}_3, \mathbf{D}_1, \mathbf{D}_2, \mathbf{D}_3, \tag{2.142}$$

which characterize the symmetry groups for the monoclinic-prismatic and rhombic-dipyramidal point groups respectively. Constitutive equations for these groups will be pointed out in the course of deriving the representation for the hexoctahedral point group, (2.140).

Before beginning, an important fact to recall is that axial vectors transform under rotations $\mathbf{Q} \in O(3, \mathbb{R})$ as

$$\bar{\mathbf{v}} = \det \mathbf{Q} \mathbf{Q} \mathbf{v}. \tag{2.143}$$

For example, under the reflection $\mathbf{R}_1 = \mathbf{I} - 2\mathbf{e}_1 \otimes \mathbf{e}_1$ we have

$$\bar{\mathbf{v}} = -1(\mathbf{v} - 2\mathbf{v} \cdot \mathbf{e}_1 \mathbf{e}_1) = -\mathbf{v} + 2\mathbf{e}_1 \mathbf{v} \cdot \mathbf{e}_1. \tag{2.144}$$

Therefore these transformations differ from those of vectors (Green and Adkins, 1970, section 1.6).

Integrity basis for cubic crystals. In this section, the general function whose integrity basis we are seeking is the function

$$F = F(\mathbf{A}, \mathbf{B}, \mathbf{v}), \tag{2.145}$$

for which F linear in $\mathbf{v}, \mathbf{B}$, and quadratic in $\mathbf{A}$. This function represents the spin function $\boldsymbol{\Omega}(\mathbf{S}, \dot{\mathbf{S}})$ for the rate independent version in (2.110). The linearity in $\mathbf{v}, \mathbf{B}$ follows from the fact that we are after a skew tensor $\boldsymbol{\Omega}$ and that we have rate independence. The quadratic dependence in $\mathbf{A}$ is largely arbitrary. These restrictions are crucial to keep in mind, otherwise the computational task increases greatly. This function is more complicated than most examples seen in the literature (Green and Adkins, 1970; Spencer, 1971), which focus on single arguments, and so is a useful example to provide. Some familiarity with Green and Adkins (1970) is useful to refer to as a simpler case of the following procedure. The derivation of the function (2.145) also serves as something of a workhorse in this document, since many steps can be retraced with slight modifications for other functions in Table 2.1 which we will make use of.

To begin, consider the effect of the reflection symmetries on F. Under $\mathbf{R}_1$, we have the component transformations

$$\begin{array}{rlll} & \bar{v}_1 = v_1 & \bar{v}_2 = -v_2 & \bar{v}_3 = -v_3 \\ \mathbf{R}_1 : & \bar{A}_{11} = A_{11} & \bar{A}_{22} = A_{22} & \bar{A}_{33} = A_{33} \\ & \bar{A}_{23} = A_{23} & \bar{A}_{13} = -A_{13} & \bar{A}_{12} = -A_{12}. \end{array} \tag{2.146}$$

The transformation properties in (2.146) are the same for $\mathbf{B}$ as $\mathbf{A}$, so we will not list them here. Also note that (2.143) implies that the transformation of $\mathbf{v}$ under $\mathbf{D}_1$ is the same as (2.146), which is not true for a normal vector.

Based on the results of the transformation (2.146), we use Theorem 1 with

$$(y_1, y_2, y_3, y_4, y_5, y_6) = (A_{12}, A_{13}, B_{12}, B_{13}, v_2, v_3)$$

and

$$(z_1, z_2, z_3, z_4, z_5, z_6) = (-A_{12}, -A_{13}, -B_{12}, -B_{13}, -v_2, -v_3),$$

and obtain the following invariant terms, organized in the symmetric array (see (2.133))

$$[K_{ij}](\mathbf{R}_1) = \begin{bmatrix} A_{12}^2 & A_{12}A_{13} & A_{12}B_{12} & A_{12}B_{13} & A_{12}v_2 & A_{12}v_3 \\ & A_{13}^2 & A_{13}B_{12} & A_{13}B_{13} & A_{13}v_2 & A_{13}v_3 \\ & & B_{12}^2 & B_{12}B_{13} & B_{12}v_2 & B_{12}v_3 \\ & & & B_{13}^2 & B_{13}v_2 & B_{13}v_3 \\ & & & & v_2^2 & v_2v_3 \\ \text{sym} & & & & & v_3^2 \end{bmatrix}. \tag{2.147}$$

Next, $\mathbf{D}_2$ gives the transformations (equivalent to $\mathbf{R}_2$)

$$\mathbf{D}_2: \begin{array}{lll} \bar{v}_1 = -v_1 & \bar{v}_2 = v_2 & \bar{v}_3 = -v_3 \\ \bar{A}_{11} = A_{11} & \bar{A}_{22} = A_{22} & \bar{A}_{33} = A_{33} \\ \bar{A}_{23} = -A_{23} & \bar{A}_{13} = A_{13} & \bar{A}_{12} = -A_{12}. \end{array} \tag{2.148}$$

In the function we require for the current analysis, the product v_2v_3 will not appear at the order we are considering. The result of the transformation $\mathbf{D}_2$, indicates again using Theorem 1, with $\{y_i\}, \{z_i\} = (\pm)\{A_{23}, B_{23}, v_1, A_{13}A_{12}, A_{13}B_{12}, A_{12}B_{13}, A_{12}v_2, A_{13}v_3, B_{12}v_2, B_{13}v_3\}$ and obtain the new integrity elements

$[K_{ij}](\mathbf{D}_2) =$

$$\begin{array}{cccccccccc} A_{23}^2 & A_{23}B_{23} & [A_{23}v_1] & A_{23}A_{12}B_{13} & A_{23}A_{13}B_{12} & [A_{23}A_{12}v_2] & [A_{23}A_{13}v_3] & [A_{23}B_{12}v_2] & [A_{23}B_{13}v_3] & A_{23}A_{12}A_{13} \\ & B_{23}^2 & [B_{23}v_1] & B_{23}A_{12}B_{13} & B_{23}A_{13}B_{12} & [B_{23}A_{12}v_2] & [B_{23}A_{13}v_3] & B_{23}B_{12}v_2 & B_{23}B_{13}v_3 & B_{23}A_{12}A_{13} \\ & & v_1^2 & [v_1A_{12}B_{13}] & [v_1A_{13}B_{12}] & v_1A_{12}v_2 & v_1A_{13}v_3 & v_1B_{12}v_2 & v_1B_{13}v_3 & v_1A_{12}A_{13} \\ & & & A_{12}^2B_{13}^2 & A_{12}B_{13}A_{13}B_{12} & A_{12}B_{13}A_{12}v_2 & A_{12}B_{13}A_{13}v_3 & A_{12}B_{13}B_{12}v_2 & A_{12}B_{13}B_{13}v_3 & A_{12}B_{13}A_{12}A_{13} \\ & & & & A_{13}^2B_{12}^2 & A_{13}B_{12}A_{12}v_2 & A_{13}B_{12}A_{13}v_3 & A_{13}B_{12}B_{12}v_2 & A_{13}B_{12}B_{13}v_3 & B_{12}A_{13}A_{12}A_{13} \\ & & & & & A_{12}^2v_2^2 & A_{12}v_2A_{13}v_3 & A_{12}v_2B_{12}v_2 & A_{12}v_2B_{13}v_3 & A_{12}v_2A_{12}A_{13} \\ & & & & & & A_{13}^2v_3^2 & A_{13}v_3B_{12}v_2 & A_{13}v_3B_{13}v_3 & A_{13}v_3A_{12}A_{13} \\ & & & & & & & B_{12}^2v_2^2 & B_{12}v_2B_{13}v_3 & B_{12}v_2A_{12}A_{13} \\ & & & & & & & & B_{13}^2v_3^{2\,2} & B_{13}v_3A_{12}A_{13} \\ sym & & & & & & & & & \end{array} \tag{2.149}$$

Next, we can reduce the basis elements developed in Equations (2.147), (2.149). For example, in calculating $\boldsymbol{\Omega}(\mathbf{S}, \dot{\mathbf{S}})$ we need terms which multiply $\mathbf{v}$ linearly (since in the end we apply Equation (2.129)). It is required to carry out the reductions with this in mind; else we would be clearly be buried in symbols. The other requirement to recall is that we want a linear function in $\mathbf{B}$, ($\mathbf{B}$ represents $\dot{\mathbf{S}}$), which we must have for rate independence, see (2.92). Therefore, we will look at expansions up to order $(2, 1, 1)$, where the indices in the array of polynomial order, (i, j, k), indicates that entries of $\mathbf{A}$ have index i, entries of $\mathbf{B}$ have index j, and entries of $\mathbf{v}$ have index k. With this we can immediately drop from consideration terms which have higher order terms in $\mathbf{B}, \mathbf{v}$. In (2.149), terms which we will accept in the representation of F are highlighted by braces [()]. After this reduction we have the function

$$F = F\left(\begin{array}{l} A_{11}, A_{22}, A_{33}, B_{11}, B_{22}, B_{33}, A_{23}v_1, A_{13}v_2, A_{12}v_3, B_{23}v_1, B_{13}v_2, B_{12}v_3 \\ v_1A_{12}B_{13}, v_1A_{13}B_{12}, B_{23}A_{12}v_2, A_{23}B_{12}v_2, B_{23}A_{13}v_3, A_{23}B_{13}v_3, \\ A_{12}^2, A_{13}^2, A_{23}^2, A_{12}B_{12}, A_{13}B_{13}, A_{23}B_{23}, A_{23}A_{12}v_2, A_{23}A_{13}v_3, v_1A_{12}A_{13} \end{array}\right). \tag{2.150}$$

Equation (2.150) turns out to also be invariant under $\mathbf{D}_3$. Equation (2.150) therefore characterizes the integrity basis for the plastic spin $\boldsymbol{\Omega}(\mathbf{S}, \dot{\mathbf{S}})$ through the rhombic classes, (2.142). To completely write down the function, apply the expansion technique of (2.139) up to order $(2, 1, 1)$ in $\mathbf{A}, \mathbf{B}, \mathbf{v}$. Then executing (2.129) gives the spin. This expansion is also sufficient to characterize the yield function incorporating dislocation content, $y(\mathbf{E}, \boldsymbol{\xi})$, with the caveat that we have not retained quadratic powers of $\boldsymbol{\xi}$. Since quadratic dependence on $\boldsymbol{\xi}$ is probably desirable, we revisit this issue in a later discussion. The spin function for the monoclinic class (2.141) would be obtained by taking all terms in (2.147) which are of order ≤ 1 in powers of v_i.

To complete the constitutive framework for the rhombic and monoclinic classes, we can consider the functions $W(\mathbf{E}), y(\mathbf{E})$, to quadratic order in a single symmetric argument. Following the previous steps with these functional arguments we have the integrity basis

$$F = F(A_{11}, A_{22}, A_{33}, A_{23}^2, A_{13}^2, A_{12}^2). \tag{2.151}$$

Taking this a step further, of relevance to $y(\mathcal{E}') = y(\text{sym } \mathcal{E}', \text{skw } \mathcal{E}')$ to quadratic order, we have the integrity basis

$$F = F(A_{11}, A_{22}, A_{33}, A_{23}v_1, A_{13}v_2, A_{12}v_3, A_{23}^2, A_{13}^2, A_{12}^2, v_1^2, v_2^2, v_3^2). \tag{2.152}$$

The basis elements in (2.151) and (2.152) are also invariant under the transformations $\mathbf{R}_3, \mathbf{D}_3$. Therefore these functions are completed up to the rhombic point group symmetry. For the monoclinic system these same two functions are given by the forms

$$F = F(A_{11}, A_{22}, A_{33}, A_{23}, A_{13}^2, A_{12}^2, A_{12}A_{13}) \tag{2.153}$$

and

$$F = F(A_{11}, A_{22}, A_{33}, A_{23}, A_{13}^2, A_{12}^2, A_{12}A_{13}, v_1, v_2v_3, v_2^2, v_3^2, A_{13}v_2, A_{13}v_3, A_{12}v_2, A_{12}v_3). \tag{2.154}$$

Again, to completely write down the polynomial function, we would apply the expansion technique of (2.139). For the yield function we would look at order 2 in $\mathbf{A}$, and for the function based on Eshelby stress we would go to the order $(2, 0)$, $(0, 2)$, $(1, 1)$ in $\mathbf{A}, \mathbf{v}$. Clearly these constitutive functions represent experimental challenges in terms of validation for low symmetry crystals, since an enormous number of material parameters are rapidly required, each of which must be measured. Things improve somewhat for cubic symmetry; we now continue the derivation leading to that result.

To briefly summarize to this point, after consideration of the actions of $\mathbf{D}_1$, $\mathbf{D}_2$, $\mathbf{D}_3$, $\mathbf{R}_1$, $\mathbf{R}_2$, $\mathbf{R}_3$ the invariant function for spin is given by (2.150). Next consider the action of $\mathbf{M}_1, \mathbf{M}_2$, the rotations through the cube diagonal. These actions give the transformations

$$\begin{array}{rlll} & \bar{v}_1 = v_2 & \bar{v}_2 = v_3 & \bar{v}_3 = v_1 \\ \mathbf{M}_1: & \bar{A}_{11} = A_{22} & \bar{A}_{22} = A_{33} & \bar{A}_{33} = A_{11} \\ & \bar{A}_{23} = A_{13} & \bar{A}_{13} = A_{12} & \bar{A}_{12} = A_{23}, \end{array} \tag{2.155}$$

$$\begin{array}{lccc} & \bar{v}_1 = v_3 & \bar{v}_2 = v_1 & \bar{v}_3 = v_2 \\ \mathbf{M}_2: & \bar{A}_{11} = A_{33} & \bar{A}_{22} = A_{11} & \bar{A}_{33} = A_{22} \\ & \bar{A}_{23} = A_{12} & \bar{A}_{13} = A_{23} & \bar{A}_{12} = A_{13}. \end{array} \tag{2.156}$$

Considering both transformations, we have the equivalences

$$\begin{aligned} F(\mathbf{A},\mathbf{B},\mathbf{v}) &= F\left(\begin{array}{l} A_{11}, A_{22}, A_{33}, B_{11}, B_{22}, B_{33}, A_{23}v_1, A_{13}v_2, A_{12}v_3, B_{23}v_1, B_{13}v_2, B_{12}v_3 \\ v_1A_{12}B_{13}, v_1A_{13}B_{12}, B_{23}A_{12}v_2, A_{23}B_{12}v_2, B_{23}A_{13}v_3, A_{23}B_{13}v_3, ... \end{array}\right) \\ &= F\left(\begin{array}{l} A_{22}, A_{33}, A_{11}, B_{22}, B_{33}, B_{11}, A_{13}v_2, A_{12}v_3, A_{23}v_1, B_{13}v_2, B_{12}v_3, B_{23}v_1 \\ v_3A_{13}B_{23}, v_3A_{23}B_{13}, B_{12}A_{13}v_1, A_{12}B_{13}v_1, B_{12}A_{23}v_1, A_{12}B_{23}v_2, ... \end{array}\right) \\ &= F\left(\begin{array}{l} A_{33}, A_{11}, A_{22}, B_{33}, B_{11}, B_{22}, A_{23}v_1, A_{13}v_2, A_{12}v_3, B_{23}v_1, B_{13}v_2, B_{12}v_3 \\ v_2A_{23}B_{12}, v_2A_{12}B_{23}, B_{13}A_{23}v_3, A_{13}B_{23}v_3, B_{13}A_{12}v_2, A_{13}B_{12}v_1, ... \end{array}\right). \end{aligned} \tag{2.157}$$

The transformations of (2.157) are therefore cyclic in the grouped quantities

$$\begin{array}{l} (A_{11}, A_{22}, A_{33}), (B_{11}, B_{22}, B_{33}), (A_{23}v_1, A_{13}v_2, A_{12}v_3), (B_{23}v_1, B_{13}v_2, B_{12}v_3), \\ (v_1A_{12}B_{13}, v_3A_{13}B_{23}, v_2A_{23}B_{12}), (v_1A_{13}B_{12}, v_3A_{23}B_{13}, v_2A_{12}B_{23}), (A_{12}^2, A_{13}^2, A_{23}^2), \\ (A_{12}B_{12}, A_{13}B_{13}, A_{23}B_{23}), (A_{23}A_{12}v_2, A_{23}A_{13}v_3, v_1A_{12}A_{13}). \end{array} \tag{2.158}$$

We see that these satisfy the conditions of Theorem 6. Restricting attention only up to order (2,1,1), we see from Theorem 6, which includes (2.134), that the lowest order terms $(2.134)_1$ are given by the sums of the 9 cycles in (2.158):

$$\begin{array}{l} (A_{11} + A_{22} + A_{33}), (B_{11} + B_{22} + B_{33}), (A_{23}v_1 + A_{13}v_2 + A_{12}v_3), (B_{23}v_1 + B_{13}v_2 + B_{12}v_3), \\ (v_1A_{12}B_{13} + v_3A_{13}B_{23} + v_2A_{23}B_{12}), (v_1A_{13}B_{12} + v_3A_{23}B_{13} + v_2A_{12}B_{23}), (A_{12}^2 + A_{13}^2 + A_{23}^2), \\ (A_{12}B_{12} + A_{13}B_{13} + A_{23}B_{23}), (A_{23}A_{12}v_2 + A_{23}A_{13}v_3 + v_1A_{12}A_{13}). \end{array} \tag{2.159}$$

Due to the appearance of the term $|\epsilon_{ijk}|B_{ij}v_k$ in (2.159) we also need to retain the quadratic combination of (A_{11}, A_{22}, A_{33}) in the final expansion for F, so we must also include the term

$$A_{11}A_{33} + A_{22}A_{33} + A_{33}A_{11}. \tag{2.160}$$

We now examine the higher order combinations between terms in (2.158). For purposes of shorthand convenience, denote the cyclic triples in (2.158) by the designations (in respective order)

$$A, B, Av, Bv, (vAB)_1, (vAB)_2, A^2, AB, A^2v. \tag{2.161}$$

Then taking a combination of terms in (2.161) we use the notation (for the terms A, B in (2.161))

$$A, B : [...] \tag{2.162}$$

where [...] follows from applying Theorem 6, which includes for example (2.135) and (2.137). If the combination would produce a term of order greater than (2,1,1), that term is not

recorded in the following. Therefore, taking all combinations of terms in (2.161) gives

$$\begin{array}{l} A,(vA):(A_{11},A_{22},A_{33}),(A_{23}v_1,A_{13}v_2,A_{12}v_3): \\ A_{11}A_{23}v_1+A_{22}A_{13}v_2+A_{33}A_{12}v_3, \\ A_{23}v_1(A_{22}-A_{33})+A_{13}v_2(A_{33}-A_{11})+A_{12}v_3(A_{11}-A_{22}), \end{array} \tag{2.163}$$

$$\begin{array}{l} A,(vAB)_1:(A_{11},A_{22},A_{33}),(v_1A_{12}B_{13},v_2A_{23}B_{12},v_3A_{13}B_{23}),: \\ v_1A_{12}B_{13}A_{11}+v_2A_{23}B_{12}A_{22}+v_3A_{13}B_{23}A_{33}, \\ v_1A_{12}B_{13}\left(A_{22}-A_{33}\right)+v_2A_{23}B_{12}\left(A_{33}-A_{11}\right)+v_3A_{13}B_{23}\left(A_{11}-A_{22}\right), \end{array} \tag{2.164}$$

$$\begin{array}{l} A,(vAB)_2:(v_1A_{13}B_{12},v_2A_{12}B_{23},v_3A_{23}B_{13}),(A_{11},A_{22},A_{33}): \\ v_1A_{13}B_{12}A_{11}+v_2A_{12}B_{23}A_{22}+v_3A_{23}B_{13}A_{33}, \\ v_1A_{13}B_{12}\left(A_{22}-A_{33}\right)+v_2A_{12}B_{23}\left(A_{33}-A_{11}\right)+v_3A_{23}B_{13}\left(A_{11}-A_{22}\right), \end{array} \tag{2.165}$$

$$\begin{array}{l} A,vB:(B_{23}v_1,B_{13}v_2,B_{12}v_3),(A_{11},A_{22},A_{33}): \\ B_{23}v_1A_{11}+B_{13}v_2A_{22}+B_{12}v_3A_{33}, \\ B_{23}v_1A_{22}A_{33}+B_{13}v_2A_{33}A_{11}+B_{12}v_3A_{11}A_{22}, \\ B_{23}v_1\left(A_{22}-A_{33}\right)+B_{13}v_2\left(A_{33}-A_{11}\right)+B_{12}v_3\left(A_{11}-A_{22}\right), \\ A_{22}A_{33}\left(B_{13}v_2-B_{12}v_3\right)+A_{33}A_{11}\left(B_{12}v_3-B_{23}v_1\right)+A_{11}A_{22}\left(B_{23}v_1-B_{13}v_2\right), \end{array} \tag{2.166}$$

$$\begin{array}{l} Av,B:B_{11},B_{22},B_{33},A_{23}v_1,A_{13}v_2,A_{12}v_3 \\ A_{23}v_1B_{11}+A_{13}v_2B_{22}+A_{12}v_3B_{33}, \\ A_{23}v_1\left(B_{22}-B_{33}\right)+A_{13}v_2\left(B_{33}-B_{11}\right)+A_{12}v_3\left(B_{11}-B_{22}\right), \end{array} \tag{2.167}$$

$$\begin{array}{l} A^2,vB:(B_{23}v_1,B_{13}v_2,B_{12}v_3),(A_{12}^2,A_{13}^2,A_{23}^2): \\ B_{23}v_1A_{12}^2+B_{13}v_2A_{13}^2+B_{12}v_3A_{23}^2, \\ B_{23}v_1\left(A_{13}^2-A_{23}^2\right)+B_{13}v_2\left(A_{23}^2-A_{12}^2\right)+B_{12}v_3\left(A_{12}^2-A_{13}^2\right), \end{array} \tag{2.168}$$

$$\begin{array}{l} AB,vA:(A_{23}B_{23},A_{13}B_{13},A_{12}B_{12}),(A_{23}v_1,A_{13}v_2,A_{12}v_3): \\ A_{23}v_1A_{23}B_{23}+A_{13}v_2A_{13}B_{13}+A_{12}v_3A_{12}B_{12}, \\ A_{23}v_1\left(A_{13}B_{13}-A_{12}B_{12}\right)+A_{13}v_2\left(A_{12}B_{12}-A_{23}B_{23}\right)+A_{12}v_3\left(A_{23}B_{23}-A_{13}B_{13}\right), \end{array} \tag{2.169}$$

$$\begin{array}{l} A^2v,B:(v_1A_{12}A_{13},A_{23}A_{12}v_2,A_{23}A_{13}v_3),(B_{11},B_{22},B_{33}): \\ v_1A_{12}A_{13}B_{11}+A_{23}A_{12}v_2B_{22}+A_{23}A_{13}v_3B_{33}, \\ v_1A_{12}A_{13}\left(B_{22}-B_{33}\right)+A_{23}A_{12}v_2\left(B_{33}-B_{11}\right)+A_{23}A_{13}v_3\left(B_{11}-B_{22}\right), \end{array} \tag{2.170}$$

and

$$\begin{array}{l} B,A,Av:(B_{11},B_{22},B_{33}),(A_{11},A_{22},A_{33}),(A_{23}v_1,A_{13}v_2,A_{12}v_3), \\ B_{11}A_{11}A_{23}v_1+B_{22}A_{22}A_{13}v_2+B_{33}A_{33}A_{12}v_3, \\ B_{11}A_{11}\left(A_{13}v_2-A_{12}v_3\right)+B_{22}A_{22}\left(A_{12}v_3-A_{23}v_1\right)+B_{33}A_{33}\left(A_{23}v_1-A_{13}v_2\right). \end{array} \tag{2.171}$$

The integrity elements listed thus far in (2.164) to (2.171) are representative of the tetartoidal and diploidal point groups in the cubic class. Continuing our march to hexoctahedral, we

consider the element $\mathbf{T}_3$. We have the transformation

$$\begin{array}{rlll} & \bar{v}_1 = v_2 & \bar{v}_2 = v_1 & \bar{v}_3 = -v_3 \\ \mathbf{T}_3: & \bar{A}_{11} = A_{22} & \bar{A}_{22} = A_{11} & \bar{A}_{33} = A_{33} \\ & \bar{A}_{23} = -A_{13} & \bar{A}_{13} = -A_{23} & \bar{A}_{12} = A_{12}. \end{array} \tag{2.172}$$

In passing, note that these are different results for $\mathbf{T}_3$ than given in (Green and Adkins, 1970, p. 12), however we believe his results reporting the strain energy function in the end were correct, perhaps since he was only considering single arguments into the scalar function. We need to also consider the transformation of the terms of (2.159). Upon the action of $\mathbf{T}_3$ we have the results

$$\begin{array}{l} \bar{A}_{23}\bar{v}_1 + \bar{A}_{13}\bar{v}_2 + \bar{A}_{12}\bar{v}_3 = -A_{13}v_2 - A_{23}v_1 - A_{12}v_3 \\ \bar{A}_{23}\bar{A}_{12}\bar{v}_2 + \bar{A}_{23}\bar{A}_{13}\bar{v}_3 + \bar{v}_1\bar{A}_{12}\bar{A}_{13} = -A_{13}A_{12}v_1 - A_{13}A_{23}v_3 - v_1A_{12}A_{13} \\ \bar{v}_1\bar{A}_{12}\bar{B}_{13}, \bar{v}_3\bar{A}_{13}\bar{B}_{23}, \bar{v}_2\bar{A}_{23}\bar{B}_{12} = -v_2A_{12}B_{23} - v_3A_{23}B_{13} - v_1A_{13}B_{12} \\ \bar{v}_1\bar{A}_{13}\bar{B}_{12}, \bar{v}_3\bar{A}_{23}\bar{B}_{13}, \bar{v}_2\bar{A}_{12}\bar{B}_{23} = -v_2A_{23}B_{12} - v_3A_{13}B_{23} - v_1A_{12}B_{13}. \end{array} \tag{2.173}$$

Therefore, upon application of Theorem 1, the first two invariants in (2.173) thus disappear from consideration since they are only retained as terms of order (2,0,2) and (4,0,2), respectively. The second two terms in (2.173) are retained by Theorem 1. Additionally, the term analogous to $(2.173)_1$, $|\epsilon_{ijk}|B_{ij}v_k$, is removed. With no terms of order $(0,1,1)$ remaining, we can also remove the (2,0,0) term (2.160). Now consider the transformation of the higher order terms under $\mathbf{T}_3$. In these transformations the terms on the left hand side are considered in the $(\bar{\cdot})$ frame.

$$\begin{array}{l} A, (vA) : (A_{11}, A_{22}, A_{33}), (A_{23}v_1, A_{13}v_2, A_{12}v_3) : \\ A_{11}A_{23}v_1 + A_{22}A_{13}v_2 + A_{33}A_{12}v_3 \rightarrow \\ -A_{22}A_{13}v_2 - A_{11}A_{23}v_1 - A_{33}A_{12}v_3, \\ A_{23}v_1(A_{22} - A_{33}) + A_{13}v_2(A_{33} - A_{11}) + A_{12}v_3(A_{11} - A_{22}) \rightarrow \\ -A_{13}v_2(A_{11} - A_{33}) - A_{23}v_1(A_{33} - A_{22}) - A_{12}v_3(A_{22} - A_{11}) \end{array} \tag{2.174}$$

$$\begin{array}{l} A, vAB_1 : (v_1A_{12}B_{13}, v_2A_{23}B_{12}, v_3A_{13}B_{23}), (A_{11}, A_{22}, A_{33}) : \\ v_1A_{12}B_{13}A_{11} + v_2A_{23}B_{12}A_{22} + v_3A_{13}B_{23}A_{33} \rightarrow -v_2A_{12}B_{23}A_{22} - v_1A_{13}B_{12}A_{11} - v_3A_{23}B_{13}A_{33}, \\ v_1A_{12}B_{13}(A_{22} - A_{33}) + v_2A_{23}B_{12}(A_{33} - A_{11}) + v_3A_{13}B_{23}(A_{11} - A_{22}) \rightarrow \\ -v_2A_{12}B_{23}(A_{11} - A_{33}) - v_1A_{13}B_{12}(A_{33} - A_{22}) - v_3A_{23}B_{13}(A_{22} - A_{11}) \end{array} \tag{2.175}$$

$$\begin{array}{l} A, vAB_2 : (v_1A_{13}B_{12}, v_2A_{12}B_{23}, v_3A_{23}B_{13}), (A_{11}, A_{22}, A_{33}) : \\ v_1A_{13}B_{12}A_{11} + v_2A_{12}B_{23}A_{22} + v_3A_{23}B_{13}A_{33} \rightarrow -v_2A_{23}B_{12}A_{22} - v_1A_{12}B_{13}A_{11} - v_3A_{13}B_{23}A_{33}, \\ v_1A_{13}B_{12}(A_{22} - A_{33}) + v_2A_{12}B_{23}(A_{33} - A_{11}) + v_3A_{23}B_{13}(A_{11} - A_{22}) \rightarrow \\ -v_2A_{23}B_{12}(A_{11} - A_{33}) - v_1A_{12}B_{13}(A_{33} - A_{22}) - v_3A_{13}B_{23}(A_{22} - A_{11}) \end{array} \tag{2.176}$$

$$
\begin{array}{l}
A, vB : \left(B_{23}v_1, B_{13}v_2, B_{12}v_3\right), \left(A_{11}, A_{22}, A_{33}\right) : \\
B_{23}v_1A_{11} + B_{13}v_2A_{22} + B_{12}v_3A_{33} \rightarrow -B_{13}v_2A_{22} - B_{23}v_1A_{11} - B_{12}v_3A_{33}, \\
B_{23}v_1A_{22}A_{33} + B_{13}v_2A_{33}A_{11} + B_{12}v_3A_{11}A_{22} \rightarrow -B_{13}v_2A_{11}A_{33} - B_{23}v_1A_{33}A_{22} - B_{12}v_3A_{22}A_{11}, \\
B_{23}v_1\left(A_{22} - A_{33}\right) + B_{13}v_2\left(A_{33} - A_{11}\right) + B_{12}v_3\left(A_{11} - A_{22}\right) \rightarrow \\
-B_{13}v_2\left(A_{11} - A_{33}\right) - B_{23}v_1\left(A_{33} - A_{22}\right) - B_{12}v_3\left(A_{22} - A_{11}\right), \\
A_{22}A_{33}\left(B_{13}v_2 - B_{12}v_3\right) + A_{33}A_{11}\left(B_{12}v_3 - B_{23}v_1\right) + A_{11}A_{22}\left(B_{23}v_1 - B_{13}v_2\right) \rightarrow \\
-A_{11}A_{33}\left(B_{23}v_1 - B_{12}v_3\right) - A_{33}A_{22}\left(B_{12}v_3 - B_{13}v_2\right) - A_{22}A_{11}\left(B_{13}v_2 - B_{23}v_1\right)
\end{array}
\tag{2.177}
$$

$$
\begin{array}{l}
Av, B : \left(B_{11}, B_{22}, B_{33}\right), \left(A_{23}v_1, A_{13}v_2, A_{12}v_3\right) \\
A_{23}v_1B_{11} + A_{13}v_2B_{22} + A_{12}v_3B_{33} \rightarrow -A_{13}v_2B_{22} - A_{23}v_1B_{11} - A_{12}v_3B_{33}, \\
A_{23}v_1\left(B_{22} - B_{33}\right) + A_{13}v_2\left(B_{33} - B_{11}\right) + A_{12}v_3\left(B_{11} - B_{22}\right) \rightarrow \\
-A_{13}v_2\left(B_{11} - B_{33}\right) - A_{23}v_1\left(B_{33} - B_{22}\right) - A_{12}v_3\left(B_{22} - B_{11}\right)
\end{array}
\tag{2.178}
$$

$$
\begin{array}{l}
A^2, vB : \left(B_{23}v_1, B_{13}v_2, B_{12}v_3\right), \left(A_{12}^2, A_{13}^2, A_{23}^2\right) : \\
B_{23}v_1A_{12}^2 + B_{13}v_2A_{13}^2 + B_{12}v_3A_{23}^2 \rightarrow -B_{13}v_2A_{12}^2 - B_{23}v_1A_{23}^2 - B_{12}v_3A_{13}^2, \\
B_{23}v_1\left(A_{13}^2 - A_{12}^2\right) + B_{13}v_2\left(A_{12}^2 - A_{23}^2\right) + B_{12}v_3\left(A_{23}^2 - A_{13}^2\right) \rightarrow \\
-B_{13}v_2\left(A_{23}^2 - A_{12}^2\right) - B_{23}v_1\left(A_{12}^2 - A_{13}^2\right) - B_{12}v_3\left(A_{13}^2 - A_{23}^2\right)
\end{array}
\tag{2.179}
$$

$$
\begin{array}{l}
AB, vA : \left(A_{23}B_{23}, A_{13}B_{13}, A_{12}B_{12}\right), \left(A_{23}v_1, A_{13}v_2, A_{12}v_3\right) : \\
A_{23}v_1A_{23}B_{23} + A_{13}v_2A_{13}B_{13} + A_{12}v_3A_{12}B_{12} \rightarrow -A_{13}v_2A_{13}B_{13} - A_{23}v_1A_{23}B_{23} - A_{12}v_3A_{12}B_{12}, \\
A_{23}v_1\left(A_{13}B_{13} - A_{12}B_{12}\right) + A_{13}v_2\left(A_{12}B_{12} - A_{23}B_{23}\right) + A_{12}v_3\left(A_{23}B_{23} - A_{13}B_{13}\right) \rightarrow \\
-A_{13}v_2\left(A_{23}B_{23} - A_{12}B_{12}\right) - A_{23}v_1\left(A_{12}B_{12} - A_{13}B_{13}\right) - A_{12}v_3\left(A_{13}B_{13} - A_{23}B_{23}\right)
\end{array}
\tag{2.180}
$$

$$
\begin{array}{l}
A^2v, B : \left(v_1A_{12}A_{13}, A_{23}A_{12}v_2, A_{23}A_{13}v_3\right), \left(B_{11}, B_{22}, B_{33}\right) : \\
v_1A_{12}A_{13}B_{11} + A_{23}A_{12}v_2B_{22} + A_{23}A_{13}v_3B_{33} \rightarrow \\
-v_2A_{12}A_{23}B_{22} - A_{13}A_{12}v_1B_{11} - A_{13}A_{23}v_3B_{33}, \\
v_1A_{12}A_{13}\left(B_{22} - B_{33}\right) + A_{23}A_{12}v_2\left(B_{33} - B_{11}\right) + A_{23}A_{13}v_3\left(B_{11} - B_{22}\right) \rightarrow \\
-v_2A_{12}A_{23}\left(B_{11} - B_{33}\right) - A_{13}A_{12}v_1\left(B_{33} - B_{22}\right) - A_{13}A_{23}v_3\left(B_{22} - B_{11}\right)
\end{array}
\tag{2.181}
$$

$$
\begin{array}{l}
A, B, Av : \left(A_{11}, A_{22}, A_{33}\right), \left(B_{11}, B_{22}, B_{33}\right), \left(A_{23}v_1, A_{13}v_2, A_{12}v_3\right) : \\
B_{11}A_{11}A_{23}v_1 + B_{22}A_{22}A_{13}v_2 + B_{33}A_{33}A_{12}v_3 \rightarrow \\
-B_{22}A_{22}A_{13}v_2 - B_{11}A_{11}A_{23}v_1 - B_{33}A_{33}A_{12}v_3, \\
B_{11}A_{11}\left(A_{13}v_2 - A_{12}v_3\right) + B_{22}A_{22}\left(A_{12}v_3 - A_{23}v_1\right) + B_{33}A_{33}\left(A_{23}v_1 - A_{13}v_2\right) \rightarrow \\
-B_{22}A_{22}\left(A_{23}v_1 - A_{12}v_3\right) - B_{11}A_{11}\left(A_{12}v_3 - A_{13}v_1\right) - B_{33}A_{33}\left(A_{13}v_2 - A_{23}v_1\right)
\end{array}
\tag{2.182}
$$

Applying Theorem 1_1 to the results gives the final integrity basis elements. Theorem 1_2 need not be considered since it gives higher order contributions, as encountered previously in the text after Equation (2.173). In other words, many terms are eliminated after use of Theorem 1, since they must be squared after elimination by Theorem 1_1 and hence are no longer linear in v. Final terms in the integrity basis are the terms given by the higher order

combinations with shorthand designations

$$\begin{array}{l} i_0 = (A, vA)_2, i_1 = (A, vAB_1)_1 - (A, vAB_2)_1, \quad i_2 = (A, vAB_1)_2 - (A, vAB_2)_2, \\ i_3 = (A, vB)_3, \quad i_4 = (A, vB)_4, \quad i_5 = (Av, B)_2, \quad i_6 = (A^2, Bv)_2, \\ i_7 = (AB, Av)_2, \quad i_8 = (A^2v, B)_2, \quad i_9 = (B, A, Av)_2, \quad i_{10} = vAB_1 - vAB_2, \end{array} \tag{2.183}$$

where the subscripts (e.g. the 2 in the shorthand $(A, vA)_2$) denotes the line in the associated result from the previous equations; in the particular case of $(A, vA)_2$, $(A, vA)_2$ denotes the first term from line 2 of Equation (2.174), which (2.174) demonstrates is invariant under $\mathbf{T}_3$. The explicit integrity elements from $i_0, ..., i_{10}$ in (2.183) are denoted as

$$\begin{array}{l} w_1^{(2,0,1)} = A_{23}v_1(A_{22} - A_{33}) + A_{13}v_2(A_{33} - A_{11}) + A_{12}v_3(A_{11} - A_{22}) \\ y_1^{(1,1,1)} = v_1A_{13}B_{12} + v_3A_{23}B_{13} + v_2A_{12}B_{23} - v_2A_{23}B_{12} - v_3A_{13}B_{23} - v_1A_{12}B_{13} \\ y_2^{(1,1,1)} = B_{23}v_1\left(A_{22} - A_{33}\right) + B_{13}v_2\left(A_{33} - A_{11}\right) + B_{12}v_3\left(A_{11} - A_{22}\right) \\ y_3^{(1,1,1)} = A_{23}v_1\left(B_{22} - B_{33}\right) + A_{13}v_2\left(B_{33} - B_{11}\right) + A_{12}v_3\left(B_{11} - B_{22}\right) \\ z_1^{(2,1,1)} = v_1A_{12}B_{13}A_{11} + v_2A_{23}B_{12}A_{22} + v_3A_{13}B_{23}A_{33} \\ -v_1A_{13}B_{12}A_{11} - v_2A_{12}B_{23}A_{22} - v_3A_{23}B_{13}A_{33} \\ z_2^{(2,1,1)} = v_1A_{12}B_{13}(A_{22} - A_{33}) + v_2A_{23}B_{12}(A_{33} - A_{11}) + v_3A_{13}B_{23}(A_{11} - A_{22}) \\ -v_2A_{12}B_{23}(A_{11} - A_{33}) - v_1A_{13}B_{12}(A_{33} - A_{22}) - v_3A_{23}B_{13}(A_{22} - A_{11}) \\ z_3^{(2,1,1)} = A_{22}A_{33}\left(B_{13}v_2 - B_{12}v_3\right) + A_{33}A_{11}\left(B_{12}v_3 - B_{23}v_1\right) + A_{11}A_{22}\left(B_{23}v_1 - B_{13}v_2\right) \\ z_4^{(2,1,1)} = B_{23}v_1\left(A_{13}^2 - A_{12}^2\right) + B_{13}v_2\left(A_{12}^2 - A_{23}^2\right) + B_{12}v_3\left(A_{23}^2 - A_{13}^2\right) \\ z_5^{(2,1,1)} = A_{23}v_1\left(A_{13}B_{13} - A_{12}B_{12}\right) + A_{13}v_2\left(A_{12}B_{12} - A_{23}B_{23}\right) + A_{12}v_3\left(A_{23}B_{23} - A_{13}B_{13}\right) \\ z_6^{(2,1,1)} = v_1A_{12}A_{13}\left(B_{22} - B_{33}\right) + A_{23}A_{12}v_2\left(B_{33} - B_{11}\right) + A_{23}A_{13}v_3\left(B_{11} - B_{22}\right) \\ z_7^{(2,1,1)} = B_{11}A_{11}\left(A_{13}v_2 - A_{12}v_3\right) + B_{22}A_{22}\left(A_{12}v_3 - A_{23}v_1\right) + B_{33}A_{33}\left(A_{23}v_1 - A_{13}v_2\right), \end{array} \tag{2.184}$$

where the notation $(\cdot)^{(i,j,k)}$ denotes the order of the term in powers of $\mathbf{A}, \mathbf{B}, \mathbf{v}$, as used previously in this section. To complete the expansion we also need accounting of the lower order terms

$$\begin{array}{l} x_1^{(1,0,0)} = A_{11} + A_{22} + A_{33} \\ x_1^{(0,1,0)} = B_{11} + B_{22} + B_{33}. \end{array} \tag{2.185}$$

Putting it all together, in (2.184) we have the expansion

$$F(\mathbf{A}, \mathbf{B}, \mathbf{v}) = \sum_i \sum_j b_{ij}^{(1,0,0)} x_i^{(1,0,0)} y_j + \sum_i \sum_j b_{ij}^{(0,1,0)} x_i^{(0,1,0)} w_j + \sum_i c_i z_i \tag{2.186}$$

for a total of $(|\{b_{ij}^{(1,0,0)}\}| = 3) + (|\{b_{ij}^{(0,1,0)}\}| = 1) + (|\{c_i\}| = 7) = 11$ constants. This basis holds under all other transformations in the hexoctahedral point group, so it is indeed the integrity basis. Additionally, it is valid for hextetrahedral and gyroidal point groups as well. The spin $\mathbf{\Omega}$ is finally given by executing Equation (2.129) on (2.186). The tensor components of the spin are

$$\Omega_{23} = -\partial F/\partial v_1 \quad \Omega_{13} = \partial F/\partial v_2 \quad \Omega_{12} = -\partial F/\partial v_3 \tag{2.187}$$

with the matrix representation

$$[\mathbf{\Omega}] = \begin{bmatrix} 0 & \Omega_{12} & \Omega_{13} \\ -\Omega_{12} & 0 & \Omega_{23} \\ -\Omega_{13} & -\Omega_{23} & 0 \end{bmatrix}. \tag{2.188}$$

In our applications we assume that reorientation functions depend on the stress and the stress rate, so that $\mathbf{\Omega} = \mathbf{\Omega}(\mathbf{S}, \dot{\mathbf{S}})$ is given by using (2.184), (2.185), (2.186), (2.187) and (2.188) with the replacements $A_{ij} = S_{ij}$, and $B_{ij} = \dot{S}_{ij}$. The material parameters are given by the arrays $\{b_{ij}^{(1,0,0)}\}, \{b_{ij}^{(0,1,0)}\}, \{c_i\}$ in (2.186). To complete the flow rule (2.110), we now consider the yield function using the polynomial framework established thus far.

The yield function and strain energy function, both of the form $F(\mathbf{A})$ for cubic symmetry, are obtained by applying the same sequence. Considering first $\mathbf{R}_1, \mathbf{D}_2$, we obtained (2.151). Then upon considering $\mathbf{M}_1, \mathbf{M}_2, \mathbf{T}_3, \mathbf{T}_2$, we can use Theorem 2 directly, and obtain the integrity basis to quadratic order as

$$F(\mathbf{A}) = F(A_{11} + A_{22} + A_{33}, A_{23}^2 + A_{13}^2 + A_{12}^2, A_{22}A_{33} + A_{33}A_{11} + A_{11}A_{22}). \tag{2.189}$$

The polynomial is then written as

$$F(\mathbf{A}) = \sum_i \sum_j b_{ij}^y x_i^y x_j^y + \sum_i c_i^y y_i^y \tag{2.190}$$

for constants b_{ij}^y, c_i^y, with the superscript y used to designate these constants relate to yield. The basis terms are

$$x_1^y \equiv A_{11} + A_{22} + A_{33}, \tag{2.191}$$

and

$$y_1^y \equiv A_{23}^2 + A_{13}^2 + A_{12}^2 \tag{2.192}$$

$$y_2^y \equiv A_{22}A_{33} + A_{33}A_{11} + A_{11}A_{22}, \tag{2.193}$$

so that $|\{b_{ij}^y\}| = 1$, $|\{c_i^y\}| = 2$, for a total of three constants (at quadratic order in $\mathbf{A}$). We therefore have $y(\mathbf{S})$ for hexoctahedral symmetry being specified by three constants, and similarly for the strain energy function $W(\mathbf{E})$. The coefficients C_{ijkl} from the array (2.85) can be related to the constants in (2.190) by computing,

$$C_{ijkl} = \left. \frac{\partial^2 F}{\partial A_{ij} \partial A_{kl}} \right|_{\mathbf{A}=\mathbf{0}}$$

through the direct use of (2.190).

Applied to yield functions, it proves convenient to use the equivalence

$$(x_1^y)^2 = A_{11}^2 + A_{22}^2 + A_{33}^2 + 2y_2^y \tag{2.194}$$

so we can replace y_2^y with the basis element

$$(y^y)_2' = A_{11}^2 + A_{22}^2 + A_{33}^2, \tag{2.195}$$

while everything else goes through unchanged in the expansion (2.190). Next we consider some other theoretically and empirically motivated aspects to encode in the form of the yield function.

Positive dissipation. First, to match the stated requirements of the optimization problem associated with the maximum dissipation postulate, (2.103), we must have $y(\mathbf{S}) = 0$ indicating a state of yielding. Therefore we subtract off a fourth material constant $y_{\max}$ from the polynomial expansion which is quadratic in $\mathbf{S}$. Secondly, there is experimental evidence that pressure does not lead to yield[5]. Therefore we remove the dependence on the first basis element x_1^y from the expansion. With this change, applying (2.190) for the yield function gives

$$y(\mathbf{S}) = c_1^y(S_{23}^2 + S_{13}^2 + S_{12}^2) + c_2^y(S_{11}^2 + S_{22}^2 + S_{33}^2) - y_{\max}. \tag{2.196}$$

The thermodynamic requirement of positive dissipation states that

$$\frac{\partial y}{\partial \mathbf{S}} \cdot \mathbf{S} > 0. \tag{2.197}$$

Using (2.196), we have (Gupta et al., 2011)

$$\begin{aligned} D &= 2c_1^y(S_{23}^2 + S_{13}^2 + S_{12}^2 + S_{11}^2 + S_{22}^2 + S_{33}^2) + 2(c_2^y - c_1^y)(S_{11}^2 + S_{22}^2 + S_{33}^2) \\ &= 2c_1^y\|\mathbf{S}\|^2 + 2(c_2^y - c_1^y)(S_{11}^2 + S_{22}^2 + S_{33}^2). \end{aligned} \tag{2.198}$$

Imposing $D > 0$ then requires that $c_1^y > 0$ and $c_2^y > c_1^y$, where in Gupta et al. (2011) they used the deviatoric stress $\bar{\mathbf{S}}$ in (2.198). Based on the simple quadratic form for y, we could get a similar result without imposing deviatoric stress by considering that (2.196) is of the form

$$y(\mathbf{S}) = \frac{1}{2}Y_{ijkl}S_{ij}S_{kl} - y_{\max} \tag{2.199}$$

for material constants $Y_{ijkl}(c_1^y, c_2^y)$. Then the dissipation restriction simply states that

$$D > 0 \implies Y_{ijkl}S_{ij}S_{kl} > 0 \tag{2.200}$$

so that the eigenvalues of Y_{ijkl} must be positive. Relating Y_{ijkl} to c_1^y, c_2^y through the use of, e.g. $Y_{ijkl} = \partial^2 y/\partial S_{ij}\partial S_{kl}$ thus gives the restriction $c_1^y > 0, c_2^y > 0$.

[5]But it can affect when yield occurs.

Plastic incompressibility. Finally, plastic incompressibility (that is, no volumetric flow during plastic deformation) requires that $\text{tr}\ \mathbf{K}^{-1}\dot{\mathbf{K}} = 0$, hence we have the restriction

$$0 = \text{tr}\ \frac{\partial y}{\partial \mathbf{S}} = 2c_2^y(S_{11} + S_{22} + S_{33}). \tag{2.201}$$

This equation can be satisfied by replacing the functional dependence of the yield function on $\mathbf{S}$ by the deviatoric stress

$$\bar{\mathbf{S}} = \mathbf{S} - 1/3(\text{tr}\ \mathbf{S})\mathbf{I}.$$

The lattice spin could likewise be considered as dependent upon the deviatoric stress, $\boldsymbol{\Omega} = \boldsymbol{\Omega}(\bar{\mathbf{S}}, \dot{\bar{\mathbf{S}}})$, however, this is an additional assumption which may or may not be borne out in experimental observations. We note that the crystal plasticity model of (2.6) is naturally only dependent upon the deviatoric stress since $\mathbf{S}\cdot\mathbf{s}_0^\alpha \otimes \mathbf{n}_0^\alpha = \bar{\mathbf{S}}\cdot\mathbf{s}_0^\alpha \otimes \mathbf{n}_0^\alpha$, since $\mathbf{I}\cdot\mathbf{s}_0^\alpha \otimes \mathbf{n}_0^\alpha = \mathbf{s}_0^\alpha \cdot \mathbf{n}_0^\alpha = 0$

Summary. Taking all restrictions together, the yield function for cubic symmetry, at quadratic order in its argument ($\mathbf{S}$ or $\mathbf{E}$), with the form $y(\mathbf{S}) = 0$ defining the boundary of the elastic region, satisfying the dissipation inequality and isochoric plastic flow is written as

$$y(\mathbf{S}) = c_1^y(\bar{S}_{23}^2 + \bar{S}_{13}^2 + \bar{S}_{12}^2) + c_2^y(\bar{S}_{11}^2 + \bar{S}_{22}^2 + \bar{S}_{33}^2) - y_{\max}. \tag{2.202}$$

with the restrictions $c_1^y > 0, c_2^y > c_1^y$, and with a contribution to the flow rule of

$$\frac{\partial y}{\partial \mathbf{S}} = 2\begin{bmatrix} c_2^y\bar{S}_{11} & c_1^y\bar{S}_{12} & c_1^y\bar{S}_{13} \\ & c_2^y\bar{S}_{22} & c_1^y\bar{S}_{23} \\ \text{sym} & & c_2^y\bar{S}_{33} \end{bmatrix}. \tag{2.203}$$

The material parameters in the model are then $c_1^y, c_2^y, y_{\max}$. The values for these parameters can only be obtained from experimental data.

We had previously raised questions as to the physicality of the rate independent flow rule developed here, $\boldsymbol{\Omega}(\mathbf{S}, \dot{\mathbf{S}})$ and resulting in (2.186), see §2.2.3.3. The problem is that this form is not guaranteed to have the property that the spin reverses upon change of loading direction. Therefore we now consider other forms for the spin which more clearly capture this crucial property.

Alternative formulations for the spin

In this section we investigate lattice reorientation functions derived from scalar functions of the form

$$F = F(\mathbf{A}, \mathbf{v}). \tag{2.204}$$

This enables spin functions of the form $\boldsymbol{\Omega} = \boldsymbol{\Omega}(\mathbf{S})$, which by construction satisfies the physical requirement $\boldsymbol{\Omega}(\mathbf{S}) = -\boldsymbol{\Omega}(-\mathbf{S})$. Rate independence can be satisfied by modifying

the flow rule from (2.110) to be written

$$\mathbf{K}^{-1}\dot{\mathbf{K}} = -\lambda\left(\frac{\partial y}{\partial \mathbf{S}} + \boldsymbol{\Omega}(\mathbf{S})\right). \tag{2.205}$$

Factoring out λ gives the rate independent phenomenology, since λ is solved for based on the constraint from the yield surface, independent of any material-dependent time scale.

Previously we considered developing the constitutive function (2.145) out to order (2,1,1) in powers of $\mathbf{A}, \mathbf{B}, \mathbf{v}$ for hexoctahedral point group symmetry. In this section we consider expansions up to order $(3,1)$ and $(5,1)$ in $\mathbf{A}, \mathbf{v}$. This is because for hexoctahedral symmetry there is no such function

$$\Omega_{ij} = W_{ijkl}A_{kl} \tag{2.206}$$

for a symmetric tensor A_{kl} and skew symmetric Ω_{ij}. Therefore we need to consider at least the cubic order expansion

$$\Omega_{ij} = W_{ijklmnop}A_{kl}A_{mn}A_{op}. \tag{2.207}$$

Cubic order integrity basis. Much of the same derivation used to obtain (2.186) applies here. To prove that there are no contributions to the spin at linear order for hexoctahedral symmetry, from our previous derivation note that there are no terms in the integrity basis which are linear in $\mathbf{A}, \mathbf{v}$ due to the required invariance under the $\mathbf{T}_i, i = 1,2,3$ transformations, see Equation (2.172) and (2.173). On the other hand, the cubic groups tetartoidal and diploidal classes do not have any $\mathbf{T}_i$ rotation elements and a linear contribution of the form (2.206) would be anticipated for those cases.

Following the same prescription as done previously for $F(\mathbf{A}, \mathbf{B}, \mathbf{v})$, we eventually obtain the integrity basis elements

$$\begin{array}{l} F(\mathbf{A}, \mathbf{v}): \\ x_1^{\text{cube}} = A_{11} + A_{22} + A_{33} \\ y_1^{\text{cube}} = A_{11}(A_{13}v_2 - A_{12}v_3) + A_{22}(A_{12}v_3 - A_{23}v_1) + A_{33}(A_{23}v_1 - A_{13}v_2), \\ z_1^{\text{cube}} = A_{22}A_{33}(A_{13}v_2 - A_{12}v_3) + A_{33}A_{11}(A_{12}v_3 - A_{23}v_1) + A_{11}A_{22}(A_{23}v_1 - A_{13}v_2), \\ z_2^{\text{cube}} = A_{23}^2(A_{13}v_2 - A_{12}v_3) + A_{13}^2(A_{12}v_3 - A_{23}v_1) + A_{12}^2(A_{23}v_1 - A_{13}v_2), \\ z_3^{\text{cube}} = A_{11}(A_{23}A_{12}v_2 - A_{23}A_{13}v_3) + A_{22}(A_{23}A_{13}v_3 - v_1A_{12}A_{13}) + A_{33}(v_1A_{12}A_{13} - A_{23}A_{12}v_2) \end{array}, \tag{2.208}$$

with associated polynomial expansion

$$F(\mathbf{A}, \mathbf{v})) = \sum_{i=1}^{1}\sum_{j=1}^{1} b_{ij}^{\text{cube}} x_i^{\text{cube}} y_j^{\text{cube}} + \sum_{i=1}^{3} c_i^{\text{cube}} z_i^{\text{cube}}, \tag{2.209}$$

where the arrays $b_{ij}^{\text{cube}}, c_i^{\text{cube}}$ are material constants. The associated spin vector $\boldsymbol{\omega} = \langle\boldsymbol{\Omega}\rangle =$

$\omega_i \mathbf{e}_i$ has components

$$\begin{aligned}
\omega_1 &= b_{11}^{\text{cube}} \left(A_{11}+A_{22}+A_{33}\right)\left(A_{33}A_{23}-A_{23}A_{22}\right) + c_1^{\text{cube}} \left(A_{11}A_{22}A_{23}-A_{23}A_{33}A_{11}\right) \\
&\quad + c_2^{\text{cube}} \left(-A_{23}A_{13}^2+A_{12}^2A_{23}\right) + c_3^{\text{cube}} \left(-A_{22}A_{12}A_{13}+A_{33}A_{12}A_{13}\right) \\
\omega_2 &= b_{11}^{\text{cube}} \left(A_{11}+A_{22}+A_{33}\right)\left(A_{11}A_{13}-A_{13}A_{33}\right) + c_1^{\text{cube}} \left(A_{22}A_{33}A_{13}-A_{13}A_{11}A_{22}\right) \\
&\quad + c_2^{\text{cube}} \left(A_{23}^2A_{13}-A_{12}^2A_{13}\right) + c_3^{\text{cube}} \left(A_{11}A_{23}A_{12}-A_{33}A_{23}A_{12}\right) \\
\omega_3 &= b_{11}^{\text{cube}} \left(A_{11}+A_{22}+A_{33}\right)\left(A_{22}A_{12}-A_{11}A_{12}\right) + c_1^{\text{cube}} \left(A_{33}A_{11}A_{12}-A_{12}A_{22}A_{33}\right) \\
&\quad + c_2^{\text{cube}} \left(-A_{23}^2A_{12}+A_{13}^2A_{12}\right) + c_3^{\text{cube}} \left(-A_{11}A_{23}A_{13}+A_{22}A_{23}A_{13}\right).
\end{aligned} \tag{2.210}$$

The spin tensor $\mathbf{\Omega}$ components are related to ω_i by

$$\Omega_{12} = -\omega_3 \qquad \Omega_{13} = \omega_2 \qquad \Omega_{23} = -\omega_1. \tag{2.211}$$

with final matrix representation in Equation (2.188).

Quintic order integrity basis As long as the iron is hot, so to speak, we continue expanding up to the quintic order. In the parameter calibrations performed in the next section, we were interested in if there was improvement in the phenomenological match to the crystal plasticity data by adding additional functional flexibility. Carrying out the same procedure as before, the required integrity basis terms for a function up to order 5 in a single argument for cubic symmetry are given by:

$$\begin{aligned}
x_1 &= A_{11}+A_{22}+A_{33} \\
y_1 &= A_{11}^2+A_{22}^2+A_{33}^2 \\
y_2 &= A_{23}^2+A_{13}^2+A_{12}^2 \\
z_1 &= A_{11}A_{22}A_{33} \\
z_2 &= A_{12}A_{13}A_{23} \\
z_3 &= A_{11}A_{23}^2+A_{22}A_{13}^2+A_{33}A_{12}^2 \\
xy_1 &= A_{23}v_1\left(A_{22}-A_{33}\right)+A_{13}v_2\left(A_{33}-A_{11}\right)+A_{12}v_3\left(A_{11}-A_{22}\right) \\
xz_1 &= A_{23}v_1\left(A_{13}^2-A_{12}^2\right)+A_{13}v_2\left(A_{12}^2-A_{23}^2\right)+A_{12}v_3\left(A_{23}^2-A_{13}^2\right), \\
xz_2 &= v_1A_{12}A_{13}\left(A_{22}-A_{33}\right)+A_{23}A_{12}v_2\left(A_{33}-A_{11}\right)+A_{23}A_{13}v_3\left(A_{11}-A_{22}\right), \\
xz_3 &= A_{22}A_{33}\left(A_{13}v_2-A_{12}v_3\right)+A_{33}A_{11}\left(A_{12}v_3-A_{23}v_1\right)+A_{11}A_{22}\left(A_{23}v_1-A_{13}v_2\right) \\
xw_1 &= A_{22}A_{33}\left(A_{23}A_{12}v_2-A_{23}A_{13}v_3\right)+A_{33}A_{11}\left(A_{23}A_{13}v_3-v_1A_{12}A_{13}\right)+ \\
&\quad A_{11}A_{22}\left(v_1A_{12}A_{13}-A_{23}A_{12}v_2\right) \\
xw_2 &= v_1A_{12}A_{13}\left(A_{13}^2-A_{12}^2\right)+A_{23}A_{12}v_2\left(A_{12}^2-A_{23}^2\right)+A_{23}A_{13}v_3\left(A_{23}^2-A_{13}^2\right) \\
xw_3 &= A_{11}A_{23}v_1\left(A_{23}^2-A_{12}^2\right)+A_{22}A_{13}v_2\left(A_{12}^2-A_{23}^2\right)+A_{33}A_{12}v_3\left(A_{23}^2-A_{13}^2\right) \\
xv_1 &= A_{13}^2A_{12}^2\left(A_{13}v_2-A_{12}v_3\right)+A_{12}^2A_{23}^2\left(A_{12}v_3-A_{23}v_1\right)+A_{23}^2A_{13}^2\left(A_{23}v_1-A_{13}v_2\right) \\
xv_2 &= A_{11}v_1A_{12}A_{13}\left(A_{23}^2-A_{12}^2\right)+A_{22}A_{23}A_{12}v_2\left(A_{13}^2-A_{23}^2\right)+A_{33}A_{23}A_{13}v_3\left(A_{12}^2-A_{13}^2\right).
\end{aligned} \tag{2.212}$$

We consider deviatoric dependence only, therefore we do not include the basis element x_1 in the expansion. Then the polynomial function is written as

$$F(\mathbf{A}) = xz(3) + xy * z(3) + xz * y(6) + xv(2), \tag{2.213}$$

where we are using the shorthand $a*b$ to denote polynomial combinations between the terms a and terms b. For example, $xz*y \equiv c_{ij}xz_iy_j$ for 6 constants c_{ij}. The number of constants required for the given combination is denoted by the notation $xz*y(6)$ in (2.213). Therefore (2.213) has a total of 14 total constants, with the assigned pairings

$$\begin{aligned} &a_i : xz_i \\ &b_i : (xy_1 * z_i) \\ &c_{ij} : (xz)_i y_j \\ &d_i : xv_i. \end{aligned} \tag{2.214}$$

Hardening phenomenology, backstress

Next, we consider a possible constitutive formulation to capture experimentally observed phenomena such as the Bauschinger effect, kinematic and isotropic hardening. In our framework this phenomenology enters into evolution of the yield function. Based on the polycrystalline plasticity literature (Chaboche, 1987, 2008) a typical approach is to pose the yield function as

$$y = y(\mathbf{S}_{ij} - \chi_{ij}), \tag{2.215}$$

where χ_{ij} is a phenomenological quantity called the backstress. The center of the yield surface is translated in its domain space when there is a non-zero backstress, thus leading to kinematic hardening phenomenology. A possible explanation for the microscopic origin of kinematic hardening is an evolving dislocation density. Therefore, it seems reasonable to assume that the backstress is some function of the geometrically necessary dislocation content, $\boldsymbol{\xi}$. Therefore, we consider yield functions of the form

$$y = \hat{y}(\mathbf{S} - \boldsymbol{\chi}(\boldsymbol{\xi})) - h(\boldsymbol{\xi}), \tag{2.216}$$

where $\boldsymbol{\chi} : \mathbb{R}^9 \to \text{sym}$ is the backstress, associated with kinematic hardening and $h : \mathbb{R}^9 \to \mathbb{R}^+$ is the radius of the yield surface, associated with isotropic hardening. The function $\boldsymbol{\chi}$ is of the form $F(\mathbf{A}, \mathbf{B}, \mathbf{v})$, from Table 2.1, see (2.131).

$$\boldsymbol{\chi}(\boldsymbol{\xi}) = \left.\frac{\partial F}{\partial \mathbf{B}}\right|_{\mathbf{B}=\mathbf{0}}, \tag{2.217}$$

with the interpretations $\mathbf{A} = \text{sym}\ \boldsymbol{\xi}$, $\mathbf{v} = \langle \text{skw}\ \boldsymbol{\xi} \rangle$. The requirements on $F(\mathbf{A}, \mathbf{B}, \mathbf{v})$ we consider are then: (1) linear in $\mathbf{B}$, in recognition of (2.217) (2) up to quadratic order in either of $\mathbf{A}, \mathbf{v}$, for computational expedience. Using our previous notation we need integrity basis elements of the orders $(2, 1, 0), (1, 1, 1), (0, 1, 2)$, and order below this. The development leading to (2.150) is valid to consider, with some modifications, in order to obtain the required integrity basis.

First off, we can directly retain the $\mathbf{R}_1$-invariant terms recorded in Equation (2.147). Note in passing that this completes the monoclinic class specification for the constitutive

function for $\boldsymbol{\chi}$. Next, considering the terms leading to (2.149) we have an additional factor. This is generated from including v_2v_3 in the integrity basis, which we did not have to do previously. Carrying out the modifications to (2.149), the expression analogous to (2.150) is then

$$F = F\left(\begin{array}{l} A_{11}, A_{22}, A_{33}, B_{11}, B_{22}, B_{33}, A_{23}v_1, A_{13}v_2, A_{12}v_3, B_{23}v_1, B_{13}v_2, B_{12}v_3 \\ v_1A_{12}B_{13}, v_1A_{13}B_{12}, B_{23}A_{12}v_2, A_{23}B_{12}v_2, B_{23}A_{13}v_3, A_{23}B_{13}v_3, \\ A_{12}^2, A_{13}^2, A_{23}^2, A_{12}B_{12}, A_{13}B_{13}, A_{23}B_{23}, A_{23}A_{13}B_{12}, A_{23}A_{12}B_{13}, B_{23}A_{12}A_{13}, \\ v_1^2, v_2^2, v_3^2, B_{23}v_2v_3, B_{13}v_3v_1, B_{12}v_2v_1 \end{array}\right). \tag{2.218}$$

As before, under $\mathbf{M}_1, \mathbf{M}_2$, the function (2.218) is cyclic in the quantities

$$\begin{array}{l} (A_{11}, A_{22}, A_{33}), (B_{11}, B_{22}, B_{33}), (A_{23}v_1, A_{13}v_2, A_{12}v_3), (B_{23}v_1, B_{13}v_2, B_{12}v_3), \\ (v_1A_{12}B_{13}, v_2A_{23}B_{12}, v_3A_{13}B_{23}), (v_1A_{13}B_{12}, v_2A_{12}B_{23}, v_3A_{23}B_{13}), (A_{23}^2, A_{13}^2, A_{12}^2), \\ (v_1^2, v_2^2, v_3^2), (A_{23}B_{23}, A_{13}B_{13}, A_{12}B_{12}), (B_{23}A_{12}A_{13}, A_{23}A_{12}B_{13}, A_{23}A_{13}B_{12}), \\ (B_{23}v_2v_3, B_{13}v_3v_1, B_{12}v_2v_1). \end{array} \tag{2.219}$$

After applying Theorems 5 and 6 we obtain the following integrity basis, with the order of the basis terms indicated

$$\begin{array}{l} x_1^{(1,0,0)} : A_{11} + A_{22} + A_{33}, \\ x_1^{(0,1,0)} : B_{11} + B_{22} + B_{33} \\ y_1^{(2,0,0)} : A_{22}A_{33} + A_{33}A_{11} + A_{11}A_{22} \\ y_2^{(2,0,0)} : A_{12}^2 + A_{23}^2 + A_{13}^2 \\ y_1^{(0,0,2)} : v_1^2 + v_2^2 + v_3^2 \\ x_1^{(1,1,0)} : A_{22}B_{22} + A_{11}B_{11} + A_{33}B_{33}, \\ x_2^{(1,1,0)} : A_{23}B_{23} + A_{13}B_{13} + A_{12}B_{12} \\ y_1^{(1,1,1)} : A_{23}v_1\left(B_{22} - B_{33}\right) + A_{13}v_2\left(B_{33} - B_{11}\right) + A_{12}v_3\left(B_{11} - B_{22}\right) \\ y_2^{(1,1,1)} : B_{23}v_1\left(A_{22} - A_{33}\right) + B_{13}v_2\left(A_{33} - A_{11}\right) + B_{12}v_3\left(A_{11} - A_{22}\right) \\ y_3^{(1,1,1)} : v_1A_{12}B_{13} + v_2A_{23}B_{12} + v_3A_{13}B_{23} - v_2A_{13}B_{23} - v_1A_{13}B_{12} - v_3A_{23}B_{13} \\ z_1^{(0,1,2)} : B_{23}v_2v_3 + B_{13}v_3v_1 + B_{12}v_2v_1 \\ z_2^{(0,1,2)} : B_{11}v_1^2 + B_{22}v_2^2 + B_{33}v_3^2 \\ z_1^{(2,1,0)} : A_{11}A_{33}B_{22} + A_{33}A_{22}B_{11} + A_{22}A_{11}B_{33}, \\ z_2^{(2,1,0)} : B_{11}A_{23}^2 + B_{22}A_{13}^2 + B_{33}A_{12}^2 \\ z_3^{(2,1,0)} : A_{11}A_{23}B_{23} + A_{22}A_{13}B_{13} + A_{33}A_{12}B_{12} \\ z_4^{(2,1,0)} : A_{23}B_{23}\left(A_{22} - A_{33}\right) + A_{13}B_{13}\left(A_{33} - A_{11}\right) + A_{12}B_{12}\left(A_{11} - A_{22}\right) \\ z_5^{(2,1,0)} : B_{23}A_{12}A_{13} + A_{23}A_{12}B_{13} + A_{23}A_{13}B_{12}, \end{array} \tag{2.220}$$

the polynomial expansion is then written as

$$F(\mathbf{A},\mathbf{B},\mathbf{v}) = a_{ij}^{(0,1,0),(1,0,0)} x_i^{(0,1,0)} x_j^{(1,0,0)} + b_{ij}^{(0,1,0),(2,0,0)} x_i^{(0,1,0)} y_j^{(2,0,0)} + b_{ij}^{(0,1,0),(0,0,2)} x_i^{(0,1,0)} y_j^{(0,0,2)} + c_i^{(1,1,0)} x_i^{(1,1,0)} + c_{ij}^{(1,1,0)(1,0,0)} x_i^{(1,1,0)} x_j^{(1,0,0)} + d_i^{(1,1,1)} y_i^{(1,1,1)} + e_i^{(0,1,2)} z_i^{(0,1,2)} + f_i^{(2,1,0)} z_i^{(2,1,0)}, \tag{2.221}$$

where $a_{ij}^{(\cdot)}, b_{ij}^{(\cdot)}, c_i^{(\cdot)}, c_{ij}^{(\cdot)}, d_i^{(\cdot)}, e_i^{(\cdot)}, f_i^{(\cdot)}$ constitute a set of 18 material constants.

2.3.4 Discussion

In this section we have given several detailed examples of generating several constitutive functions from Table 2.1 for hexoctahedral symmetry (maximum cubic symmetry). During the course of the derivations, we also arrived at integrity basis forms for rhombic and monoclinic classes, as well as several lower order groups from the cubic class. These examples are useful to give since the procedures are not well documented in the literature, (Green and Adkins, 1970; Spencer, 1971), and we found the structural tensor approach to be unattractive when dealing with multiple functional arguments due to the tendency to generate redundant basis elements. Such lack of examples may be one reason why the present approach to single crystal plasticity has not been completed prior to this study.

Later in this document we perform similar analysis for the other practically important yet difficult to analyze crystal class: the hexagonal system. In §3.5.1.2 we examine the yield function for this system. Then in §A.5 we give a detailed treatment of the spin function of the form $\mathbf{\Omega} = \mathbf{\Omega}(\mathbf{S})$ up to cubic order for dihexagonal-dipyramidal point group symmetry (maximum hexagonal symmetry).

Since the hexoctahedral and dihexagonal-dipyramidal classes represent the groups with the most symmetry out of the 32 crystallographic point groups, lower symmetry groups can readily be picked off at various stages of the given derivations. This was done with monoclinic and rhombic symmetry in this section, for example. All these examples taken together from this thesis should therefore provide enough reference material to allow other researchers interested in implementing this constitutive framework to generate complete integrity basis elements for any of the 32 crystal point groups.

For those familiar with crystal plasticity implementations, it may be of interest to emphasize that this constitutive framework does not explicitly distinguish between for example FCC and BCC crystals. Here, constitutive equations are generated based on the point group symmetry, which is of the cubic class in both cases. In the next section we calibrate the plasticity model defined by (2.110) against crystal plasticity models for FCC and BCC crystals from the literature. According to crystal plasticity theory, FCC and BCC crystals have different slip systems in (2.5), and therefore different reorientation behavior under the same conditions. In our framework, this distinction will have to come out in the numerical values of the material constants in the constitutive equations we are considering. Therefore it will

be interesting to see how well our functions capture the different reorientation behavior between FCC and BCC. After these calibrations, we perform plane strain simulations in order to assess the model in qualitatively simple yet informative boundary value problems.

2.4 Numerical simulations

In this section we exercise the plasticity model in numerical simulations. We ground the model in reality by first calibrating our constitutive equations for plastic flow. Then we develop a simple numerical method for executing plane strain simulations, incorporating dislocation $\boldsymbol{\xi}$, as derived from the plastic deformation field, rather than as a primitive variable. Results from several simple but informative boundary value problems are shown.

2.4.1 Calibration of constitutive functions; material point simulations

First we calibrate the constitutive formulas for yield and plastic flow developed in the previous section against available data. Due to a lack of usable data (Bell and Green, 1967) our best recourse is to calibrate against a crystal plasticity model from the literature. We calibrate these parameters by performing one of the simplest possible simulations, a spatially homogeneous isochoric uniaxial extension. This simulation has the benefit of having a degree of experimental feasibility. We now describe the algorithm used to update the plastic variables such as the lattice reorientation. This algorithm will be used again in the plane strain simulations.

2.4.1.1 Numerical algorithm

We calibrate the evolution of $\mathbf{K}$ between the phenomenological and crystal plasticity models by simulating an isochoric extension of the form

$$\mathbf{F}(s) = s\mathbf{e}_1 \otimes \mathbf{e}_1 + \frac{1}{\sqrt{s}}(\mathbf{e}_2 \otimes \mathbf{e}_2 + \mathbf{e}_3 \otimes \mathbf{e}_3). \tag{2.222}$$

Although this homogeneous deformation does not necessarily correspond to the material deformation in a uniaxial extension or compression test, it is close enough to be considered representative of such tests. The discussion in §2.2.3.3 surrounding lattice reorientation in axial extension experiments is pertinant to review, as this deformation results in non-zero lattice reorientation from the crystal plasticity model.

The material is initialized at $s = s_0 = 1$ with $\mathbf{K}(0) = \mathbf{K}_0$. The initial plastic deformation is set at $\mathbf{K}_0 \in \mathrm{SO}(3, \mathbb{R})$ in recognition of the experimental fact that only initial orientations are detectable using X-ray diffraction, see the summary paragraph of §2.2.1. A constant

extension rate parameter $\dot{s} = \text{const}$ is specified, so that the extension is discretized as

$$s^{(i+1)} = s^{(i)} + \dot{s}\Delta t \tag{2.223}$$

for an assigned temporal increment Δt. Then $\mathbf{F}^{(i+1)} \equiv \mathbf{F}(s^{(i+1)})$ is updated using (2.222). Next, given $\mathbf{K}^{(i)}, \mathbf{H}^{(i)}, \mathbf{F}^{(i+1)}$, we perform what is usually referred to as a predictor corrector scheme to stay on the yield surface, although it is really just solving a system of nonlinear equations. The procedure is as follows. First, assume the increment $\mathbf{F}^{(i)} \to \mathbf{F}^{(i+1)}$ constitutes elastic deformation. That is, set $\mathbf{K}^{(i+1)} = \mathbf{K}^{(i)}$, compute $\mathbf{H}^{(i+1)} = \mathbf{F}^{(i+1)}\mathbf{K}^{(i+1)}$, and evaluate the yield function $y = y(\mathbf{S}^{(i+1)})$. Note here that the trial stress is dependent on $\mathbf{K}^{(i+1)}$ through the sequence $\mathbf{S}^{(i+1)} \equiv \mathbf{S}(\mathbf{H}^{(i+1)}) = \mathbf{S}(\mathbf{F}^{(i+1)}\mathbf{K}^{(i+1)})$. If the yield condition $y(\mathbf{S}^{(i+1)}) < 0$ is satisfied, accept $\mathbf{K}^{(i+1)} = \mathbf{K}^{(i)}$ and go to the next $\mathbf{F}$-step by incrementing s through (2.223). If the yield condition is violated by the new elastic state, so that $y > 0$, then solve the following system of equations for $\lambda, \mathbf{K}^{(i+1)}$, where we are using the flow rule of (2.205)

$$\begin{aligned} &(\mathbf{K}^{(i+1)})^{-1}\dot{\mathbf{K}}^{(i+1)} = -\lambda\left(\frac{\partial y}{\partial \mathbf{S}} + \boldsymbol{\Omega}(\mathbf{S}^{(i+1)})\right) \\ &y(\mathbf{S}^{(i+1)}) = 0 \end{aligned} \tag{2.224}$$

where $\dot{\mathbf{K}}^{(i+1)} = (\mathbf{K}^{(i+1)} - \mathbf{K}^{(i)})/\Delta t$, and $\dot{\mathbf{S}} = (\mathbf{S}^{(i+1)} - \mathbf{S}^{(i)})/\Delta t$. The implicit form of (2.224) is motivated by our initial studies of flow rules of the form (2.110), in which having $\boldsymbol{\Omega} = \boldsymbol{\Omega}(\mathbf{S}, \dot{\mathbf{S}})$ to achieve rate independence would necessitate an implicit solve.

The equation $(2.224)_2$ enforces the yield constraint. Alternatively, instead of adding $(2.224)_2$ to the system of equations, to solve for λ we could use the so-called consistency condition in the form

$$0 = \dot{y} = \frac{\partial y}{\partial \mathbf{S}} \cdot \frac{\partial \mathbf{S}}{\partial \mathbf{E}} \cdot \dot{\mathbf{E}} \tag{2.225}$$

where

$$2\dot{\mathbf{E}} = \dot{\mathbf{C}} = \dot{\mathbf{K}}^{\mathrm{T}}\mathbf{F}^{\mathrm{T}}\mathbf{F}\mathbf{K} + \mathbf{K}^{\mathrm{T}}\dot{\mathbf{F}}^{\mathrm{T}}\mathbf{F}\mathbf{K} + \mathbf{K}^{\mathrm{T}}\mathbf{F}^{\mathrm{T}}\dot{\mathbf{F}}\mathbf{K} + \mathbf{K}^{\mathrm{T}}\mathbf{F}^{\mathrm{T}}\mathbf{F}\dot{\mathbf{K}}.$$

Next, $\dot{\mathbf{K}}$ is given by the flow rule (2.205),

$$\dot{\mathbf{K}} = -\mathbf{K}\lambda\left(\frac{\partial y}{\partial \mathbf{S}} + \boldsymbol{\Omega}\right), \tag{2.226}$$

which gives

$$\begin{aligned} \dot{\mathbf{C}} = \; & -\lambda\left[\left(\frac{\partial y}{\partial \mathbf{S}} - \boldsymbol{\Omega}\right)\mathbf{K}^{\mathrm{T}}\mathbf{F}^{\mathrm{T}}\mathbf{F}\mathbf{K} + \mathbf{K}^{\mathrm{T}}\mathbf{F}^{\mathrm{T}}\mathbf{F}\mathbf{K}\left(\frac{\partial y}{\partial \mathbf{S}} + \boldsymbol{\Omega}\right)\right] \\ & + \mathbf{K}^{\mathrm{T}}\dot{\mathbf{F}}^{\mathrm{T}}\mathbf{F}\mathbf{K} + \mathbf{K}^{\mathrm{T}}\mathbf{F}^{\mathrm{T}}\dot{\mathbf{F}}\mathbf{K}. \end{aligned} \tag{2.227}$$

Then, substitution of (2.227) into (2.225) and solving for λ gives

$$\lambda = \frac{\left[\frac{\partial y}{\partial \mathbf{S}} \cdot \frac{\partial \mathbf{S}}{\partial \mathbf{E}} \cdot \left(\mathbf{K}^{\mathrm{T}}\dot{\mathbf{F}}^{\mathrm{T}}\mathbf{F}\mathbf{K} + \mathbf{K}^{\mathrm{T}}\mathbf{F}^{\mathrm{T}}\dot{\mathbf{F}}\mathbf{K}\right)\right]}{\frac{\partial y}{\partial \mathbf{S}} \cdot \frac{\partial \mathbf{S}}{\partial \mathbf{E}} \cdot \left[\left(\frac{\partial y}{\partial \mathbf{S}} - \boldsymbol{\Omega}\right)\mathbf{K}^{\mathrm{T}}\mathbf{F}^{\mathrm{T}}\mathbf{F}\mathbf{K} + \mathbf{K}^{\mathrm{T}}\mathbf{F}^{\mathrm{T}}\mathbf{F}\mathbf{K}\left(\frac{\partial y}{\partial \mathbf{S}} + \boldsymbol{\Omega}\right)\right]}. \tag{2.228}$$

Equation (2.228) can be used to evaluate the multiplier λ and thereby reduces the number of equations in the system (2.224) by one, but we find it more straightforward and as effective to simply enforce remaining on the yield surface at the end of the iteration in the system of equations. Equation (2.228) can also be used to incorporate rate independence into explicit schemes. The solution of the equations (2.224) is obtained by Newton Raphson iterations from initial guesses $\mathbf{K}_0^{(i+1)} = \mathbf{K}^{(i)}$, and taking $\lambda^{(i+1)}$ from (2.228). Taking a positive number for the initial guess $\lambda_0^{(i+1)}$ generally works, but for some boundary value problems successful convergence of the solution was found to be dependent on the numerical value for $\lambda_0^{(i+1)}$. Therefore for robustness we use Equation (2.228) to give the initial guess for $\lambda^{(i+1)}$.

Crystal plasticity model As mentioned previously, the raw experimental data we desire to calibrate against was not readily available. However crystal plasticity models which have apparently been calibrated against experimental data are generally available in the literature. Therefore we use these models to generate simulated data in order to furnish the calibration.

Although raw experimental data would be more meaningful to calibrate against, matching the phenomenological lattice reorientation function $\mathbf{\Omega}$ and yield function y against crystal plasticity models which have been calibrated against data is the best we can do at this time. In order to relate the two models more clearly, we have the equivalence $\mathbf{K}^{-1} = \mathbf{F}^{\mathrm{p}}$, where $\mathbf{F} = \mathbf{F}^{\mathrm{p}}\mathbf{F}^{\mathrm{e}}$ is the multiplicative decomposition of $\mathbf{F}$. Then in our notation the crystal plasticity flow rule, Equation (2.5), becomes written as

$$\dot{\mathbf{K}^{-1}}\mathbf{K} = \sum_{\alpha}^{N_{\mathrm{slips}}} \dot{\gamma}^{\alpha}\mathbf{s}_0^{\alpha} \otimes \mathbf{n}_0^{\alpha}, \tag{2.229}$$

where the summation is over the slip systems in the crystal, obtained from the space group symmetry of the crystal. The shear rate $\dot{\gamma}^{\alpha}$ is typically given by (Anand et al., 1997)

$$\dot{\gamma}^{\alpha} = \dot{\gamma}_0 \left(\frac{|\tau^{\alpha}|}{s^{\alpha}} \right)^{1/m} \mathrm{sign}(\tau^{\alpha}), \tag{2.230}$$

where τ^{α} is the resolved shear stress on the slip system, computed from the second Piola Kirchoff stress as $\tau^{\alpha} = \mathbf{S} \cdot \mathbf{s}_0^{\alpha} \otimes \mathbf{n}_0^{\alpha}$. s^{α} is the flow resistance for the slip system, $\dot{\gamma}_0$ is a material property representing material viscosity, and m is a rate sensitivity parameter. The Miller indices for the slip system vectors $\mathbf{s}_0^{\alpha}$, $\mathbf{n}_0^{\alpha}$, $\alpha = 1, 2, ..., N_{\mathrm{slips}}$ for FCC (N_{slips}= 12) and BCC (N_{slips}= 24) space group symmetry are recorded in Table A.1 and Table A.2, respectively. Due to the cubic symmetry, directional indices common in crystallography moniker are closely related to the Cartesian components of crystallographic vectors, so that $1, \bar{1}, 1 = 1/\sqrt{3}\,(\mathbf{e}_1 - \mathbf{e}_2 + \mathbf{e}_3)$ and $1, 2, 1 = 1/4(\mathbf{e}_1 + 2\mathbf{e}_2 + \mathbf{e}_3)$ for example (Hosford, 1993).

The flow parameters in (2.230) for BCC and FCC crystals are given in Table 2.2; these parameters are from Anand et al. (1997); Barton et al. (2005). The slip systems used are recorded in Tables A.1, A.2 for FCC and BCC crystals respectively. The plastic state update is obtained from the integration of (2.229) and (2.230) during the extension (2.222).

Table 2.2: Table of crystal plasticity parameters from (Barton et al., 2005; Anand et al., 1997).

crystal type	m	$\dot{\gamma}_0[s^{-1}]$	$s_0[$ MPa]
BCC	0.05	0.003	250
FCC	0.012	0.001	16

2.4.1.2 Results

In order to calibrate the phenomenological model we performed the uniaxial deformation simulation described by (2.222) from a several random initial orientation, $\mathbf{K}_0 \in \mathrm{SO}(3,\mathbb{R})$. From these initial orientations tests were performed to a total material stretches of $s_{\max} = 1.1, 0.9$ in (2.222). These two cases represent isochoric extension and contraction, respectively. The phenomenological model was calibrated to the crystal plasticity model by using a standard least squares method, see §3.4.1. In order to determine the phenomenological parameters we decoupled the considerations of the yield parameters $c_1^y, c_2^y, y_{\max}$, introduced in (2.202), from the lattice reorientation parameters $b_{11}^{\text{cube}}, c_1^{\text{cube}}, c_2^{\text{cube}}, c_3^{\text{cube}}$ which were introduced in (2.209). That is, we used separate calibration criteria for the two in order to get initial guesses for the parameters.

2.4.1.2.1 Calibration of yield parameters. For the yield parameters of (2.202), the residuals were formed by taking differences in the axial Cauchy stress $\mathbf{T}$, so that the residual contribution, r, from one initial orientation is written

$$r^{s_k}(\boldsymbol{\Theta}^y) = (\mathbf{T}_{\text{cp}}(s_k))_{11} - (\mathbf{T}_{\text{phen}}(\boldsymbol{\Theta}^y)(s_k))_{11}, \tag{2.231}$$

where $\mathbf{T}_{\text{cp}}$ is the Cauchy stress from the crystal plasticity model and $\mathbf{T}_{\text{phen}}$ is the Cauchy stress from the phenomenological model. The free parameters are

$$\boldsymbol{\Theta}^y \equiv (c_1^y, c_2^y, y_{\max}) \tag{2.232}$$

from (2.202). The least squares objective function associated to the residual (2.231) is written

$$\Phi(\boldsymbol{\Theta}^y) = \sum_m^{N_{\text{grains}}} \sum_k^{N_{\text{steps}}} \left[(r^{s_k})_m\right]^2, \tag{2.233}$$

where N_{grains} is the number of initial grains taken through the simulation (2.222) and N_{steps} is the number of steps s^i in (2.223) where comparison between data and simulation is made, respectively. We found that this approach works in terms of fitting the stress data, but that there is an undesirable flexibility in the absolute numerical values of $c_1^y, c_2^y, y_{\max}$. That this makes sense is seen by dividing the yield equation (2.202) by any arbitrary constant, which gives the same elastic region. To set a meaningful scale for the magnitude of the parameters

Table 2.3: Best fit material parameters for $y(\mathbf{S})$ for hexoctahedral symmetry, from (2.202).

crystal	c_1^y	c_2^y	$y_{\max}[\text{GPa}^2]$
BCC	0.396	0.463	0.106
FCC	0.412	0.412	0.00041

(2.232), we take insight from the classical J_2 theory of plasticity. There, the yield function is of the form

$$y(\mathbf{S}) = \bar{\mathbf{S}} \cdot \bar{\mathbf{S}} - k^2 \tag{2.234}$$

where it can be shown that (Malvern, 1969, p. 338)

$$k = \frac{Y}{\sqrt{3}} \tag{2.235}$$

where Y is the yield stress in tension. In our formulation we would like to have something similar, such as

$$y_{\max} \approx k^2 = Y^2/3, \tag{2.236}$$

in order to give an order of magnitude guess for $y_{\max}$, with subsequent effect on the values of c_1^y, c_2^y. To facilitate this, to the objective function (2.233) we add the residual equation

$$r_i = y_{\max} - \frac{1}{3}(T_{\text{phen}})_y^2, \tag{2.237}$$

where $(T_{\text{phen}})_y$ is the axial Cauchy stress at yield, determined from the T_{11}vs$s$ curve. Should there be confusion it is emphasized that the procedure of assigning the extra residual (2.237) is used simply to get more numerically intuitive values for the parameters in the yield function.

The final results for a BCC and FCC crystal are given in Table 2.3. In these results the number of initial orientations simultaneously incorporated into the objective function was $N_{\text{grains}} = 7$. Since the crystal plasticity model does not have uncertainties associated with the model parameters, we cannot assess quantitative precisions to the best fit parameters; this being something of an unfortunately common occurrence in the literature. After calibration, the Cauchy stress curves for tension and compression were plotted in Figure 2.7 and Figure 2.8. There are only two parameters in the yield function, so fully matching the crystal plasticity result which has corners in the yield surface is not possible. Higher order polynomial forms for the yield function may give further improvements in the calibration, but this is not as straightforward a proposition as might be thought. More comments on these issues are in the discussion section following the calibration results.

2.4.1.2.2 Calibration of lattice reorientation function For the lattice reorientation function, $\boldsymbol{\Omega}$, the residuals for the objective function were formed from the difference in

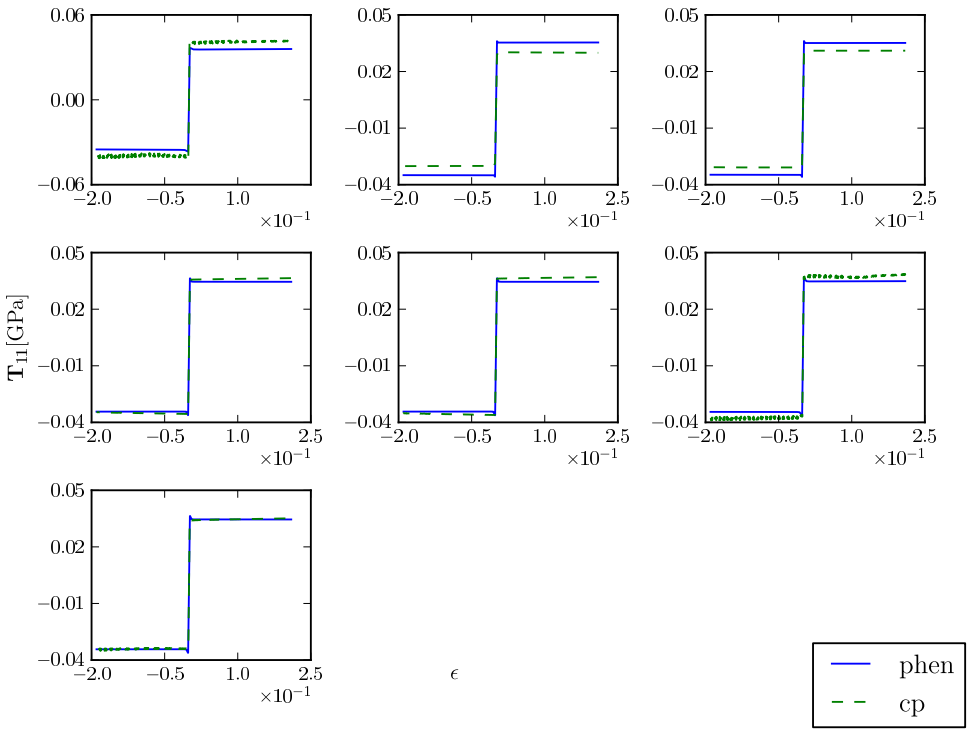

Figure 2.7: T_{11} Cauchy stress components for the FCC crystal plasticity model in Table 2.2 and best fit phenomenological yield function for seven initial orientations $\mathbf{K}_0 \in \mathrm{SO}(3,\mathbb{R})$. Both extension and contraction behavior was used to calibrate the model as indicated in the figure. Solid lines are results of the phenomenological model, the dashed lines are the crystal plasticity model.

Cartesian components of the plastic deformation $\mathbf{K}$ at various states of the deformation $s_k, k = 1, 2, ..., N_{\text{steps}}$. For an individual grain the residual array is

$$r_{ij}^{s_k}(\boldsymbol{\Theta}) = \left[\mathbf{K}_{\text{cp}}(s_k) - \mathbf{K}_{\text{phen}}(\boldsymbol{\Theta})(s_k)\right]_{ij}, \tag{2.238}$$

where $\boldsymbol{\Theta} = (b_{11}^{\text{cube}}, c_1^{\text{cube}}, c_2^{\text{cube}}, c_3^{\text{cube}})$ are the reorientation parameters from (2.209), $\mathbf{K}_{\text{cp}}(s)$ is the plastic deformation according to integrating the crystal plasticity flow rule (2.229) and $\mathbf{K}_{\text{phen}}(s)$ is the plastic deformation according to the phenomenological flow rule (2.205) with the yield parameters of Table 2.3. The objective function for the lattice reorientation parameters is then written

$$\Phi(\boldsymbol{\Theta}) = \sum_{m}^{N_{\text{grains}}} \sum_{k}^{N_{\text{steps}}} \sum_{i}^{3} \sum_{j}^{3} \left[\left(r_{ij}^{s_k}(\boldsymbol{\Theta})\right)_m\right]^2. \tag{2.239}$$

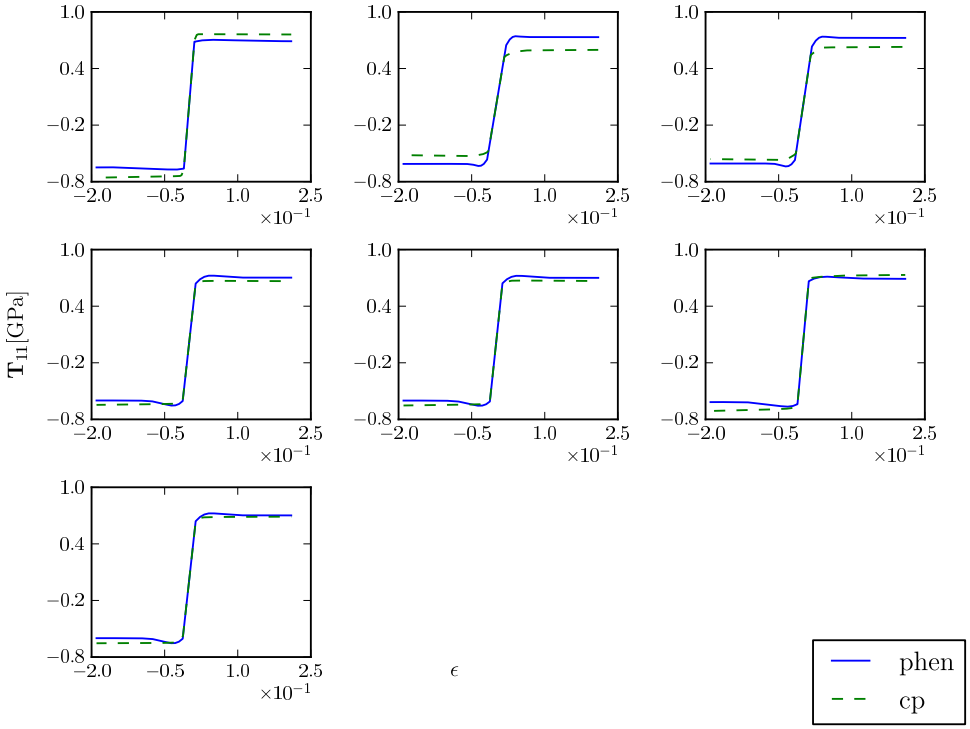

Figure 2.8: T_{11} Cauchy stress components for the BCC crystal plasticity model of Table 2.2 and best fit phenomenological yield function for seven initial orientation $\mathbf{K}_0 \in \mathrm{SO}(3,\mathbb{R})$. Both extension and contraction behavior was used to calibrate the model as indicated. Solid lines are results of the phenomenological model, the dashed lines are the crystal plasticity model.

In these results the number of initial orientations tested was $N_{\text{grains}} = 7$, and the plastic deformation was sampled at $N_{\text{steps}} = 10$ data points. The best fit parameters are given in Table 2.4. The units are such that the flow rule makes sense, e.g. we have $\partial y/\partial \mathbf{S}$ of the same units as $\mathbf{\Omega}(\mathbf{S})$, so since $\mathbf{\Omega}(\mathbf{S})$ has cubic expressions of $\mathbf{S}$, the constants in $\mathbf{\Omega}$ must be units of stress^{-2} to match the linear-in-stress $\partial y/\partial \mathbf{S}$. The numerical differences between the BCC and FCC models have to do with with the stress values present during plastic flow, compare for example Figure 2.7 and Figure 2.8. The last column entry Φ^* denotes the objective function value at the optimal solution. This value is mostly useful for comparisons between models.

Next, the calibrated parameters are used to qualitatively assess the ability to capture the reorientation behavior of the single crystal. In Figure 2.9 and Figure 2.10 are shown the extension axis $\mathbf{e}_1$ of (2.222) projected into the crystal reference configuration κ_i; an inverse

Table 2.4: Best fit material parameters for $\mathbf{\Omega}(\mathbf{S})$. The units are [GPa^{-2}], as required by the flow rule.

crystal	b_{11}	c_1	c_2	c_3	Φ^*
BCC	0.452	9.73	-7.72	-0.961	0.207
FCC	432.93	-1740.61	1092.45	198.73	0.227

Table 2.5: Best fit material parameters for $\mathbf{\Omega}(\bar{\mathbf{S}})$ up to quintic order. The units are [GPa^{-2}], [GPa^{-4}] as required by the flow rule.

crystal	a_1	a_2	a_3	b_1	b_2	b_3	c_{11}
BCC	52.3	-20.2	-0.12	0.88	99.9	21.0	-50.4
FCC	-1488.4	921.8	109.4	-5.4	-29.7	27.8	-1.3
c_{12}	c_{21}	c_{22}	c_{31}	c_{32}	d_1	d_2	Φ^*
-178.4	28.1	59.7	-5.9	5.1	-48.5	-99.7	0.14
$5.5 \cdot 10^{-4}$	17.5	-7.6	17.1	-49.6	23.8	23.4	0.23

pole figure. The inset figure is a zoomed in region from the figure. Blue and black circles represent the crystal plasticity prediction in extension, contraction respectively; red and purple crosses represent the phenomenological model prediction in extension, contraction respectively. On a visual basis the agreement is generally very good for the BCC crystal. The FCC crystal captures the sense of reorientation decently well, but the final reorientation on the inverse pole figure is of less magnitude than the crystal plasticity model.

We also tabulate calibration results from the other constitutive models for lattice reorientation. Table 2.5 shows the results from the quinitic order reorientation function, $\mathbf{\Omega}(\bar{\mathbf{S}})$, in (2.213), (2.212). Table 2.6 shows the results based on the function $\mathbf{\Omega}(\bar{\mathbf{S}}, \dot{\bar{\mathbf{S}}})$ in (2.186), (2.184), with the reduction

$$F(\mathbf{A}, \mathbf{B}, \mathbf{v}) = \sum_i c_i z_i. \tag{2.240}$$

Equation (2.240) follows from (2.186) after considering only deviatoric stress and stress rate contributions.

2.4.1.2.3 Viscoplastic extension Using the same material point simulation, (2.222), we can exercise the viscoplastic extension of the model and the evolution to the rate inde-

Table 2.6: Best fit material parameters for $\mathbf{\Omega}(\bar{\mathbf{S}}, \dot{\bar{\mathbf{S}}})$ up to order (2,1) in $\bar{\mathbf{S}}, \dot{\bar{\mathbf{S}}}$.

crystal	c_1	c_2	c_3	c_4	c_5	c_6	c_7	Φ^*
BCC	0.045	0.16	0.002	0.079	-0.122	-1.97	0.02	0.194
FCC	35.2	77.4	25.2	-70.5	292.2	-384.4	$= 169.9$	0.211

pendent limit. The viscoplastic extension uses flow rule of the form

$$\mathbf{K}^{-1}\dot{\mathbf{K}} = -\frac{1}{\nu}\left(\frac{\partial y}{\partial \mathbf{S}} + \mathbf{\Omega}\right), \tag{2.241}$$

where ν is a material constant representing viscosity of plastic flow. Note that the rate independent limit is $\nu \to 0$, which we achieve in practice by executing the algorithm in (2.224). Also note that this extension is an example of a simple Perzyna-type overstress model, see (2.98). For example, taking a stress dependent viscosity of the form $\nu = \nu(\mathbf{S})$ and generating constitutive equations from the methods in §2.3.3.1 would be another admissible formulation of the model mentioned in (2.98).

In (2.241), the yield condition $y(\mathbf{S})$ is the same as for the rate independent case; the calibrated parameters from Table 2.3 are used. The axial deformation in (2.222) at different deformation rates can be characterized by the fixed parameter $\dot{s}$. In Figure 2.11, the axial ($\mathbf{e}_1$) stress behavior as a function of the ratio of the extension rate $\dot{s}$ to the material viscosity ν is plotted. As the viscosity ν decreases, the rate independent limit is reached. As an important point, Figure 2.11 shows that the assumptions of small elastic strain in (2.107) may not be satisfied for certain material viscosities or for sufficiently high rates of loading. In the rate independent case, there is a natural restriction to stress states to be within the elastic region defined by $y(\mathbf{S}) \leq 0$, see (2.103). However in the overstress model of (2.241), there is no restriction of stress states to the elastic region. Therefore with viscoplastic simulations the strains should be checked to make sure that the conditions presumed to be valid in the theoretical construction are indeed still valid; in this case, that elastic strains are small $< 1\%$.

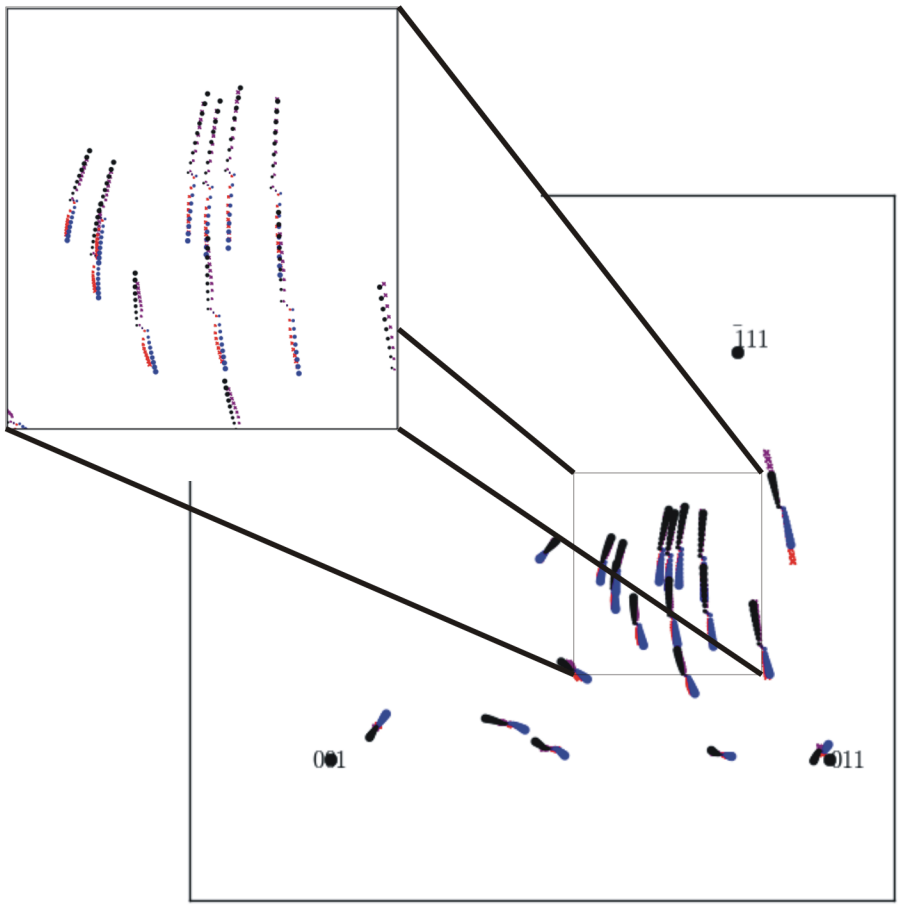

Figure 2.9: Inverse pole figure for extension axis $\mathbf{e}_1$ with $s \in [1, 1.1]$ in for extension and $s \in [1, 0.9]$ for compression, for BCC crystal. Blue and black circles are the crystal plasticity prediction in extension, contraction resp.;red and purple crosses are the phenomenological prediction in extension, contraction.

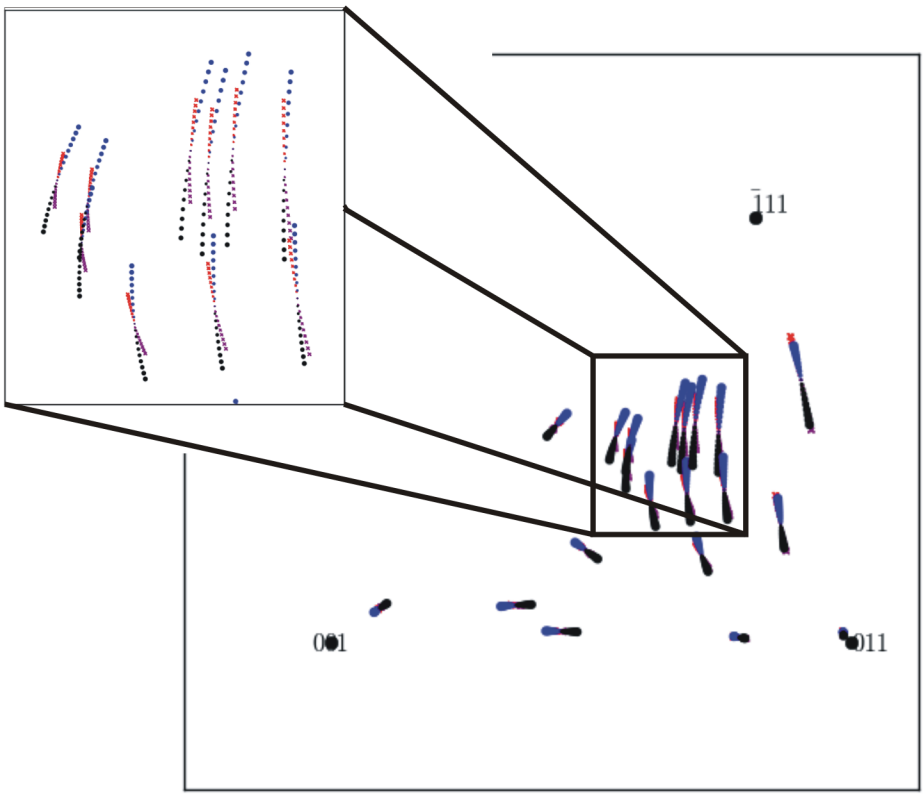

Figure 2.10: Inverse pole figure for extension axis $\mathbf{e}_1$ up to $s \in [1, 1.1]$ in extension and $s \in [1, 0.9]$ in contraction, for FCC crystal. Blue and black circles are the crystal plasticity prediction in extension, contraction resp.; red and purple crosses are the phenomenological prediction in extension, contraction.

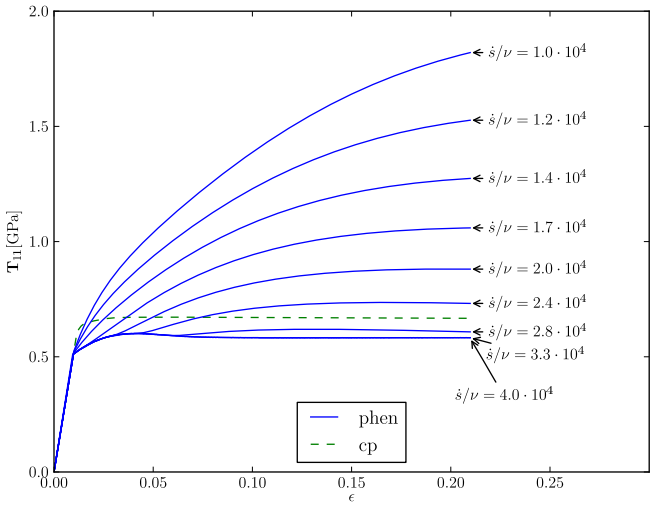

Figure 2.11: Material point simulations of the viscoplastic overstress model (2.98) with flow rule (2.241). The figure indicates that elastic strains may not be small depending on the material viscosity and/or rate of loading, thereby requiring use of (2.104). Such conditions must be checked if simulation results are to be trusted.

2.4.1.3 Discussion

In this section, constitutive functions requested by the phenomenological theory of §2.2 were grounded in reality by calibrating against a prediction from a crystal plasticity model which is regarded as experimental data. This calibration was constructed in recognition of the fact that lattice deformation is measurable using X-ray diffraction, so a theory which predicts how the lattice evolves can, in principle, be related to experimental observations[6]. We obtained reasonable agreement with the crystal plasticity model. The BCC fit in Figure 2.9 was qualitatively better than the FCC fit of Figure 2.10, in terms of matching the reorientation behavior (see figure insets). One reason this may be is because the BCC crystal plasticity model we were calibrating against had 24 slip systems, while the FCC model had 12 slip systems, see Tables A.1, A.2. The increased number of slip systems to consider makes the BCC model more isotropic in some sense.

One question we were curious in investigating was how the model would handle the different reorientation behavior of FCC and BCC crystals. For example, according to crystal plasticity, the point group symmetry of the crystal is largely irrelevant in determining plastic flow; it is the space group symmetry determines the slip systems and the flow in (2.229). Therefore, the plastic flow evolution for FCC and BCC crystals have seemingly little in common from this viewpoint. However in classical phenomenological thinking, we only require information about the point group symmetry of the material. Therefore the distinction between BCC and FCC must come out in the constitutive equations; for the same type of constitutive equation this must be evidenced in the numerical values of the material parameters associated to the constitutive equation. This was indeed borne out in our calibration, where we achieved reasonable matching of both FCC and BCC crystal plasticity models with our seven parameter model, $c_1^y, c_2^y, y_{\max}, b_{11}^{\text{cube}}, c_1^{\text{cube}}, c_2^{\text{cube}}, c_3^{\text{cube}}$. Interestingly, in Table 2.4 the signs of the dominant parameters $c_1^{\text{cube}}, c_2^{\text{cube}}$ are opposite one another, in terms of sign, for the FCC and BCC cases. This is consistent with the crystal plasticity based observation that the skew part of the flow rule differs between FCC and BCC crystals, see Table A.1 and Table A.2 and note that $\mathbf{n}_0^i(\text{BCC}) \cong \mathbf{s}_0^i(\text{FCC})$ and $\mathbf{s}_0^i(\text{BCC}) \cong \mathbf{n}_0^i(\text{FCC})$, so that $(\text{skw } \mathbf{K}^{-1}\dot{\mathbf{K}})_{\text{BCC}} \approx -(\text{skw } \mathbf{K}^{-1}\dot{\mathbf{K}})_{\text{FCC}}$.

Clearly the phenomenological model cannot compete with the simple shear deformations predicted by crystal plasticity in the simple material point simulation employed for calibration in this paper. However as more complicated crystal plasticity models are proposed to describe experimental observations the phenomenological model may prove to be more attractive. In fact, viewed through the same lens as our phenomenological theory, crystal plasticity has many more parameters: 3 for each $\mathbf{s}_0^\alpha \otimes \mathbf{n}_0^\alpha$ system note ($\|\mathbf{s}_0^\alpha\| = \|\mathbf{n}_0^\alpha\| = 1$, and $\mathbf{s}_0^\alpha \cdot \mathbf{n}_0^\alpha = 0$), along with the two parameters $\dot{\gamma}_0, m$, for a total of 38 parameters for the FCC model. The phenomenological theory here has seven parameters, which shows some promise for improving the constitutive framework.

It is important to note that an open question is whether the best fit parameters are

[6]See Chapter 3 for a thorough treatment of this task from the experimental side of the equation.

the best fit in a global or local sense of optimization. The phenomenological function for $\mathbf{\Omega}$ was surely among the simplest consistent with the core requirements of hexoctahedral symmetry and the requirement $\mathbf{\Omega}(\mathbf{S}) = -\mathbf{\Omega}(-\mathbf{S})$. Even so, the four material parameters available to the material, $(b_{11}^{\text{cube}}, c_1^{\text{cube}}, c_2^{\text{cube}}, c_3^{\text{cube}})$, constitute a large parameter search space; and there are no thermodynamic restrictions on these parameters which might otherwise reduce the search region. As a preliminary effort to examine if there were effects of local optimum, we tested various initial conditions, but did not observe any better parameter combinations. However, this is not proof that there does not exist better parameter values. Roughly speaking, the more parameters introduced into the phenomenological model in the format suggested here, the more the question of whether an optimum value is a global vs local maximum will arise. With more parameters included in the model, a more exhaustive genetic algorithm is suggested. This is a general issue in constitutive parameter determination (Liu and Han, 2003).

We also investigated other functional forms for the lattice reorientation $\mathbf{\Omega}(\mathbf{S})$. For example, the crystal plasticity flow rule has a lattice reorientation analogous to ours, with $\mathbf{\Omega} \approx \text{skw}\, \mathbf{K}^{-1}\dot{\mathbf{K}}$. In the crystal plasticity flow rule however, this is related to the symmetric part of the flow, $\text{sym}\, \mathbf{K}^{-1}\dot{\mathbf{K}}$, through the shear rates $\dot{\gamma}$. That is, both skew-symmetric and symmetric parts of the flow $\mathbf{K}^{-1}\dot{\mathbf{K}}$ originate from one function, the so called hidden variable γ (Rice, 1971). Inspired by this coupling, we attempted to fit parameters to reorientation functions of the form

$$\mathbf{\Omega} = \hat{\mathbf{\Omega}}\left(\frac{\partial y}{\partial \mathbf{S}}\right) \tag{2.242}$$

which uses the same constitutive framework as that resulting in (2.209), e.g. we simply repace $\mathbf{A} \to y_{,\mathbf{S}}$. This was also used in a similar context for sheet metal plasticity by Cleja-Tigoiu and Iancu (2011). No significant improvements in the ability to match the crystal plasticity model with this form for $\mathbf{\Omega}$ were observed upon executing the same fitting algorithm with this modification. There was perhaps a modest $< 5\%$ improvement, judged by comparing optimal residual values, which may or may not be significant. The slightly better matching may simply be a symptom of the fact that the crystal plasticity model naturally encodes such coupling, which may or may not be borne out in raw experimental data. Further study of applications will judge whether such a reorientation function is to be preferred, but it has a certain intrinsic appeal.

A final point to make is that the residuals used to calibrate the lattice reorientation in (2.238) have a non-trivial dependence on the accuracy of the matching to the yield function. That is, it is possible that our attention should be drawn to improving the yield function fits of Figure 2.7 and Figure 2.8 instead of focusing on improving the lattice reorientation. Higher order polynomials for the yield function have additional material constants and may get better fits to experimental data. For that investigation to proceed, a good starting point would be the publications like Soare and Barlat (2010), in regard to yield functions for sheet metals. This community has developed the techniques to ensure that they obtain convex yield surfaces.

In order to facilitate initial studies, that is, to get estimates for the yield and lattice reorientation functions, we recommend using the two stage estimation method employed in this section. That is, first fit the yield function parameters using (2.233), and then the lattice reorientation, (2.239). From these initial estimates, further refining both sets of parameters simultaneously, in a global optimum search may be a useful framework to explore.

In the next section, we implement the model into plane strain simulations, in order to examine predictions from the model. To our knowledge this constitutes the first attempt at implementing classical models along the lines of Fox (1968) into simulations.

2.4.2 Plane strain simulations

In this section we solve for the motion of an elastic-plastic body according to the theory of §2.2. We obtain $\boldsymbol{\chi}(\mathbf{X},t), \mathbf{K}(\mathbf{X},t)$ by numerically integrating the equation of motion (2.17), along with the flow rule, (2.19). We test out the calibrated constitutive models from §2.4.1.2. In this introduction we give a short overview of the numerical formulation of the problem. Later we give details such as which particular constitutive functions were tested.

Overview of numerical formulation. To reduce computational resource requirements we consider plane strain boundary value problems, so that

$$\chi_3(\mathbf{X},t) = X_3 \tag{2.243}$$

and

$$\chi_\alpha(\mathbf{X},t) = \chi_\alpha(X_1,X_2,t), \qquad \alpha = 1,2. \tag{2.244}$$

These requirements imply that the deformation gradient $\mathbf{F}$ is of the form

$$\mathbf{F} = \nabla\boldsymbol{\chi} = \begin{bmatrix} \partial\chi_1/\partial X_1 & \partial\chi_1/\partial X_2 & 0 \\ \partial\chi_2/\partial X_1 & \partial\chi_2/\partial X_2 & 0 \\ 0 & 0 & 1 \end{bmatrix}. \tag{2.245}$$

We also consider plastic deformation to be of the form

$$\mathbf{K}(\mathbf{X},t) = \hat{\mathbf{K}}(X_1,X_2,t), \tag{2.246}$$

and for simplicity take the restriction

$$\mathbf{K} = \begin{bmatrix} K_{11} & K_{12} & 0 \\ K_{21} & K_{22} & 0 \\ 0 & 0 & 1 \end{bmatrix}. \tag{2.247}$$

The lattice deformation is computed from $\mathbf{F},\mathbf{K}$ using (2.12), so that

$$\mathbf{H} = \mathbf{F}\mathbf{K} = (\nabla\boldsymbol{\chi})\,\mathbf{K}. \tag{2.248}$$

In overview of the method, we discretize the material and time domain $\mathbf{X}, t$ and solve for the correspondingly discretized functions $\boldsymbol{\chi}(\mathbf{X}, t), \mathbf{K}(\mathbf{X}, t)$. Then these fields can be integrated in time using a simple forward Euler scheme. For example, we need the velocity of the material

$$\dot{\boldsymbol{\chi}} \equiv \mathbf{v}^{(i)} = \frac{\mathbf{x}^{(i+1)} - \mathbf{x}^{(i)}}{\Delta t}, \tag{2.249}$$

from which the position field $\mathbf{x}$ is updated at the step $(i+1)$, the acceleration

$$\ddot{\boldsymbol{\chi}} = \dot{\mathbf{v}}^{(i)} = \frac{\mathbf{v}^{(i+1)} - \mathbf{v}^{(i)}}{\Delta t} \tag{2.250}$$

which updates the velocities $\mathbf{v}$ at the next step $(i+1)$, by using the balance of linear momentum equation (2.17), and

$$\dot{\mathbf{K}}^{(i)} = \frac{\mathbf{K}^{(i+1)} - \mathbf{K}^{(i)}}{\Delta t} \tag{2.251}$$

is the evolution of the plastic deformation, which updates the plastic deformation using the flow rule (2.19). Taking (2.249), (2.250), (2.251) we have the staggered update equations Herrmann and Bertholf (1983)

$$\mathbf{x}^{(i+1)} = \mathbf{v}^{(i+1)}\Delta t + \mathbf{x}^{(i)} \tag{2.252}$$

$$\dot{\mathbf{v}}^{(i+1)} = \frac{1}{\rho_0}\left(\operatorname{Div}\mathbf{P}(\mathbf{H}, \mathbf{K})^{(i)} + \rho_0 \mathbf{b}^{(i)}\right)\Delta t + \dot{\mathbf{v}}^{(i)} \tag{2.253}$$

$$\mathbf{K}^{(i+1)} = \dot{\mathbf{K}}^{(i)}\Delta t + \mathbf{K}^{(i)}, \tag{2.254}$$

where $\mathbf{P}(\mathbf{H}, \mathbf{K})$ and $\dot{\mathbf{K}}$ are given by constitutive functions which are given later. We now describe the discretization scheme employed in this study, which is an explicit Lagrangian framework. Literature discussions of the method can be found in the reviews (Herrmann and Bertholf, 1983; Silling, 1988). For completeness we describe our take on the method here; for other details consult Herrmann and Bertholf (1983); Silling (1988).

2.4.2.1 Computational grid and data storage

The computational grid used in the solution of Equations 2.252 to 2.254 is described in this section. Discretization of the material domain is performed; the nodes of subsequent domain carry information on $\mathbf{x}, \mathbf{v}$, or more simply, the function $\boldsymbol{\chi}(\mathbf{X}, t)$. Zonal values carry information on the deformation gradient and plastic deformation, $\mathbf{F}, \mathbf{K}$, and hence the lattice deformation and stress response $\mathbf{H}, \mathbf{P}$. The proposed computational grid is shown in Figure 2.12, the solid dots are the nodes, and the rectangular regions are the zones. On the left side of the figure is the fixed material domain where computation is performed. Under the motion $\boldsymbol{\chi}$ the rectangular grid in the material domain gets distorted as shown on the right side of the figure.

Our consideration of plane strain (2.244) allows the use of Green's theorem in the plane to relate nodal values $\boldsymbol{\chi}$ to zonal values $\mathbf{F}$ in a manner consistent with the discretization, We now describe in detail how we compute the quantities $\mathbf{F}, \mathrm{Div}\,\mathbf{P}, \boldsymbol{\xi}$, which enter into the formulation.

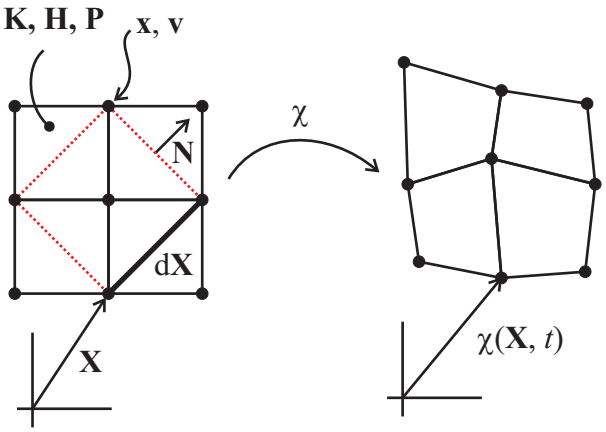

Figure 2.12: Illustration of the computational grid for the plane strain simulations. The nodes store position and velocity, $\mathbf{x}, \mathbf{v}$, while zones store $\mathbf{F}, \mathbf{K}$, and hence $\mathbf{H}, \mathbf{P}$. Since $\boldsymbol{\xi}$ may be used in the yield function, it needs to be determined on the zones as well.

Determination of F. The gradient of the material motion $\mathbf{F} = \nabla\boldsymbol{\chi}$ is given by

$$\mathbf{F} = \frac{1}{A}\int_{\Omega} \nabla\boldsymbol{\chi}\mathrm{d}A = \frac{1}{A}\int_{\partial\Omega} \boldsymbol{\chi}\otimes\mathbf{N}\mathrm{d}A, \tag{2.255}$$

where $\mathbf{F}$ is the zone volume averaged deformation gradient over Ω, $\mathbf{N}$ is the normal vector in the fixed material reference configuration, set by the initial discretization of the material domain. We have used Green's theorem in the plane to arrive at $(2.255)_2$. The zonal area A is obtained by Gaussian quadrature over the reference discretization of the material domain, see §A.4 for further information.

In Figure 2.13 is illustrated the method used to obtain $\mathbf{F}$ from the nodal data of $\boldsymbol{\chi}$. The boundary of a zonal region, $\partial\Omega$, is indicated by the solid dark line. The local nodal points are labeled $0, 1, 2, 3$ in a counterclockwise ordering. The mapped region $\boldsymbol{\chi}(\Omega)$ is shown on the right hand side of the figure, with the values of $\boldsymbol{\chi}$ at the local nodes indicated. Integration of $\boldsymbol{\chi}\otimes\mathbf{N}$ over the boundary $\partial\Omega$ with nodal locations $0, 1, 2, 3$ is accomplished by decomposition along each edge, e.g.

$$\int_{\partial\Omega} \boldsymbol{\chi}\otimes\mathbf{N} = \int_{0,1} \boldsymbol{\chi}\otimes\mathbf{N}\mathrm{d}A + \int_{1,2} \boldsymbol{\chi}\otimes\mathbf{N}\mathrm{d}A + \int_{2,3} \boldsymbol{\chi}\otimes\mathbf{N}\mathrm{d}A + \int_{3,0} \boldsymbol{\chi}\otimes\mathbf{N}\mathrm{d}A. \tag{2.256}$$

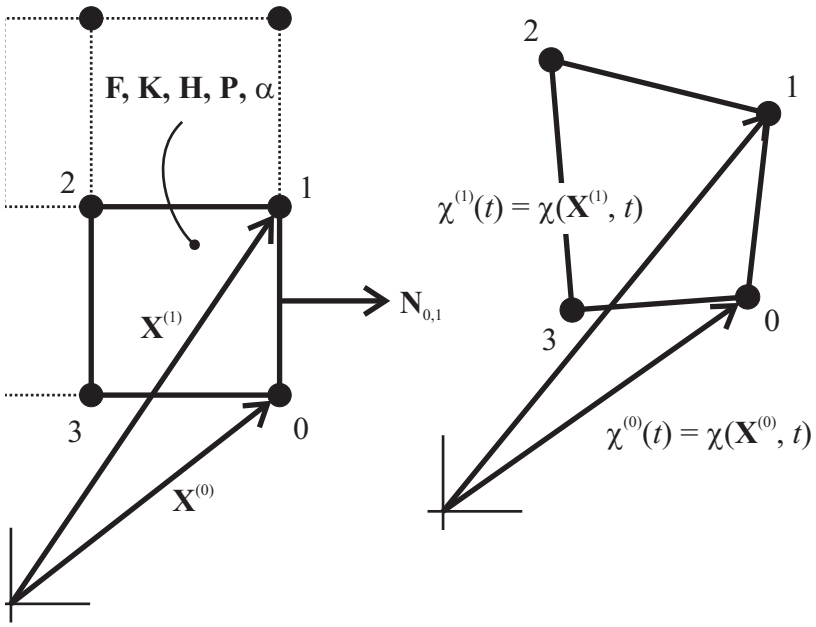

Figure 2.13: Computational grid, highlighting the integration curve used for obtaining the zonal value of $\mathbf{F}$.

For illustration, take one term from the right hand side of (2.256). We have

$$\int_{0,1} \boldsymbol{\chi} \otimes \mathbf{N} \mathrm{d}A = \int_{0,1} \boldsymbol{\chi}(s) \otimes \mathbf{N} \mathrm{d}s, \tag{2.257}$$

where the area integral is reduced to the form $\mathrm{d}A = 1 \cdot \mathrm{d}s$ from the imposition of plane strain, and along the edge $0, 1$ we have the linear approximation

$$\boldsymbol{\chi}(s) = \boldsymbol{\chi}^{(0)} + (\boldsymbol{\chi}^{(1)} - \boldsymbol{\chi}^{(0)})s, \tag{2.258}$$

where $\boldsymbol{\chi}^{(0)}$ is the value of $\boldsymbol{\chi}$ at local node 0 and $\boldsymbol{\chi}^{(1)}$ is the value of $\boldsymbol{\chi}$ at local node 1, see Figure 2.13. Using (2.258) in (2.257) gives

$$\int_{0,1} \boldsymbol{\chi} \otimes \mathbf{N} \mathrm{d}A = \boldsymbol{\chi}^{(0)} s + (\boldsymbol{\chi}^{(1)} - \boldsymbol{\chi}^{(0)}) \frac{s^2}{2}\bigg|_0^1 \otimes \mathbf{N}_{0,1} \tag{2.259}$$

$$= \boldsymbol{\chi}^{(0)} + (\boldsymbol{\chi}^{(1)} - \boldsymbol{\chi}^{(0)}) \frac{1}{2} \otimes \mathbf{N}_{0,1} \tag{2.260}$$

$$= \frac{1}{2}(\boldsymbol{\chi}^{(0)} + \boldsymbol{\chi}^{(1)}) \otimes \mathbf{N}_{0,1}, \tag{2.261}$$

where $\mathbf{N}_{0,1}$ is fixed based on the initial discretization of the material reference configuration. It can be computed from

$$\mathbf{N}_{0,1} = (\mathbf{X}^{(1)} - \mathbf{X}^{(0)}) \times \mathbf{e}_3 / \|(\mathbf{X}^{(1)} - \mathbf{X}^{(0)}) \times \mathbf{e}_3\|. \tag{2.262}$$

Therefore we can compute $\mathbf{F}$ on the zonal data structure. Like $\mathbf{F}$, the plastic deformation $\mathbf{K}$ is stored on the zonal data structure. Hence, so is $\mathbf{H} = \mathbf{F}\mathbf{K}$, the lattice deformation.

Determination of $\mathrm{Div}\,\mathbf{P}$**.** The divergence of the stress at the nodal locations is obtained by using the sequence

$$(\mathrm{Div}\,\mathbf{P})_{\text{node}} = \frac{1}{A}\int_{\Omega} \mathrm{Div}\,\mathbf{P}\mathrm{d}A = \frac{1}{A}\int_{\partial\Omega} \mathbf{P}\mathbf{N}\mathrm{d}A, \tag{2.263}$$

where we have again used Green's theorem in arriving at $(2.263)_2$. To compute the integration of $(2.263)_2$, we employ a similar decomposition as in (2.256), although with a different local numbering scheme, as shown in Figure 2.14. Taking one term to illustrate, we have

$$\int_{0,1} \mathbf{P}\mathbf{N}\mathrm{d}A = \int_{0,1} \mathbf{P}(s)\otimes\mathbf{N}(s)\mathrm{d}s, \tag{2.264}$$

with $\mathbf{P}(s) = \mathbf{P}_{0,1} = \hat{\mathbf{P}}(\mathbf{H}_{0,1}, \mathbf{K}_{(0,1)})$ given by a constitutive equation, (2.39), and $\mathbf{N}(s) = \mathbf{N}_{0,1}$ is computed as in (2.262). Figure 2.14 illustrates the described integration procedure. The solid red line is the boundary $\partial\Omega$, with local nodes labeled $0, 1, 2, 3$ in counterclockwise order. The nodal points $\mathbf{X}^{(0)}, \mathbf{X}^{(1)}$ are indicated in the figure. The required normal vector $\mathbf{N}_{0,1}$ is also shown. The result of the integration is the vector $\mathrm{Div}\,\mathbf{P}$, shown at the center of the integration region. This nodal force is coupled to the nodal acceleration through the equation of motion, (2.253).

From (2.253) we also require nodal densities, which are defined on the zones. The nodal density in (2.253) is obtained from the equation

$$A(\rho_0)_{\text{node}} = \frac{1}{4}(A_{0,1}\rho_{0,1} + A_{1,2}\rho_{1,2} + A_{2,3}\rho_{2,3} + A_{3,0}\rho_{3,0}), \tag{2.265}$$

where A is obtained from the methods of §A.4 for the stencil shown in Figure 2.14, $\rho_{i,j}$ are the (fixed) material densities in the zonal area, and $A_{i,j}$ are the zonal areas obtained from the stencil in Figure 2.13.

Determination of $\boldsymbol{\xi}$**.** Finally, we consider the dislocation content $\boldsymbol{\xi}$, (2.16), which is reprinted here for convenience

$$\boldsymbol{\xi} = J_K\mathbf{K}^{-1}\mathrm{Curl}\,\mathbf{K}^{-1}. \tag{2.266}$$

The computation of $\boldsymbol{\xi}$ is new in the plasticity literature, see Lele and Anand (2009) for a version of this for isotropic materials using ABAQUS. We seek to directly incorporate $\boldsymbol{\xi}$ derived from the plastic deformation field into hardening phenomenology, see §2.3.3.1, which to our knowledge is a new effort.

In the present numerical framework, $\boldsymbol{\xi}$ is obtained by considering the Cartesian component expressions

$$\mathbf{K}^{-1} = (\mathbf{K}^{-1})_{ij}\mathbf{e}_i\otimes\mathbf{e}_j,$$

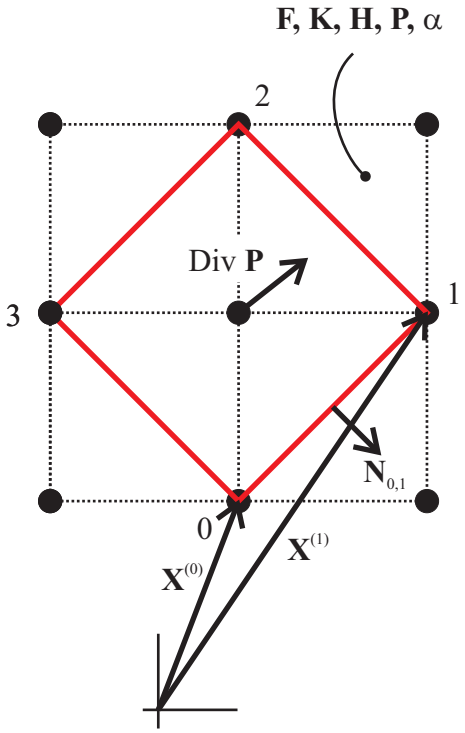

Figure 2.14: Computational grid for Div $\mathbf{P}$. The solid line shows the integration region used to obtain the vector Div $\mathbf{P}$ at the required node location.

$$\begin{aligned}\nabla \times \mathbf{K}^{-1} &= (\mathbf{K}^{-1})_{ij,k}\mathbf{e}_i \otimes \mathbf{e}_j \times \mathbf{e}_k \\ &= \epsilon_{jkm}(\mathbf{K}^{-1})_{ij,k}\mathbf{e}_i \otimes \mathbf{e}_m. \end{aligned} \tag{2.267}$$

For the plane strain case under consideration given by Equation (2.247), (2.267) simplifies to

$$\begin{aligned}\nabla \times \mathbf{K}^{-1} &= (\mathbf{K}^{-1})_{i1,2}\mathbf{e}_i \otimes \mathbf{e}_3 - (\mathbf{K}^{-1})_{i2,1}\mathbf{e}_i \otimes \mathbf{e}_3 \\ &= [(\mathbf{K}^{-1})_{11,2} - (\mathbf{K}^{-1})_{12,1}]\mathbf{e}_1 \otimes \mathbf{e}_3 + [(\mathbf{K}^{-1})_{21,2} - (\mathbf{K}^{-1})_{22,1}]\mathbf{e}_2 \otimes \mathbf{e}_3. \end{aligned} \tag{2.268}$$

This quantity can be computed for the present numerical grid in the following manner. Consider Stokes' theorem,

$$\int_A \mathbf{n} \cdot \nabla \times \mathbf{v} = \int_{\partial A} \mathbf{v} \cdot \mathrm{d}\mathbf{l}, \tag{2.269}$$

where $\mathbf{l}$ is the tangent vector to the boundary ∂A. We wish to apply the theorem to $\mathbf{K}^{-1}$. Therefore take $\mathbf{v} = (\mathbf{K}^{-1})^{\mathrm{T}}\mathbf{a}$, for $\mathbf{a}$ a constant vector. Then Stokes' theorem reads

$$\int_A \mathbf{n} \cdot \nabla \times \mathbf{K}^{-\mathrm{T}}\mathbf{a} = \int_{\partial A} \mathbf{K}^{-\mathrm{T}}\mathbf{a} \cdot \mathrm{d}\mathbf{l}. \tag{2.270}$$

Since $\mathbf{a}$ is constant, the right hand side is written

$$\int_{\partial A} \mathbf{K}^{-\mathrm{T}}\mathbf{a}\cdot \mathrm{d}\mathbf{l} = \mathbf{a}\cdot\int_{\partial A}\mathbf{K}^{-1}\cdot\mathrm{d}\mathbf{l}, \tag{2.271}$$

which can be computed with our computational grid using techniques similar to those already employed. The left hand side of (2.270) is written in components as

$$\begin{aligned}\int_A \mathbf{n}\cdot\nabla\times\mathbf{K}^{-\mathrm{T}}\mathbf{a} &= \int_A \epsilon_{ijk}\partial_i(\mathbf{K}^{-1})_{mj}a_m n_k \mathrm{d}A \\ &= \mathbf{a}\cdot\int_A \epsilon_{ijk}\partial_i(\mathbf{K}^{-1})_{mj}n_k\mathbf{e}_m\mathrm{d}A.\end{aligned} \tag{2.272}$$

For the plane strain case, the normal $\mathbf{n}$ in Stokes' theorem is $\mathbf{n}=\mathbf{e}_3$, so (2.272) becomes

$$\mathbf{a}\cdot\int_A \epsilon_{ijk}\partial_i(\mathbf{K}^{-1})_{mj}n_k\mathrm{d}A\mathbf{e}_m = \mathbf{a}\cdot\int_A\left[\epsilon_{ij3}\partial_i(\mathbf{K}^{-1})_{mj}\mathbf{e}_m\right]\mathrm{d}A. \tag{2.273}$$

The quantity in brackets on the right hand side is expanded out as

$$\begin{aligned}\epsilon_{ij3}\partial_i(\mathbf{K}^{-1})_{mj}\mathbf{e}_m &= \partial_1(\mathbf{K}^{-1})_{12}\mathbf{e}_1 + \partial_1(\mathbf{K}^{-1})_{22}\mathbf{e}_2 - \partial_2(\mathbf{K}^{-1})_{11}\mathbf{e}_1 - \partial_2(\mathbf{K}^{-1})_{21}\mathbf{e}_2 \\ &= [\partial_1(\mathbf{K}^{-1})_{12} - \partial_2(\mathbf{K}^{-1})_{11}]\mathbf{e}_1 + [\partial_1(\mathbf{K}^{-1})_{22} - \partial_2(\mathbf{K}^{-1})_{21}]\mathbf{e}_2,\end{aligned} \tag{2.274}$$

a vector whose components are the required quantity in the expression for $\nabla\times\mathbf{K}^{-1}$, in (2.268). Therefore (2.274) and (2.268), along with (2.273), (2.272), and (2.270), (2.271) we have

$$\frac{1}{A}\int_{\partial A}\mathbf{K}^{-1}\cdot\mathrm{d}\mathbf{l} = -(\overline{\nabla\times\mathbf{K}^{-1}})_{13}\mathbf{e}_1 - (\overline{\nabla\times\mathbf{K}^{-1}})_{23}\mathbf{e}_2, \tag{2.275}$$

where $\overline{\nabla\times\mathbf{K}^{-1}}$ represents the area average of $\nabla\times\mathbf{K}^{-1}$ on the left hand side of (2.270), and the factor $1/A$ comes from pulling out this area average from (2.270).

We now compute the left hand side of (2.275). We integrate piecewise around the loop depicted in Figure 2.15 in a fashion again similar to (2.256). A single term of which is written

$$\int_{0,1}\mathbf{K}^{-1}\cdot\mathrm{d}\mathbf{l} = \int_{0,1}\mathbf{K}^{-1}(s)\cdot\mathrm{d}\mathbf{l}, \tag{2.276}$$

where in this equation $\mathbf{K}^{-1}(s)=\mathbf{K}_{0,1}^{-1}$ and $\mathrm{d}\mathbf{l}=(\mathbf{X}^{(1)}-\mathbf{X}^{(0)})\mathrm{d}s$. The net result of one piece of the integration is

$$\int_{0,1}\mathbf{K}^{-1}\cdot\mathrm{d}\mathbf{l} = \mathbf{K}_{0,1}^{-1}\cdot(\mathbf{X}^{(1)}-\mathbf{X}^{(0)}). \tag{2.277}$$

Repeating (2.277) for the other integration segments gives the nodal values of $\overline{\nabla\times\mathbf{K}^{-1}}$. The computational stencil is illustrated in Figure 2.15, which shows the integration region in solid red line, with one element $\mathrm{d}\mathbf{X}_{0,1}=\mathbf{X}^{(1)}-\mathbf{X}^{(0)}$. The vector $\nabla\times\mathbf{K}^{-1}$ is shown at the center of the integration region. The values of $\boldsymbol{\xi}$ at the zones are found by integrating the nodal values of $\boldsymbol{\xi}$ in the manner of §A.4, which results in a simple numerical average of the nodal values for $\boldsymbol{\xi}$.

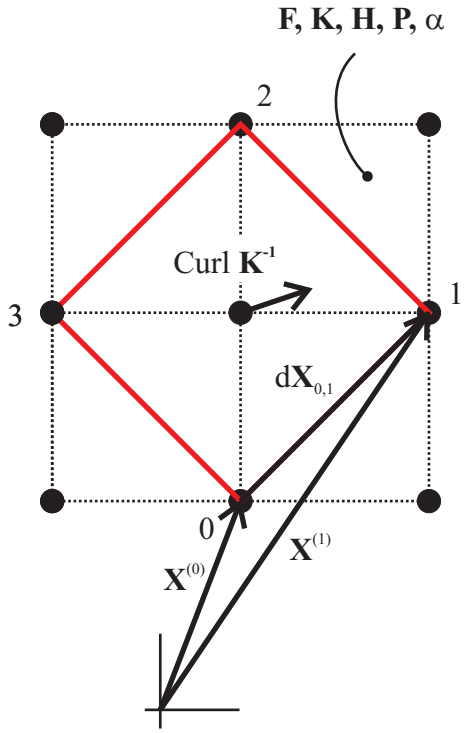

Figure 2.15: Computational grid for $\nabla \times \mathbf{K}^{-1}$, which is required for computing $\boldsymbol{\xi}$, the dislocation content.

Summary. In this section we have described how to obtain the required terms in the state update equations (2.252), (2.253) according to our simple discretization approach. To recap, the deformation gradient at the zones is obtained from (2.255), which incorporates the nodal quantities $\boldsymbol{\chi}$. The lattice deformation $\mathbf{H}$ is obtained from $\mathbf{F}$ along with the zonal values of $\mathbf{K}$, through $\mathbf{H} = \mathbf{FK}$, (2.248). The Piola stress $\mathbf{P}$ is obtained from (2.39) which requires $\mathbf{H}, \mathbf{K}$ and an assigned strain energy function. The divergence of the Piola stress is given at the nodes by (2.263), which couples to the evolution of the nodal data $\boldsymbol{\chi}$ through (2.253). The plastic deformation is updated from (2.254) through the flow rule. We have mentioned two methods of updating the plastic deformation. For the rate independent constitutive model, described in §2.2.3.2.1, (2.104), the plastic deformation flow rule is integrated by solving the equations (2.224), with the additional constraint that $\mathbf{K}^{(i+1)}$ is of the form (2.247). Therefore, for the plane strain case under consideration Equation (2.224) represents five equations for the five unknowns $\lambda, (\mathbf{K}^{-1})_{11}, (\mathbf{K}^{-1})_{12}, (\mathbf{K}^{-1})_{21}, (\mathbf{K}^{-1})_{22}$. The viscoplastic rate dependent model is described in (2.241), which does not require the solution of a set of nonlinear equations.

This completes the explanation of the numerical discretization algorithm. The theory requires the specification of the initial values for $\mathbf{K}(\mathbf{X}, t)$, as discussed in §2.2.1. In the next

section, we give an account of the algorithm used to generate these simple microstructures.

2.4.2.1.1 Microstructure generation algorithm In this section we describe the algorithm used to seed the plane strain simulations with initial grain orientations. The initial microstructure will be an interesting parameter to consider when examining the results of the simulations. Classical experimental observations including the Bauschinger effect and Hall-Petch relation may be sensitive to such microstructural details. Different initial grain orientations sets up elastic anisotropy, which causes strain localization phenomena.

To define the microstructure, we require initial values for the plastic deformation field at time $t = t_0$. In an X-ray diffraction experiment, the reference material configuration is defined to be the observed configuration - so that $\mathbf{F}(t = t_0) = \mathbf{I}$. Therefore (2.12) implies $\mathbf{K}(t = t_0) = \mathbf{H}(t = t_0)$. For small elastic strains, $\mathbf{H} \approx \mathbf{R}$, for $\mathbf{R} \in \mathrm{SO}(3, \mathbb{R})$, where in experiments $\mathbf{H}$ is determined by X-ray diffraction. In recognition of the experimental realities, we seed our numerical simulations with $\mathbf{K}(t = t_0) \in \mathrm{SO}(3, \mathbb{R})$. The following prescription for generating the microstructure is simple and is easily generated with pseudorandom numbers, so that Monte Carlo simulations may be performed over ensembles of microstructures, if so desired.

Given a spatial region parametrized by coordinates $\mathbf{x}$ which we wish to fill with crystals, we first generate an array of random locations in the mesh, $\{\mathbf{x}^{(i)} : i = 1, 2, ..., N_{\text{grains}}\}$, which represent the grain center positions. We also assign random orientations

$$A = \{\theta^{(i)} : i = 1, 2, ..., N_{\text{grains}}\} \tag{2.278}$$

to these locations by using the one dimensional orientation parametrization

$$\mathbf{K}_0(\theta) = \hat{\mathbf{R}}(\mathbf{e}_3, \theta), \tag{2.279}$$

where the axis of rotation $\mathbf{e}_3$ is the out of plane direction. Finally, we assign random sizes (according to a specified distribution function) to the locations, which represents something akin to the grain diameters, D, so that we generate the set

$$B = \{D^{(i)} : i = 1, 2, ..., N_{\text{grains}}\}. \tag{2.280}$$

The sizes are incorporated into matrices which represent a distance metric g_{ij}, so that we write

$$[g_{kl}^{(i)}(D^{(i)})] = \begin{bmatrix} D^{(i)} & 0 \\ 0 & D^{(i)} \end{bmatrix}. \tag{2.281}$$

The isotropic metric in (2.281) can be modified to be anisotropic ($g_{11} \neq g_{22}$, for example). Non isotropic metrics might be used if elongated grains are known to exist, or if experiments can give such information. Finally, the initial microstructural data is expressed by the set

$$C = \{(\mathbf{x}, \theta, D, g_{kl}(D))^{(i)} : i = 1, 2, ..., N_{\text{grains}}\}. \tag{2.282}$$

Given the seed data, C, the algorithm to specify the rest of the microstructure is given as follows. For each zone in the mesh, with center position $\mathbf{x}_{\text{zone}}$, compute the 'closest' seed point and give that zone the orientation, θ, corresponding to that closest seed point. Here 'closeness', denoted δ, is determined by the distance metric to the seed point, written

$$\delta^{(i)} \equiv g_{kl}^{(i)}(\mathbf{x}_{\text{zone}} - \mathbf{x}^{(i)})_k(\mathbf{x}_{\text{zone}} - \mathbf{x}^{(i)})_l. \tag{2.283}$$

The minimum distance is then given by

$$\min \delta \equiv \min\{g_{kl}^{(i)}(\mathbf{x}_{\text{zone}} - \mathbf{x}^{(i)})_k(\mathbf{x}_{\text{zone}} - \mathbf{x}^{(i)})_l : i = 1, 2, ..., N_{\text{grains}}\}, \tag{2.284}$$

so that $\theta(\mathbf{x}_{\text{zone}}) = \theta^*$, where θ^* is the orientation of the closest seed point, determined by (2.284). Carrying out this procedure for all zones in the mesh completes the assignment of the initial plastic deformation, $\mathbf{K}(t = t_0)$. An example microstructure generated from this procedure is shown in Figure 2.16.

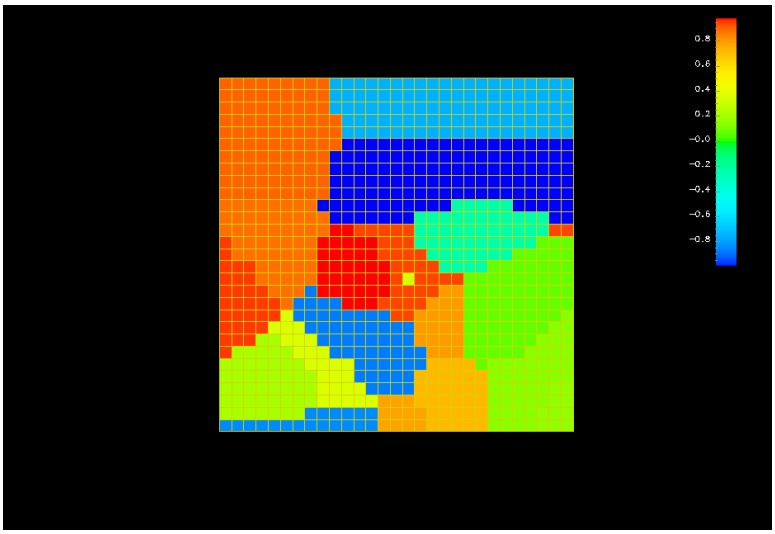

Figure 2.16: Microstructure generated by the algorithm described in the text leading to (2.284). The $K_{11}(0)$ component is visualized by the colormap.

2.4.2.2 Boundary value problems

We tested the numerical method in several simple boundary value problems. We used a square material domain, as shown in Figure 2.16 to perform the tests. In this section we describe the variety of boundary conditions imposed to the material, the exact constitutive equations used, and two methods of implementing hardening phenomenology.

2.4.2.2.1 Boundary conditions The boundary conditions used were one of the following

1. Extension - contraction cycles
2. Axial extension
3. Simple shear
4. Shock contraction

The axial extension, extension-contraction, and shock contraction boundary conditions were simulated by prescribing nodal velocities on the right hand edge, see Figure 2.17. The horizontal velocity v_1 on the left hand edge nodes was set to zero, while the velocity v_2 on the same edge was not fixed by boundary conditions. In other words, this is a roller type boundary condition. We also experimented with fixed placement boundary conditions on the left hand edge. The top and bottom boundaries were traction free. Surface tractions, if desired, would be implemented into the nodal force balance equations of (2.253), as described by Silling (1988).

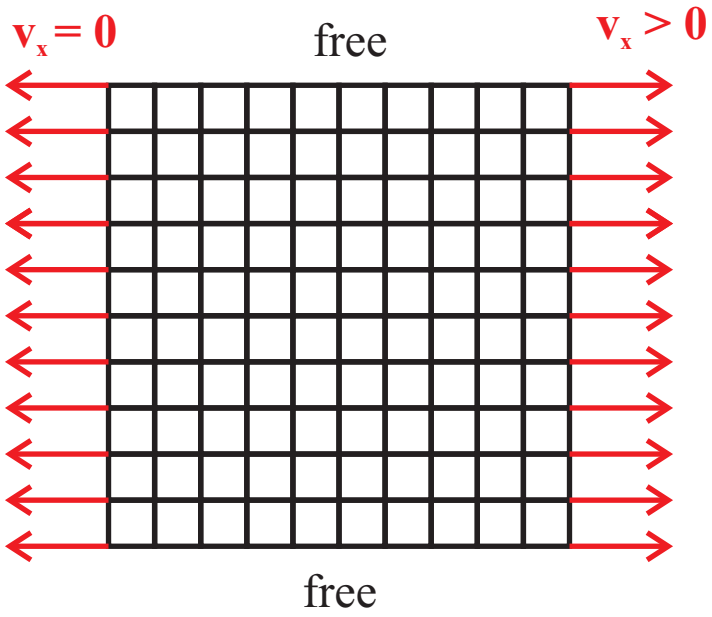

Figure 2.17: Illustration of typical boundary conditions for the plane strain simulations. The horizontal velocity was prescribed on the left and right boundaries; on the left it is zero, on the right it is generally non-zero.

The extension-contraction cycles were constructed to investigate work hardening phenomenology, which is described in the next paragraph. An example right hand edge velocity

cycle is shown in Figure 2.18. The difference between the axial extension and shock contraction boundary conditions is simply one of time-scale: boundary velocities for the shock contraction condition were high in comparison to the elastic wave speed of the material. We tested both single crystals and polycrystalline domains using the microstructure generation of §2.4.2.1.1.

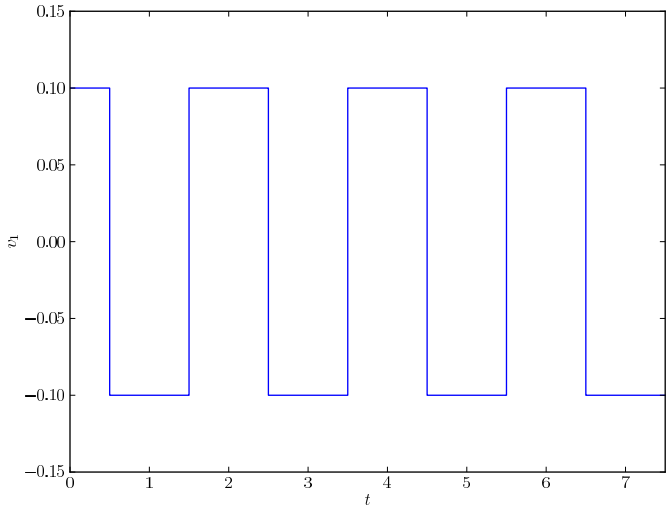

Figure 2.18: Right edge boundary condition for $\mathbf{e}_1$ component of boundary nodal velocity. This boundary condition was used to investigate the effect of different constitutive relations for hardening phenomenology.

2.4.2.2.2 Constitutive equations

Stress response The constitutive formulation requires the stress response from (2.39), (2.40) and (2.190). Therefore for hexoctahedral cubic crystals there are three elastic constants. The elastic constants are normally presented based on the Voigt form

$$S_I = C_{IJ} E_J, \tag{2.285}$$

where $(E_I) = (E_{11}, E_{22}, E_{33}, 2E_{23}, 2E_{13}, 2E_{12})$ and $S_I = (S_{11}, S_{22}, S_{33}, S_{23}, S_{13}, S_{12})$, and where C_{IJ} is a matrix of elastic constants given by

$$C_{IJ} = \begin{bmatrix} C_{11} & C_{12} & C_{13} & C_{14} & C_{15} & C_{16} \\ & C_{22} & C_{23} & C_{24} & C_{25} & C_{26} \\ & & C_{33} & C_{34} & C_{35} & C_{36} \\ & & & C_{44} & C_{45} & C_{46} \\ & & & & C_{55} & C_{56} \\ \text{sym} & & & & & C_{66} \end{bmatrix}. \tag{2.286}$$

For hexoctahedral symmetry, we have

$$C_{11} = C_{22} = C_{33},$$

$$C_{12} = C_{13} = C_{23}$$

$$C_{14} = C_{15} = C_{16} = C_{24} = C_{25} = C_{26} = C_{34} = C_{35} = C_{36} = C_{45} = C_{46} = C_{56} = 0,$$

and

$$C_{44} = C_{55} = C_{66}.$$

The Piola stress in the lattice configuration is given by evaluating

$$\mathbf{P_H} = \mathbf{HS}, \tag{2.287}$$

with $\mathbf{S}$ given by (2.285). Equation (2.39) then gives the stress response for use in the equation of motion, (2.253). The values for the elastic constants were taken as $C_{11} = 226$ GPa, $C_{12} = 140$ GPa, $C_{44} = 116$ GPa, which are representative of iron (BCC).

Plastic response. For plasticity equations, we need equations for the yield function y and lattice reorientation, $\mathbf{\Omega}$. The yield function is obtained from (2.196), with calibrated parameters Table 2.3. We also tested hardening relations based on (2.216). In particular we report on isotropic hardening relations of the form

$$y(\mathbf{S}, \boldsymbol{\xi}) = y(\mathbf{S}) - y_{\max}(1 + k_{\text{iso}}\|\boldsymbol{\xi}\|)^{A_3}, \tag{2.288}$$

where $k_{\text{iso}} \in \mathbb{R}$ has the dimensions of L, and the parameter A_3 is modified in our parameter investigations. Here y is the quadratic polynomial presented in (2.202). Equation (2.288) is of the form (2.216) with $\boldsymbol{\chi}(\boldsymbol{\xi}) = \mathbf{0}$ and $h(\boldsymbol{\xi}) = y_{\max}(1 + k_{\text{iso}}\|\boldsymbol{\xi}\|)^{A_3}$.

We also used the plastic work to account for hardening phenomenology (Malvern, 1969; Dowling, 1999), which is computed from

$$W_{\text{p}} = \int D \mathrm{d}t, \tag{2.289}$$

where $D = -\mathbf{S} \cdot \mathbf{K}^{-1}\dot{\mathbf{K}}$ is the dissipation, see (2.47), since $\mathcal{E}' \approx -\mathbf{S}$ for the small elastic strain model. Then we use yield functions of the form

$$y(\mathbf{S}, W_{\mathrm{p}}) = y(\mathbf{S}) - y_{\max}(1 + k_{\mathrm{p}} W_{\mathrm{p}})^{A_3}, \tag{2.290}$$

where k_{p} has dimensions of Energy^{-1}. The form of (2.290) is in recognition of the fact that $\boldsymbol{\xi}$ does not capture all dislocation content, and there are statistically stored dislocations below the length scale revealed by the integration loop of (2.275).

Finally, the lattice reorientation function we used is taken from Equations (2.209), (2.210) and (2.211), which represent the cubic order spin $\boldsymbol{\Omega} = \boldsymbol{\Omega}(\mathbf{S})$. Calibrated constitutive parameters are from Table 2.4. We used the BCC model results from the table for both lattice spin and yield function.

2.4.2.3 Results

In this section we discuss the results from the plane strain simulations for the boundary conditions and constitutive formulations described in the previous section.

2.4.2.3.1 Extension-contraction cycling In this section we give the results from the cyclic loading tests. In Figure 2.19 is shown the initial microstructure of a polycrystal at a 10×10 grid resolution. The component $K_{11}(t = 0)$ is visualized by the colormap. We tested the velocity cycling program specified in Figure 2.18 to this microstructure, and tested the hardening relations (2.288) and (2.290). The rate independent plastic flow model, (2.224), was used, with the reorientation function of (2.205).

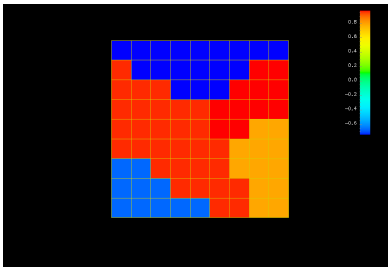

Figure 2.19: Initial microstructure for cyclic tests. 10×10 grid.

Effect of $\boldsymbol{\xi}$. Due to the nature of the computation of $\boldsymbol{\xi}$, the grain boundaries of Figure 2.19 are equivalent to high concentrations of geometrically necessary dislocations. The representative visualization of $\boldsymbol{\xi}$-concentration is shown in Figure 2.20 which plots $\|\boldsymbol{\xi}\|$ in the colormap. Comparing this to Figure 2.19 clearly shows the correlation between grain boundaries and the computed $\|\boldsymbol{\xi}\|$ using Equation (2.275). In Figure 2.21 the value of $\|\mathbf{K}\|$ is visualized at the same stage of deformation, for the values $A_3 = 0, 0.1, 0.5$ from left to right.

The influence of the parameter A_3 on the plastic deformation is clearly evident based on the relative locations of plastic deformation from these figures. For example, in Figure 2.21(a) plastic deformation is heterogeneous, but evenly distributed throughout the polycrystal. In Figure 2.21(b), for $A_3 = 0.1$, plastic deformation is isolated in a band which passes through the large grain in Figure 2.19, without crossing grain boundaries. In Figure 2.21(c), similar behavior is seen. To examine the influence of hardening on stress strain hysteresis,

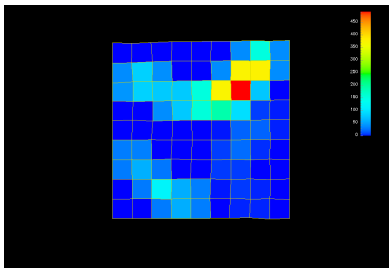

Figure 2.20: Initial picture of $\|\boldsymbol{\xi}\|^2$ for the microstructure of Figure 2.19. Grain boundaries serve as high dislocation density sites using the numerical stencil of (2.275).

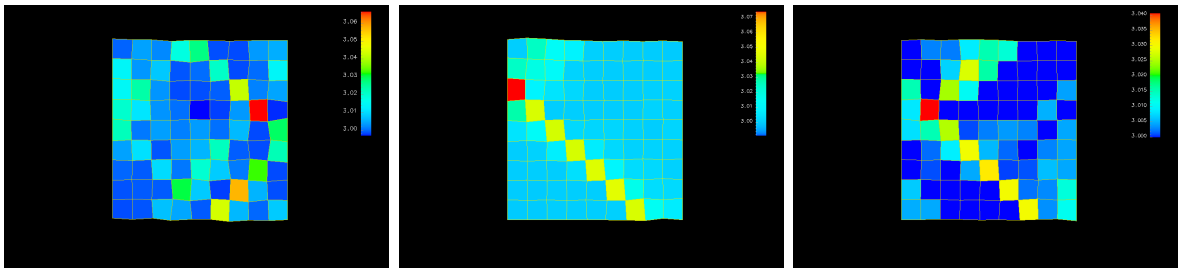

(a) Plot of $\|\mathbf{K}\|$ for the case $A_3 = 0$ in (2.288). Plastic deformation is heterogeneous but evenly distributed in the polycrystal.

(b) Plot of $\|\mathbf{K}\|$ during plastic flow, for $A_3 = 0.1$. The plastic deformation is localized to a region with low $\boldsymbol{\xi}$ content, see Figure 2.20.

(c) Plot of $\|\mathbf{K}\|$ during plastic flow, for $A_3 = 0.5$. The plastic deformation is localized to a region with low $\boldsymbol{\xi}$ content, see Figure 2.20.

Figure 2.21: Images of $\|\mathbf{K}\|$ for various exponents A_3 in Equation (2.288).

a measure of the total force on the right hand boundary is shown in Figures 2.22 to 2.24 for the cases $A_3 = 0, 0.1, 0.5$, respectively. This force quantity is plotted to get an idea of the axial stress response. From these figures, the hardening behavior induced by the model (2.288) is not very strong. Most of the determination of the yield is dominated by the initial microstructure; deformation dependent hardening is largely absent.

Next we examine similar data using the plastic work-based hardening of Equation (2.290). In Figures 2.25 - 2.27 are shown the axial stress vs. axial stretch for the microstructure shown in Figure 2.19. The yield function used was (2.290), with hardening exponent $A_3 = 1, 3, 10$

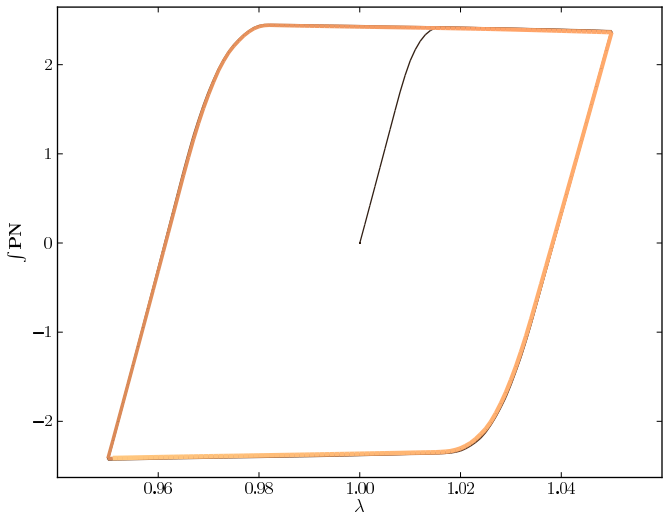

Figure 2.22: Plot of axial stress vs. extension for the microstructure shown in Figure 2.19. The yield function used was (2.288). The hardening parameter was $A_3 = 0$. There is no hardening effect.

respectively in the figures. Qualitative agreement with notions of isotropic hardening are good with the hardening model, better than for (2.288). Finally, in Figure 2.28, the same cyclic test is performed for the rate dependent model, (2.241), with viscosity $\nu = 2.5 \cdot 10^{-4}\text{GPa}^{-1} \cdot s$. The mesh is refined from 10×10 to 40×40 to 50×50. Convergence of the integrated stress vs. stretch relation is rapid.

Next, in Figures 2.29 - 2.33 are the hysteresis plots for the 11 -parameter lattice reorientation model of (2.186), $\boldsymbol{\Omega} = \boldsymbol{\Omega}(\mathbf{S}, \dot{\mathbf{S}})$ from (2.205). Figures 2.29 - 2.30 used (2.288), and Figures 2.31 - 2.33 used (2.290). Although calibrated in the same fashion as $\boldsymbol{\Omega}(\mathbf{S})$, there is a bias towards certain lattice reorientation, evidenced by the changing slope in the load extension curve. This indicates that there is a net reorientation in the crystal upon tension and compression cycling, since anisotropic elasticity causes a resulting change in stress-strain slope. This serves as further justification that reorientation functions of the form $\boldsymbol{\Omega} = \boldsymbol{\Omega}(\mathbf{S}, \dot{\mathbf{S}})$ should be used with caution, if at all, in applications.

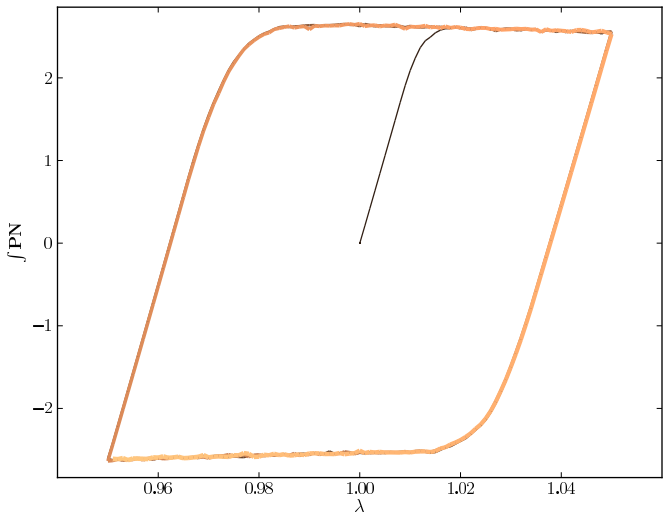

Figure 2.23: Plot of axial stress vs. extension for the microstructure shown in Figure 2.19. The yield function used was (2.288). The hardening parameter was $A_3 = 0.1$. The isotropic hardening effect is not modeled as well as for Equation (2.290).

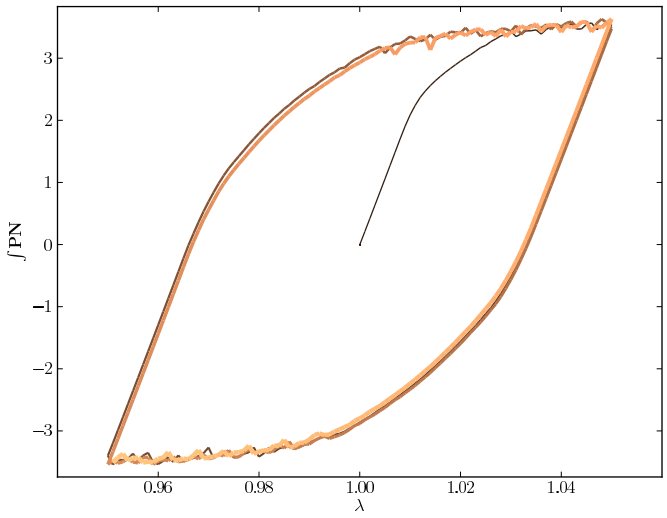

Figure 2.24: Plot of axial stress vs. extension for the microstructure shown in Figure 2.19. The yield function used was (2.288). The hardening parameter was $A_3 = 0.5$. The isotropic hardening effect is not modeled as well as for Equation (2.290), there is only a dependence on the initial yield point as the exponent increases.

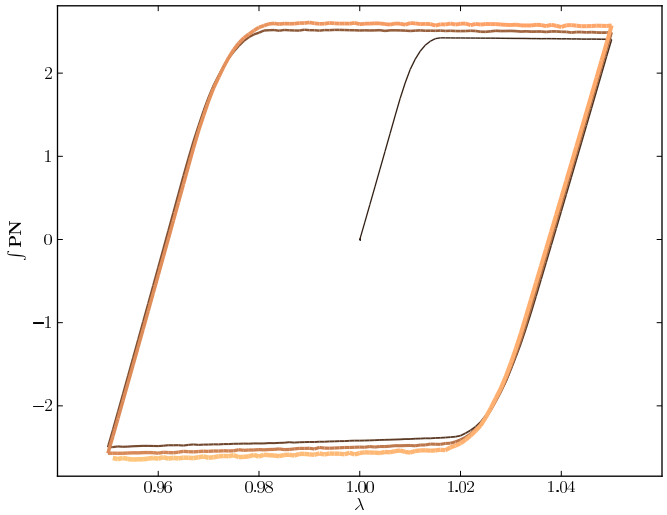

Figure 2.25: Plot of axial stress vs. axial stretch, for the microstructure shown in Figure 2.19. The yield function was (2.290). The hardening parameter was $A_3 = 1$. A small amount of isotropic hardening is evident.

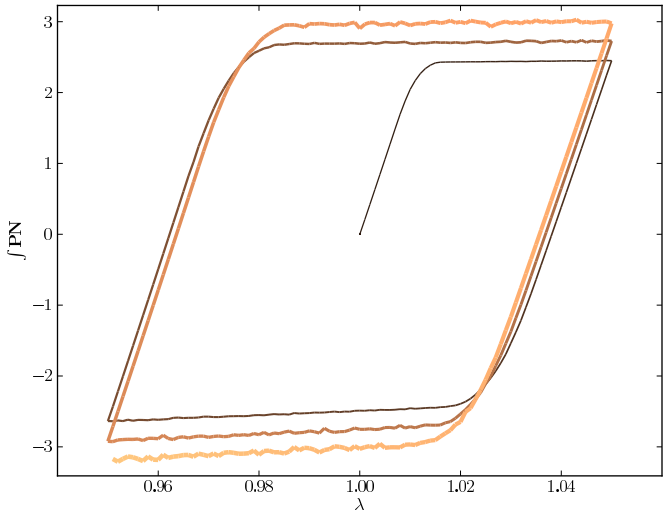

Figure 2.26: Plot of axial stress vs. axial stretch, for the microstructure shown in Figure 2.19. The yield function was (2.290). The hardening parameter was $A_3 = 3$. A larger amount of isotropic hardening than for Figure 2.25 is evident.

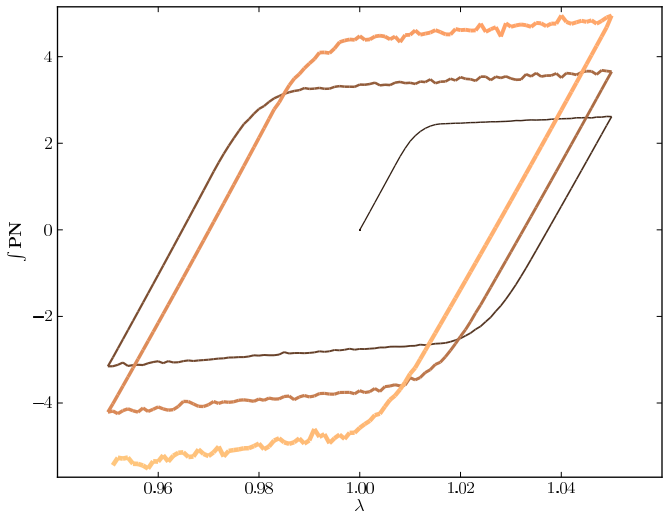

Figure 2.27: Plot of axial stress vs. axial stretch, for the microstructure shown in Figure 2.19. The yield function was (2.290). The hardening parameter was $A_3 = 10$. The increase in isotropic hardening is clearly monotonic with A_3, by comparing Figures 2.25, 2.26.

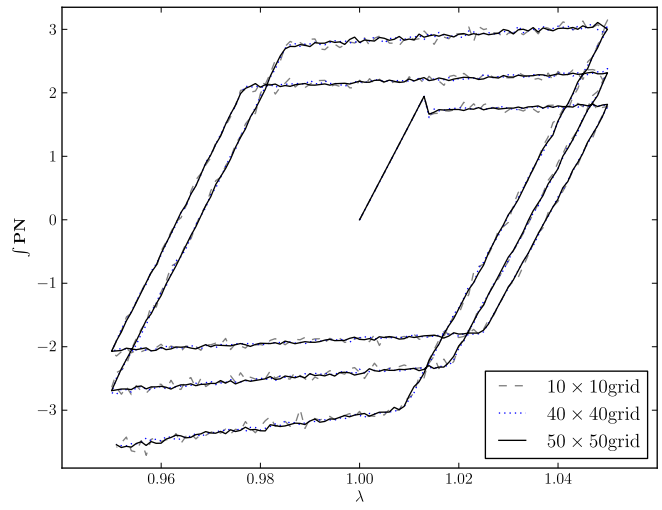

Figure 2.28: Plot of axial stress vs. extension, for the microstructure shown in Figure 2.19 for several mesh resolutions. The yield function was (2.290). A rate dependent model was used. The parameter $A_3 = 10$. Convergence of the macroscopic stress vs. stretch is rapid.

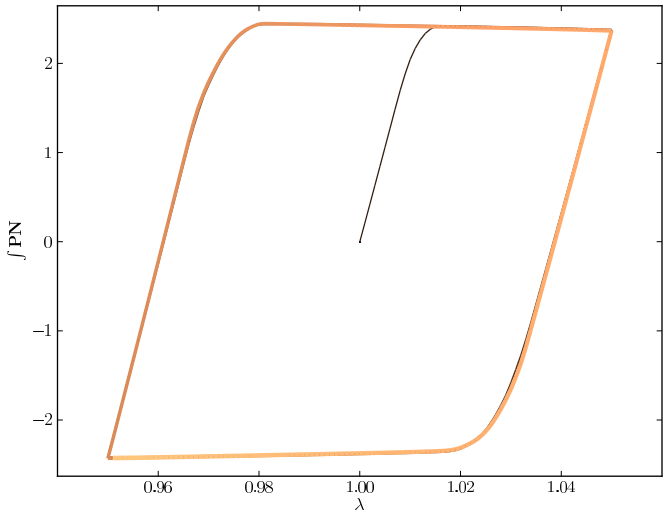

Figure 2.29: Plot of axial stress vs. extension, for the microstructure shown in Figure 2.19 with the reorientation function from (2.186), $\mathbf{\Omega} = \mathbf{\Omega}(\mathbf{S}, \dot{\mathbf{S}})$. The yield function was (2.288). The parameter $A_3 = 0$.

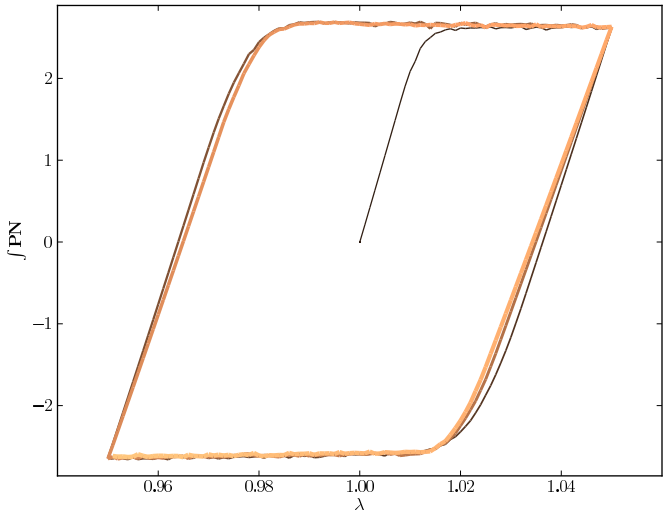

Figure 2.30: Plot of axial stress vs. extension, for the microstructure shown in Figure 2.19 with the reorientation function from (2.186), $\mathbf{\Omega} = \mathbf{\Omega}(\mathbf{S}, \dot{\mathbf{S}})$. The yield function was (2.288). The parameter $A_3 = 0.1$.

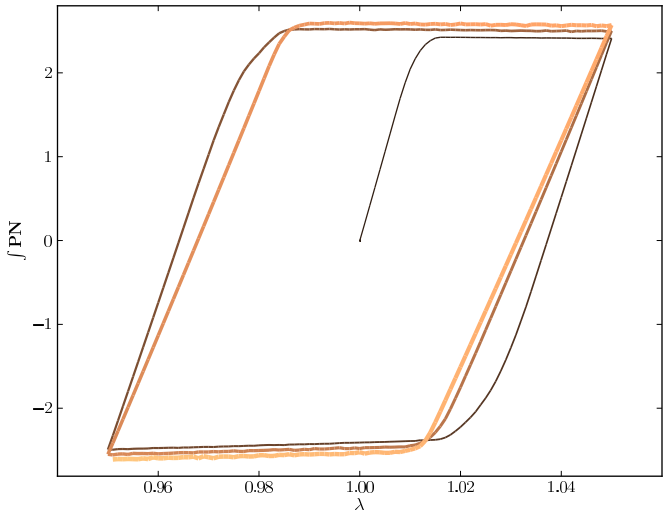

Figure 2.31: Plot of axial stress vs. extension, for the microstructure shown in Figure 2.19 with the reorientation function from (2.186), $\mathbf{\Omega} = \mathbf{\Omega}(\mathbf{S}, \dot{\mathbf{S}})$. The yield function was (2.290). The parameter $A_3 = 1$.

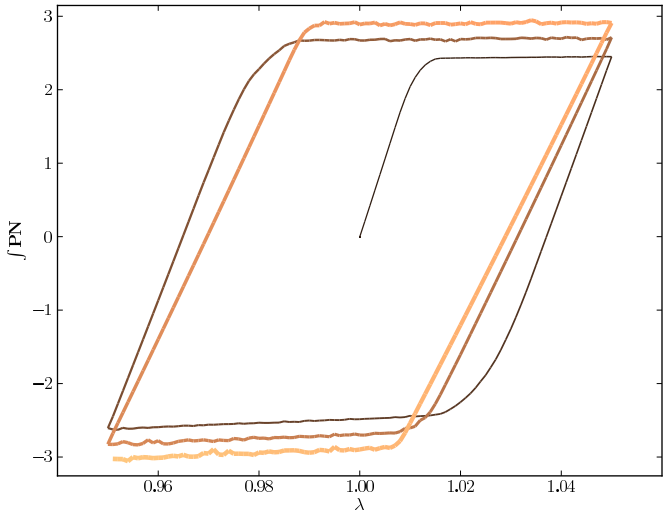

Figure 2.32: Plot of axial stress vs. extension, for the microstructure shown in Figure 2.19 with the reorientation function from (2.186), $\mathbf{\Omega} = \mathbf{\Omega}(\mathbf{S}, \dot{\mathbf{S}})$. The yield function was (2.290). The parameter $A_3 = 3$.

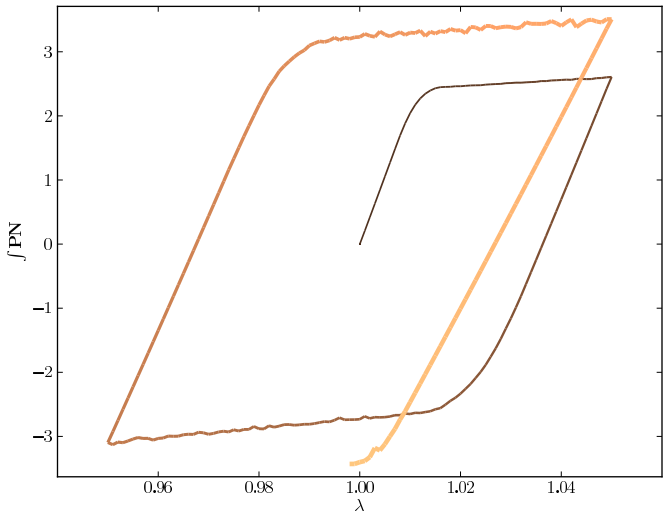

Figure 2.33: Plot of axial stress vs. extension, for the microstructure shown in Figure 2.19 with the reorientation function from (2.186), $\mathbf{\Omega} = \mathbf{\Omega}(\mathbf{S}, \dot{\mathbf{S}})$. The yield function was (2.290). The parameter $A_3 = 10$. The simulation failed to integrate the rate independent equations at the final point in the simulation.

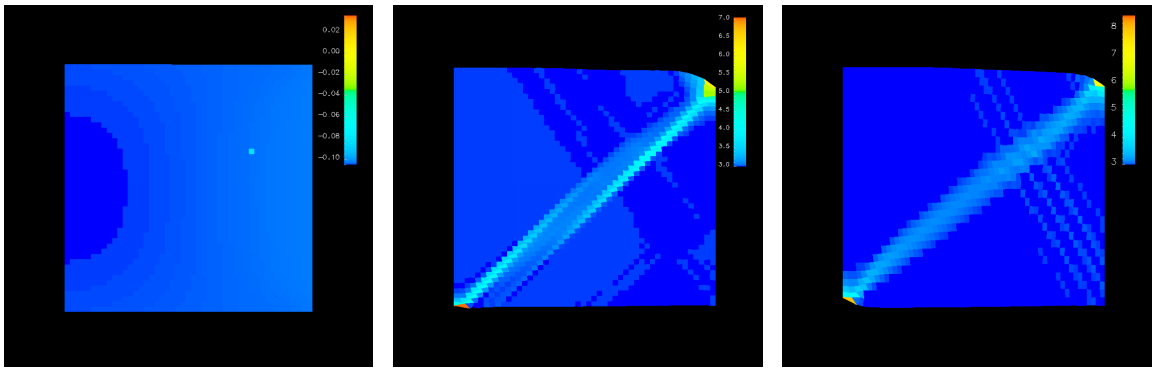

(a) $y(\mathbf{S})$, 48×48 mesh (b) $\|\mathbf{K}\|$, 48×48 mesh (c) $\|\mathbf{K}\|$, 30×60 mesh

Figure 2.34: On the left, the color map is of $y(\mathbf{S})$ near the beginning stage of deformation. The lightened pixel indicates where the material has been weakened by changing the value of $y_{\max}$. The right two figures are a comparison of $\|\mathbf{K}\|$ for 48×48 mesh along side a 30×60 mesh. The location and orientation of the localization band is the same for both cases.

2.4.2.3.2 Investigation of mesh dependence Based on statements by Silling (1988), we were interested in investigating the effect of mesh dependence on simulation results. Silling (1988) stated that results regarding, for example, localization bands can be mesh geometry dependent if there is not a strong localization effect in the model. His context was not precisely the present one, but it is close enough to presume that similar observations apply to our physics. To examine mesh dependence, we constructed a mesh where the material is weakened in a particular zone Ω^* by setting $y_{\max}(\Omega^*) < y_{\max}$. Recall that $y_{\max}$ is the nominal yield parameter in Equations (2.288), (2.290), which are of the form $y(\mathbf{S}) = y'(\mathbf{S}) - y_{\max}$. The microstructure was a constant lattice orientation of $\theta = 20°$, see (2.279). The boundary conditions were of the axial extension nature, velocity prescribed on right edge, traction free top and bottom. In Figure 2.34 is shown the value of $y(\mathbf{S})$ for an early stage of deformation on the left; the right two figures are plots of $\|\mathbf{K}\|$ at identical stage of deformation. The center figure is a 48×48 mesh, the right figure is a 30×60 mesh. The orientation of the localization band in the figures is the same in both cases, giving some comfort in the predictions from the numerical framework.

Next, in order to investigate the issues of convergence we tested the same weakened material in $12\times12, 24\times24,$ and48×48 mesh resolutions. We again used $\theta_0 = 20°$, and used the rate dependent model with $\nu = 0.0003$ GPa$^{-1}\cdot s$. We used the yield function based on (2.288), which incorporates $\boldsymbol{\xi}$ into the hardening. In Figures 2.35 - 2.41, 2.42 - 2.48 are plotted $\|\mathbf{K}\|$, $\|\boldsymbol{\xi}\|^2$ respectively for a hardening exponent $A_3 = 0$, representing no hardening. In Figures 2.49 - 2.55, 2.56 - 2.62 are the same displayed data, at the same stages in deformation, but with $A_3 = 0.1$. In the captions of these figures, the parameter 'hardeningmode' refers to the use of either plastic work hardening, Equation (2.290) (hardeningmode = 0), or $\boldsymbol{\xi}$-based hardening, (2.288) (hardeningmode = 1). This designation of 'hardeningmode' will be in effect for the rest of the document. The addition of the hardening exponent in the simulations appears to give better convergence properties. Since the viscoplastic model was used, elastic strain should be checked for compliance with the small elastic strain theory; this was indeed the case for these quasistatic simulations. Other examples from these simulations for different grain orientations are given in the appendix.

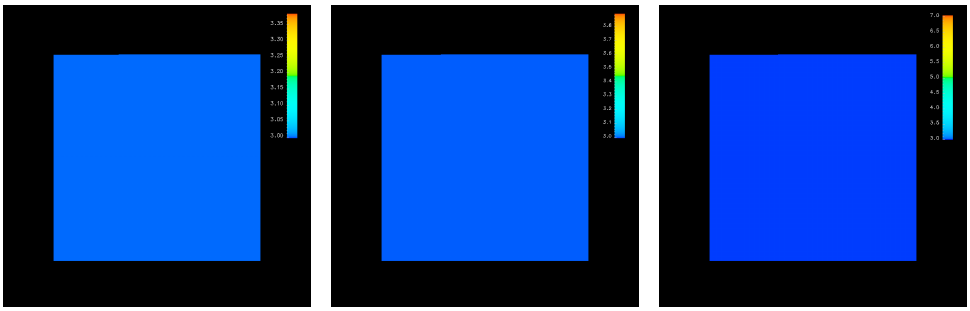

(a) 12×12 mesh (b) 24×24 mesh (c) 48×48 mesh

Figure 2.35: Mesh resolution comparison for axial extension with local weakening. The colormap shows $\|\mathbf{K}\|$ $A_3 = 0$, $\nu = 0.0003$, hardeningmode=1, $\theta_0 = 20$, sequence number =0

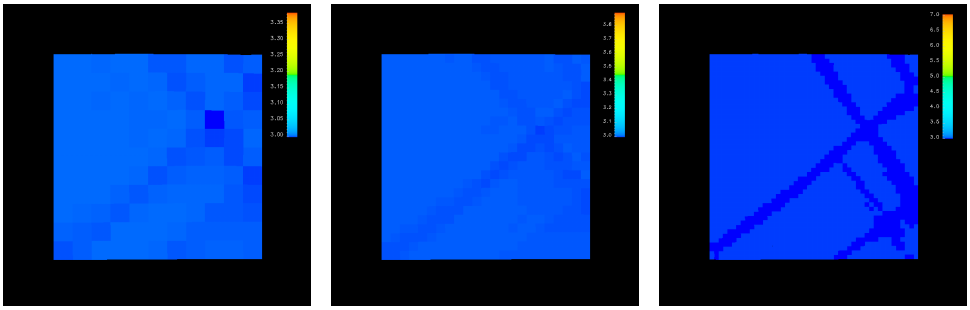

(a) 12×12 mesh (b) 24×24 mesh (c) 48×48 mesh

Figure 2.36: Mesh resolution comparison for axial extension with local weakening. The colormap shows $\|\mathbf{K}\|$ $A_3 = 0$, $\nu = 0.0003$, hardeningmode=1, $\theta_0 = 20$, sequence number =1

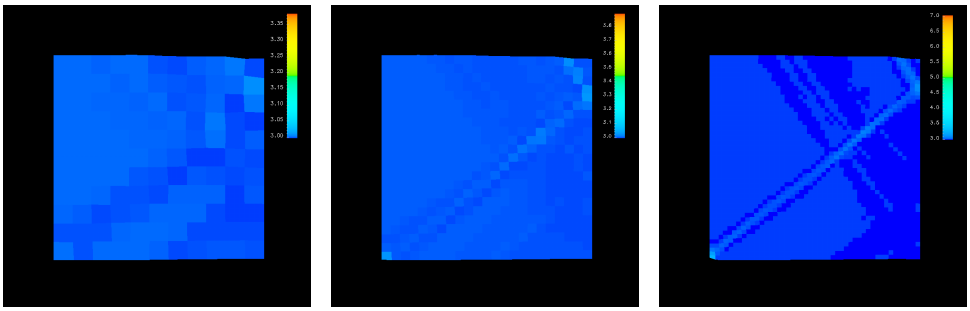

(a) 12×12 mesh (b) 24×24 mesh (c) 48×48 mesh

Figure 2.37: Mesh resolution comparison for axial extension with local weakening. The colormap shows $\|\mathbf{K}\|$ $A_3 = 0$, $\nu = 0.0003$, hardeningmode=1, $\theta_0 = 20$, sequence number =2

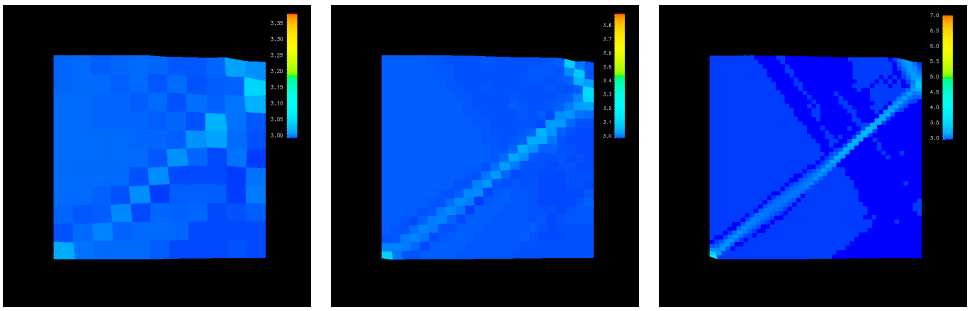

(a) 12×12 mesh (b) 24×24 mesh (c) 48×48 mesh

Figure 2.38: Mesh resolution comparison for axial extension with local weakening. The colormap shows $\|\mathbf{K}\|$ $A_3 = 0$, $\nu = 0.0003$, hardeningmode=1, $\theta_0 = 20$, sequence number =3

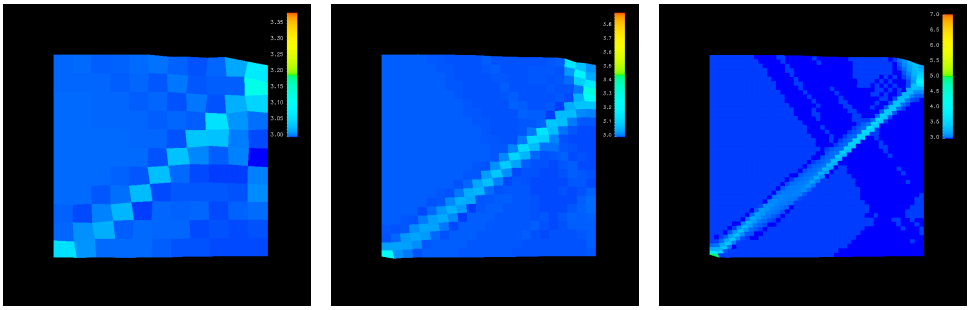

(a) 12×12 mesh (b) 24×24 mesh (c) 48×48 mesh

Figure 2.39: Mesh resolution comparison for axial extension with local weakening. The colormap shows $\|\mathbf{K}\|$ $A_3 = 0$, $\nu = 0.0003$, hardeningmode=1, $\theta_0 = 20$, sequence number =4

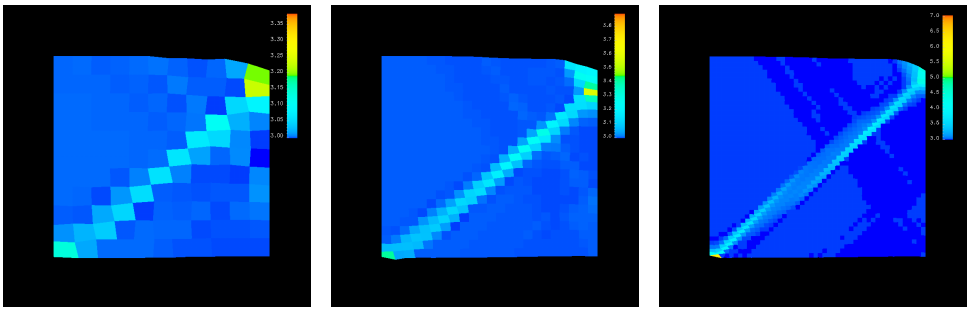

(a) 12×12 mesh (b) 24×24 mesh (c) 48×48 mesh

Figure 2.40: Mesh resolution comparison for axial extension with local weakening. The colormap shows $\|\mathbf{K}\|$ $A_3 = 0$, $\nu = 0.0003$, hardeningmode=1, $\theta_0 = 20$, sequence number =5

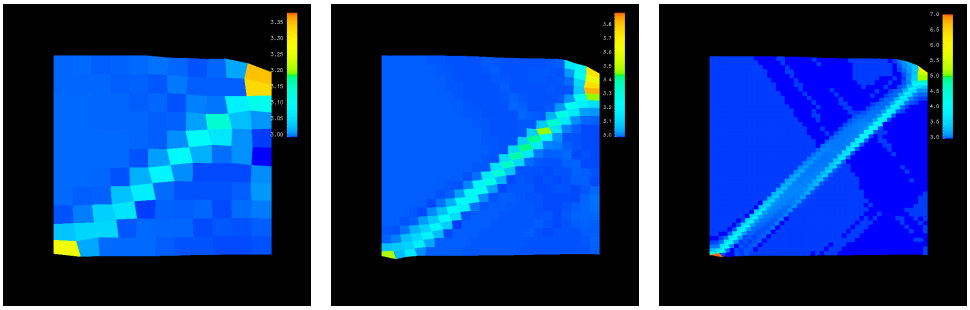

(a) 12×12 mesh (b) 24×24 mesh (c) 48×48 mesh

Figure 2.41: Mesh resolution comparison for axial extension with local weakening. The colormap shows $\|\mathbf{K}\|$ $A_3 = 0$, $\nu = 0.0003$, hardeningmode=1, $\theta_0 = 20$, sequence number =6

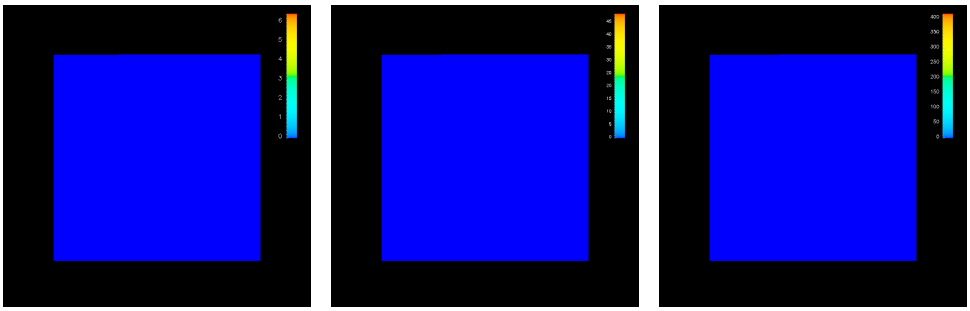

(a) 12×12 mesh (b) 24×24 mesh (c) 48×48 mesh

Figure 2.42: Mesh resolution comparison for axial extension with local weakening. The colormap shows $\|\boldsymbol{\xi}\|^2$ $A_3 = 0$, $\nu = 0.0003$, hardeningmode=1, $\theta_0 = 20$, sequence number =0

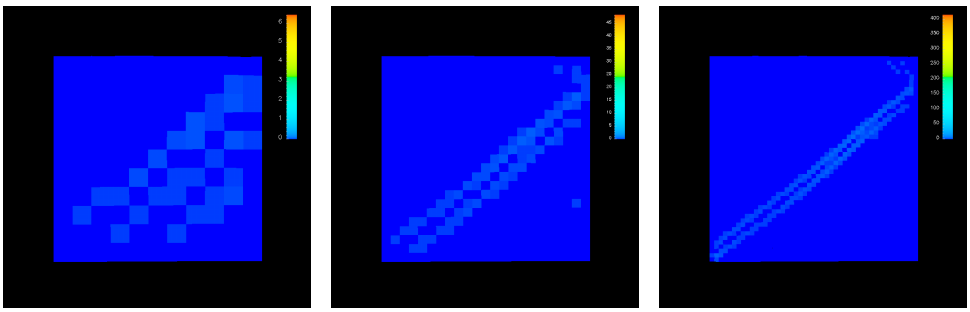

(a) 12×12 mesh (b) 24×24 mesh (c) 48×48 mesh

Figure 2.43: Mesh resolution comparison for axial extension with local weakening. The colormap shows $\|\boldsymbol{\xi}\|^2$ $A_3 = 0$, $\nu = 0.0003$, hardeningmode=1, $\theta_0 = 20$, sequence number =1

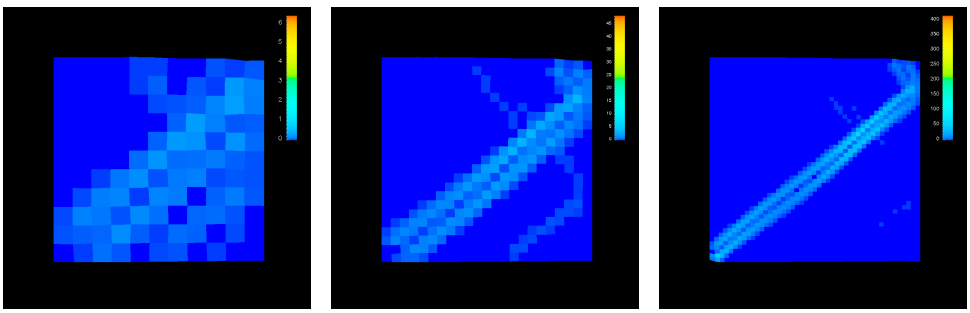

(a) 12×12 mesh (b) 24×24 mesh (c) 48×48 mesh

Figure 2.44: Mesh resolution comparison for axial extension with local weakening. The colormap shows $\|\boldsymbol{\xi}\|^2$ $A_3 = 0$, $\nu = 0.0003$, hardeningmode=1, $\theta_0 = 20$, sequence number =2

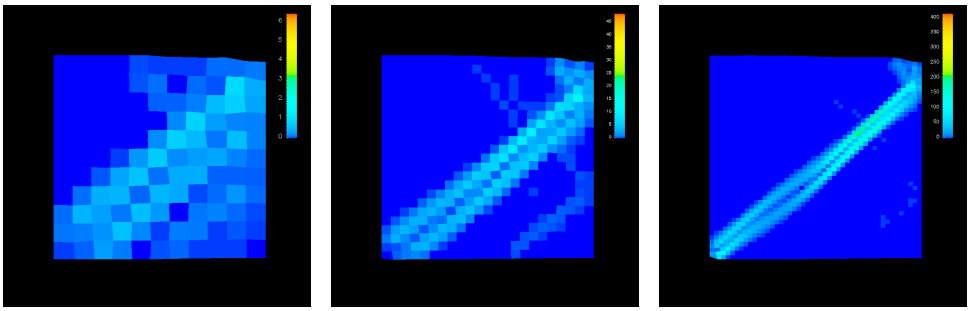

(a) 12×12 mesh (b) 24×24 mesh (c) 48×48 mesh

Figure 2.45: Mesh resolution comparison for axial extension with local weakening. The colormap shows $\|\boldsymbol{\xi}\|^2$ $A_3 = 0$, $\nu = 0.0003$, hardeningmode=1, $\theta_0 = 20$, sequence number =3

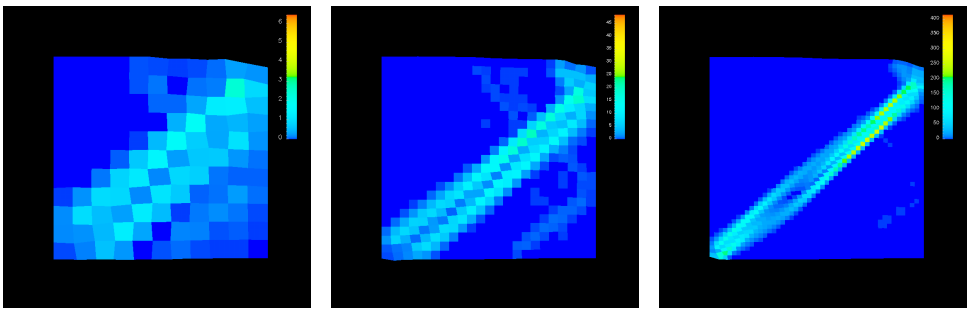

(a) 12×12 mesh (b) 24×24 mesh (c) 48×48 mesh

Figure 2.46: Mesh resolution comparison for axial extension with local weakening. The colormap shows $\|\boldsymbol{\xi}\|^2$ $A_3 = 0$, $\nu = 0.0003$, hardeningmode=1, $\theta_0 = 20$, sequence number =4

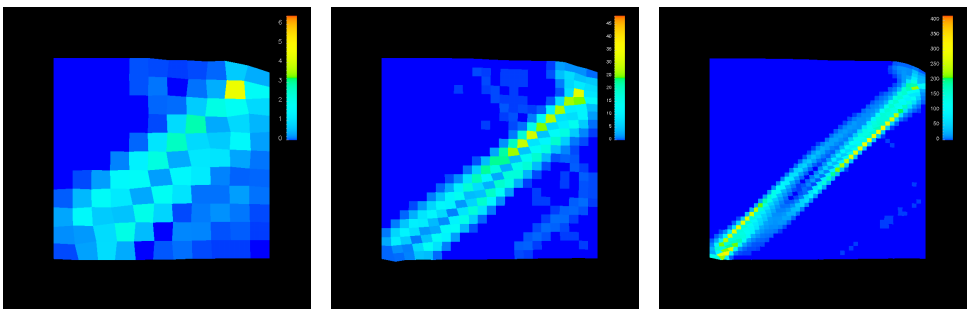

(a) 12×12 mesh (b) 24×24 mesh (c) 48×48 mesh

Figure 2.47: Mesh resolution comparison for axial extension with local weakening. The colormap shows $\|\boldsymbol{\xi}\|^2$ $A_3 = 0$, $\nu = 0.0003$, hardeningmode=1, $\theta_0 = 20$, sequence number =5

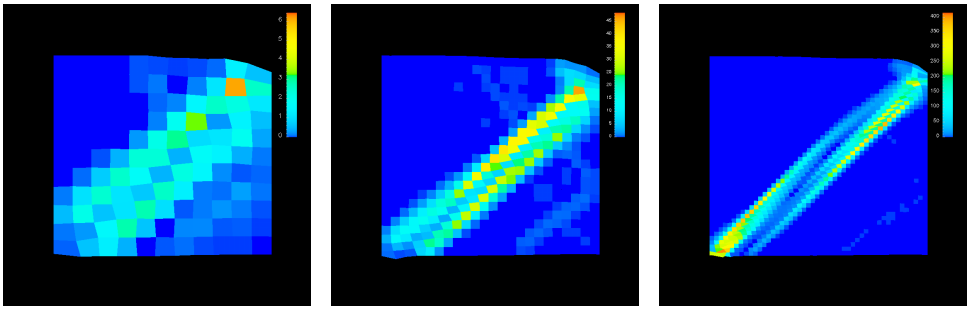

(a) 12×12 mesh (b) 24×24 mesh (c) 48×48 mesh

Figure 2.48: Mesh resolution comparison for axial extension with local weakening. The colormap shows $\|\boldsymbol{\xi}\|^2$ $A_3 = 0$, $\nu = 0.0003$, hardeningmode=1, $\theta_0 = 20$, sequence number =6

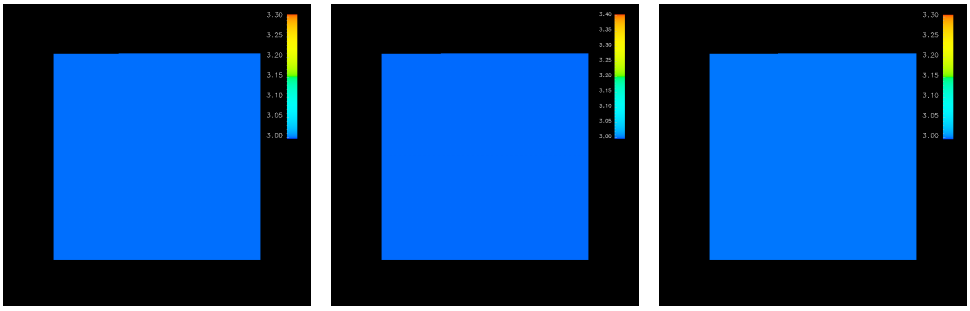

(a) 12×12 mesh (b) 24×24 mesh (c) 48×48 mesh

Figure 2.49: Mesh resolution comparison for axial extension with local weakening. The colormap shows $\|\mathbf{K}\|$ $A_3 = 0.1$, $\nu = 0.0003$, hardeningmode=1, $\theta_0 = 20$, sequence number =0

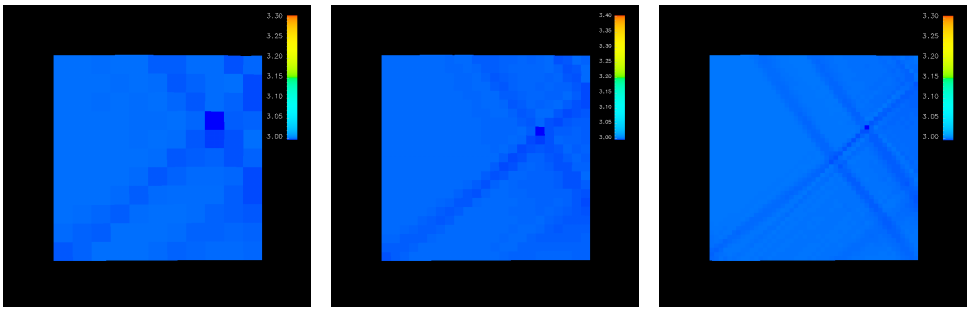

(a) 12×12 mesh (b) 24×24 mesh (c) 48×48 mesh

Figure 2.50: Mesh resolution comparison for axial extension with local weakening. The colormap shows $\|\mathbf{K}\|$ $A_3 = 0.1$, $\nu = 0.0003$, hardeningmode=1, $\theta_0 = 20$, sequence number =1

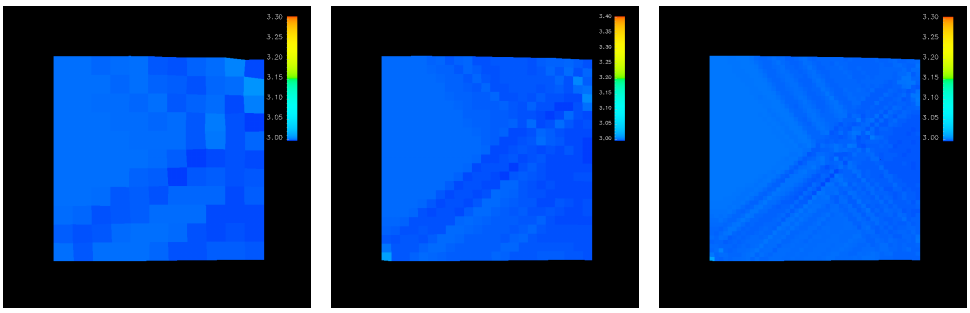

(a) 12×12 mesh (b) 24×24 mesh (c) 48×48 mesh

Figure 2.51: Mesh resolution comparison for axial extension with local weakening. The colormap shows $\|\mathbf{K}\|$ $A_3 = 0.1$, $\nu = 0.0003$, hardeningmode=1, $\theta_0 = 20$, sequence number =2

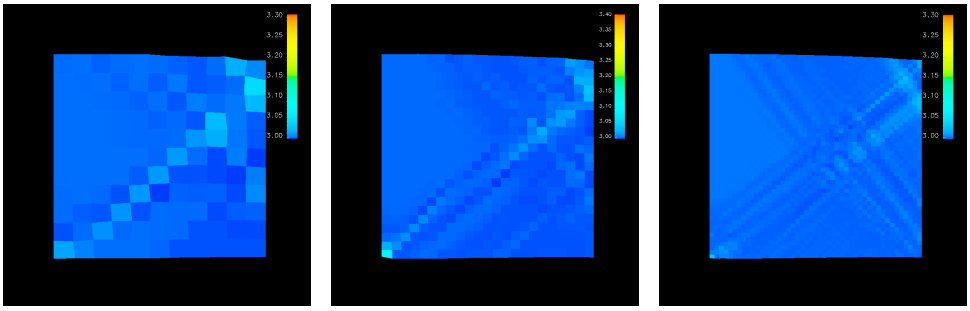

(a) 12×12 mesh (b) 24×24 mesh (c) 48×48 mesh

Figure 2.52: Mesh resolution comparison for axial extension with local weakening. The colormap shows $\|\mathbf{K}\|$ $A_3 = 0.1$, $\nu = 0.0003$, hardeningmode=1, $\theta_0 = 20$, sequence number =3

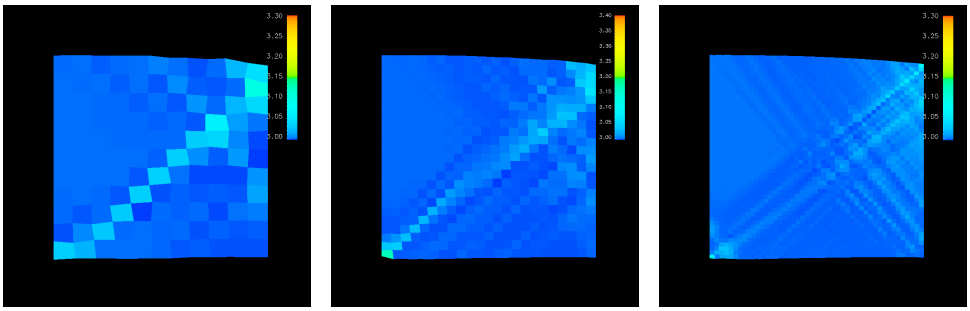

(a) 12×12 mesh (b) 24×24 mesh (c) 48×48 mesh

Figure 2.53: Mesh resolution comparison for axial extension with local weakening. The colormap shows $\|\mathbf{K}\|$ $A_3 = 0.1$, $\nu = 0.0003$, hardeningmode=1, $\theta_0 = 20$, sequence number =4

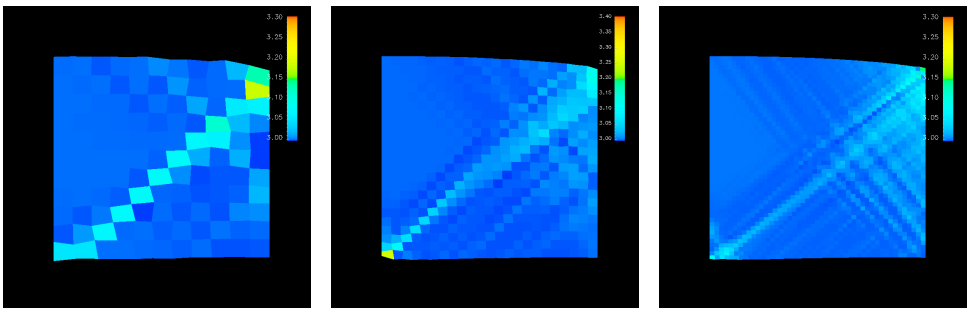

(a) 12×12 mesh (b) 24×24 mesh (c) 48×48 mesh

Figure 2.54: Mesh resolution comparison for axial extension with local weakening. The colormap shows $\|\mathbf{K}\|$ $A_3 = 0.1$, $\nu = 0.0003$, hardeningmode=1, $\theta_0 = 20$, sequence number =5

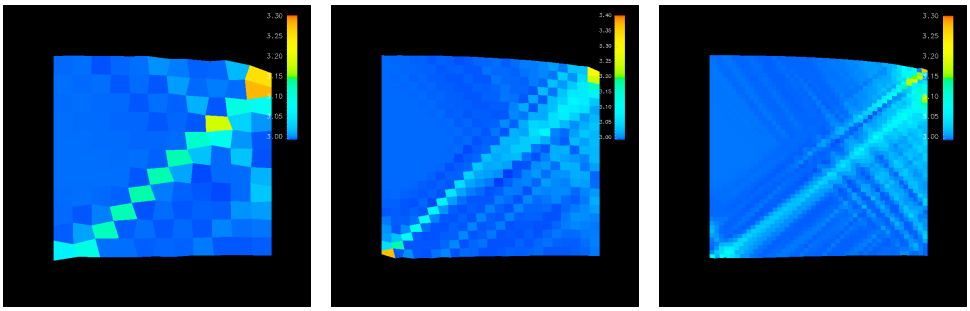

(a) 12×12 mesh (b) 24×24 mesh (c) 48×48 mesh

Figure 2.55: Mesh resolution comparison for axial extension with local weakening. The colormap shows $\|\mathbf{K}\|$ $A_3 = 0.1$, $\nu = 0.0003$, hardeningmode=1, $\theta_0 = 20$, sequence number =6

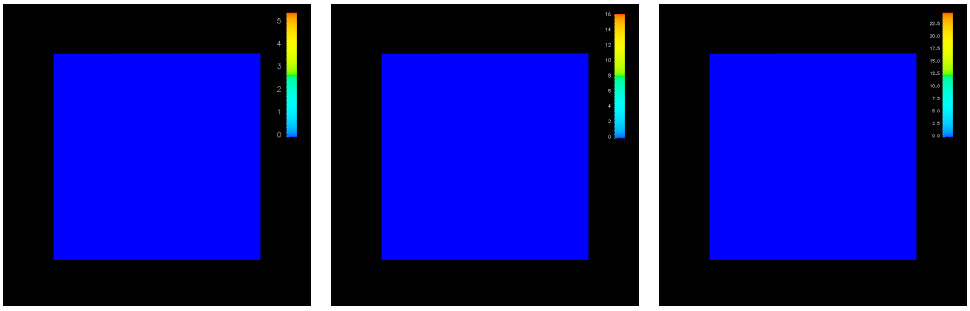

(a) 12×12 mesh (b) 24×24 mesh (c) 48×48 mesh

Figure 2.56: Mesh resolution comparison for axial extension with local weakening. The colormap shows $\|\boldsymbol{\xi}\|^2$ $A_3 = 0.1$, $\nu = 0.0003$, hardeningmode=1, $\theta_0 = 20$, sequence number =0

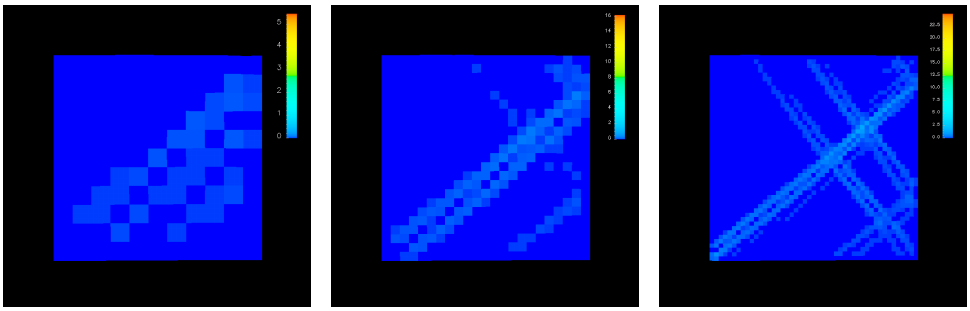

(a) 12×12 mesh (b) 24×24 mesh (c) 48×48 mesh

Figure 2.57: Mesh resolution comparison for axial extension with local weakening. The colormap shows $\|\boldsymbol{\xi}\|^2$ $A_3 = 0.1$, $\nu = 0.0003$, hardeningmode=1, $\theta_0 = 20$, sequence number =1

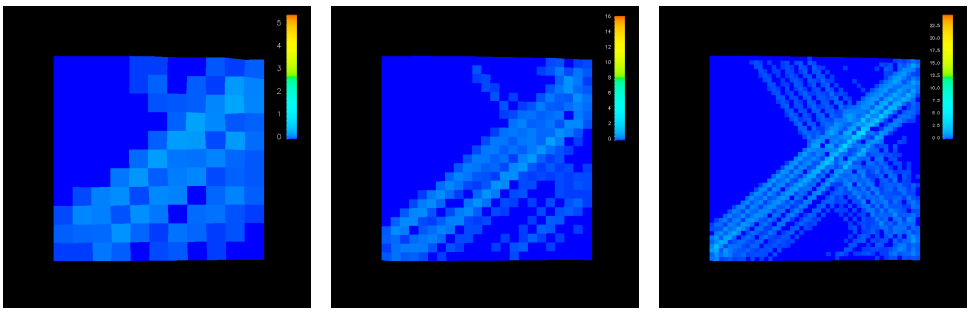

(a) 12×12 mesh (b) 24×24 mesh (c) 48×48 mesh

Figure 2.58: Mesh resolution comparison for axial extension with local weakening. The colormap shows $\|\boldsymbol{\xi}\|^2$ $A_3 = 0.1$, $\nu = 0.0003$, hardeningmode=1, $\theta_0 = 20$, sequence number =2

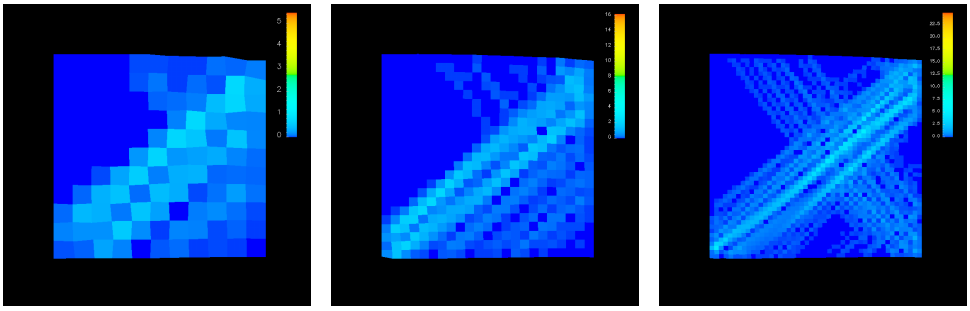

(a) 12×12 mesh (b) 24×24 mesh (c) 48×48 mesh

Figure 2.59: Mesh resolution comparison for axial extension with local weakening. The colormap shows $\|\boldsymbol{\xi}\|^2$ $A_3 = 0.1$, $\nu = 0.0003$, hardeningmode=1, $\theta_0 = 20$, sequence number =3

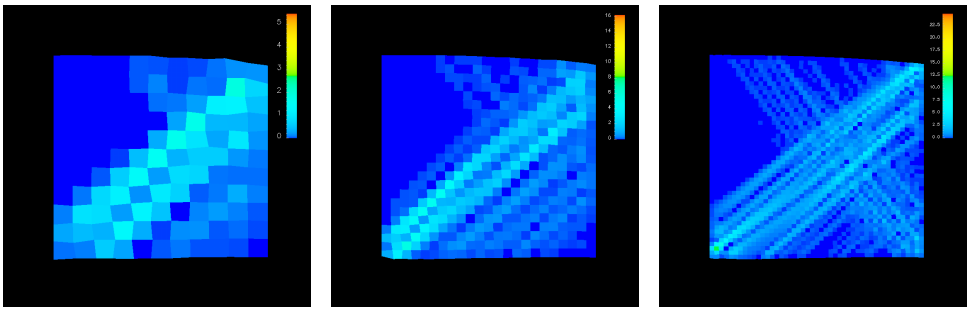

(a) 12×12 mesh (b) 24×24 mesh (c) 48×48 mesh

Figure 2.60: Mesh resolution comparison for axial extension with local weakening. The colormap shows $\|\boldsymbol{\xi}\|^2$ $A_3 = 0.1$, $\nu = 0.0003$, hardeningmode=1, $\theta_0 = 20$, sequence number =4

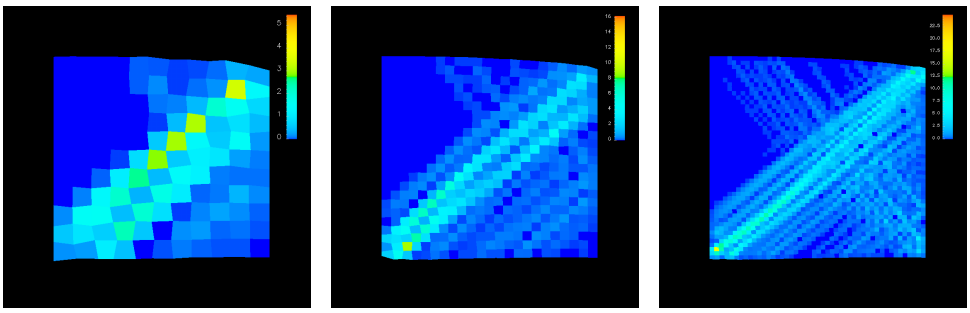

(a) 12×12 mesh (b) 24×24 mesh (c) 48×48 mesh

Figure 2.61: Mesh resolution comparison for axial extension with local weakening. The colormap shows $\|\boldsymbol{\xi}\|^2$ $A_3 = 0.1$, $\nu = 0.0003$, hardeningmode=1, $\theta_0 = 20$, sequence number =5

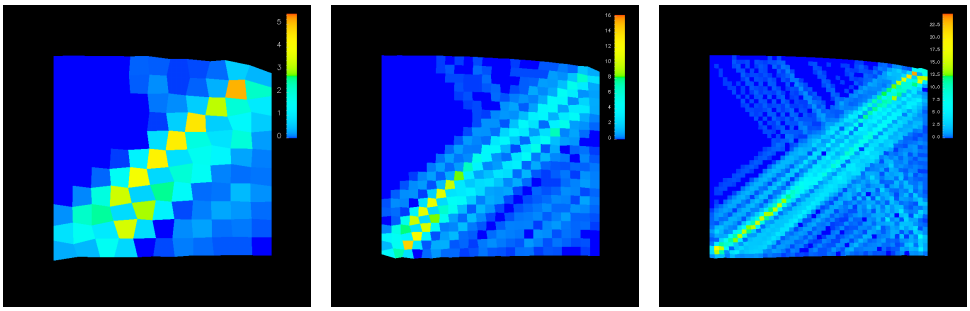

(a) 12×12 mesh (b) 24×24 mesh (c) 48×48 mesh

Figure 2.62: Mesh resolution comparison for axial extension with local weakening. The colormap shows $\|\boldsymbol{\xi}\|^2$ $A_3 = 0.1$, $\nu = 0.0003$, hardeningmode=1, $\theta_0 = 20$, sequence number =6

2.4.2.3.3 Shock contraction Next, we simulate a high velocity impact loading on a single crystal. The crystal is oriented at $\theta_0 = 10^\circ$. The boundary conditions are the same as for the previous simulations, except the horizontal velocity is amplified to be on the order of the elastic wave speed. Additionally, the duration of this velocity pulse is short, after which the right edge becomes traction free. The time step is dropped to a level where dynamic behavior is accurately captured. In the following images the rate independent flow rule is used, based on (2.205). In Figure 2.63 and Figure 2.64 is shown the pressure, tr $\mathbf{S}$, at several time steps. In Figure 2.65 and Figure 2.66 is shown the geometrically necessary dislocation content, in the form $\|\boldsymbol{\xi}\|^2$, at the same time steps as in Figure 2.63, Figure 2.64. In Figure 2.67 and Figure 2.68 is shown the plastic deformation in the form $||\mathbf{K}||$, again at the same time steps. In applications, the $\boldsymbol{\xi}$ content can be measured with X-ray diffraction experiments or the related EBSD. See Kysar et al. (2007) for recent experiments where geometrically necessary dislocation content was measured. Therefore, if the shock loading were produced experimentally, the sample could be post mordem sectioned and compared to simulations to validate high strain rate constitutive behavior. Further examples of the shock contraction boundary condition can be found in the appendix.

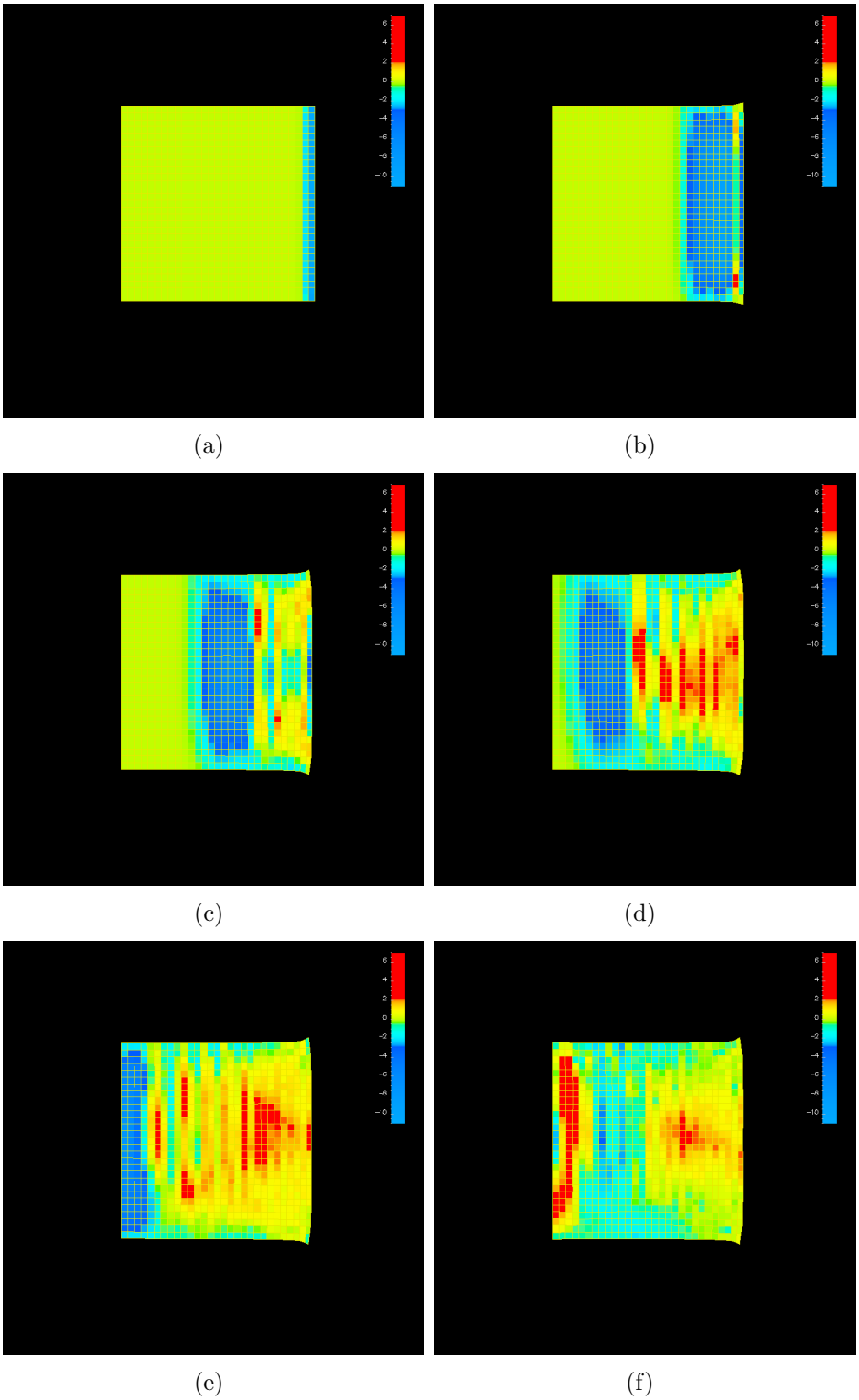

Figure 2.63: Shock animation frames, color bar is the pressure, tr **S**. Incident pressure wave propagation is depicted

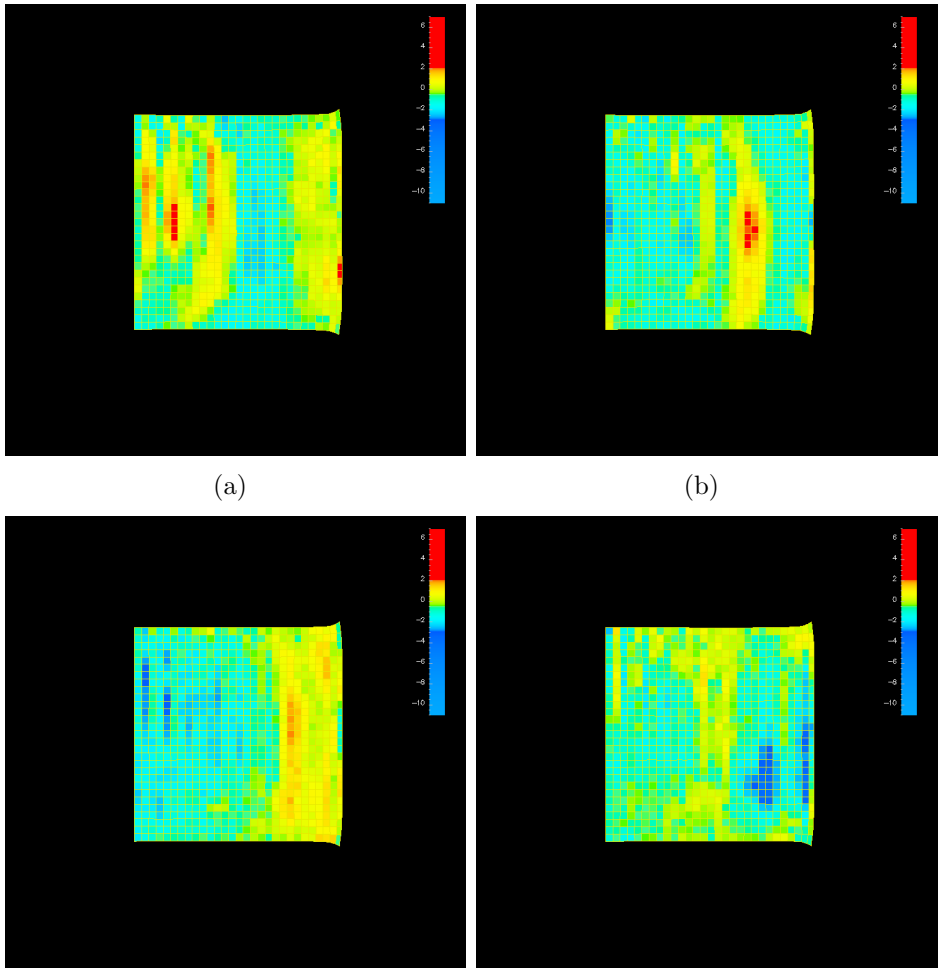

(a) (b)

(c) (d)

Figure 2.64: Shock animation frames (cont'd)

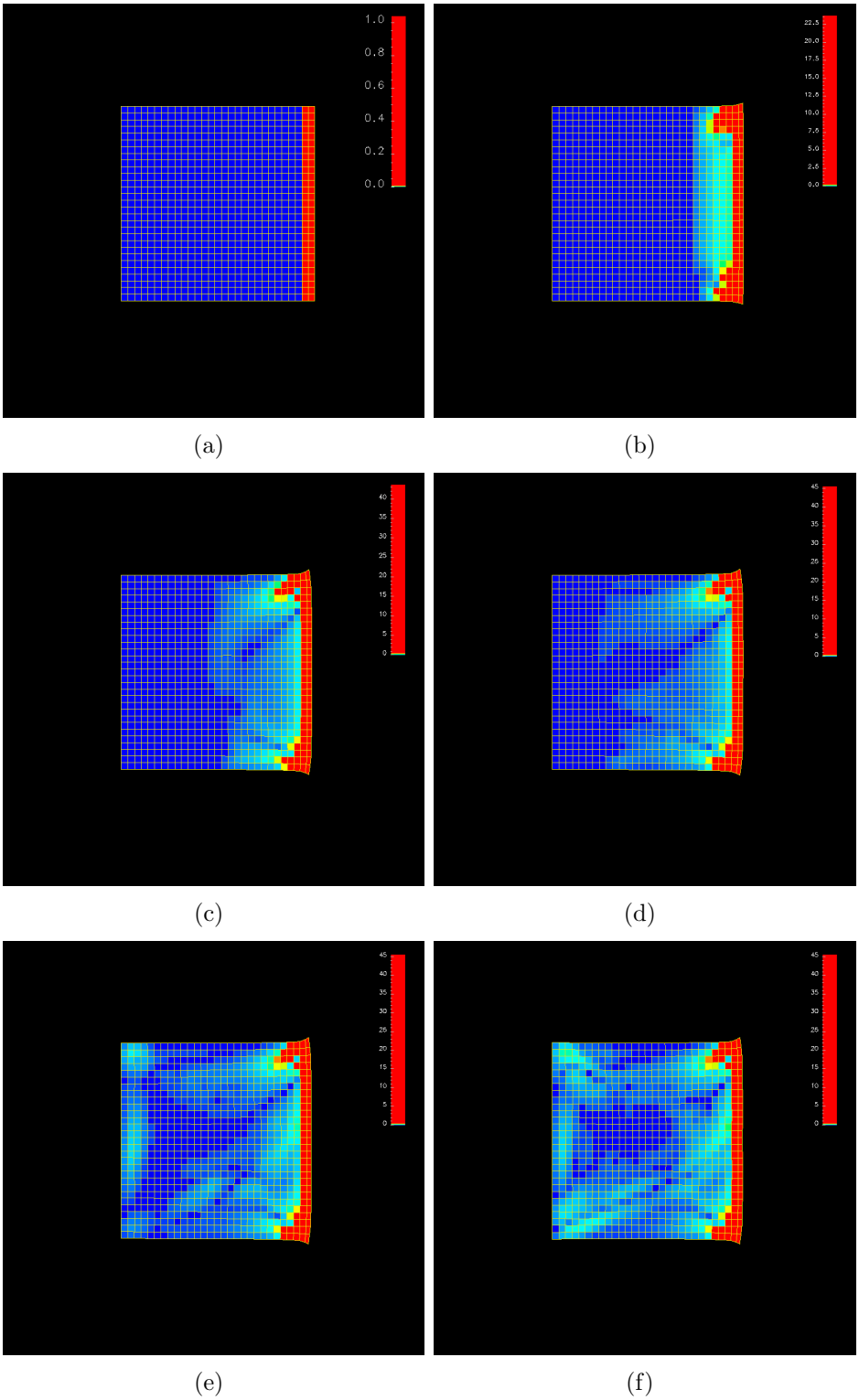

Figure 2.65: Shock animation frames, color bar is a measure of the geometrically necessary dislocation content, $||\boldsymbol{\xi}||$. Same frames as for the previous figure. The color map has been modified to better visualize the fine scale structures.

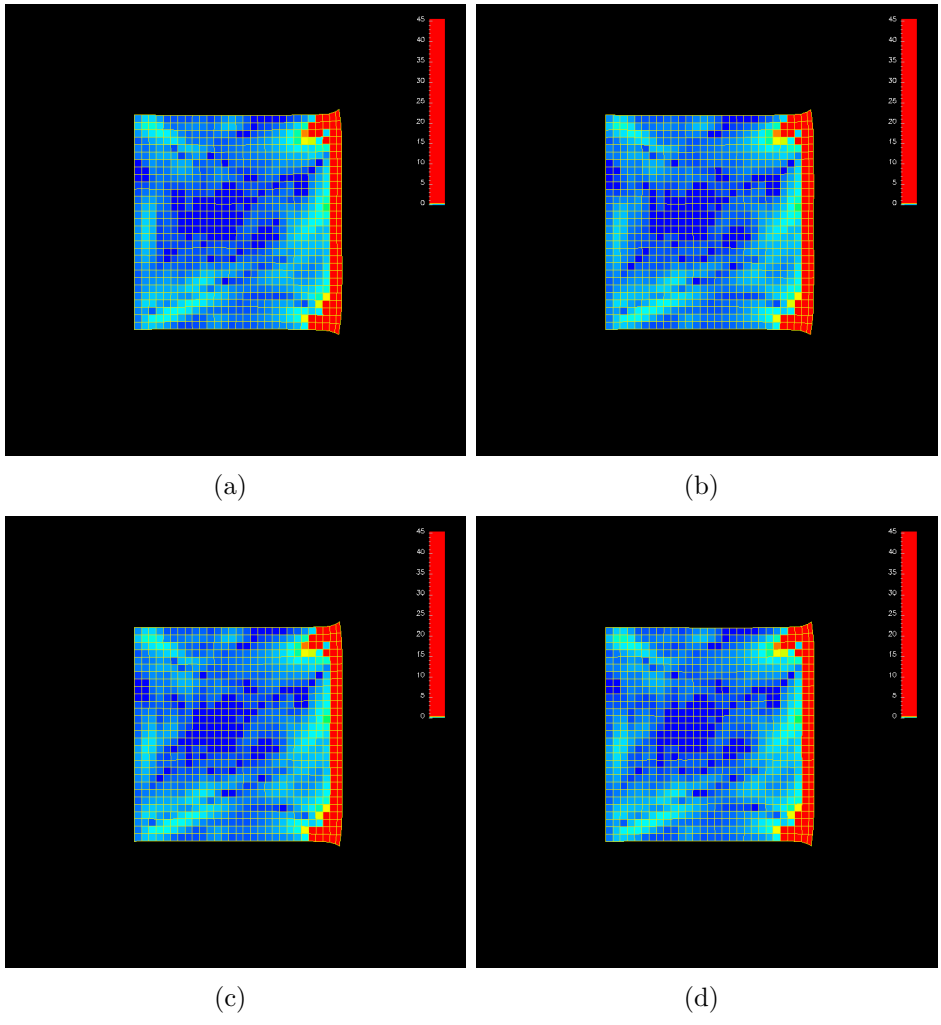

(a) (b)

(c) (d)

Figure 2.66: Shock animation frames, $||\boldsymbol{\xi}||$ (cont'd),

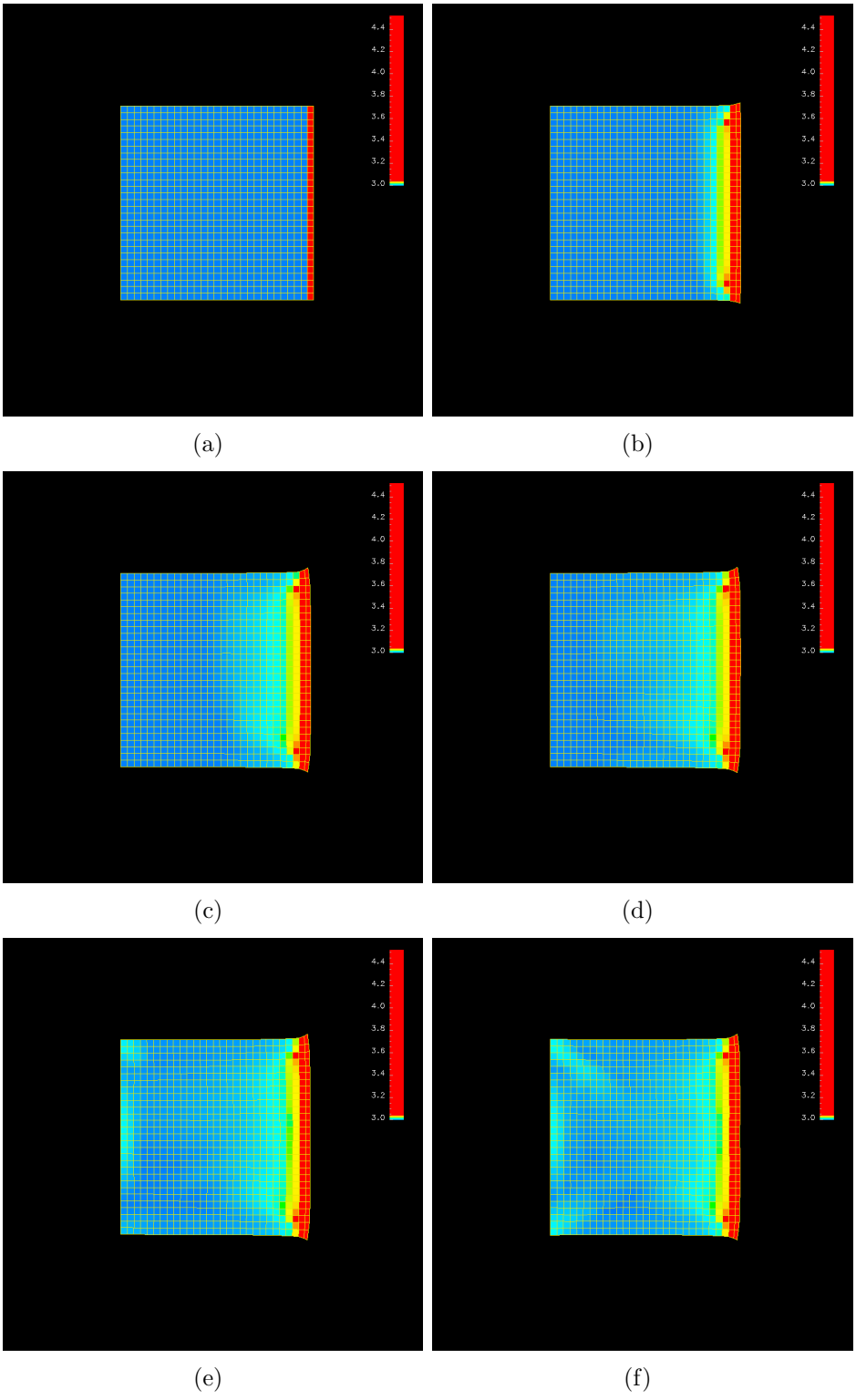

Figure 2.67: Shock animation frames, color bar is $||\mathbf{K}||$. Snapshots are at the same time as the previous figures in this series. The color map has been modified to better visualize the fine scale structures.

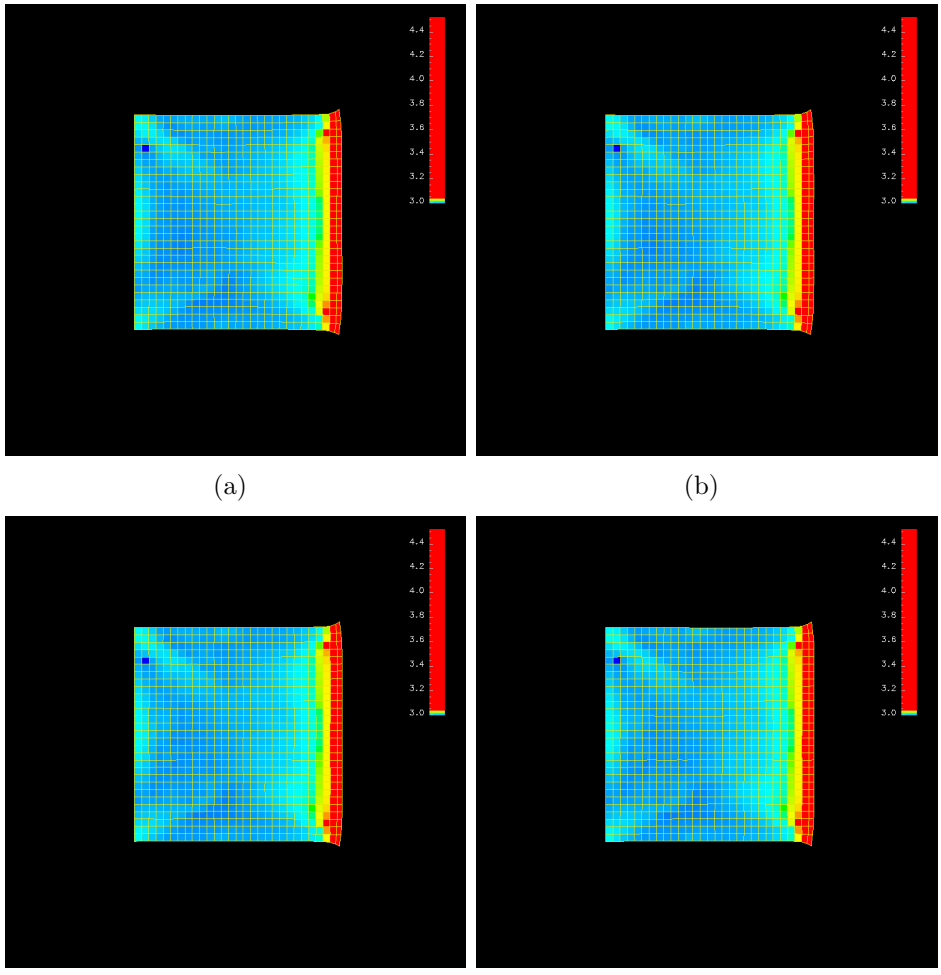

Figure 2.68: Shock animation frames, $||\mathbf{K}||$ (cont'd)

2.4.2.3.4 Shear deformation We also show results from shear boundary condition. The nodal velocity on the right is set in the vertical $\mathbf{e}_2$ direction, with the same cycling as in Figure 2.18. The top and bottom boundaries are traction free, and the left edge is fixed. In Figures 2.69-2.72 are shown the results for several initial orientations of θ_0, with $A_3 = 0.1$, with $\|\boldsymbol{\xi}\|^2$ plotted in the colormap. The localization of plastic flow is evident due to the boundary conditions at the edges. In Figures 2.73-2.76 the same simulation is plotted with $\|\mathbf{K}\|$ shown.

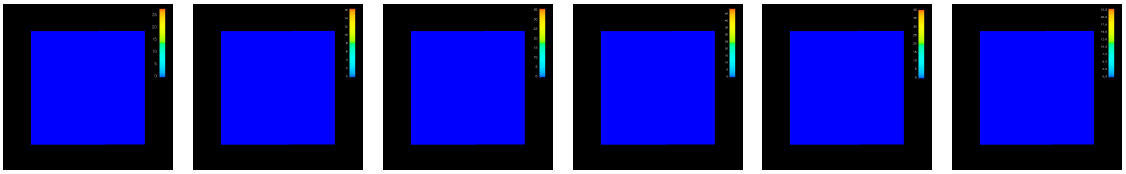

(a) $\theta = 0$ (b) $\theta = 10$ (c) $\theta = 20$ (d) $\theta = 30$ (e) $\theta = 40$ (f) $\theta = 45$

Figure 2.69: Comparison of θ-dependence for shear boundary condition. The colormap shows $\|\boldsymbol{\xi}\|^2$. $A_3 = 0.1$, $\nu = 0.0010$, hardening mode=1, $\theta_0 = 45$, sequence number = 0

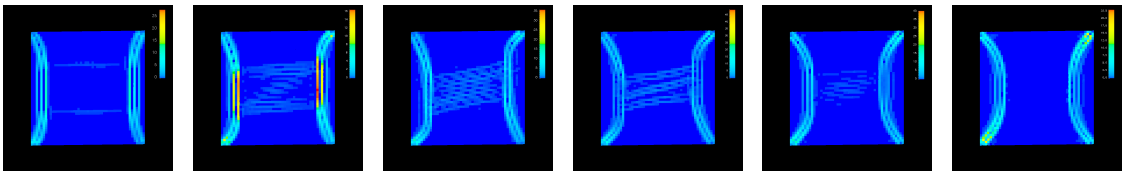

(a) $\theta = 0$ (b) $\theta = 10$ (c) $\theta = 20$ (d) $\theta = 30$ (e) $\theta = 40$ (f) $\theta = 45$

Figure 2.70: Comparison of θ-dependence for shear boundary condition. The colormap shows $\|\boldsymbol{\xi}\|^2$. $A_3 = 0.1$, $\nu = 0.0010$, hardening mode=1, $\theta_0 = 45$, sequence number = 1

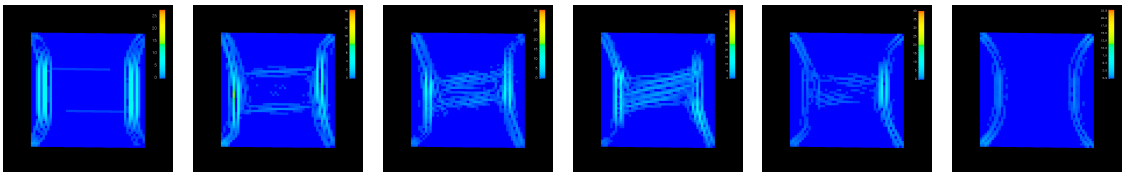

(a) $\theta = 0$ (b) $\theta = 10$ (c) $\theta = 20$ (d) $\theta = 30$ (e) $\theta = 40$ (f) $\theta = 45$

Figure 2.71: Comparison of θ-dependence for shear boundary condition. The colormap shows $\|\boldsymbol{\xi}\|^2$. $A_3 = 0.1$, $\nu = 0.0010$, hardening mode=1, $\theta_0 = 45$, sequence number = 2

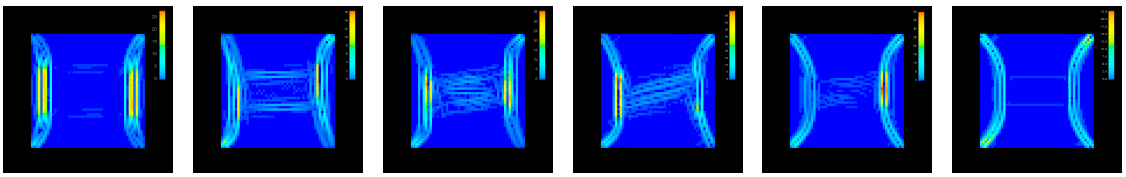

(a) $\theta = 0$ (b) $\theta = 10$ (c) $\theta = 20$ (d) $\theta = 30$ (e) $\theta = 40$ (f) $\theta = 45$

Figure 2.72: Comparison of θ-dependence for shear boundary condition. The colormap shows $\|\boldsymbol{\xi}\|^2$. $A_3 = 0.1$, $\nu = 0.0010$, hardening mode=1, $\theta_0 = 45$, sequence number = 3

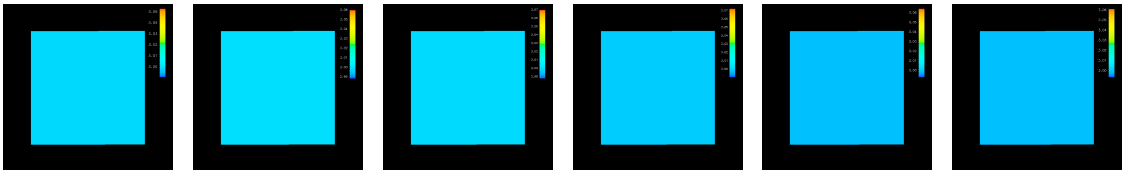

(a) $\theta = 0$ (b) $\theta = 10$ (c) $\theta = 20$ (d) $\theta = 30$ (e) $\theta = 40$ (f) $\theta = 45$

Figure 2.73: Comparison of θ-dependence for shear boundary condition. The colormap shows $\|\mathbf{K}\|$. $A_3 = 0.1$, $\nu = 0.0010$, hardening mode=1, $\theta_0 = 45$, sequence number = 0

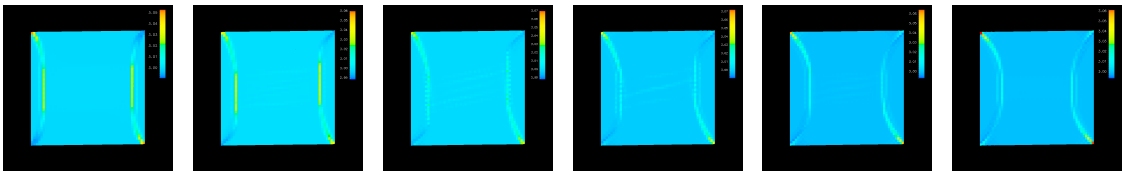

(a) $\theta = 0$ (b) $\theta = 10$ (c) $\theta = 20$ (d) $\theta = 30$ (e) $\theta = 40$ (f) $\theta = 45$

Figure 2.74: Comparison of θ-dependence for shear boundary condition. The colormap shows $\|\mathbf{K}\|$. $A_3 = 0.1$, $\nu = 0.0010$, hardening mode=1, $\theta_0 = 45$, sequence number = 1

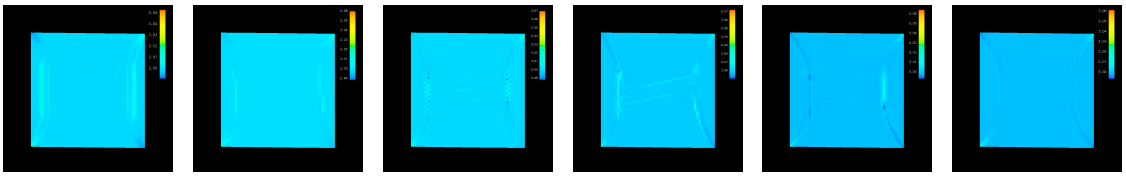

(a) $\theta = 0$ (b) $\theta = 10$ (c) $\theta = 20$ (d) $\theta = 30$ (e) $\theta = 40$ (f) $\theta = 45$

Figure 2.75: Comparison of θ-dependence for shear boundary condition. The colormap shows $\|\mathbf{K}\|$. $A_3 = 0.1$, $\nu = 0.0010$, hardening mode=1, $\theta_0 = 45$, sequence number = 2

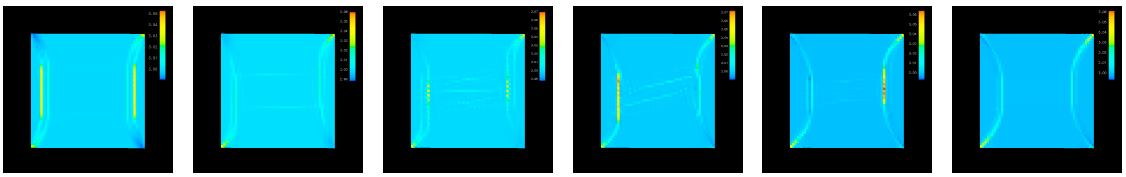

(a) $\theta = 0$ (b) $\theta = 10$ (c) $\theta = 20$ (d) $\theta = 30$ (e) $\theta = 40$ (f) $\theta = 45$

Figure 2.76: Comparison of θ-dependence for shear boundary condition. The colormap shows $\|\mathbf{K}\|$. $A_3 = 0.1$, $\nu = 0.0010$, hardening mode=1, $\theta_0 = 45$, sequence number = 3

2.4.2.4 Discussion

We now summarize and discuss the results from these simulations. First, the results of §2.4.2.3.1 indicated several things. (1) plastic work hardening based on (2.290) gives better isotropic hardening phenomenology than hardening based on $\boldsymbol{\xi}$, (2.288), and (2) reorientation functions of the form $\boldsymbol{\Omega}(\mathbf{S})$ in the flow rule (2.205) should definitely be preferred to functions of the form $\boldsymbol{\Omega}(\mathbf{S}, \dot{\mathbf{S}})$ of (2.110), unless experiments otherwise dictate. This is because the reorientation behavior of the net material using (2.110) were not equal and opposite in extension-contraction simulations, thus leading to a changing slope of the elastic region due to the anisotropic crystal structure.

Second, we performed simulations based on weakening the material in a fixed location. This caused plastic deformation to be localized in a consistent region with out mesh dependent effects entering in. Convergence upon mesh refinement was qualitatively better when imposing a parameter of $A_3 \geq 0.1$ in the $\boldsymbol{\xi}$-based yield function of (2.288), rather than having no such hardening. Further study of the implications of well known convergence issues of localization phenomena in plasticity, as they pertain to the current model, is required.

On the positive side, the deformation bands in e.g. Figure 2.34 and following images is reminiscent of experimental images such as Figure 2.77 from Spitzig (1981) showing the fracture pattern of Fe-Ti-Mn single crystals (BCC).

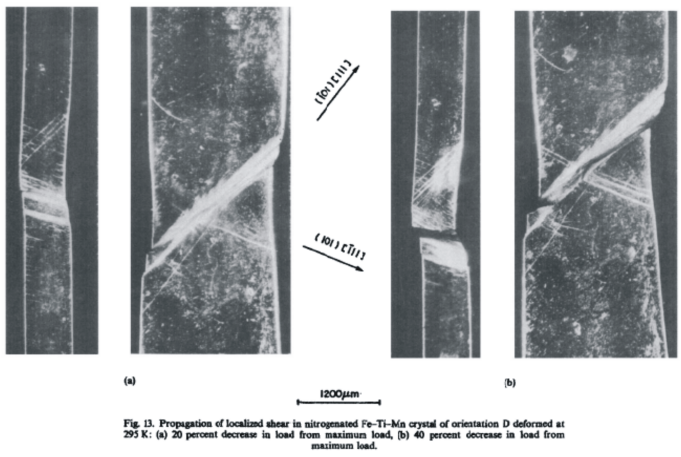

Fig. 13. Propagation of localized shear in nitrogenated Fe-Ti-Mn crystal of orientation D deformed at 295 K: (a) 20 percent decrease in load from maximum load, (b) 40 percent decrease in load from maximum load.

Figure 2.77: Fracture of Fe-Ti-Mn single crystal in qualitative agreement with Figure 2.34. From (Spitzig, 1981). Reprinted with permission from Elsevier.

Thirdly, the notion of treating geometrically necessary dislocations at grain boundaries in the same fashion as in a bulk crystal in this framework should be further analyzed. For

instance, in the determination of $\boldsymbol{\xi}$ based on (2.275), the dimensions of $\boldsymbol{\xi}$ are on the order

$$\boldsymbol{\xi} \propto \frac{1}{A} \int_{\partial A} \mathbf{K}^{-1} \cdot \mathrm{d}\mathbf{l} \approx \frac{1}{h} \Delta \mathbf{K}^{-1} \tag{2.291}$$

where h is a characteristic mesh dimension and $\Delta \mathbf{K}^{-1}$ is some measure of the difference in $\mathbf{K}^{-1}$ around the integration loop ∂A. At a grain boundary, $\Delta \mathbf{K}^{-1}$ is fixed by the difference in orientations, irrespective of the mesh resolution, and as $h \to 0$, $\boldsymbol{\xi} \to \infty$. In yield functions based on (2.288), for a fixed $y_{\max}$ there will therefore be a mesh resolution at which no plastic deformation is expected at grain boundaries. This numerical behavior may or may not be a problem in practice. At worst, the elements on the boundary of the grains will not achieve flow in the simulations, but adjacent ones certainly will. As $h \to 0$, this lack of flow at the exact boundary material becomes irrelevant. We don't believe that treating grain boundary based hardening in a different fashion than $\boldsymbol{\xi}$ seems physically appealing, as hardening should only depend on local neighbors. Such a study of grain boundaries on yield behavior may be crucial to developing simulations which predict phenomenological effects such as the Hall-Petch effect (Lim et al., 2011) which relates polycrystalline yield strength to the grain size diameter.

The numerical simulations developed here are probably most efficiently suited for the shock contraction simulations, due to the retention of dynamics information. At large plastic deformations, the Lagrangian mesh becomes distorted, and additional computational steps which were beyond the current scope are required to prevent problems. For shocks however the numerical performance was qualitatively excellent. We previously stated that plastic deformations in the current theory can only be experimentally determined from an initial state. In shock compression experiments, measuring in situ elastic and total material strain as suggested for quasistatic experiments is far beyond current capabilities. However the calculation of $\boldsymbol{\xi}$ can serve as an independent indicator of past plastic deformation. Given an initially perfect crystal, after shock loading geometrically necessary dislocation content can be deduced by post mordem analysis like EBSD or X-ray diffraction. High resolution EBSD measurements are only recently becoming available (Kysar et al., 2007), but they have the advantage of being more readily available than synchrotron sources. Therefore the shock simulations and prediction of $\boldsymbol{\xi}$ from this work can be directly compared against experimental data, even if $\mathbf{K}$ cannot. In our visualizations we have normally plotted $\|\boldsymbol{\xi}\|^2$. However we can also plot directly the Burgers vectors from the integration loop, compare (2.13) and (2.275), shown in Figure 2.78. We were not able to discern any implications from this type of data visualization, besides that the Burgers vectors typically collect in $+/-$ pair orientations instead of monotonically aligning in a certain direction.

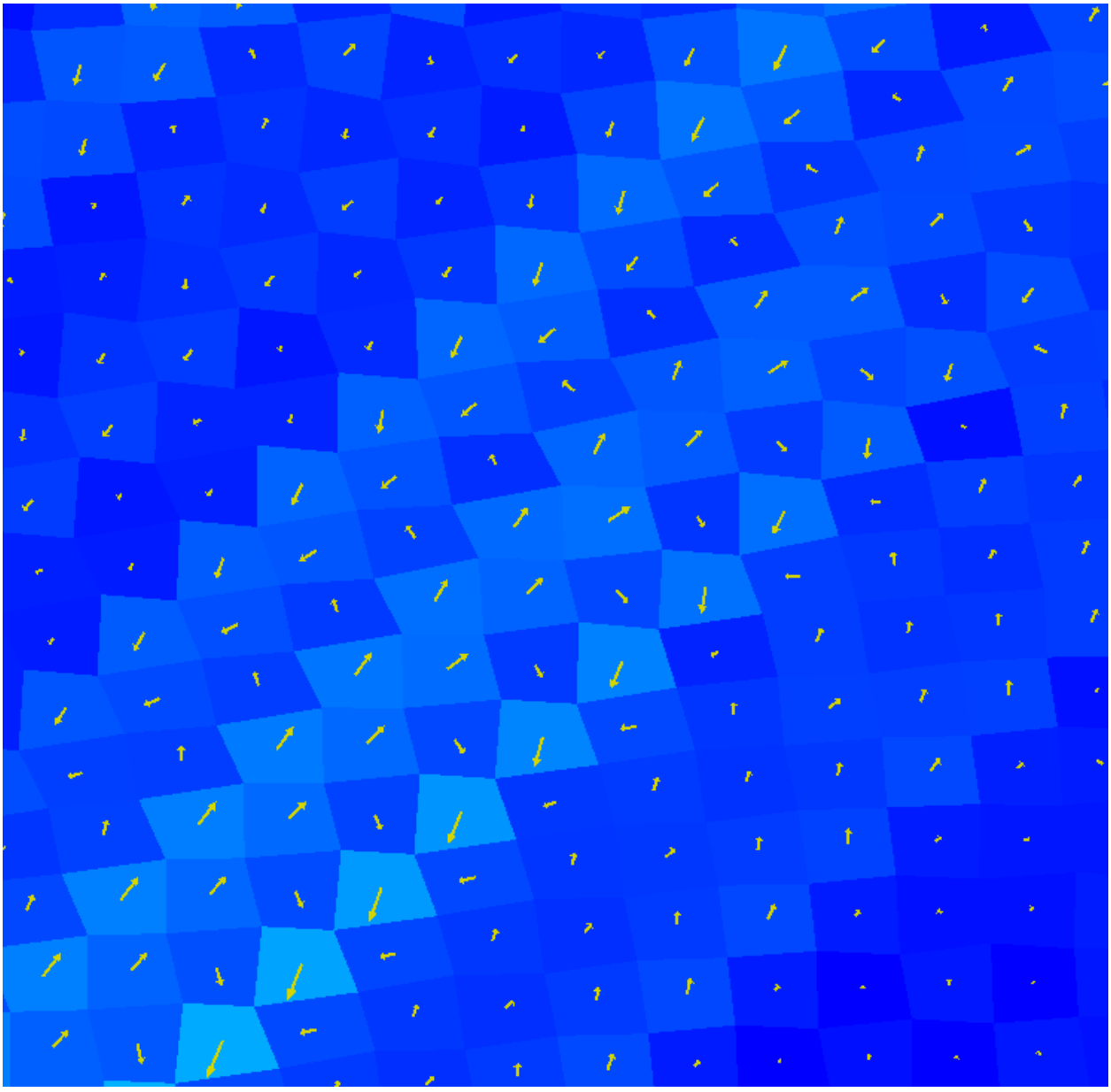

Figure 2.78: Burgers vectors, (2.13), from numerical simulation. The color map is based on $\|\boldsymbol{\xi}\|^2$.

2.5 Conclusion

In this chapter we have completed the specification of a proposed theory of elastic-plastic deformation based on the model of Fox (1968). This model was infused with the maximum dissipation postulate and applied to symmetry groups characteristic of single crystals. The intended application of the model is identical to that the situations in which crystal plasticity is used.

The differences between the formulations are most generally viewed as being of a constitutive nature. The flow rule of crystal plasticity is given by (2.229), (2.230), whereas our flow rule is given by (2.205) or (2.110). Crystal plasticity elegantly reduces to the single slip theory based on observations from Taylor and Elam (1923). However it's ability to predict data in more complicated situations such as embedded grains in a polycrystal has not been verified by available experimental methods. Based on the mechanics community's past experience with other aspects of continuum physics, physically motivated theories have been at times inadequate in comparison to experimental data (Treloar, 1974). Therefore until the experimental investigation of plasticity becomes of a more quantitative than qualitative nature, there will remain some uncertainty as to which plasticity formulations are successful in certain situations. Even before that however, there are still many phenomenological observations in plasticity which have not been adequately answered by current modeling approaches, such as the Hall-Petch effect (Lim et al., 2011). For most engineering applications, macroscopic phenomenology is more important than the modeling methodology used to obtain the answer; our approach still shows the ability to model strain localization and geometrically necessary dislocations which was raised as a potential reason not to implement such theories, in §2.1.4. Our view is that as long as theories remain true to the most fundamental principles of physics they should be investigated; which has not been the case for the proposed formulation of single crystal plasticity. Therefore this model seeks to serve as a viable alternative framework for such situations where crystal plasticity becomes cumbersome to deal with or is found to be inadequate in capturing data.

The primary contribution in this chapter is the constitutive framework needed to complete the theory and make predictions. Of the 32 crystallographic point groups, we focused on the cubic class due to the importance of cubic crystals in engineering. For cubics, we found examining polynomial integrity basis elements to be more attractive than using structural tensors (Liu, 1982). We gave detailed examples of constitutive function generation, building off of similar examples given in the literature (Green and Adkins, 1970; Spencer, 1971). We obtained expressions for lattice reorientation as well as yield functions incorporating hardening phenomenology. The hope is providing these examples makes the constitutive framework more friendly to future investigation.

Lattice orientation is a fundamental observable in experimental plasticity using X-ray diffraction; our theory seeks to make predictions of the orientation evolution due to plastic flow. With this experimental situation in mind a simple extension experiment should be sufficient to calibrate the model to experimental data. Such an experiment is feasible given

proper resources but here we calibrated our constitutive equations for yield and plastic flow to simulated data from a crystal plasticity model using a material point simulation of isochoric extension.

The resulting constitutive model was implemented into plane strain simulations to investigate predictions from the theory in simple boundary value problems. We used an explicit Lagrangian numerical method (Herrmann and Bertholf, 1983; Silling, 1988) which was straightforward to implement into code, gave a measurement of $\boldsymbol{\xi}$, and proved to be generally useful for early investigations of the model. The simulations passed several consistency checks, such as mesh dependence of strain localization bands and convergence of the solution. We learned several things about our plasticity model from these simulations. First, we learned that rate independent reorientation function of (2.205) appears to be must more attractive than that initially established in (2.110), since it assures that the lattice reorientation direction reverses upon reversal of the load. This behavior is naturally encoded in crystal plasticity flow rules. Second, we learned that flow localizations are naturally predicted in the model, giving some counter to the statement by Yang and Lee (1993) that such microstructural information could not be deduced from phenomenological theories, see §2.1.4, item number 3. The numerical method also gave predictions for geometrically necessary dislocation content, $\boldsymbol{\xi}$, which in this theory is derived based on the spatial gradients in the plastic deformation field and not stored as an independent state variable. This information is only recently being incorporated into numerical simulations (Lele and Anand, 2009). Experimentalists have suggested that the development of $\boldsymbol{\xi}$ is responsible for many phenomenological observations, the modeling of which is still open to improvements. The present model may prove to be helpful in providing flexibility to constitutive frameworks in the presence of such complexity.

In the next chapter we give a detailed treatment of the experimental method which is naturally coupled to this model of plasticity - X-ray diffraction.

Chapter 3

Experimental: X-ray Diffraction

Chapter overview. The major areas of scientific research work activity consist of theoretical development, numerical simulation, and experiments. In the previous chapter we developed a theory for the plasticity of single crystals, and gave numerical predictions. This chapter describes considerations associated with investigating the model experimentally.

Experiments serve two primary functions in research. One function is that experiments enable the discovery of new behaviors and properties of materials. The second function is that experiments provide the physical data needed to ground theoretical models in reality. In particular, the values of material parameters in constitutive models cannot be obtained without the input of experimental data at some stage. After obtaining such values, numerical studies can be performed. This is useful because simulations are a cost-effective way to inform design processes, for example. However, quite often the constitutive models required by a given theory are left unfounded by experiment. This is particularly true, historically speaking, for phenomenological continuum plasticity. In this situation, promising numerical simulations have to be performed with unknown constitutive parameters (Papadopoulos and Lu, 2001). In this chapter we seek to determine constitutive parameters for the theory in Chapter 2 directly from experiments.

The experimental technique addressed in this chapter is high energy synchrotron X-ray experimentation. This is a relative newcomer to the array of methods available for experimentation (Poulsen et al., 1997). To date, much attention has been given to using the experiments to make novel observations (Jakobsen et al., 2006), but little attention is given to experiments where quantifiable information is derived. In this chapter we analyze the data from some recent high energy X-ray diffraction experiments to determine constitutive behaviors in materials of interest. We also give a thorough background to the method, to serve as a reference for crossover researchers from mechanics to applied crystallography.

3.1 Introduction

In the following sections we discuss theoretical and practical aspects of X-ray diffraction experiments for analysis of the plasticity theory developed in Chapter 2. We provide a thorough introduction to basic X-ray diffraction theory, so that researchers from a mechanics background can use this as a concise translation between mechanics and crystallographic notions and terminologies.

As noted in the introduction to this thesis, experimental investigation of plasticity theories is challenging. Techniques to quantitatively validate theories of plasticity for length scales at which crucial mechanical details purported to be modeled by the theory manifest themselves simply do not exist or are not widely available. This is particularly true for the investigation of polycrystalline behavior.

Although a synchrotron is not a common instrument to have available in a small research lab (!), synchrotron X-ray diffraction is one of the most promising experimental tools available to investigate these theories. For example, the brilliance of modern third generation synchrotron sources (Mills et al., 2005), in combination with improvement in hardware technology, has opened up the field to *in situ* testing at comparatively fine temporal resolutions appropriate for quasistatic processes. This enables the quantitative study of interesting deformation processes or phase changes (Margulies et al., 2001; Larsen et al., 2004; Offerman et al., 2006; Aydiner et al., 2009). Scans sufficient to characterize a polycrystal can now be completed on time scales on the order of tens of seconds at Sector 1 of the Advanced Photon Source, Argonne National Lab.

The core contributions of the following sections are summarized by three major points. These are:

1. Advancing the community's understanding of the quantitative capabilities of the high energy X-ray diffraction technique by developing the analytical tools to estimate uncertainty in the measurements.

2. Developing an improved modeling methodology to increase the amount of kinematic information able to be deduced from X-ray diffraction data.

3. Using X-ray diffraction data from experiments on polycrystalline materials to extract single crystal constitutive parameters.

To elaborate on (1): as we shall soon see, the output from X-ray diffraction measurements are estimates of the lattice deformation with respect to the fixed reference configuration, which we called $\mathbf{H}$ in Chapter 2. This is accomplished by measuring the locations of reciprocal vectors, which are functions of the ambient lattice structure and the lattice deformation $\mathbf{H}$. At the high X-ray energies we will consider (50 -100 keV), the available resolution of reciprocal space is poor. Therefore there is a relatively large degree of uncertainty associated with the measurements of $\mathbf{H}$. For constitutive determination, this uncertainty must be

quantified in order to be a useful experimental tool. This uncertainty has not been quantified before in the hierarchical framework we will propose later in this chapter.

On (2): In conventional methods of X-ray diffraction analysis, the principal output, **H**, is assumed to be spatially homogeneous on a grain averaged basis. Associated with the homogeneity assumption, each diffraction peak is assumed to represent a single location in reciprocal space. This simplification is acceptable for many studies. However for plastically deformed crystals, the diffraction peaks smear out as a symptom of the single crystal breaking up - that is, the single crystal becomes spatially inhomogeneous. The diffraction technique considered in this chapter cannot measure the lattice deformation state on the length scales required to quantify this spatial inhomogeneity. However by projecting the inhomogeneity into **H**-space, and forward modeling the diffraction pattern from this projection, we can make deductions about the plastic deformation processes having occurred in the crystal. This modeling approach adds to the list of capabilities of the X-ray diffraction technique, increasing the profitability of pursuing such experiments.

For (3): we first motivate why single crystal properties are of interest, since polycrystalline materials are the materials most often encountered in applications. Polycrystals typically have better mechanical properties than a single crystal of the same material, have less anisotropy, and are easier and cheaper to produce. Clearly, accurate prediction of polycrystalline behavior is of interest in many fields of study. Advances in computational capabilities have led to methods of numerical simulation which discretize polycrystals at length scales which require constitutive information about the single crystal. Therefore obtaining constitutive information of single crystals is required for these sorts of numerical studies. This is, of course, in addition to the situations where single crystals are directly required to be employed in an engineering application (e.g. silicon-based microelectronics).

When large (macroscopic) single crystals are cheaply available, obtaining the single crystal properties is only a matter of executing the experiments to obtain material properties, such as the constants in the strain energy function. However many materials of interest to engineering applications, such as complicated alloy mixtures, may be difficult to possess as a large single crystal due to the required heat treatments, etc. Therefore having the capability to extract single crystal properties from a more readily available polycrystalline sample would be desirable.

We present these topics in 5 sections.

1. In §3.2 we give the requisite background of X-ray diffraction theory used in this study. The presentation of §3.2 constitutes only a subset of a fully general treatment of X-ray diffraction, but one that is relevant to full understanding of the results and concepts behind the type of experiment used in the present work. The most useful outcome of §3.2 is that we derive the Fourier transform of the crystal lattice which leads to the reciprocal lattice description. Once the reciprocal lattice is obtained, we can then rapidly translate all required quantities to a style in line with continuum mechanics notions of deformation analysis. We also derive the expression for scattering intensity,

including structure factors, Thomson polarization factor, and Lorentz polarization factors. These factors are needed, for example, in order to estimate the relative volume of grains in the polycrystal for microstructure reconstruction. In addition, developing the general structure of analysis afforded by the Fourier transform leads to an elegant and practically useful model of X-ray diffraction for the forward modeling of diffraction peaks, (see item (2) in the previous list).

2. In §3.3 we apply the theory developed in §3.2 to describe technical details of a class of synchrotron X-ray diffraction experiments. In the literature this technique is referred to as 3DXRD or HEDM (High Energy Diffraction Microscopy). At their essence these techniques basically describe the classical rotating crystal method; the distinctive features being the high X-ray energies, from synchrotron sources. We describe the explicit mapping from observations of diffracted beams to reciprocal lattice vectors in preparation for grain indexing and estimating lattice deformations. We discuss general approaches to grain indexing, and suggest a novel indexing algorithm. We describe techniques for refining the lattice deformation measurement, and compare and contrast the approaches of a crystallographer with that of a mechanics perspective.

3. In §3.4 we present the framework for estimating kinematic information such as lattice deformation from X-ray diffraction. In effect, this section explains how to 'read' the strain gauge enabled by X-ray diffraction. We give a brief review of weighted least squares, which is used extensively in this chapter. We present two methods for extracting information from X-ray diffraction data: a grain averaged approach and a forward modeling approach.

   The grain averaged approach leads to an efficient framework for estimating the uncertainty associated with X-ray diffraction measurements of the lattice deformation $\mathbf{H}$. We implement a hierarchical method in which uncertainties in the locations of diffraction peaks are communicated to the lattice stretch and rotation parameters by using the classical method of weighted least squares. This enables the uncertainty of the lattice stretch and rotation parameters to be estimated based on a single full rotation scan. We apply our framework to diffraction data obtained from a ruby single crystal and a titanium polycrystal. We are able to state precisions for lattice orientation and strain of 0.1° and $200 \cdot 10^{-6}$ respectively, which were found to be comparable to statistical analysis of repeated measurements. Our analysis also shows that we are able to identify the source of maximum uncertainty of our measurements, in order to inform experimental methodologies and improvements to the experimental configuration. The basic framework of the uncertainty analysis is generally applicable to any experimental program, although specific results are unique to monochromatic X-ray diffraction experiments.

   The forward modeling approach has a certain aesthetic appeal over the grain averaged approach. In this method, simulated diffraction peaks are forward modeled based on

the collective information from all measured diffraction peaks, rather than having each peak be a separate entity. Such modeling gives kinematic information inaccessible from the grain averaged approach, such as the intragranular misorientation. The intragranular misorientation can be interpreted to provide a measure of the plastic deformation history in the grain. By the relationship between the misorientation and the unit cell of the lattice, we can obtain a direct indication of the plastic deformation processes in the crystal. The addition of this capability makes the high energy technique attractive for experiments.

4. In §3.5 we attempt constitutive parameter extraction from a uniaxial tension test of a titanium alloy (Ti-7Al, HCP). This undertaking closes the loop between Chapter 2 and the present chapter by relating experiment with the plasticity model. From the measurements of $\mathbf{H}$, we use independently obtained elastic moduli to compute grain averaged stresses. We fit phenomenological constitutive parameters for the yield function, according to the theory in Chapter 2. We perform a similar analysis adopting crystal plasticity theory, where we can project these stresses on the slip systems in the material in order to obtain evidence of critical shear stress for a given slip system. The resulting comparison between models is informative.

5. Concluding remarks are given in §3.6.

We begin with the background discussion of X-ray diffraction that closely follows the treatment of Guiner (1963).

3.2 Background - X-ray diffraction theory

In this section we present background information for an efficient description of X-ray diffraction. The main outcome of this section is that we derive the importance of the reciprocal lattice construction for description of diffraction observations.

We start from considering the radiation scattered by an entity such as an atom, eventually deriving the reciprocal lattice by taking the Fourier transform of a spatial distribution of atoms. Once the reciprocal lattice description is established, we can then effectively abandon the formal computation of the Fourier transform and use standard notions from differential geometry in Euclidean space to give a more computationally efficient description of the reciprocal lattice and its evolution due to elastic deformation.[1] Once this description is obtained, we can then derive the evolution of the reciprocal lattice under elastic deformations in a straightforward manner. That is, we derive the relation

$$\mathbf{l}^{(i)} = \mathbf{H}^{-\mathrm{T}}\mathbf{L}^{(i)} \tag{3.1}$$

[1]This description works well for the type of X-ray diffraction conditions undertaken in subsequently presented experiments - these conditions being far field detector, high energy, synchrotron radiation, and known a priori crystallographic symmetry and structure.

where $\mathbf{L}^{(i)}$ is an arbitrary reciprocal lattice vector of the reference lattice configuration, $\mathbf{l}^{(i)}$ is a reciprocal lattice vector of the current lattice configuration, and $\mathbf{H}$ is the lattice deformation between configurations. A relation analogous to (3.1) which should be familiar to mechanicians is the relation between reference and deformed material vectors,

$$\mathbf{g}_{(i)} = \mathbf{F}\mathbf{G}_{(i)}, \tag{3.2}$$

where $\mathbf{G}_{(i)}, \mathbf{g}_{(i)}$ are the reference and current material tangent vectors. This equation is of importance in the use of bonded resistance strain gages, whose readings track the deformation of material elements on the surface of the material. This relation between (3.1) and (3.2) suggests a reassuring analogy for mechanicians not familiar with X-ray diffraction procedures: the processing of X-ray diffraction images can be considered to be readings from an three dimensional strain gage, which has been implanted into each grain. We examine this analogy in greater detail in §3.2.3.

The kinematic linking between elastic deformation and evolution of reciprocal lattice vectors was long observed in theoretically minded papers by previous authors. However the description in this section lays down in one place the relationship between a classical X-ray diffraction treatment and a more modern approach, and applies the analysis to data. The communication of X-ray diffraction data in terms of finite deformations as in (3.1) is somewhat recent (Edmiston et al., 2012).

We give the background presentation in 3 sections. First, in §3.2.1 we state the assumptions necessary to simplify the X-ray diffraction analysis, assumptions appropriate for the experiments undertaken in this work. We record the effect on radiated waves of a single and then multiple scattering entities. We also give results regarding the effect of a finite material size. This is a negligible effect in our experiments, but the derivation of this illustrates the usefulness of the Fourier transform. In §3.2.2, we apply the Fourier transform concept to atoms arranged in a crystal lattice, and derive the relevance of the reciprocal lattice for X-ray diffraction. We introduce the structure factor of the unit cell, and give an example computation. We then proceed to derive the scattering power from a body, as a function of the diffraction angles. This will be used later on in §3.5 to estimate the size of grains in a polycrystal and generate an experimentally suggested polycrystalline microstructure. In §3.2.3 we give a convenient description of the lattice using notions from continuum mechanics. This will enable us to complete the transition from Fourier transforms to computationally easier differential geometric constructions. We record expressions for the evolution of reciprocal lattice vectors to elastic deformation of the crystal lattice. We compare and contrast X-ray diffraction kinematic analysis with the conventional macroscopic tool, the strain gage rosette. Before beginning, we first list some caveats of the approach we are taking to X-ray diffraction theory.

X-ray diffraction background - preliminaries. In this background we are considering the kinematic theory of X-ray diffraction. This is the classical formulation given in most

introductory books on the subject (Azaroff et al., 1974; Cullity, 1978; Guiner, 1963). The kinematic theory is the simplest useful model for X-ray diffraction; it is also readily pushed into a continuum mechanics friendly framework. It should be noted that, being a simplified model, we do lose generality, and cannot characterize effects such as Compton or incoherent scattering. The restrictions of the kinematic treatment are well explained in Azaroff et al. (1974), but for completeness we repeat these here:

1. Small scattering amplitude - implies that the interaction between the incident beam and the scattered beam may be neglected. If interactions between the incident and diffracted beams may not be neglected the dynamic theory of diffraction is used, see Azaroff et al. (1974).

2. Plane-wave approximation - implies that the incident beam has a plane wave front as opposed to a spherical front.

3. Coherent scattering - implies that the wavelength does not change due to scattering. This is crucial since the entire kinematical theory is built on the idea of extinctions of diffracted waves in particular directions - an effect which is strongly dependent upon a uniform wavelength.

An additional important restriction on the advertised generality of the background theory presented here is that we are assuming the crystal structure is known from prior studies. In the course of our background treatment, we will introduce some of the notions needed to give an abstract proposition of the full structure determination problem, but will not go into any details of this. With the limitations of the current theory established, we now begin with the description of the X-ray diffraction problem.

3.2.1 Description of X-ray diffraction, interference computations

An X-ray diffraction experiment may be simply stated as the simultaneous processes of (1) bombardment of a material sample under electromagnetic radiation with X-ray wavelength, together with (2) measuring the resulting response of the material and electromagnetic field.

From this perspective, the response of the material and field are then obtained by solving the differential equations for electromagnetism (and associated material response), which accounts for the positions of each of the individual atoms and electrons. However in the absence of omniscient experimental or computational capabilities, we can get a very good approximation for the electromagnetic field diffracted by a distribution of atoms with a much simpler model than the general boundary value problem.

The simplified model considered here is called the kinematical theory of X-ray diffraction. The crucial assumptions required for this framework are enumerated in the introduction to this section. We refer to Azaroff et al. (1974) for a detailed account of the assumptions made upon employing the kinematical theory.

In the following sections we first focus on the primary characteristic of a scattering problem which unlocks the general boundary value problem of electromagneto-mechanics to a tractable form: consideration of the electromagnetic wave interference between diffracting species - in our case, atoms. From this basic interference model, we can derive the important conclusions of the kinematical theory: the concept of a Fourier transform of a spatial distribution of atoms, and the related description of reciprocal space. Generalization of this model to consider a crystal lattice eventually allows us to relate experimental X-ray diffraction patterns to an averaged state of deformation in the crystal. From a mechanical point of view, this gives us kinematic information about deformation processes in the crystal. And, in relation to the theory set out in Chapter 2, this kinematic information gives us direct measurements of $\mathbf{H}$, which can be used to validate constitutive theories of elastic-plastic deformation of crystals.

We first we consider the effect of a single scatterer on the electromagnetic field in §3.2.1.1.

3.2.1.1 Single scatterer

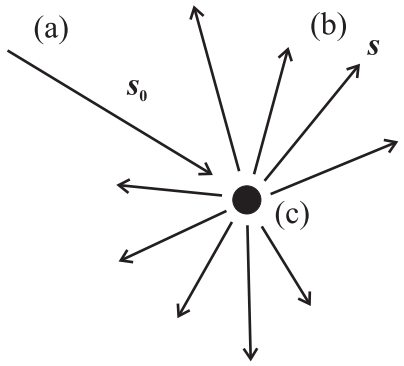

Figure 3.1: (a) Incident beam with unit vector direction $\mathbf{s}_0$ (b) diffracted beam with unit vector direction $\mathbf{s}$ (c) scattering particle

In this section we consider the effect of a single scattering entity, such as an atom, in a propagating electromagnetic wave. Figure 3.1 illustrates a schematic representation of an beam with direction $\mathbf{s}_0 \in \mathrm{S}^2$ incident upon a single scatterer. The diffracted wave propagates in all directions $\mathbf{s} \in \mathrm{S}^2$. Let

$$A(t) = A_0 \cos 2\pi\nu t \tag{3.3}$$

be the amplitude of incident radiation at the scattering point $\mathbf{x}$, where t is time, ν is frequency, and A_0 is the intensity factor. This is simply an arbitrary periodic function of the type that solves the wave equation. The amplitude of the scattered wave a distance r from $\mathbf{x}$ is (Azaroff et al., 1974)

$$A(t;\mathbf{x}) = f A_0 \cos\left[2\pi\nu\left(t - \frac{r}{c}\right) - \psi\right], \tag{3.4}$$

where f is called the scattering factor, it is the ratio between incident and scattered amplitudes, ψ is the phase shift, and c is the speed of light. As an example, when the scattering center is a free electron, the phase shift $\psi = \pi$ (Guiner, 1963). In the book by Guiner (1963) it is stated that even for atoms, $\psi = \pi$ is a good approximation. We can write (3.4) in complex form as (Guiner, 1963)

$$A = f \exp(-i\psi) A_0 \exp\left[2\pi i\nu \left(t - \frac{r}{c}\right)\right]. \tag{3.5}$$

From the periodicity of the above amplitude function, it is evident that an interference relation is set up when more than one scatter is present. Depending on the relative spatial location of these entities, the interference may have different effects, between constructive and destructive interference. In the next section we consider how this interference leads to the notion of reciprocal space and the Ewald or reflection sphere.

3.2.1.2 Scattering pair, Ewald sphere.

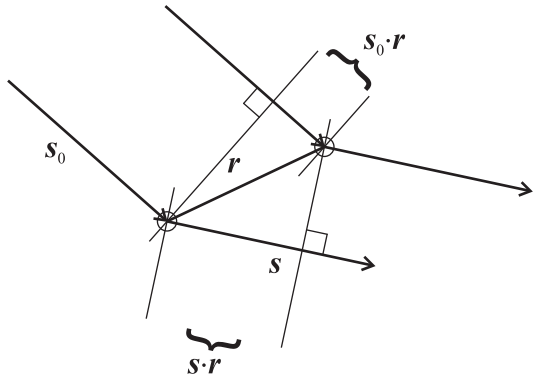

Figure 3.2: Pair of scattering entities. The relative position of the scatterers, $\mathbf{r}$, determines the phase shift between diffracted waves.

Fundamental to understanding X-ray diffraction experiments is consideration of the interactions between the scattered waves set up by individual waves of the form (3.5). The simplest example demonstrating this scenario is to consider the scattered intensity from a pair of atoms, separated by a spatial position vector $\mathbf{r}$, as depicted in Figure 3.2. The incident radiation wave propagation direction is denoted by $\mathbf{s}_0$, and the scattering wave propagation direction is denoted $\mathbf{s}$. Both $\mathbf{s}$ and $\mathbf{s}_0$ are unit vectors, as in Figure 3.1. The wave fronts are denoted in the figure by the lines perpendicular to the vectors $\mathbf{s}$, $\mathbf{s}_0$. The wave fronts coincide up to the points indicated in the figure, where a perpendicular is dropped. The path difference obtained from the incident and scattered beams between the two scatterers, δ, is obtained from geometry, by computing the projections of the separation $\mathbf{r}$ onto the wave direction unit vectors $\mathbf{s}, \mathbf{s}_0$ as

$$\delta = \mathbf{s} \cdot \mathbf{r} - \mathbf{s}_0 \cdot \mathbf{r}. \tag{3.6}$$

Since we are concerned with periodic functions, the path difference, δ, is essentially equivalent to a phase shift, ϕ (modulo the period), multiplied by the common wavelength, λ, e.g.

$$\delta = \frac{\phi}{2\pi}\lambda,$$

the phase shift ϕ is then given by

$$\phi = 2\pi\frac{\delta}{\lambda} = -2\pi\frac{\mathbf{s}\cdot\mathbf{r} - \mathbf{s}_0\cdot\mathbf{r}}{\lambda}, \tag{3.7}$$

where we have used (3.6). We note in passing that the wavelength λ being common to the incident and diffracted beams is a consequence of the kinematic theory requirement of wave coherence, see the introduction to this section. Next, define the vector $\mathbf{g}$ by

$$\mathbf{g} \equiv \frac{\mathbf{s} - \mathbf{s}_0}{\lambda}, \tag{3.8}$$

and apply (3.8) to (3.7). This gives the phase shift function $\phi(\mathbf{g};\mathbf{r})$ as

$$\phi = -2\pi\mathbf{g}\cdot\mathbf{r}. \tag{3.9}$$

The vector $\mathbf{g}$ will be crucially important to the following analysis. (3.9) indicates that phase differences between scattering entities depends only on the combination $\mathbf{g}(\mathbf{s}, \mathbf{s}_0, \lambda)$, and not independently on wavelength λ, $\mathbf{s}$, or $\mathbf{s}_0$.

One can gather from (3.9) and considering illustrative periodic functions of the form

$$A(t) = A_1 \cos 2\pi\nu_1 t + A_2 \cos 2\pi\nu_2(t + \phi)$$

that integral values of $\mathbf{g}\cdot\mathbf{r}$ will lead to constructive interference as a result of the spatial positions of the scatterers, and that non integer values will exhibit some degree of destructive interference. Therefore one can to begin to conceive in the abstract of the notion of an intensity function $I(\mathbf{g};\mathbf{r})$ which will have a structure induced by the spatial structure of the scatterers. Certain scattering directions will have constructive interference, so that the value of $I(\mathbf{g};\mathbf{r})$ will be high, and other directions will have destructive interference, so that $I(\mathbf{g};\mathbf{r}) = 0$. The space parametrized by $\mathbf{g} \in \mathbb{R}^3$ is called reciprocal space, G^3, and will be a useful construction throughout the all sections in this chapter.

In fact it may be stated that the intensity of radiation scattered at each $\mathbf{g}$, that is, the function $I(\mathbf{g})$ over reciprocal space, is the principle result diffraction measurements seek to obtain. Later on, we will relate this function to the distribution of scatterers in the sample (e.g. the material structure). In §3.2.2 we will also see that a crystal lattice in real space has a corresponding reciprocal lattice in G^3. Denote the reciprocal lattice set by L. Therefore for crystals, the function $I(\mathbf{g})$ will be similar to an array of Dirac δ-functions, with high intensity at the nodes of L and low intensity elsewhere. The deviations in the crystal lattice structure due to elastic strains will be of interest for our mechanical analysis.

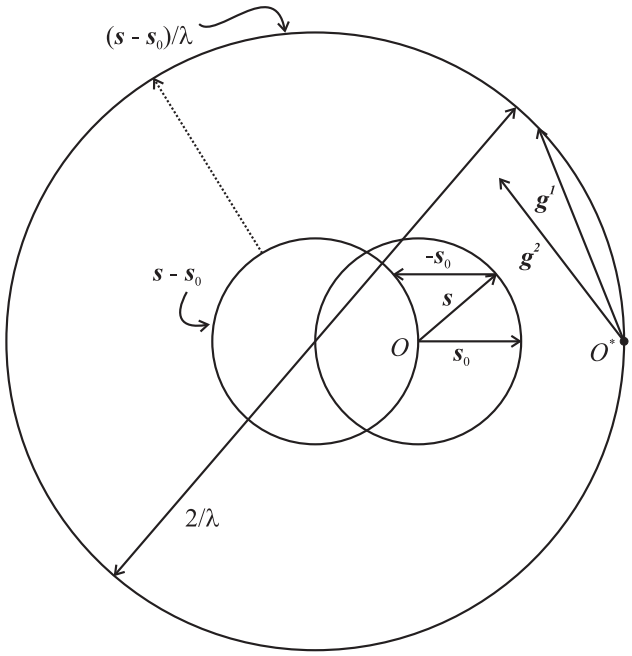

Figure 3.3: Ewald sphere depiction. The reciprocal space 'positions' $\mathbf{g}^1, \mathbf{g}^2$ are respectively on and slightly off the sphere for this combination of $\mathbf{s}_0, \lambda$.

In practical experiments, one typically deals with a fixed experimental setup, so that $\mathbf{s}_0$ and λ are fixed or otherwise known from independent control systems. Then, for a given input vector $\mathbf{s}_0$ and wavelength λ, we can trace the path of $\mathbf{g}(\mathbf{s}; \mathbf{s}_0, \lambda)$ for all test directions, $\mathbf{s}$. Considering all test directions $\mathbf{s}(\theta, \phi)$ traces out a unit sphere in physical space, centered at the position of the scattering material, where θ, ϕ are spherical polar coordinates. This unit sphere, under the function $\mathbf{g}(\cdot; \mathbf{s}_0, \lambda) : \mathbb{R}^3 \to \mathrm{G}^3$, maps to a sphere in reciprocal space, $\mathbf{g}(\mathbf{s}(\theta, \phi); \mathbf{s}_0, \lambda)$, which is constructed in Figure 3.3. Denote this sphere in reciprocal space by S. This is called the Ewald or reflection sphere. From an experimental perspective, if all diffracted radiation was captured via some detector bounding the inside of a spherical cavity centered at the material sample, then $I(\mathbf{g})$ would be completely quantified in the two dimensional region in reciprocal space defined by the Ewald sphere.

To illustrate, in Figure 3.3 is shown the (two dimensional projection of) the Ewald sphere defined by a fixed wavelength λ and a fixed incident beam $\mathbf{s}_0$. $\mathbf{s}$ is defined to be a unit vector, so its limiting surface is depicted as originating from the origin O. The sphere defined by $\mathbf{s} - \mathbf{s}_0$ is also shown in Figure 3.3; it is simply constructed by adding $-\mathbf{s}_0$ to the sphere defining all possible $\mathbf{s}$. To generate the corresponding $\mathbf{g}$ sphere in reciprocal space (Ewald sphere), recalling (3.8), the sphere $\mathbf{s}-\mathbf{s}_0$ is amplified by the factor λ^{-1} as shown in Figure 3.3. Then this Ewald sphere, whose surface passes through the origin in reciprocal space, O^*, is the set of points where the diffraction condition is satisfied. For a fixed $\lambda, \mathbf{s}_0$, all $\mathbf{g} \in \mathrm{G}^3$

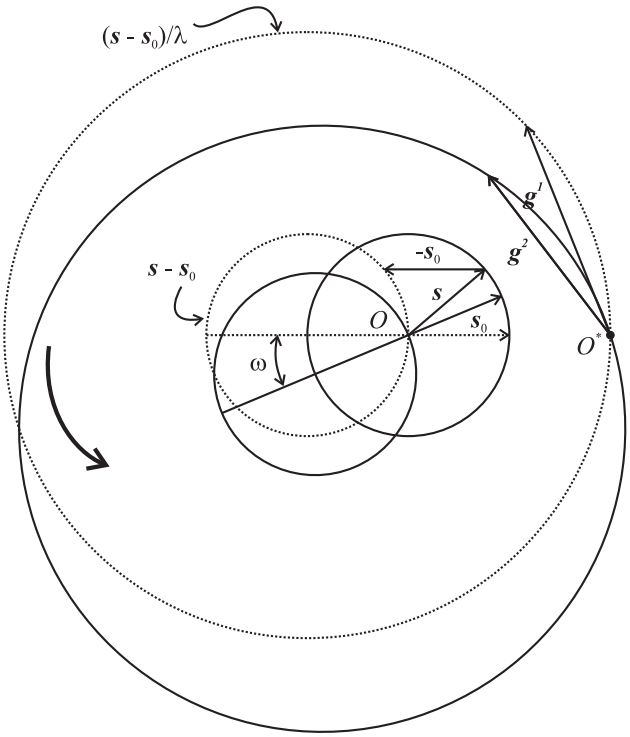

Figure 3.4: Ewald sphere depiction after a rotation of $\mathbf{s}_0$ through an angle ω, compared to Figure 3.3. The reciprocal space 'positions' $\mathbf{g}^1, \mathbf{g}^2$ are now respectively off and on the sphere for this combination of $\mathbf{s}_0, \lambda$. This rotation is necessary to probe the entire reciprocal space (bring all $\mathbf{g}^i$ onto reflection sphere).

which emanate from O^* and terminate on the sphere surface would produce constructive interference. Conversely, given $\mathbf{g}$ on the sphere, the direction of diffracted radiation $\mathbf{s}$ can be forward mapped by rearranging (3.8) as

$$\mathbf{s}(\mathbf{g}; \mathbf{s}_0, \lambda) = \lambda \mathbf{g} + \mathbf{s}_0. \tag{3.10}$$

For a fixed $\mathbf{s}_0, \lambda$, the intersection of the diffraction sphere and reciprocal lattice points may be empty, $S \cap L = \emptyset$. For example, the reciprocal space point $\mathbf{g}^2$ in Figure 3.3 is off the sphere, but after rotating the incident beam $\mathbf{s}_0$ through an angle ω, as depicted in Figure 3.4, we arrive at a condition where the diffraction sphere intersects $\mathbf{g}^2$. This is the reason that in monochromatic experiments we must rotate the crystal, c.f. the rotating crystal method (Cullity, 1978). Conversely, in polychromatic wavelength experiments, the reflection sphere becomes effectively a spherical annulus, e.g., a continuum of Ewald spheres for each wavelength. In these experiments more points in reciprocal space are accessible from a single $\mathbf{s}_0$, and no rotation of the material is required.

By going to lower and lower wavelengths, i.e., higher beam energies, the total volume in reciprocal space which is possible to probe by physically rotating the sample is given by

the spherical ball with radius $1/\lambda$. It is computed simply as $(4\pi/3)\lambda^{-3}$. As the wavelength decreases, the reciprocal space volume which may be probed increases. However, as a trade off, with the same detection capabilities, the precision with which the determination of $I(\mathbf{g})$ is made decreases along with the wavelength. In our experiments we use a relatively low wavelength (high energy) of about $\hat{\lambda}(50\text{keV}) \approx 0.0238$ nm, so the precision of our measurements is important to quantify. In particular, we need to determine how precision in the measurements of $I(\mathbf{g})$ corresponds to precision in the grain averaged deformation, $\mathbf{H}$. We will consider this issue in §3.4. It should be noted that an important benefit of using higher beam energies is that we have greater penetration depths into the sample, which is usually a primary factor to consider.

3.2.1.2.1 Multiple scatterers Returning to the consideration of interference computations, we now consider an arbitrary array of scatterers. Starting from the equation (3.5), for an array of scattering entities with different scattering factors f_i we can arrive at the amplitude function (Guiner, 1963)

$$A(\mathbf{g}) = A_0 \sum_{i=1}^{n} f_i \exp i\phi_i(\mathbf{g}), \tag{3.11}$$

where $\phi_i(\mathbf{g}) = \phi(\mathbf{g}; \mathbf{r}_i)$ is given from (3.9), with $\mathbf{r}_i$ the position of the scatterer with respect to an arbitrary common origin (fig).

Next we specialize to solid crystals, by computing the intensity $I(\mathbf{g})$ for a group of atoms organized in a regular lattice. Assign a distinguished atom by setting the origin at its location. Then assigning position vectors $\mathbf{x}_i$, and scattering factors f_i we have the amplitude function expressed as

$$F(\mathbf{g}) = \sum_{i=1}^{N} f_i \exp(-2\pi i \mathbf{g} \cdot \mathbf{x}_i), \tag{3.12}$$

where N is the number of atoms in the distribution, and where we have used (3.9) and (3.11) with $\mathbf{r} \equiv \mathbf{x}_i$. The function $F(\mathbf{g})$ is called the structure factor for this grouping of atoms; it is simply the amplitude function $A(\mathbf{g})$ for the array, (3.11). An example practical computation of the structure factor for a BCC material will be given in §3.2.2.3.

We have seen that the structure factor in equation (3.12) depends on the choice of origin for computing $\mathbf{x}_i$. However, the intensity, defined to be the square of the modulus of the amplitude function, $A(\mathbf{g})$, that is

$$I(\mathbf{g}) = |A(\mathbf{g})|^2 = A(\mathbf{g})A^*(\mathbf{g}), \tag{3.13}$$

where A^* is the complex conjugate of A, is independent of the choice of origin. To see this, we compute the intensity of the distribution using (3.12) in (3.13). The result is given as

(Guiner, 1963)

$$I(\mathbf{g}) = (F \cdot F^*)(\mathbf{g}) = \sum_i \sum_j f_i f_j \exp(-2\pi i \mathbf{g} \cdot (\mathbf{x}_i - \mathbf{x}_j)), \tag{3.14}$$

which depends only on relative positions between the atoms, $\mathbf{x}_i - \mathbf{x}_j$. In fact, the intensity is the only measurable quantity from a diffraction experiment - as phase information $\phi_i(\mathbf{g})$ is not available with conventional diffraction experiments. Were phase information detectable, as noted in Guiner (1963), X-ray diffraction experiments would perform as a microscope to directly visualize and probe the lattice structure.

We pause here to examine (3.14) for the case of a spatially homogeneous deformation of the scatterers $\mathbf{x}_i$. We adopt terminology typically used in mechanics, see Liu (2002). For a reference configuration position $\mathbf{X}$, the current position is simply $\mathbf{x} = \mathbf{F}\mathbf{X}$, modulo some translation. Here $\mathbf{F}$ is a spatially homogeneous deformation gradient. Any translational offset will not matter in the end since we need relative positions in the intensity expression, (3.14). Therefore we have the kinematic equivalence

$$\mathbf{x}_i - \mathbf{x}_j = \mathbf{F}(\mathbf{X}_i - \mathbf{X}_j),$$

which gives

$$I(\mathbf{g}) = (F \cdot F^*)(\mathbf{g}) = \sum_i \sum_j f_i f_j \exp(-2\pi i \mathbf{g} \cdot \mathbf{F}(\mathbf{X}_i - \mathbf{X}_j)). \tag{3.15}$$

For an infinite summation in (3.15) , $I(\mathbf{g})$ will be zero unless $\mathbf{g} = \mathbf{F}^{-\mathrm{T}}\mathbf{G}$, for some $\mathbf{G} \in \mathbb{G}^3$, the reciprocal space of the reference configuration. To see this, consider the sequence

$$\begin{aligned} \mathbf{g} \cdot \mathbf{F}(\mathbf{X}_i - \mathbf{X}_j) &= \mathbf{F}^{-\mathrm{T}}\mathbf{G} \cdot \mathbf{F}\Delta\mathbf{X} \\ &= \mathbf{G} \cdot \mathbf{F}^{-1}\mathbf{F}\Delta\mathbf{X} \\ &= \mathbf{G} \cdot \Delta\mathbf{X} \\ &= HA + KB + LC \in \mathbb{Z}, \end{aligned} \tag{3.16}$$

where $\Delta\mathbf{X} = A\mathbf{G}_1 + B\mathbf{G}_2 + C\mathbf{G}_3$, and $\mathbf{G} = H\mathbf{G}^1 + K\mathbf{G}^2 + L\mathbf{G}^3$ are parametrizations of the direct and reciprocal reference lattices. The result (3.16) implies that $I(\mathbf{g})$ will differ from zero since $\exp(-2\pi i n) = 1$ for $n \in \mathbb{Z}$. Translating (3.15) into the reference configuration, the intensity distribution over reference reciprocal space is given by

$$I(\mathbf{G}) = (F \cdot F^*)(\mathbf{G}) = \sum_i \sum_j f_i f_j \exp(-2\pi i \mathbf{G} \cdot (\mathbf{X}_i - \mathbf{X}_j)). \tag{3.17}$$

The computations in (3.16) will be more evident after the discussion in §3.2.3.

3.2.1.3 Continuous distribution of scatterers, Fourier transforms

The diffracted intensity from a discrete distribution of scatterers (3.11) can be generalized by passing to a continuous distribution with spatial density $\rho(\mathbf{x})$. In this case we have, using (3.9) in (3.11) and passing to the continuous limit,

$$A(\mathbf{g}) = \int \rho(\mathbf{x}) \exp(-2\pi i \mathbf{g} \cdot \mathbf{x}) \mathrm{d}\mathbf{x}. \tag{3.18}$$

In usual usage $\rho(\mathbf{x})$ is the electron density function (per unit spatial volume), and the integral extends to all physical space, $\mathbf{x} \in \mathbb{R}^3$. The practically important case of a finite body is interesting to consider; we will look at this problem in the next section.

Upon passing to the continuous limit, (3.18) indicates that the amplitude function $A(\mathbf{g})$ is the Fourier transform of the spatial distribution of scattering particles $\rho(\mathbf{x})$. The notion of taking the Fourier transform of a crystal is useful from a conceptual and computational perspective. It will also enable us to eventually derive the reciprocal lattice, which will be a fundamental construct in passing to a geometric/mechanics-centric analysis of X-ray diffraction.

We pause here to note another significant aspect of (3.18), at least in terms of providing motivation for the general crystal structure determination problem. Hypothetically speaking, the critical step in the task of determining structure from X-ray analysis is stated as taking the inverse Fourier transformation of the amplitude $A(\mathbf{g})$ in order to determine the spatial distribution $\rho(\mathbf{x})$,

$$\rho(\mathbf{x}) = \int A(\mathbf{g}) \exp(2\pi i \mathbf{g} \cdot \mathbf{x}) \mathrm{d}\mathbf{g}. \tag{3.19}$$

The determination of $\rho(\mathbf{x})$ is then equivalent to determining the atomic structure of the material being studied. It bears restating - were phase information available, (3.19) could be used to turn X-ray diffraction data into a microscope where the distribution of scatterers is known precisely. Ultimately however, this procedure cannot work since the function $A(\mathbf{g})$ cannot be observed. X-ray diffraction does not measure the relative phases of the diffracted waves, so that the amplitude function cannot be measured directly, and $\rho(\mathbf{x})$ is therefore inaccessible by using (3.19). Only total intensity, e.g. $I(\mathbf{g}) = AA^*$ is measured. See (Guiner, 1963) for an informative treatment for this general case. Fortunately, in this study, the structure of the material may be assumed to be known from prior experimental studies, so a full structure determination framework is overly general for our purposes here. Our interests are in the evolution of the lattice structure due to deformation (strain) and not in the determination of the structure without prior knowledge.

Before considering computational details of the Fourier transform of a crystal lattice in §3.2.2, we first consider the practically important effect of a finite object on the theory developed thus far. This will be useful in the section on forward modeling, §3.4.2.2.

3.2.1.4 Finite size effect.

As a final background point before applying the Fourier transform framework to crystal lattices, it is interesting to consider the effect of a finite object on the diffraction pattern.

Consider an object, denoted as V, where $\rho(\mathbf{x}) \neq 0$, $\mathbf{x} \in V$, and $\rho(\mathbf{x}) = 0, \mathbf{x} \notin V$. The spatial density of scatterers $\rho(\mathbf{x})$ may then written as the product

$$\rho(\mathbf{x}) = (\rho_\infty \sigma)(\mathbf{x}), \tag{3.20}$$

where

$$\sigma(\mathbf{x}) = \begin{cases} 1 & \text{if } \mathbf{x} \in V \\ 0 & \text{if } \mathbf{x} \notin V \end{cases} \tag{3.21}$$

is called the indicator function, and ρ_∞ is the scatterer density, extended to infinite spatial domain. Next, denote $A(\mathbf{g}) = \text{trans}[\rho(\mathbf{x})]$, where trans : $f(\mathbf{x}) \rightarrow F(\mathbf{g})$, is the Fourier transform defined by (3.18). Then we have, taking the transform of (3.20)

$$A(\mathbf{g}) = \int \rho_\infty(\mathbf{x})\sigma(\mathbf{x}) \exp(-2\pi i \mathbf{g} \cdot \mathbf{x}) \mathrm{d}\mathbf{x}. \tag{3.22}$$

Using the Faltung product, (3.22) becomes

$$A(\mathbf{g}) = \Sigma(\mathbf{g}) * A_\infty(\mathbf{g}), \tag{3.23}$$

where $\Sigma(\mathbf{g}) = \text{trans}[\sigma(\mathbf{x})]$ and $A_\infty(\mathbf{g}) = \text{trans}[\rho_\infty(\mathbf{x})]$. The Faltung product or convolution in (3.23) has the interpretation that the amplitude $A(\mathbf{g})$ is essentially superposition of the transform $\Sigma(\mathbf{g})$ placed at each point of the amplitude function which would be nonzero if the material were infinite.

As a simple intuitive example of the Faltung/convolution integral for a different case, consider a problem of a light beam, shining on a planar surface. Given an appropriate sensor, one could measure the intensity of light falling on the surface as a function of position on the surface. Denote this intensity function as $F = F(x)$, where x is a position coordinate, and F is the intensity. Next consider a spatial array of lights. Let the spatial density of these lights be $\rho(x)$. The resultant intensity on the wall is given by the convolution of the two functions, $F_{\text{tot}} = F * \rho$. Equation (3.23) suggests a similar behavior to this example. Practically speaking, once the transform $A_\infty(\mathbf{g})$ is characterized for idealized, infinite solid crystals, for finite bodies (e.g. the practical case), diffraction peaks are not mathematically sharp points but have some width corresponding to the finite size effect, $\Sigma(\mathbf{g})$. It should be noted that this size effect is in addition to other sources which create finite peak widths, such as spatial gradients in the lattice deformation.

In an ideal situation (3.23) would be enough to quantify the size effect of the crystallites[2]. However since the amplitude $A(\mathbf{g})$ is not experimentally accessible, we must consider the effect of the finite size on the integrated intensity $I(\mathbf{g})$, which is a more complicated problem.

[2]In the following we will use the terms crystallite in several situations. We basically use crystallite to imply a small coherently diffracting crystalline domain. The length scale of the material at which the term applies in this context may vary from that microns to the dimension for a grain of a polycrystal.

We now compute the finite size effect on the intensity, $I(\mathbf{g})$. The following comes from the description in Guiner (1963), where the derivations are carried out with greater detail. First we require the expression for the diffracted intensity. We have

$$\begin{aligned} I_N(\mathbf{g}) &= A^* A \\ &= \int \rho(\mathbf{u}) \exp(2\pi i \mathbf{g}\cdot\mathbf{u}) \mathrm{d}\mathbf{u} \int \rho(\mathbf{v}) \exp(-2\pi i \mathbf{g}\cdot\mathbf{v}) \mathrm{d}\mathbf{v} \\ &= \int\int \rho(\mathbf{u})\rho(\mathbf{v}) \exp(-2\pi i \mathbf{g}\cdot(\mathbf{v}-\mathbf{u})) \mathrm{d}\mathbf{u}\mathrm{d}\mathbf{v}, \end{aligned} \tag{3.24}$$

where we have used (3.18), and where I_N is the total diffraction intensity. Defining $\mathbf{x} \equiv \mathbf{v}-\mathbf{u}$ we have from (3.24)

$$\begin{aligned} I_N(\mathbf{g}) &= \int\int \rho(\mathbf{u})\rho(\mathbf{x}+\mathbf{u}) \exp(-2\pi i \mathbf{g}\cdot\mathbf{x}) \mathrm{d}\mathbf{x}\mathrm{d}\mathbf{u} \\ &= \int \mathcal{P}(\mathbf{x}) \exp(-2\pi i \mathbf{g}\cdot\mathbf{x}) \mathrm{d}\mathbf{x}, \end{aligned} \tag{3.25}$$

where

$$\mathcal{P}(\mathbf{x}) \equiv \int \rho(\mathbf{u})\rho(\mathbf{x}+\mathbf{u}) \mathrm{d}\mathbf{u} \tag{3.26}$$

is called a Patterson function. Inverting (3.25) via Fourier transform we obtain

$$\mathcal{P}(\mathbf{x}) = \int I(\mathbf{g}) \exp(2\pi i \mathbf{g}\cdot\mathbf{x}) \mathrm{d}\mathbf{g}. \tag{3.27}$$

As stated before, X-ray diffraction experiments measure $I(\mathbf{g})$. Therefore the function $\mathcal{P}(\mathbf{x})$ is obtained experimentally.

With a finite object, (3.26) becomes

$$\mathcal{P}(\mathbf{x}) = \int \sigma(\mathbf{u})\sigma(\mathbf{u}+\mathbf{x})\rho_\infty(\mathbf{u})\rho_\infty(\mathbf{x}+\mathbf{u}) \mathrm{d}\mathbf{u}. \tag{3.28}$$

Due to the nature of the indicator function σ, we have that we can write (3.28) as

$$\mathcal{P}(\mathbf{x}) = \int_{\mathcal{V}(\mathbf{x})} \rho_\infty(\mathbf{u})\rho_\infty(\mathbf{u}+\mathbf{x}), \tag{3.29}$$

where the volume $\mathcal{V}(\mathbf{x})$ is the region in $\mathbb{R}^3$ where $\sigma(\mathbf{u})\sigma(\mathbf{u}+\mathbf{x}) = 1$. Therefore we define

$$\mathcal{V}(\mathbf{x}) = \int \sigma(\mathbf{u})\sigma(\mathbf{u}+\mathbf{x}) \mathrm{d}\mathbf{u} \equiv V \cdot V(\mathbf{x}). \tag{3.30}$$

We give the following additional interpretation to $V \cdot V(\mathbf{x})$ in(3.30) from Guiner (1963). $V \cdot V(\mathbf{x})$ is the volume common to the physical diffraction object and to its 'ghost' obtained by displacing the object a distance $\mathbf{x}$. With this intuitive picture in mind we state the following properties which will be used later

1. $V(0) = 1$, since at $\mathbf{x} = 0$, $V \cdot V(\mathbf{x}) = V$
2. $V(\mathbf{x}) = V(-\mathbf{x})$
3. $V(\mathbf{x})$ is decreasing, becoming zero when $\mathbf{x}$ is greater than the diameter of the object in the direction $\mathbf{x}$

From (3.30) we have

$$V \cdot V(\mathbf{x}) = \int \sigma(\mathbf{w})\sigma(-(\mathbf{x}-\mathbf{w}))\mathrm{d}\mathbf{w}. \tag{3.31}$$

Recalling that from the properties of a Faltung, (A.11), we have

$$\begin{aligned}\int \sigma(\mathbf{w})\sigma(-(\mathbf{x}-\mathbf{w}))\mathrm{d}\mathbf{w} &= \int \sigma(\mathbf{w})(\sigma \circ 1^{-1})(\mathbf{x}-\mathbf{w})\mathrm{d}\mathbf{w} \\ &= \sigma(\mathbf{x}) * (\sigma \circ 1^{-1})(\mathbf{x}) \\ &= \sigma(\mathbf{x}) * \sigma(-\mathbf{x}),\end{aligned} \tag{3.32}$$

where the inversion function $1^{-1} : A \to A, 1^{-1}(x) = -x$, for a group A (here $A = (\mathbb{R}^3, +)$). The transform of $V(\mathbf{x})$ is then given by, with (3.31) and (3.32),

$$V(\mathbf{x}) = \frac{1}{V}\sigma(\mathbf{x}) * \sigma(-\mathbf{x}). \tag{3.33}$$

Now $\mathrm{trans}[\sigma(\mathbf{x})] = \Sigma(\mathbf{g})$, $\mathrm{trans}[\sigma(-\mathbf{x})] = \Sigma^*(\mathbf{g})$ and using the Faltung theorem, (A.12), Equation (3.33) gives

$$\begin{aligned}\mathrm{trans}[V(\mathbf{x})] &= \frac{1}{V}\Sigma(\mathbf{g})\Sigma^*(\mathbf{g}) \\ &= \frac{1}{V}|\Sigma(\mathbf{g})|^2.\end{aligned} \tag{3.34}$$

Writing out the left hand side of Equation (3.34) and rearranging gives

$$|\Sigma(\mathbf{g})|^2 = V \int V(\mathbf{x}) \exp(-2\pi i \mathbf{g} \cdot \mathbf{x})\mathrm{d}\mathbf{x}. \tag{3.35}$$

Recall also the expression for the Fourier transform of $\sigma(\mathbf{x})$:

$$\Sigma(\mathbf{g}) = \int \sigma(\mathbf{x}) \exp(-2\pi i \mathbf{g} \cdot \mathbf{x})\mathrm{d}\mathbf{x}, \tag{3.36}$$

so that

$$\Sigma(0) = \int \sigma(\mathbf{x})\mathrm{d}\mathbf{x} = V, \tag{3.37}$$

which implies

$$|\Sigma(0)|^2 = V^2. \tag{3.38}$$

Next, we can show that $|\Sigma(\mathbf{g})|^2$ is centrosymmetric. Since $\sigma(\mathbf{x}) \in \mathbb{R} \implies \Sigma(\mathbf{g}) = \Sigma^*(-\mathbf{g})$, we have

$$|\Sigma(-\mathbf{g})|^2 = \Sigma(-\mathbf{g})\Sigma^*(-\mathbf{g}) = \Sigma^*(\mathbf{g})\Sigma(\mathbf{g}) = |\Sigma(\mathbf{g})|^2, \tag{3.39}$$

symmetry being shown.

Now, if the physical object were large, say $V(\mathbf{x}) = 1, \text{with} \|\mathbf{x}\| \to \infty$, then from (3.35) $|\Sigma(\mathbf{g})|^2$ would essentially be a Dirac-delta function in $\mathbf{g}$-space, see (A.10). From this viewpoint we conclude that $|\Sigma(\mathbf{g})|^2$ is a rapidly decreasing function from its maximum at $\mathbf{g} = 0$. Therefore the maximum is given by (3.38), V^2. Transforming $|\Sigma(\mathbf{g})|^2$ gives

$$V(\mathbf{x}) = \frac{1}{V} \int |\Sigma(\mathbf{g})|^2 \exp 2\pi i \mathbf{g} \cdot \mathbf{x} \mathrm{d}\mathbf{x}, \tag{3.40}$$

and $V(0) = 1$ from the previously stated properties of $V(\mathbf{x})$ so that we have the result

$$\int |\Sigma(\mathbf{g})|^2 \mathrm{d}\mathbf{g} = V, \tag{3.41}$$

where V is the spatial volume of the diffracting material, which will be used later, and the integral is over all reciprocal space. From the established properties of $|\Sigma(\mathbf{g})|^2$, approximating $|\Sigma(\mathbf{g})|^2$ by its maximum, V^2, in a small nonzero (reciprocal space) volume, w centered at $\mathbf{g} = 0$, is a useful exercise and gives

$$\int |\Sigma(\mathbf{g})|^2 \mathrm{d}\mathbf{g} = V^2 \int \mathrm{d}\mathbf{g} = wV^2, \tag{3.42}$$

where w is the volume of the region in reciprocal space where the approximation for $|\Sigma(\mathbf{g})|^2 = V^2$ holds. Then equating (3.42) and (3.41) gives

$$w = \frac{1}{V}. \tag{3.43}$$

The actual width of the function $\Sigma(\mathbf{g})$ in reciprocal space is then estimated by taking w to be a three dimensional cube with side length $2s_0$, which with (3.43) gives

$$(2s_0)^3 = \frac{1}{V} = \frac{1}{r^3}, \tag{3.44}$$

where we have used $V = r^3$, with r the size of the material in physical space, e.g. the cube edge length, and s_0 is the size of the region of volume w. Rearranging (3.44) gives

$$s_0 = \frac{1}{2r}. \tag{3.45}$$

For a given wavelength, λ, the angular spread in the diffraction peak coordinate θ due to the finite size of the object can be computed from Bragg's law, with $d = s_0^{-1}$ through the relation

$$s_0 = \frac{2\sin\theta}{\lambda}. \tag{3.46}$$

Solving (3.46) for $\theta(s_0(r))$, with (3.45) then gives the angular spread in the diffraction peak due to the particle size effect. This data is plotted on log scale in Figure 3.5, for $\lambda = \lambda(50\text{keV}) = 0.0238\text{nm}$. Figure 3.5 indicates that finite size effects become most important

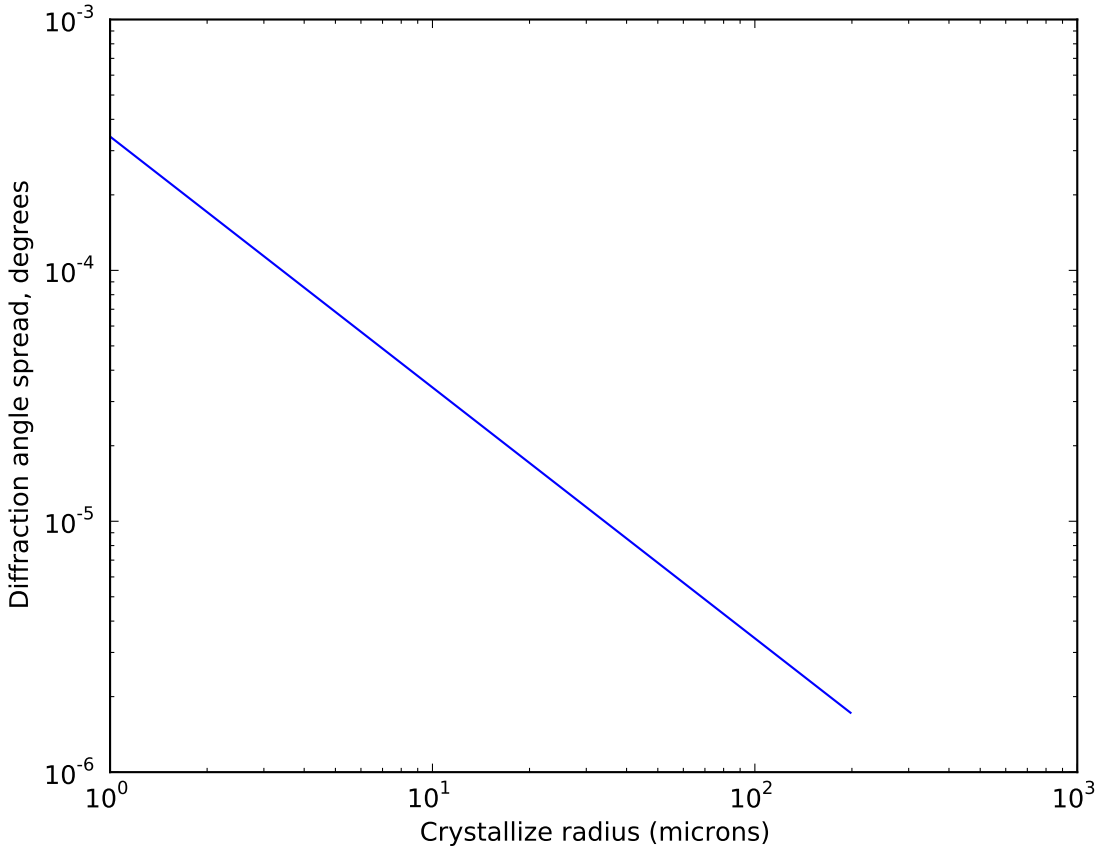

Figure 3.5: Trend of crystallite size effect on the spread in the Bragg angle, θ, from (3.46).

for submicron (nano) grain sizes. Our grains are on the order of a hundred microns, so size effects due to sub-grain or crystallite breakdown will not be a critical ingredient in the modeling required for this work. We will however use the formal consideration of size effects in the development of a forward model, see §3.4.2.2.

To further justify neglecting size effects, we have to introduce some details of the experimental configuration. The geometry of the setup is described in Figure 3.13, §3.3. Consider the resolution determined by the pixel size, p/L, where p is the pixel size and L is the sample to detector distance. From the far field geometry, the resolution in the Bragg angle θ is approximately p/L. Bragg's law gives that the corresponding reciprocal space resolution is $2\theta = \lambda s_0 \implies s_0 \approx 2p/(\lambda L)$. And (3.46) gives that size effects become detectable for $\lambda/(2r) \approx 2p/L$. With typical pixel size and detector distances, $p/L \approx 0.2 \cdot 10^{-3}$, and $\lambda = 0.0238$nm, this occurs for $r \approx 0.03$ μm. For an alternate treatment see Warren (1969), where they report

$$\theta_{\text{FWHM}} = \frac{0.94\lambda}{r \cos\theta},$$

where FWHM denotes full width at half max of the Bragg angle spread. FWHM can be related to the standard deviation parameter of a Gaussian distribution. With this, $\theta_{\text{FWHM}} \approx p/L \approx 0.2 \cdot 10^{-3}$, and $\theta_{\max} \approx 0.1$ gives a detectable particle dimension of detection of 0.1 μm, which is in the same order of magnitude as the previous estimate. From these estimates, broadening due to particle size effects will not be significantly detectable in our experiments. Observable broadening will instead come from a variety of factors, collectively grouped under the category 'instrumental broadening', (Warren, 1969). For example the deviation in wavelength λ from monochromatic experiments will cause some broadening effect. See §3.4.2.2 for more information.

In the next section, we apply the general framework developed thus far to the regular array of atoms found in a solid crystal. We will use the Fourier transform concept from Equation (3.18) in order to derive the reciprocal lattice associated with the physical crystal lattice. Once we obtain the reciprocal lattice description we can apply analytical techniques following from considerations of diffeomorphisms of differentiable manifolds representing the lattice structure to deduce the effect of lattice deformations on the diffraction pattern. This geometric framework will be more convenient for computations of lattice strain, for example, than using the more cumbersome Fourier transforms.

3.2.2 Application to crystalline lattices.

In this section we consider the theory of diffraction resulting from crystal lattices. Crystalline materials are of primary interest to solid mechanics studies. For example, important structural metals such as iron, titanium, and aluminum are naturally crystalline. Although normal processing procedures induce a polycrystalline structure, the single crystal domains, called grains, can be analyzed with the framework we develop in this section.

A primary outcome of this section is the derived importance of the reciprocal lattice description of the crystal. We first begin with the general notion of a crystal lattice in the spatial configuration. The following formulation and description works without caveat for simple lattices such as simple cubic, but the results can be applied to more complicated

structures easily[3]. Simple lattices are considered to make the notation and discussion less cumbersome.

3.2.2.1 Spatial crystalline lattice

In this section we derive the Fourier transform of the crystal lattice. First we must characterize the spatial distribution of atoms in a crystal, in order to obtain an expression for the scattering density $\rho(\mathbf{x})$. This quantity was introduced in (3.18).

Figure 3.6 depicts a simple lattice. The origin of the spatial coordinate system is set

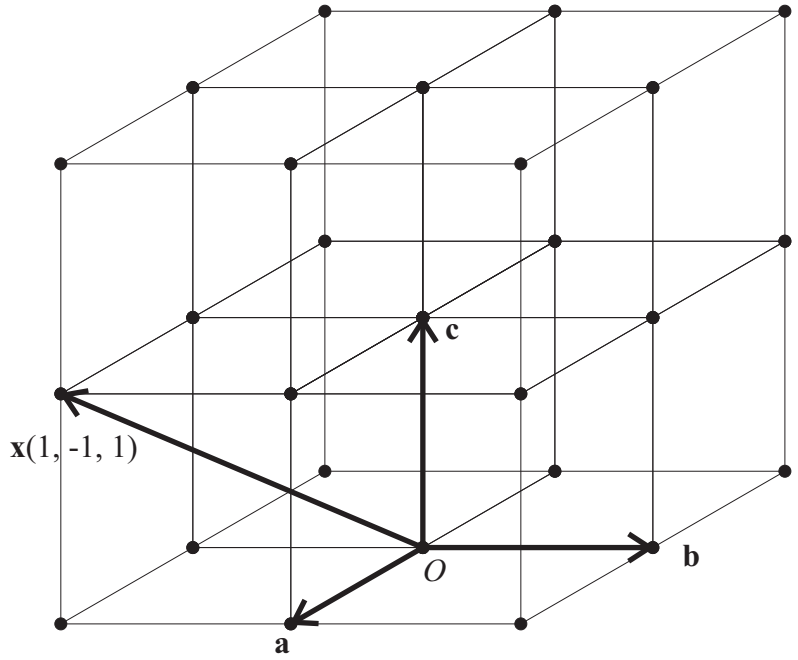

Figure 3.6: The lattice of a simple cubic crystal. The lattice vectors $\mathbf{a}, \mathbf{b}, \mathbf{c}$ for a basis. Positions $\mathbf{x}$ can be described relative to the basis, as shown for the vector $\mathbf{x}(1, -1, 1) = \mathbf{a} - \mathbf{b} + \mathbf{c}$. In this basis integral coefficients of the basis vectors correspond to lattice points.

on a node of the lattice, as shown in the figure. The linearly independent vectors $\mathbf{a}, \mathbf{b}, \mathbf{c}$ generate the lattice by translations; they are called the lattice vectors. The position field in the crystal lattice, $\mathbf{x}$, may be described by the function

$$\mathbf{x}(\boldsymbol{\theta}) = \theta_1 \mathbf{a} + \theta_2 \mathbf{b} + \theta_3 \mathbf{c}, \tag{3.47}$$

where $\mathbf{x}$ is the spatial position and $\boldsymbol{\theta} = (\theta_1, \theta_2, \theta_3) \in \mathbb{R}^3$. Generally $\boldsymbol{\theta}$ range freely, but $\boldsymbol{\theta} \in \mathbb{Z}^3$ on lattice sites. To apply the Fourier transform to such arrays of atoms, we divide

[3]Non simple lattices have non trivial extinction reflections which must be considered. The set of active reflections comes from the structure factor calculation. An example is given later in this section.

the description of the crystal into the (Faltung) product of unit cells at each lattice site, so that the scattering density $\rho(\mathbf{x})$ may be expressed as the convolution of two terms,

$$\rho(\mathbf{x}) = \rho_c(\mathbf{x}) * [z(\mathbf{x})\sigma(\mathbf{x})], \tag{3.48}$$

where $\rho_c(\mathbf{x})$ is the local electron density defined over the unit cell, the lattice function $z(\mathbf{x})$ is nonzero only on lattice sites, and $\sigma(\mathbf{x})$ is the indicator function introduced in (3.21) which accounts for the macroscopically finite size of the crystal. The lattice function $z(\mathbf{x})$ can be described by a combination of Dirac-delta functions, written as

$$z(\mathbf{x}) = \sum_{\boldsymbol{\theta}^*} \delta(\mathbf{x} - \mathbf{x}(\boldsymbol{\theta}^*)), \tag{3.49}$$

where $\boldsymbol{\theta}^* \in \mathbb{Z}^3$. Should there be confusion with what is meant by (3.49), we are using the shorthand

$$\sum_{\boldsymbol{\theta}^*} \delta(\mathbf{x} - \mathbf{x}(\boldsymbol{\theta}^*)) \equiv \sum_m \sum_n \sum_p \delta(\mathbf{x} - \mathbf{x}_{mnp}), \tag{3.50}$$

where

$$\mathbf{x}_{mnp} \equiv m\mathbf{a} + n\mathbf{b} + p\mathbf{c} \tag{3.51}$$

for $m, n, p \in \mathbb{Z}$. Recalling the intuitive example of convolutions given in §3.2.1.4, we can see that the operation given in Equation (3.48) has the mathematical features we are looking for in describing a lattice (population of a locally nonzero function at discrete lattice points)

Next, recall the general expression for the amplitude function regarded as a Fourier transform of the scatterer density. That is, $A(\mathbf{g}) = \text{trans}[\rho(\mathbf{x})]$, see Equation (3.18). Further recall that the magnitude of the amplitude gives the diffraction intensity, $I(\mathbf{g}) = |A(\mathbf{g})|^2$, which is the observable in a diffraction experiment. Therefore to compute the intensity we must first compute the Fourier transform of $\rho(\mathbf{x})$ of the combination in Equation (3.48), and then take the modulus. Using the property of Fourier transforms in (A.12), (A.13), $A(\mathbf{g})$ is given by the product,

$$A(\mathbf{g}) = F(\mathbf{g})[Z(\mathbf{g}) * \Sigma(\mathbf{g})], \tag{3.52}$$

where $F(\mathbf{g}) \equiv \text{trans}[\rho_c(\mathbf{x})]$ is the transform of $\rho_c(\mathbf{x})$ over the unit cell and is called the structure factor, and $\Sigma(\mathbf{g})$ is the transform of the indicator function over the crystal, described in §3.2.1.4. We previously introduced the structure factor for the unit cell in Equation (3.12) in the previous section. We will return to the structure factor calculation shortly and give an example computation; first let us examine $Z(\mathbf{g}) \equiv \text{trans}[z(\mathbf{x})]$, as this will lead to the reciprocal lattice construction which is more crucial to the rest of the framework.

3.2.2.2 Reciprocal lattice

From Equation (3.49) and Equation (3.52) we need to compute the transform of $z(\mathbf{x})$ in order to compute the amplitude, $A(\mathbf{g})$. Using the definition of the transform and (3.49), we

have

$$\begin{aligned} Z(\mathbf{g}) &= \int z(\mathbf{x}) \exp(-2\pi i \mathbf{g}\cdot\mathbf{x}) \mathrm{d}\mathbf{x} \\ &= \int \sum_{\boldsymbol{\theta}^*} \delta(\mathbf{x} - \mathbf{x}(\boldsymbol{\theta}^*)) \exp(-2\pi i \mathbf{g}\cdot\mathbf{x}) \mathrm{d}\mathbf{x} \\ &= \sum_{\boldsymbol{\theta}^*} \exp[-2\pi i \mathbf{g}\cdot\mathbf{x}(\boldsymbol{\theta}^*)], \end{aligned} \tag{3.53}$$

where we have used the properties of the Dirac delta function, given by

$$\int \delta(\mathbf{x} - \mathbf{x}^*) f(\mathbf{x}) \mathrm{d}\mathbf{x} = f(\mathbf{x}^*). \tag{3.54}$$

Then, using (3.47) in (3.53), and with evaluations of $\mathbf{x}$ on lattice sites, $\mathbf{x}(\boldsymbol{\theta}^*)$ given by (3.51), Equation (3.53) becomes

$$Z(\mathbf{g}) = \left(\sum_m \exp[-2\pi i m \mathbf{g}\cdot\mathbf{a}]\right)\left(\sum_n \exp[-2\pi i n \mathbf{g}\cdot\mathbf{b}]\right)\left(\sum_p \exp[-2\pi i p \mathbf{g}\cdot\mathbf{c}]\right). \tag{3.55}$$

It can be shown (see Guiner (1963)) that by taking the summation limits in (3.55) from $-N/2$ to $N/2$, $N \in \mathbb{N}$, the result of a single summation factor from (3.55) can be simplified to

$$\sum_{m=-N/2}^{N/2} \exp[-2\pi i m \mathbf{g}\cdot\mathbf{a}] = 1 + 2\sum_{m=1}^{N/2} \cos\left[2\pi m(\mathbf{g}\cdot\mathbf{a})\right] \tag{3.56}$$

$$= \frac{\sin\left[(N+1)\pi \mathbf{g}\cdot\mathbf{a}\right]}{\sin\left[\pi(\mathbf{g}\cdot\mathbf{a})\right]}. \tag{3.57}$$

The terms $\sin[2\pi m \mathbf{g}\cdot\mathbf{a}]$ drop out of (3.56) since sin is an odd function, e.g. $\sin(x) + \sin(-x) = 0$. The final expression Equation (3.57) is plotted vs $\mathbf{g}\cdot\mathbf{a}$ in Figure 3.7 for various values of N. Equation (3.57) has a discontinuity at integral values of $\mathbf{g}\cdot\mathbf{a}$, but the right and left hand limits at these points are the same at integral values of $\mathbf{g}\cdot\mathbf{a}$. Therefore by taking the limit as $\mathbf{g}\cdot\mathbf{a}$ approaches an arbitrary integer, we obtain the result

$$\lim_{\mathbf{g}\cdot\mathbf{a}\to\mathbb{Z}^+} \frac{\sin\left[(N+1)\pi \mathbf{g}\cdot\mathbf{a}\right]}{\sin\left[\pi(\mathbf{g}\cdot\mathbf{a})\right]} = \lim_{\mathbf{g}\cdot\mathbf{a}\to\mathbb{Z}^-} \frac{\sin\left[(N+1)\pi \mathbf{g}\cdot\mathbf{a}\right]}{\sin\left[\pi(\mathbf{g}\cdot\mathbf{a})\right]} = N + 1. \tag{3.58}$$

The width of the peaks at the integral values of $\mathbf{g}\cdot\mathbf{a}$ is obtained by considering the zeros of the numerator of (3.57). Rewriting the numerator gives

$$\sin(N+1)\pi \mathbf{g}\cdot\mathbf{a} = \sin 2\pi f \mathbf{g}\cdot\mathbf{a}, \tag{3.59}$$

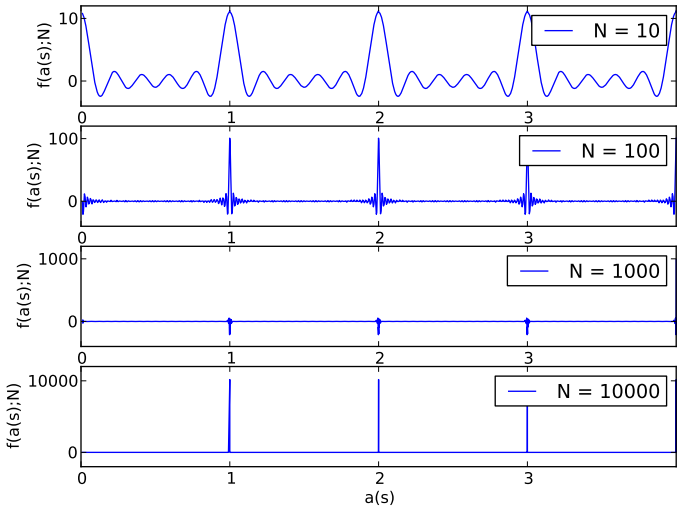

Figure 3.7: Plot of Equation (3.57) for various values of N. The limiting behavior is qualitatively similar to Dirac-delta functions at the integral values of $\mathbf{g} \cdot \mathbf{a}$

where $f = (N+1)/2$ is the frequency. Then (3.59) has a full period, T, of

$$T = \frac{1}{f} = \frac{2}{N+1}, \tag{3.60}$$

and a half period (i.e. peak width, w) of

$$w = \frac{T}{2} = \frac{1}{N+1}. \tag{3.61}$$

With the interpretations provided by (3.61) and (3.58), Equation (3.57) clearly represents something akin to a Dirac delta function, see Figure 3.7. In other words, as $N \to \infty$, then for $\mathbf{g} \cdot \mathbf{a} \in \mathbb{Z}$, (3.57) tends to a large number, and for $\mathbf{g} \cdot \mathbf{a} \notin \mathbb{Z}$, with fixed $\mathbf{g}$, the summation tends to zero (Guiner, 1963). Applying these observations to each of the summations in the product (3.55) gives the result that (3.55) becomes

$$Z(\mathbf{g}) = \begin{cases} K & \text{if } (\mathbf{g} \cdot \mathbf{a},\, \mathbf{g} \cdot \mathbf{b},\, \mathbf{g} \cdot \mathbf{c}) \in \mathbb{Z}^3 \\ 0 & \text{else,} \end{cases} \tag{3.62}$$

where K is a constant which will eventually be related to the physical size of the unit cell later in this section. In other words, $Z(\mathbf{g})$ is zero unless we have the simultaneous conditions

$$\mathbf{g} \cdot \mathbf{a} = h, \qquad \mathbf{g} \cdot \mathbf{b} = k, \qquad \mathbf{g} \cdot \mathbf{c} = l, \tag{3.63}$$

where $h, k, l \in \mathbb{Z}$. This is a restriction on the reciprocal vectors which give rise to non zero intensities, (see the discussion in §3.2.1.2.

At this point it is useful to introduce a formal parametrization for reciprocal space. We resolve $\mathbf{g}$ on the dual basis to the lattice vectors $\mathbf{a}, \mathbf{b}, \mathbf{c}$, giving the representation (see Equation (A.15))

$$\mathbf{g} = (\mathbf{g} \cdot \mathbf{a})\mathbf{a}^* + (\mathbf{g} \cdot \mathbf{b})\mathbf{b}^* + (\mathbf{g} \cdot \mathbf{c})\mathbf{c}^*, \tag{3.64}$$

where $\mathbf{a}^*, \mathbf{b}^*, \mathbf{c}^*$ are the reciprocal basis to $\mathbf{a}, \mathbf{b}, \mathbf{c}$. Then using the results of (3.63) in (3.64) we have the form

$$\mathbf{g} = h\mathbf{a}^* + k\mathbf{b}^* + l\mathbf{c}^*. \tag{3.65}$$

Ranging h, k, l over the integers and noting the values given by (3.65) represents a lattice in reciprocal space. More generally, we can parametrize reciprocal space by

$$\mathbf{g}(\boldsymbol{\beta}) = \beta_1\mathbf{a}^* + \beta_2\mathbf{b}^* + \beta_3\mathbf{c}^*, \tag{3.66}$$

where here $\boldsymbol{\beta} \in \mathbb{R}^3$, and $\boldsymbol{\beta}_i, i = 1, 2, 3$ are the components of $\boldsymbol{\beta}$. Equation (3.66) simply reflects the fact that $\mathbf{a}^*, \mathbf{b}^*, \mathbf{c}^*$ are a basis for reciprocal space. With (3.66) parametrizing reciprocal space, the results of (3.62) and (3.63) are rewritten as

$$Z(\mathbf{g}(\boldsymbol{\beta})) = 0 \qquad \boldsymbol{\beta} \notin \mathbb{Z}^3$$

and

$$Z(\mathbf{g}(\boldsymbol{\beta})) \neq 0, \qquad \boldsymbol{\beta} \in \mathbb{Z}^3.$$

The parametrization given by (3.66) thus forms a lattice in reciprocal space much as Equation (3.47) does in the physical space, with lattice points at $\boldsymbol{\beta} \in \mathbb{Z}^3$. This lattice will be referred to as the dual or reciprocal lattice, and vectors on reciprocal lattice sites will be referred to as reciprocal lattice vectors.

Denoting $\boldsymbol{\beta} \in \mathbb{Z}^3$ by $\boldsymbol{\beta} = \boldsymbol{\beta}^*$ we now rewrite (3.62) as

$$Z(\mathbf{g}) = K \sum_{\boldsymbol{\beta}^*} \delta(\mathbf{g} - \mathbf{g}(\boldsymbol{\beta}^*)). \tag{3.67}$$

In (3.67) we are using the shorthand similar to that used previously for the spatial lattice, Equation (3.50). That is,

$$\sum_{\boldsymbol{\beta}^*} \delta(\mathbf{g} - \mathbf{g}(\boldsymbol{\beta}^*)) \equiv \sum_h \sum_k \sum_l \delta(\mathbf{g} - \mathbf{g}_{hkl}), \tag{3.68}$$

where

$$\mathbf{g}_{hkl} \equiv h\mathbf{a}^* + k\mathbf{b}^* + l\mathbf{c}^* \tag{3.69}$$

denotes a reciprocal lattice node, $h, k, l \in \mathbb{Z}$. We now compute the scaling constant K required in Equations (3.62), (3.67).

Computation of scaling constant

To compute the value of K in (3.67) we integrate $Z(\mathbf{g})$ around an h, k, l node of the reciprocal lattice. By the properties of the Dirac delta function,

$$K = \int_{\text{node}} Z(\mathbf{g}) \mathrm{d}\mathbf{g}. \tag{3.70}$$

We now write out the integral on the right hand side. To simplify the notation we replace the parametrization of reciprocal space in (3.66) by

$$\mathbf{g}(g_1, g_2, g_3) = g_1\mathbf{g}^1 + g_2\mathbf{g}^2 + g_3\mathbf{g}^3 = g_i\mathbf{g}^i, \tag{3.71}$$

where $g_i \in \mathbb{R}, i = 1, 2, 3$, and $\mathbf{g}^1, \mathbf{g}^2, \mathbf{g}^3 \equiv \mathbf{a}^*, \mathbf{b}^*, \mathbf{c}^*$, respectively. Next we have, by (3.55) with (3.57) and (3.71), for some large natural number N,

$$Z(\mathbf{g}; N) = \left(\frac{\sin\left[(N+1)\pi g_1\right]}{\sin\left[\pi(g_1)\right]}\right)\left(\frac{\sin\left[(N+1)\pi g_2\right]}{\sin\left[\pi(g_2)\right]}\right)\left(\frac{\sin\left[(N+1)\pi g_3\right]}{\sin\left[\pi(g_3)\right]}\right). \tag{3.72}$$

Around a particular $\mathbf{g}_{hkl}$ node of the reciprocal lattice, we take an integration box with dimension $\pm\epsilon$. Using the expressions for peak height and width from (3.58) and (3.61), considering a single factor in (3.72) gives

$$\int_{g_1(hkl)-\epsilon}^{g_1(hkl)+\epsilon} \frac{\sin\left[(N+1)\pi g_1\right]}{\sin\left[\pi(g_1)\right]} \mathrm{d}g_1 \approx (N+1)\frac{1}{N+1} = 1. \tag{3.73}$$

Next, we have

$$\begin{aligned}
\int_{\text{node}} Z(\mathbf{g}) \mathrm{d}\mathbf{g} &= \int_{\text{node}} Z(\mathbf{g})[\mathbf{g}^1 \cdot \mathbf{g}^2 \times \mathbf{g}^3] && (3.74)\\
&= \int_{\text{node}} Z(\mathbf{g}) \det \mathbf{F}_c^* \mathrm{d}g_1 \wedge \mathrm{d}g_2 \wedge \mathrm{d}g_3 \\
&= \int_{\text{node}} Z(\mathbf{g}) V_c^* \mathrm{d}g_1 \wedge \mathrm{d}g_2 \wedge \mathrm{d}g_3 \\
&= V_c^* \int_{\text{node}} Z(\mathbf{g}) \mathrm{d}g_1 \wedge \mathrm{d}g_2 \wedge \mathrm{d}g_3 && (3.75)\\
&= V_c^* \cdot 1 \\
&= V_c^*, && (3.76)
\end{aligned}$$

where we have used (3.73) in arriving at (3.76). Here

$$\mathbf{F}_c^* \equiv \frac{\partial \mathbf{g}}{\partial g_j} \otimes \mathbf{e}_j,$$

and where $V_c^* = \det \mathbf{F}_c^*$ is the volume form of the reciprocal unit cell. Should further explanation of the above operations be helpful, the volume element d$\mathbf{g}$ in (3.74) is represented by the parallelepiped with edges given by $\mathbf{g}^i, i = 1, 2, 3$. The integral in (3.75) is over the natural coordinates $g_i, i = 1, 2, 3$, hence the Jacobian $\mathbf{F}_c^*$ is introduced. With this, Equation (3.76) taken with (3.70) gives

$$K = V_c^*. \tag{3.77}$$

When we introduce the differential geometry for crystalline lattices, in §3.2.3, we will see that we have the relation

$$V_c^* = \frac{1}{V_c}, \tag{3.78}$$

where V_c is the unit cell volume in physical space. Taking Equation (3.78) in (3.77) gives

$$K = \frac{1}{V_c}, \tag{3.79}$$

so that (3.67) is written as

$$Z(\mathbf{g}) = \frac{1}{V_c} \sum_{\boldsymbol{\beta}^*} \delta(\mathbf{g} - \mathbf{g}(\boldsymbol{\beta}^*)). \tag{3.80}$$

We have therefore completed the determination of the transform $Z(\mathbf{g})$. We now return to considering the rest of the terms in Equation (3.52). First, the Faltung product in (3.52) is simplified by using a property of Faltung with Dirac-delta functions, see Guiner (1963, Appendix), yielding

$$Z(\mathbf{g}) * \Sigma(\mathbf{g}) = \frac{1}{V_c} \sum_{\boldsymbol{\beta}^*} \delta(\mathbf{g} - \mathbf{g}(\boldsymbol{\beta}^*)) * \Sigma(\mathbf{g}) \tag{3.81}$$

$$= \frac{1}{V_c} \sum_{\boldsymbol{\beta}^*} \Sigma(\mathbf{g} - \mathbf{g}(\boldsymbol{\beta}^*)). \tag{3.82}$$

Next, recall from §3.2.1.4 that $\Sigma(\mathbf{g})$ is a rapidly decreasing function with non zero value in a volume around the origin of reciprocal space. The volume of the region where $\Sigma(\mathbf{g})$ differs from zero was shown to be approximately $1/V$ where V is the physical volume of the entire crystal. Therefore, the Faltung of the lattice transform with the size effect, $Z(\mathbf{g}) * \Sigma(\mathbf{g})$, broadens the sharp points of $Z(\mathbf{g})$ to distributions with width proportional to the physical size of the crystal. For future use, following Guiner (1963), we denote this Faltung by

$$R(\mathbf{g}) \equiv Z(\mathbf{g}) * \Sigma(\mathbf{g}) == \frac{1}{V_c} \sum_{\boldsymbol{\beta}^*} \Sigma(\mathbf{g} - \mathbf{g}(\boldsymbol{\beta}^*)). \tag{3.83}$$

To complete the specification of the amplitude function in (3.52) we now consider the structure factor of the unit cell, $F(\mathbf{g})$, i.e. the transform of the electron density function $\rho(\mathbf{x})$.

3.2.2.3 Structure factor computation

In Equation (3.52) we need the transform of the electron density over the unit cell,

$$F(\mathbf{g}) = \int \rho(\mathbf{x}) \exp(-2\pi i \mathbf{g} \cdot \mathbf{x}) \mathrm{d}\mathbf{x}. \tag{3.84}$$

Using Equation (3.83) in (3.52), we rewrite (3.52) as

$$A(\mathbf{g}) = F(\mathbf{g}) R(\mathbf{g}), \tag{3.85}$$

where $R(\mathbf{g})$, defined by (3.83), is a sharp function around the reciprocal lattice nodes at $\mathbf{g} = \mathbf{g}(\boldsymbol{\beta}^*) = \mathbf{g}_{hkl}$. Since $R(\mathbf{g})$ is sharp, we can simplify (3.85) by considering the approximation to $F(\mathbf{g})$ at a reciprocal lattice node, giving

$$\begin{aligned} A(\mathbf{g}) &\approx F(\mathbf{g}(\boldsymbol{\beta}^*)) R(\mathbf{g}) && (3.86)\\ &= F(\mathbf{g}^*) R(\mathbf{g}), && (3.87) \end{aligned}$$

where $\mathbf{g}^* = \mathbf{g}_{hkl}$, see (3.69). Then

$$\begin{aligned} F(\mathbf{g}^*) &= \int \rho(\mathbf{x}) \exp(-2\pi i \mathbf{g}_{hkl} \cdot \mathbf{x}) \mathrm{d}\mathbf{x} \\ &\equiv F_{hkl}, && (3.88) \end{aligned}$$

where F_{hkl} is the structure factor of the unit cell. From Equation (3.88) each h, k, l node of reciprocal space has a corresponding structure factor, differing from point to point, according to the atomic structure described by the unit cell. For a discrete crystal lattice with unit cell containing N atoms at the lattice points enumerated by $\mathbf{x}(\boldsymbol{\theta}_i^*), i = 1, 2, ..., N$, the structure factor from (3.88) can be written as, (Cullity, 1978)

$$\begin{aligned} F_{hkl} &= \sum_{j=1}^{N} f_j \exp(2\pi i \mathbf{g}_{hkl} \cdot \mathbf{x}(\boldsymbol{\theta}_j^*)) && (3.89)\\ &= \sum_{j=1}^{N} f_j \exp(2\pi i (h m_j + k n_j + l p_j)), && (3.90) \end{aligned}$$

where we have used Equation (3.51), (3.65), and the property of the reciprocal and direct lattice encoded by the relations $\mathbf{g}_i \cdot \mathbf{g}^j = \delta_i^j$.

Structure factor - example computation. For completeness an example of the computation of structure factor described by (3.90) is given. Consider the lattice motif in Figure 3.8. This is the motif for a body centered cubic lattice. There are two atoms per unit cell, hence the motif has two atoms. The lattice points $\mathbf{x}_1, \mathbf{x}_2$ have the coordinates

$$\mathbf{x}_1 = \mathbf{0},$$

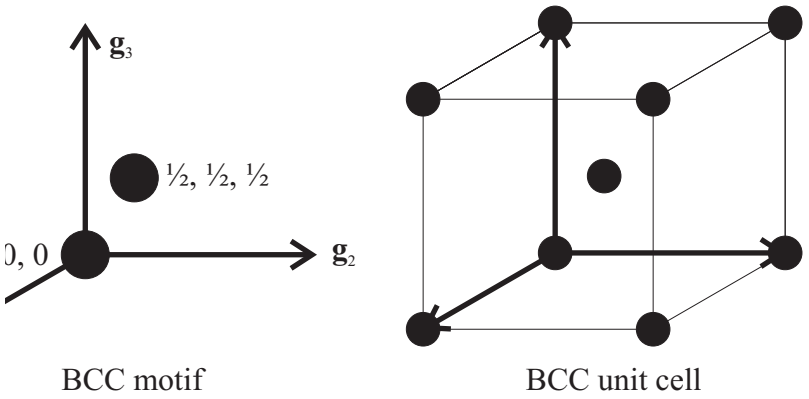

Figure 3.8: On the left, the BCC lattice motif for structure factor calculation. On the right, the BCC unit cell.

$$\mathbf{x}_2 = \frac{1}{2}(\mathbf{g}_1 + \mathbf{g}_2 + \mathbf{g}_3).$$

A reciprocal vector is given by the parametrization

$$\mathbf{g} = h\mathbf{g}^1 + k\mathbf{g}^2 + l\mathbf{g}^3$$

so that Equation (3.90) is computed as

$$\begin{aligned} F_{hkl} &= f_1 + f_2 \exp 2\pi i(h/2 + k/2 + l/2) \\ &= f_1 + f_2 \exp \pi i(h + k + l). \end{aligned} \tag{3.91}$$

For simplicity, take $f_1 = f_2 = f$, e.g. the same atoms are at both points of the motif. This would be the case for elemental iron, for example, along with many other important metals. By inspection of Equation (3.91), setting $h + k + l = even$ gives

$$F_{hkl} = f(1 + 1) = 2f,$$

and for $h + k + l$=*odd*, (3.91) gives

$$F_{hkl} = f(1 + -1) = 0.$$

Therefore, in consideration of the reciprocal lattice parametrization from (3.65), we have some reciprocal nodes h, k, l where there is no diffraction. This is because the BCC lattice is not a simple lattice. For BCC, the extinctions are described by, e.g., $h, k, l = (1, 0, 0), (1, 1, 1)$, etc., and diffraction will occur for, e.g., $h, k, l = (1, 1, 0), (2, 0, 0)$, etc.. In this way, the generation of the h, k, l indices for which diffraction occurs generates the reciprocal lattice by using the integral parametrization $\mathbf{g} = h\mathbf{g}^1 + k\mathbf{g}^2 + l\mathbf{g}^3$. □

Equations (3.88) and (3.82) now completely specify the amplitude function we are after, (3.52),

$$A(\mathbf{g}) = F(\mathbf{g})[Z(\mathbf{g}) * \Sigma(\mathbf{g})].$$

As mentioned several times, the amplitude $A(\mathbf{g})$ is not measurable in an X-ray diffraction experiment, however the intensity, $I(\mathbf{g}) = |A(\mathbf{g})|^2$ is. In the next section we consider the scattering power for a given reflection, which is proportional to $I(\mathbf{g})$. This calculation will give the true integrated intensity picked up by the detector, hence it is the directly measured quantity in the X-ray diffraction experiments we are considering. We will also introduce the Lorentz and Thomson polarization factors, which also contribute to the experimentally measured intensity.

3.2.2.4 Scattering power

The intensity at a point in reciprocal space is given by taking the modulus of Equation (3.85),

$$\begin{aligned} I_N(\mathbf{g}) &= A(\mathbf{g})A^*(\mathbf{g}) \\ &= F(\mathbf{g})F^*(\mathbf{g})R(\mathbf{g})R^*(\mathbf{g}) \\ &= \frac{1}{V_c^2}\sum_i F_{hkl}^2 |\Sigma(\mathbf{g} - \mathbf{g}(\boldsymbol{\beta}_i^*))|^2, \end{aligned} \tag{3.92}$$

where we have used

$$F(\mathbf{g})F^*(\mathbf{g}) = |F_{hkl}|^2 \tag{3.93}$$

along with a simplification of the product

$$R(\mathbf{g})R^*(\mathbf{g}) = \frac{1}{V_c}\sum_i \Sigma(\mathbf{g} - \mathbf{g}(\boldsymbol{\beta}_i^*))\frac{1}{V_c}\sum_j \Sigma^*(\mathbf{g} - \mathbf{g}(\boldsymbol{\beta}_j^*)). \tag{3.94}$$

Derivation of (3.92) To simplify Equation (3.94) we use the following logic. Since the functions $\Sigma(\mathbf{g})$ are confined to the neighborhoods of the lattice nodes, via the results of the finite size computation from (3.46), we can take the i, j overlaps between the summations in (3.94) to be zero. This gives the following sequence of reductions,

$$\begin{aligned} R(\mathbf{g})R^*(\mathbf{g}) &= \frac{1}{V_c}\sum_i \Sigma(\mathbf{g} - \mathbf{g}(\boldsymbol{\beta}_i^*))\frac{1}{V_c}\sum_j \Sigma^*(\mathbf{g} - \mathbf{g}(\boldsymbol{\beta}_j^*)) \\ &= \frac{1}{V_c^2}\sum_i\sum_j \Sigma(\mathbf{g} - \mathbf{g}(\boldsymbol{\beta}_i^*))\Sigma^*(\mathbf{g} - \mathbf{g}(\boldsymbol{\beta}_j^*))\delta_{ij} \\ &= \frac{1}{V_c^2}\sum_i \Sigma(\mathbf{g} - \mathbf{g}(\boldsymbol{\beta}_i^*))\Sigma^*(\mathbf{g} - \mathbf{g}(\boldsymbol{\beta}_i^*)) \\ &= \frac{1}{V_c^2}\sum_i |\Sigma(\mathbf{g} - \mathbf{g}(\boldsymbol{\beta}_i^*))|^2. \end{aligned} \tag{3.95}$$

Now, starting from Equation (3.52), we use (3.88) along with (3.82) and (3.95). The result (3.92) then follows. □

The scattering intensity (power per solid angle) per unit cell is obtained by dividing (3.92) by the total number of unit cells N. For a body of volume V, and unit cell volume V_c there are $N = V/V_c$ unit cells. This gives

$$\begin{aligned} I(\mathbf{g}) &= \frac{I_N}{V/V_c} \\ &= \frac{1}{VV_c}\sum_i F_{hkl}^2 |\Sigma(\mathbf{g} - \mathbf{g}(\boldsymbol{\beta}_i^*))|^2. \end{aligned} \tag{3.96}$$

We now consider the scattering power from a finite crystal. A general reciprocal lattice peak where $I(\mathbf{g}) \neq 0$ is indicated in Figure 3.9, where the Ewald sphere is also indicated. We will return to this figure in a subsequent discussion. As shown previously, for monochromatic radiation one must physically rotate the crystal to have the Ewald sphere intersect the reciprocal lattice vector. The geometry of how the reciprocal lattice vector intersects the Ewald sphere has implications for the scattering intensity produced by the reciprocal lattice vector passing through the Ewald sphere. To simplify the geometry of this intersection process, in Figure 3.9 we first consider a reciprocal lattice vector which is in the plane of rotation, and derive the expression for the scattering power. We then generalize to the case when the reciprocal vector is not in the plane of rotation, depicted in Figure 3.10.

Rotation in-plane analysis Let us assume that the crystal is rotating with angular rate $\dot{\omega}$. The energy transmitted, per unit cell, E, by going through a diffraction condition is given by

$$E = \int_{\Delta\omega} \frac{1}{\dot{\omega}} \mathrm{d}\omega \wedge \int_{\Omega} I_e I(\mathbf{g}) \mathrm{d}\Omega, \tag{3.97}$$

where I_e is the Thomson polarization factor, see §A.2, $I(\mathbf{g})$ is the scattering power per unit cell given by Equation (3.96), understood as power per solid angle, and $\mathrm{d}\Omega$ is the solid angle area element. In terms of the geometry of the Ewald sphere the solid angle is related to the angular coordinates θ, η, see §3.3.2 by

$$\mathrm{d}\Omega = \sin 2\theta \mathrm{d}(2\theta) \wedge \mathrm{d}\eta. \tag{3.98}$$

We would like to convert the integral of (3.97) over the coordinates $\mathrm{d}\omega \wedge \mathrm{d}\Omega$ into an integral over reciprocal space coordinates, $\mathrm{d}\mathbf{g}$, so that we obtain an expression of the form

$$E = \hat{E}\left(\int I(\mathbf{g}) \mathrm{d}\mathbf{g}\right). \tag{3.99}$$

Then we can use (3.96) to simplify (3.99).

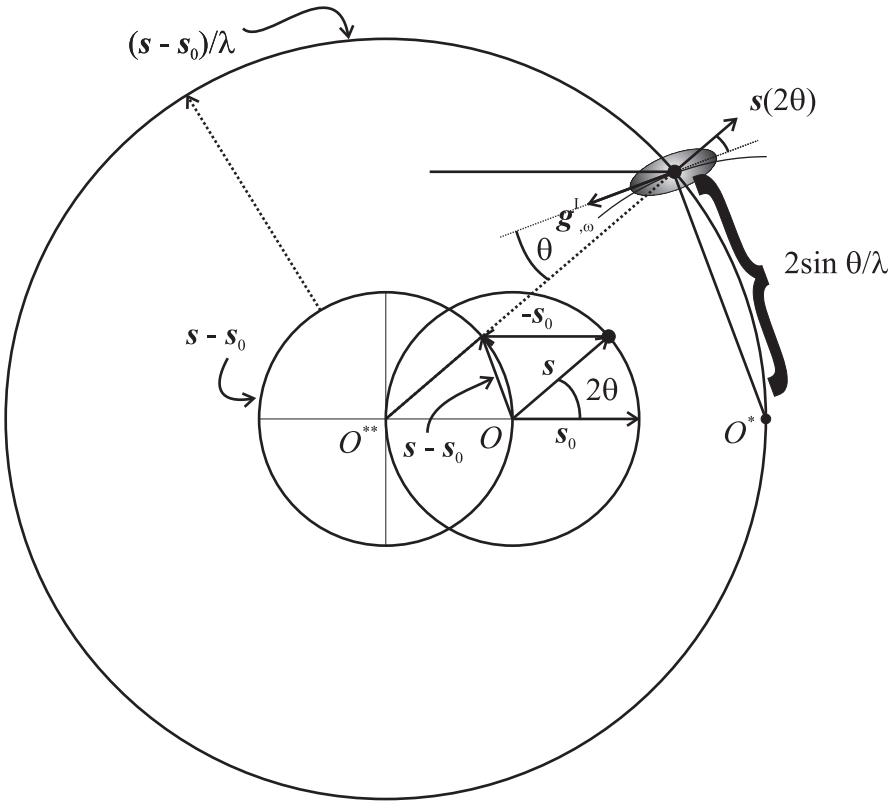

Figure 3.9: Ewald sphere construction of a diffraction event, with reciprocal vector $\mathbf{g}^i$ in the plane of rotation generated by $\dot{\omega}$. The geometry of the construction of crossing the Ewald sphere determines the diffracted power received by the detector. The geometric factor the power is only a function of θ-location of the peak in this case.

To do this, we will compute the volume element induced by tracing the path of $\mathbf{g}^I$ through small changes in ω, and multiply by the solid angle area element in Equation (3.98). See also (Cochran, 1948) for a similar method of computation.

The equation of the Ewald sphere gives that the magnitude of the reciprocal vector $\mathbf{g}^I$ is

$$|\mathbf{g}^I| = \left|\frac{\mathbf{s} - \mathbf{s}_0}{\lambda}\right| = \frac{2\sin\theta}{\lambda}, \tag{3.100}$$

where $\mathbf{s} \cdot \mathbf{s}_0 = \cos 2\theta$, see Figure 3.13 and discussion associated with a general experimental setup. As the crystal rotates, the reciprocal vector $\mathbf{g}^I$ likewise rotates; the arc of this rotation is traced in reciprocal space, as indicated in Figure 3.9. The tangent vector to the arc traced by the reciprocal vector, projected on the normal to the Ewald sphere, $\mathbf{s}$, is given by $\cos\theta$, as indicated in Figure 3.9. This can be seen by geometric construction. Therefore the reciprocal

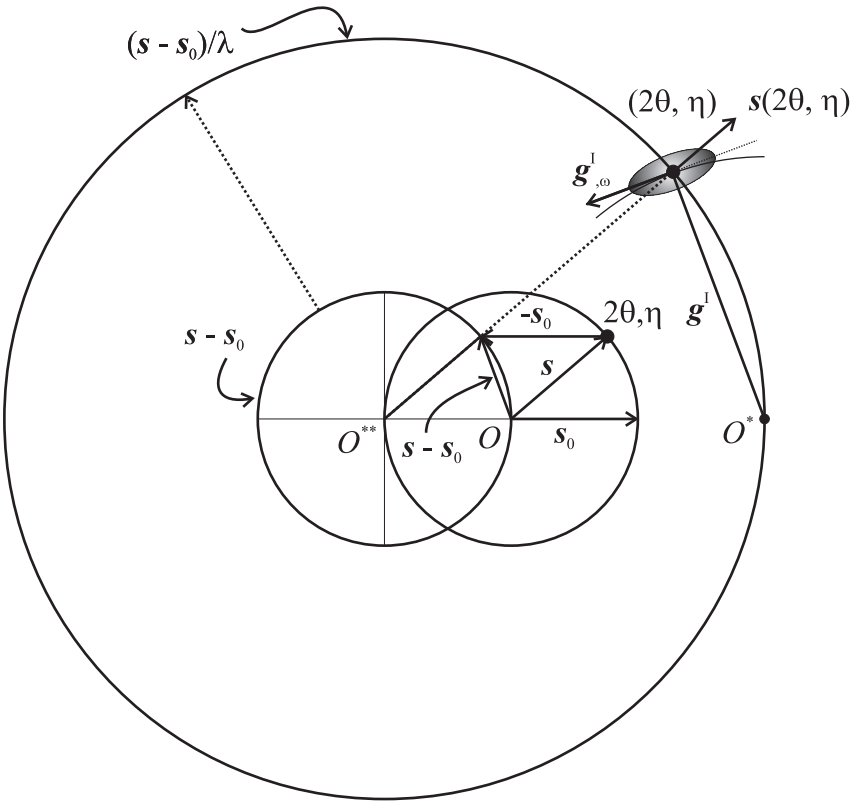

Figure 3.10: Ewald sphere construction of a diffraction event, as in Figure 3.9, for the general case when the reciprocal vector $\mathbf{g}^i$ is not in the plane of rotation induced by $\dot{\omega}$. The diffracted power received by the detector is determined by the η-location of the peak as well as by the θ-location.

space volume element in the angular coordinates is given by

$$\mathrm{d}\mathbf{g} = -|\mathbf{g}|\mathrm{d}\sigma \wedge \mathbf{g}_{,\omega} \cdot \mathbf{s}\mathrm{d}\omega \tag{3.101}$$

$$= \frac{2\sin\theta}{\lambda}\cos\theta \mathrm{d}\omega \wedge \mathrm{d}\sigma, \tag{3.102}$$

where $\mathrm{d}\sigma$ is the solid angle on the reflection sphere. It is related to the solid angle on the unit sphere by

$$\mathrm{d}\sigma = \frac{\mathrm{d}\Omega}{\lambda^2} = \frac{\sin 2\theta}{\lambda^2}\mathrm{d}(2\theta) \wedge \mathrm{d}\eta. \tag{3.103}$$

With Equation (3.103) and (3.102) we can rewrite the expression for total energy, (3.97), as

$$E = \frac{I_e}{\dot{\omega}}\frac{\lambda^3}{\sin 2\theta}\int I(\mathbf{g})\mathrm{d}\mathbf{g}. \tag{3.104}$$

In (3.104) we are making the assumption that the peak is tight enough so that the θ-broadening is negligible, letting us remove it from the integration. For small particle applications, we may wish to integrate directly over the angular coordinates $2\theta, \eta, \omega$. In that case using (3.102) with (3.103) gives the volume element as

$$\mathrm{d}\mathbf{g} = \frac{1}{\lambda^3}\sin^2 2\theta \mathrm{d}(2\theta) \wedge \mathrm{d}\eta \wedge \mathrm{d}\omega. \tag{3.105}$$

Therefore combining (3.102) and (3.103), the total integrated energy using intensity over angular coordinates becomes

$$E = \frac{I_e \lambda^3}{\dot{\omega}} \int \frac{I(2\theta, \eta, \omega)}{\sin^2 2\theta} \mathrm{d}(2\theta) \wedge \mathrm{d}\eta \wedge \mathrm{d}\omega. \tag{3.106}$$

Recall that the total energy computed in Equations (3.104), (3.106) were for the case of the reciprocal vector in the plane of rotation of the crystal. Next we consider the general case, where the reciprocal vector is not in the plane of rotation. The same computational ideas apply - we seek the volume element generated by extruding the solid angle element on the Ewald sphere along the tangent vector traced by a reciprocal vector as the crystal is rotated, in order to relate the angular coordinates to the integrated intensity.

Out-of-plane rotation analysis. In this case it is convenient to formally parametrize reciprocal space in terms of the diffraction angles, $2\theta, \eta, \omega$ as

$$\mathbf{g}(2\theta, \eta, \omega) = \frac{1}{\lambda}(s_1(2\theta, \eta, \omega)\mathbf{e}_1 + s_2(2\theta, \eta, \omega)\mathbf{e}_2 + s_3(2\theta, \eta, \omega)\mathbf{e}_3), \tag{3.107}$$

where

$$s_1 = -\sin\omega(1 - \cos 2\theta) + \cos\eta\cos\omega\sin 2\theta \tag{3.108}$$

$$s_2 = \sin\eta\sin 2\theta \tag{3.109}$$

$$s_3 = \cos\omega(1 - \cos 2\theta) + \cos\eta\sin\omega\sin 2\theta. \tag{3.110}$$

Note that the array (s_1, s_2, s_3) is not a unit vector. These equations are obtained from the analysis in §3.3.3. The normal on the reflection sphere is parameterized by $2\theta, \eta$ as

$$\mathbf{s} = \mathbf{e}_\rho(2\theta, \eta; -\mathbf{e}_3, \mathbf{e}_1, \mathbf{e}_2), \tag{3.111}$$

where $\mathbf{e}_\rho(\cdot)$ is defined in (A.1). In the expression for energy given by (3.97) the solid angle $\mathrm{d}\Omega$ is unchanged, but the result of the volume extrusion is changed from (3.102), which was obtained for an in plane reciprocal vector. It is computed by forming first the path of the reciprocal vector upon rotation, ω as

$$\frac{d}{d\omega}\mathbf{Q}(\omega)\mathbf{g}^I\Big|_{\omega=\omega^*} = \dot{\mathbf{Q}}(\omega)\mathbf{g}^I, \tag{3.112}$$

where ω^* is the value of ω upon bringing $\mathbf{g}^I$ onto the Ewald sphere, and $\mathbf{Q}(\omega) \equiv \hat{\mathbf{R}}(\mathbf{e}_2, \omega)$ is the induced physical rotation of the sample by the stage. Then the volume element is computed by projecting the path of the rotating reciprocal vector on the normal to the Ewald sphere, which gives

$$\mathrm{d}\mathbf{g} = \mathrm{d}\Omega \wedge \left(\frac{d}{d\omega} \mathbf{Q}(\omega) \mathbf{g}^I \Big|_{\omega=\omega^*} \cdot \mathbf{s} \right) \mathrm{d}\omega \tag{3.113}$$

$$= \mathrm{d}\Omega \wedge \left(\frac{\cos\eta \sin 2\theta}{\lambda^3} \right) \mathrm{d}\omega \tag{3.114}$$

$$= \left(\frac{\cos\eta \sin^2 2\theta}{\lambda^3} \right) \mathrm{d}(2\theta) \wedge \mathrm{d}\eta \wedge \mathrm{d}\omega, \tag{3.115}$$

where we have again used

$$\mathrm{d}\sigma = \frac{\mathrm{d}\Omega}{\lambda^2}$$

and

$$\mathrm{d}\Omega = \sin 2\theta \mathrm{d}(2\theta) \wedge \mathrm{d}\eta.$$

Then using the expression for the volume element from (3.114), the energy, (3.97), becomes

$$E = \frac{I_e}{\dot{\omega}} \frac{\lambda^3}{\sin 2\theta \cos\eta} \int I(\mathbf{g}) \mathrm{d}\mathbf{g}, \tag{3.116}$$

where we are using the assumption of negligible angular broadening of the diffraction peak. Should this not be the case, re-expressing (3.116) on angular coordinates using (3.115) gives that (3.97) becomes

$$E = \int_{\Delta\omega} \frac{1}{\dot{\omega}} \mathrm{d}\omega \wedge \int_{\Omega} I_e I(\mathbf{g}) \mathrm{d}\Omega \tag{3.117}$$

$$= \left(\frac{I_e \lambda^3}{\dot{\omega}} \right) \int \frac{I(2\theta, \eta, \omega)}{\sin^2 2\theta \cos\eta} \mathrm{d}2\theta \wedge \mathrm{d}\eta \wedge \mathrm{d}\omega. \tag{3.118}$$

We can also arrive at (3.115) in a much cleaner fashion by considering the diffeomorphism between manifolds representing reciprocal space, being parametrized by the map $\boldsymbol{\xi}(2\theta, \eta, \omega) = (s_1, s_2, s_3)$ where $s_i, i = 1, 2, 3$ are given by (3.108)-(3.110). Then the volume element is given by the standard formula

$$\mathrm{d}\mathbf{g} = \left(\sqrt{\det \boldsymbol{\Xi}} \right) \mathrm{d}2\theta \wedge \mathrm{d}\eta \wedge \mathrm{d}\omega, \tag{3.119}$$

where $\boldsymbol{\Xi}_{ij} \equiv \boldsymbol{\xi}_{,i} \cdot \boldsymbol{\xi}_{,j}$. This computation is executed in Mathematica and results in

$$\mathrm{d}\mathbf{g} = \left(\frac{\sin^2 2\theta \cos\eta}{\lambda^3} \right) \mathrm{d}2\theta \wedge \mathrm{d}\eta \wedge \mathrm{d}\omega, \tag{3.120}$$

which is equivalent to (3.115).

We have now an expression for the total energy integrated from a reciprocal lattice vector, given by (3.104), and the more general (3.116). We now compute (3.99), the total energy for a node. Using Equation (3.96) we have, after some rearrangement,

$$\begin{aligned}\int I(\mathbf{g})\mathrm{d}\mathbf{g} &= \frac{1}{VV_c}F_{hkl}^2\int|\Sigma(\mathbf{g})|^2\mathrm{d}\mathbf{g}\\ &= \frac{1}{V_c}F_{hkl}^2,\end{aligned}\tag{3.121}$$

where we have used (3.41). The energy per unit cell is computed from (3.121) and (3.116) as

$$E = \left(\frac{I_e}{\dot{\omega}}\right)\left(\frac{\lambda^3}{\sin 2\theta\cos\eta}\right)\left(\frac{1}{V_c}F_{hkl}^2\right).\tag{3.122}$$

The total reflected energy for the whole crystal is then given by taking the product of (3.122) times the number of unit cells

$$E_{\mathrm{tot}} = E\frac{V}{V_c},\tag{3.123}$$

where V is the total spatial volume of the crystal. Therefore for the same crystal (e.g. unit cell is constant), increasing the macroscopic volume increases the diffracted intensity (linearly). To complete Equations (3.122), (3.123), the Thomson formula gives, for an initially unpolarized beam[4]

$$I_e = I_0 r_e^2\left(\frac{1+\cos^2 2\theta}{2}\right),\tag{3.124}$$

where I_0 is the nominal beam intensity. The full power is given by

$$P = \frac{E_{\mathrm{tot}}\dot{\omega}}{I_0} = r_e^2\left(\frac{1+\cos^2 2\theta}{2}\right)\left(\frac{\lambda^3}{\sin 2\theta\cos\eta}\right)\left(\frac{1}{V_c^2}\right)F_{hkl}^2V\tag{3.125}$$

$$= Q_{hkl}V,\tag{3.126}$$

where

$$Q_{hkl} = r_e^2\left(\frac{1+\cos^2 2\theta}{2}\right)\left(\frac{\lambda^3}{\sin 2\theta\cos\eta}\right)\left(\frac{1}{V_c^2}\right)F_{hkl}^2.\tag{3.127}$$

The factor $(1+\cos^2 2\theta)/(2\sin 2\theta\cos\eta)$ is called the Lorentz factor (Guiner, 1963; Warren, 1969). When using a monochrometer, the Thomson formula does not apply and a correction factor must multiply (3.127) in order to get the absolute intensity correctly. For details, see Guiner (1963, p. 100). For the purposes of this work, we only use relative intensities so the numerical value of this correction factor does not matter to the present work. The most important results from the derivations leading to (3.127) are that we can now relate the intensity picked up on a pixel of the detector to (1) the structure factor of the reflection, (2) the diffraction angles of the peak, and (3) the physical volume of the crystal. These factors will be important to consider in §3.5.

[4]see §A.2 for details

Summary. In this section we have arrived at the relationship between the reciprocal lattice and X-ray diffraction intensity, using the Fourier transform operation. The reciprocal lattice is an array of points in reciprocal space, corresponding to the spatial distribution of lattice points in physical space. The importance of the reciprocal construction was revealed when we showed that we can formulate the description of diffraction processes in a geometric fashion: that diffraction occurs when a reciprocal lattice vector lies on the Ewald sphere. To complete a predictive model of diffraction, we derived the resulting total energy recorded by a detector, as a reciprocal lattice vector passed through the diffraction condition. This required the introductions of the structure factor and Lorentz polarization factor, which were both provided. This description for diffraction in terms of Fourier transforms will be important to consider in §3.4.2.2 when we describe a forward model to simulate diffraction intensities.

In the next section we further build on the deductions from this section, and recast the reciprocal lattice in a more geometric context. Upon taking this perspective we can reformulate some notions of experimental X-ray diffraction without using Fourier transforms, in a framework more natural to mechanics work. We now present the details.

3.2.3 Geometric description for X-ray diffraction

In §3.2.2 we used the physics of coherent scattering of an array of atoms to motivate computation of the Fourier transform of the physical lattice. It was shown that constructive interference occurs for diffraction vectors, $\mathbf{g}$, which are located on reciprocal lattice sites; equivalently, when reciprocal lattice sites are coincident with the Ewald sphere. The relevance of the reciprocal lattice to diffraction experiments was therefore established. In this section the crystalline lattice is reexamined from a geometric point of view. This point of view is natural to consider in order to couple the framework of continuum mechanics with X-ray diffraction analysis.

We will first restate the basic formulation of a crystal lattice, and then quickly derive the geometric construction of the reciprocal lattice. We then derive some kinematic results which were suggested in the previous section, see Equation (3.15). Many of the results in this section exist in other forms in the mechanics literature. In order to keep the treatment simple for now, we will restrict the treatment to elastic deformations, so notions of material deformation and lattice deformation will be identical. When plasticity occurs, lattice deformation and material deformation are not equivalent, as was described in Chapter 2. However the results of this section still carry over very well to that case, differing only in some details. A final note is that in this section, the use of the term kinematic will be used to denote the idea of deformation, and does not refer to the kinematic theory of diffraction, a term used previously in this chapter.

As we have seen, a primary notion in the geometry of crystals is the existence of an array of atoms which are generated by combinations of translations of three linearly independent position vectors. To relate this array to a continuum field description, we can assign the

position field according to the parametrization (see (3.47))

$$\mathbf{x}(\theta^1, \theta^2, \theta^3) = \theta^1 \mathbf{a} + \theta^2 \mathbf{b} + \theta^3 \mathbf{c}, \tag{3.128}$$

where $\mathbf{a}, \mathbf{b}, \mathbf{c}$ are constant lattice vectors, $\theta_i \in \mathbb{R}, i = 1, 2, 3$ and the position field $\mathbf{x}$ has the property that a lattice point is defined to be at $\boldsymbol{\theta} \in \mathbb{Z}^3$. Therefore $\theta_i, i = 1, 2, 3$ may be considered the material coordinates for the body, a common construction in mechanics analysis. In this convected coordinate formulation, the point defined by a particular values of $\boldsymbol{\theta}$ is the same material point throughout any deformation of the body. This is done so that we can bring in the machinery from differential geometry and apply it to the mechanics of the crystal, which we now proceed to exercise.

Having established the position field in the crystal by (3.128), the material tangent vectors are defined by the traditional formula

$$\mathbf{g}_i = \frac{\partial \mathbf{x}}{\partial \theta^i}. \tag{3.129}$$

Applying (3.129) to (3.128) gives that $\mathbf{a} \equiv \mathbf{g}_1$, $\mathbf{b} \equiv \mathbf{g}_2$, $\mathbf{c} \equiv \mathbf{g}_3$. Therefore we have the equivalent, compact representation of position referred to the lattice vectors as

$$\mathbf{x}(\boldsymbol{\theta}) = \theta^i \mathbf{g}_{\boldsymbol{i}}, \tag{3.130}$$

where we are using the Einstein summation convention on repeated indices.

The kinematic metric of interest in material coordinates θ^i is induced by the Euclidean metric, $\boldsymbol{\delta}$, in the spatial configuration,

$$\boldsymbol{\delta} = \mathrm{d}\mathbf{x}^i \otimes \mathrm{d}\mathbf{x}^i, \tag{3.131}$$

where we are using the notation of exterior calculus to denote the basis elements $\mathrm{d}\mathbf{x}^i$. Using the mapping from material coordinates to spatial coordinates, $\boldsymbol{\chi} : \mathbb{R}^3 \to \mathbb{R}^3, \boldsymbol{\chi}(\boldsymbol{\theta}) \mapsto \mathbf{x}$ is given by

$$\begin{aligned} \boldsymbol{g} &= \boldsymbol{\chi}^* \boldsymbol{\delta} \\ &= \mathbf{g}_i \cdot \mathbf{g}_j \mathrm{d}\theta^i \otimes \mathrm{d}\theta^j, \end{aligned} \tag{3.132}$$

where $()^*$ denotes the pullback map. So that in material coordinates therefore the metric components are

$$g_{ij} = \mathbf{g}_i \cdot \mathbf{g}_j. \tag{3.133}$$

To generate the reciprocal lattice, we can use the lattice vectors $\mathbf{g}_i$ and use the relations

$$\mathbf{g}^i = \mathbf{I}\mathbf{g}^i = \mathbf{g}_j \otimes \mathbf{g}^j \cdot \mathbf{g}^i = (g^{ij})\mathbf{g}_j. \tag{3.134}$$

Using $g_{ij} g^{jk} = \delta_i^k$, and the uniqueness of matrix inverses, (3.134) gives the reciprocal vector in terms of the lattice vectors as

$$\mathbf{g}^i = \hat{\mathbf{g}}^i(\mathbf{g}_1, \mathbf{g}_2, \mathbf{g}_3) = [g_{ij}]^{-1} \mathbf{g}_j, \tag{3.135}$$

where $[g_{ij}]$ denotes the matrix constructed from the components g_{ij}. The volume of the unit cell, V_c, in physical space can be computed from

$$V_c = [\mathbf{g}_1, \mathbf{g}_2, \mathbf{g}_3] = \sqrt{\det g_{ij}}. \tag{3.136}$$

Likewise, the volume of the reciprocal unit cell, in reciprocal space can be computed from

$$V_c^* = [\mathbf{g}^1, \mathbf{g}^2, \mathbf{g}^3]. \tag{3.137}$$

To relate Equations (3.136), (3.137), we use (3.135) and the relations

$$\begin{aligned}
[\mathbf{g}^1, \mathbf{g}^2, \mathbf{g}^3] &= [\mathbf{g}^{1j}\mathbf{g}_j, \mathbf{g}^{2k}\mathbf{g}_k, \mathbf{g}^{3m}\mathbf{g}_m] \\
&= \mathbf{g}^{1j}\mathbf{g}^{2k}\mathbf{g}^{3m}\epsilon_{jkm}\sqrt{g} \\
&= \det[\mathbf{g}^{ij}]\sqrt{g} \\
&= \det(\mathbf{g}_{ij})^{-1}\sqrt{g} \\
&= (\sqrt{g})^{-1},
\end{aligned} \tag{3.138}$$

where

$$g \equiv \det g_{ij} = V_c^2, \tag{3.139}$$

so that after substitutions (3.138) gives the result

$$V_c = \frac{1}{V_c^*}. \tag{3.140}$$

This was a required relation in (3.78). From another direction, we can consider a structural deformation mapping from a Cartesian material coordinate system with coordinate directions $\mathbf{e}_1, \mathbf{e}_2, \mathbf{e}_3$ into the lattice configuration, $\mathbf{g}_1, \mathbf{g}_2, \mathbf{g}_3$. This construction is developed further in §3.3.5. Denoted this mapping as $\mathbf{F}_\mathrm{s}$, we have the sequence

$$V_c = [\mathbf{g}_1, \mathbf{g}_2, \mathbf{g}_3] = [\mathbf{F}_\mathrm{s}\mathbf{e}_1, \mathbf{F}_\mathrm{s}\mathbf{e}_2, \mathbf{F}_\mathrm{s}\mathbf{e}_3] = \det\mathbf{F}_\mathrm{s}[\mathbf{e}_1, \mathbf{e}_2, \mathbf{e}_3] = \det\mathbf{F}_\mathrm{s}. \tag{3.141}$$

On the reciprocal vectors we have

$$\mathbf{g}^i = \mathbf{F}_\mathrm{s}^{-\mathrm{T}}\mathbf{e}_i, \tag{3.142}$$

so that

$$V_c^* = [\mathbf{g}^1, \mathbf{g}^2, \mathbf{g}^3] = [\mathbf{F}_\mathrm{s}^{-\mathrm{T}}\mathbf{e}_1, \mathbf{F}_\mathrm{s}^{-\mathrm{T}}\mathbf{e}_2, \mathbf{F}_\mathrm{s}^{-\mathrm{T}}\mathbf{e}_3] \tag{3.143}$$

$$= \det\mathbf{F}_\mathrm{s}^{-\mathrm{T}}[\mathbf{e}_1, \mathbf{e}_2, \mathbf{e}_3] \tag{3.144}$$

$$= V_c^{-1}. \tag{3.145}$$

We record here some further kinematic results relating the reciprocal lattice vectors to the direct lattice vectors. For any three independent lattice vectors $\mathbf{g}_i$ we can construct a

reference configuration based around the measured state $\mathbf{g}_i$. Following common conventions, we denote this triad by $\mathbf{G}_i$. Then the evolution of lattice vectors occurs through the action of a deformation gradient, $\mathbf{F}$. In equation form, we have

$$\mathbf{g}_i = \mathbf{F}\mathbf{G}_i \tag{3.146}$$

for $i = 1, 2, 3$. Since the choice of the triad $\mathbf{G}_i$ is an arbitrary basis for the lattice (see Figure 3.6, the relation (3.146) holds for any lattice vector $\mathbf{G}_i$. Based on Equation (3.146) and properties of the reciprocal lattice, a representation for $\mathbf{F}$ is given by

$$\mathbf{F} = \mathbf{g}_i \otimes \mathbf{G}^i. \tag{3.147}$$

By direct computation, $\mathbf{F}\mathbf{F}^{-1} = \mathbf{I}$ so that

$$\mathbf{F}^{-1} = \mathbf{G}_i \otimes \mathbf{g}^i, \tag{3.148}$$

and

$$\mathbf{F}^{-\mathrm{T}} = \mathbf{g}^i \otimes \mathbf{G}_i, \tag{3.149}$$

so that apparently

$$\mathbf{F}^{-\mathrm{T}}\mathbf{G}^i = \mathbf{g}^i. \tag{3.150}$$

That is, (3.150) maps reference reciprocal lattice vectors to their state in the current configuration. Based on the arbitrariness of the sublattice $\mathbf{G}_i$, (3.150) holds for any associated pair $\mathbf{G}^i, \mathbf{g}^i$. Therefore we can write

$$\mathbf{F}^{-\mathrm{T}}\mathbf{G}^{(i)} = \mathbf{g}^{(i)}, \tag{3.151}$$

where (i) denotes the index into an enumeration of the reciprocal lattice points. For non-simple lattices this enumeration is determined by the h, k, l extinctions from the structure factor for the unit cell, see §3.2.2.3 for an example. Recalling that X-ray diffraction measurements detect reciprocal lattice vectors, we can see that (3.150) forms the basis for strain analysis using X-ray diffraction measurements of the reciprocal lattice.

Furthermore, only three reciprocal vectors suffice to determine $\mathbf{F}$, once a reference configuration has been defined. To see this, from (3.147), we can use

$$\mathbf{g}_i = [\mathbf{g}_i \cdot \mathbf{g}_j]\mathbf{g}^j = (g^{ij})^{-1}\mathbf{g}^j, \tag{3.152}$$

where $g^{ij} = \mathbf{g}^i \cdot \mathbf{g}^j = [g_{ij}]^{-1}$ is the reciprocal metric tensor. Therefore Equation (3.152) in (3.147) gives $\mathbf{F}$ as

$$\mathbf{F} = (\mathbf{g}^i \cdot \mathbf{g}^j)^{-1}\mathbf{g}^j \otimes \mathbf{G}^i, \tag{3.153}$$

an expression only in terms of the reciprocal lattice vectors, which are measurable from X-ray diffraction.

To relate this with other methods of strain determination, in traditional studies on bulk materials, some components of the deformation $\mathbf{F}$ described by (3.146) may be obtained experimentally with the use of a bonded resistance strain gage. The strain gauges measure the deformation on the surface of the material. For crystalline materials we have an analogous X-ray diffraction measurement, with the kinematic relationship for any reciprocal lattice vector given by (3.151). Therefore, X-ray diffraction experiments operate like a three dimensional strain gage rosette. A difference is that the diffraction measurement has many more 'gauges' than is possible with a strain gage rosette: one gauge for each reciprocal lattice vector.

More explicitly, for a strain gage rosette, the deformation of material lines is measured. Since they are bonded, the gauge stretches along with the material. The resistance in the gauge wire thereby changes. This change in resistance then gives an indication of the (surface) strain in the material. To relate this to $\mathbf{F}$, take a given gage element of length L, aligned with the in plane direction $\mathbf{e}_1$. The gage element is described by the vector $L\mathbf{e}_1$. Upon deformation by $\mathbf{F}$, using (3.146), the new length of that line element is given by

$$l^2 = L^2\mathbf{F}\mathbf{e}_1 \cdot \mathbf{F}\mathbf{e}_1 = L^2\mathbf{C} \cdot \mathbf{e}_1 \otimes \mathbf{e}_1, \tag{3.154}$$

where l is the deformed gage length, and $\mathbf{C} \equiv \mathbf{F}^{\mathrm{T}}\mathbf{F}$. The stretch in the gage is given by

$$\frac{l_1}{L_1} = \sqrt{\mathbf{C} \cdot \mathbf{e}_1 \otimes \mathbf{e}_1} = \sqrt{C_{11}}. \tag{3.155}$$

Computing the same quantity for a gage oriented in the direction orthogonal to $\mathbf{e}_1$ gives

$$\frac{l_2}{L_2} = \sqrt{\mathbf{C} \cdot \mathbf{e}_2 \otimes \mathbf{e}_2} = \sqrt{C_{22}}. \tag{3.156}$$

For a gage initially aligned with a third direction, coplanar with $\mathbf{e}_1, \mathbf{e}_2$, oriented at

$$\mathbf{e}_r(\theta \ = \ \pi/4; \ \mathbf{e}_1, \ \mathbf{e}_2),$$

we will introduce mixed terms so that

$$\left(\frac{l}{L}\right)_{\theta=\pi/4} = \frac{1}{\sqrt{2}}\sqrt{\mathbf{C} \cdot (\mathbf{e}_1 + \mathbf{e}_2) \otimes (\mathbf{e}_1 + \mathbf{e}_2)} = \frac{1}{\sqrt{2}}\sqrt{C_{11} + C_{22} + 2C_{12}}. \tag{3.157}$$

Solving the three equations (3.155) - (3.157) for C_{11}, C_{12}, C_{22} gives a measurement of the (surface) strain in the material. Similarly, for X-ray diffraction, we have the kinematic relation (3.151) As in the strain gage example, equation (3.151) could be used with only three measurements of reciprocal lattice vectors in the deformed and current configuration. But generally these computations will have large errors, and there are more measurements available since there are many reciprocal vectors than the amount of strain gages which could be simultaneously bonded to the same spatial location. Since (3.151) holds for any associated

pair $\mathbf{g}^{(i)}, \mathbf{G}^{(i)}$, we can form a least squares system over all detected pairs to determine the $\mathbf{F}$ which minimizes the difference between the model ((3.151) and the experiment.

Thus, strain gage and X-ray diffraction measurements each characterize the deformation of a material. Whereas strain gages measure the deformation of material lines, X-ray diffraction measures the deformation of reciprocal vectors. There are differences which should be pointed out here between the two measurements. First, it is evident that material rotation is not accessible from the basic strain gage method. This is evident from the fact that only $\mathbf{C}$ was involved in the gauge equations. Arguing intuitively, the bonded gage rotates with the material, and the electrical resistance does not change due to such rotations. For X-ray diffraction, equation (3.206) enables both strain and rotation to be determined experimentally. Secondly, the strain gage measurement is a measurement of total material strain. That is, strain gages measure the deformation of material lines, and not just of lattice vectors. This is an important distinction when considering plasticity of crystals. In plasticity theory, the total deformation is given by $\mathbf{F} = \mathbf{H}\mathbf{K}^{-1}$, see Chapter 2, where $\mathbf{H}$ is called the lattice deformation, $\mathbf{K}$ the plastic deformation. X-rays measure only lattice deformations $\mathbf{H}$. Therefore, the use of diffraction measurements in experimental plasticity must be complemented by a simultaneous measurement of the total material deformation if one desires to measure all kinematic variables. This is precisely what Taylor did in his fundamental studies (Taylor and Elam, 1923), where material lines were scribed on the surface of the material and visually measured at various stages of deformation, see Figure 1.1. Promising modern techniques for such simultaneous studies include digital image correlation, where the spatial position of points from a speckle pattern are tracked by a high resolution camera. By combining these measurements with X-ray diffraction, the full deformation field can be measured in an elastic-plastic deformation.

Vector bundle depiction of elastic-plastic body In Figure 3.11 is a depiction of the vector bundle $M \xrightarrow{\pi} B$ characterizing the geometry of an elastic plastic body. The state of the body is described by its spatial location coordinate $\mathbf{x}$, the local lattice deformation $\mathbf{H}$ and local plastic deformation $\mathbf{K}$. Equivalently, $\mathbf{H}, \mathbf{K}$ can be replaced by the lattice deformation and material deformation, $\mathbf{H}, \mathbf{F}$. Denote the bundle space by $M = \mathbb{R}^3 \times \mathrm{GL}(3,\mathbb{R}) \times \mathrm{GL}(3,\mathbb{R})$. The projections $\pi : M \to \Omega, \pi_{\mathbf{F}} : M \to T\Omega \cong \mathrm{GL}(3,\mathbb{R}), \pi_{\mathbf{H}} : M \to \mathrm{GL}(3,\mathbb{R})$ correspond to the projections of the point of the body to spatial position, local material deformation gradient, and local lattice deformation, respectively. X-ray diffraction measurements represent the action of the function $\pi_{\mathbf{H}}$, with a weak coupling to the spatial projection π, as will be shown later. Strain gauge or digital image correlation measurements represent the action of the function $\pi_{\mathbf{F}}$, giving the material deformation. Digital image correlation experiments also expose the projection π. In order to characterize the state of the body fully, all functions $\pi, \pi_{\mathbf{F}}, \pi_{\mathbf{H}}$ must be probed experimentally, through a combination of X-ray diffraction with digital image correlation for example.

The picture of Figure 3.11 is an idealization, since there is no mention of the experimental

limits on the resolution on the base space, Ω. In Figure 3.12, the action of X-ray diffraction is more accurately depicted. A finite beam of width w probes the base space of the material, $\mathbf{x}$. Therefore X-ray diffraction measurements over a finite volume of material represent the projection of the function $\mathbf{H}(\mathbf{x})$ into $\mathbf{H}$-space. The incorporation of this projection into analysis codes is recent; we give an in depth look at how to squeeze out some additional information from the projection in §3.4.2.2.

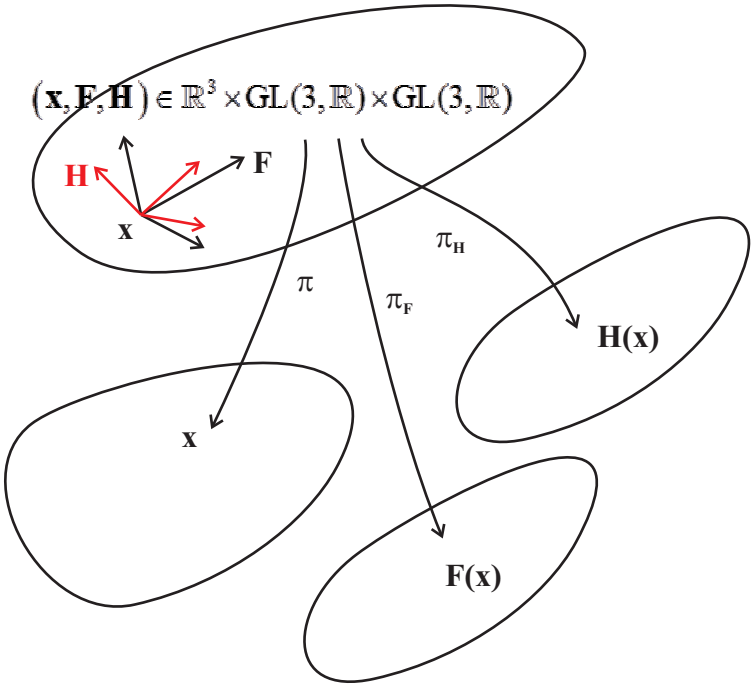

Figure 3.11: Fiber bundle picture of elastic plastic bodies with application to X-ray diffraction. The bundle is of the structure $M \xrightarrow{\pi} B$ where $M = \mathbb{R}^3 \times \mathrm{GL}(3,\mathbb{R}) \times \mathrm{GL}(3,\mathbb{R})$ is the bundle space and B is the spatial configuration of the manifold. The material tangent space is coordinitized by $\mathbf{F}$ (through the material tangent vectors $\mathbf{m}_i$), the lattice tangent space by $\mathbf{H} \cong \mathbf{l}$. X-ray diffraction techniques measure the projection $\pi_{\mathbf{H}}$, other techniques are required to obtain $\pi_{\mathbf{F}}$ such as digital image correlation.

Summary. This completes the geometric description of crystal lattices. We now may envision lattice deformation in a crystal equally as the evolution of the physical lattice under $\mathbf{F}$ or of the reciprocal lattice under $\mathbf{F}^{-\mathrm{T}}$, by using (3.151). The modifications of this treatment for elastic plastic bodies are simply that $\mathbf{F}$ is replaced by $\mathbf{H}$ in (3.151). See §2.2.1 for more background.

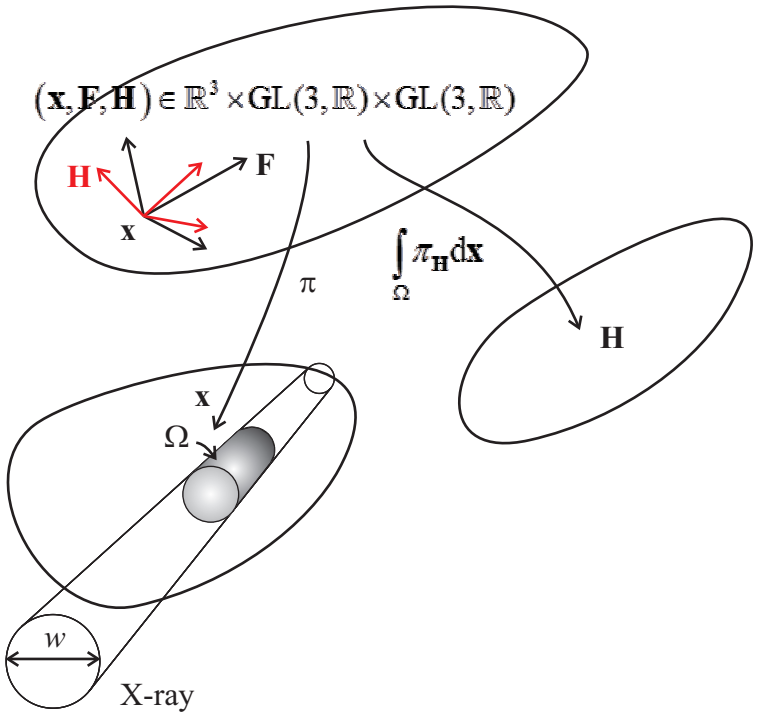

Figure 3.12: Fiber bundle picture of X-ray diffraction. The X-ray beam has finite width w. This means that the projection $\pi_{\mathbf{H}}$ probed by X-ray diffraction is really the projection $\int_{\Omega(w)} \pi_{\mathbf{H}}$ over a finite volume of material $\Omega(w)$ in the base space.

3.3 Experimental - practical application

In this section details of the X-ray diffraction procedure used in this study are described. We present data from several experiments performed at the Advanced Photon Source, Sector 1-ID, Argonne National Lab. These experiments represent current state of the art capabilities in high energy X-ray diffraction.

We previously made the analogy between X-ray diffraction measurements and electrical resistance strain gauges. The reading of the X-ray diffraction 'gauge' is more complicated than for the resistance strain gauge and hence requires the background development we cover in this section. Although numerous software programs exist for analyzing X-ray diffraction data of this sort (Gotz et al., 2000; Oddershede et al., 2010), the type of measurements taken for this work required the writing of in house codes and analytical software tools. For instance, a major undertaking for this thesis was spent developing analytical software tools to analyze the data taken from such experiments in unexplored directions: quantifying experimental precision and developing a modeling approach to quantify intragranular texture of single grains in a polycrystal.

The experimental technique which will be focused on is a far field technique, which uses high energy, monochromatic X-rays, (50-100 keV) produced by a synchrotron source. In simplified terms, the outputs of the experiments in this study are the grain averaged measurements of the lattice deformation $\mathbf{H}$. See §3.2 for general background on X-ray diffraction, and Chapter 2 for background on elastic-plastic deformation. We are also able to obtain estimates for the grain averaged center of mass position, useful for reconstruction of the polycrystalline configuration.

We begin with an introductory level overview of the particular class of X-ray diffraction experiment used in this study. We will describe how one converts from the raw diffraction data, the electromagnetic field intensity, to an estimate for the local lattice deformation. We refer to this conversion from raw data to useful physical estimates as the data reduction process. The diffraction images files are large $O(\text{GB})$ and hence impractical to use in a raw state, hence the term data reduction has relevance. We give a detailed exposition of the relationship between observed diffraction peaks and reciprocal lattice vectors. We also give a brief discussion of grain indexing methods and illustrate a novel algorithm for indexing a polycrystal. We also discuss general considerations of the lattice refinement procedure for estimating grain averaged deformation from the X-ray measurements, as these procedures differ between crystallographers and mechanics researchers.

3.3.1 XRD experiment overview

Generally stated, for our goals the purpose of an X-ray diffraction experiment is to obtain the lattice deformation $\mathbf{H}$ of the crystal lattice, with respect to a fixed lattice configuration. The electromagnetic field intensity diffracted by the material is the primitive experimentally measured quantity which must be analyzed to obtain this output. In §3.2 we described how

the spatial state of the atomic configuration affects the X-ray diffraction pattern, and we derived the reciprocal lattice description. In this section, we will describe how one converts from the raw diffraction data, the electromagnetic field intensity, (see Equation (3.122)) to an estimate for the local lattice deformation. We refer to this conversion from raw data to useful physical estimates as the data reduction procedure. This procedure involves many steps which will each be explained in this section. We introduce a generic coordinate system, useful for describing X-ray diffraction patterns, in order to facilitate quantitative descriptions.

3.3.1.1 General procedure.

In this section, an overview of standard methodologies for reducing data from raw diffraction images to lattice structure information is given. In addition to general background information, this exposition motivates the structure of the uncertainty analysis presented in §3.4.2.1. In that section, uncertainty in the data at each step affects results derived from that data, hence the hierarchical nature of the reduction procedure is emphasized here.

We specialize the foregoing discussion of X-ray diffraction experiment procedure to the rotating crystal method (Milch and Minor, 1974; Cullity, 1978; Kabsch, 1988). Although the details of experimental setups may vary from the setup used here, the general nature of the treatment given in this particular case should serve as an example of the sort of computations which must be undertaken in processing data from any X-ray diffraction experiment.

Before describing the experimental setup, we recall an important consideration for the rotating crystal method. As described previously, in §3.2, for monochromatic radiation the Ewald sphere is defined by the incident beam, $\mathbf{s}_0$ and the wavelength λ, see Figure 3.3. The orientation of $\mathbf{s}_0$ with respect to the sample must be changed in order to allow more reciprocal vectors to pass through the Ewald sphere surface, and thereby be observed as a diffraction peak, see Figures 3.3-3.4. Physically rotating the crystal (instead of moving the beam) is the easiest way to accomplish this procedure; more will be said shortly. Lastly, we consider high energy (50-100 keV) X-rays, which have the effect of compressing the Bragg angles to a small solid angle, so that a two dimensional detector may be used to record much of the reciprocal space of the lattice (Poulsen et al., 1997; Poulsen, 2004). This compression has the consequence of relatively poor reciprocal space precision, so that uncertainty analysis is an important consideration. There are benefits to using high energy X-rays as well. For one, deeper penetration into the material is possible, so that bulk deformation processes can be probed by the method.

The main steps in the data reduction we consider are

1. assigning locations to the diffraction peaks (peak detection),
2. indexing the resulting dataset of peak locations to lattice orientations (grain indexing)
3. refining the parameters which characterize the lattice orientation and stretch, the deformation parameters (lattice refinement).

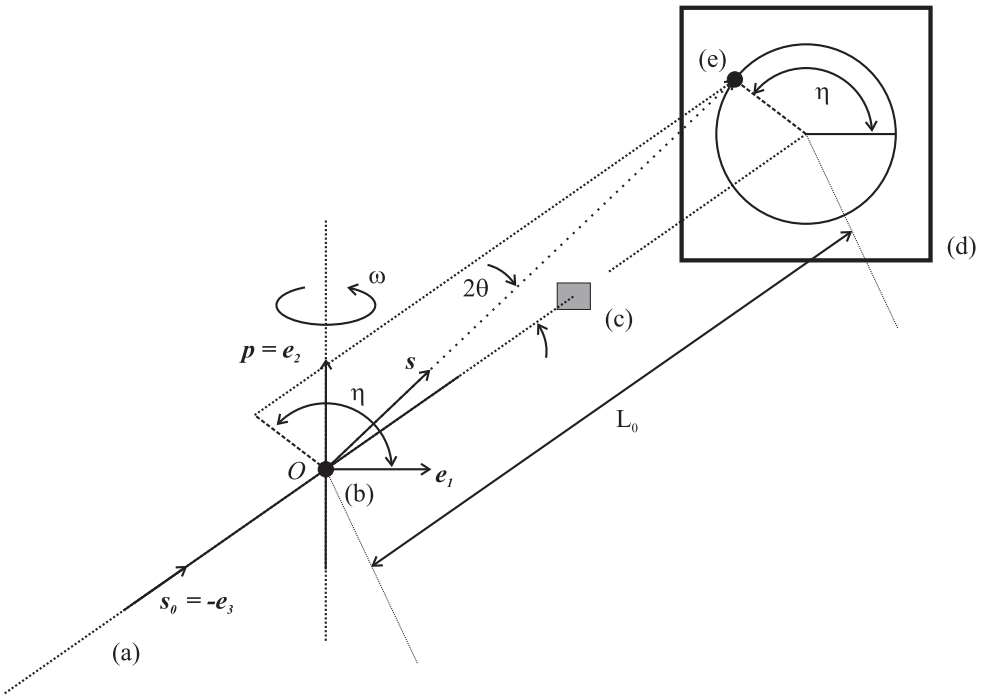

Figure 3.13: Experimental setup for far field, high energy, monochromatic X-ray diffraction. (a) X-ray beam with wavelength λ, direction $\mathbf{s}_0 = -\mathbf{e}_3$, (b) sample, mounted on rotation stage with rotation axis $\mathbf{p} = \mathbf{e}_2$, and rotation coordinate ω, (c) beam stop, (d) detector, at a distance L_0 from the rotation axis, (e) diffraction peak corresponding to a diffracted beam with unit direction $\mathbf{s}(2\theta, \eta)$.

We now describe each of these steps in greater detail, beginning with a general experimental setup.

3.3.1.2 Lab geometry.

A schematic experimental setup is shown in Figure 3.13. Only major aspects of this figure will be described in this section, further details will be given in §3.3.2. The components of the experiment are the X-ray beam (a), the sample, mounted on a rotation stage (b), the beam stop (c), and an area detector (d). A diffraction peak is indicated at (e). The incident beam propagates in the direction $\mathbf{s}_0 \equiv -\mathbf{e}_3$ with wavelength λ. The rotation stage has rotation axis $\mathbf{p} \equiv \mathbf{e}_2$, and the angular rotation about that axis, induced by a stage motor, is denoted by the coordinate ω. The intersection of the rotation axis and the beam center is denoted O. In the general case, the center of mass of the sample may be precessed with respect to the rotation axis, see Bernier et al. (2011) for further details required to handle this situation. Precession is also addressed later in this chapter.

The detector is positioned a known position relative to O, and has a known orientation,

e.g. in Figure 3.13 the detector is spanned by $(\mathbf{e}_1, \mathbf{e}_2)$. The distance and orientation of the detector are estimated from a calibration procedure by using the powder diffraction pattern from a material such as LaB_6, see (Bernier et al., 2011) for further details on the detector calibration. Typically the distance to the center of the detector is described along the beam direction, so that the detector is a distance L_0, from O along $\mathbf{s}_0$. For our experiments, L_0 is on the order of 1 meter.

The detector consists of an array of X-ray sensitive pixels. In our experiments the size of an individual pixel is approximately 200 μm. As the sample is rotated through an amount $\delta\omega$, incident radiation diffracted by the sample is recorded by the pixels. We refer to the intensity recorded by the pixel, integrated over an increment of rotation, $\delta\omega$, as the integrated intensity. The magnitude of $\delta\omega$ used is determined by experimenter choice apart from hardware limitations at small $\delta\omega$. Typically, $\delta\omega$ increments are chosen from the range $\delta\omega \in [0.25, 1]$ degrees.

We now break down the steps in the data reduction.

3.3.1.3 Raw data collection

The pixel data recorded after each $\delta\omega$ step constitutes a two dimensional array of integrated intensity values, each array is referred to here as a diffraction image. See Figure 3.14 for an example of a diffraction image from a polycrystalline titanium alloy. These images are recorded for a specified range of rotation angles, $\omega \in [\omega_0, \omega_\mathrm{f}]$, where ω_0 is the starting position for the scan, and ω_f is the final position of the scan.

The entire set of images obtained for the chosen scanning range of ω constitutes what will be referred to as the detector image stack. Define $\Delta\omega = \omega_\mathrm{f} - \omega_)$. Then, for example, there are $\Delta\omega/\delta\omega$ images like that in Figure 3.14 constituting the detector image stack. These images are recorded for a specified range of rotation angles ω. Note that a complete scan of the reciprocal lattice would require $\omega \in [0, \pi)$. This range may be restricted based on experimental factors such as if a load frame is in use, which would prevent a full $\omega \in [0, \pi)$ scan. In radial diamond anvil cell experiments, which may be the most angular-restrictive experiment in common use, $\omega \in [0, 2\pi/3]$ is still readily possible with special design of the diamond anvil cell. In the experiments presented later on, a tensile load frame was used, which was restricted to $\omega \in [0, 2\pi/3]$.

3.3.1.4 Peak detection.

The detector image stack described in the previous paragraph, an element of which is shown in Figure 3.14, represents the fundamental layer of diffraction data. The information encoded in this data can be concisely described by a field of integrated intensity over image stack coordinates as

$$E = E(p_1, p_2, \omega), \tag{3.158}$$

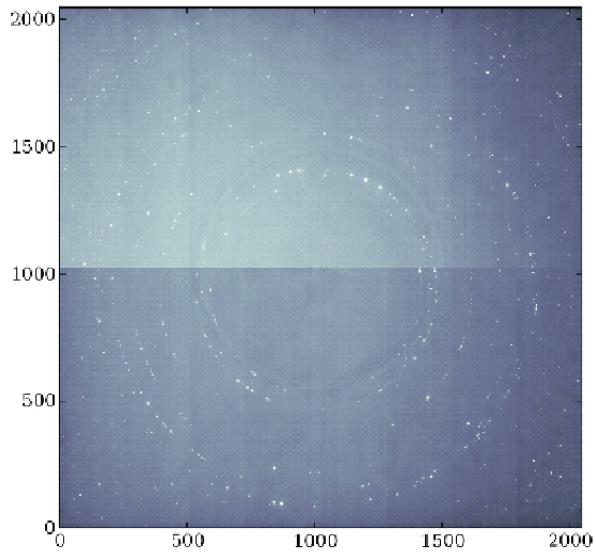

Figure 3.14: An example image of the diffraction data from a single $\delta\omega$ step. This image is from polycrystalline titanium. The x and y values represent pixel coordinates on the 2048 by 2048 detector.

where E is the integrated intensity and p_1, p_2 denote general position coordinates on the detector plane. In the peak detection step, the integrated intensity field is searched for peaks; that is, where the recorded intensity is above some chosen threshold value,

$$E(p_1, p_2, \omega) > E_{\min},$$

where $E_{\min}$ is the threshold intensity specified by the data analyst. The value of $E_{\min}$ can be chosen to suppress unwanted background signals for example. The peaks with intensity above the threshold value are then located and isolated from each other, substantially reducing the size of the dataset.

Next, the data contained in each individual diffraction peak is (usually) further reduced by fitting a local intensity distribution to a model. Conventional methods require simply computing the intensity weighted average of the distribution, however we use a slightly more informative approach. We describe the diffraction peak model we employed in greater detail in §3.4.2.1. At this stage it is sufficient to understand that upon fitting the intensity distribution to a model, the location of the center of the i^{th} peak is expressed by an array of three numbers $(\bar{p_1}, \bar{p_2}, \bar{\omega})^{(i)}$. In §3.3.3 we will show how these coordinates are related to a reciprocal lattice vector $\mathbf{g}^{(i)}$, which contains kinematic information about the state of strain in the crystal.

3.3.1.5 Indexing and fitting lattice deformation.

After the centers of all diffraction peaks in the image stack are obtained, giving the set $\{(\bar{p_1}, \bar{p_2}, \bar{\omega})^{(i)} : i = 1, 2, ..., N_{\text{peaks}}\}$, we assign peaks to grains until all peaks are processed. This is known as indexing the pattern, and is generally a challenging task for the case of a polycrystal. See Lauridsen et al. (2001); Poulsen (2004) for further information on indexing techniques.

The set of diffraction peaks assigned to a particular lattice orientation constitutes the input data for obtaining the lattice deformation parameters, i.e., the orientation and stretch of the lattice. As established in §2.2.1, the orientation and stretch parameters we are characterizing are the components of a linear transformation from a chosen reference configuration, $\boldsymbol{\kappa}$, into the current configuration where diffraction was observed. This transformation may be denoted $\mathbf{H}_{\boldsymbol{\kappa}}$ to emphasize the dependence on the reference lattice $\boldsymbol{\kappa}$. For elastic deformations, the transformation $\mathbf{H}_{\boldsymbol{\kappa}}$ is equivalent to the deformation gradient, (Liu, 2002)

$$\mathbf{F}_{\boldsymbol{\kappa}} = \text{Grad}_{\boldsymbol{\kappa}}\, \mathbf{y} = \frac{\partial y^i}{\partial x^j} \mathbf{e}_i \otimes \mathbf{e}_j, \quad i, j = 1, 2, 3, \tag{3.159}$$

where $\mathbf{x} = x^i \mathbf{e}_i$ denotes position of a material point in the reference configuration, and $\mathbf{y} = y^i \mathbf{e}_i$ denotes position of the same material point in the physical configuration. However for plastic deformations, $\mathbf{H}_{\boldsymbol{\kappa}}$ is not the gradient of a deformation (see Chapter 2, so (3.159) can't be directly applied for such cases. The parameters for $\mathbf{H}_{\boldsymbol{\kappa}}$ are obtained by a procedure called lattice refinement; more details of this procedure which will be explained later in this section.

Upon obtaining $\mathbf{H}_{\boldsymbol{\kappa}}$ for a particular grain, the data reduction is complete. One may obtain stresses from $\mathbf{H}_{\boldsymbol{\kappa}}$ measurements by using an elasticity model for the material under consideration. For example, the Piola stress with respect to κ, $\mathbf{P}_{\kappa}$ may be obtained by specifying a strain energy function, $W_{\kappa}(\mathbf{H})$ for the material and computing

$$\mathbf{P}_{\kappa}(\mathbf{H}) = \frac{\partial W_{\kappa}}{\partial \mathbf{H}}(\mathbf{H}). \tag{3.160}$$

In the rest of the section all quantities can be assumed to be dependent upon choice of κ and we suppress the subscript.

3.3.1.6 Summary.

We summarize the data reduction process in the following flowchart:

$$E(p_1, p_2, \omega) \mapsto \left\{ (\bar{p_1}, \bar{p_2}, \bar{\omega})^{(i)} \right\},\ i = 1, ..., N_{\text{peaks}} \mapsto \left\{ H_{ij}^{(k)} \right\},\ k = 1, ..., N_{\text{grains}}, \tag{3.161}$$

where $E(p_1, p_2, \omega)$ is the intensity distribution in the image stack, $(\bar{p_1}, \bar{p_2}, \bar{\omega})^{(i)}$ are parameters which represent the location of the i^{th} diffraction peak, and $H_{ij}^{(k)}$ are the i, j components

of the lattice deformation for the k^{th} grain. Experimental variance at the first layer of data, $E(p_1, p_2, \omega)$, will affect the uncertainty in the peak center, $(\bar{p_1}, \bar{p_2}, \bar{\omega})$, which will affect the uncertainty in the lattice deformation parameters, the H_{ij}. One of our goals in this chapter is to implement a framework which systematically communicates uncertainty from the diffraction intensity to the overall lattice deformation parameters, and to be able to state confidence intervals for the lattice deformation parameters based on a single rotation scan through a range of ω. The uncertainties on the components H_{ij} can then be used to form confidence intervals on quantities derived from $\mathbf{H}$, such as orientation relationships and stresses, (3.160). Having confidence intervals on orientation relationships and stresses directly influences the strength of conclusions that experimentalists can draw from their observations, and completes the experimental program.

In the next sections we describe the data reduction steps introduced here in more details. First we introduce a coordinate system which is natural to use for analysis of this class of X-ray diffraction experiments. This coordinate system naturally parametrizes the location of diffraction peaks, and hence, parametrizes reciprocal space. We will first describe the coordinate system, and then give a general derivation of the conversion from this coordinate system to reciprocal space. We will then describe indexing procedures and techniques. Finally we will describe further details of the lattice refinement.

3.3.2 Angular coordinates

In this section we introduce an angular coordinate system which is useful for describing the location of diffraction peak intensity distributions. We again consider the experimental geometry shown in Figure 3.13, where the detector panel has been aligned so that its surface is spanned by the vectors $\{\mathbf{e}_1, \mathbf{e}_2\}$. Note that in general, these vectors may not be the same as the global Cartesian basis $\mathbf{e}_1, \mathbf{e}_2$. We consider the aspect of detector tilt in §3.3.3. Incident radiation (a) propagates in a direction $\mathbf{s}_0 = -\mathbf{e}_3$, with wavelength λ. For simplicity consider the case of a grain centered at the intersection of the rotation axis and beam at O, (b). We will provide the analysis for the more general case of a precessed grain in §3.3.3. A diffraction peak (e) is indicated on the detector (d). The unit vector representing the direction of the diffracted beam, $\mathbf{s}$, is conveniently parametrized with a spherical polar coordinate system constructed on the bases $(-\mathbf{e}_3, \mathbf{e}_1, \mathbf{e}_2)$. The azimuth is measured from $-\mathbf{e}_3$ and is denoted 2θ, and polar angle from $\mathbf{e}_1$ is denoted η, so that we have

$$\mathbf{s}(2\theta, \eta) = \cos(2\theta)(-\mathbf{e}_3) + \sin(2\theta)(\cos\eta\mathbf{e}_1 + \sin\eta\mathbf{e}_2). \tag{3.162}$$

Note that the azimuthal angle 2θ also serves as the Bragg angle in the classical Bragg's law

$$2d^{(i)}\sin\theta^{(i)} = \lambda, \tag{3.163}$$

where $d^{(i)}$ is the planar spacing on the i^{th} plane and $\theta^{(i)}$ is the Bragg angle for this plane.

Proof. This can be seen by using the diffraction condition in the form (Boumann, 1957)

$$\frac{\mathbf{s}-\mathbf{s}_0}{\lambda} = \mathbf{g}^i, \tag{3.164}$$

where $\mathbf{g}^i$ is the i^{th} reciprocal lattice vector. Using the relation

$$\mathbf{g}^i \cdot \mathbf{g}^i = \left(d^{(i)}\right)^{-2}, \tag{3.165}$$

and taking inner products of both sides of (3.164) gives

$$\begin{aligned} \frac{\lambda^2}{d^2} &= (\mathbf{s}-\mathbf{s}_0)\cdot(\mathbf{s}-\mathbf{s}_0) \\ &= 4\sin^2\theta, \end{aligned} \tag{3.166}$$

where we have used $\mathbf{s}\cdot\mathbf{s}_0 = \cos 2\theta = 1 - 2\sin^2\theta$ in obtaining (3.166). Simplification of (3.166) recovers Bragg's law in the form (3.163). □

Motivation for introducing these angular coordinates is evident when the diffraction peaks are spread out due to intragranular mosaicity. An example diffraction peak is shown in Figure 3.15. The order of the tiles in the figure is such that the ω-location of the diffraction image increases from left to right and top to bottom. Such curved peaks with spread along the angular coordinate directions become approximately ellipsoidal distributions of intensity in angular coordinates. Loosely, the spreading of a diffraction peak along the η direction, as

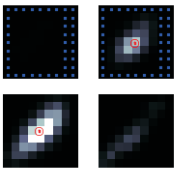

Figure 3.15: Image of a spot spread out in angular coordinates. The ω frames allocated to the peak are also shown in increasing order, from left to right and top to bottom.

in Figure 3.15, is due to the presence of spatial gradients in the orientation of the crystal. Spreading along the 2θ direction corresponds to gradients in the lattice strain. It is noteworthy that conventional methods of diffraction peak analysis do not differentiate between peaks that are spread out and peaks which remain tight - for both cases, the intensity weighted average is used. There is clearly potentially useful microstructural information in the nature in which the peaks may be spread out. In §3.4 we give two different approaches which seek to utilize this information.

In the next section we describe in detail how one may transfer between angular coordinates of a peak $(2\theta, \eta, \omega)^{(i)}$and a reciprocal lattice vector $\mathbf{g}^{(i)}$. This transfer is the first

step in the data reduction where error propagation should be considered, since identifying a particular location to the peak in Figure 3.15 must necessarily come with some uncertainty in that location. The process of converting to a reciprocal vector also involves calibration constants representative of the experimental setup, whose uncertainty also contributes to the final uncertainty in the components of the reciprocal vector.

3.3.3 Conversion to reciprocal space coordinates

In this section we give a treatment of the conversion between the spatial location of a diffraction peak and its preimage in reciprocal space. The motivation for including this section is that it is common in the crystallography literature to give confusing algebraic formula with a low degree of what we would call, 'invariance of application'; that is, the type of information which can be applied to different situations which may differ from those presented in the literature contributions. Here, we use a concise geometric construction, so that those with comfort in direct vector notation can readily apply the following relations for their particular geometry.

In addition to the two dimensions used to describe diffraction peaks in the previous section, p_1, p_2 or $2\theta, \eta$, the experimental stage rotation coordinate ω is appended to fully parametrize the observation of diffraction peaks[5]. Aspects of this stage rotation were described in §3.3.1.1. In this section we also account for grains offset from the rotation axis, so that the grain averaged center of mass location is denoted by $\mathbf{x} = \hat{\mathbf{x}}(\omega)$. Incorporating the stage rotation, whose action is denoted by $\mathbf{Q}$, and the precession, and consulting Figure 3.13, the position of a diffraction peak relative to O may be written as

$$\mathbf{r} = \mathbf{Q}(\mathbf{p}, \omega)\mathbf{x}_0 + \rho\mathbf{s}(2\theta, \eta), \tag{3.167}$$

where $\mathbf{r}$ is the spatial position of the diffraction peak relative to O, $\mathbf{Q}(\mathbf{p}, \omega)$ is the stage axis rotation about $\mathbf{p}$ with angular coordinate ω, and $\mathbf{x}_0$ is the position of the diffracting material at $\omega = \omega_0$, some reference ω location, ρ is the spatial distance between the diffracting material (grain center-of-volume) at the ω location of the observation, and $\mathbf{s}$ is the unit vector describing the direction of the diffracting beam relative to the ω location of the observation. We suppress the functional dependencies for $\mathbf{Q}$, $\mathbf{s}$, and ρ in the rest of this section for reasons of appearance. Also note that in (3.167) we are using slightly different angular coordinates than that depicted in Figure 3.13: here the angles $2\theta, \eta$ are defined with respect to the current grain position $\mathbf{x} = \mathbf{Q}\mathbf{x}_0$ instead of the intersection of the rotation axis and the beam, O.

[5]It bears repeated that for a diffraction peak as shown in Figure 3.15, describing the location of the diffraction peak by a three dimensional parametrization $2\theta, \eta, \omega$ is associated with some loss of information, and some uncertainty in the precise location of the peak. This uncertainty will then be communicated to the lattice deformation estimate. We will examine the effect of this peak location uncertainty in §3.4.2.1. We will also describe an approach to analyzing more of the local integrated intensity, using a forward model prediction of the lattice state, in §3.4.2.2.

Consider the rectangular pixel array constituting detector to be aligned with the orthonormal basis $\mathbf{e}'_1, \mathbf{e}'_2$, which generally differ from the laboratory basis $\mathbf{e}_1, \mathbf{e}_2$ due to errors in beam-detector alignment. The detector basis is related to the laboratory basis by

$$\mathbf{e}'_{\mathrm{i}} \equiv \mathbf{R}_{\mathrm{t}} \mathbf{e}_{\mathrm{i}},$$

where $\mathbf{R}_{\mathrm{t}} \in \mathrm{SO}(3, \mathbb{R})$ is the tilt of the detector panel. $\mathbf{R}_{\mathrm{t}}$ is described by a parametrization of $\mathrm{SO}(3, \mathbb{R})$, written as $\mathbf{R}_{\mathrm{t}} = \hat{\mathbf{R}}_{\mathrm{t}}(t_1, t_2, t_3)$. The detector image stack is parametrized by p_1, p_2, ω. Positions of peaks in the detector image stack, (p_1, p_2, ω) are related to $(2\theta, \eta, \omega)$ coordinates by the geometrically equivalent statements

$$\mathbf{r} = p_1 \mathbf{e}'_1 + p_2 \mathbf{e}'_2 + L_0(-\mathbf{e}_3) = \|\mathbf{r}\| \left[\cos 2\theta(-\mathbf{e}_3) + \sin 2\theta(\cos\eta \mathbf{e}_1 + \sin\eta \mathbf{e}_2)\right], \tag{3.168}$$

where $\|\mathbf{r}\| = \sqrt{\mathbf{r} \cdot \mathbf{r}}$ is the spatial distance between O and the detector position (p_1, p_2) are defined relative to the beam location on the detector (projection of O along $\mathbf{s}_0$ on the detector). Given the p_1, p_2 location of the peak, the functions $\eta = \hat{\eta}(p_1, p_2, L_0), 2\theta = 2\hat{\theta}(p_1, p_2, L_0)$ can be solved for by taking inner products of (3.168) with $\mathbf{e}_1, \mathbf{e}_3$ in succession and solving the resulting equations.

Next we relate the position of a peak $\mathbf{r}$ to the reciprocal space vector preimage, $\mathbf{g}^{(i)}$. There is much geometric information contained in Equation (3.167). First consider the inner product with the incidence beam direction $\mathbf{s}_0 \equiv -\mathbf{e}_3$. To avoid cluttering the equations, let us consider the effect of no detector tilt, so that $\mathbf{r} \cdot \mathbf{s} = L_0$, from $(3.168)_1$. We obtain

$$\begin{aligned} \mathbf{r} \cdot \mathbf{s}_0 = \mathbf{Q}\mathbf{x}_0 \cdot \mathbf{s}_0 + \rho \mathbf{s} \cdot \mathbf{s}_0 \implies \\ L_0 = \mathbf{Q}\mathbf{x}_0 \cdot \mathbf{s}_0 + \rho \cos 2\theta. \end{aligned} \tag{3.169}$$

Furthermore, solving for ρ and noting that $\|\mathbf{s}\| = 1$ we have

$$\rho = \|\mathbf{r} - \mathbf{Q}\mathbf{x}_0\|. \tag{3.170}$$

The parametrization of the stage rotation $\mathbf{Q}$ can be profitably written as

$$\mathbf{Q} = \mathbf{e}_2 \otimes \mathbf{e}_2 + (\mathbf{e}_1 \otimes \mathbf{e}_1 + \mathbf{e}_3 \otimes \mathbf{e}_3) \cos\omega - (\mathbf{e}_3 \otimes \mathbf{e}_1 - \mathbf{e}_1 \otimes \mathbf{e}_3) \sin\omega. \tag{3.171}$$

Next consider the diffraction requirements that for diffraction to occur, a reciprocal vector must lie on the Ewald sphere, see §3.2. Therefore a diffraction peak, located by $\mathbf{s}$ must satisfy

$$\frac{\mathbf{s} - \mathbf{s}_0}{\lambda} = \mathbf{g}^i, \tag{3.172}$$

where $\mathbf{g}^i$ is a reciprocal lattice vector in the current (rotated by $\mathbf{Q}$) state of the crystal. At the reference location $\omega = \omega_0$ we have the relation

$$\mathbf{g}^i = \mathbf{Q}\mathbf{g}^i, \tag{3.173}$$

where $\mathbf{g}^i$ is the reciprocal vector in the spatial configuration of the lattice at the reference rotation $\omega = \omega_0$. Rearranging (3.172) and use of (3.173) gives the forward model

$$\mathbf{s} = \lambda \mathbf{Q} \mathbf{g}^i + \mathbf{s}_0, \tag{3.174}$$

which will be used later in §3.4.2.2, where we simulate diffraction peak intensities based on the state of the crystal lattice (hence $\mathbf{g}^i$). Returning to the inverse problem, determining $\mathbf{g}^i(\mathbf{s}, ...)$, from (3.167), we have the geometric statement

$$\mathbf{s}(L_0, \omega, \mathbf{t}, \mathbf{x}_0, p_1, p_2) = \frac{\mathbf{r}(p_1, p_2, L_0, \mathbf{t}) - \mathbf{Q}(\omega)\mathbf{x}_0}{|\mathbf{r} - \mathbf{Q}\mathbf{x}_0|}, \tag{3.175}$$

where all functional dependencies are highlighted, $\mathbf{r}$ is given by (3.168), and $\mathbf{t} = (t_1, t_2, t_3)$. From (3.172) and (3.173) we have the relation between reciprocal space and geometry written as

$$\mathbf{g}^i(L_0, \omega, \mathbf{t}, \mathbf{x}_0, p_1, p_2, \lambda, \mathbf{s}_0) = \frac{1}{\lambda}\mathbf{Q}^{\mathrm{T}}[\mathbf{s}(L_0, \omega, \mathbf{t}, \mathbf{x}_0, p_1, p_2) - \mathbf{s}_0], \tag{3.176}$$

where $\mathbf{s}$ is given by (3.175). Clearly any error in any of the fundamental arguments L_0, ω, $\mathbf{t}$, $\mathbf{x}_0$, p_1, p_2, λ, $\mathbf{s}_0$ will lead to error in the computation of $\mathbf{g}^i$. The formula simplify when the precession is neglected, by taking $\mathbf{x}_0 = \mathbf{0}$. In that case we can use

$$\lambda \mathbf{g}^i \cdot \mathbf{p} = \mathbf{Q}^{\mathrm{T}}(\mathbf{s} - \mathbf{s}_0) \cdot \mathbf{p}, \tag{3.177}$$

and with (3.171) we have

$$\lambda \mathbf{g}^i \cdot \mathbf{p} = \mathbf{p} \cdot \mathbf{s}, \tag{3.178}$$

noting that $\mathbf{p} \equiv \mathbf{e}_2$. Then we have

$$\lambda \mathbf{g}^i_2 = \mathbf{p} \cdot \mathbf{s} = \sin 2\theta \sin \eta, \tag{3.179}$$

$$\lambda \mathbf{g}^i_1 = \mathbf{Q}^{\mathrm{T}}(\mathbf{s} - \mathbf{s}_0) \cdot \mathbf{e}_1, \tag{3.180}$$

and

$$\lambda \mathbf{g}^i_3 = \mathbf{Q}^{\mathrm{T}}(\mathbf{s} - \mathbf{s}_0) \cdot \mathbf{e}_3. \tag{3.181}$$

With the representation for $\mathbf{Q}$ in (3.171) and the spherical polar parametrization for $\mathbf{s}$ as

$$\mathbf{s}(2\theta, \eta) = \cos 2\theta(-\mathbf{e}_3) + \sin 2\theta(\cos \eta \mathbf{e}_1 + \sin \eta \mathbf{e}_2), \tag{3.182}$$

we have

$$\begin{aligned} \mathbf{Q}^{\mathrm{T}}\mathbf{s} = {} & \mathbf{e}_2 \sin 2\theta \sin \eta \\ & + \mathbf{e}_1(\sin 2\theta \cos \eta \cos \omega + \sin \omega \cos 2\theta) \\ & + \mathbf{e}_3(\sin \omega \sin 2\theta \cos \eta + \cos \omega \cos 2\theta), \end{aligned} \tag{3.183}$$

and

$$\mathbf{Q}^{\mathrm{T}}\mathbf{s}_0 = \mathbf{e}_1 \sin\omega - \mathbf{e}_3 \cos\omega. \tag{3.184}$$

Therefore

$$\mathbf{Q}^{\mathrm{T}}(\mathbf{s}-\mathbf{s}_0) = (-(1-\cos 2\theta)\sin\omega + \cos\eta\cos\omega\sin 2\theta)\mathbf{e}_1 \tag{3.185}$$

$$+ \sin\eta \sin 2\theta \mathbf{e}_2 \tag{3.186}$$

$$+ (\cos\omega(1-\cos 2\theta) + \cos\eta\sin\omega)\mathbf{e}_3. \tag{3.187}$$

So finally Equation (3.176) is established where the second factor on the right hand side is given by (3.187).

The presence of lattice deformation alters the components of the reciprocal vector, $\mathbf{g}^i$ with respect to the configuration $\boldsymbol{\kappa}$. The measured reciprocal vector $\mathbf{g}^i$ has preimage in the reference configuration, denoted $\mathbf{G}^i$. The mapping between $\mathbf{G}^i$ and $\mathbf{g}^i$ will be shown to be given by

$$\mathbf{g}^i = \mathbf{H}^{-\mathrm{T}}\mathbf{G}^i. \tag{3.188}$$

Therefore with respect to a reference configuration the forward model (3.174) becomes

$$\mathbf{s} = \lambda \mathbf{Q}(\omega)\mathbf{H}^{-\mathrm{T}}(\boldsymbol{\Theta})\mathbf{G}^i + \mathbf{s}_0, \tag{3.189}$$

where $\boldsymbol{\Theta}$ denotes parameters characterizing the deformation. In a later section we will use $\boldsymbol{\Theta} = (\mathbf{R}, \mathbf{U})$, where $\mathbf{H} = \mathbf{R}\mathbf{U}$ is the polar decomposition of the non-singular transformation $\mathbf{H}$. In a traditional crystallographers approach, $\boldsymbol{\Theta} = (\mathbf{H}_{\mathrm{s}}, \mathbf{R})$, where $\mathbf{H}_{\mathrm{s}}$ is the structural map from a reference cube to the prerotated configuration. Both approaches have $\dim \boldsymbol{\Theta} = 9$. A comparison and translation between the two methods is described in §3.3.5. For the case of a precessed grain, the use of (3.189) is combined with (3.175). The refinement problem is then over the array $\boldsymbol{\Theta} = (\mathbf{H}, \mathbf{x})$ so that $\dim \boldsymbol{\Theta} = 12$. Looking ahead, in §3.4.2.2 the list of parameters $\boldsymbol{\Theta}$ is further expanded to account for the presence of spatial inhomogeneities in the lattice deformation, $\mathbf{H} = \hat{\mathbf{H}}(\mathbf{x})$.

Once the data in the form of diffraction peaks locations have been converted to the form of reciprocal lattice vectors (e.g. components), the lattice deformation may be estimated based on the relations (3.188). Starting from the raw list of reciprocal vectors, the refinement is typically done in two steps. The methods for the two steps differ greatly from each other. This is because at the first stage of analysis, we do not know the membership correspondence between reciprocal vectors in the data and grains in the polycrystal. We only have a collection of diffraction peaks (and hence, reciprocal vectors).In other words, for each $\mathbf{g}^i$ we do not know the corresponding $\mathbf{G}^i$ in the reference lattice configuration, since such information requires knowledge of $\mathbf{H}$ through (3.188).

In the next section we will discuss the first step, called grain indexing. The function of indexing is to obtain the unknown associations between $\mathbf{g}^i, \mathbf{G}^i$. Following that, we will describe the final lattice refinement procedure which gives a finer estimate for $\mathbf{H}$, but requires the completion of grain indexing before attempting.

3.3.4 Indexing

In this section we briefly describe grain indexing procedures for the analysis of X-ray diffraction data. Grain indexing algorithms are an interesting topic of applied mathematics in their own right, but are a vital component for diffraction experiments when the states of single crystals must be independently distinguished from a polycrystal. From a semantic point of view, we can describe the indexing program as coarse lattice refinement, in that we obtain an estimate for the rotation component, $\mathbf{R}$ of $\mathbf{H} = \mathbf{RU}$. The final stage of lattice refinement is discussed in §3.3.5, but indexing must be performed for the final refinement to be possible. The primary task of the indexing step is creating the pairs $\left(\mathbf{G}^i, \mathbf{g}^i\right)$, between reciprocal lattice vectors in the configuration $\boldsymbol{\kappa}$ and the current configuration, at a reference state of the rotation stage, $\mathbf{Q} = \mathbf{Q}(\omega_0)$. This process is easier in terms of computational algorithms with a single grain than for a polycrystal (< 1000 grains) but the procedures are the same for both.

We briefly summarize conventionally deployed indexing algorithms, and suggest a proposed novel formulation. Conventional methods are generally excellent; the different formulation is given here mostly as an interesting example of applications of the geometry of orientation space.

3.3.4.1 Standard indexing method.

In §3.3.1.1 and §3.3.3 we described how raw diffraction data is transformed into reciprocal vectors. The reciprocal vector data is then the fundamental data for the indexing algorithm. The X-ray diffraction data set is then written

$$M = \{\mathbf{g}^i : \mathrm{i} = 1, 2, ..., N_{\mathrm{obs}}\},$$

where N_{obs} is the number of observed reciprocal lattice vectors in the entire sample.

A hypothetical indexing procedure can be stated as follows. First, define the set of observable reciprocal lattice vectors in $\boldsymbol{\kappa}$ by

$$H \equiv \{\mathbf{G}^i, \mathrm{i} = 1, 2, ..., N_{\mathrm{refl}}(\lambda)\},$$

where $N_{\mathrm{refl}}(\lambda)$ emphasizes the dependence of the size of the observable reference lattice on the chosen wavelength. This definition is meaningful because lattice strains are generally small, otherwise the observable set would be dependent upon the lattice strain.

Then, for each $\mathbf{H} \in \mathrm{GL}(3, \mathbb{R})$, test the data set M for the membership

$$\mathbf{H}^{-\mathrm{T}}\mathbf{G}^i \in M \tag{3.190}$$

for all observable $\mathbf{G}^i \in H$. Since this is experimental data, the condition in (3.190) must involve some tolerance, denoted by tol. Then the indexing problem is stated as determining the set

$$\{\mathbf{H} : \text{for } \mathbf{G}^i \in H : \|\mathbf{H}^{-\mathrm{T}}\mathbf{G}^i - \mathbf{g}^i\| < \mathrm{tol}\}, \tag{3.191}$$

where $\|\cdot\|$ is an appropriate norm (the Euclidean norm is fine). The function evaluations prescribed by Equation (3.191) is prohibitively expensive to compute - the space $\dim \mathrm{GL}(3,\mathbb{R}) = 9$ is large. However since elastic deformations are typically small, we can simplify the search space by taking $\mathbf{H} \approx \mathbf{R}$, where $\mathbf{R} \in \mathrm{SO}(3,\mathbb{R})$. Then since $\dim \mathrm{SO}(3,\mathbb{R}) = 3$, the computational search space is tractable. Considerations of material symmetry further reduce the size of the space which must be probed.

We summarize the above indexing problem in words: rotation space $\mathrm{SO}(3,\mathbb{R})$ is parametrized via Euler angles or angle axis parameters, and we search this space for rotations which have good agreement between the mapped reference configuration reciprocal vectors $\mathbf{H}^{-\mathrm{T}}\mathbf{G}^i$ and the observed reciprocal vectors $\mathbf{g}^i$. The indexed set is written

$$\{\mathbf{H} : \mathbf{H} \in \mathrm{SO}(3,\mathbb{R}), \text{and for } \mathbf{G}^i \in H : \|\mathbf{H}^{-\mathrm{T}}\mathbf{G}^i - \mathbf{g}^i\| < \mathrm{tol}\}. \tag{3.192}$$

One approach to practically solving the indexing problem is clearly a brute force method: discretize the three dimensional rotation space with some chosen resolution, and test each nodal point in the discretized space for agreement with the data. Here 'agreement' is determined by: for each trial $\mathbf{H}$, the percentage of $\mathbf{G}^i \in H$ which are found to have images in M. If agreement is above a threshold of completeness, remove the matched reciprocal vectors from M and continue. A typically used threshold might be 75%. For polycrystals, results of the indexing can be sensitive to tolerances on testing the membership condition $\mathbf{H}^{-\mathrm{T}}\mathbf{G}^i \in M$. Too stringent of a tolerance and zero grains may be found, too loose a tolerance and many spurious grains may be found in the data, leading to erroneous results.

As an alternative, we next present an approach which is based on calculation of the distance between two orientation fibers. If the fibers intersect, this point defines a trial orientation to test for completeness, (3.192). Essentially, the fiber intersection in this approach boils down to computing eigenvalues of a 2×2 matrix, which, at least on simulated data, is faster than the other indexing methods which require some notion of discretization and subsequent probing of some space.

3.3.4.2 Alternate indexing approach - introduction.

In the following treatment, we will denote $\mathbf{R}_{\mathrm{g}} \in \mathrm{SO}(3,\mathbb{R})$ as the orientation of the grain we are seeking to determine. As stated in the previous section, given an arbitrary measured reciprocal vector $\mathbf{g}^i$, we can extract the possible family of reciprocal vectors in the reference lattice configuration by knowledge of the reference crystal structure, which gives the set of $\{\mathbf{G}^i\}$, the reciprocal vectors characteristic of that particular structure. Specifically, the magnitude of the measured vector $\mathbf{g}^i$ can be used to subset the possible $\mathbf{G}^i$ which have the same magnitude and are possible generators for that particular measured vector through the mapping $\mathbf{g}^i = \mathbf{R}_{\mathrm{g}}\mathbf{G}^i$. Note that $\mathbf{R}_{\mathrm{g}} \in \mathrm{SO}(3,\mathbb{R}) \implies \mathbf{R}_{\mathrm{g}}^{-\mathrm{T}} = \mathbf{R}_{\mathrm{g}}$, when applying (3.188).

Next, given a potential correspondence $\mathbf{G}^i \to \mathbf{g}^i$ we can generate a one parameter family of rotations which give identically the correspondence $\mathbf{G}^i \to \mathbf{g}^i$. We can see this by observing

that the set

$$R = \{\mathbf{R}_s : \mathbf{R}_s \mathbf{G}^i = \mathbf{g}^i\} \tag{3.193}$$

has $|R| > 1$ To see this, given an $\mathbf{R}_s$ which satisfies (3.193) we can operate by a second rotation with rotation axis $\mathbf{g}^i$ without changing the result, e.g. the equation

$$\mathbf{g}^i = \hat{\mathbf{R}}(\mathbf{g}^i, \theta)\mathbf{R}_s \mathbf{G}^i \tag{3.194}$$

is valid for any value of θ. Here recall that the function $\hat{\mathbf{R}}(\mathbf{g}^i, \theta)$ is the rotation tensor with rotation axis being the unit vector parallel to $\mathbf{g}^i$, and with rotation angle θ, see (A.5). We can construct an rotation $\mathbf{R}_s$ which satisfies (3.193) in a unique way by computing a rotation taking $\mathbf{G}^i$ to $\mathbf{g}^i$ as the rotation about the axis defined by $\mathbf{G}^i \times \mathbf{g}^i$ with rotation angle $\cos^{-1}(\hat{\mathbf{G}}^i \cdot \hat{\mathbf{g}}^i)$. Define this rotation by $\mathbf{R}_{\text{base}}(\mathbf{G}^i, \mathbf{g}^i)$. In terms of angle axis parameters

$$\mathbf{R}_{\text{base}}(\mathbf{G}^i, \mathbf{g}^i) = \hat{\mathbf{R}}(\mathbf{G}^i \times \mathbf{g}^i, \cos^{-1}(\hat{\mathbf{G}}^i \cdot \hat{\mathbf{g}}^i)). \tag{3.195}$$

We can then operate on the rotation $\mathbf{R}_{\text{base}}$ by a rotation with axis $\mathbf{g}^i$ and any rotation angle $\theta \in [0, 2\pi]$. The result of this combination is a one parameter family of rotations which map $\mathbf{G}^i \to \mathbf{g}^i$. In other words, we have the family of rotations satisfying $\mathbf{g}^i = \mathbf{R}_{\text{test}}\mathbf{G}^i$ where

$$\mathbf{R}_{\text{test}}(\theta; \mathbf{G}^i, \mathbf{g}^i) = \hat{\mathbf{R}}(\mathbf{g}^i, \theta)\mathbf{R}_{\text{base}}(\mathbf{G}^i, \mathbf{g}^i). \tag{3.196}$$

The family of rotations parametrized by (3.196) is called an orientation fiber. The question of grain indexing previously stated thus can be restated as: given two measured reciprocal vectors, $\mathbf{g}^1$, $\mathbf{g}^2$, and two possible generator reciprocal vectors for those measurements, $\mathbf{G}^1$, $\mathbf{G}^2$, does there exist, for each fiber $\mathbf{R}_{\text{test}_i}(\mathbf{G}^i, \mathbf{g}^i), i = 1, 2$, a point of intersection between the two one parameter families of rotations. That is, for some θ_1, θ_2 along the two respective fibers, (3.196), do we have

$$\mathbf{R}_{\text{test}_1}(\theta_1) =? \mathbf{R}_{\text{test}_2}(\theta_2). \tag{3.197}$$

If (3.197) is true, then there is evidence to suggest that there exists a grain with $\mathbf{R}_g = \mathbf{R}_{\text{test}1}(\theta_1) = \mathbf{R}_{\text{test}2}(\theta_2)$. The data structure M can then be probed by this $\mathbf{R}_g$ to see if the completeness condition is met at this intersection point.

We now reduce the problem of fiber intersections to determining the eigenvalues of a 2 by 2 matrix. Here we use quaternion geometry for describing elements of $\text{SO}(3, \mathbb{R})$. The quaternions have a one-to-one correspondence with S^3, the unit sphere in $\mathbb{R}^4$, and doing all operations in $\mathbb{R}^4$ lends some profitable reductions in the problem formulation. Therefore, from here on, any multiplication involving quaternions should not be confused with quaternion multiplication; only their representation on $\text{S}^3 \subset \mathbb{R}^4$ is used to do some vector operations.

The one parameter family of rotations given by $\mathbf{R}_{\text{test}}(\theta, \mathbf{G}^i, \mathbf{g}^i)$ in (3.196) generates a path around S^3 which is a geodesic. Employing a hyper-spherical-coordinate chart on S^3 exposes

the geodesics in a simple way, and we can achieve some nice benefits from this property. The coordinitization used for a quaternion $\mathbf{p}$ is

$$\mathbf{p}(\alpha,\beta,\gamma) = \cos\alpha\mathbf{e}_4 + \sin\alpha(\cos\beta\mathbf{e}_3 + \sin\beta(\cos\gamma\mathbf{e}_1 + \sin\gamma\mathbf{e}_2), \tag{3.198}$$

where $\alpha,\beta \in [0,\pi], \gamma \in [0,2\pi]$ and the basis vectors $\mathbf{e}_\alpha, \alpha = 1,2,3,4$ are orthonormal under the standard Euclidean metric, e.g. $\mathbf{e}_\alpha \cdot \mathbf{e}_\beta = \delta_{\alpha\beta}$. That this parametrization 'exposes' the geodesics in a simple way is a result of the following viewpoint: the equator of S^3 may be described by the one parameter path given by $\mathbf{p}(\pi/2,\pi/2,2\pi t), t \in [0,1]$. Noting that any geodesic on S^3 can be reduced to this 'equatorial' form with a corresponding re-association, that is, an $\mathbb{R}^4 \to \mathbb{R}^4$ rotation of the 4-basis $\{\mathbf{e}_\alpha\}$. In other words, when the basis elements $\{\mathbf{e}_\alpha\}$ are aligned correctly with the one-parameter fiber path traced out by the rotations, the path is simply given by $\mathbf{p}(\theta) = \cos\theta\mathbf{e}_1 + \sin\theta\mathbf{e}_2$, $\theta \in \{0, 2\pi\}$. Note that $\mathbf{e}_1, \mathbf{e}_2 \in S^3 \subset \mathbb{R}^4$, and the way the basis $\mathbf{e}_1, \mathbf{e}_2$ may be found in terms of the fiber will be explained next.

3.3.4.3 Fiber plane basis construction

The construction of the basis vectors $\mathbf{e}_1, \mathbf{e}_2$ which span the plane in $\mathbb{R}^4$ on which the one parameter family of quaternions lies can be generated in the following procedure, which is essentially a Gram-Schmidt basis construction procedure. Recall that the fiber is given in terms of rotation matrices as $\mathbf{R}_{\text{test}}(\theta;\mathbf{G}^i,\mathbf{g}^i) = \hat{\mathbf{R}}(\mathbf{g}^i,\theta)\mathbf{R}_{\text{base}}(\mathbf{G}^i,\mathbf{g}^i)$, and that $\mathbf{R}_{\text{test}}(0;\mathbf{G}^i,\mathbf{g}^i) = \mathbf{R}_{\text{base}}(\mathbf{G}^i,\mathbf{g}^i)$ since $\hat{\mathbf{R}}(\mathbf{g}^i,0) = \mathbf{I}$. The quaternion representation for $\mathbf{R}_{\text{test}}(0;\mathbf{G}^i,\mathbf{g}^i)$ will be denoted as $\mathbf{q}_0$. By the parametrization $\mathbf{p}(\theta) = \cos\theta\mathbf{e}_1 + \sin\theta\mathbf{e}_2$, where at each θ, $\mathbf{p}(\theta)$ gives the quaternion representation for $\mathbf{R}_{\text{test}}(\theta;\mathbf{G}^i,\mathbf{g}^i)$, it is evident that a logical choice for $\mathbf{e}_1$ is $\mathbf{q}_0$, so hereby define

$$\mathbf{e}_1 \equiv \mathbf{q}_0 \equiv \mathbf{R}_{\text{test}}(0;\mathbf{G}^i,\mathbf{g}^i). \tag{3.199}$$

Next use the fact that for $\mathbf{R}_{\text{test}}(\theta;\mathbf{G}^i,\mathbf{g}^i), \theta \neq 0$, the resulting quaternion form of $\mathbf{R}_{\text{test}}$, denoted as $\mathbf{q}_\theta$ lies in its geodesic plane P, with $P = \{\mathbf{p}|\mathbf{p} \in \text{span}(\mathbf{e}_1,\mathbf{e}_2)\}$. By removing the $\mathbf{q}_\theta$ component along $\mathbf{e}_1$ via a projection, the leftover component $\mathbf{q}_{\text{proj}}$ is written

$$\mathbf{q}_{\text{proj}} = \mathbf{1}[\mathbf{e}_1]\mathbf{q}_\theta, \tag{3.200}$$

and is orthogonal to $\mathbf{e}_1$. By unitizing $\mathbf{q}_{\text{proj}}$ we obtain the basis vector $\mathbf{e}_2$, e.g.

$$\mathbf{e}_2 \equiv \frac{\mathbf{q}_{\text{proj}}}{\|\mathbf{q}_{\text{proj}}\|}, \tag{3.201}$$

With these bases, $\mathbf{e}_1, \mathbf{e}_2$ given by (3.199), (3.201), $\mathbf{q}_\theta \in P$ for all $\theta \in [0, 2\pi]$.

3.3.4.4 Distance to fiber computation.

Now we consider the comparison of two fibers, constructed from the pairs $(\mathbf{G}^1,\mathbf{g}^1), (\mathbf{G}^2,\mathbf{g}^2)$. Denote the fiber constructed from $(\mathbf{G}^1,\mathbf{g}^1)$ as f^1, and the fiber constructed from $\mathbf{G}^2,\mathbf{g}^2$ as

f^2. Denote the basis vectors for f^1 as $\mathbf{a}_1, \mathbf{a}_2 \in \mathbb{R}^4$ and for f^2 as $\mathbf{b}_1, \mathbf{b}_2 \in \mathbb{R}^4$, where these bases are constructed through the procedure described in the previous paragraph. We are using $\mathbf{a}_i, \mathbf{b}_i$ for the basis in preference to something like $\mathbf{e}_i^1, \mathbf{e}_i^2$. We seek to find if the fibers intersect at a point along their path, and if so, what the rotation corresponding to that point is.

To accomplish this, consider the following procedure: take one of the fibers (f^1, say) as the native space on which to do the distance-to-fiber comparison. As f^2 is traversed (by adjusting θ), project the quaternion described by f^2 onto the plane containing f^1, by the projection tensor with represented as $\mathbf{a}_1 \otimes \mathbf{a}_1 + \mathbf{a}_2 \otimes \mathbf{a}_2$. This tensor takes any $\mathbf{x} \in \mathbb{R}^4$ and projects it onto the plane containing f^1. Since the fiber f^2 can be described in terms of its basis $\{\mathbf{b}_1, \mathbf{b}_2\}$ as $\mathbf{p}(\theta) = \cos\theta\mathbf{b}_1 + \sin\theta\mathbf{b}_2$, we write out the projection operation as:

$$\begin{aligned}\mathbf{1p}(\theta) &= (\mathbf{a}_1 \otimes \mathbf{a}_1 + \mathbf{a}_2 \otimes \mathbf{a}_2)[\cos\theta\mathbf{b}_1 + \sin\theta\mathbf{b}_2] \\ &= (\mathbf{a}_1 \cdot \mathbf{b}_1 \cos\theta + \mathbf{a}_1 \cdot \mathbf{b}_2 \sin\theta)\mathbf{a}_1 + (\mathbf{a}_2 \cdot \mathbf{b}_1 \cos\theta + \mathbf{a}_2 \cdot \mathbf{b}_2 \sin\theta)\mathbf{a}_2. \end{aligned} \tag{3.202}$$

In other words, if $\mathbf{x} = x_1\mathbf{b}_1 + x_2\mathbf{b}_2$ is the initial point along the f^2 geodesic, the projection onto $\mathbf{a}_1, \mathbf{a}_2$ is given by

$$\hat{\mathbf{x}} = \mathbf{1x} = (x_1\mathbf{a}_1 \cdot \mathbf{b}_1 + x_2\mathbf{a}_1 \cdot \mathbf{b}_2)\mathbf{a}_1 + (x_1\mathbf{a}_2 \cdot \mathbf{b}_1 + x_2\mathbf{a}_2 \cdot \mathbf{b}_2)\mathbf{a}_2. \tag{3.203}$$

This may be viewed more clearly as a linear transformation from $\mathbf{x} \in \text{span}(\mathbf{b}_1, \mathbf{b}_2) \to \hat{\mathbf{x}} = \mathbf{F}^{(\text{p})}\mathbf{x} \in \text{span}(\mathbf{a}_1, \mathbf{a}_2)$ where

$$\mathbf{F}^{(\text{p})} = \begin{bmatrix} c_{11} & c_{12} \\ c_{21} & c_{22} \end{bmatrix}, \tag{3.204}$$

with $c_{11} = \mathbf{a}_1 \cdot \mathbf{b}_1$, $c_{12} = \mathbf{a}_1 \cdot \mathbf{b}_2$, $c_{21} = \mathbf{a}_2 \cdot \mathbf{b}_1$, $c_{22} = \mathbf{a}_2 \cdot \mathbf{b}_2$. Here the superscript (p) is used to convey the idea of projection. When $\mathbf{F}^{(\text{p})}$ is non singular, which will generally be true, barring pathological cases which can be handled by examining other fibers, the polar decomposition theorem applies. Therefore we can find an orthogonal matrix $\mathbf{R}^{(\text{p})}$, and symmetric positive definite matrix $\mathbf{U}^{(\text{p})}$ such that $\mathbf{F}^{(\text{p})} = \mathbf{R}^{(\text{p})}\mathbf{U}^{(\text{p})}$. We can construct $\mathbf{U}^{(\text{p})}$ via a spectral decomposition of $\mathbf{C}^{(\text{p})} = (\mathbf{F}^{(\text{p})})^{\text{T}}\mathbf{F}^{(\text{p})} = \sum_i^2(\lambda_i\mathbf{u}_i \otimes \mathbf{u}_i)$, through $\mathbf{U}^{(\text{p})} = (\mathbf{C}^{(\text{p})})^{1/2} = \sum_i^2 \sqrt{\lambda_i}\mathbf{u}_i \otimes \mathbf{u}_i$, and $\mathbf{R}^{(\text{p})}$ via $\mathbf{R}^{(\text{p})} = \mathbf{F}^{(\text{p})}(\mathbf{U}^{(\text{p})})^{-1}$. This is useful because the closest distance between f^1 and f^2 is proportional to the largest eigenvalue of $\mathbf{U}^{(\text{p})}$. If $\mathbf{U}^{(\text{p})}$ has an eigenvalue of 1, then the two fibers do in fact intersect somewhere along their trajectories on S^3. The value of the quaternion at this intersection point is found by letting $\mathbf{R}^{(\text{p})}$ operate on the eigenvector of $\mathbf{U}^{(\text{p})}$ which has eigenvalue 1, and then expressing this on the $\mathbb{R}^4$ basis $\mathbf{a}_1, \mathbf{a}_2$ to obtain the quaternion at the intersection. This intersection quaternion is then mapped to the fundamental region, Q_{fund} for the crystal and denoted as the generating $\mathbf{R}_{\text{g}} \in Q_{\text{fund}}$. The fundamental region is defined operationally in §A.1. By repeating this process for each pair of fibers in M the grains' orientation can be found.

3.3.4.5 Examples

Here is shown a few plots of the fiber previously denoted as f^1 (as it is traversed by $\theta \in [0, 2\pi]$), plotting on its own plane with basis $\mathbf{a}_1, \mathbf{a}_2 \in \mathbb{R}^4$, along with a second fiber f^2 traversing its own plane spanned by basis $\mathbf{b}_1, \mathbf{b}_2 \in \mathbb{R}^4$, but with points on the fiber f^2 projected into the basis $\mathbf{a}_1, \mathbf{a}_2$. This was shown in the previous paragraphs to define a linear transformation with a polar decomposition into $\mathbf{R}^{(\mathrm{p})}, \mathbf{U}^{(\mathrm{p})}$. The symmetric positive definite multiplicative factor ($\mathbf{U}^{(\mathrm{p})}$) has real eigenvalues with useful interpretation: if an eigenvalue is 1 then the fibers f^1, f^2 intersect at some quaternion, thus indicating they came from the same grain orientation. This quaternion at the intersection is described by the operation of $\mathbf{R}^{(\mathrm{p})}\mathbf{u}_1$, where $\mathbf{u}_1$ is the eigenvector of $\mathbf{U}^{(\mathrm{p})}$ associated with the eigenvalue of value 1. To get the quaternion, recognize that $\mathbf{R}^{(\mathrm{p})}\mathbf{u}_1$ was expressed on the basis $\mathbf{a}_1, \mathbf{a}_2$, so the representation for this quaternion would be

$$\mathbf{q}_{\mathrm{isect}} = (\mathbf{R}^{(\mathrm{p})}\mathbf{u}_1 \cdot \mathbf{a}_1)\mathbf{a}_1 + (\mathbf{R}^{(\mathrm{p})}\mathbf{u}_1 \cdot \mathbf{a}_2)\mathbf{a}_2, \tag{3.205}$$

that is we simply resolve the intersection point $\mathbf{R}^{(\mathrm{p})}\mathbf{u}_1$ on the basis $\mathbf{a}_1, \mathbf{a}_2$.

Figure 3.16 shows the results of plotting f^2 on the basis generated by f^1 for two reciprocal vectors which where constructed as originating from the same grain. Therefore the fiber projections are seen to intersect at a given quaternion. The fiber f^1 in its plane span $(\mathbf{a}_1, \mathbf{a}_2)$ is a circle, as expected. The straight lines across the diagonal denote the maximum eigenvector of $\mathbf{U}^{(\mathrm{p})}$, and the mapped vector $\mathbf{R}^{(\mathrm{p})}\mathbf{u}_1$. In the figure it is clear that $\mathbf{R}^{(\mathrm{p})}\mathbf{u}_1$, the major axis of the projected ellipse, is hitting the correct intersection point between f^1, f^2. In an indexing algorithm, the intersection point $\mathbf{R}^{(\mathrm{p})}\mathbf{u}_1$ would then be used to test for completeness in M.

Figure 3.17 and Figure 3.18 show the resulting geodesic projections for two fibers which come from different base orientations, $\mathbf{R}_{\mathrm{g}}$, so that there is no intersection. The maximum eigenvalue for $\mathbf{U}^{(\mathrm{p})}$ upon calculating the polar decomposition of (3.204) would therefore be less than 1. In an indexing algorithm, these two fibers would then not be used to generate a trial orientation to test for completeness; the algorithm would proceed to the next pair of trial fibers and repeat the calculation.

3.3.4.6 Summary

This section has described the ideas behind the indexing of diffraction patterns coming from polycrystalline materials, and has suggested an indexing algorithm. The viability of indexing methods is measured by the computational efficiency and effectiveness of the algorithm. In this method, the main computational expense comes from

1. Solving for eigenvalues of $(\mathbf{F}^{(\mathrm{p})})^{\mathrm{T}}\mathbf{F}^{(\mathrm{p})}$ ($\mathbf{F}^{(\mathrm{p})}$ as defined in (3.204))
2. Gram-Schmidt construction to find the basis for the plane containing the fiber f^i

These requirements are therefore more attractive than the brute force search methods, since a check of the eigenvalues of a 2-by-2 matrix takes fewer computational time than querying

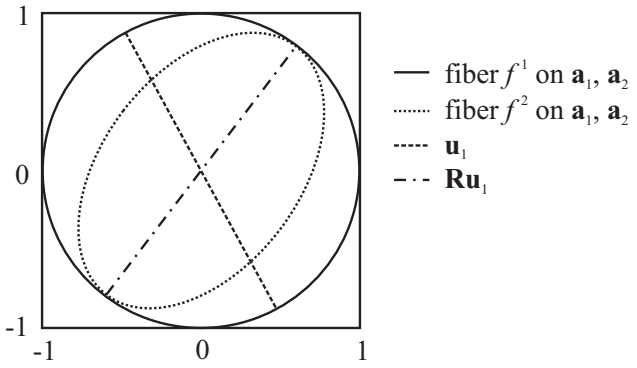

Figure 3.16: Diagram of the projection of fiber f^2 onto the plane containing fiber f^1 for $\mathbf{G}^1, \mathbf{g}^1$ and $\mathbf{G}^2, \mathbf{g}^2$ coming from the same grain orientation. The eigenvector of $\mathbf{U}^{(\mathrm{p})}, \mathbf{u}_1$ is plotted, along with $\mathbf{R}^{(\mathrm{p})}\mathbf{u}_1$, the major axis of the ellipse. Notice the intersection since these fibers come from the same grain rotation.

the entire reflection data structure for completeness. In simulations, this method is faster and more efficient than such brute force methods. However, when applied to experimental data which contains noise, the precision at which fiber intersections is determined by obtaining the eigenvalues of $\mathbf{U}^{(\mathrm{p})}$ is lacking. The tolerance on the eigenvalue check of $\mathbf{U}^{(\mathrm{p})}(f^1, f^2)$ must be opened up to the point where the potential advantages of the method in reducing the amount of trial orientations disappear rapidly, since many spurious orientations are still tested for completeness. It is possible with further tweaking of the tolerances that a robust solution can be found. In any case, the method has some interesting features that may prove useful for the indexing of certain materials. A potential application might be for the indexing of low symmetry materials, where the probe space required for a brute force approach is large (since there are few reductions in the size of the orientation space).

This concludes the information on grain indexing, which constituted the first step of lattice refinement by obtaining estimates for $\mathbf{H}$ from the data set of reciprocal vectors, M. In the next section, we consider the second step of lattice refinement. The finite deformation framework described here differs from conventional approaches, from both crystallographers' approach, and from a conventional infinitesimal strain approach. We describe our approach and compare the other approaches. We describe how our approach reduces to the infinitesimal strain approach, and we quantify the error made in the infinitesimal strain approach.

3.3.5 Lattice refinement strategies

In this section[6]we consider the final step of lattice refinement, after the indexed pairs in the reference lattice configuration $\mathbf{g}^i, \mathbf{G}^i$ have been obtained. After grain indexing, we have an approximation for the rotation factor $\mathbf{R}$ of the lattice deformation $\mathbf{H}$, effectively assuming

[6]Some of this section is taken from (Edmiston et al., 2012)

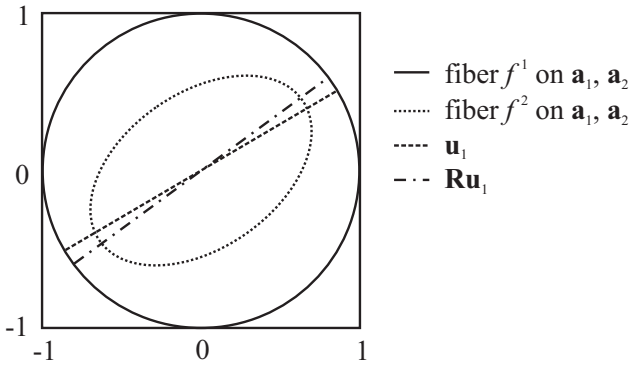

Figure 3.17: Plot of the projection of fiber f^2 onto the plane containing fiber f^1 for $\mathbf{G}^1, \mathbf{g}^1$ and $\mathbf{G}^2, \mathbf{g}^2$ coming from the different grain orientation. The projected geodesic does not intersect the base geodesic, and the eigenvalues of the projection tensor (3.204) would therefore be less than one. In algorithms, this indicates that these fibers do not come from the same grain, and the next fiber is then checked.

$\mathbf{U} \approx \mathbf{I}$. We now would like to obtain a more accurate estimate of $\mathbf{H}$, by refining the estimates for $\mathbf{R}, \mathbf{U}$. The basic relation we exploit is

$$\mathbf{g}^i = \mathbf{H}^{-\mathrm{T}} \mathbf{G}^i, \tag{3.206}$$

which holds for the pairs $\mathbf{g}^i, \mathbf{G}^i$. These pairings are available after the indexing step described in §3.3.4.

There are various ways of implementing the kinematic relation (3.206) in order to obtain an experimental estimate of $\mathbf{H}$. To motivate different ways we may use this relation, consider the traditional decomposition for a deformation $\mathbf{F}$,

$$\mathbf{F} = \mathbf{m}_i \otimes \mathbf{M}^i, \tag{3.207}$$

where $i = 1, 2, 3$, and the pairs $\mathbf{m}_i, \mathbf{M}^i$ are specifically chosen tangent and reciprocal tangent vectors in the deformed and reference configurations. In this formulation, one only needs to select the reference reciprocals $\mathbf{M}^i$, obtaining the reference tangent vectors $\mathbf{M}_i$ from these. Then the $\mathbf{m}_i$ are defined by convecting $\mathbf{M}_i$ through the action of $\mathbf{F}$:

$$\mathbf{m}_i \equiv \mathbf{F}\mathbf{M}_i. \tag{3.208}$$

For the present consideration of X-ray diffraction analysis, we are interesting in applying this result to lattice and reciprocal lattice vectors. Therefore we similarly write

$$\mathbf{H} = \mathbf{g}_i \otimes \mathbf{G}^i, \tag{3.209}$$

where the pairs $\mathbf{g}_i, \mathbf{G}^i$ are interpreted lattice and reciprocal lattice vectors in the deformed and reference configuration, respectively. Although X-ray diffraction only directly measures

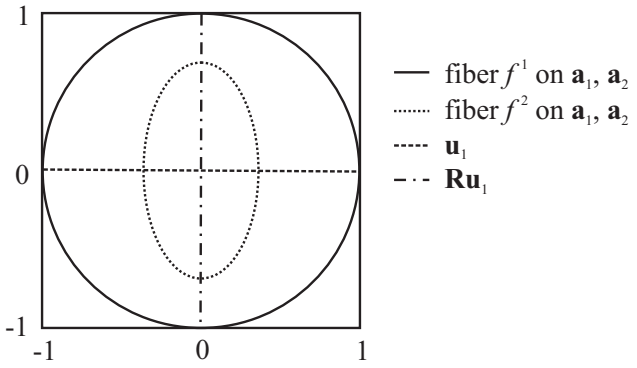

Figure 3.18: A second plot of the projection of non-matching grain orientations for the two fibers f^1, f^2 . There is a distinct gap between the fiber f^1's path and fiber f^2's path, with no intersections.

the reciprocals $\mathbf{g}^i, \mathbf{G}^i$, we can compute the lattice vectors $\mathbf{g}_i$ by the simple relations

$$g^{ij} = \mathbf{g}^i \cdot \mathbf{g}^j \tag{3.210}$$

and

$$g_{ij} = (g^{ij})^{-1}, \tag{3.211}$$

giving

$$\mathbf{g}_i = g_{ij}\mathbf{g}^j = [g_{ij}]^{-1}\mathbf{g}^j, \tag{3.212}$$

so that

$$\begin{aligned} \mathbf{H} &= \mathbf{g}_i \otimes \mathbf{G}^i \\ &= (g^{ij})^{-1}\mathbf{g}^j \otimes \mathbf{G}^i. \end{aligned} \tag{3.213}$$

Here g_{ij} is the lattice metric tensor, and g^{ij} is the reciprocal lattice metric tensor. Equation (3.213) therefore only contains information which can be directly obtained from X-ray diffraction measurements, that is, from measurements of reciprocal lattice vectors in the deformed and reference state. From (3.213), it is evident that only six reciprocal vector measurements are required to fully characterize the lattice deformation $\mathbf{H}$: $\mathbf{g}^i, \mathbf{G}^i, i = 1, 2, 3$, by measuring a reciprocal lattice vector in a reference state with the same reciprocal lattice vector in the deformed state. If the reference structure is known before hand, only three observations are required. However, we will see later that (3.213) is not actually all that useful in experimental crystallography, due to the requirement of needing to index a crystal initially to actually obtain the pairs $\mathbf{g}^i, \mathbf{G}^i$ which make constructing (3.213) possible in the first place. In addition, using (3.213) directly would be prone to errors in the individual measurements of the reciprocal vectors $\mathbf{g}^i$. In order to increase the precision of the measurements, one would like to be able to apply (3.213) to all the observed reciprocal vectors, instead of only three, thus arriving at an averaged estimate of $\mathbf{H}$.

To accomplish this, note that the selection of the $\mathbf{G}^i$ in (3.209) is largely arbitrary, apart from the requirement that the set $\mathbf{G}^i$ must be linearly independent (hence a basis). Any other set of linearly independent vectors $\mathbf{G}^i$ must also give (3.209). Therefore, we have the relation

$$\mathbf{g}^{(i)} = \mathbf{H}^{-\mathrm{T}}\mathbf{G}^{(i)} \tag{3.214}$$

holding for any indexed pair $\mathbf{g}^{(i)}, \mathbf{G}^{(i)}$. The superscript (i) is used to denote the enumeration into the array of observable reflections, as determined by a structure factor calculation, §3.2.2.3. Then, we can use (3.214) as the modeling equation in a least squares algorithm to determine the value of $\mathbf{H}$ such that residual equations of the form

$$\boldsymbol{r}(\mathbf{G}^i, \mathbf{g}^i, \mathbf{H}) = \mathbf{g}^i - \mathbf{H}^{-\mathrm{T}}\mathbf{G}^i \tag{3.215}$$

are minimized for all indexed pairs $\mathbf{g}^i, \mathbf{G}^i$. We describe least squares estimation analysis based on equations like (3.215) in greater detail in §3.4.

In summary, the overall strategy in our approach is to:

1. Assign a reference configuration $\boldsymbol{\kappa}$ where one generates $\mathbf{G}^{(\mathrm{i})}$, $i = 1, 2, ..., \infty$, where i is an index into the particular reciprocal lattice node. The nodes of the reciprocal lattice are one-to-one with an h, k, l index, see (3.65). The h,k,l indices which produce diffraction are determined from the structure factor, (3.90). We have

   $$\mathbf{G}^{(i)}(h, k, l) = h\mathbf{L}^1 + k\mathbf{L}^2 + l\mathbf{L}^3, \tag{3.216}$$

   where $\mathbf{L}^1, \mathbf{L}^2, \mathbf{L}^3$ are the reciprocal vectors based on the unit cell geometry. We will return to this concept in the next section.

2. The crystal is indexed and the pairs are created, $\mathbf{g}^i, \mathbf{G}^i$, $i = 1, 2, ..., N_{\mathrm{vis}}$, where $N_{\mathrm{vis}} < \infty$ is the the number of experimentally visible reciprocal lattice vectors, which will be a function of the wavelength, λ, crystal structure g_κ, and angular rotation range $\Delta\omega$ for the rotating crystal method, see §3.3.1.1.

3. The data $\mathbf{g}^i, \mathbf{G}^i$ are implemented into an optimization algorithm based on solving equations based on (3.214). The result of the optimization problem are to obtain the deformation $\mathbf{H}$ which best satisfies, (3.214): that is the $\mathbf{H}$ which best matches the data.

It should be pointed out that the transformation $\mathbf{H}$ is the elastic deformation in the model for elastic plastic deformation developed in Chapter 2. With an appropriately chosen configuration $\boldsymbol{\kappa}$, stresses are readily computed through constitutive equations using $\mathbf{H}_{\boldsymbol{\kappa}}$, see Equation (3.160). This synergy makes X-ray diffraction attractive for the investigation of the model in Chapter 2.

Some details of the strategy to lattice refinement prescribed here differs from the traditional methods in the crystallography literature. In these methods, one performs a similar

optimization problem to refine the lattice, but the optimization occurs over the internal angles and lengths of a unit cell, along with an orientation operation, instead of the components of $\mathbf{H}$. We can relate these two approaches by translating the unit cell parameters into the present language - we now describe the details.

3.3.5.1 Construction of structural map.

For simple lattices we can clearly link the approaches of refinement between the mechanics approach and the crystallographic approach, as shown in Figure 2.6.

To achieve this we first consider a reference cube aligned with a Cartesian basis $\mathbf{e}_1, \mathbf{e}_2, \mathbf{e}_3$. For later use, the reciprocal vectors in this configuration are trivial due to orthonormality of the Cartesian system; we have

$$\mathbf{e}_1^* = \mathbf{e}_1, \ \mathbf{e}_2^* = \mathbf{e}_2, \ \mathbf{e}_3^* = \mathbf{e}_3, \tag{3.217}$$

where $\mathbf{e}_i^*, i = 1, 2, 3$ are the reciprocal basis vectors to $\mathbf{e}_i$. Throughout this section, reciprocal vectors will be distinguished by the notation $(\cdot)^*$. This cube is mapped by a structural map, $\mathbf{H}_\mathrm{s}$, which takes the unit cube into its conventionally prescribed lattice parameter configuration. This configuration is defined by the three length changes of the cube axes, a, b, c, and the internal angles of the cell, α, β, γ. We construct this deformation according to the following definitions:

$$\mathbf{H}_\mathrm{s}\mathbf{e}_1 \equiv \mathbf{a} = a\mathbf{e}_1 \tag{3.218}$$
$$\mathbf{H}_\mathrm{s}\mathbf{e}_2 \equiv \mathbf{b} = b\mathbf{e}_r(\gamma; \mathbf{e}_1, \mathbf{e}_2) \tag{3.219}$$
$$\mathbf{H}_\mathrm{s}\mathbf{e}_3 \equiv \mathbf{c} = c\hat{\mathbf{c}}(\alpha, \beta, \gamma), \tag{3.220}$$

where $\mathbf{a}, \mathbf{b}, \mathbf{c}$ are the unit cell edges after the structural map, and where we are using the assignment of the polar coordinate unit vector $\mathbf{e}_r$ defined by

$$\mathbf{e}_r(\gamma; \mathbf{e}_1, \mathbf{e}_2) = \cos\gamma\mathbf{e}_1 + \sin\gamma\mathbf{e}_2. \tag{3.221}$$

The Cartesian representation for $\mathbf{c}$, which is defined off of the internal angles α, β, γ, is lengthy to compute; details are provided in the Appendix, see Equation (A.39). Also consult Neustadt et al. (1968) for an alternative point of view on this computation.

Now returning to the consideration of Equations (3.218)-(3.220), recall that Equation (3.217) defines the reciprocal basis $\mathbf{G}^i (\equiv \mathbf{e}_i^*)$ with respect to the reference cube configuration. Then we can apply (3.207) to Equations (3.218)-(3.220), observe that $\mathbf{a} \equiv \mathbf{g}_1$, $\mathbf{b} \equiv \mathbf{g}_2$, and $\mathbf{c} \equiv \mathbf{g}_3$, and see that $\mathbf{H}_\mathrm{s}$ has the representation

$$\begin{aligned}\mathbf{H}_\mathrm{s} &= \mathbf{a} \otimes \mathbf{e}_1 + \mathbf{b} \otimes \mathbf{e}_2 + \mathbf{c} \otimes \mathbf{e}_3 \\ &= a\mathbf{e}_1 \otimes \mathbf{e}_1 + b\mathbf{e}_r(\alpha; \mathbf{e}_1, \mathbf{e}_2) \otimes \mathbf{e}_2 + c\hat{\mathbf{c}}(\alpha, \beta, \gamma) \otimes \mathbf{e}_3.\end{aligned} \tag{3.222}$$

As an example we display Equation (3.222) in matrix form for the general triclinic case. Resolving on the Cartesian basis $\mathbf{e}_i$ gives

$$\mathbf{H}_{\mathrm{s}} = \begin{bmatrix} a & b\cos\gamma & c\cos\beta \\ 0 & b\sin\gamma & c(\cos\alpha - \cos\beta\cos\gamma)/\sin\gamma \\ 0 & 0 & c\left(1 + 2\cos\alpha\cos\beta\cos\gamma - \cos^2\alpha - \cos^2\beta - \cos^2\gamma\right)^{1/2}/\sin\gamma \end{bmatrix}_{\mathbf{e}_i\otimes\mathbf{e}_j}, \tag{3.223}$$

where $\mathbf{e}_i \otimes \mathbf{e}_j$ denotes the tensorial basis being used. Details of the computations leading to Equation (3.223) are provided in the Appendix, §A.3. Finally, the reciprocal basis in (3.216), $\mathbf{L}^1, \mathbf{L}^2, \mathbf{L}^3$ are generated from the equations

$$\mathbf{L}^i = \mathbf{H}_{\mathrm{s}}^{-\mathrm{T}}\mathbf{e}_i^*, \qquad i = 1, 2, 3. \tag{3.224}$$

So far we have only related unit cell parameters to the structural map of a convenient artificial reference cube. To complete the lattice refinement problem we must be able to account for the orientation of the physical configuration of the lattice when the X-ray observation is made. Therefore to go from the structural map configuration to an arbitrary current configuration, an additional rotation operation, denoted by $\bar{\mathbf{R}} \in \mathrm{SO}(3, \mathbb{R})$, is required. This rotation tensor may be parametrized by three coordinates, e.g. Euler angles or angle axis parameters, see (A.5). Finally, the full set of parameters characterizing the deformation from the reference cube to the current configuration are summarized by

$$\mathbf{H}_{\mathrm{cube}}(r_1, r_2, r_3, a, b, c, \alpha, \beta, \gamma) = \bar{\mathbf{R}}(r_1, r_2, r_3)\mathbf{H}_{\mathrm{s}}(a, b, c, \alpha, \beta, \gamma), \tag{3.225}$$

where r_1, r_2, r_3 are e.g. the angle axis parameters for a rotation. The lattice refinement procedure then occurs on the array $r_1, r_2, r_3, a, b, c, \alpha, \beta, \gamma$; that is, these values are modified to match experimental diffraction data via an algorithm such as least squares. The entire process is depicted in Figure 3.19, where the actions of the structural map $\mathbf{H}_{\mathrm{s}}$ and rotation $\bar{\mathbf{R}}$ are illustrated, arriving at the final configuration where the diffraction measurement is made.

An approach more in line with the mechanics view would be to fix the lattice parameters from the structural map corresponding to a chosen reference state, (e.g. let $\mathbf{H}_{\mathrm{s},0}$ define the reference state!) and then simply evolve this structure with an unrestricted transformation $\mathbf{H}_{\boldsymbol{\kappa}}$. Then the map from the fixed reference configuration to the current configuration is parameterized by

$$\mathbf{H}_{\boldsymbol{\kappa}}(\mathbf{R}, \mathbf{U}) = \mathbf{R}\mathbf{U}, \tag{3.226}$$

where $\mathbf{R}$ is parametrized by three coordinates, and $\mathbf{U}$ is parameterized by six coordinates due to symmetry. See Figure 3.20 for a depiction of this situation.

Comparing Figure 3.20 and Figure 3.19 shows that in theory either approach works as well as the other, since the final solutions for the deformation relative to the unit cube would

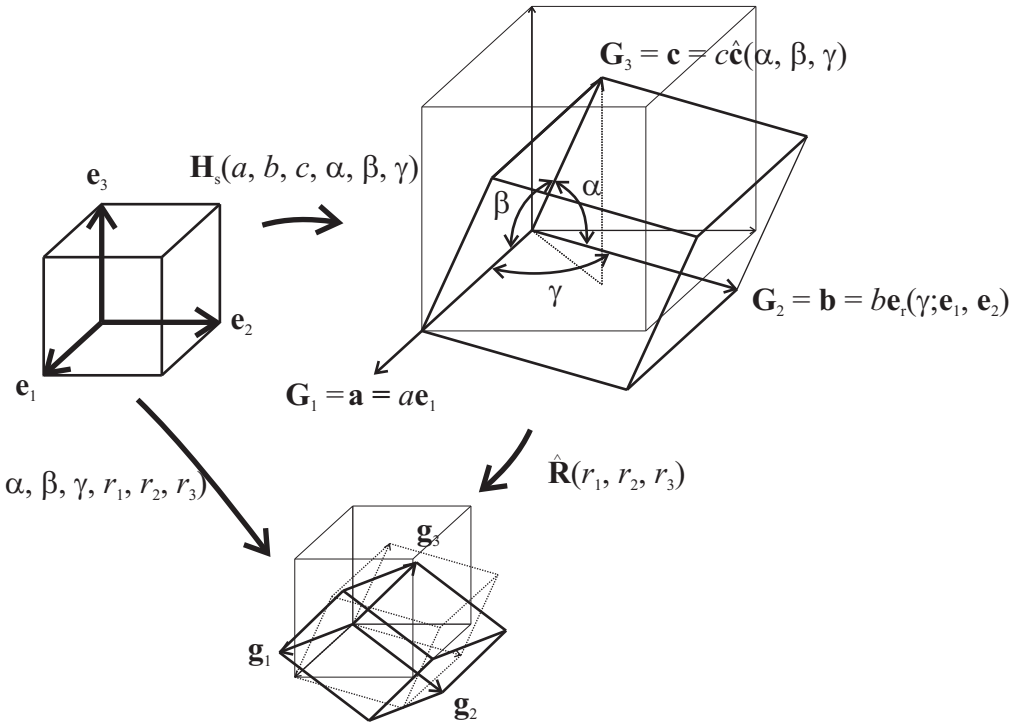

Figure 3.19: Depiction of the lattice refinement procedure using six unit cell parameters $a, b, c, \alpha, \beta, \gamma$ and three rotation parameters r_1, r_2, r_3 to arrive at the physical configuration of the crystal where diffraction is measured. The final state based on evolution from the initial cube is given by the mapping $\mathbf{H}_{\text{cube}} = \bar{\mathbf{R}}\mathbf{H}_{\text{s}}$. The evolution of lattice vectors from the reference cube to the physical configuration is shown by $\mathbf{e}_i \rightarrow \mathbf{G}_i \rightarrow \mathbf{g}_i$

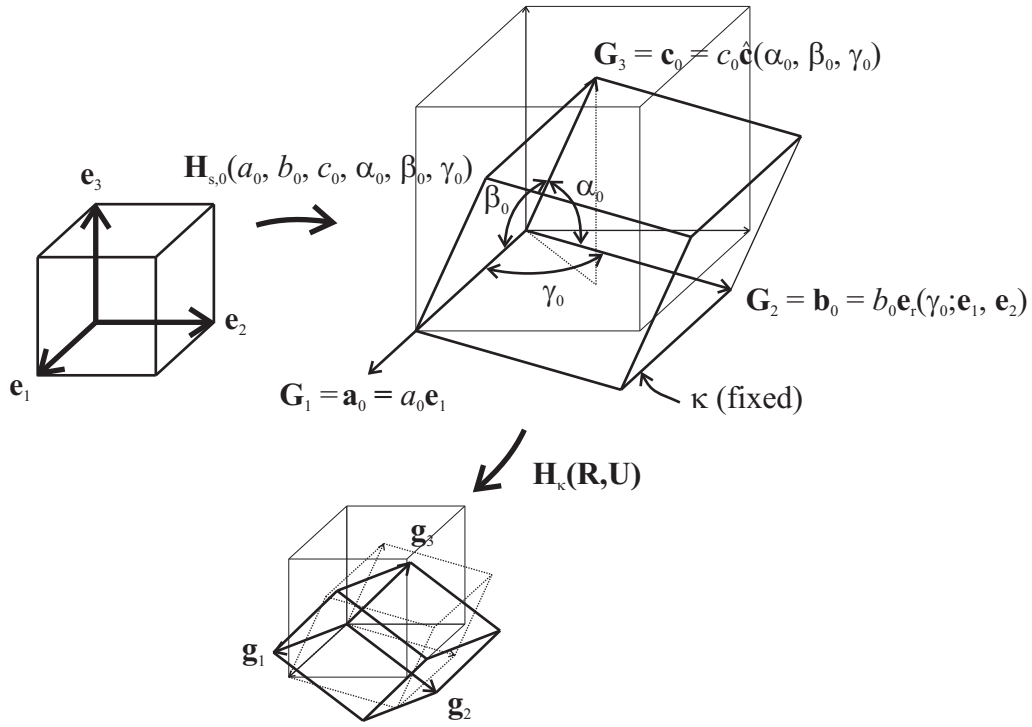

Figure 3.20: Depiction of the lattice refinement procedure using the lattice deformation **H** from a fixed reference configuration $\boldsymbol{\kappa}$. The reference lattice is generated from the structural map at a convenient state, fixing $a_0, b_0, c_0, \alpha_0, \beta_0, \gamma_0$. The reference parameters typically define a stress free state (the material may be a powder) so that constitutive equations defined with respect to $\boldsymbol{\kappa}$ are easily interpreted.

be equivalent. We can relate both approaches with respect to the initial reference cube, giving the equivalence

$$\mathbf{H}_{\text{cube}} = \mathbf{H}_{\boldsymbol{\kappa}}\mathbf{H}_{\text{s},0} = \mathbf{R}\mathbf{H}_{\text{s}}. \tag{3.227}$$

However upon consideration of the structural map in (3.223), in the crystallographic approach modification of the unit cell parameters induce both stretch and rotation, (3.223). In the mechanics approach, these kinematically meaningful quantities are decoupled, by the direct use of the polar decomposition. Therefore these two techniques can have quantitative difference when it comes to calculating uncertainties, a consideration which will be explored in §3.4.2.1. Therefore the mechanics perspective of fixing $\boldsymbol{\kappa}$ with reference unit cell parameters and refining $\mathbf{H}_{\boldsymbol{\kappa}}$ based on the data is preferred in this study. See Edmiston et al. (2012) for further details of these comparison.

A common approximation made in the literature on diffraction based stress analysis is to use infinitesimal strain kinematics to account for lattice strain. In the next section we investigate this approximation and compare it to the finite deformation result preferred here.

3.3.5.2 Error in small strain estimate.

We now consider typical expressions used for infinitesimal strain based analysis of diffraction data in the literature. These equations differ in appearance from Equation (3.206). For example, common methodologies for strain analysis take fundamental relation

$$\boldsymbol{\varepsilon} \cdot \mathbf{N}^{(i)} \otimes \mathbf{N}^{(i)} = \frac{\delta d^{(i)}}{d_0^{(i)}}, \tag{3.228}$$

where $||\boldsymbol{\varepsilon}|| << 1$ is the infinitesimal strain tensor, $\mathbf{N}^{(i)}$ is the normal vector to the ith lattice plane, and $\delta d^{(i)} \equiv d_{\text{f}}^{(i)} - d_0^{(i)}$ is the change in planar spacing for the ith reflection. Here $d_{\text{f}}^{(i)}$ is the deformed spacing, and $d_0^{(i)}$ is the initial spacing. Then a least squares algorithm is formed from residuals based on Equation (3.228) in order to solve for $\boldsymbol{\varepsilon}$. Most crystalline materials yield before reaching the levels of distortion which would make infinitesimal strain measures such as (3.228) unacceptably erroneous compared to a finite deformation measure such as $\mathbf{H}_{\boldsymbol{\kappa}}$. However recent experiments are pushing this envelope. Large elastic strains are possible for short time scale studies such as impact loading, where plastic flow is absent (Kalantar et al., 2005; Hawreliak et al., 2011), or when high hydrostatic pressures are imposed, such as those attained in diamond anvil cell experiments (Jayaraman, 1983; Yamanaka et al., 2001; Katrusiak, 2008). Although to date the error in using infinitesimal kinematic measures has been acceptable, since typically $\|\boldsymbol{\varepsilon}\| < 1$ %, finite deformation measures may become important to consider as experimental techniques enable large-strain studies.

Furthermore, upon critical examination of Equation (3.228), these kinematics are objectionable from the outset. Traditional definitions of strain tensors do not operate on planar normals, but on tangent vectors or line elements, and these have different behavior under

the same transformation. For example, consider the Lagrangian strain tensor given by

$$\mathbf{E} = \frac{1}{2}\left(\mathbf{H}^{\mathrm{T}}\mathbf{H} - \mathbf{I}\right). \tag{3.229}$$

Noting from Equation (3.213) that $\mathbf{H}$ operates on line elements, Equation (3.229) indicates that $\mathbf{E}$ likewise operates on line elements. Instead, the appropriate kinematic relationship for planar normals is obtained from Nanson's formula (Chadwick, 1999)

$$(\det \mathbf{H})\mathbf{H}^{-\mathrm{T}}\mathbf{N}^{(i)} = \mu^{(i)}\mathbf{n}^{(i)},$$

where $\mathbf{n}^{(i)}$ is the deformed unit normal, $\mu^{(i)} = \left(\mathbf{C}^{-1} \cdot \mathbf{N}^{(i)} \otimes \mathbf{N}^{(i)}\right)^{1/2}$ is the area ratio, and $\mathbf{C} \equiv \mathbf{H}^{\mathrm{T}}\mathbf{H} = \mathbf{U}^2$.

We do not in the end seriously object to the use of Equation (3.228) for small strain studies, which is the most common situation to date. We point out the deficiency should experimental conditions advance to the point where using Equation (3.228) would give distinguishable errors, or for the large elastic strain cases noted in the introduction. In the next section we will show that Equation (3.206) reassuringly reduces to Equation (3.228) upon linear approximation. We find these computations useful to elucidate, since this equivalence may not be evident upon first comparing (3.228) to (3.206).

Linear approximation procedure.

We now derive the error made when replacing the general kinematics given by Equation (3.206) with the approximate kinematics in Equation (3.228). The linearization method shown here gives is less rigorous than the general approach given by Hughes and Pister (1978), but gives the same results. The result of the procedure is that the kinematics of Equation (3.228) are correct to within an error of order $\boldsymbol{\varepsilon}^2$. For a rough idea of the meaning of this, let's assume we have strains of $\boldsymbol{\varepsilon} \approx 1\% = 0.01$, with error $\Delta\boldsymbol{\varepsilon} = \boldsymbol{\varepsilon}^2 \approx 1 \cdot 10^{-4}$. Then for a material with elastic modulus $E \approx 100$ GPa, the nominal stress level would be $\sigma \approx 1$ GPa and the error in the stress would be $\Delta\sigma \approx 10$ MPa. This error is currently below the magnitude of error arising from other sources such as precision uncertainty (Edmiston et al., 2011); however as instrumentation and data analysis algorithms improve this may not always be the case. From another perspective, at the higher stress levels which may be obtained in diamond anvil cell or shock experiments, where $\sigma \approx 10$ GPa this error may also be detectable.

We begin by considering with the relative change in spacing for a given lattice plane, e.g. the right hand side of Equation (3.228),

$$\frac{\delta d}{d_0} = \frac{d - d_0}{d_0}. \tag{3.230}$$

In Equation (3.230) and all the following equations, the superscript (i) designating the lattice plane will be suppressed to clean the notation. Next we employ the finite deformation

kinematics of Equation (3.206) to linearize Equation (3.230) about the reference state. We have the typical requirements of $\mathbf{R} = \mathbf{I}$, and use a simple expansion for the stretch,

$$\mathbf{U} = \mathbf{I} + \boldsymbol{\varepsilon}. \tag{3.231}$$

In practice we obtain $\mathbf{R} = \mathbf{I}$ effectively by rotating the reference configuration $\boldsymbol{\kappa}$. To compute $\delta d/d_0$ from Equation (3.230) we expand the planar spacing in the deformed configuration, d, giving

$$d = d_0 + \left.\frac{\partial d}{\partial \boldsymbol{\varepsilon}}\right|_{\boldsymbol{\varepsilon}=0} \cdot \boldsymbol{\varepsilon} + O(\boldsymbol{\varepsilon}^2). \tag{3.232}$$

Using Equation (3.232) in Equation (3.230) gives the leading order expansion for the relative change in spacing as

$$\frac{\delta d}{d_0} = d_0^{-1} \left.\frac{\partial d}{\partial \boldsymbol{\varepsilon}}\right|_{\boldsymbol{\varepsilon}=0} \cdot \boldsymbol{\varepsilon} + O(\boldsymbol{\varepsilon}^2). \tag{3.233}$$

Next, it can be shown that lattice planar spacing, d, is related to the magnitude of a reciprocal lattice vector $\mathbf{g}^*$ by the equation

$$(d) = \|\mathbf{g}^*\|\|^{-1}. \tag{3.234}$$

Substitution of Equation (3.206) in Equation (3.234) gives

$$\begin{aligned} d &= |\mathbf{g}^*|^{-1} \\ &= \left(\mathbf{H}^{-\mathrm{T}}\mathbf{G}^* \cdot \mathbf{H}^{-\mathrm{T}}\mathbf{G}^*\right)^{-1/2} \\ &= \left(\mathbf{C}^{-1} \cdot \mathbf{G}^* \otimes \mathbf{G}^*\right)^{-1/2}. \end{aligned} \tag{3.235}$$

For later use, we note that in the reference state, similar computations give $d_0 = |\mathbf{G}^*|^{-1}$. Then using Equation (3.235) with the chain rule we compute

$$\frac{\partial d}{\partial \varepsilon_{kl}} = -\left(\frac{1}{2}\right) \frac{1}{\left(\mathbf{C}^{-1} \cdot \mathbf{G}^* \otimes \mathbf{G}^*\right)^{3/2}} \left(\frac{\partial (\mathbf{C}^{-1})_{mn} G_m^* G_n^*}{\partial \varepsilon_{kl}}\right), \tag{3.236}$$

where $G_m^* \equiv \mathbf{G}^* \cdot \mathbf{e}_m$, is notation for projection on the Cartesian basis. Similarly $(\mathbf{C}^{-1})_{mn} = \mathbf{C}^{-1} \cdot \mathbf{e}_m \otimes \mathbf{e}_n$. Next, we use $\mathbf{C} = \mathbf{U}^2$, the initial expansion for the stretch in Equation (3.231), and the result $(\mathbf{I} + \boldsymbol{\varepsilon})^{-1} = \mathbf{I} - \boldsymbol{\varepsilon} + O(\boldsymbol{\varepsilon}^2)$ (Liu, 2002, p. 261), giving

$$\mathbf{C}^{-1} = \mathbf{I} - 2\boldsymbol{\varepsilon} + O(\boldsymbol{\varepsilon}^2). \tag{3.237}$$

Then substitution of Equation (3.237) in Equation (3.236) and evaluating at $\boldsymbol{\varepsilon} = 0$ so that $\mathbf{C} \approx \mathbf{I}$ gives

$$\left.\frac{\partial d}{\partial \varepsilon_{kl}}\right|_{\boldsymbol{\varepsilon}=0} = \frac{1}{\left(|\mathbf{G}^*|\right)^3} G_k^* G_l^*. \tag{3.238}$$

Now we write $\mathbf{G}^* = |\mathbf{G}^*|\hat{\mathbf{G}}^*$ where $\hat{\mathbf{G}}^*$ is the unit vector associated with $\mathbf{G}^*$. The properties of reciprocal space geometry are such that $\hat{\mathbf{G}}^* = \mathbf{N}$, where $\mathbf{N}$ is the unit normal to the lattice plane. Using this property, Equation (3.238) and $d_0 = |\mathbf{G}^*|^{-1}$ in Equation (3.233) gives, after simplifications,

$$\frac{\delta d}{d_0} = \boldsymbol{\varepsilon} \cdot \mathbf{N} \otimes \mathbf{N} + O(\boldsymbol{\varepsilon}^2). \tag{3.239}$$

Thus we have shown that the finite deformation expression of Equation (3.206) reduces to the conventional expression of Equation (3.228) upon a linearization procedure. The infinitesimal relation in Equation (3.228) is therefore demonstrated to be correct to within an error of $O(\boldsymbol{\varepsilon}^2)$. The detailed form of the error term is a complicated function and is too lengthy to report here. Should there be desire to compute these higher order terms by continuing the expansion, we suggest simply using the finite deformation framework from the beginning.

3.3.5.3 Summary

In this section, we have derived the relations between the descriptions of lattice distortion based on unit cell parameters and that based on a lattice deformation tensor relative to a fixed reference configuration, $\boldsymbol{\kappa}$. This was done to establish the equivalences of the two approaches in order to assist in communications and collaborations between mechanics and crystallography communities. We pointed out that the lattice deformation tensor approach should be preferred for studies where constitutive quantities such as stress tensors are eventually required. This is because the constitutive formula for phenomenological continuum theories are explicitly expressed in terms of tensor functions of $\mathbf{H}$; in addition in this framework the uncertainties for lattice stretch and rotation are naturally decoupled (Edmiston et al., 2011).

We have also derived the evolution relation for reciprocal lattice vectors under finite lattice deformations, $\mathbf{H}$. This result enabled the demonstration that the finite deformation relations of Equation (3.206) reduce to the more commonly used infinitesimal kinematic relations of (3.228) upon linearization about the reference state. The error term in using the infinitesimal kinematic relations was shown to be $O(\boldsymbol{\varepsilon}^2)$. Recognition of this error when using small strain kinematics is becoming more important to consider as experimental precisions improve and as higher lattice strain levels are probed. The implementation of Equation (3.206) into analysis codes is a suggested course of action to avoid this error, should there be sufficient need.

3.3.6 Conclusion

In this section we have developed the core ingredients to analyze X-ray diffraction patterns. We have described aspects of each step in the data reduction procedure which takes the

detector images from polycrystalline materials, shown in Figure 3.14, in order to produce estimates for the lattice deformation $\mathbf{H}$. We have described how the geometry of the experimental setup is used in converting the pixel location of a peak on the detector image to a reciprocal lattice vector, including grains offset from the rotation axis and tilt of the detector panel. We gave background information on the indexing of diffraction patterns, and described an indexing algorithm which may be of use in certain applications. Finally, we described the method of lattice refinement based on linear transformations from a meaningfully chosen reference lattice, $\boldsymbol{\kappa}$. This transformation was denoted $\mathbf{H}$, which can be interpreted as the elastic strain in the model for elastic-plastic deformation developed in Chapter 2. We related this approach to the refinement problem with the traditional crystallographic approach of refining on unit cell parameters, and showed our equations to be equivalent to infinitesimal strain equations after a linearization procedure.

In several places in this section we mentioned the use of least squares methods in to estimate quantities such as the transformation $\mathbf{H}$. In the next section we describe the background and implementation of these methods, including uncertainty quantification. We also suggest two methods for the estimation of $\mathbf{H}$ from diffraction data which offer increased capabilities over conventional methods.

3.4 Kinematic parameter estimation

This section describes details of the incorporation of X-ray diffraction data in algorithms to make estimates on quantities such as the lattice deformation $\mathbf{H}$ in §3.3.5. In §3.5 the kinematic estimates obtained from the methods in this section are used with constitutive models to extract material parameters.

The most common method of parameter estimation are least squares methods (Bard, 1974). Both this section and §3.5 use least squares methods extensively. In overview these methods are described by defining a model, using the model to predict experimentally observable values as a result of given input data, and carrying out an algorithm to change model parameters to minimize the difference between these predicted and experimentally measured values. With an appropriate formulation, the least squares method also gives uncertainties on the best-fit model parameters. In the next section we describe the weighted least squares method in some generality; we then apply the method to X-ray diffraction data in various applications in this section and in §3.5. The style of presentation and terminology for this background section closely follows that of Bard (1974).

3.4.1 Background - weighted least squares

We briefly summarize several basic results from the method of weighted least squares, and refer to Bard (1974) for further details. The basic entity of the theory given in Bard (1974)

are the structural equations for the model,

$$\mathbf{r}(\mathbf{z}_1, \mathbf{z}_2, \mathbf{\Theta}) = \mathbf{0}, \tag{3.240}$$

where the m dimensional array $\mathbf{z}_1$ represents independent variables, the n dimensional array $\mathbf{z}_2$ are dependent variables, and the l dimensional array $\mathbf{\Theta}$ are the model parameters. Here both $\mathbf{z}_1$ and $\mathbf{z}_2$ are considered experimentally measured or derived quantities. Equality in (3.240) only holds if both the model $\mathbf{r}(\cdot, \mathbf{\Theta})$ and the data $(\mathbf{z}_1, \mathbf{z}_2)$ are exact and free of errors. When the model is in error or the data has scatter, the model may be written as

$$\mathbf{r}(\mathbf{z}_1, \mathbf{z}_2, \mathbf{\Theta}) = \mathbf{e}_\mu(\mathbf{z}_1, \mathbf{z}_2, \mathbf{\Theta}), \tag{3.241}$$

where $\mathbf{e}_\mu(\mathbf{z}_1, \mathbf{z}_2, \mathbf{\Theta})$ is called the residual for the μ^{th} experiment. For convenience we will suppress denoting the $\mathbf{z}_1, \mathbf{z}_2$ dependence of $\mathbf{e}_\mu(\mathbf{z}_1, \mathbf{z}_2, \mathbf{\Theta})$, and simply write the residual as $\mathbf{e}_\mu(\mathbf{\Theta})$. In many cases the structural equation, (3.240), can be rewritten in reduced form as

$$\mathbf{r}(\mathbf{z}_1, \mathbf{z}_2, \mathbf{\Theta}) = \mathbf{z}_2 - \mathbf{f}(\mathbf{z}_1, \mathbf{\Theta}). \tag{3.242}$$

Therefore for the reduced equations (3.242), the residual $\mathbf{e}_\mu(\mathbf{\Theta})$ is interpreted simply as the difference between measured and predicted data for the μ^{th} experiment. As an example, recall Equation (3.215), which is written in the form of (3.240) and (3.242).

The method of least squares can be stated as finding the minimum of an objective function $\Phi(\mathbf{\Theta})$, where the general objective function is of the form (Bard, 1974)

$$\Phi(\mathbf{\Theta}) = \sum_{a=1}^{M}\sum_{b=1}^{M}\sum_{\mu=1}^{N}\sum_{\eta=1}^{N} B_{(\mu a)(\eta b)} e_{\mu a}(\mathbf{\Theta}) e_{\eta b}(\mathbf{\Theta}), \tag{3.243}$$

where $B_{(\mu a)(\eta b)}$ are the weight coefficients, and $e_{\mu a}(\mathbf{\Theta})$ are multidimensional residual functions. The indices μ, η indicate the experiment index, and the indices a, b indicate indexes into the residuals from the $\mu^{\text{th}}, \eta^{\text{th}}$ experiment, respectively. For example, in (3.243) we have indicated that N experiments were made, each resulting in an M-dimensional residual array.

The optimal model parameters are estimated by solving the equation

$$\left.\frac{\partial \Phi}{\partial \mathbf{\Theta}}\right|_{\mathbf{\Theta}^*} = \mathbf{0}, \tag{3.244}$$

where $\mathbf{\Theta}^*$ denotes the solution parameters. This solution is obtained by, e.g. Newton iterations, or any other optimization technique. The covariance matrix of the solution parameters $\mathbf{\Theta}^*$ can be estimated by computing the inverse of the Hessian of Φ (Bard, 1974),

$$\mathbf{V}_{\mathbf{\Theta}^*} \approx \left.\left(\frac{\partial^2 \Phi}{\partial \mathbf{\Theta}^2}\right)^{-1}\right|_{\mathbf{\Theta}^*}. \tag{3.245}$$

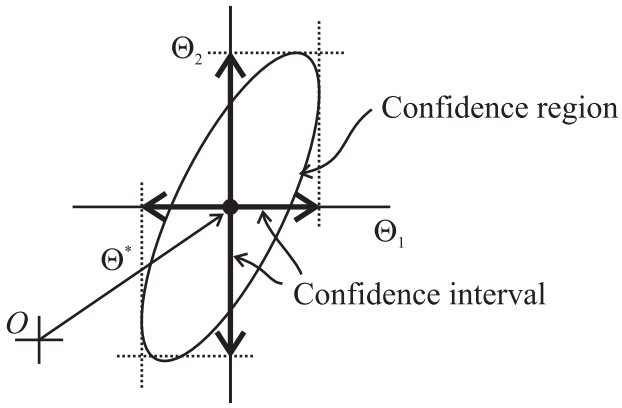

Figure 3.21: Schematic of the ellipsoidal confidence region described by (3.246) for dim$\boldsymbol{\Theta} = 2$. The maximum projections of the ellipse on the $\boldsymbol{\Theta}$-coordinate axes are one method, among many, to report the uncertainty in $\boldsymbol{\Theta}^*$.

The covariance matrix is important if uncertainties in the solution parameters $\boldsymbol{\Theta}^*$ are of interest, which for constitutive determination is certainly the case (Zohdi, 2001). The covariance matrix $\mathbf{V}_{\boldsymbol{\Theta}^*}$ defines a confidence region in $\boldsymbol{\Theta}$-space around the optimal solution $\boldsymbol{\Theta}^*$ which is described by the ellipsoid (Bard, 1974)

$$(\boldsymbol{\Theta} - \boldsymbol{\Theta}^*)^{\mathrm{T}} \mathbf{V}_{\boldsymbol{\Theta}}^{-1} (\boldsymbol{\Theta} - \boldsymbol{\Theta}^*) \leq \chi^2_{\alpha,l}, \tag{3.246}$$

where $\chi^2_{\alpha,l}$ is the upper point of a chi squared distribution with l degrees of freedom, and α is the chosen confidence level.

Figure 3.21 depicts a schematic confidence region described by (3.246) for $l = 2$. When $\mathbf{V}_{\boldsymbol{\Theta}^*}$ is such that the principal axes are not coaxial with the $\boldsymbol{\Theta}$ coordinate axes, as depicted in Figure 3.21, there is some discretion in how to quantify the confidence interval for a particular component of $\boldsymbol{\Theta}^*$. In the present work, as an estimate, we find the bounds of $\mathbf{V}_{\boldsymbol{\Theta}^*}$ in the directions of the eigenvectors of $\mathbf{V}_{\boldsymbol{\Theta}^*}$, and project these extents onto each $\boldsymbol{\Theta}$ coordinate axis. The maximum distance achieved by this procedure for each $\boldsymbol{\Theta}$-coordinate is then assigned as the uncertainty interval for that particular parameter. With this, the solution parameter is stated as $\boldsymbol{\Theta}_i^* = \boldsymbol{\Theta}_i^* \pm u_{\boldsymbol{\Theta}_i^*}$, where $u_{\boldsymbol{\Theta}_i^*}$ is the uncertainty in the solution value.

The background presented in this section is general for any consideration of fine tuning model parameters. For the present application, we are mostly interested in obtaining estimates of the lattice deformation $\mathbf{H}$. We also are interested in estimates of the grain precession, $\mathbf{x}$, see §3.3.3. We therefore form residuals of the form (3.242) by comparing predicted and measured diffraction vectors, such as Equation (3.215). In the next section we describe the forms of the model functions used for least squares algorithms in this study. These model functions differ from conventionally employed methods, and provide information beyond that obtained by standard analysis.

3.4.2 Model equations and objective functions

In this section we describe the detailed model functions (3.240) which will be used during the course of analysis of experimental X-ray diffraction data. We will describe two models for estimating the lattice state, a grain averaged approach and a forward modeling approach. The motivations for these two approaches differ from one another. The grain averaged approach is targeted at efficient uncertainty analysis, and the goal of the forward modeling approach is to extract data of intragranular inhomogeneity from single crystals. Both are novel formulations to the field for this class of X-ray diffraction experiments.

The grain averaged approach is summarized by the following description: we determine the location of diffraction peaks, and minimize the difference between predicted and measured locations by using the kinematic relation (3.206). The location of the peak could be characterized by the reciprocal vector components or the angular location §3.3.2. In either case, the process of assigning a 'location' to a diffraction peak requires some further explanation. To this end, consider Figure 3.22, which shows a diffraction peak for a perfect ruby single crystal. Even with the simple, uniform shape of the local intensity distribution, there is clearly some leeway in ascribing the pixel location of the diffraction peak. In Figure 3.23 we show a diffraction peak which has smeared out due to plastic deformation in the crystal. There is uncertainty in the location of the diffraction peak in both cases, but more so with plastic deformation. The goal of this modeling approach is to convey this uncertainty in the diffraction peak location to the uncertainty in the overall lattice deformation $\mathbf{H}$. All else being equal, the data in Figure 3.23 should result in increased uncertainty in $\mathbf{H}$ over that in Figure 3.22.

To accomplish this in the grain averaged approach we fit a local intensity distribution to each diffraction peak. In powder diffraction experiments, where integrated intensity is only a $1-D$ function, $I(2\theta)$, as opposed to the 3D function here $I(2\theta, \eta, \omega)$, much attention is paid to the precise functional form of $I(2\theta)$. For example, there is much hand wringing over what functional form this local intensity distribution should take, either Gaussian or Voigt (Will, 2006). In the high energy experiments we are considering, we do not have the reciprocal space resolution required to distinguish these forms however, so any function with a maximum and some breadth works. For example, for an undistorted crystal, there may only be only on the order of 10 pixels to describe the diffraction peak, making quantitative distinction between local intensity shapes produced by Gaussian or Voigt functions impossible on a rigorous basis. No matter what form is chosen, we fit a local intensity function to the data.

Although crude, this method of fitting local intensity distributions to each peak is novel compared to traditionally used forms of X-ray diffraction analysis. Normally, the pixel location of the diffraction peak is assigned based on the intensity weighted average. The grain averaged approach has appeal in that uncertainty in the local fit of the diffraction peak propagates to uncertainty in the location of the diffraction peak, information which can be used as weights in the overall lattice refinement, (3.243) and (3.245).

The forward modeling approach we present takes a slightly different point of view but

the motivation is the same: analyze the data in such a way to extract more information than is possible with the intensity weighted average. In the grain averaged approach, by allowing each diffraction peak to have its own model parameters according to a local intensity distribution, we are not taking advantage of the physical fact that the diffraction peaks under consideration are originating from the same crystal. For example in Figure 3.23, where plastic deformation has occurred, spatial gradients in the intragranular lattice deformation are the primary cause of the angular spread of the diffraction peak. This information may be important to capture for a variety of studies relating to the development of intragranular texture, which has not been quantitatively explored to a great degree for these type of diffraction experiments. Therefore instead of fitting independent parameters to each individual peak, we assign parameters according to certain structural properties of the grain itself, for example, parameters corresponding to an intragranular orientation distribution. We use the microstructural information to make predictions of the pixel by pixel diffracted intensity, and compare experimental and prediction in a residual on a pixel by pixel basis.

Besides a certain aesthetic/holistic appeal, this approach has several benefits: First, it introduces a larger set of data to minimize over in the least squares algorithm, and hence increases the precision of the lattice deformation estimates over the grain averaged approach. Second, the microstructural information obtained can be used as a trailing indicator of plastic deformation, as we will see upon application to data. Of course, this approach has relative shortcomings as well. The forward modeling approach is computationally expensive, so with current technology it should not be used as the de facto grain refinement algorithm. However, in these sort of applications, obtaining best fit parameters for experimental data, it makes sense to use a sequence of models of increasing sophistication in order to obtain the final parameter values. For one reason this is because good initial conditions are crucial in determining the success of an optimization algorithms for nonlinear problems. We have already seen an example of this increasing sophistication in §3.3.1.1 with respect to lattice refinement to determine $\mathbf{H}$. Grain indexing is the coarse level estimate for $\mathbf{R} \approx \mathbf{H}$, followed by the procedure discussed here, the final refinement for $\mathbf{H} \in \mathrm{GL}(3, \mathbb{R})$. For example, we may first perform a fit based on the intensity weighted peak locations, followed by the local intensity distribution, and finally the forward model.

In summary, both methods of extracting data from X-ray diffraction experiments discussed in this section have unique attributes , with different costs and benefits to weigh, but they are also compatible with one another. In the following sections, for each least squares model required we will describe: (1) the data involved $\mathbf{z}_1, \mathbf{z}_2$, (2) the functional form of the residual (3.242), and (3) the unknown parameters $\boldsymbol{\Theta}$, which the least squares algorithm seeks to determine. We also examine aspects of uncertainty estimates based on (3.246). For example (3.246) is dependent upon the form for the objective function Φ, so the uncertainty predictions from several model equations may be compared. We begin by addressing the grain averaged approach to lattice refinement, followed by the forward modeling approach.

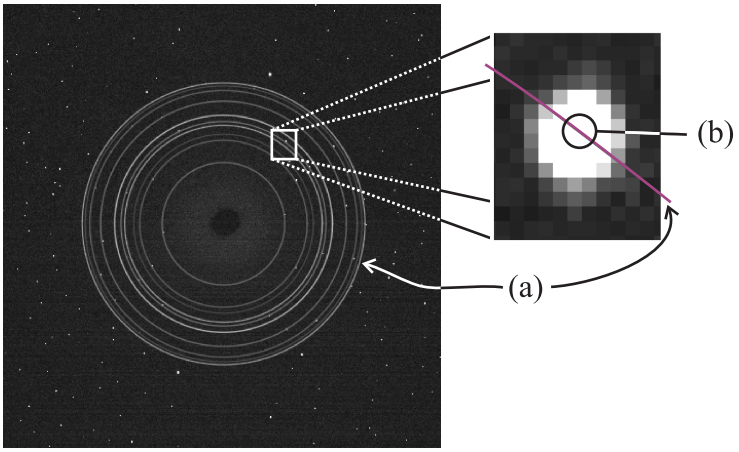

Figure 3.22: Diffraction image taken from area detector (see Figure 3.13), with $2\theta = \text{const}$ rings drawn on the detector (a). A diffraction peak is highlighted at (b). The uncertainty in the location of the diffraction peaks leads to uncertainty in the lattice deformation.

3.4.2.1 Grain averaged approach

In this section we describe the grain averaged approach to estimating model parameters, $\mathbf{H}$. As a brief review: recall that the main output we are seeking from the diffraction data is the lattice deformation, $\mathbf{H}$. Additionally, the geometric analysis in §3.3.3 allows the grain center of mass position $\mathbf{x}$ to be determined. Therefore in the language of (3.240), the model parameters accessible in this model are $\boldsymbol{\Theta} = (\mathbf{H}, \mathbf{x})$, both quantities on a grain averaged basis. As mentioned previously, the grain averaged approach fits a local intensity distribution to a diffraction peak. Uncertainty in the location of the center of the distribution is then communicated to the lattice refinement step by using weighted least squares. This enables a systematic determination of the precision uncertainty associated with high energy X-ray diffraction experiments. We now describe the details.

3.4.2.1.1 Diffraction peak model. In this section we introduce the diffraction peak model used to fit local intensity distributions recorded in the detector image stack, introduced in §3.3.1.1. An example of a local intensity distribution is shown in Figure 3.22, Figure 3.23. In a polycrystal it is certainly possible for diffraction peaks from different individual grains to overlap at the same location on the detector. This complicates the analysis, and is a limiting factor in our framework, as it is with any conventional approach of diffraction analysis. In this discussion of local intensity distributions we consider peak overlap to be previously accounted for. For example, by carefully selecting a threshold level which enables separation of nearby peaks.

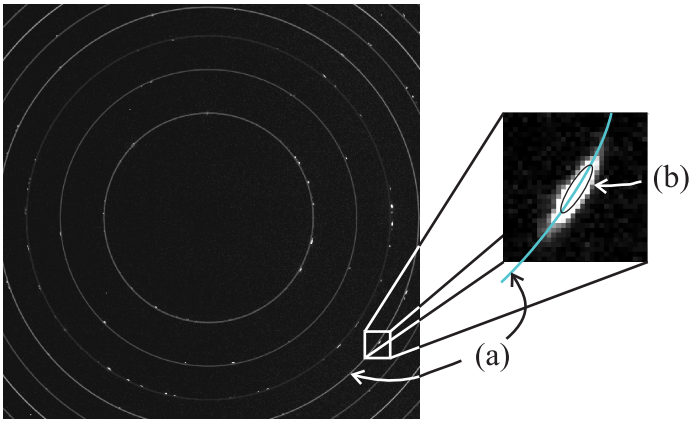

Figure 3.23: A diffraction image from a titanium alloy experiment, with 2θ = const rings drawn on the detector (a). A diffraction peak is highlighted at (b). The peak is elongated along the η direction of the detector plane due to plastic deformation suffered during tensile deformation.

In standard methods, the location of the diffraction peak is obtained from computing the intensity weighted average of the location in angular or pixel coordinates. That is, in practical terms,

$$\mathbf{x} = \frac{1}{\bar{E}} \sum_{i=1}^{N} E_i \mathbf{x}_i, \tag{3.247}$$

where $\mathbf{x}$ is the intensity weighted estimate of the location of the peak E_i is the intensity of the i^{th} pixel, $\bar{E} = \sum_i E_i$ is the total integrated intensity and $\mathbf{x}_i$ is the location of the i^{th} pixel. In contrast to this approach, in our method we assume an anisotropic functional form for the local integrated intensity: a three dimensional Gaussian along the angular directions, e.g. $E(2\theta, \eta, \omega)$. This formulation is supported by observations that diffraction peaks tend to be spread out along the η, ω coordinate directions. The choice of a Gaussian is primarily due to their long history of usage in X-ray diffraction; at the pixel resolution we use the precise functional form does not matter. We use

$$E(\theta, \eta, \omega) = E_0 \exp\left[-\left(\left(\frac{2\theta - 2\bar{\theta}}{s_{2\theta}}\right)^2 + \left(\frac{\eta - \bar{\eta}}{s_\eta}\right)^2 + \left(\frac{\omega - \bar{\omega}}{s_\omega}\right)^2\right)\right] + C, \tag{3.248}$$

where $2\bar{\theta}, \bar{\eta}, \bar{\omega}$ are the centers of the intensity distribution in angular coordinates, $s_{2\theta}, s_\eta, s_\omega$ are the angular widths, E_0 represents the intensity scaling of the peak and C represents the background radiation. In relation to the discussion in §3.4.1, $E(\cdot)$ is an example of the function $\mathbf{f}(\cdot)$ given in Equation (3.242). Inspection of Equation (3.248) reveals that the model parameters for the diffraction peak function are the array

$$\boldsymbol{\Theta}_{\text{peak}} = (2\bar{\theta}, \bar{\eta}, \bar{\omega}, s_{2\theta}, s_\eta, s_\omega, E_0, C), \tag{3.249}$$

and the independent variables ($\mathbf{z}_1$ in (3.241)) are the coordinates θ, η, ω.

We now incorporate (3.248) in a weighted least squares objective function of the form (3.243) to solve for $\mathbf{\Theta}^*_{\text{peak}}$. The residual for the diffraction peak objective function is formed on the measured integrated pixel intensity, written as

$$e_\tau(\mathbf{\Theta}_{\text{peak}}) = E_{\text{meas},\tau} - \int_{\Omega_\tau} E(\theta, \eta, \omega; \mathbf{\Theta}_{\text{peak}}) \mathrm{d}\Omega_\tau, \tag{3.250}$$

where $E_{\text{meas},\tau}$ is the measured integrated intensity for the τ^{th} pixel, $E(\theta, \eta, \omega; \mathbf{\Theta}_{\text{peak}})$ is given by the Gaussian distribution (3.248), with model parameters $\mathbf{\Theta}_{\text{peak}}$, (3.249), and Ω_τ denotes the $2\theta, \eta, \omega$ domain of the τ^{th} pixel. The integral in (3.250) is performed by standard numerical quadrature methods, with the number of quadrature points in each direction chosen to accurately capture the variation of the intensity over the pixel.

The weights, $B_{(\tau a)(\nu b)}$, are found using information about the distribution of E_{meas} estimated from repeated measurements. We denote the standard deviation of the intensity read by a pixel normalized to intensity as σ_E, so that the weights in (3.243) are given by

$$B_{(\tau)(\nu)} = \frac{1}{\sigma_E^2}, \tau = \nu \qquad B_{(\tau)(\nu)} \equiv 0, \tau \neq \nu. \tag{3.251}$$

In $(3.251)_1$ we have assumed that all pixels have the same variation in response to incident X-rays; assuming that the cross correlation between pixels is zero gives $(3.251)_2$. To quantify this, based on analyzing repeated scans of diffraction peaks at varying intensities we used a conservative estimate for σ_E to be given by $\sigma_E = 0.2 E_{\text{meas}}$. Using Equation (3.250), (3.251) in (3.243) gives the weighted least squares objective function

$$\Phi_{\text{peak}}(\mathbf{\Theta}_{\text{peak}}) = \sum_{\tau=1}^{N_{\text{pixels}}} \left(\frac{E_{\text{meas},\tau} - \int_{\Omega_\tau} E(2\theta, \eta, \omega; \mathbf{\Theta}_{\text{peak}}) \mathrm{d}\Omega_\tau}{\sigma_E} \right)^2, \tag{3.252}$$

where τ denotes the pixel index, and where N_{pixels} is the number of pixels assigned to the diffraction peak. Upon execution of the least squares algorithm to find $\mathbf{\Theta}^*_{\text{peak}}$ uncertainties for the model parameters at the solution are found from (3.246). In particular, the uncertainties of the parameters representing the center of the peak, $(\bar{2\theta}, \bar{\eta}, \bar{\omega})$ will be of importance in subsequent discussion in this section, and are denoted $(\sigma_{2\theta}, \sigma_\eta, \sigma_\omega)$. In the next section we implement the lattice deformation model equations into a weighted least squares framework.

3.4.2.1.2 Weighted lattice deformation model. In this section we briefly review the model used to estimate lattice deformation parameters given diffraction peak locations. We review the kinematics relating to the evolution of reciprocal vectors under finite lattice deformations. We then incorporate these relations into objective functions for use in the

weighted least squares method. We will propose several different objective functions in this section, examining the properties of each as they pertain to our uncertainty analysis in §3.4.2.1.3.

We have established the kinematic relations required to determine the lattice deformation in Chapter 2 and §3.3.5. To reiterate, we wish to describe the deformed state of the lattice in terms of the lattice deformation $\mathbf{H}$ with respect to a reference lattice configuration $\boldsymbol{\kappa}$. The configuration $\boldsymbol{\kappa}$ is obtained from §3.3.5.1 and (3.223), with $a, b, c, \alpha, \beta, \gamma$ set from literature values, which have most likely been obtained at a stress free state (e.g. powder pattern). The lattice in $\boldsymbol{\kappa}$ can equivalently be described by specifying a set of reciprocal vectors $\mathbf{G}^{(i)}$ for some labels (i). In the physical, or deformed configuration, the reference reciprocal vector $\mathbf{G}^{(i)}$ evolves due to deformation and becomes denoted as $\mathbf{g}^{(i)}$. The kinematic relation between the pair $\left(\mathbf{g}^{(i)}, \mathbf{G}^{(i)}\right)$ is given by

$$\mathbf{g}^{(i)} = \mathbf{H}^{-\mathrm{T}}\mathbf{G}^{(i)}, \tag{3.253}$$

where $\mathbf{H}^{-\mathrm{T}}$ denotes the inverse transpose of $\mathbf{H}$. We refer to Chadwick (1999); Holzapfel (2000); Liu (2002) as modern references for finite deformation kinematics.

The relation (3.253) is used as the foundation for forming residual equations describing the state of the lattice, which are then incorporated into a weighted least squares objective function. The model parameters here are evidently the components of the deformation gradient,

$$(\boldsymbol{\Theta}_{\text{lattice}})_{ij} \equiv (\mathbf{H})_{ij}, \quad i, j = 1, 2, 3, \tag{3.254}$$

although parameters equivalent to a deformation gradient may also be used. For example, from the polar decomposition theorem, we have $\mathbf{H} = \mathbf{RU}$, where $\mathbf{R}$ is a unique orthogonal tensor representing the rotation factor of $\mathbf{H}$ and $\mathbf{U}$ is a unique positive definite symmetric tensor representing the stretching factor of $\mathbf{H}$[7]. Using this gives the model parameters as

$$\boldsymbol{\Theta}_{\text{lattice}} \equiv (r_1, r_2, r_3, U_{11}, U_{22}, U_{33}, U_{12}, U_{23}, U_{31}), \tag{3.255}$$

where r_β, $\beta = 1, 2, 3$ are coordinates which produce a rotation tensor such as angle axis parameters (Frank, 1992), and $U_{ij} = U_{ji}$ are the components of $\mathbf{U}$. Distinguishing rotation and stretch parameters in this fashion will be useful in interpreting the results of our uncertainty analysis.

[7]We note here that the grain indexing step briefly referred to in §3.3.1.1 essentially prescribes the rotation factor $\mathbf{R}$ of $\mathbf{H} = \mathbf{RU}$. This is necessary to be able to form the pairs $\left\{\left(\mathbf{g}^{(i)}, \mathbf{G}^{(i)}\right)\right\}$, which are then used as data to implement (3.253) in a least squares algorithm (described later in this section). Due to crystal symmetry however, one may arrive at different $\mathbf{R}$ for the same grain if one used a different indexing algorithm, hence changing the pairings $\left\{\left(\mathbf{g}^{(i)}, \mathbf{G}^{(i)}\right)\right\}$, and subsequently both $\mathbf{U}$ and $\mathbf{H}$. Equivalently, reassigning $\mathbf{R}$ to the same grain amounts to assigning different reference configurations for the material. Since the uncertainty analysis here is essentially related to local behavior (i.e. curvature) of an objective function $\Phi(\boldsymbol{\Theta})$, see §3.4.2, this issue does not present any complications for us.

As with the diffraction peak model, we now incorporate (3.253) in a weighted least squares objective function to enable the estimation of the parameters of Equation (3.255). The required data for the residuals based on (3.253) are the reciprocal vector pairings $\left\{\left(\mathbf{g}^{(i)}, \mathbf{G}^{(i)}\right)\right\}$, which are able to be formed after the diffraction data is indexed, see §3.3.4 for more on grain indexing.

Next we propose several specific residuals based on (3.253). In all residuals μ denotes the index associated with the μ^{th} diffraction peak. The first residual, $e^1_{\mu a}$, is given by

$$\{e^1_{\mu a}\} = \left\{ \begin{array}{ll} e^1_{\mu 1} & = \bar{2\theta}^{(\mu)}_{\text{meas}} - \gamma_1(\mathbf{H}^{-\text{T}}_{\boldsymbol{\kappa}}\mathbf{G}^{(\mu)}) \\ e^1_{\mu 2} & = \bar{\eta}^{(\mu)}_{\text{meas}} - \gamma_2(\mathbf{H}^{-\text{T}}_{\boldsymbol{\kappa}}\mathbf{G}^{(\mu)}) \\ e^1_{\mu 3} & = \bar{\omega}^{(\mu)}_{\text{meas}} - \gamma_3(\mathbf{H}^{-\text{T}}_{\boldsymbol{\kappa}}\mathbf{G}^{(\mu)}) \end{array} \right\}, \tag{3.256}$$

where the invertible functions $\boldsymbol{\gamma} : \mathbb{R}^3 \mapsto \mathbb{R}^3$ denote mapping the predicted reciprocal vector $\mathbf{H}^{-\text{T}}_{\boldsymbol{\kappa}}\mathbf{G}^{(\mu)}$ into angular coordinates, that is,

$$\boldsymbol{\gamma}(\mathbf{H}^{-\text{T}}_{\boldsymbol{\kappa}}\mathbf{G}^{(\mu)}) = (2\theta^{(\mu)}, \eta^{(\mu)}, \omega^{(\mu)}),$$

with the associated residual (3.256) being based on the difference between predicted and measured angular coordinates of the peak. Note that $\boldsymbol{\gamma}$ is not one-to-one (there are usually two angular solutions for a single reciprocal vector) and so the formation of the residuals with (3.256) needs to be implemented with caution. Even so, employing (3.256) has advantages which will be made evident in §3.4.2.1.3. A second proposed residual, $e^2_{\mu a}$, is given by

$$e^2_{\mu a} = \left[\mathbf{g}^{(\mu)}\right]_a - \left[\mathbf{H}^{-\text{T}}_{\boldsymbol{\kappa}}\mathbf{G}^{(\mu)}\right]_a, \tag{3.257}$$

where the notation $[\mathbf{v}]_a$, simply denotes the a^{th} component of $\mathbf{v}$ resolved on an appropriate basis. For example the values of $[\mathbf{v}]_a$ could be the Cartesian component decomposition, $[\mathbf{v}]_a = \mathbf{v} \cdot \mathbf{e}_a$, $a = 1, 2, 3$. In our implementation we found using $[\,]_a$ to denote a spherical polar coordinate decomposition with inclination angle measured from the zenith $\mathbf{e}_2$ and azimuthal angle measured from $\mathbf{e}_1$ to be useful. We we elucidate upon this in §3.4.2.1.3. The final residual we report on, $e^3_{\mu a}$, is obtained by simply forming the inner product of the kinematic relation (3.253),

$$e^3_{\mu 1} = (\mathbf{g}^{(\mu)} - \mathbf{H}^{-\text{T}}_{\boldsymbol{\kappa}}\mathbf{G}^{(\mu)}) \cdot (\mathbf{g}^{(\mu)} - \mathbf{H}^{-\text{T}}_{\boldsymbol{\kappa}}\mathbf{G}^{(\mu)}), \tag{3.258}$$

resulting in a scalar valued residual.

In all residual equations (3.256)-(3.258), the input data are the centers of the spot in angular space, the $\bar{2\theta}, \bar{\eta}, \bar{\omega}$ parameters from the solution vector $\boldsymbol{\Theta}^*_{\text{peak}}$, see (3.249). The weights for the residuals (3.256)-(3.258) are assigned using standard error propagation formula (Beckwith et al., 1995), for example,

$$\sigma_h = \sqrt{\sum\nolimits_{i=1}^{N_{\text{args}}} \left(\frac{\partial h}{\partial x^i}\sigma_{x^i}\right)^2}, \tag{3.259}$$

where the function $h = h(\{x^i\})$ is a function of the arguments $\{x^i\}$, $i = 1, 2, ...N_{\text{args}}$, which have uncertainties σ_{x^i}. Using (3.259) the weights for the residuals $e_{\mu a}$ in (3.256)-(3.258) are determined by

$$\sigma_{e_{\mu a}} = \sqrt{\left(\frac{\partial e_{\mu a}}{\partial 2\theta}\sigma_{2\theta}\right)^2 + \left(\frac{\partial e_{\mu a}}{\partial \eta}\sigma_{\eta}\right)^2 + \left(\frac{\partial e_{\mu a}}{\partial \omega}\sigma_{\omega}\right)^2}, \tag{3.260}$$

where $\sigma_{2\theta}, \sigma_{\eta}, \sigma_{\omega}$ are found from the uncertainties of the peak location by using the analysis discussed at the end of §3.4.2.1.1. That is, by applying (3.246) to the objective function for the peak, (3.252). In using (3.260) we have omitted considerations of other possible sources of error entering into $e_{\mu a}$, such as uncertainty in the detector calibration parameters, see (3.176). These factors can be incorporated as needed.

Next we put together (3.256),(3.257),(3.258) and (3.260) into three objective functions represented by

$$\Phi^{\beta}_{\text{lattice}}(\mathbf{\Theta}_{\text{lattice}}) = \sum_{\mu=1}^{N_{\text{peaks}}} \left(\frac{e^{\beta}_{\mu a}(\mathbf{\Theta}_{\text{lattice}})}{\sigma_{e^{\beta}_{\mu a}}}\right)^2, \tag{3.261}$$

where $\beta = 1, 2, 3$, $e^{\beta}_{\mu a}$ are given by (3.256),(3.257),(3.258) respectively, and $\sigma_{e^{\beta}_{\mu a}}$ is given by computing (3.260). As before, upon execution of the least squares algorithm to find $\mathbf{\Theta}^*_{\text{lattice}}$, uncertainties for the model parameters are found from (3.246). These uncertainties will be denoted as $(u_{r_1}, u_{r_2}, u_{r_3}, u_{U_{11}}, u_{U_{22}}, u_{U_{33}}, u_{U_{12}}, u_{U_{23}}, u_{U_{31}})$. The properties of the three objective functions (3.261) will be examined in §3.4.2.1.3.2, where we present results from applying our methods to experimental data taken from a ruby single crystal as an ideal case. We also give results of the application to an elastically and plastically deformed titanium polycrystal as an example.

3.4.2.1.3 Experimental application In this section we apply our grain averaged analysis framework to data obtained from two different experiments. First, we analyze an unstrained ruby single crystal, in order to take repeated measurements of a calibration material. This data consists of sharp diffraction peaks, hence the requirement of observing data across multiple pixels and omega frames for the local peak intensities is not satisfied for many peaks. However we still use this data to compare our error predictions with those based upon repeated measurements. We also use this data to suggest a preferred objective function for fitting the lattice deformation (3.261) and to examine the effect of the total angular range, $\Delta\omega \equiv \omega_{\text{f}} - \omega_0$ on the single scan uncertainty prediction. We comment on the special accommodations required to analyze the ruby data set in further detail in the next section.

Secondly, we apply our method to a polycrystalline sample of a titanium alloy, $\beta 21s$, under tensile load and after plastic deformation. This data was chosen to present since it is representative of the intended application for our method, as the diffraction peaks are spread over a relatively large angular range. We analyze a grain in the diffraction volume which was manually centered on the rotation axis and report on the uncertainties of the averaged stretch and orientation for this grain.

3.4.2.1.3.1 Ruby single crystal In this section we apply our established uncertainty framework to diffraction data taken from a ruby single crystal. We wish to find the estimated uncertainty of $\mathbf{\Theta}^*_{\text{lattice}} = \mathbf{H}^* = (\mathbf{R}^*, \mathbf{U}^*)$, based on the prescription for uncertainty developed in the previous sections. We then compare the uncertainty obtained using our method from a single scan with that attained directly from the statistical distribution of repeated scans.

We first make several comments on the ruby data analysis, since aspects of our analysis differ slightly from that described in §3.4.2.1.1 owing to the low defect content of this crystal. For the ruby, many diffraction peaks are present on only a single ω-frame, hence the Gaussian intensity distribution used in our algorithm (3.248) is altered to become two dimensional, i.e.,

$$E(\theta, \eta) = E_0 \exp\left[-\left(\left(\frac{2\theta - 2\bar{\theta}}{s_{2\theta}}\right)^2 + \left(\frac{\eta - \bar{\eta}}{s_\eta}\right)^2\right)\right] + C. \tag{3.262}$$

The values for $2\bar{\theta}, \bar{\eta}$ and the uncertainties on these are then obtained with with the same methods as described in §3.4.2. For the location of the ω coordinate, we assign $\bar{\omega}$ as halfway between the ω slices which bracket the location of the peak, and assign the uncertainty in ω as $\sigma_\omega = \pm\frac{1}{2}\delta\omega$. We then proceed with the refinement as described in §3.4.2.1.2. This is unconventional compared to other methods, which either omit the ω coordinate from the residual computation altogether, or form a residual based on the ω value obtained from the lattice deformation parameters of the previous iteration. The reason for our approach is that our uncertainty computation depends on the local curvature of the objective function, (3.245). Conventional methods for refinement cause the objective function to be locally flat at the solution $\mathbf{\Theta}^*$ with respect to deformations which change the omega coordinates of the peak. Hence, we could not use predictions of uncertainty based on the confidence region (3.246) when omitting the ω coordinate from the objective function. An alternate, dedicated framework of analysis would have to be used to rigorously handle the case of single ω frame peaks, for which previous work has been done, e.g see Winkler et al. (1979). Typically uncertainties on the ω coordinate of a peak are about a factor of 10 greater than the η coordinate uncertainty, and about a factor of 100 greater than the θ coordinate uncertainty. The implication being that we are effectively using the ω coordinate less than η, θ in refining the lattice deformation parameters. In a general sense this accomplishes the same end as conventional approaches.

Additionally, after a solution for $\mathbf{\Theta}^*_{\text{lattice}}$ is obtained, we evaluate the residual vector based on (3.261), Φ^β_{vec}, where

$$\Phi^\beta_{\text{vec}} \equiv \left(\frac{e^\beta_{1a}(\mathbf{\Theta}_{\text{lattice}})}{\sigma_{e^\beta_{1a}}}, \frac{e^\beta_{2a}(\mathbf{\Theta}_{\text{lattice}})}{\sigma_{e^\beta_{2a}}}, ..., \frac{e^\beta_{N_{\text{peaks}}a}(\mathbf{\Theta}_{\text{lattice}})}{\sigma_{e^\beta_{N_{\text{peaks}}a}}}\right).$$

We compute mean and standard deviation for Φ^β_{vec}, and then remove peaks which lie outside a specified number, N_σ, of standard deviations from the mean value of Φ^β_{vec}. We then find

the solution for $\mathbf{\Theta}^*_{\text{lattice}}$ based on this reduced data set. We repeat this procedure until no further peaks are removed. This procedure is consistent with recommendations on outlier removal in Bard (1974), who suggests a range for N_σ of $2.5 - 3$. This procedure is also seemingly used, along with other proposed criteria for outlier removal in Oddershede et al. (2010). We typically used $N_\sigma = 3$ for our tests.

Diffraction measurements were taken at Argonne National Lab, Sector 1-ID. The experimental setup used is shown schematically in Figure 3.13. For these tests we used a 150 μm ruby sphere, NIST SRM 1990. The beam size was a wide box beam, 500 μm by 200 μm. The beam energy was 80.72 keV, for a wavelength, λ, of 0.153 Å. The detector was a GE 41RT, with 2048 x 2048 pixels, and 200 μm pixel size, positioned 1100 mm from the sample. The ruby was centered on the rotation axis and then scans were taken for $\omega \in [-60°, 60°]$, with an angular rotation increment of $\delta\omega = 0.25°$. The total number of frames in the detector image stack was $\Delta\omega/\delta\omega = 120/0.25 = 480$. We repeated the scans 9 times in order to directly estimate the sampling distribution of $\mathbf{\Theta}^*_{\text{lattice}}$. This number of scans was chosen arbitrarily based on beam time limitations.

3.4.2.1.3.2 Results. In this section we present our results from the ruby experiments. In order to compute a deformation gradient, $\mathbf{H}$, (3.159) the reference configuration $\boldsymbol{\kappa}$ for the ruby was assigned using hexagonal unit cell based lattice parameters, giving $a = 4.761$ Å, $c = 12.996$ Å, see Wong-Ng et al. (2001).

Precision of $\mathbf{R}, \mathbf{U}$. The precision we attain from the rotation factor fit ranged over $0.01° - 0.02°$ for the repeated measurements. The precision we attain from the strain fit ranged from approximately $30 - 130\mu\epsilon$, where $\mu\epsilon \equiv 10^{-6}$ strain. To relate uncertainty in the stretch $\mathbf{U}$ to uncertainty in strain we have used (3.259) with

$$\mathbf{E} = \frac{1}{2}(\mathbf{U}^2 - \mathbf{I}), \tag{3.263}$$

where $\mathbf{E}$ is the Lagrange lattice strain measure, and $\mathbf{I}$ is the identity. To obtain the stated value of uncertainty in the rotation factor fit, we computed the misorientation between the solution $\mathbf{R}^* \equiv \hat{\mathbf{R}}(\boldsymbol{r}^*)$ and the rotation tensor at the furthest distance from the solution, $\mathbf{R}'$, where $\hat{\mathbf{R}} : \mathbb{R}^3 \mapsto \text{SO}(3, \mathbb{R})$ denotes the map from angle axis coordinates to rotation matrices, and $\boldsymbol{r}^* \equiv (r_1, r_2, r_3)^*$ is the projection of the solution $\mathbf{\Theta}^*_{\text{lattice}}$ into angle axis rotation space. Here $\mathbf{R}'$ is obtained by using the uncertainty in the angle axis parameters, e.g. $\mathbf{R}' = \hat{\mathbf{R}}(\mathbf{r}^* + \mathbf{u}_{\text{r}})$, where $\mathbf{u}_{\text{r}} \equiv (u_{r_1}, u_{r_2}, u_{r_3})$, i.e., it is the array formed by the uncertainties in the angle axis parameters. We compare the estimated uncertainty at 95% confidence from a single scan, i.e. using (3.261) with (3.246), to the uncertainty obtained from standard statistical analysis of repeated scans in Tables 3.1,3.2. The stated results are obtained from the objective function Φ^1_{lattice}, see (3.261). In Tables 3.1,3.2, the uncertainty based on repeated measurements is referred to as the measured uncertainty, u_{meas}, and the uncertainty based on our method will

Table 3.1: Comparison of average estimated uncertainty to that directly obtained by repeated measurements for rotation factor angle axis components. Uncertainties are computed based on a 95% confidence interval, using Φ^1_{lattice}.

	u_{r_1}	u_{r_2}	u_{r_3}
u_{estimate}	$5.1 \cdot 10^{-5}$	$1.9 \cdot 10^{-4}$	$4.1 \cdot 10^{-5}$
u_{meas}	$5.2 \cdot 10^{-4}$	$2.5 \cdot 10^{-3}$	$1.1 \cdot 10^{-4}$

Table 3.2: Comparison of average estimated uncertainty to that directly obtained by repeated measurements for stretch components. Uncertainties are computed based on a 95% confidence interval, using Φ^1_{lattice}.

	$u_{U_{11}}$	$u_{U_{22}}$	$u_{U_{33}}$	$u_{U_{12}}$	$u_{U_{23}}$	$u_{U_{31}}$
u_{estimate}	$1.2 \cdot 10^{-4}$	$6.6 \cdot 10^{-5}$	$5.2 \cdot 10^{-5}$	$5.6 \cdot 10^{-5}$	$3.3 \cdot 10^{-5}$	$5.4 \cdot 10^{-5}$
u_{meas}	$9.6 \cdot 10^{-5}$	$3.3 \cdot 10^{-5}$	$6.8 \cdot 10^{-5}$	$9.7 \cdot 10^{-5}$	$5.2 \cdot 10^{-5}$	$6.8 \cdot 10^{-5}$

be referred to as the estimated uncertainty, u_{estimate}. Our results compare favorably, being slightly underpredictive of the uncertainty on the rotation components by about a factor of 10, and being underpredictive of the stretch component uncertainty by factor of around 1.5. (Bard, 1974) states that the covariance matrices used to estimate uncertainty from a single test (3.245) should be considered correct to within an order of magnitude; our results are in line with this.

Effect of $\Delta\omega$ on precision. Next we consider the effect of the *total* ω range for the scan, $\Delta\omega$, on the estimated uncertainty. In Figure 3.24 we plot the uncertainty in the stretch component, U_{11} versus the total ω interval, $\Delta\omega$, for $\Delta\omega = (10°, 20°, ..., 120°)$. The component U_{11} was chosen to be representative of the trends in uncertainty for all stretch and rotation parameters. We see a nonlinear trend for the estimated uncertainty in U_{11}, with uncertainty decreasing as the ω range goes up, as might have been anticipated. One could use data like this to inform the selection an appropriate $\Delta\omega$ range if a target level of precision is to be weighed against the time required for a scan.

Comparison of Φ_{lattice}. We next compare results from the three objective functions Φ^1_{lattice}, Φ^2_{lattice}, Φ^3_{lattice} (3.261). To do this, we parametrize the uncertainties obtained from these three objective functions in an experimentally meaningful way by modifying the input data to simulate the effect of taking larger $\delta\omega$ steps. That is, we hypothesize larger $\delta\omega$ steps result in larger uncertainties for the ω locations of the peaks and compare error predictions resulting from each of the objective functions. Explicitly, we compare the uncertainty from objective functions

$$\Phi^{\beta}_{\text{lattice}}(\boldsymbol{\Theta}_{\text{lattice}}, t) = \sum_{\mu=1}^{N_{\text{peaks}}} \left(\frac{e^{\beta}_{\mu a}(\boldsymbol{\Theta}_{\text{lattice}})}{\sigma_{e^{\beta}_{\mu a}}(t)} \right)^2, \tag{3.264}$$

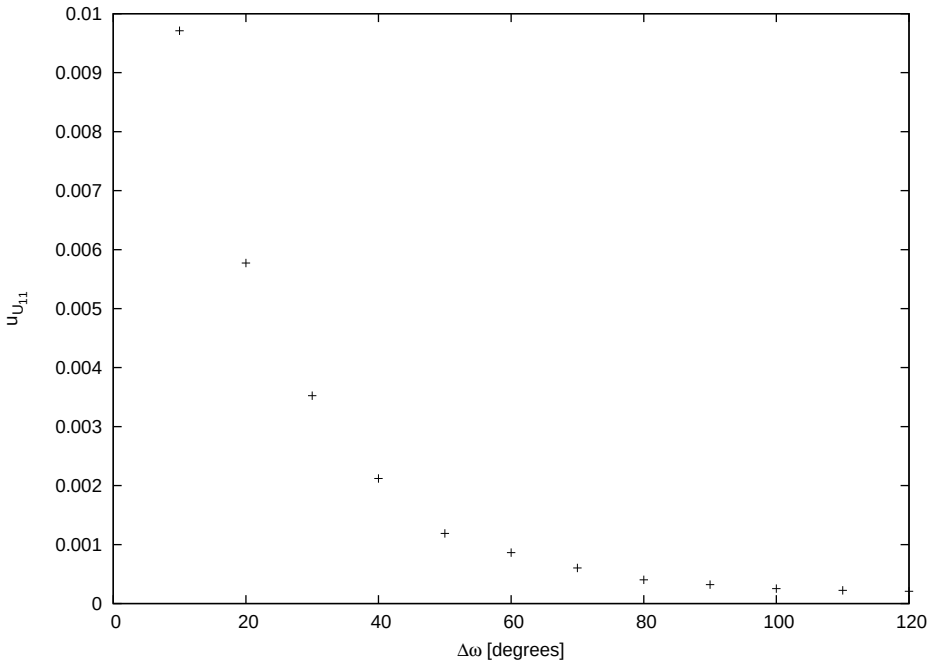

Figure 3.24: Plot of estimated uncertainty for a representative deformation parameter, U_{11} vs *total* angular sweep range, $\Delta\omega \equiv \omega_{\mathrm{f}} - \omega_0$, for the ruby single crystal experiment.

where $\beta = 1, 2, 3$, $e^{\beta}_{\mu a}$ are given by (3.256),(3.257),(3.258) respectively, and $\sigma_{e^{\beta}_{\mu a}}(t)$ is given by computing (3.260):

$$\sigma_{e_{\mu a}}(t) = \sqrt{\left(\frac{\partial e_{\mu a}}{\partial 2\theta}\sigma_{2\theta}\right)^2 + \left(\frac{\partial e_{\mu a}}{\partial \eta}\sigma_{\eta}\right)^2 + \left(\frac{\partial e_{\mu a}}{\partial \omega}\sigma_{\omega}(t)\right)^2}, \tag{3.265}$$

where $\sigma_{\omega}(t) = t$.

In Figures 3.25 and 3.26 we see the compiled error bar trends as a function of t for a rotation parameter r_1 and for a stretch parameter, U_{11} for the three objective functions. These plots should be used for qualitative comparisons between $\Phi^1_{\mathrm{lattice}}$, $\Phi^2_{\mathrm{lattice}}$, $\Phi^3_{\mathrm{lattice}}$. The objective functions $\Phi^1_{\mathrm{lattice}}, \Phi^2_{\mathrm{lattice}}$ give approximately the same behavior for both rotation and stretch. The error estimate for the rotation parameter r_1 increases upon increasing $\sigma_{\omega}(t)$ but the error estimate for the stretch parameter U_{11} is not affected. Indeed, one can show that the θ coordinate of the diffraction peak only depends on the stretching factor, $\mathbf{U}$ of $\mathbf{H}$. In other words, the uncertainties from the ω coordinate couple minimally to the stretch; this is particularly evident in the construction of $\Phi^1_{\mathrm{lattice}}$ in Equation (3.256). However Figure 3.26 indicates that the spherical polar coordinate decomposition of the reciprocal vectors used in $\Phi^2_{\mathrm{lattice}}$ also apparently decouples the ω coordinate from residuals involving $\mathbf{U}$. Finally, from Figure 3.26 we note that the objective function $\Phi^3_{\mathrm{lattice}}$ based on the inner product of

measured and predicted reciprocal vectors is not able to separate the effect of the lattice stretch from the influence of increasing σ_ω.

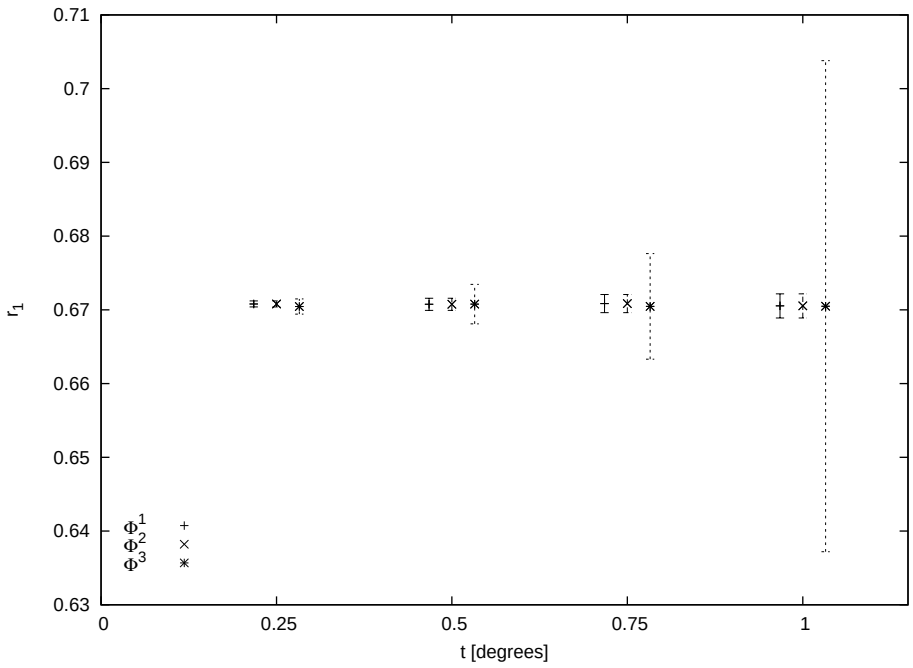

Figure 3.25: Plot of r_1 vs $\delta\omega$ for $\Phi^1_{\text{lattice}}, \Phi^2_{\text{lattice}}, \Phi^3_{\text{lattice}}$. Error bars represent 95% confidence intervals. The objective functions $\Phi^1_{\text{lattice}}, \Phi^2_{\text{lattice}}$ perform similarly, while the function Φ^3_{lattice} is associated with greater uncertainty as u_ω is increased.

To see why the spherical polar coordinate decomposition of Φ^2_{lattice} decouples ω from $\mathbf{U}$, consider the residual contribution from the μ^{th} diffraction peak, with angular coordinates $\theta^{(\mu)}, \eta^{(\mu)}, \omega^{(\mu)}$ and with corresponding reciprocal vector $\mathbf{g}^{(\mu)} = \boldsymbol{\gamma}^{-1}(\theta^{(\mu)}, \eta^{(\mu)}, \omega^{(\mu)})$. The magnitude coordinate of the μ^{th} residual equation of Φ^2_{lattice} is expressed as

$$e^2_{\mu 1} = \|\mathbf{g}^{(\mu)}\| - \|\mathbf{H}^{-T}\mathbf{G}^{(\mu)}\|, \tag{3.266}$$

where $\mathbf{g}^{(\mu)}, \mathbf{G}^{(\mu)}$ have been associated by previously indexing the diffraction peaks. The magnitude of $\mathbf{g}^{(\mu)}$ is related to the planar spacing by (Boumann, 1957)

$$\|\mathbf{g}^{(\mu)}\| = \frac{1}{d^{(\mu)}},$$

where $d^{(\mu)}$ is the planar spacing on the μ^{th} lattice plane. Furthermore, Bragg's law gives

$$\|\mathbf{g}^{(\mu)}\| = \frac{2\sin\theta^{(\mu)}}{\lambda}, \tag{3.267}$$

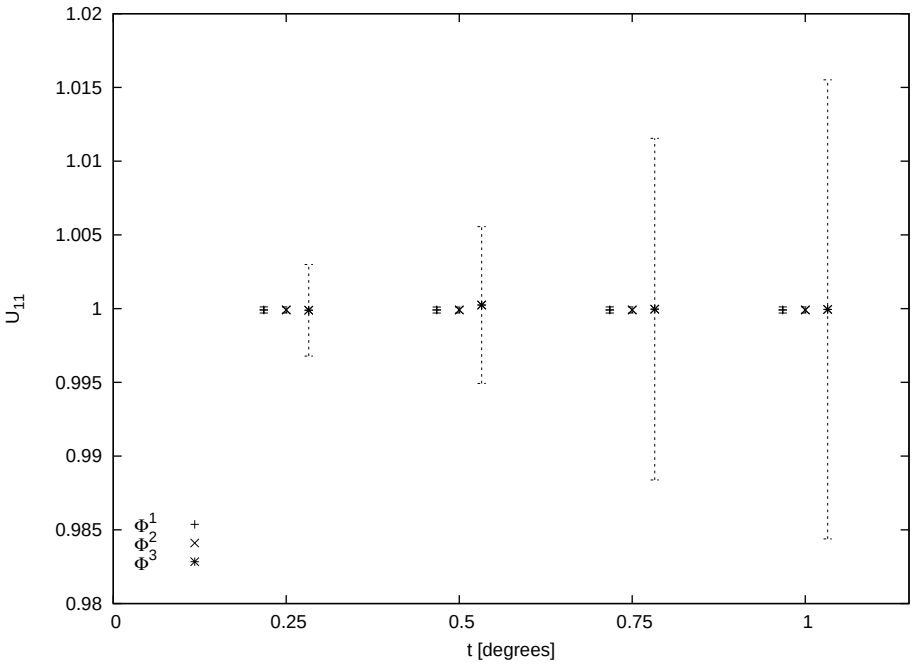

Figure 3.26: Plot of U_{11} components vs $\delta\omega$ for $\Phi^1_{\text{lattice}}, \Phi^2_{\text{lattice}}, \Phi^3_{\text{lattice}}$. Error bars represent 95% confidence intervals. The objective functions $\Phi^1_{\text{lattice}}, \Phi^2_{\text{lattice}}$ perform similarly, being independent of u_ω. The function Φ^3_{lattice} is associated with linearly increasing uncertainty as u_ω is increased.

where λ is the wavelength of radiation. The implication of (3.267) is that the magnitude component of a reciprocal vector is only a function of the θ coordinate of the peak. We also have

$$\|\mathbf{H}^{-\mathrm{T}}\mathbf{g}^{(\mu)}\| \equiv \sqrt{\mathbf{H}^{-\mathrm{T}}\mathbf{G}^{(\mu)} \cdot \mathbf{H}^{-\mathrm{T}}\mathbf{G}^{(\mu)}} = \sqrt{\mathbf{C}^{-1} \cdot \mathbf{G}^{(\mu)} \otimes \mathbf{G}^{(\mu)}}, \tag{3.268}$$

where $\mathbf{C} \equiv \mathbf{H}^{\mathrm{T}}\mathbf{H} = \mathbf{U}^2$ is the right Cauchy-Green stretch tensor for the lattice. Upon substituting (3.267) and (3.268) in (3.266) it is evident that the residual equation (3.266) thus incorporates no rotation factor information, and is only dependent upon the θ coordinate of the diffraction peak. Hence increasing the uncertainty in ω couples only weakly to the stretch factor, $\mathbf{U}$.

A more informative comparison between Φ^1_{lattice}, Φ^2_{lattice}, Φ^3_{lattice} can be observed by considering the covariance matrix at the solution, $\mathbf{V}_{\boldsymbol{\Theta}^*_{\text{lattice}}}$. For the objective functions $\Phi^1_{\text{lattice}}, \Phi^2_{\text{lattice}}$, the covariance matrix has one large eigenvalue, with the corresponding eigenvector primarily in the (r_1, r_2, r_3) subspace of the full $\boldsymbol{\Theta}_{\text{lattice}}$-space. This indicates that the rotation factor $\mathbf{R}$ is the least well determined component of $\mathbf{H}$ for the ruby data. We explore this observation further in §3.4.2.1.4.

Next, we visualize the local behavior of the objective functions by directly evaluating

Φ^2_{lattice}, Φ^3_{lattice} for model parameters near the minimizing solution $\boldsymbol{\Theta}^*_{\text{lattice}}$. We probe the r_1, r_2 plane, holding the other parameters fixed. Contour plots for Φ^2_{lattice},Φ^3_{lattice} were generated and are shown in Figures 3.27, 3.28 respectively. In these figures, 10 contours were drawn from a $\Delta\Phi_{\text{lattice}}$ range of $[0, 100]$, where

$$\Delta\Phi_{\text{lattice}}(\boldsymbol{\Theta}_{\text{lattice}}) \equiv \Phi^*_{\text{lattice}} - \Phi_{\text{lattice}}(\boldsymbol{\Theta}_{\text{lattice}}),$$

and

$$\Phi^*_{\text{lattice}} \equiv \Phi_{\text{lattice}}(\boldsymbol{\Theta}^*_{\text{lattice}}).$$

We also superimpose the confidence region defined by $\mathbf{V}_{\boldsymbol{\Theta}^*_{\text{lattice}}}$ by a dashed black line, and the confidence region defined by finding the exact bounds of $\Delta\Phi_{\text{lattice}}$ in grey. The exact boundaries of $\Delta\Phi_{\text{lattice}}$ may be shown to correspond to $\chi^2_{0.95,9}$ by the relation

$$\Delta\Phi_{\text{lattice,max}} = \frac{1}{2}\chi^2_{0.95,9}, \tag{3.269}$$

which can be seen by expanding $\Phi(\boldsymbol{\Theta})$ in a Taylor series expansion about $\boldsymbol{\Theta}^*_{\text{lattice}}$ and using (3.245),(3.246), see also (Bard, 1974). We observe that the uncertainty ellipsoid defined by the covariance matrix, (3.246), agrees well with the exact results, and provides a slightly conservative estimate of the confidence region. As suggested by the eigenvalue/eigenvector observations in the previous paragraph, Figure 3.27 visually confirms that the objective function Φ^2_{lattice} is relatively ill determined along one direction in rotation space. Contrast this with the local plot of Φ^3_{lattice} in Figure 3.28, which does not have a pronounced eigenvalue and has broader local curvature around the solution $\boldsymbol{\Theta}^*$. The conclusion is that we apparently lose information about the source of the uncertainty when forming the objective function in the fashion of Φ^3_{lattice}.

This analysis of the ruby single crystal provides validation of the overall method. Next we move on to the next section where we apply our method to a strained titanium alloy. We examine a single grains embedded in the polycrystal.

3.4.2.1.3.3 Application to strained polycrystal In this section we apply our uncertainty framework to diffraction data taken from a polycrystalline sample of a titanium alloy, $\beta 21s$ (BCC), while under tensile load and after plastic deformation. This material is representative of the intended application for the X-ray diffraction experimental configuration: analysis of bulk deformation in polycrystals.

Diffraction measurements were again taken at Argonne National Lab, Sector 1-ID, with the same detector and beam energy as for the ruby experiment, see §3.4.2.1.3.1. The tension axis was in the $\mathbf{e}_2$ direction, see Figure 3.13. The distance between the sample and the detector was 1500 mm. From the diffraction volume a grain was selected and manually centered on the rotation axis. Scans were taken for $\omega \in [-60°, 60°]$, with a rotation increment of $\delta\omega = 0.5°$. There were $\Delta\omega/\delta\omega = 240$ images in the detector image stack. We used the same outlier rejection criteria described in the ruby experiment, see §3.4.2.1.3.1.

Table 3.3: Cartesian components of the Lagrange strain tensor for the deformed titanium alloy with uncertainty at 95% confidence. (in $\mu\epsilon$)

E_{11}	E_{22}	E_{33}	E_{12}	E_{23}	E_{31}
-7000 ± 110	4800 ± 220	-2200 ± 240	-4800 ± 100	1400 ± 110	-400 ± 130

Results The reference configuration used to define $\boldsymbol{\kappa}$ for the BCC titanium alloy was constructed using a cubic unit cell with lattice parameter $a = 3.252$ Å. A representative diffraction image is shown for a single ω frame in Figure 3.23, where a diffraction peak is highlighted. The elongation of the peak along the η direction resulting spatial inhomogeneity from plastic flow is evident. In order to solve for the lattice deformation, $\mathbf{R}, \mathbf{U}$, we used the objective function Φ^2_{lattice}, (3.261), in the least squares algorithm.

Our single scan uncertainty gave the precision on the rotation factor as $0.03°$, and the precision on the stretch corresponding to a strain uncertainty in a range from $100 - 250\mu\epsilon$. The measured Lagrange strain components, (3.263), are tabulated in Table 3.3. To examine the kinematics, the right stretch tensor, $\mathbf{V} = \mathbf{R}\mathbf{U}\mathbf{R}^{\mathrm{T}}$ is more informative than $\mathbf{U}$ for comparing with anticipated results, those being extension along the loading axis, $\mathbf{e}_2$. However we note that the high anisotropy in this crystal implies that uniaxial stress doesn't imply uniaxial strain, see (Efstathiou et al., 2010). Anisotropy also produces inhomogeneous deformation in the polycrystal. Even so, we find that the eigenvectors of $\mathbf{V}$ are nearly coaxial with $\mathbf{e}_1, \mathbf{e}_2, \mathbf{e}_3$, with eigenvalues $(0.997, 1.008, 0.998)$, respectively, indicating uniaxial extension kinematics along $\mathbf{e}_2$. We examine the stress state of this grain at the end of the next section.

3.4.2.1.4 Discussion In this section we further interpret the results of the experiments described in §3.4.2.1.3. We first discuss observations resulting from the validation experiments using the ruby single crystal, and end the section with a stress analysis of the titanium alloy grain under load.

In §3.4.2.1.3 we showed that depending on the objective function used to formulate the least squares problem we obtained different confidence regions around the solution parameters $\boldsymbol{\Theta}^*_{\text{lattice}}$, see Figures 3.27, 3.28. Generally speaking, for objective functions where the residual involving ω was separated from the other residuals (e.g. Φ^2_{lattice}) the confidence region was stretched along one direction, and for objective functions where each residual depends upon ω, the confidence region was broader.

We now seek to provide an interpretation for the direction of maximum uncertainty, evident in Figure 3.27. This direction corresponds to the maximum eigenvector of the covariance matrix, $\mathbf{V}_{\boldsymbol{\Theta}^*_{\text{lattice}}}$. Based on the experimental setup and associated resolution in angular coordinates, see Figure 3.13, we might expect that one could reorient the sample by a rotation with axis $\mathbf{e}_2$ without affecting the measured diffraction peak locations significantly. More precisely stated, the resolution in ω is much less than that in 2θ or η, hence a reorientation of the sample changing ω is less detectable than a change in the sample which would affect $2\theta, \eta$. Therefore we might expect that the maximum eigenvector of $\mathbf{V}_{\boldsymbol{\Theta}^*_{\text{lattice}}}$ is associated

with a relatively poorly known rotation of the sample, $\bar{\mathbf{R}}$, such that

$$\Phi_{\text{lattice}}(\bar{\mathbf{R}}\mathbf{R}^*, \mathbf{U}^*) \approx \Phi_{\text{lattice}}(\mathbf{R}^*, \mathbf{U}^*), \tag{3.270}$$

and where the rotation axis of $\bar{\mathbf{R}}$ is aligned with the axis of the rotation stage, $\mathbf{e}_2$. In (3.270) we have used the notation $(\mathbf{R}^*, \mathbf{U}^*) = \boldsymbol{\Theta}^*_{\text{lattice}}$.

To investigate if this is true, we first project the maximal eigenvector of $\mathbf{V}_{\boldsymbol{\Theta}^*_{\text{lattice}}}$, denoted $\mathbf{v}_1$, into the (r_1, r_2, r_3) subspace of $\boldsymbol{\Theta}_{\text{lattice}}$-space, the result being denoted $\mathbf{v}'_1$. An interpretation of the maximal eigenvector is that we can walk from the solution $\boldsymbol{\Theta}^*_{\text{lattice}}$ in the direction $\mathbf{v}'_1$ for a relatively substantial distance before achieving $\Delta\Phi_{\max}$; this is the notion which defines a confidence region for multivariate least squares, see (Bard, 1974). We express this traversal of rotation space by the parametrized equation

$$\mathbf{R}_2(t) \equiv \hat{\mathbf{R}}(\mathbf{r}^* + \mathbf{v}'_1 t), \tag{3.271}$$

where $t \in \mathbb{R}$ parametrizes the path in rotation space with direction $\mathbf{v}'_1$. The misorientation between $\mathbf{R}^*$ and $\mathbf{R}_2(t)$ is denoted $\mathbf{R}'(t)$, and is expressed by

$$\mathbf{R}'(t) = \mathbf{R}_2 \mathbf{R}^{*\mathrm{T}}.$$

Then denote the axis of rotation of $\mathbf{R}'(t)$ as $\mathbf{q}(t)$. An analysis of the relationship between $\mathbf{q}(t)$ and the axis of rotation for the rotation stage, $\mathbf{e}_2$ shows that the direction of maximum uncertainty, $\mathbf{v}_1$, indeed corresponds to applying an additional rotation about $\mathbf{e_2}$, since $\mathbf{q}(t) \cdot \mathbf{e}_2 \approx 1$ for a large range of t, confirming our supposition at the end of the previous paragraph with $\mathbf{R}' \equiv \bar{\mathbf{R}}$. This data is not presented due to its simple behavior.

Next we consider the uncertainty on stress tensor components given the uncertainty on the kinematic quantities $\mathbf{R}^*, \mathbf{U}^*$. For example these computations are of interest for investigations of residual stress fields or measurements of flow stresses on slip planes. We apply our analysis to the titanium alloy described in §3.4.2.1.3.3 as an example. Since we have established a finite deformation framework in this paper, we retain this generality here.

Consider the constitutive function for hyperelastic solids, e.g. the strain energy function,

$$W = W(\mathbf{H}) = \hat{W}(\mathbf{C}) \tag{3.272}$$

where W is the strain energy per unit reference volume, and the second equality is obtained using the invariance of W under change of observer in the physical configuration. Functional forms of (3.272) for various material symmetries can be found in Green and Adkins (1970), or in Chapter 2. The Piola stress with respect to the reference configuration is given in general by the relation (Holzapfel, 2000; Liu, 2002)

$$\mathbf{P}(\mathbf{H}) = 2\mathbf{H}\frac{\partial \hat{W}}{\partial \mathbf{C}}, \tag{3.273}$$

where the Piola stress is related to the Cauchy stress, $\mathbf{T}$, by

$$\mathbf{T} = \frac{1}{J}\mathbf{P}\mathbf{H}^{\mathrm{T}}, \tag{3.274}$$

where $J \equiv \det \mathbf{H}$. Using the error propagation formula (3.259) on (3.273) gives the uncertainty in the Piola stress components as

$$u_{P_{ij}} = \sqrt{\sum_{k,l=1}^{3}\left(\frac{\partial P_{ij}}{\partial H_{kl}}u_{H_{kl}}\right)^2} = \sqrt{\sum_{k=1}^{3}\left(\frac{\partial P_{ij}}{\partial r_k}u_{r_k}\right)^2 + \sum_{k,l=1}^{3}\left(\frac{\partial P_{ij}}{\partial U_{kl}}u_{U_{kl}}\right)^2}, \tag{3.275}$$

where $i, j = 1, 2, 3$, the uncertainties $u_{r_k}, u_{U_{kl}}$ are obtained from the lattice deformation parameters uncertainties, and the Piola stress components P_{ij} are obtained from the constitutive equation (3.273). The partial derivatives in (3.275) are evaluated at the least squares solution $(\mathbf{R}^*, \mathbf{U}^*)$. For small strains with negligible rotation we have a simpler relation. The Cauchy stress is then given by

$$T_{ij} = C_{ijkl}E_{kl}, \tag{3.276}$$

where $i, j, k, l = 1, 2, 3$, $T_{ij} = T_{ji}$ is the Cauchy stress, C_{ijkl} are the elastic moduli, and E_{kl} are the strain components. The uncertainty in this case is obtained by again using (3.259) with (3.276), giving

$$u_{T_{ij}} = \sqrt{\sum_{k,l=1}^{3}\left(\frac{\partial T_{ij}}{\partial E_{kl}}u_{E_{kl}}\right)^2 + \sum_{m,n,o,p=1}^{3}\left(\frac{\partial T_{ij}}{\partial C_{mnop}}u_{C_{mnop}}\right)^2}, \tag{3.277}$$

where $u_{E_{ij}}$ are uncertainties for the strain and $u_{C_{mnop}}$ are the uncertainties on the elastic moduli.

We now carry out the described computations for the titanium alloy under load, described in §3.4.2.1.3.3. For this material, elastic moduli have recently been measured using in interesting application of HEDM by Efstathiou et al. (2010), who gives $\mathrm{M}_{11} = 110$ GPa, $\mathrm{M}_{12} = 74$ GPa, and $\mathrm{M}_{44} = 89$ GPa. The strain energy function is constructed to quadratic order using the polynomial function bases for cubic symmetry given in (Green and Adkins, 1970) defined by

$$i_1 \equiv E_{11} + E_{22} + E_{33}, \quad i_2 \equiv E_{22}E_{33} + E_{11}E_{33} + E_{11}E_{22}, \quad i_3 \equiv E_{23}^2 + E_{31}^2 + E_{12}^2.$$

The strain energy function is then written as

$$W(i_1, i_2, i_3) = c_1 i_1^2 + c_2 i_2 + c_3 i_3,$$

where in this form the material parameters c_i, $i = 1, 2, 3$ are given in terms of the traditional moduli in Voigt notation by $c_1 \equiv \mathrm{M}_{11}/2$, $c_2 \equiv \mathrm{M}_{12} - \mathrm{M}_{11}$, $c_3 \equiv \mathrm{M}_{44}$. The Cauchy stress,

Table 3.4: Cartesian components of the Cauchy stress tensor with uncertainty at 95% confidence. (in MPa)

T_{11}	T_{22}	T_{33}	T_{12}	T_{23}	T_{31}
-1200 ± 30	580 ± 30	-510 ± 30	-130 ± 10	-40 ± 15	-190 ± 15

$\mathbf{T}$, may be constructed directly using (3.274) along with error propagation from (3.259). The full symbolic expressions are too unwieldy to record here. There are no uncertainties available for the moduli of this particular titanium alloy, true to normal deficiencies in the literature, so only uncertainty in the kinematic factors, $\mathbf{R}, \mathbf{U}$, were accounted for in carrying out (3.259). In Table 3.4 we record the final Cauchy stress components (in MPa) along with their uncertainty at 95% confidence. This crystal has a high degree of elastic anisotropy, so the local stress cannot be expected to be perfectly uniaxial, see (Efstathiou et al., 2010) for further discussion. The normal stresses are compressive in the $\mathbf{e}_1, \mathbf{e}_3$ directions, and tensile in the $\mathbf{e}_2$ direction. There is approximately a 10% relative uncertainty in the stress components in Table 3.4, according to our single scan uncertainty.

3.4.2.1.5 Summary In this section we have established a grain averaged modeling framework for lattice refinement. This method provides an efficient methodology to state the precision of lattice deformation measurements using monochromatic X-ray diffraction. The framework we employ uses a weighted least squares method, with the positions of diffraction peaks as input data and with weight coefficients corresponding to uncertainties of the positions of diffraction peaks. The positions of the diffraction peaks were similarly found using the weighted least squares method, with pixel integrated intensities as input data and with weight coefficients corresponding to experimentally measured variance in the recorded intensity. Confidence intervals are found by computing the local curvature of the objective function at the solution. An important requirement for this method to be optimal is having continuous observations of diffraction peak intensity across multiple pixels and image frames.

We applied our framework to two monochromatic X-ray diffraction experiments. We analyzed a ruby single crystal as a validation case and we were able to favorably compare uncertainties from our single measurement predictions with those attained from standard statistical analysis of repeated measurements. As an example application of our method for *in situ*, high deformation studies, we also considered a deformed grain in a polycrystalline titanium alloy, and found we had a rotation uncertainty of 0.03° and a stretch uncertainty corresponding to a range from $100 - 250\mu\epsilon$. Based on the nominal strain values of Table 3.3, this uncertainty corresponds to about 5 - 20% uncertainty in the strain, with an average uncertainty between 5 - 10%. This quantitative information on the deliverables of the high energy diffraction method is crucial to determine, in order to use the technique to obtain constitutive information, see §3.5.

We investigated three proposed objective functions, $\Phi^{\beta}_{\text{lattice}}, \beta = 1, 2, 3$, (3.261) used to estimate the lattice deformation parameters, each of which made use of a simple kinematic

relation relating reciprocal lattice vectors in a chosen reference configuration to the reciprocal lattice vectors in the physical configuration (3.253). We found that the effect of error in the ω coordinate on the precision of lattice deformation parameters depends on the form of the objective function employed in the least squares algorithm. Generally speaking, formulations of Φ_{lattice} which decouple residuals using the angular rotation coordinate, ω, from those which do not are able to attain more incisive results. Furthermore, for the ruby data, the confidence regions around the solution parameters generated by our method were able to be interpreted based on physical characteristics of the experiment. Although this is an idealized data set, this confirmation gives us further verification of our method.

Next we give comments related to improving the precision of measurements using this X-ray diffraction method. As noted by Poulsen et al. (1997), due to the high energy of the X-rays, the resolution of diffraction peaks in reciprocal space is relatively poor. We have compared traditional bonded resistance strain gauges to the X-ray diffraction technique in several places in this thesis. Strain gages have uncertainties of only $< 5\%$, compared with the $< 20\%$ quoted here. Clearly there is improvement required in the high energy technique. Improving this resolution, hence improving precision on the peak locations and therefore lattice deformation parameters, may be accomplished geometrically by moving the detector further from the sample and increasing the area of the detector, or through improved instrumentation, by simply increasing the pixel density on the detector. However, neither of these solutions addresses the problem of the relatively large uncertainties in the ω-locations of the peaks. On the other hand, since this analysis has shown that the precision of the ω-coordinate has only a small effect on the precision of the lattice stretch parameters when forming an appropriate objective function, improving the $2\theta, \eta$ resolution of diffraction peaks would likely increase the precision of lattice stretch measurements to some extent.

Another topic to investigate further would be the assumptions used to derive the confidence regions, (3.246). As noted, there is some discretion in how to quantify the confidence interval for a particular parameter, which is how confidence intervals are typically stated for experimental results. The method we used to convert uncertainty regions into confidence intervals may be overly conservative for certain experiments. We also note that the uncertainty for the pixel integrated intensity has a large effect on the overall precision predicted by the method. For our tests we used a fairly conservative estimate of $\sigma_E = 0.2E_{\text{meas}}$ and applied this estimate to each pixel, see §3.4.2.1.1, If a meticulous estimate of the variation in integrated intensity is made, perhaps even considering individual pixels or regions of pixels independently, we would expect increases in the estimated precision. A major improvement to our algorithm would be to add methods to better handle the case of diffraction peaks falling on a single omega frame as noted previously in the text, see also Winkler et al. (1979). In our framework this case may require changes to the method of estimating uncertainty based on the curvature of an objective function, and instead use some notion of a digitisation of the uncertainty in the final lattice deformation parameters, corresponding to the digitisation of the diffraction peak locations.

In closing, the framework we employed to determine lattice deformation parameters on a

grain averaged basis was highly successful in providing us much quantitative information. In addition to an efficient tool to quantify uncertainty, we were able to deduce information about the fundamental limitations of our experimental method, including intrinsic measurement precision, the effect of experimentally controlled parameters, e.g. $\Delta\omega$, and the effect of an analytically controlled parameter (choice of Φ_{lattice}) on the overall precision of a single measurement.

Next, we consider the alternative to the grain averaged approach - a framework which forward models the diffraction peaks, modifying microstructural parameters to match detailed intensity data.

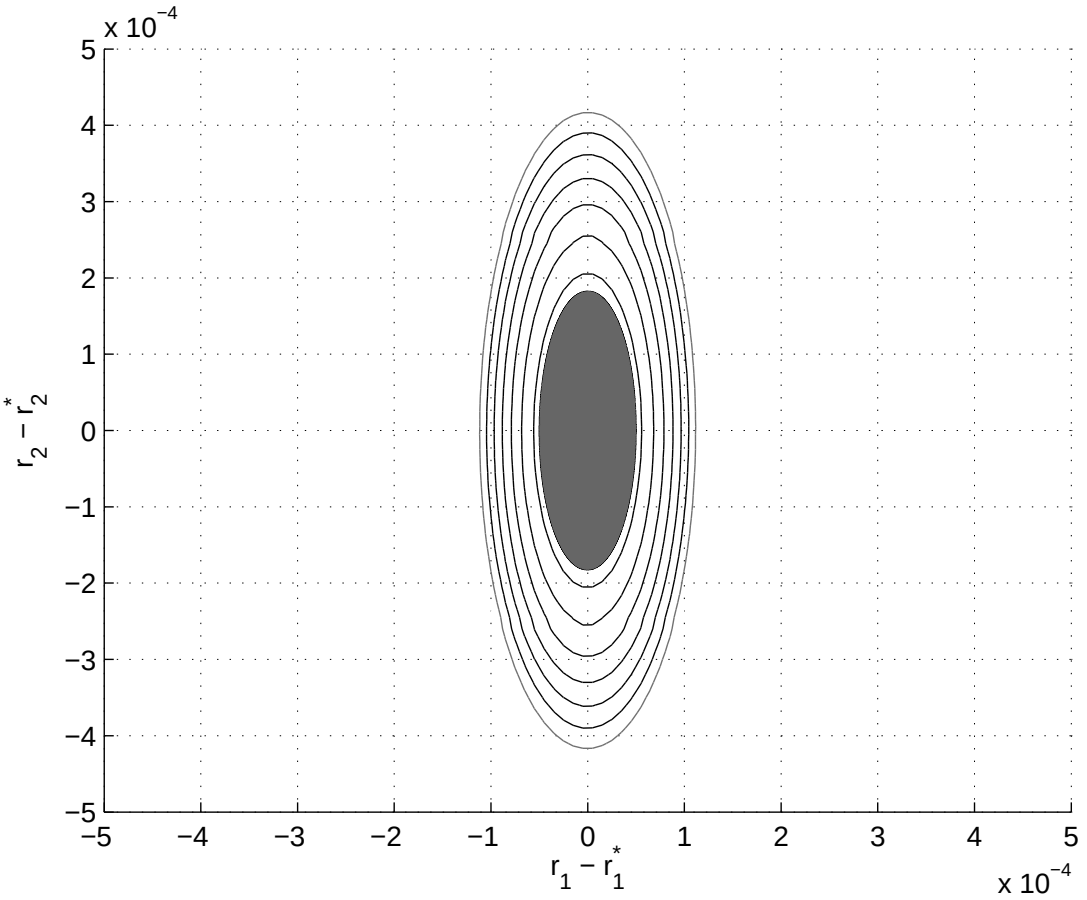

Figure 3.27: Objective function Φ^2_{lattice} in region around solution. 10 contours were drawn from a $\Delta\Phi^2_{\text{lattice}}$ range of $[0, 100]$, where $\Delta\Phi^2_{\text{lattice}} \equiv \Phi^{2*}_{\text{lattice}} - \Phi^2_{\text{lattice}}$. The grey ellipse defines exact confidence region defined by $\Delta\Phi^2_{\text{lattice}} = \frac{1}{2}\chi^2_{\alpha=0.95,l=9}$, a dashed black line defines the confidence region given by (3.246). The black ellipse is only slightly larger than the grey ellipse; they are not distinguishable at this magnification for this objective function.

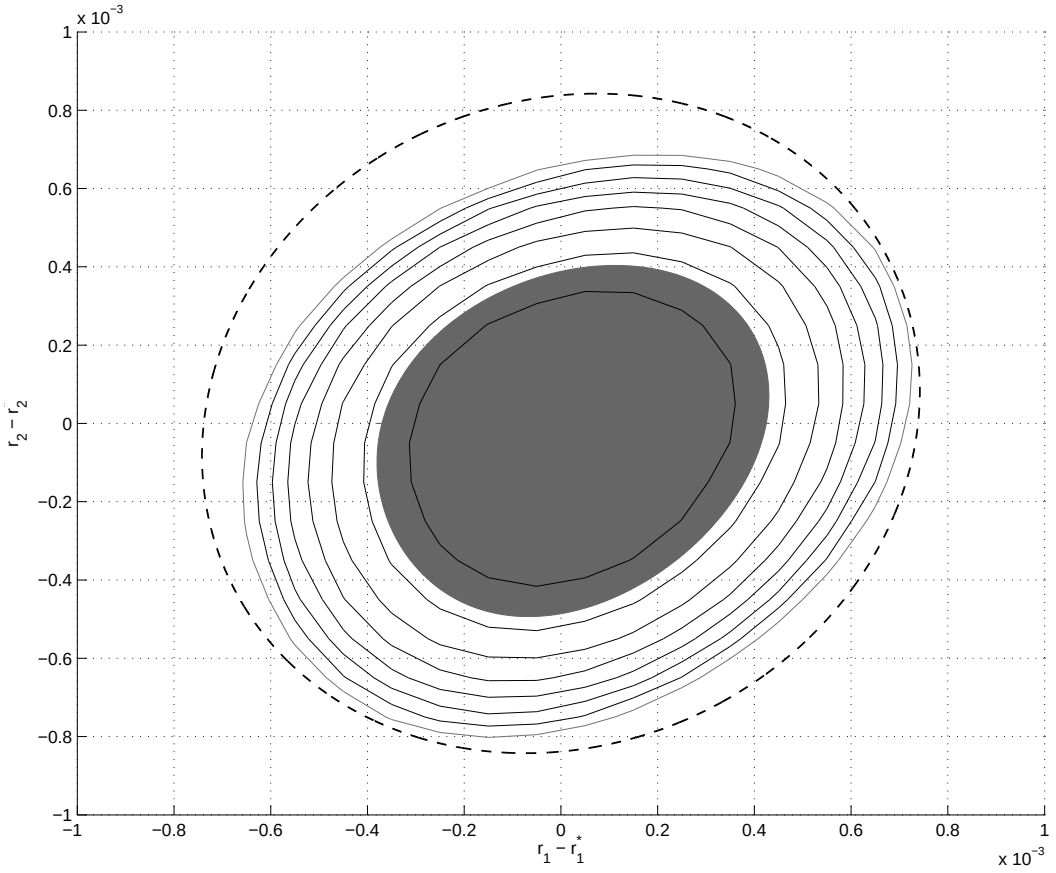

Figure 3.28: Objective function Φ^3_{lattice} in region around solution. 10 contours were drawn from a $\Delta\Phi^3_{\text{lattice}}$ range of $[0, 100]$, where $\Delta\Phi^3_{\text{lattice}} \equiv \Phi^{3*}_{\text{lattice}} - \Phi^3_{\text{lattice}}$. The grey ellipse defines the exact confidence region obtained from $\Delta\Phi^3_{\text{lattice}} = \frac{1}{2}\chi^2_{\alpha=0.95,l=9}$, the dashed black line defines the confidence region given by (3.246).

3.4.2.2 Forward modeling approach

In this section is described a modification of the grain averaged modeling approach introduced in §3.4.2.1 to obtain lattice deformation parameters along with microstructural information. The use of a sufficiently general forward model enables the determination of attributes such as the degree of intragranular misorientation for an individual grain.

In the traditional procedure of refinement, estimates for the volume averaged strain, orientation, and center of mass position are obtained - a total of twelve parameters (3 for orientation, 6 for strain, and 3 for position). These parameters may be solved for by using a least squares algorithm, where the residual equations are generated by comparing measured and predicted locations of diffraction peaks, or equivalent coordinitizations of such. Therefore for each diffraction peak there are three residual equations added to the least squares objective function, see Equations (3.256)-(3.258). In the proposed modeling approach, to the traditional list of up to twelve parameters characterizing the deformation and position of the grain we add additional parameters which characterize properties of the intragranular texture distribution. These additional parameters are used in a forward model to broaden diffraction peaks in a consistent manner for every reflection in the grain. Then we reformulate the inverse problem to solve for these parameters by forming least squares residuals based on direct raw pixel intensities, a much larger data set than the three dimensional location of the peak. For example, each peak may have pixel extents on the order of 10-100 pixels, so the data utilization is much higher than for the traditional approach. This methodology is similar in approach to the Rietveld method for whole pattern fitting of powder diffraction, applied to high energy X-ray diffraction of polycrystals.

Besides a certain intrinsic appeal, the benefits of this modeling technique are that quantifying data such as the dominant axis of intragranular misorientation becomes possible. In accordance with crystal plasticity theory such information may give quantitative insight into slip system activity in *in situ* experiments. This capability adds to the list of experimental outcomes available from X-ray diffraction data. Additionally, since the forward (+inverse) model prescribed here directly uses the raw experimental intensity data in the least squares problem, we obtain modest improvements in the estimated precision of measurements of grain averaged orientation made in this fashion.

The limitations of the approach are that the formulation becomes less quantitative as the degree of intragranular mosaicity increases, and local diffraction peaks become non smooth. Therefore the intended application for this modeling approach are in situ loading tests of bulk polycrystals from a virgin state up to moderate plastic deformation (O(2%)).

In the next section, we develop the requisite background for our modeling approach.

3.4.2.2.1 Background In this section we describe the background information and framework necessary to justify our approach to the modeling problem. Recall we require a model which incorporates intragranular texture or mosaicity to generate local intensity distributions of diffraction peaks. See §3.2 for the necessary introduction to X-ray diffrac-

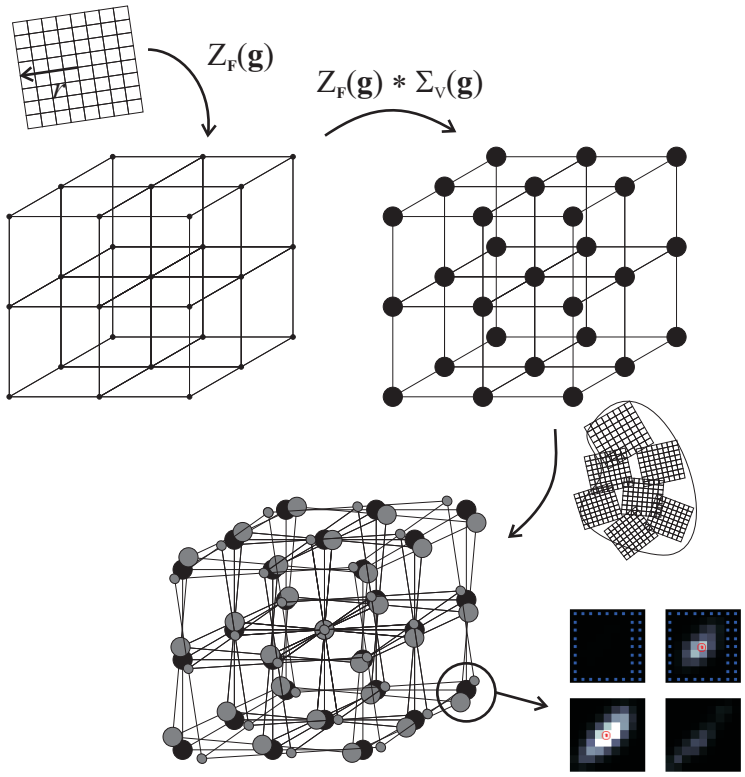

Figure 3.29: Maps of lattice of crystal, under convolution with finite size effect (or instrument broadening) and spatial inhomogeneity, resulting in a smeared diffraction peak in the lower right.

tion and Fourier transforms.

As a motivating visualization for this section, consider Figure 3.29. In the figure, a reference region of perfect crystal generates a reciprocal space lattice with Fourier transform $Z(\mathbf{g})$, where $\mathbf{g} \in \mathrm{G}^3$ denotes a vector in reciprocal space. Next, the lattice transform $Z(\mathbf{g})$ is convoluted with the finite size effect of the crystal, $\Sigma(\mathbf{g})$, to broaden the reciprocal lattice points to finite regions in reciprocal space, see §3.2.1.4. Broadening can also be considered as a phenomenological outcome of instrumentation effects (instrument broadening) (Warren, 1969). A natural example of instrument broadening is from the finite bandwidth of the incident beam intensity. Finally, the effect of the presence of multiple subdomains in the crystallite is incorporated by transformation of the broadened reference reciprocal lattice points into the current configuration. The resulting combination of all these effects results in a broadened diffraction peak, the ω-slices of which are shown in the lower right image in Figure 3.29. The details of our approach to these modeling steps are elucidated in the rest of this section. The end result will be to formalize the above description in a framework amenable to computation and application to experimental data.

3.4.2.2.1.1 Derivation of local intensity based on intragranular state. In this section we work out the details of the analytical procedure suggested by Figure 3.29. The fundamental measurement of the type of X-ray diffraction experiments considered here is the integrated intensity on a given pixel. Therefore at the end of this section we will have a model to predict integrated intensities on a given pixel, given information about the intragranular state. The prediction of pixel intensities based on microstructural information constitutes the forward model. The inverse model is a standard least squares optimization, where we compare predicted and measured individual pixel intensities to solve for the best fit microstructural parameters.

We begin the derivation by re-examining the factors contributing to determining the integrated intensity on a particular pixel, see §3.2 for additional background. Recall we are considering monochromatic X-ray diffraction experiments where rotation of the crystal is required. The physical process carried out in the rotating crystal method is the reorientation of the crystal about an axis $\mathbf{p}$ through $\omega(t)$, see Figure 3.13. The integrated energy on a pixel per unit cell, E , for a given exposure time interval is given by (compare to (3.97)):

$$\begin{aligned} E &= \int_t \int_x \int_y I_{\mathrm{e}} I(\mathbf{g}(p_1, p_2, \omega(t))) \mathrm{d}p_1 \wedge \mathrm{d}p_2 \wedge \mathrm{d}t \\ &= \int_\omega \int_x \int_y \frac{1}{\dot{\omega}} I_{\mathrm{e}} I(\mathbf{g}(p_1, p_2, \omega)) \mathrm{d}p_1 \wedge \mathrm{d}p_2 \wedge \mathrm{d}\omega, \end{aligned} \tag{3.278}$$

where $\mathbf{g} : \mathbb{R}^3 \to \mathrm{G}^3$ is regarded as the reciprocal vector associated to the pixel location, see §3.3.3, $p_1, p_2 \in \mathbb{R}^2$ are Cartesian position coordinates parametrizing the detector plane, $I_{\mathrm{e}} \in \mathbb{R}$ is Thomson polarization factor, $I : \mathrm{G}^3 \to \mathbb{R}^+$ is the diffracted intensity function over reciprocal space, and $\dot{\omega} \equiv \omega_{,t} = \text{const}$ is the angular velocity of rotation applied to the sample. In experiments $\dot{\omega}$ will be assumed constant. The total integrated energy for the pixel was previously shown to be given by multiplication of E times the number of unit cells, $N = V/V_c$, so that

$$E_{\mathrm{tot}} \equiv \frac{V}{V_c} E. \tag{3.279}$$

E_{tot} is therefore linear in the macroscopic volume of the crystal since V_c is constant for a given material. The direct use of Equation (3.278) and (3.279) therefore gives the integrated intensity on a given pixel and over a given $\delta\omega$-step. Explicitly, for the i^{th} pixel, which has a domain $p_1 \in [x_1, x_1 + \delta x]$, $p_2 \in [y_1, y_1 + \delta y]$, and $\omega \in [\omega_1, \omega_1 + \delta\omega]$ we have

$$E_{\mathrm{pixel_i},\delta\omega} = \frac{V}{V_c} \int_{\omega_i}^{\omega_i + \delta\omega} \int_{x_i}^{x_i + \delta x} \int_{y_i}^{y_i + \delta y} \frac{1}{\dot{\omega}} I_{\mathrm{e}} I(\mathbf{g}(p_1, p_2, \omega)) \mathrm{d}p_1 \wedge \mathrm{d}p_2 \wedge \mathrm{d}\omega. \tag{3.280}$$

The GE 41-RT detector used in §3.4.2.1.3.1 had $\delta x = \delta y = 200$ μm, and $\delta\omega = 0.5°$ for example. The integral of (3.280) can be carried out by standard numerical methods such as Gaussian quadrature. Therefore once we generate an expression for $I(\mathbf{g})$ we have completed the forward model giving $E_{\mathrm{pixel},\delta\omega}$, since $\dot{\omega}, I_{\mathrm{e}}$ are essentially fixed constants.

For convenience, it will be useful to incorporate the volume amplification factor V/V_c of (3.279) and (3.280) into the intensity function. Therefore we rewrite (3.280) as

$$E_{\text{pixel}_i,\delta\omega} = \int_{\omega_i}^{\omega_i+\delta\omega} \int_{x_i}^{x_i+\delta x} \int_{y_i}^{y_i+\delta y} \frac{1}{\dot{\omega}} I_e I_{\text{tot}}(\mathbf{g}(p_1, p_2, \omega)) \mathrm{d}p_1 \wedge \mathrm{d}p_2 \wedge \mathrm{d}\omega, \tag{3.281}$$

where

$$I_{\text{tot}}(\mathbf{g}(p_1, p_2, \omega)) \equiv \frac{V}{V_c} I(\mathbf{g}(p_1, p_2, \omega)) \tag{3.282}$$

is the total intensity function.

3.4.2.2.2 Intensity over reciprocal space. In Guiner (1963), see also §3.2, (3.96) the intensity per unit cell $I : \mathrm{G}^3 \to \mathbb{R}^+$is derived to be given by

$$I(\mathbf{g}) = \frac{1}{VV_c} \sum_i F^2_{hkl(i)} |\Sigma_V(\mathbf{g} - \mathbf{g}^{(i)})|^2, \tag{3.283}$$

where $hkl(i)$ is an enumeration of the nodes of reciprocal space, and $\mathbf{g}^{(i)}$ is the corresponding reciprocal lattice vector. Here the function $\Sigma_V : \mathrm{G}^3 \to \mathbb{R}^+$ is the Fourier transform of the indicator function, $\sigma(\mathbf{x})$, see Equation (3.21), which originates from the finite size effect of the crystal with volume V, and $F^2_{hkl} \in \mathbb{R}$ is the structure factor, see §3.2.2.3. Note that the definition of $\Sigma_V(\mathbf{g})$ in §3.2.1.4 is coupled to the overall volume of the crystal; the subscript V is used to emphasize this relationship.

Next, by relating reciprocal lattice vectors $\mathbf{g}$ to a fixed reference configuration, we arrive at a convenient incorporation of lattice deformation into the model. This description also enables a straightforward prescription for modeling intragranular effects. We now examine the details.

Effect of lattice deformation. We now consider the evolution of the reciprocal space intensity function I given by (3.283) under deformation of the lattice. Just to be clear, referring to lattice 'deformation' doesn't necessarily imply that a physical change in shape happens; orientation changes are also considered deformations in the sense implied here here. To facilitate the adding lattice deformation to the forward model, following normal notions in mechanics we construct a fixed reference configuration of the crystal lattice. This configuration may be thought of as being constructed from tabulated values (i.e. literature values) of lattice parameters corresponding to stress free configurations (from a powder experiment in ambient conditions for example). See §3.3.5 for a quantitative discussion of these reference configurations. In the reference lattice configuration, reciprocal space is parametrized by vectors $\mathbf{G}$, with reciprocal lattice nodes given by $\mathbf{G}^{(i)}$. In the current configuration, reciprocal space is parametrized by $\mathbf{g}$, with reciprocal lattice nodes given by

$\mathbf{g}^{(i)}$. We have previously shown that the reference and current reciprocal lattice vectors are related by (Edmiston et al., 2012)

$$\mathbf{g}^{(i)} = \mathbf{H}^{-\mathrm{T}}\mathbf{G}^{(i)}, \tag{3.284}$$

where $\mathbf{H}$ is an invertible linear transformation describing the deformation of the lattice. In our formulation of elastic plastic deformation in Chapter 2, $\mathbf{H}$ is also called the elastic deformation. Also note that under the local deformation $\mathbf{H}$, the volume of the crystal changes to $V = JV_0$, where $J \equiv \det \mathbf{H}$, and the unit cell volume changes to $V_c = JV_{c,0}$, where $V_0, V_{c,0}$ are the reference volumes of the macroscopic crystal and unit cell, respectively. In the reciprocal space of the current configuration, where diffraction is actually measured, we then modify (3.283) to read

$$I(\mathbf{g}; \mathbf{H}) = \frac{1}{J^2 V_0 V_{c,0}} \sum_i F^2_{hkl(i)} |\Sigma_{JV_0}(\mathbf{g} - \mathbf{H}^{-\mathrm{T}}\mathbf{G}^{(i)})|^2, \tag{3.285}$$

where the dependence on $\mathbf{H}$ is emphasized on the left hand side of (3.285). Equation (3.285) completes the specification of $I(\mathbf{g})$ for a perfect single crystal under lattice distortion $\mathbf{H}$.

3.4.2.2.3 A simple forward model. We now generalize (3.285) to arrive at an expression for $I(\mathbf{g})$ for a grain with intragranular texturing (i.e. spatial gradients in $\mathbf{H}(\mathbf{x})$). To simplify things we first consider diffraction from a discrete collection of macroscopic crystalline particles, each of the same material and with distinct volumes V_j. Then (3.282) shows that the intensity is given by

$$I_{\mathrm{tot}}(\mathbf{g}) = \sum_j^{N_{\mathrm{p}}} \frac{V_j}{V_c} I_j(\mathbf{g}), \tag{3.286}$$

where N_{p} is the number of particles in the distribution and

$$I_j(\mathbf{g}) = \frac{1}{J_j^2 V_{j,0} V_{c,0}} \sum_{i=1}^{N} \Sigma_{J_j V_{j,0}}(\mathbf{g} - \mathbf{H}_j^{-\mathrm{T}}\mathbf{G}^{(i)}) \tag{3.287}$$

is the intensity per unit cell over the current reciprocal space coordinates $\mathbf{g}$; adapted from (3.285). Here the j^{th} particle experiences a homogeneous lattice deformation $\mathbf{H}_j$, with associated initial volume $V_{j,0}$ and volume changes $J_j = \det \mathbf{H}_j$. The material of each particle is the same so that the unit cell volume $V_{c,0}$ is the same for all particles.

Next, taking the continuous limit of this construct to infinitesimal particle sizes, we conceive of a volume distribution function $g : \mathrm{GL}(3, \mathbb{R}) \to \mathbb{R}^+$. This function is such that for a given lattice deformation $\mathbf{H} \in \mathrm{GL}(3, \mathbb{R})$ reports the physical volume of particles with that lattice deformation. As a quick example, for the discrete particle case described in the last paragraph, $g(\mathbf{H}_j) = V_{j,0}$ since each particle had a homogeneous deformation.

The function $g(\mathbf{H})$ is an obvious generalization of the ODF function from texture analysis, which essentially is concerned with analysis of a function $m' : \mathbb{R}^3 \to \mathbb{R}^+, m = m(\mathbf{R})$, where $\mathbf{R} \in \mathrm{SO}(3, \mathbb{R})$. Motivated by this, using the distribution $g(\mathbf{H})$, we can taking the continuous limit of (3.286) and obtain

$$I_{\mathrm{tot}}(\mathbf{g}; g(\mathbf{H})) = \int_{\mathbf{H}} \frac{g(\mathbf{H})}{V_c} I(\mathbf{g}; g(\mathbf{H})) \mathrm{d}\mathbf{H}, \tag{3.288}$$

and (3.285) becomes

$$I(\mathbf{g}, g(\mathbf{H})) = \frac{1}{g(\mathbf{H})\,(J_H V_{c,0})} \sum_{i=1} \Sigma_{g(\mathbf{H})}(\mathbf{g} - \mathbf{H}^{-\mathrm{T}} \mathbf{G}^{(i)}). \tag{3.289}$$

The functions (3.289) and (3.288) in (3.281) therefore represent a forward model giving the integrated intensities for a pixel, given the distribution function g. We now describe further details of the model and consider how to implement it numerically.

First, assume we have prescribed an estimate for the volume function $g(\mathbf{H})$. With $g(\mathbf{H})$ in hand, next identify a given pixel where diffraction is expected to occur (that is, for pixels in and nearby experimentally measured diffraction peaks). Then, compute the forward modeled integrated intensity based on $g(\mathbf{H})$ by quadrature over the pixel coordinates

$$E_{\mathrm{pixel},\delta\omega}(; g(\mathbf{H})) = \int_{\omega_i}^{\omega_i+\delta\omega} \int_{x_i}^{x_i+\delta x} \int_{y_i}^{y_i+\delta y} \frac{1}{\dot{\omega}} I_{\mathrm{e}} I_{\mathrm{tot}}(\mathbf{g}(p_1, p_2, \omega); g(\mathbf{H})) \mathrm{d}p_1 \wedge \mathrm{d}p_2 \wedge \mathrm{d}\omega, \tag{3.290}$$

where $I_{\mathrm{tot}}(\mathbf{g}(p_1, p_2, \omega); g(\mathbf{H}))$ is computed from (3.288). In words: at each pixel quadrature point p_1, p_2, ω, compute the corresponding test reciprocal vector $\mathbf{g}_{\mathrm{q}} = \hat{\mathbf{g}}(p_1, p_2, \omega)$, this function is described in §3.3.3. Then at the point $\mathbf{g}_{\mathrm{q}}$ in reciprocal space, evaluate $I_{\mathrm{tot}}(\mathbf{g}_{\mathrm{q}})$ by computing (3.288). The use of (3.288) requires integrating over $\mathbf{H}$-space, via quadrature, and for each $\mathbf{G}^{(i)}$ in the reference lattice, evaluating $\Sigma_{g(\mathbf{H})}(\mathbf{g}_{\mathrm{q}} - \mathbf{H}^{-\mathrm{T}} \mathbf{G}^{(i)})$. Note that the properties of the reciprocal lattice are such that only one $\mathbf{G}^{(i)}$ is likely to contribute to the consideration at $\mathbf{g}_{\mathrm{q}}$, simplifying things somewhat (see §3.2).

Next, recall from §3.2 that the properties of Σ are such that $\Sigma(\mathbf{0}) = g(\mathbf{H}^*)$, where $\mathbf{H}^*$ is the volume averaged value of $\mathbf{H}$ and that it is a rapidly decaying function. The radius of the function $\Sigma(\mathbf{g})$ is normally assumed to be proportional to the physical radius of the finite body under consideration. Previously, in §3.2.1.4, Equation (3.45) we used the estimate $s_0 = 1/(2r)$, where r is the physical radius of the particle and s_0 is the distance in reciprocal space from a node $\mathbf{g}^*$ where $\Sigma(\mathbf{g} - \mathbf{g}^*) > 0$. In terms of the volume function $g(\mathbf{H})$ we have, for a particle with spherical volume

$$s_0 = \frac{1}{2\,(3/4\pi g(\mathbf{H}))^{1/3}}. \tag{3.291}$$

Putting these properties together, the simplest form of the size effect function $\Sigma(\mathbf{g})$ consistent with our previous analysis is

$$\Sigma(\mathbf{g}) = \begin{cases} \Sigma(0) & |\mathbf{g}| < s_0(g(\mathbf{H})) \\ \Sigma(\mathbf{g}) = 0 & \text{else,} \end{cases} \tag{3.292}$$

with $s_0(g(\mathbf{H}))$ given by (3.291). This completes the specification of the intensity contribution to the quadrature point at p_1, p_2, ω. Repeating this for all pixels gives the full, local intensity distribution predicted by the volume distribution g.

The above method, which requires two integrations (over pixels and over the crystal, $g(\mathbf{H})$) allows for incorporating the size effect from nearby crystals by explicitly using the size function Σ. However this method is expensive to compute, since to have a well behaved minimization procedure we must evaluate the forward model not just on pixels where intensity was observed but on nearby pixels as well. Many of these test points may turn out to be outside the radius s_0 so that $\Sigma(\mathbf{g}) = 0$ at those points. This adds inefficiency to the computation of the integrated pixel intensity.

Motivated to improve this, we now prescribe a more computationally efficient approach to the forward modeling problem. We obtain the intensity produced in the detector image stack, (§3.3.1.1), by the following method. We first integrate $g(\mathbf{H})$ directly over the regions where $g(\mathbf{H}) > 0$. For quadrature point of this integration, and for each $\mathbf{G}^{(i)}$ in the reciprocal lattice, compute the reciprocal vector $\mathbf{H}^{-\mathrm{T}}\mathbf{G}^{(i)}$, and find the p_1, p_2, ω voxel where diffraction will be observed. The intensity at that voxel is then obtained from product of the structure factor of the $\mathbf{G}^{(i)}$ and the volume $g(\mathbf{H})$ at the quadrature point, and the nominal beam intensity, I_0. Explicitly, this voxel location is obtained from solving (3.189) and (3.175) for $\hat{\mathbf{r}_{\mathrm{p}}}$, the position on the detector. This method is more efficient than the previous description since the pixel integration does not require any Gaussian quadrature over the pixel locations per se, merely a summation over contributions to a given $p_1, p_2, \delta\omega$ voxel.

We now describe this methodology more precisely. We begin by ignoring the formal size effect. This is a practically useful simplification for the type of experiments for which the present model is meant to apply, where finite size effects are not likely to be measurable, see Figure 3.5 and associated text for example. Upon this simple case we show how contributions to peak broadening such as the finite size effect can be easily added on to the basic framework of analysis.

We directly express the integrated intensity field over all p_1, p_2, ω space in the form

$$E(p_1, p_2, \omega; g(\mathbf{H}), \mathbf{x}) = \frac{1}{\dot{\omega}} \sum_{i=1}^{N} \int_{\mathbf{H}} \frac{g(\mathbf{H})}{V_c} \hat{\mathbf{r}_{\mathrm{p}}}(\mathbf{H}^{-\mathrm{T}}\mathbf{G}^{(i)}, \mathbf{x}) I_0 c(\mathbf{H}^{-\mathrm{T}}\mathbf{G}^{(i)}, \mathbf{x}) F^2_{hkl(i)}, \tag{3.293}$$

where $\hat{\mathbf{r}_{\mathrm{p}}} : \mathrm{G}^3 \to \mathbb{R}^3$ maps reciprocal vectors to pixel locations in the image stack, and is a function of the precession $\mathbf{x}$, I_0 is the nominal beam intensity, and c is the polarization correction, proportional to $\lambda^3/(\sin 2\theta \cos \eta)$ where θ, η are the angular coordinates of the

pixel, see (3.116). See §3.3.3 for background information on the conversion function $\hat{\mathbf{r}_{\mathrm{p}}}$. Since it is difficult to convey formally, the function $E(p_1, p_2, \omega; g(\mathbf{H}), \mathbf{x})$ evaluates to zero when there is no diffraction condition possible given the available microstructure. The summation in (3.293) is over all reciprocal lattice vectors $\mathbf{G}^{(i)}$. This formulation is more efficient than the previous formulation because we compute the integrated intensity on a particular pixel (e.g. a particular (p_1, p_2, ω) voxel) by summing contributions to individual pixel domains from the quadrature evaluations of the integration on the right hand side of (3.293). Essentially, in this form, the integration over pixels is reduced to a simple quadrature over the function $g(\mathbf{H})$, and the resolution of the local pixel intensity value is governed by the number of quadrature points over the integration region in $\mathbf{H}$-space. We investigate the influence of the quadrature resolution on the forward simulated diffraction peaks in the results section.

We now add on additional factors to (3.293) which may be relevant to consider. To incorporate modeling of size effects, we add an additional integration step over each node $\mathbf{G}^{(i)}$, so that we have

$$E(g(\mathbf{H})) = \sum_{i=1} \int_{\mathbf{G},\mathrm{node}} \int_{\mathbf{H}} \left[\frac{1}{g(\mathbf{H})} \Sigma_{g(\mathbf{H})}(\mathbf{G} - \mathbf{G}^{(i)}) \right] g(\mathbf{H}) \hat{\mathbf{r}_{\mathrm{p}}}(\mathbf{H}^{-\mathrm{T}} \mathbf{G}^{(i)}, \mathbf{x}) I_0 c F^2_{hkl(i)}. \quad (3.294)$$

To add in the wavelength effect (a component of instrument broadening) add an additional integration layer

$$E = \sum_{i=1} \int_{\lambda} \int_{\mathbf{G},\mathrm{node}} \int_{\mathbf{H}} \left[\frac{1}{g(\mathbf{H})} \Sigma_{g(\mathbf{H})}(\mathbf{G} - \mathbf{G}^{(i)}) \right] g(\mathbf{H}) \hat{\mathbf{r}_{\mathrm{p}}}(\mathbf{H}^{-\mathrm{T}} \mathbf{G}^{(i)}, \mathbf{x}) I(\lambda) c F^2_{hkl(i)}, \quad (3.295)$$

where the input intensity spread is expressed in reduced dimensional form by

$$I(\lambda) = I_0 \exp \left[- \left(\frac{\lambda - \bar{\lambda}}{\sigma_\lambda} \right)^2 \right], \quad (3.296)$$

where $\bar{\lambda}$ is the nominal wavelength, and σ_λ is the spread in the wavelengths. A typical spread at Sector 1, Advanced Photon Source is $\sigma_\lambda \approx 0.001 \bar{\lambda}$. In order to account for instrumentation broadening apart from the wavelength effect, this effect can be acceptably modeled by an additional term of the form Σ_{inst}:

$$E(g(\mathbf{H})) = \sum\nolimits_{i=1} \int_{\mathbf{G},\mathrm{node}} \Sigma_{\mathrm{inst}}(\mathbf{G} - \mathbf{G}^{(i)}) \int_{\lambda} I(\lambda) \int_{\mathbf{G},\mathrm{node}} \int_{\mathbf{H}} \left[\frac{1}{g(\mathbf{H})} \Sigma_{g(\mathbf{H})}(\mathbf{G} - \mathbf{G}^{(i)}) \right] \cdot$$
$$g(\mathbf{H}) \hat{\mathbf{r}_{\mathrm{p}}}(\mathbf{H}^{-\mathrm{T}} \mathbf{G}^{(i)}, \mathbf{x}) c F^2_{hkl(i)}. \quad (3.297)$$

Although clearly similar in its resulting effect on the diffraction pattern to the size effect Σ, isotropic broadening from Σ_{inst} is in principle distinguishable from size broadening $\Sigma_{g(\mathbf{H})}$ since it remains constant throughout the test. Therefore it can likely be extracted from a calibration procedure, although this was not attempted for the current contribution.

3.4.2.2.3.1 Model equations In this section, we include the least squares model to complete the treatment and lead into applications. In the traditional lattice refinement procedure (Edmiston et al., 2011), the model parameters consist of the array

$$\begin{aligned}\boldsymbol{\Theta} &= (r_1, r_2, r_3, U_{11}, U_{22}, U_{33}, U_{23}, U_{13}, U_{12}, p_1, p_2, p_3) && (3.298)\\ &= (\mathbf{R}, \mathbf{U}, \mathbf{x}), && (3.299)\end{aligned}$$

where $\mathbf{R}(r_1, r_2, r_3), \mathbf{U}(U_{11}, U_{22}, U_{33}, U_{23}, U_{13}, U_{12})$ are the orthogonal and symmetric positive definite, resp., polar decomposition factors of the volume averaged $\mathbf{H}$ and $\mathbf{x} = (x_1, x_2, x_3)$ is the precession or center of mass of the grain. These standard model parameters were utilized in §3.4.2.1. Residuals in the objective function (3.243) in that case were based on the locations of the center of a Gaussian function fit to the local intensity, see (3.256)-(3.258).

In contrast, the present model requires residuals to instead be formed directly on pixel intensities, with additional parameters added to the $\boldsymbol{\Theta}$ defined in (3.299) which contain functional information for approximating $g(\mathbf{H})$. In effect, the broadening which was modeled with the Gaussian functions in §3.4.2.1, and shown in Figure 3.23, is now modeled by the specification of $g(\mathbf{H})$. To form residuals, let $A_{\text{data}} = \{p_x, p_y, \omega : I_{\text{data}}(p_x, p_y, \omega) > I_{\text{thresh}}\}$ be the set of voxels which have been indexed to a particular grain, according to the experimental measurement and let $B_{\text{sim}} = \{p_x, p_y, \omega : I_{\text{sim}}(p_x, p_y, \omega) > 0\}$ be the set of voxels representing the forward modeled intensity from the same grain. Here $I_{\text{data}}, I_{\text{sim}}$ represent the values for integrated intensity on the voxel. Then the residual for the νth diffraction peak is efficiently expressed as

$$e_\mu^\nu = \begin{cases} (I_{\text{data}} - I_{\text{sim}})(p_x, p_y, \omega)^{(\mu)} & (p_x, p_y, \omega)^{(\mu)} \in A_{\text{data}} \cap B_{\text{sim}} \\ (I_{\text{data}}(p_x, p_y, \omega)^{(\mu)} & (p_x, p_y, \omega)^{(\mu)} \in A_{\text{data}} - B_{\text{sim}} \\ (I_{\text{sim}}(p_x, p_y, \omega)^{(\mu)} & (p_x, p_y, \omega)^{(\mu)} \in B_{\text{sim}} - A_{\text{data}}, \end{cases} \tag{3.300}$$

where μ is an index into the number of pixels in $A_{\text{data}} \cup B_{\text{sim}}$ In other words, we penalize the forward modeled intensity in the obvious way where simulation and data overlap, and also for having a broader extent than the experimental data. The success of this approach is contingent upon getting good initial guesses for the data, so that the simulated intensity and experimental intensity distributions overlap. The objective function based on (3.300) is written as

$$\Phi(\boldsymbol{\Theta}) = \sum_{\nu=1}^{N} \sum_{\mu=1}^{N^\nu} \left(e_\mu^\nu\right)^2, \tag{3.301}$$

where N_ν is the number of pixels in the νth diffraction peak. Uncertainty can be incorporated into the objective function as was done in §3.4.2.1.1.

Summary. In this section we have developed the framework for computing a forward modeled diffraction pattern given the intragranular volume distribution function $g(\mathbf{H})$. The

functions (3.289), (3.288), in (3.281) represents a forward model giving the integrated intensities on detector pixels, which can be compared to experimental pixel values. We described a general algorithm for generating the integrated intensities from these functions, through (3.288). This was found to be computationally inefficient, so that the methods culminating in (3.297) were found to give a more efficient implementation. We also described the usage of the forward model in a least squares system by assigning residual equations (3.300). Thus far the core new component over the analysis in §3.4.2.1 is the volume distribution function $g(\mathbf{H})$, which has not been addressed in terms of implementation.

In the next section we describe suggested methods for assigning $g(\mathbf{H})$ by introducing reduced degree of freedom specification for the function. This limits the method from modeling arbitrary intensity distributions. Based on experimental observations, however, this is not a limitation to deduce insightful material behavior up to moderate plastic strain.

3.4.2.2.4 DOF reduction and numerical implementation. In the previous section, we developed a forward modeling approach to determine the local intensity of diffraction peaks. In essence, we have reduced question of simulating diffraction peak intensities to the determination of the volume distribution function over **H**-space, $g(\mathbf{H})$, see Equation (3.281). The function g represents the projection of spatial inhomogeneity into the space which the considered class of X-ray diffraction experiments can measure, **H**-space, see Figure 3.12. In this section we investigate suggested forms for $g(\mathbf{H})$ which can give us a quantification of the anisotropic broadening of the diffraction peaks.Anisotropic broadening is of interest since it is clearly distinguishable from size effect or instrument broadening, and originates from microstructural phenomena.

Philosophically, determining $g(\mathbf{H})$ is no different than curve fitting any function $\mathbb{R}^9 \to \mathbb{R}^+$. However, fitting a fully nine-dimensional $g(\mathbf{H})$ would be computationally prohibitive. Besides, the nature of the experimental resolution we can attain limits the ability to accurately quantify many dimensions of **H**; strain broadening will be difficult to pick up and separate from wavelength broadening for example. Therefore instead of the full fitting a function over $9-$dimensional space we consider a subspace $\mathbf{H}(\boldsymbol{\theta})$, parametrized by $\boldsymbol{\theta}$, with $\dim \boldsymbol{\theta} \leq \dim \mathbf{H} = 9$. For example, we can use the polar decomposition of **H** to suggest the three dimensional subspace parametrized by

$$\mathbf{H}(\boldsymbol{\theta}) = \mathbf{R}(\boldsymbol{\theta})\mathbf{U}, \tag{3.302}$$

where $\boldsymbol{\theta} \in \mathbb{R}^3$ parametrizes orientation space via angle axis parameters, for example. Therefore with the parametrization of **H**-space given by (3.302), $g(\mathbf{H}(\boldsymbol{\theta})) = g(\boldsymbol{\theta})$ would represent very much akin to the orientation distribution function from classical texture analysis, although our function is not understood as a probability density function. As a potentially useful extension of this, the sensitivity of our experiments to volumetric lattice strain is greater than for isochoric strains, which motivates the possibility of adding to the orientation parameters a degree of freedom for volumetric changes. Therefore we may also suggest

the four dimensional subspace parametrization

$$\mathbf{H}(\boldsymbol{\theta}) = \mathbf{R}(\theta_1, \theta_2, \theta_3)\mathbf{U}(\theta_4), \tag{3.303}$$

where e.g. $\mathbf{U}(\theta_4) = \theta_4^{1/3}\bar{\mathbf{U}}$, and $\bar{\mathbf{U}}$ is the isochoric part of $\mathbf{U}$.

No matter which space $g(\boldsymbol{\theta})$ is represented over, it should be understood that the determination of $g(\boldsymbol{\theta})$ has many potential avenues for exploration, but it is essentially a problem of curve fitting, separate from any governing rules of physics besides the requirement $g(\boldsymbol{\theta}) \geq 0$. For a quite general approximation to $g(\boldsymbol{\theta})$ we may use a finite element inspired discretization over $\boldsymbol{\theta}$-space. For example, for the standard linear interpolation functions, we discretize $\boldsymbol{\theta}$-domain assign the N nodal points $\boldsymbol{\theta}^i, i = 1, 2, ..., N$, basis functions $\Phi^i(\boldsymbol{\theta})$, with $\Phi^i(\boldsymbol{\theta}_j) = \delta^i_j$, and solve for the nodal values $g(\boldsymbol{\theta}^i) \equiv g^i$. Then with the assigned basis functions $\Phi^i(\boldsymbol{\theta})$ we generate the entire distribution by

$$g(\boldsymbol{\theta}) = \sum_i^N g^i \Phi^i(\boldsymbol{\theta}). \tag{3.304}$$

The number of degrees of freedom allowed to $g(\boldsymbol{\theta})$ is only limited by computational expense and experimental resolution, by the number of dimensions to allow $\boldsymbol{\theta}$ as well as the number of nodal points taken per dimension.

As an alternative to the brute force expansion (3.304) we attempt to describe $g(\boldsymbol{\theta})$ based on only a few degrees of freedom. Essentially, we Taylor expand $g(\boldsymbol{\theta})$ about a point in $\boldsymbol{\theta}$-space which corresponds to the maximum physical volume of crystal content. An example would be to expand around the grain volume averaged deformation, $\mathbf{H}^*$. This is similar in idea to that given in Eschner (1993). We will consider this method using the orientation space parametrization using (3.302). This is because the orientation subspace is most familiar to existing literature, has the most experimental resolution, and has the convenient property of being three dimensional, so that the space involved is readily visualized. We work out the details in the next section.

3.4.2.2.5 ODF deformation. Here now examine restricted domain volume function $g(\boldsymbol{\theta})$, defined over the orientation subspace of $\mathbf{H}$-space, and parametrized by (3.302). For motivation of the proposed view, consider approximate shapes for the projection of spatial inhomogeneity of a grain into orientation space. See Figure 3.12 for a depiction of the projection $\pi_{\mathbf{H}}$. Intuitively, for an perfect, undeformed grain, the image of $\pi_{\mathbf{H}}$ in orientation space would be a sphere with small radius, centered at a point $\mathbf{r}^*$ representing the grain averaged orientation. We can coordinitize this initial sphere by the unit ball B^3. As the grain deforms plastically in the physical space, the orientation image of the grain is translated and stretched and rotated into roughly an ellipsoid. For a schematic example of the evolution from a perfect crystal to a deformed one compare the diffraction peaks in Figure 3.22 to Figure 3.23. Such a deformation process can be described by the action of a symmetric 3 by

3 matrix $\mathbf{A}$ on the reference projection of the crystal, the spherical region of the nearly perfect state, much as the linear transformation $\mathbf{H}$ acts on the reference lattice vectors in §3.3.5. In order to make this discussion more precise we must prescribe coordinate conventions.

Orientation coordinates The orientation space we consider here is $\mathrm{SO}(3,\mathbb{R})$. The overall coordinate transformations required are depicted in Figure 3.30. We impose an orientation-reference configuration, γ, as a spherical ball of radius one, B^3. In γ, coordinates are denoted as $\boldsymbol{\gamma} = \gamma_1, \gamma_2, \gamma_3$. We can then impose the natural spherical polar coordinates for the ball, R, Θ, Φ according to the standard spherical polar map

$$\boldsymbol{\gamma}' : (R, \Theta, \Phi) \to (\gamma_1, \gamma_2, \gamma_3) | \boldsymbol{\gamma}'(R, \Theta, \Phi) = R\mathbf{e}_\rho(\Theta, \Phi), \tag{3.305}$$

with the spherical polar map defined in (A.1). Formally speaking, the spherical polar system with coordinates R, Θ, Φ may be considered another reference configuration γ', with $\boldsymbol{\gamma}' : \gamma' \mapsto \gamma$ given by (3.305)

We pause here to note that the choice of a spherical reference region γ is guided only by the physically reasonable assertion that the orientation distribution of a grain has a dominant mean value and other orientations in the grain are modeled as perturbations from the mean value. Other prescribed regions, such as cubic, may also be useful or give better fits to the data. If these details are important a broader orientation region can be modeled with the approach of (3.304). For the goals of the present work we only would like to quantify the anisotropic broadening, so the choice of the reference region does not greatly effect the phenomena we are attempting to capture.

Next, we must consider the map from the unit reference ball, γ to orientation space, denoted

$$\boldsymbol{\theta} : \gamma \to \mathrm{SO}(3,\mathbb{R}) | \boldsymbol{\theta}(\boldsymbol{\gamma}) = \hat{\mathbf{r}} \in \mathrm{SO}(3,\mathbb{R}), \tag{3.306}$$

see Figure 3.30. The mapping $\boldsymbol{\theta}$ into orientation space is of the form

$$\boldsymbol{\theta}(\boldsymbol{\gamma}) = \boldsymbol{\theta}_0 + \Delta(\boldsymbol{\gamma}), \tag{3.307}$$

where $\boldsymbol{\theta}_0$ represents the volume averaged center of the projection of the grain into $\mathrm{SO}(3,\mathbb{R})$, and $\Delta(\boldsymbol{\gamma})$ represents deviations from the center point.

Next we present several potential avenues for advancement of the model by prescribing $\Delta(\boldsymbol{\gamma})$. Generally speaking, like in the theory of elastic-plastic deformation of Chapter 2, we can assign a field $\mathbf{A}(\boldsymbol{\gamma})$, where $\mathbf{A} \in$ sym , so that relative to the base point $\boldsymbol{\theta}_0$, and for a path in γ parametrized by $\boldsymbol{\gamma}(s)$ as we have the mapped location

$$\boldsymbol{\theta}(\boldsymbol{\gamma}(s)) = \boldsymbol{\theta}_0 + \int_0^s \mathbf{A}(\boldsymbol{\gamma}(s)) \frac{d\boldsymbol{\gamma}}{ds} ds, \tag{3.308}$$

where $\boldsymbol{\theta}_0 \equiv \boldsymbol{\theta}(\mathbf{0})$. However being required to determine a field $\mathbf{A}(\boldsymbol{\gamma})$ clearly does not giving any reduction in degrees of freedom over a general ODF, (3.304). Therefore we further

restrict the degrees of freedom afforded to $\boldsymbol{\theta}$ and impose an $\mathbf{A}$ which is homogeneous over the reference region γ, reducing (3.308) to

$$\boldsymbol{\theta}(\boldsymbol{\gamma}) = \boldsymbol{\theta}_0 + \mathbf{A}\boldsymbol{\gamma}, \tag{3.309}$$

since

$$\int_0^s \mathbf{A}(\boldsymbol{\gamma}(s))\frac{\mathrm{d}\boldsymbol{\gamma}}{\mathrm{d}s}\mathrm{d}s = \mathbf{A}\int_0^s \frac{\mathrm{d}\boldsymbol{\gamma}}{\mathrm{d}s}\mathrm{d}s = \mathbf{A}\int_0^\gamma \mathrm{d}\boldsymbol{\gamma} = \mathbf{A}\boldsymbol{\gamma}. \tag{3.310}$$

The mapping prescribed by (3.309) would be enough to obtain the type of information sought by this model, therefore we can move on to applications. However for a given crystal, fitting $\mathbf{A}$ according to the expression (3.309) is not invariant under changes of frame. For example changes of frame which would clearly assign different values for $\boldsymbol{\theta}_0$. Then, due to the curvature of orientation space, for each point $\boldsymbol{\theta}_0$ associated with a particular frame, executing the least squares algorithm for $\mathbf{A}$ could potentially give different results for $\mathbf{A}$ for the same crystal. For the purposes of the present study where we only want to fit intragranular misorientations in any fashion, this is not really a concern, but invariance of $\mathbf{A}$ under different reference configurations would be a desirable feature to build into our construction. This is because then $\mathbf{A}$ would be eligible to serve as a proper constitutive variable for theories of deformable bodies intended to operate at the length scales probed by these experiments. For example, several authors have proposed including the geometrically necessary dislocation content, $\boldsymbol{\xi}$ in constitutive equations for plastic flow and yield, see Chapter 2. The physical character of $\mathbf{A}$ is very similar to $\boldsymbol{\xi}$ in that it connotes an idea of misorientation. In the future, if the phenomenological theories of plasticity incorporating $\boldsymbol{\xi}$ are to be useful, experimental studies must be able to measure $\boldsymbol{\xi}$, by spatially probing the lattice at a finer resolution than is used for these experiments. However these measurements will always have an associated length scale of observation below which spatial resolution cannot be obtained, see Figure 3.12. Therefore the modeling of the present section is still of use to those studies as well, in which case the projection of the homogeneity in the form of $\mathbf{A}$ is crucial.

To make $\mathbf{A}$ frame invariant, we remove the dependence of $\mathbf{A}$ from $\boldsymbol{\theta}_0$ by using a slightly different construction for $\boldsymbol{\theta}$ than in (3.309). We consider mappings through $\mathbf{A}$ from γ, as before, but we restrict the mappings to the origin of $\mathrm{SO}(3,\mathbb{R})$, instead of near to the point $\boldsymbol{\theta}_0$. Then, to get to the final point in orientation space $\boldsymbol{\theta}(\boldsymbol{\gamma})$, in place of the summation through $\boldsymbol{\theta}_0$ we map from the point $\mathbf{A}\boldsymbol{\gamma}$ by matrix multiplying the rotation tensor corresponding to $\mathbf{A}\boldsymbol{\gamma}$ and the grain averaged orientation $\mathbf{R}(\boldsymbol{\theta}_0)$. Explicitly instead of (3.309) we have

$$\boldsymbol{\theta}(\boldsymbol{\gamma}) = \boldsymbol{\theta}(\boldsymbol{\gamma}; \mathbf{A}, \boldsymbol{\theta}_0) = \hat{\mathbf{r}}(\mathbf{R}_0\hat{\mathbf{R}}(\mathbf{A}\boldsymbol{\gamma})), \tag{3.311}$$

where $\hat{\mathbf{r}}$ denotes the map from rotation tensors to angle axis parameters, $\hat{\mathbf{R}}$ denotes the map from angle axis parameters to rotation tensors, and $\mathbf{R}_0 \equiv \hat{\mathbf{R}}(\boldsymbol{\theta}_0)$ is the rotation tensor for the grain center of volume. In summary, we perform the matrix operation between the perturbation from $\mathbf{A}$ and the grain averaged orientation $\mathbf{R}_0$ and then remap to orientation

space to arrive at $\boldsymbol{\theta}(\boldsymbol{\gamma})$. Under this construction, $\mathbf{A}$ will be as close to invariant under changes of reference frame as possible, since changes of frame and their distortions of orientation space will naturally be nominally accounted for by using the product mapping via $\mathbf{R}_0$. There are small discrepancies upon change of frame due to the non zero curvature of $\mathrm{SO}(3,\mathbb{R})$ even at the origin, but these are unavoidable and acceptably small.

Next we consider the effect of g under the prescribed transformations. The full map from spherical polar coordinates reference configuration γ' to orientation space is given by the composition

$$\psi = \boldsymbol{\theta} \circ \boldsymbol{\gamma}', \tag{3.312}$$

where $\boldsymbol{\theta}_0 : \mathbb{R}^3 \to \mathrm{SO}(3,\mathbb{R}) | \boldsymbol{\theta}(\boldsymbol{\gamma}) = \hat{\mathbf{r}}(\hat{\mathbf{R}}(\boldsymbol{\theta}_0)\hat{\mathbf{R}}(\mathbf{A}\boldsymbol{\gamma}))$ is the positioning of the center of the ellipse in the full parameter space. Frame invariance requires that the volume distribution function $g(\boldsymbol{\theta})$ be only a function of $\mathbf{A}$ and not $\boldsymbol{\theta}_0$. $g(\boldsymbol{\theta})$ may then be written over the coordinates in γ' by taking

$$g(\boldsymbol{\theta}) = (g \circ \boldsymbol{\theta} \circ \boldsymbol{\gamma}')(R,\Theta,\Phi) = g(\mathbf{A}[R\mathbf{e}_\rho(\Theta,\Phi)]) = \bar{g}(R,\Theta,\Phi;\mathbf{A}). \tag{3.313}$$

As an aside, the important question of frame invariance does not arise when considering excursions into the strain subspace such as (3.303), since $\mathbf{U}$ is already observer invariant. Figure 3.30 depicts the analysis in this section, showing the projection of spatial inhomogeneity into the orientation subspace, and the approximation from $g(\boldsymbol{\theta})$.

Next we consider specific functional forms for $\bar{g}(R,\Theta,\Phi;\mathbf{A})$, in order to expose its specification to a least squares algorithm, §3.4.1.

Forms for intragranular ODF Suggestions for the functional representation of the intragranular ODF $\bar{g}$ are described in this section. A simple sufficiently useful form is the anisotropic Gaussian function

$$g(R,\Theta,\Phi) = g_0 \exp\left[-(\boldsymbol{\gamma} \cdot \mathbf{A}^{\mathrm{T}}\mathbf{A}\boldsymbol{\gamma})\right], \tag{3.314}$$

where $\boldsymbol{\gamma} = \boldsymbol{\gamma}'(R,\Theta,\Phi)$ is the position in γ using a spherical polar coordinate chart, and $g_0 \in \mathbb{R}^+$ is a scaling factor. Equation (3.314) is useful because it exposes anisotropic evolution of intragranular texture; if the eigenvalues of $\mathbf{A}$ differ from one another then anisotropy is present. Furthermore, Gaussian functions have enjoyed a long history of usage in crystallography, and it automatically satisfies the condition $g \geq 0$. In Bunge (1999, eqn 20, p 425) the exponential form like (3.314) is also used in a classical texture exposition. The model parameters for (3.314) are the 6 components of the symmetric $\mathbf{A}$. Other potential forms include separate constructions for $\mathbf{A}$ and $\bar{g}$, such as taking

$$\bar{g}(R,\Theta,\Phi) = (k_0 + k_1 R)^2, \tag{3.315}$$

along with an isotropic texture evolution,

$$\mathbf{A}(\alpha) = \alpha\mathbf{I}. \tag{3.316}$$

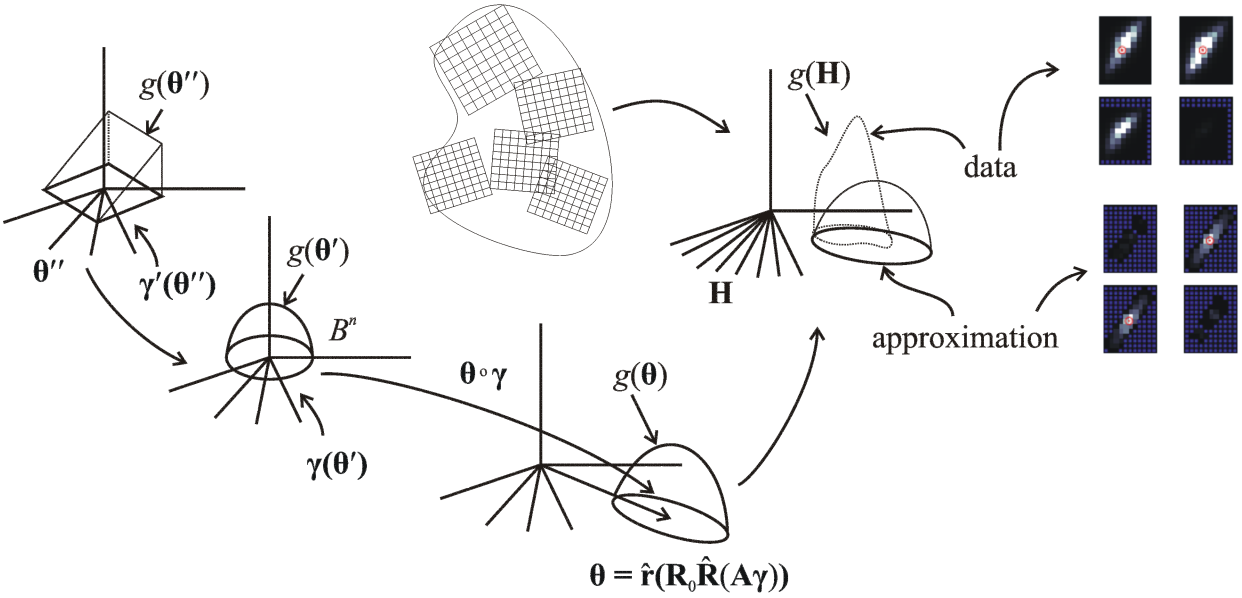

Figure 3.30: Maps of configurations over which the function g is defined, which produce the final diffraction peaks. The projection of spatial inhomogeneity into a subspace of **H**-space gives rise to the function g. The domain of this function is defined to be the result of the linear transformation **A** operating on a reference ball in the configuration γ, thereby giving microstructural content to the estimated values for **A**.

By construction, (3.315) also enforces the condition $g \geq 0$. A third proposed formulation extending (3.316), is that we could introduce a variable number of degrees of freedom for $\mathbf{A}$, between one and six. The form selected for $\bar{g}$ will have implications for the type of microstructural information which can be extracted from this modeling technique. In this study we found the form (3.314) to be sufficient and effective.

Dislocation content In theories of mechanics of elastic plastic deformation, several authors have postulated the dependence of the yield function on the local dislocation content, $\boldsymbol{\xi}$, (Acharya and Bassani, 2000; Gupta et al., 2007). Since plastic behavior is to a great extent determined by the yield function, experimentally quantifying $\boldsymbol{\xi}$ would be of interest when fitting constitutive functions to data. In our experiments, the X-ray beam is larger than the grain size. Therefore we can obtain an estimate for the volume of the grain based on the integrated intensity of the pixel, see Equation (3.127). This enables the determination of a length scale for the individual grain measurements, based on the grain diameter, $d_{\text{grain}}\ V^{1/3}$, where V is the grain volume. If the beam size were small enough to probe local microstructure, then the available length scale would be the beam diameter, w, see Figure 3.12. This length scale information in conjunction with the modeling technique presented here, we are able to thereby obtain a quantity which at least captures the flavor of a dislocation content. To see this we can compute the volume weighted moment of the intragranular volume distribution over $\mathbf{H}$-space as

$$\Sigma_{\mathbf{H}} = \int_{\mathbf{H}} g(\mathbf{H})(\mathbf{H} - \bar{\mathbf{H}}) \otimes (\mathbf{H} - \bar{\mathbf{H}}) \mathrm{d}\mathbf{H}, \tag{3.317}$$

which represents a measure of the spreading of the grain in $\mathbf{H}$-space (or a subspace, $\mathbf{H}(\boldsymbol{\theta})$. Dividing by the available length scale, d, where d is either grain diameter or beam width then gives

$$\frac{1}{d}\Sigma_{\mathbf{H}} = \Sigma_{\mathbf{H},d}[L^2], \tag{3.318}$$

where the notation $[\cdot]$ denotes units of the particular expression. The integral (3.317) has units of L^3 since g has units of volume. The dimension of $\Sigma_{\mathbf{H},d}$ has the same dimensions as the volume integral of the dislocation content introduced in (2.16),

$$\boldsymbol{\xi} = \int_V \boldsymbol{\xi} \mathrm{d}V. \tag{3.319}$$

Then taking (3.314) in (3.317), evaluating at the origin of orientation space so that the moment is $\mathbf{H} - \bar{\mathbf{H}} \approx \mathbf{A}\boldsymbol{\gamma}$ gives

$$\Sigma_{\boldsymbol{\gamma}} = \int_{\mathbf{x}} \exp\left[-(\boldsymbol{\gamma} \cdot \mathbf{A}^{\mathrm{T}}\mathbf{A}\boldsymbol{\gamma})\right] \mathbf{A}\boldsymbol{\gamma} \otimes \mathbf{A}\boldsymbol{\gamma} \mathrm{d}\boldsymbol{\gamma}, \tag{3.320}$$

$$\Sigma_{\boldsymbol{\gamma}} = \mathbf{A} \left(\int_{\boldsymbol{\gamma}} \exp\left[-(\boldsymbol{\gamma} \cdot \mathbf{A}^{\mathrm{T}}\mathbf{A}\boldsymbol{\gamma})\right] \boldsymbol{\gamma} \otimes \boldsymbol{\gamma} \mathrm{d}\boldsymbol{\gamma} \right) \mathbf{A}^{\mathrm{T}}. \tag{3.321}$$

In the next section we test out the model on experimental data.

3.4.2.2.6 Experimental application. In this section we apply the modeling methodology developed in the previous sections to experimental data. We tested a titanium (HCP) alloy with in-situ tension into the plastic region to about 2% strain. The original objectives of the creators of the experiment (Matt Miller, Cornell University) were to compare two heat treatments for a Ti-7Al alloy using a tension experiment with X-ray diffraction *in situ* . One alloy was an air cooled specimen and the other a ice water quenched specimen, which had different macroscopic behaviors with regard to plastic properties such as yield strength and hardening. These experiments were performed in collaboration with the group at LLNL of which I participate. I am grateful for their allowing me access to the data from the experiment.

Description of experimental method. The experiments were performed at the Advanced Photon Source, sector 1-ID. The basic procedure is to load the sample in uniaxial tension into the plastic region while taking XRD measurements. In a previous study, they found that halting the extension of the sample in order to take diffraction measurements led to undesirable drops in the sample tension due to relaxation in the load frame. The development of new hardware capabilities at this particular beamline which greatly reduces the time required for each full rotation scan, to on the order on 30 seconds. Therefore this team decided to attempt a continuous load scan, where the load frame extension rate was kept as constant as possible, with diffraction measurements taken continuously throughout the deformation. This avoided the load frame relaxation problem they observed in the previous study. For example, the macroscopic load curve is indicated in Figure 3.31. The macroscopic stress on the vertical axis is measured by the external load frame, solid points indicate where diffraction measurements were taken. The stress level is plotted versus the diffraction images themselves in Figure 3.32. The finite speed at which the diffraction measurement can be taken (the time required to scan $\Delta\omega$) introduces some error into this process. However the macroscopic extension rate was set slow enough so that this error was deemed acceptable.

There are other challenges in the experiment which should be addressed. In this thesis we have frequently compared the high energy X-ray diffraction measurements with a bonded strain gage, in §3.4.2.1.5 for example. Appealing to this comparison again, unlike a strain gage, the X-ray diffraction volume in the present experiment is not naturally fixed to the material. Therefore the diffraction volume can change due to relative translations between the incident beam and the material. In the present experiment, the beam was kept centered on the same material location by tracking the precession vectors $\mathbf{x}$ for the grains, and keeping a designated master grain in as close to the same position as possible. This analysis was complemented by simple visual verification of surface features on the sample by a high resolution camera. In the end, the researchers found that the simpler visual technique was sufficient for keeping the same material in the diffraction volume. The grain tracking takes longer time than the scan itself since it requires analysis of the X-ray diffraction images, therefore the visual sufficiency was an important learning step.

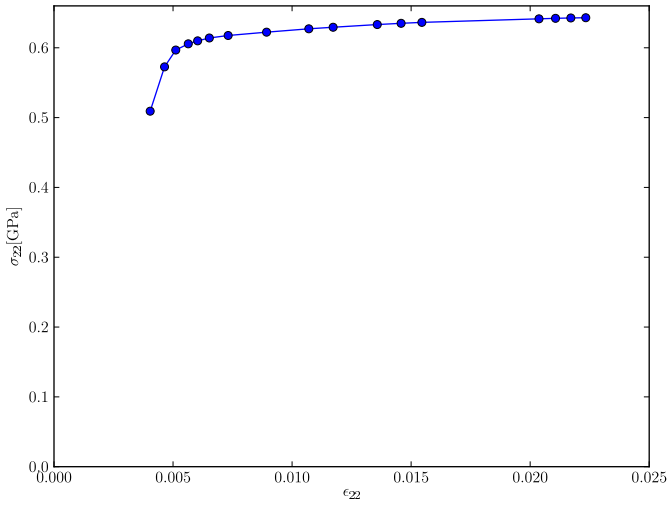

Figure 3.31: σ vs ε for the continuous load scan. Solid points indicate where diffraction measurements were taken.

The detector was the same GE 41RT detector used in §3.4.2.1.3.1, with 2048 x 2048 pixels, and 200 μm pixel size. The beam energy was 50keV. The Ti-7Al sample had a 1 mm by 1 mm cross section. The sample was positioned 880 mm from the specimen. The beam size was 1 mm by 300 μm, fully encompassing the cross section of the material. Approximately 300 grains were present in this diffraction volume. A master grain was selected in the sample and was centered on the rotation axis. The scans were taken for $\omega \in [-60°, 60°]$, in 240 steps for an angular rotation increment of $\delta\omega = 0.5°$. The data analysis was complicated somewhat by the fact that diffraction scans were taken at three vertical positions along the sample, at $0, \pm 150\mu$m, these displacements zeroed to the master grain position. This was done in order to assure that at least the master grain was sampled throughout the test. Figure 3.33 depicts the experimental situation. The master grain in the polycrystal is schematically illustrated. The three different scan regions are also shown relative to the master grain. The limitation on the vertical beam size of 300 μm is due to limitations in data analysis capabilities as more grains are in the diffraction volume. Due to the sequential vertical scanning, the net time interval for which the same region was sampled was approximately three minutes. The load rate was chosen to match this time scale, in order to limit the error introduced by measuring the lattice at a varying load.

3.4.2.2.7 Results We now present the analysis of the experimental data. In Figure 3.34 we show the evolution of a representative diffraction peak as it is tracked throughout the deformation. The images represent raw pixel intensities on the detector. Each quadrant in

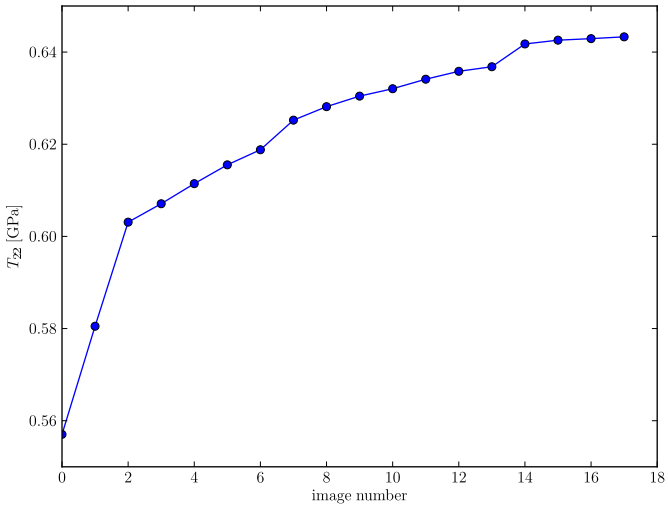

Figure 3.32: Uniaxial stress vs image number for continuous load scan. This is a transformation of the data in Figure 3.31 to show the stress at the times when diffraction measurements were taken.

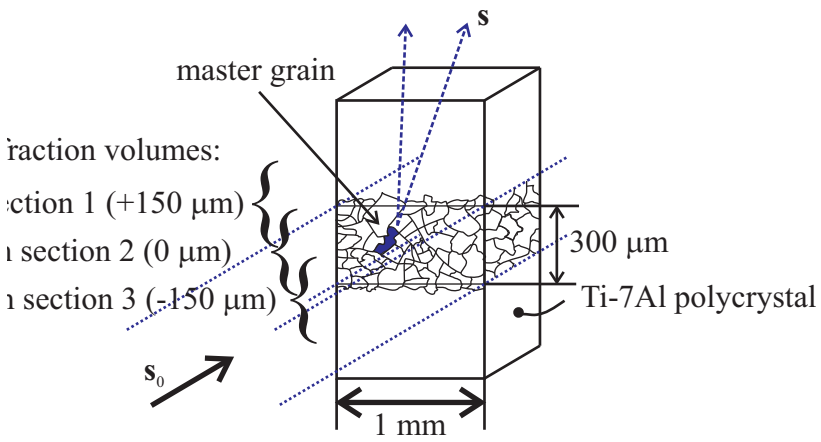

Figure 3.33: Depiction of continuous load scan used to test the forward model. The beam encompasses the width of the material specimen, 1 mm and is 300 μm tall. The beam was scanned in a sequence of three positions at $0, \pm 150$ μm relative to the master grain to ensure that the master grain would not be lost in the data due to relative displacements between the material and beam.

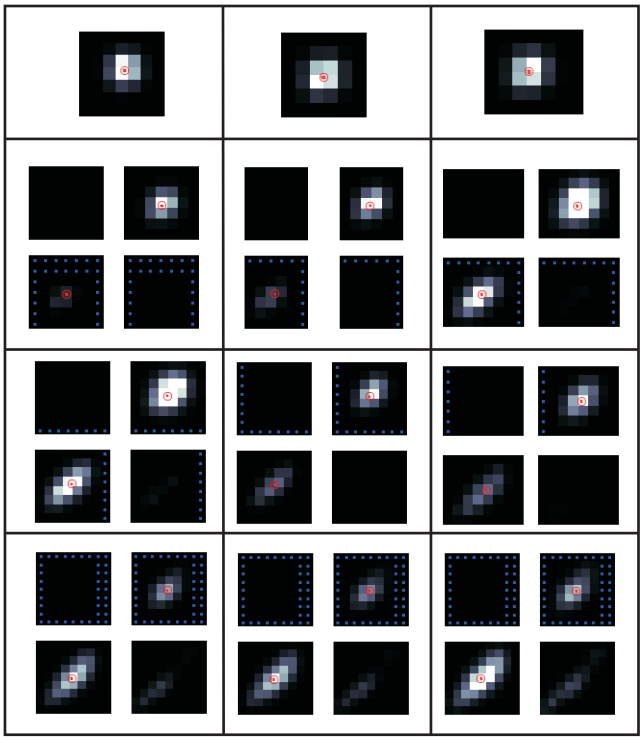

Figure 3.34: Raw data reflections from the continuous loading. ω-slices of the peak are shown in each box. The spreading in the peak is due to evolving spatial inhomogeneity in the grain. The brightness of the peak changes during the load, this is because the nominal intensity to the sample was changed as the test was executed do counteract dimming relative to the threshold value from plastic deformation.

the figure, separated by solid lines, represents the diffraction peak at a different load step. See Figure 3.32 for the stress level at each load step. Multiple tiles in a quadrant indicate that the peak fell over multiple ω-slices. In these cases the sequence should be read in the comic strip order left-right, top-bottom, as ω increases. Blue points in the figure indicate that intensities were below the thresholding level for that particular image. The red mark indicates the location of the center of the diffraction peak, using the local Gaussian fitting described in §3.4.2.1. The increasing angular smearing of the peak has microstructural origin; this is the motivation for pursuing the modeling contained in this section. Also note that the brightness of the peak changes during the loading; this is because the nominal intensity to the sample was changed as the test was executed do counteract dimming relative to the threshold value as a result of plastic deformation.

In application of the model to data we used the simplest possible modeling framework, starting from the combination given by (3.293). Therefore we ignore broadening due to particle size effects. We add wavelength broadening by using the nominal intensity function

(3.296) with $\sigma_\lambda = 0.001\bar{\lambda}$. All together, the pixel intensities use an integrated intensity distribution of the form of (3.293), with the field

$$E_{\text{tot}}(p_1, p_2, \omega; g(\boldsymbol{\theta})) = k \sum_{i=1}^{N} \int_\lambda \int_{\boldsymbol{\theta}} g(\boldsymbol{\theta}) \hat{\mathbf{r}}_{\text{p}}(\mathbf{H}(\boldsymbol{\theta})^{-\text{T}} \mathbf{G}^{(i)}, \mathbf{x}) I(\lambda) c(\mathbf{H}(\boldsymbol{\theta})^{-\text{T}} \mathbf{G}^{(i)}) F^2_{hkl(i)} \mathrm{d}\lambda \wedge \mathrm{d}\boldsymbol{\theta} \tag{3.322}$$

$$= \sum_{i=1}^{N} k \int_\lambda \int_{R \times \Theta \times \Phi} \left(g(R, \bar{\Theta}, \Phi; \mathbf{A}) \hat{\mathbf{r}}_{\text{p}}(\mathbf{H}(\boldsymbol{\theta}(R, \Theta, \Phi))^{-\text{T}} \mathbf{G}^{(i)}, \mathbf{x}) I(\lambda) \right) \cdot \left(c^{(i)} F^2_{hkl(i)} \left(\det \frac{\partial \boldsymbol{\theta}}{\partial \boldsymbol{\eta}} \right) \mathrm{d}\lambda \wedge \mathrm{d}R \wedge \mathrm{d}\Theta \wedge \mathrm{d}\Phi \right), \tag{3.323}$$

where $\boldsymbol{\eta} = R, \Theta, \Phi$, we use the short hand $c^{(i)} \equiv c(\mathbf{H}(\boldsymbol{\theta})^{-\text{T}} \mathbf{G}^{(i)})$, and where the constant $k \equiv 1/(\dot{\omega} V_c)$, and $\mathbf{H}(\boldsymbol{\theta}) = \mathbf{R}(\boldsymbol{\theta}) \mathbf{U}^*$, where $\mathbf{U}^*$ is regarded as a constant tensor representing the best grain averaged lattice strain fit. In other words, in passing from (3.322) to (3.323) we pull back the integration over $\boldsymbol{\theta}$-space to the reference orientation subspace, see (3.302) and (3.305), and use $g(\boldsymbol{\theta})$ given by the anisotropic Gaussian, (3.314). The Jacobian is obtained from (3.311) and is written out as

$$\frac{\partial \boldsymbol{\theta}}{\partial \boldsymbol{\eta}} = \left. \frac{\partial \mathbf{r}}{\partial \mathbf{R}} \right|_{\mathbf{R}_0 \hat{\mathbf{R}}(\mathbf{A}\boldsymbol{\gamma})} \frac{\partial \mathbf{R}_0 \hat{\mathbf{R}}(\mathbf{A}\boldsymbol{\gamma})}{\partial \boldsymbol{\eta}}, \tag{3.324}$$

and

$$\frac{\partial \mathbf{R}_0 \hat{\mathbf{R}}(\mathbf{A}\boldsymbol{\gamma})}{\partial \boldsymbol{\eta}} = \mathbf{R}_0 \left. \frac{\partial \hat{\mathbf{R}}}{\partial \mathbf{r}} \right|_{\mathbf{A}\boldsymbol{\gamma}} \frac{\partial \mathbf{A}\boldsymbol{\gamma}}{\partial \boldsymbol{\eta}}, \tag{3.325}$$

where

$$\frac{\partial \mathbf{A}\boldsymbol{\gamma}}{\partial \boldsymbol{\eta}} = \mathbf{A} \frac{\partial R \mathbf{e}_\rho(\Theta, \Phi)}{\partial \boldsymbol{\eta}}. \tag{3.326}$$

Therefore

$$\frac{\partial \boldsymbol{\theta}}{\partial \boldsymbol{\eta}} = \left(\left. \frac{\partial \mathbf{r}}{\partial \mathbf{R}} \right|_{\mathbf{R}_0 \hat{\mathbf{R}}(\mathbf{A}\boldsymbol{\gamma})} \mathbf{R}_0 \left. \frac{\partial \hat{\mathbf{R}}}{\partial \mathbf{r}} \right|_{\mathbf{A}\boldsymbol{\gamma}} \right) \mathbf{A} \left(\frac{\partial R \mathbf{e}_\rho(\Theta, \Phi)}{\partial \boldsymbol{\eta}} \right). \tag{3.327}$$

Taking the determinant gives

$$\begin{aligned} \det \frac{\partial \boldsymbol{\theta}}{\partial \boldsymbol{\eta}} &= \det \boldsymbol{\Gamma} \det \mathbf{A} \det \frac{\partial R \mathbf{e}_\rho(\Theta, \Phi)}{\partial \boldsymbol{\eta}} \\ &= \det \boldsymbol{\Gamma} \det \mathbf{A} \left(R^2 \sin \Theta \right), \end{aligned} \tag{3.328}$$

where

$$\mathbf{\Gamma} \equiv \left(\frac{\partial \hat{\mathbf{r}}}{\partial \mathbf{R}}\bigg|_{\mathbf{R}_0 \hat{\mathbf{R}}(\mathbf{A}\boldsymbol{\gamma})} \mathbf{R}_0 \, \frac{\partial \hat{\mathbf{R}}}{\partial \mathbf{r}}\bigg|_{\mathbf{A}\boldsymbol{\gamma}} \right),$$

and we have used (A.2). The value of $\det \mathbf{\Gamma}$ depends on the value of $\mathbf{R}_0$, which is not frame invariant. At $\mathbf{R}_0 = \mathbf{I}$, $\det \mathbf{\Gamma} = 1$, otherwise it differs from 1. Considering the analysis of individual grains, we can always rotate the fixed lattice configuration $\boldsymbol{\kappa}$ to make $\mathbf{R}_0 = \mathbf{I}$. This is fine, but should be used with caution, as the definitions for $\mathbf{H}$ also change with this procedure.

The integration region in (3.323) is over the reference orientation subspace γ' and domain of wavelength spread, written as

$$\gamma' \times \lambda = (\Delta R \times \Delta\Theta \times \Delta\Phi) \times \Delta\lambda,$$

where for the unit ball of γ', $\Delta R = [0, 1]$, $\Delta\Theta = [0, \pi]$, $\Delta\Phi = [0, 2\pi]$, and for the wavelength we take $\Delta\lambda = \bar{\lambda} + [-2\sigma_\lambda, 2\sigma_\lambda]$, see (3.296). This integration region is discretized following 4-dimensional Gaussian quadrature. After fitting the grain averaged quantities $\mathbf{H}_0, \mathbf{x}_0$ using the methods of §3.4.2.1, the intragranular optimization occurs with the 9 free parameters $\mathbf{R}_0, \mathbf{A}$. The residuals for the least squares optimization are formed from (3.300) and (3.301). To dull the influence of scalar factors in the integrated pixel intensity in (3.323), we modify the residuals to only compare peak intensities normalized to the maximum intensity in the peak. This has the effect of modifying the model parameters $\mathbf{R}_0, \mathbf{A}$ in a fashion to match the intensity profile curvature over the pixels, which is what we are after anyway. We used $N = 10$ diffraction peaks in (3.301); more peaks became computationally prohibitive with only modest changes in the final optimal estimates for $\mathbf{R}_0, \mathbf{A}$.

In the next section, we present simulation results of the forward model with a range of quadrature points along each dimension, to ascertain the amount of discretization necessary to sufficiently model smeared diffraction peaks. We also show results of the forward modeling for tracking the evolving intragranular misorientation.

Forward simulation results In this section we present results of the forward modeling for producing simulated diffraction peaks. The results from increasing the number of quadrature points are given in Figure 3.35. The number of quadrature point selected for the integration in Equation (3.323) influences the speed of the computation and the accuracy of the simulated peak. Qualitative examination of Figure 3.35 suggested that 12 point quadrature along each of the integration domain variables R, Θ, Φ, λ in (3.323) gave acceptable smoothness and coverage of the forward modeled intensity, with reasonable computation cost.

Next we show the results of different reflections from the same grain, in Figures 3.36-3.41. These peaks were simultaneously used in the forward model. These figures show raw intensity data for different reflection types in the crystal alongside the forward model intensity distributions after the parameter refinement. Also note that the forward model qualitatively captures the geometric distortions of the reciprocal vector to pixel map in Figure 3.39.

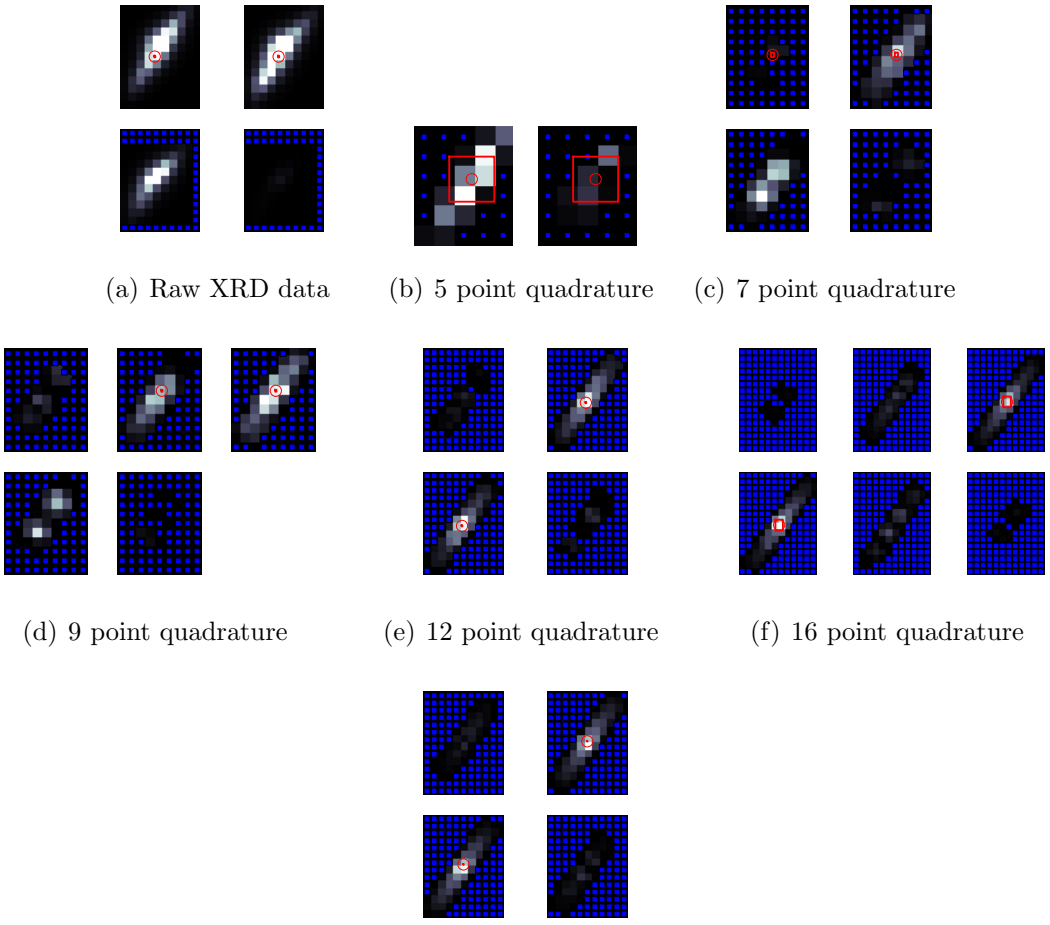

(a) Raw XRD data (b) 5 point quadrature (c) 7 point quadrature

(d) 9 point quadrature (e) 12 point quadrature (f) 16 point quadrature

(g) 20 point quadrature

Figure 3.35: Comparison of predicted and simulated normalized intensity as a function of the quadrature over the domain $\gamma' \times \lambda$. The simulated intensities are obtained according to (3.322) and (3.323).

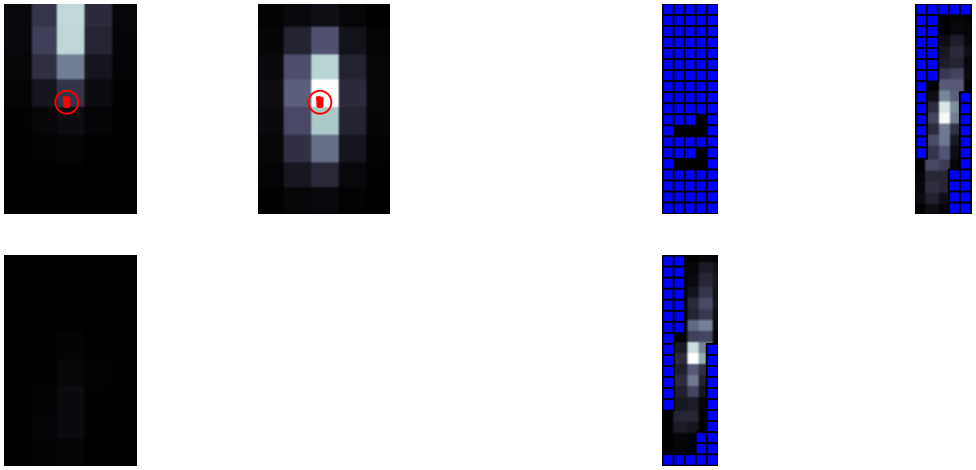

(a) Raw XRD intensity data

(b) Simulated intensity data

Figure 3.36: Comparison of predicted and simulated normalized intensity, hkl = 1, -1, 0. Forward modeling from (3.323).

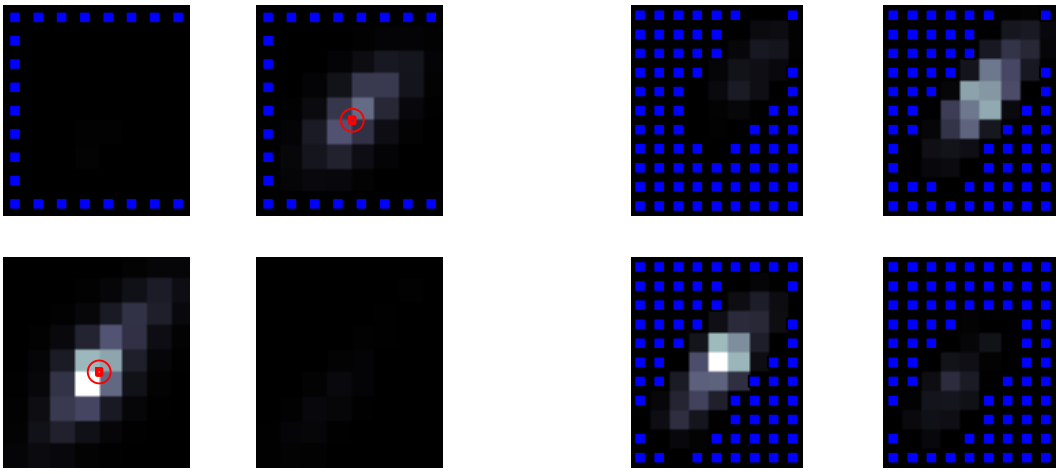

(a) Raw XRD intensity data

(b) Simulated intensity data

Figure 3.37: Comparison of predicted and simulated normalized intensity, hkl = 0, 0, -2. Forward modeling from (3.323).

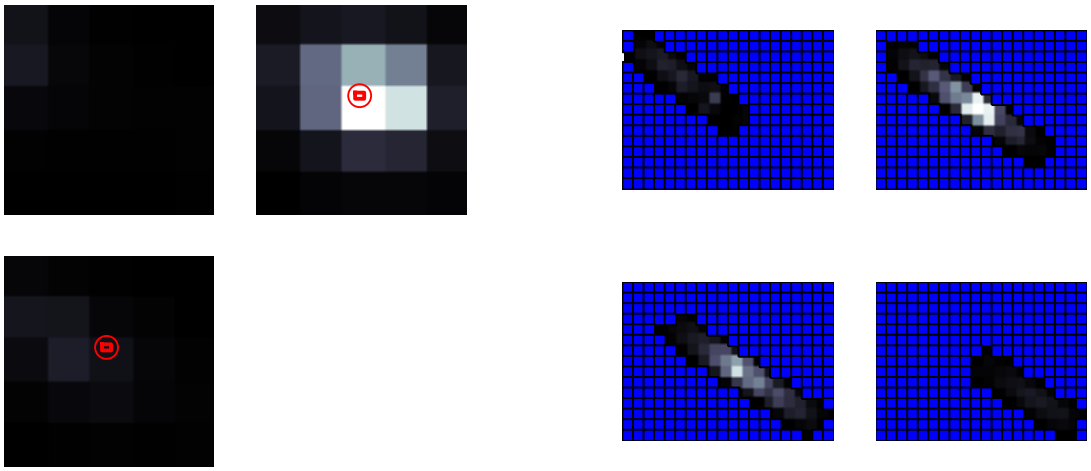

(a) Raw XRD intensity data

(b) Simulated intensity data

Figure 3.38: Comparison of predicted and simulated normalized intensity, hkl = -1, 0, 1. Forward modeling from (3.323).

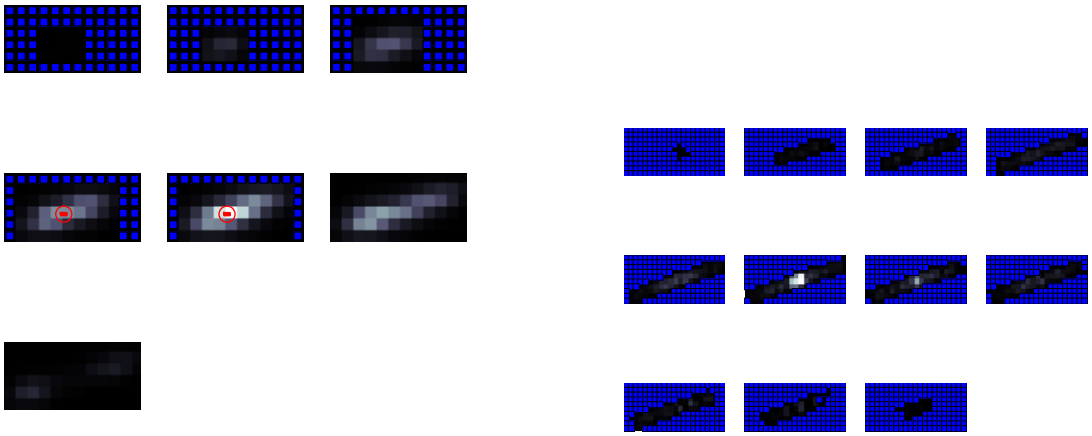

(a) Raw XRD intensity data

(b) Simulated intensity data

Figure 3.39: Comparison of predicted and simulated normalized intensity, hkl = 0, 1, -1.Forward modeling from (3.323).

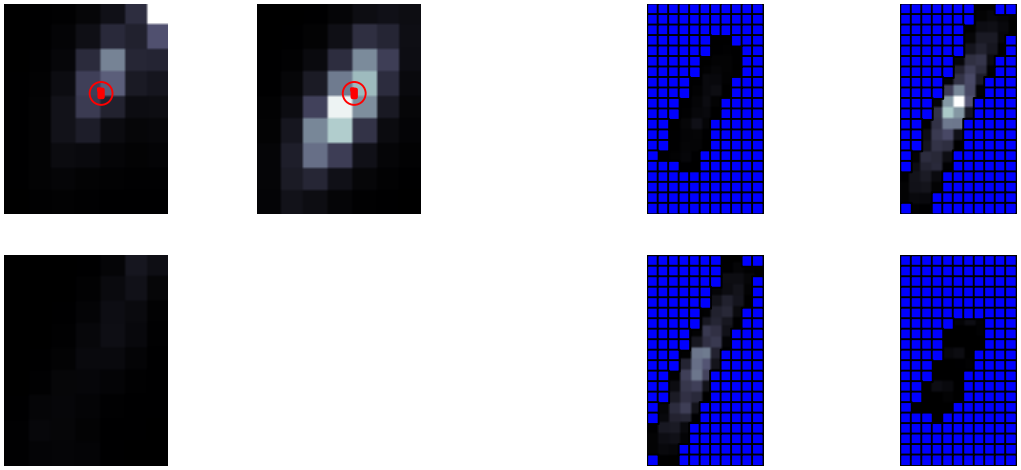

(a) Raw XRD intensity data

(b) Simulated intensity data

Figure 3.40: Comparison of predicted and simulated normalized intensity, hkl = -1, 1, -1. Forward modeling from (3.323).

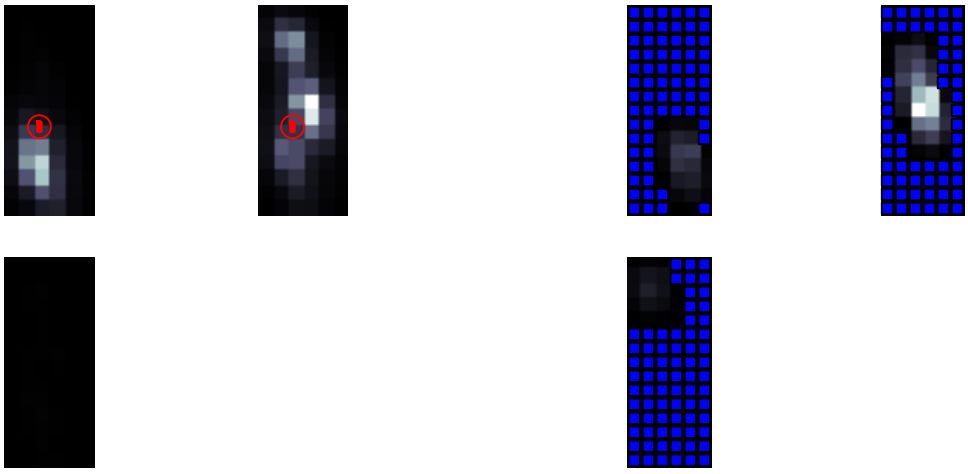

(a) Raw XRD intensity data

(b) Simulated intensity data

Figure 3.41: Comparison of predicted and simulated normalized intensity, hkl = 1, 0, 1. Forward modeling from (3.323).

Next we consider the uncertainty prediction from the forward model. There are more residual entries into the objective function than the grain averaged approach (as the residual is formed on pixel intensities instead of a single pixel tuple). Therefore it seems reasonable to expect the precision uncertainty to fall off for the forward model with respect to the grain averaged approach. This is shown in Figure 3.42, where the uncertainty in a rotation component r_1 from the forward model fit based on 10, 20, and 30 reflections is plotted against the grain averaged fit. The uncertainty from the grain averaged fit is computed from using all available reflections. There is about an order of magnitude increase in the estimated precision from the method if all reflections are incorporated into the forward model.

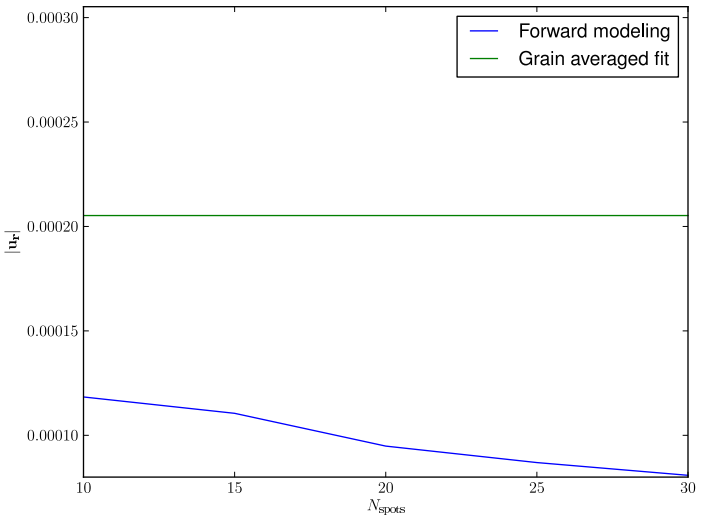

Figure 3.42: Comparison of the uncertainty in $\mathbf{R}_0$ for the forward model vs. the grain averaged fitting. The increase in the size of the residual leads to an increase in the stated precision of measurement.

Thus far we have shown the forward model method to be qualitatively interesting in that we have the flexibility to capture anisotropic broadening in the diffraction peaks based on the coarse detector. We investigated the influence of the resolution of the integration required to produce the forward model, arriving at a compromise between smooth intensity distributions with acceptable computational cost. Figures 3.36-3.41 show promise for the approach, in comparison with the grain averaged approach. We now examine potential informative uses for the modeling technique.

Intragranular misorientation We have shown the capability to capture the diffraction intensities given model parameters in the form of the symmetric matrix $\mathbf{A}$, which is constructed to respect invariance under change of frame. Therefore $\mathbf{A}$ represents an efficient

measure of the amount of spatial inhomogeneity in the crystal, or an indication of the projection $\pi_{\mathbf{H}}$ of Figure 3.12.

Since the initial state of the crystal is known from the initial measurements, Figure 3.34, spatial inhomogeneity in the lattice deformation must arise due to gradients in the plastic flow. That plastic deformation is present is evident based on the macroscopic stress strain curve, Figure 3.31, since we are clearly out of the elastic region in the stress-strain curve. The two phenomena (development of spatial inhomogeneity, plastic flow) are therefore clearly correlated in the experimental data.

In Figure 3.43 is shown the familiar schematic illustration we have used previously in Figure 2.6, generalized to demonstrate spatial inhomogeneity. In this figure the fixed reference configuration is shown, with its implant in the material reference configuration at two different material points $\mathbf{X}_{(1)}, \mathbf{X}_{(2)}$. These points experience different plastic deformations $\mathbf{K}(\mathbf{X}_{(1)}), \mathbf{K}(\mathbf{X}_{(2)})$, and hence the lattice deformations $\mathbf{H}(\mathbf{X}_{(1)}), \mathbf{H}(\mathbf{X}_{(2)})$ in the current state differ spatially. The relative lattice deformation taking the lattice from one material location with lattice deformation $\mathbf{H}_1 = \mathbf{H}(\mathbf{X}_1)$ to another $\mathbf{H}_2 = \mathbf{H}(\mathbf{X}_2)$ is given by $\Delta\mathbf{H}\mathbf{H}_1 = \mathbf{H}_2 \implies$

$$\Delta\mathbf{H} = \mathbf{H}_1(\mathbf{H}_2)^{-1}. \tag{3.329}$$

This transformation is depicted in the lower right of Figure 3.43. Considering only spatial inhomogeneity in the orientation factor, from the polar decomposition we have $\mathbf{U}_1 = \mathbf{U}_2 \implies$

$$\Delta\mathbf{H} \approx \mathbf{R}_1\mathbf{U}_1\mathbf{U}_2)^{-1}(\mathbf{R}_2)^{-1} = \mathbf{R}_1(\mathbf{R}_2)^{-1}. \tag{3.330}$$

Therefore $\Delta\mathbf{H}$ defines the misorientation tensor between orientations,

$$\boldsymbol{\Omega} = \mathbf{R}_1(\mathbf{R}_2)^{-1}, \tag{3.331}$$

with $\boldsymbol{\Omega} \in \mathrm{SO}(3,\mathbb{R})$. We can define the misorientation axis, $\boldsymbol{\omega}$, using the projection of $\mathrm{SO}(3,\mathbb{R}) \to \mathbb{R}^3$ given by the angle-axis map. Therefore $\boldsymbol{\omega}(\boldsymbol{\Omega})$ is the misorientation axis of the spatial inhomogeneity as shown in the lower right of Figure 3.43.

Now we relate the microstructural $\boldsymbol{\omega}$ to the X-ray diffraction quantity $\mathbf{A}$. The eigenvectors of $\mathbf{A}$ represent the directions of largest spatial misorientation. Therefore the largest eigenvector and eigenvalue of $\mathbf{A}$ represent the dominant directions of spatial inhomogeneity and can be used to compute $\boldsymbol{\omega}$. We now analyze the continuous load scan data with this line of analysis.

Application to continuous load The misorientation axes $\boldsymbol{\omega}$ corresponding to the eigenvectors of the largest eigenvalues of $\mathbf{A}$ can be plotted in various projections into the unit cell. The eigenvectors of $\mathbf{A}$ are frame invariant, so to project onto the unit cell we need to use the bulk orientation of the grain, $\mathbf{R}_0$ in order to project onto the unit cell. For example, let $\mathbf{u}_1$ be the maximum eigenvector of $\mathbf{A}$. Then we compute

$$\mathbf{R}^{(1)} = \mathbf{R}_0\mathbf{A}\mathbf{u}_1 \tag{3.332}$$

and

$$\mathbf{R}^{(2)} = \mathbf{R}_0\mathbf{A}(-\mathbf{u}_1). \tag{3.333}$$

We then compute the misorientation

$$\boldsymbol{\omega} = \hat{\boldsymbol{\omega}}(\mathbf{R}^{(1)}(\mathbf{R}^{(2)})^{-1}) \tag{3.334}$$

by evaluating the angle axis representation of $\mathbf{R}^{(1)}(\mathbf{R}^{(2)})^{-1}$. Next, projection of $\boldsymbol{\omega}$ on the crystal basis vectors $\mathbf{L}_1, \mathbf{L}_2, \mathbf{L}_3$ is accomplished by

$$\boldsymbol{\omega} = (\boldsymbol{\omega} \cdot \mathbf{R}_0^{-\mathrm{T}}\hat{\mathbf{L}}^{i})\mathbf{R}_0\hat{\mathbf{L}}_i, \tag{3.335}$$

where $\hat{\mathbf{L}}_i$ is the unit vector associated with the lattice vector $\mathbf{L}_i$, and $\hat{\mathbf{L}}^{i}$ is the unit vector associated with the reciprocal lattice vector $\mathbf{L}^i$, see (A.4). With the decomposition (3.335) we can visualize the evolution of $\boldsymbol{\omega}$ on various views of the crystal unit cell. For example taking $\mathbf{L}_1$ in the basal plane and $\mathbf{L}_3$ along the c-axis gives a view of the misorientation axis through the side of the unit cell. Equivalently, we can resolve everything on the image of the orthonormal basis $\mathbf{e}_1, \mathbf{e}_2, \mathbf{e}_3 \in \boldsymbol{\kappa}$ which is mapped to the physical configuration by $\mathbf{R}_0$, giving

$$\boldsymbol{\omega} = (\boldsymbol{\omega} \cdot \mathbf{R}_0^{-\mathrm{T}}\mathbf{e}_i)\mathbf{R}_0\mathbf{e}_i. \tag{3.336}$$

The orthonormal construction in (3.336) avoids the geometric complexity of the reciprocal unit basis in (3.335), and is depicted in Figure 3.44. The microstructural significance of this analysis of spatial inhomogeneity, the intragranular misorientation should be a trailing indicator of plastic deformation. Consider Figure 3.45, which shows a cartoon picture of lattice reorientation due to single slip, (Yang and Lee, 1993). If the stress field is inhomogeneous, then regions of crystal experience different amounts of slip, hence different amounts of reorientation in the same grain, see Figure 3.46. Therefore there is a spatial inhomogeneity in the lattice deformation, and the projection of this spatial inhomogeneity into the orientation subspace of **H**-space gives rise to the misorientation $\boldsymbol{\omega}$. This logic supports the notion that $\boldsymbol{\omega}$ represents a trailing indicator of plastic deformation.

To see this, according to crystal plasticity theory, plastic deformation is restricted to the slip systems of the material. Therefore each slip system $\mathbf{s}^\alpha \otimes \mathbf{n}^\alpha$ defines a likely candidate for the misorientation axis, via $\boldsymbol{\omega} \parallel \mathbf{s}^\alpha \times \mathbf{n}^\alpha$ where $\parallel$ denotes the parallel relation. Comparing to the results Figure 3.52, the misorientation axes cluster at the c-axis. This is consistent with a history of prismatic slip.

We now examine the projections of the several hundred grains which were forward modeled for each step of the test. In the following figures, there are several small images, which represent the load steps where images were taken. See Figure 3.32 for a plot of the far field stress at each load step. In Figure 3.54, the projection is on the image of the lab frame basis $\mathbf{e}_1, \mathbf{e}_3$. This represents a view of the misorientation development from the lab frame based $\mathbf{e}_2$ direction, the loading direction. Due to symmetry, for a given misorientation $\hat{\boldsymbol{\omega}}$ the opposite sign misorientation $-\hat{\boldsymbol{\omega}}$ was also added to the figure. The behavior is for the misorientation

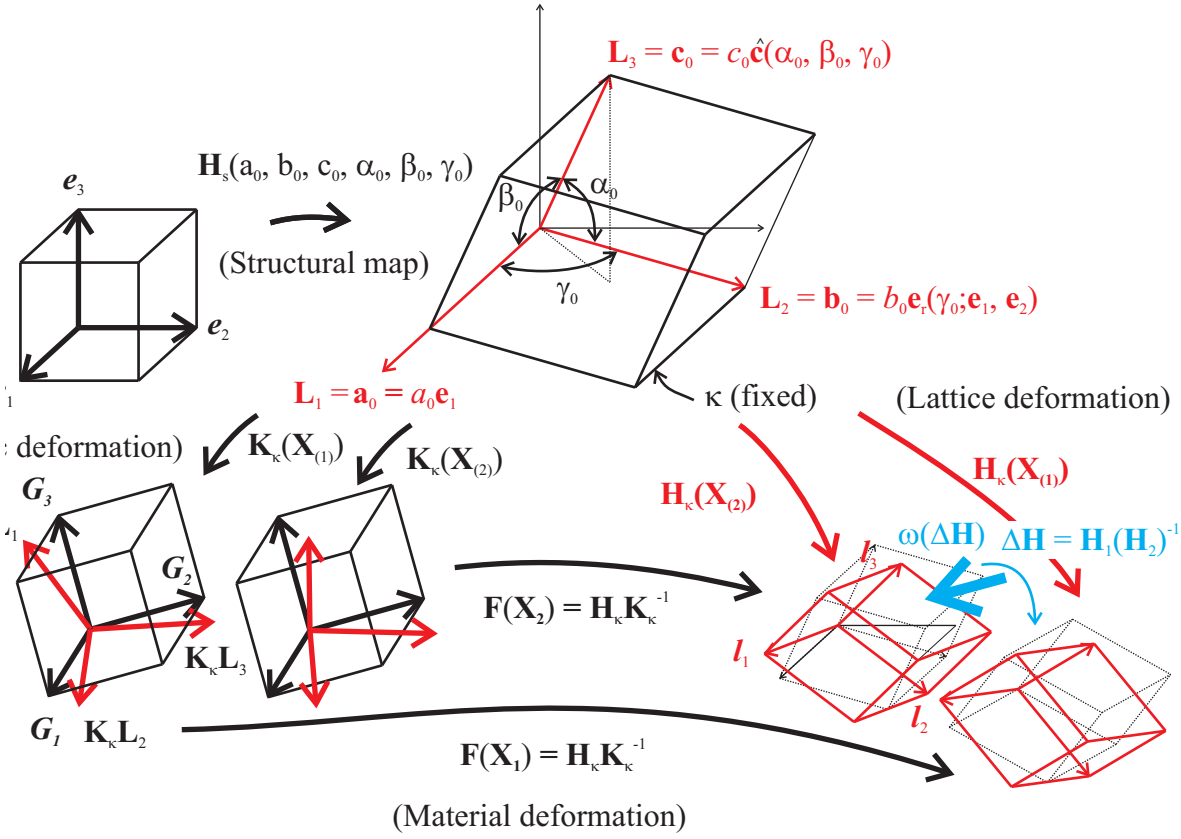

Figure 3.43: Illustration of the misorientation vector $\boldsymbol{\omega}$ introduced by spatial inhomogeneity in the plastic deformation, hence lattice deformation. This figure was initially introduced in Figure 2.6. $\mathbf{X}_{(1),(2)}$ denote material position vectors in the material reference configuration, which are nearby in the physical configuration. The intragranular function $\mathbf{A}$ introduced in the present section represents the projection of the spatial inhomogeneity in this figure into the orientation subspace of $\mathbf{H}$-space.

axes to fall to an equatorial position. Next we look at resolving the misorientations on intrinsic crystal bases. In Figure 3.47 is a schematic of the three prismatic and basal slip systems in the HCP unit cell. There are three prismatic systems $\mathbf{s}^{(i)} \otimes \mathbf{n}^{(i)}, i = 1, 2, 3$ and three basal systems $i = 4, 5, 6$. The slip plane normals $\mathbf{n}$ are denoted in red, the slip directions $\mathbf{s}$ in blue. The misorientation axis $\boldsymbol{\omega}$ suggested from the action of these slips is indicated by the dashed black line, see Figure 3.46 for this motivation. Therefore a history of heterogeneous prismatic slip is expected to have $\boldsymbol{\omega}$ parallel to the c-axis, while basal slip would have $\boldsymbol{\omega}$ in the equatorial plane $\mathbf{e}_1, \mathbf{e}_2$.

We now examine the $\boldsymbol{\omega}$ extracted from several hundred grains in the titanium polycrystal. We project $\boldsymbol{\omega}$ on various views of the unit cell in order to visualize its evolution. In the following figures the location of the data point indicates the projection of $\hat{\boldsymbol{\omega}}$ onto the

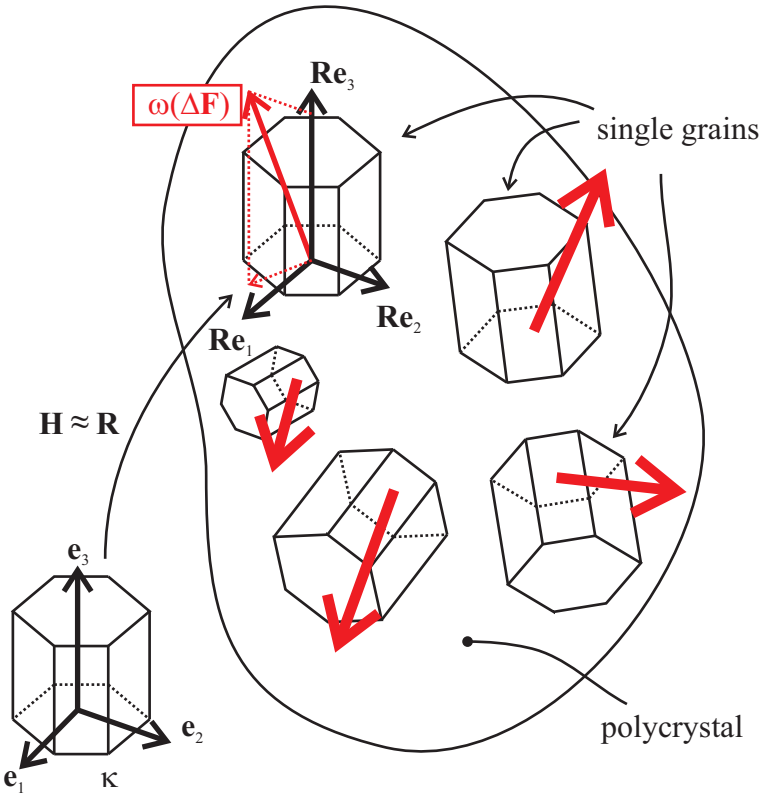

Figure 3.44: Illustration of the misorientation vector $\boldsymbol{\omega}$ introduced by spatial inhomogeneity in the plastic deformation, resolved on the crystal basis.

visualization basis. The size of the data point indicates the magnitude of misorientation, proportional to $\|\boldsymbol{\omega}\|$. The colormap can be ignored. In Figure 3.48 we see the projection of $\hat{\boldsymbol{\omega}}$ onto the $\mathbf{R}_0\mathbf{e}_1, \mathbf{R}_0\mathbf{e}_3$ basis for each of the 18 load steps. This is the visualization projection for one of the basal systems, according to Figure 3.46. Initially the misorientations are random, but as plastic deformation accumulates and the grains break up, the misorientation axes begin to show a detectable anisotropy. It appears that the tendency is for the misorientation axes to cluster around the c-axis. This is consistent with a history of prismatic slip. To verify this, in Figure 3.49, Figure 3.50, and Figure 3.51are visualization projections for the three prismatic systems. These figures show projections looking down from the c-axis, and the basis vectors for obtaining the projection are $\mathbf{R}_0\mathbf{e}_1, \mathbf{R}_0\mathbf{e}_2$. The prismatic slip history is again indicated, as the misorientation axes cluster at the c-axis. In Figure 3.52 we again see the projection of $\hat{\boldsymbol{\omega}}$ onto the basal visualization, with basis $\mathbf{R}_0\mathbf{e}_1, \mathbf{R}_0\mathbf{e}_3$ in greater resolution. The loadsteps 1,6,12,15 were selected as representative. In Figure 3.53 are the same load steps with the prismatic visualization. These two figures are added for better resolution in comparison with the previous coarse figures. The clustering of the misorientation axes $\boldsymbol{\omega}$ around the c-axis reflects a history of prismatic slip activity. Finally in Figure 3.54 the

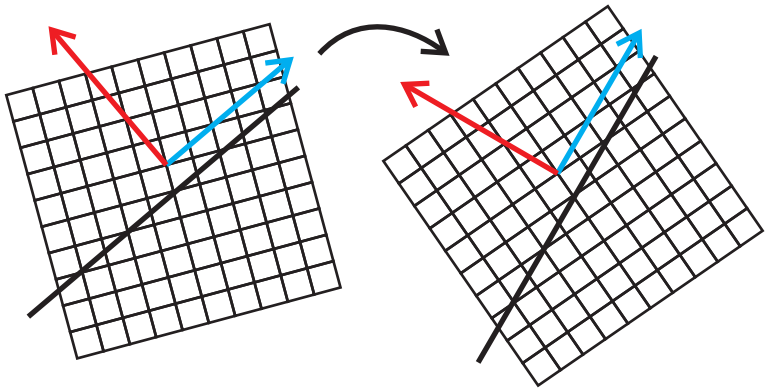

Figure 3.45: Schematic illustration of the reorientation of the lattice under single slip.

misorientation data is plotted on the external (fixed) lab frame $\mathbf{e}_1, \mathbf{e}_3$. The evolution of the misorientation is to fall on the equatorial plane. The evolution based on the intrinsic unit cell orientation is apparently successful, so that this equatorial evolution is probably more an effect of anisotropic texture in the polycrystal than a property of the boundary value problem.

To get a better visualization of the evolution of $\boldsymbol{\omega}$, Figure 3.55 represents the same data as in Figure 3.52 but plotted on a spherical polar coordinate chart. This is natural because the unit vectors on S^2 naturally occupy a two dimensional manifold, by the parametrization of Equation (A.1). The coordinates β, α from this parametrization are plotted on the horizontal and vertical axes respectively. The north pole in the parametrization used for Figure 3.52 is in the basal plane, so the c axis is at $\beta = \pi/2$. The clustering at the c-axis is clearly depicted in the figure. Finally, in Figure 3.56 the projections of the misorientation on the fixed lab frame basis is similarly plotted in spherical polar coordinates. The poles are defined at $\pm\mathbf{e}_2$. The evolution of the misorientation to the equatorial plane at $\beta = \pi/2$ is more evident than in Figure 3.54.

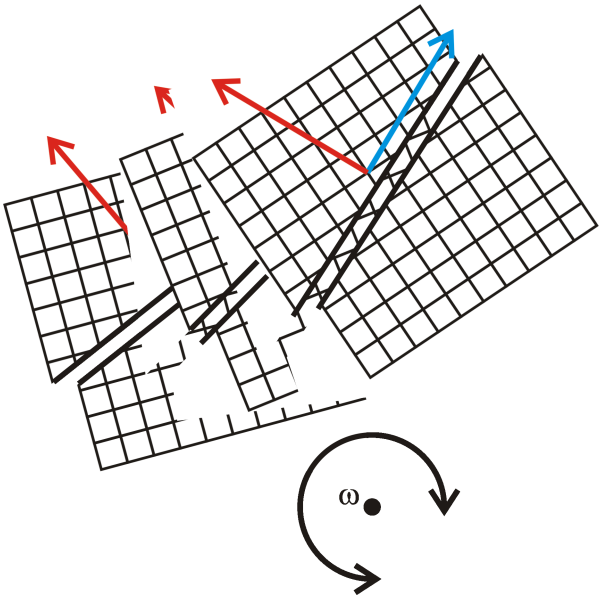

Figure 3.46: Schematic illus-traction of differences in the local slip causing spatial misorientation in the lattice. In the figure the resulting misorientation axis $\boldsymbol{\omega}$ is coming out of the page; it is orthogonal to the slip system.

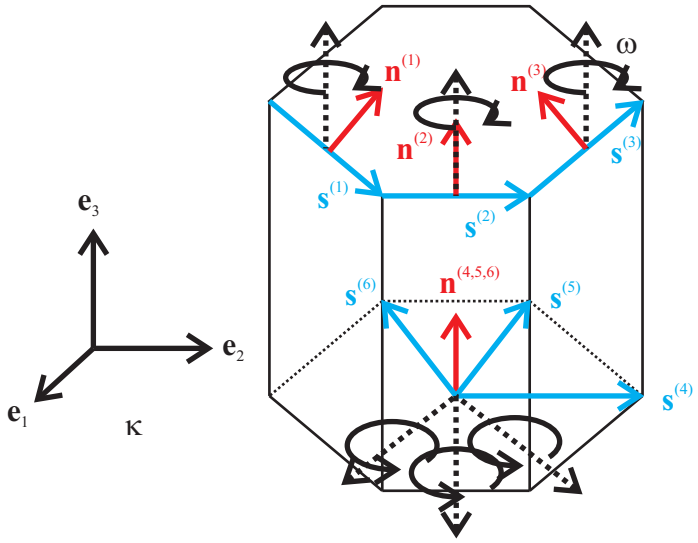

Figure 3.47: Schematic view of HCP unit cell with several slip systems indicated. The misorientation axis $\boldsymbol{\omega}$ suggested from the action of these slips, according to Figure 3.46 is indicated by the dashed black line. Therefore prismatic slip is expected to have $\boldsymbol{\omega}$ parallel to the c-axis and basal slip any thing in the equatorial plane.

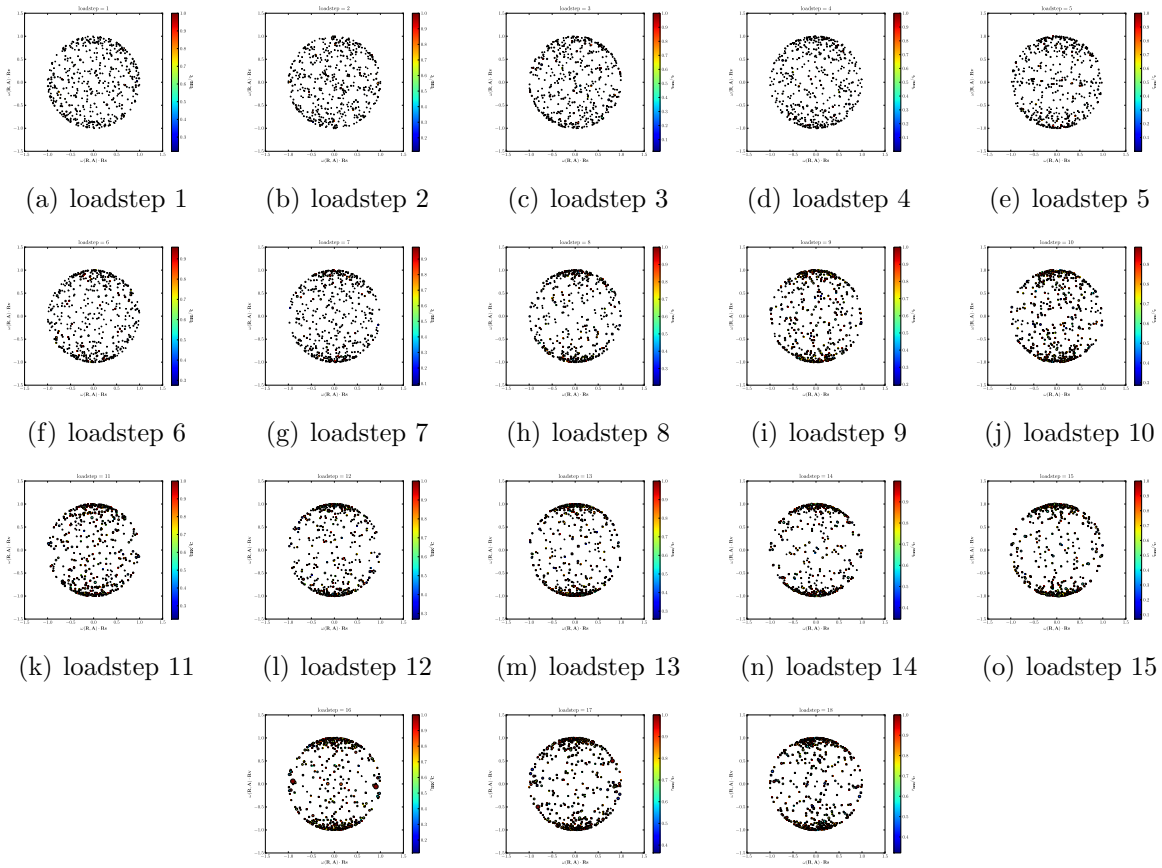

(a) loadstep 1 (b) loadstep 2 (c) loadstep 3 (d) loadstep 4 (e) loadstep 5

(f) loadstep 6 (g) loadstep 7 (h) loadstep 8 (i) loadstep 9 (j) loadstep 10

(k) loadstep 11 (l) loadstep 12 (m) loadstep 13 (n) loadstep 14 (o) loadstep 15

(p) loadstep 16 (q) loadstep 17 (r) loadstep 18

Figure 3.48: $\hat{\boldsymbol{\omega}}$ axes projected on to a basal visualization direction. Location of the data points indicates the projection of $\hat{\boldsymbol{\omega}}$ on the selected basis. The size of the data points indicates the magnitude of misorientation, $\|\boldsymbol{\omega}\|$. The misorientation axes cluster around the c-axis of the unit cell, indicating a history of prismatic slip.

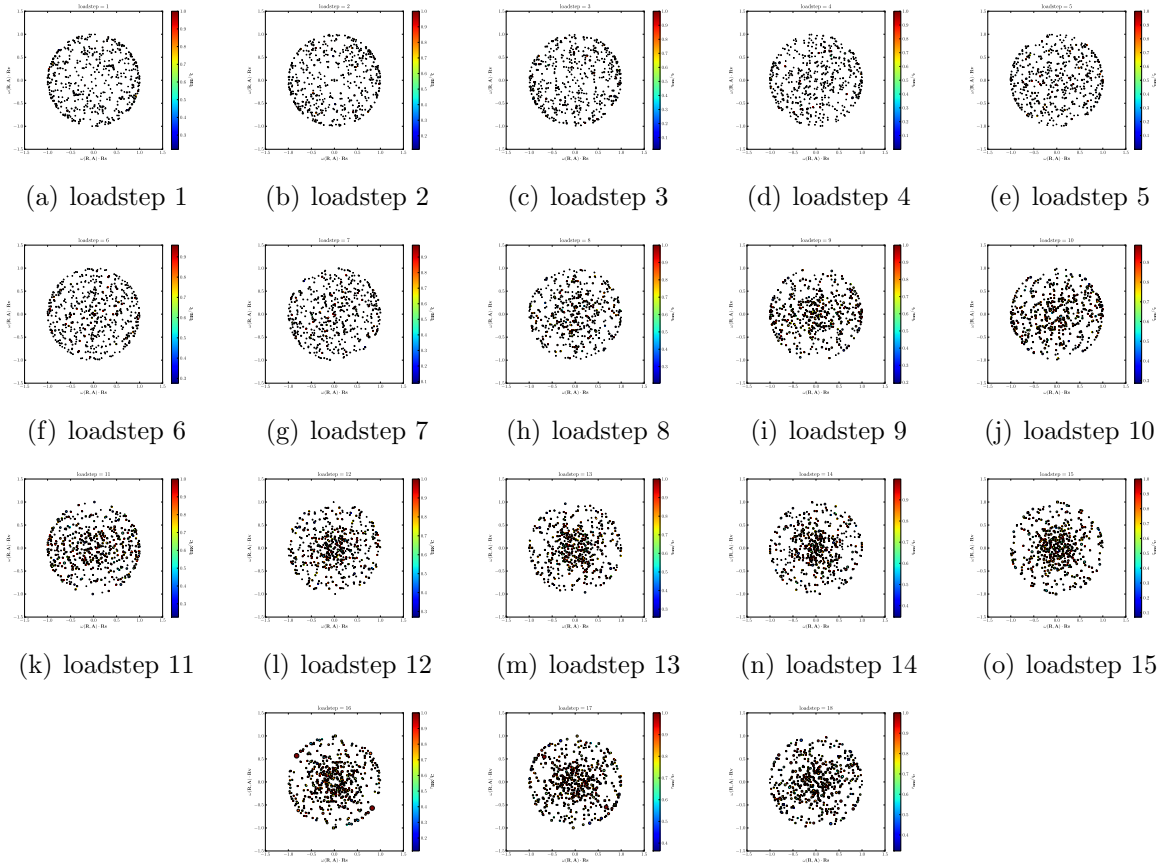

(a) loadstep 1 (b) loadstep 2 (c) loadstep 3 (d) loadstep 4 (e) loadstep 5

(f) loadstep 6 (g) loadstep 7 (h) loadstep 8 (i) loadstep 9 (j) loadstep 10

(k) loadstep 11 (l) loadstep 12 (m) loadstep 13 (n) loadstep 14 (o) loadstep 15

(p) loadstep 16 (q) loadstep 17 (r) loadstep 18

Figure 3.49: $\hat{\boldsymbol{\omega}}$ axes projected on to a basal visualization direction. Location of the data points indicates the projection of $\hat{\boldsymbol{\omega}}$ on the selected basis. The size of the data points indicates the magnitude of misorientation, $\|\boldsymbol{\omega}\|$. The misorientation axes cluster around the c-axis of the unit cell, indicating a history of prismatic slip.

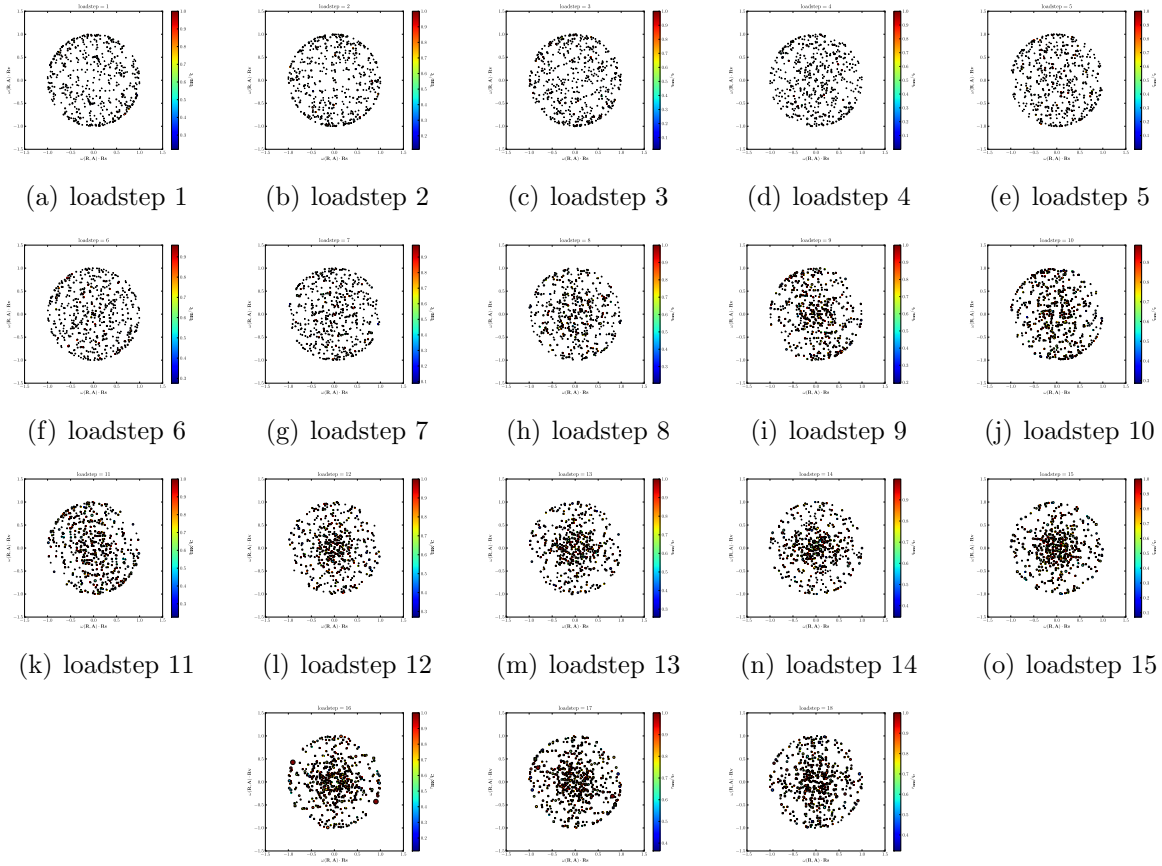

(a) loadstep 1 (b) loadstep 2 (c) loadstep 3 (d) loadstep 4 (e) loadstep 5

(f) loadstep 6 (g) loadstep 7 (h) loadstep 8 (i) loadstep 9 (j) loadstep 10

(k) loadstep 11 (l) loadstep 12 (m) loadstep 13 (n) loadstep 14 (o) loadstep 15

(p) loadstep 16 (q) loadstep 17 (r) loadstep 18

Figure 3.50: $\hat{\boldsymbol{\omega}}$ axes projected on to a basal visualization direction. Location of the data points indicates the projection of $\hat{\boldsymbol{\omega}}$ on the selected basis. The size of the data points indicates the magnitude of misorientation, $\|\boldsymbol{\omega}\|$. The misorientation axes cluster around the c-axis of the unit cell, indicating a history of prismatic slip.

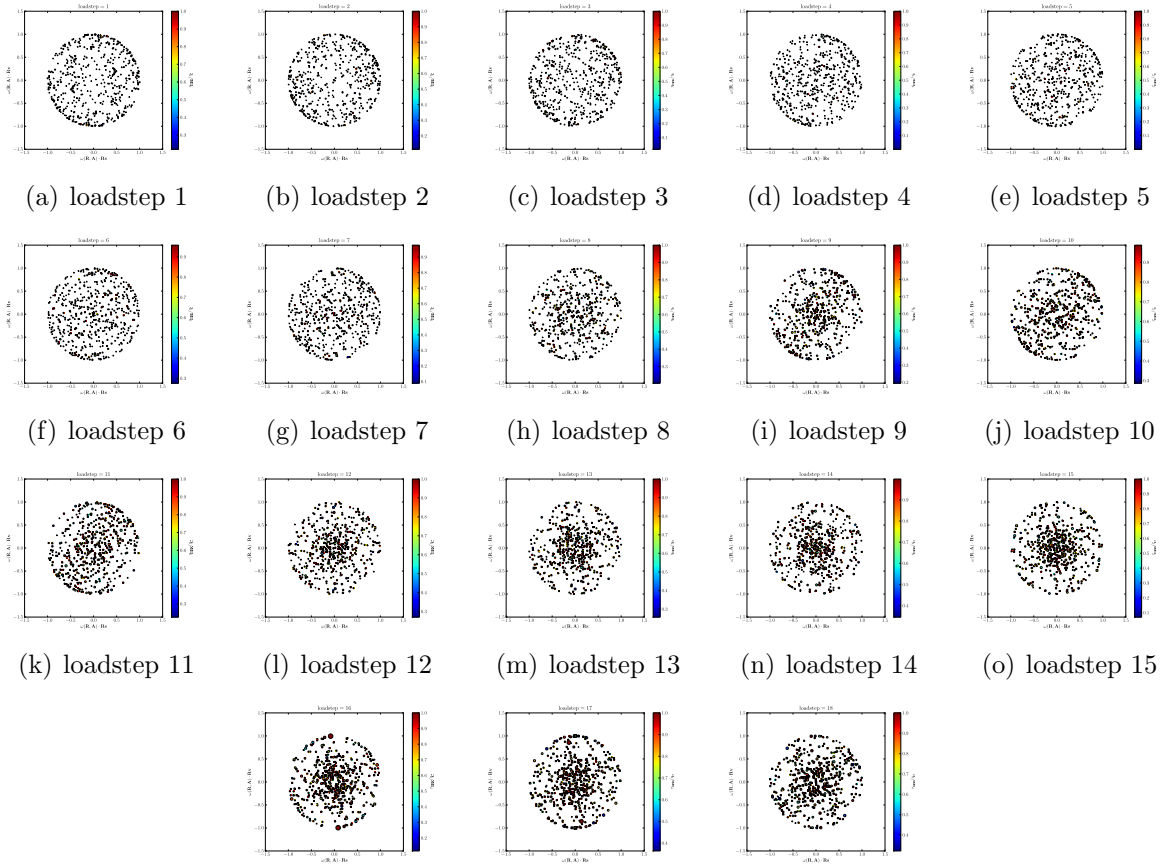

(a) loadstep 1 (b) loadstep 2 (c) loadstep 3 (d) loadstep 4 (e) loadstep 5

(f) loadstep 6 (g) loadstep 7 (h) loadstep 8 (i) loadstep 9 (j) loadstep 10

(k) loadstep 11 (l) loadstep 12 (m) loadstep 13 (n) loadstep 14 (o) loadstep 15

(p) loadstep 16 (q) loadstep 17 (r) loadstep 18

Figure 3.51: $\hat{\boldsymbol{\omega}}$ axes projected on to a prismatic visualization direction. Location of the data points indicates the projection of $\hat{\boldsymbol{\omega}}$ on the selected basis. The size of the data points indicates the magnitude of misorientation, $\|\boldsymbol{\omega}\|$. The misorientation axes cluster around the c-axis of the unit cell, indicating a history of prismatic slip.

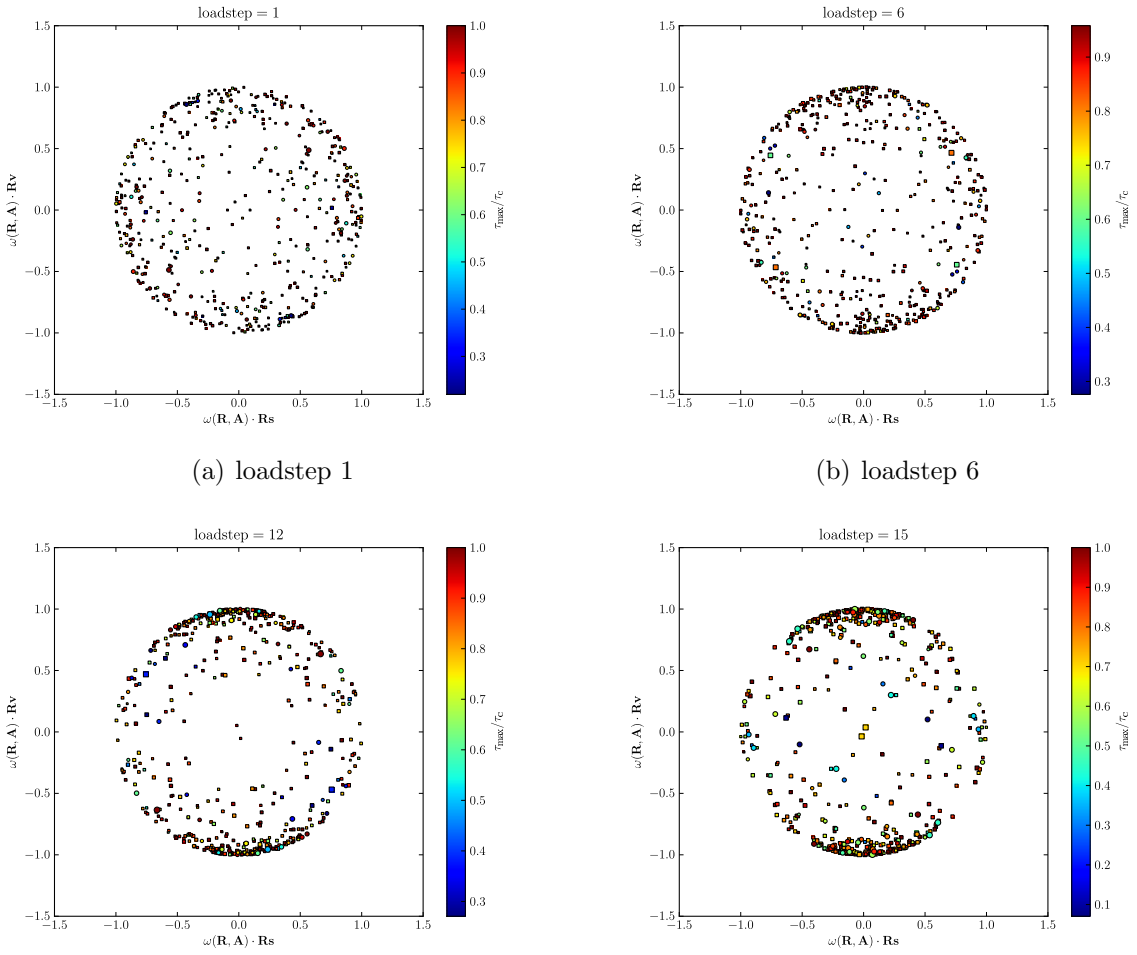

(a) loadstep 1

(b) loadstep 6

(c) loadstep 12

(d) loadstep 15

Figure 3.52: $\hat{\boldsymbol{\omega}}$ axes projected on to a basal visualization direction. Location of the data points indicates the projection of $\hat{\boldsymbol{\omega}}$ on the selected basis. The size of the data points indicates the magnitude of misorientation, $\|\boldsymbol{\omega}\|$. The misorientation axes cluster around the c-axis of the unit cell, indicating a history of prismatic slip.

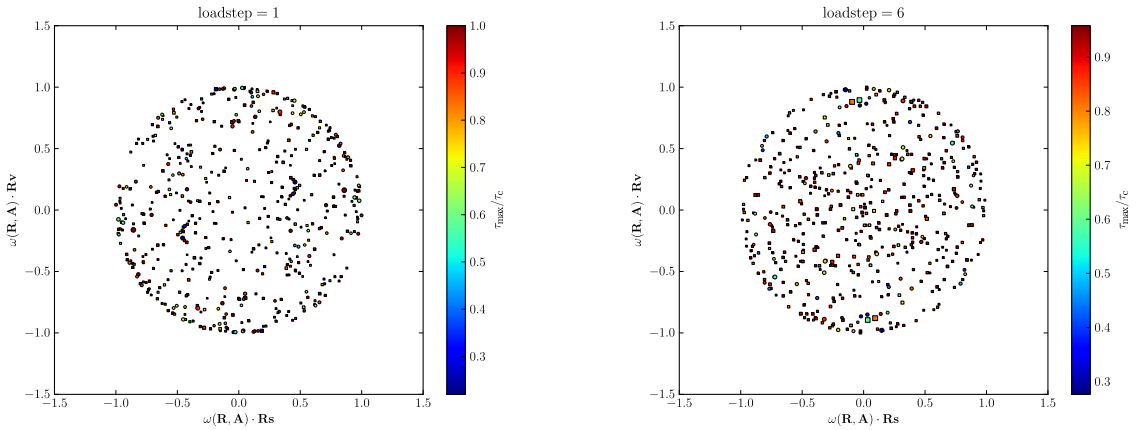

(a) loadstep 1

(b) loadstep 6

(c) loadstep 12

(d) loadstep 15

Figure 3.53: $\hat{\boldsymbol{\omega}}$ axes projected on to a prismatic visualization direction. Location of the data points indicates the projection of $\hat{\boldsymbol{\omega}}$ on the selected basis. The size of the data points indicates the magnitude of misorientation, $\|\boldsymbol{\omega}\|$. The misorientation axes cluster around the c-axis of the unit cell, indicating a history of prismatic slip.

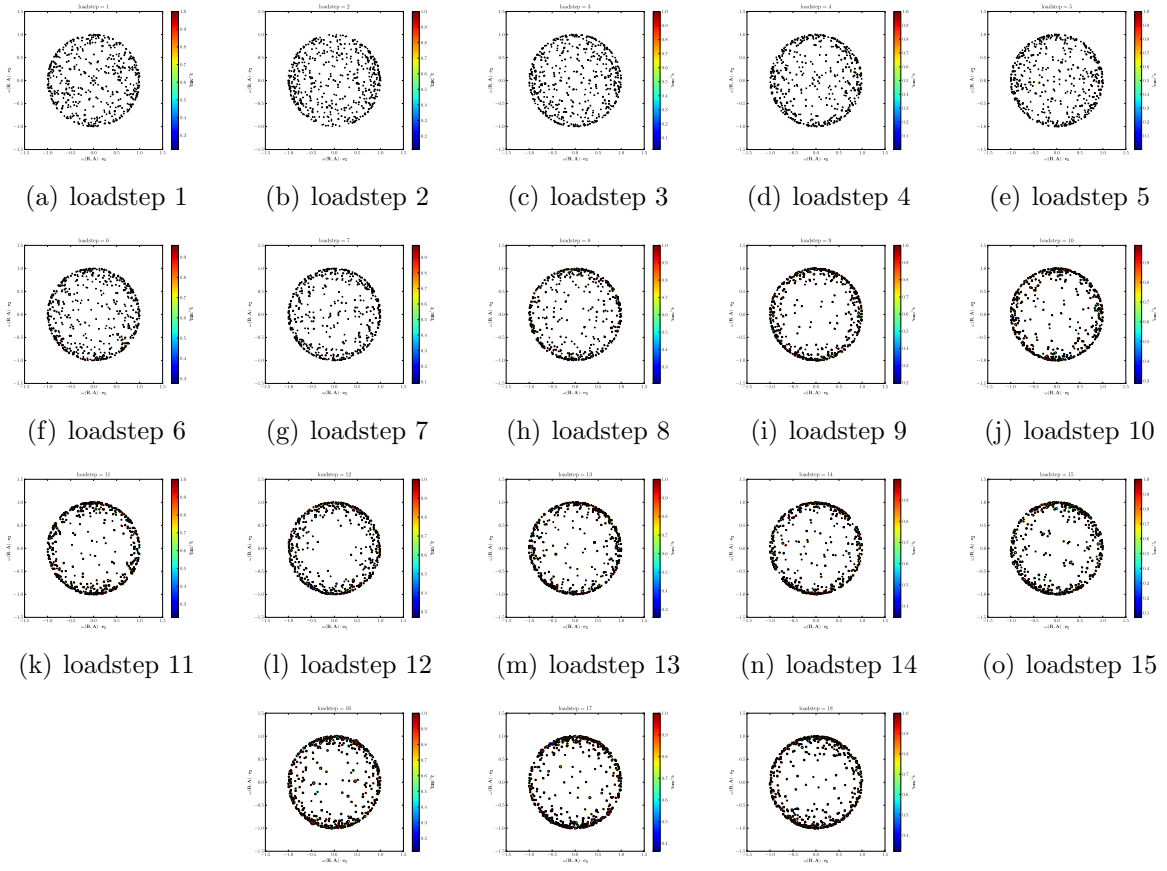

(a) loadstep 1 (b) loadstep 2 (c) loadstep 3 (d) loadstep 4 (e) loadstep 5

(f) loadstep 6 (g) loadstep 7 (h) loadstep 8 (i) loadstep 9 (j) loadstep 10

(k) loadstep 11 (l) loadstep 12 (m) loadstep 13 (n) loadstep 14 (o) loadstep 15

(p) loadstep 16 (q) loadstep 17 (r) loadstep 18

Figure 3.54: $\hat{\boldsymbol{\omega}}$ axes projected on to the fixed lab frame. The view is looking down on the polycrystal from the load axis, $\mathbf{e}_2$. The size of the data points indicates the magnitude of misorientation, $\|\boldsymbol{\omega}\|$.

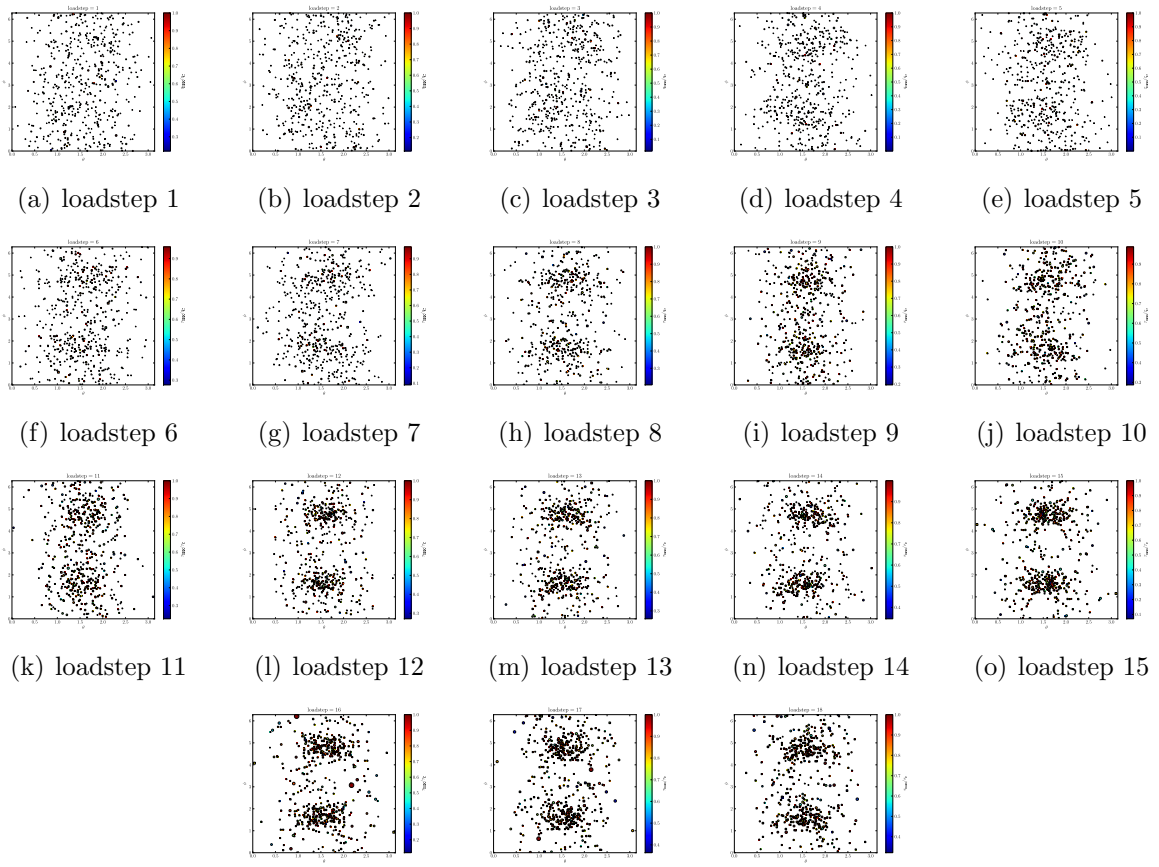

(a) loadstep 1 (b) loadstep 2 (c) loadstep 3 (d) loadstep 4 (e) loadstep 5

(f) loadstep 6 (g) loadstep 7 (h) loadstep 8 (i) loadstep 9 (j) loadstep 10

(k) loadstep 11 (l) loadstep 12 (m) loadstep 13 (n) loadstep 14 (o) loadstep 15

(p) loadstep 16 (q) loadstep 17 (r) loadstep 18

Figure 3.55: $\hat{\boldsymbol{\omega}}$ axes visualized on spherical polar coordinates. The north pole $\beta = 0$ is in the basal plane. Location of the data points indicates the α, β coordinates of the unit vector according to (A.1). The size of the data points indicates the magnitude of misorientation, $\|\boldsymbol{\omega}\|$. The misorientation axes cluster around the c-axis, indicating a history of prismatic slip.

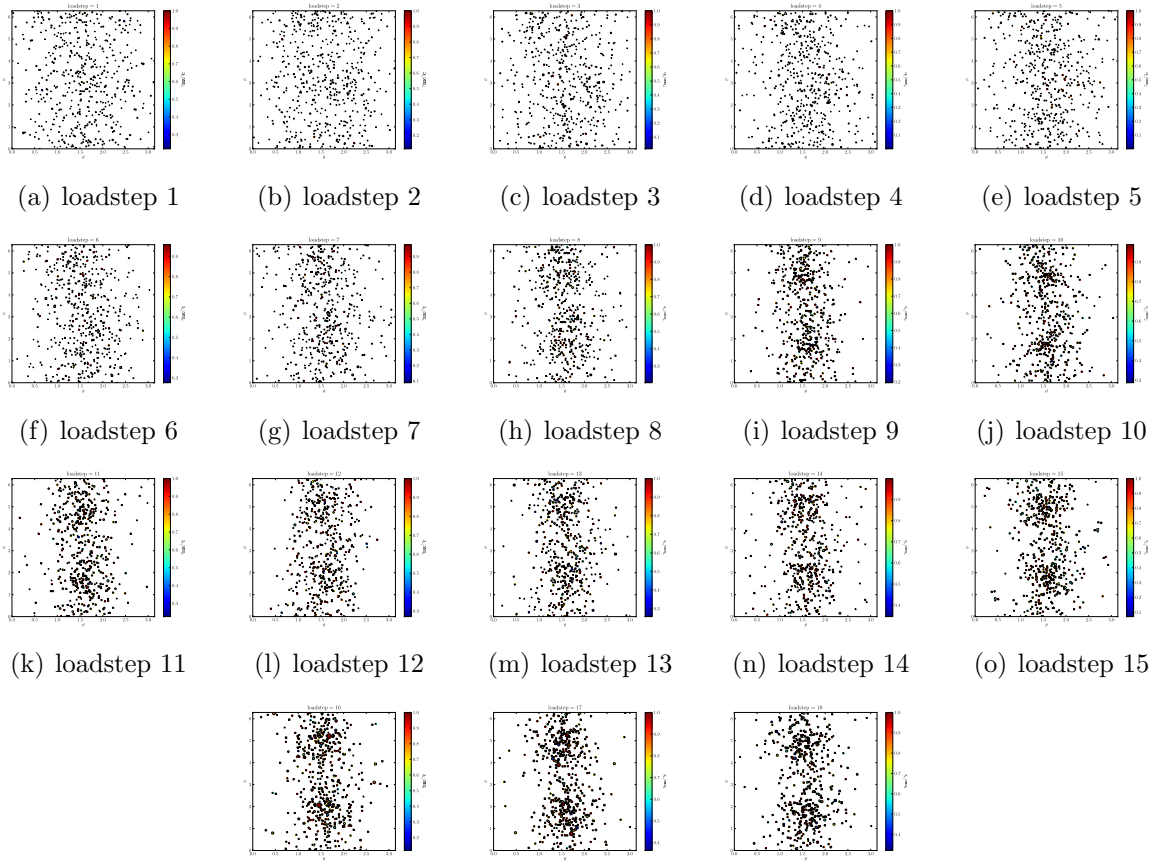

(a) loadstep 1 (b) loadstep 2 (c) loadstep 3 (d) loadstep 4 (e) loadstep 5

(f) loadstep 6 (g) loadstep 7 (h) loadstep 8 (i) loadstep 9 (j) loadstep 10

(k) loadstep 11 (l) loadstep 12 (m) loadstep 13 (n) loadstep 14 (o) loadstep 15

(p) loadstep 16 (q) loadstep 17 (r) loadstep 18

Figure 3.56: $\hat{\boldsymbol{\omega}}$ axes visualized on spherical polar coordinates based on the fixed lab frame, with north pole $\mathbf{e}_2$. Location of the data points indicates the α, β coordinates of the unit vector according to (A.1). The size of the data points indicates the magnitude of misorientation, $\|\boldsymbol{\omega}\|$. The misorientation axes cluster at the equator at $\beta = \pi/2$.

3.4.2.2.8 Discussion We now discuss a few aspects from the results of the forward simulation technique. The intragranular misorientation direction was able to be obtained using the standard tools of the far field detector. Figures 3.48 - Figure 3.56 indicate that this modeling leads to the reporting of anisotropic intragranular texture development in single grains. This anisotropy was derived from a model which does not impose the effect of slip systems a priori, as done in Barabash et al. (2002). With assumptions about the relationship between spatial inhomogeneity in the amount of slip, we found prismatic slip to be indicated in the data. In §3.5 the activity of prismatic systems is suggested from a complementary computation based on resolved shear stresses. Therefore this modeling approach has been successful in adding to the possible data one may obtain from the far field high energy X-ray techniques.

Now we give observations of areas the technique could be improved. The last three images in the full frames of Figures 3.48 - Figure 3.56 tend to lose a clear indication of anisotropy in the the intragranular texture. Comparing this to Figure 3.31 indicates that the ability of the technique to accurately capture intragranular misorientation reaches a peak at about 2% strain. Note that isotropic broadening is monotonic as indicated by the increasing size of the data points in the figures, but the clear indication of anisotropy begins to get lost. This may be for several reasons. First, as plastic deformation commences, the local diffraction peaks can become multimodal, as the grains divide into discrete subdomains. The formulation of the residuals in (3.300), (3.301) or the overall choice of a gradient solution method for the objective function may not be optimal. One particular peak may get fit preferentially in the algorithm due to a the gradient algorithm being unable to get to a global optimum intensity distribution. A global optimization technique may be useful to investigate in further studies. Secondly, the pixels of the detector can get easily saturated without careful control of the intensity. At the later load steps, many local diffraction peaks are completely saturated, therefore all details of the anisotropic nature of the local peaks is lost. It is difficult for the objective function used here to retain anisotropy in the intragranular estimate if all the reflections saturate their pixels.

The latter point brings up another suggested improvement to the experimental technique. In Figure 3.34 we noted the changing brightness of the diffraction images, due to true changes in the experimental configuration of the incident beam. These changes in the intensity alter the numerical values of $\mathbf{A}$, at least isotropically. The intensity recorded at each load increment was not available in the data; therefore in future tests independent measurements of the incident intensity would be useful for investigation of the forward model.

As noted previously, the computational cost of the approach is expensive relative to the grain averaged modeling in §3.4.2.1. The coding used python's multiprocessing module to take advantage of multiple cores. On a quad-core processor, a single forward modeling least squares refinement can take 20 minutes with 12 quadrature points per dimension in (3.323). This compares with the grain averaged refinement time of 30 seconds. Algorithmic optimizations have not been deeply investigated. Addressing this can surely reduce the computational cost greatly, although using a global optimization technique mentioned earlier

in this discussion would more likely add to the cost. This underscores that this modeling approach is not meant for rapid processing of the data, but for the extra mining of information contained in the fundamental experiments at the synchrotron.

3.4.2.2.9 Summary. The results of the forward modeling method described in this paper are positive. We developed a model to predict the integrated energy at individual pixels on the detector which was sensitive to lattice deformation and microstructural effects. We reduced this forward modeling problem to the determination of a volume distribution $g(\mathbf{H})$ which represents the projection of spatial inhomogeneity $\pi_{\mathbf{H}}$ into $\mathbf{H}$-space. We applied the model to X-ray data from a continuously loaded polycrystalline titanium alloy. In this application we considered a reduced degree of freedom expression for the volume distribution $g(\mathbf{H})$, over the orientation subspace $\mathbf{H}(\boldsymbol{\theta}) = \mathbf{R}(\boldsymbol{\theta})\mathbf{U}$. We investigated the effect of the number of quadrature points taken in the forward model, and demonstrated the ability to capture estimates of intragranular misorientation. This misorientation was related to intrinsic aspects of the single crystal: that prismatic slip is the dominant plastic deformation mechanism. This outcome is notable because we did not require a separate experimental methodology, such as the independent use of high resolution detectors to obtain this information. These additional measurements would ideally be used to validate the far-field method of analysis. For the time being, however, the standard far field technique appears to suffice.

Overall, this method exhibits greater data utilization than the approach taken in §3.4.2.1, at the cost of increased computational time. However, this is not much of a detractor, since synchrotron experiments such as the one generating this data may be mined for years after the initial experiment. This modeling technique enables researchers to have one more tool of analysis at their disposal, increasing the profitability of executing such experiments.

3.4.3 Conclusion

This concludes the discussion of methods for the estimation of direct kinematic parameters from high energy X-ray diffraction experiments. The sought after parameters described in this section include the lattice deformation $\mathbf{H}$ and the intragranular texture deformation $\mathbf{A}$. The term kinematic is used in recognition of the fact that these quantities are obtained from geometric properties of the lattice of the crystal, and are independent of constitutive relations.

We gave a general background overview of weighted least squares based parameter estimation, including uncertainty analysis. We then described two novel modeling approaches for X-ray diffraction data.

The grain averaged approach was an efficient method for incorporating uncertainty in the location of a diffraction peak to uncertainty in the overall lattice deformation estimate $\mathbf{H}$. The uncertainty in the strain of $5 - 20\%$ is greater than uncertainties from a method such as a standard resistance strain gauge, which has a relative uncertainty of $< 5\%$. Being able

to quantify these uncertainties in the lattice strain estimates is crucially important when considering constitutive parameter determination.

The forward modeling approach allowed the extraction of intragranular texture information from the single crystal. Based on a reduced degree-of-freedom assumption for the texture function, diffraction peaks are forward modeled. Then these simulated intensity distributions can be directly compared to pixel intensity data on the detector. This forms the basis for a least squares based estimation of a projection of the spatial distribution of lattice deformation into a subspace of $\mathrm{GL}(3,\mathbb{R}) \times \mathbb{R}$ (the volume distribution $g(\mathbf{H})$). This projection, essentially an indication of spatial inhomogeneity, was shown to exhibit microstructural information such as the history of plastic deformation according to crystal plasticity theory. In application to an experiment, it revealed a history of prismatic slip to be indicated in a continuously loaded titanium polycrystal. Additionally, this projection was constructed to be frame invariant, so that it can serve as a constitutive variable in potential granular based models of polycrystals.

In the next section, the kinematic data obtained by the methods described here is used in conjunction with the model of elastic-plastic deformation developed in Chapter 2 to estimate single crystal constitutive parameters from a polycrystal. Most literature publications have used the high energy technique for discovery-type research. Therefore the ability of the method to obtain equally important constitutive information has not been widely demonstrated. The capability to use these X-ray techniques to extract constitutive parameters would be a boon to studies of complicated materials where single crystal constitutive parameters are poorly quantified. The fact that this method can be applied to a polycrystal only increases the potential payoff of this line of experimentation.

3.5 Constitutive parameter extraction

Experiments play two primary roles in research. The first role is of providing fundamental discoveries of material behavior. The second role is closing the gap between theoretical models and applications by measuring constitutive functions requested by the theory. The determination of constitutive functions is particularly crucial for phenomenological continuum mechanics, where any underlying physics present at, say, the discrete atomic level is smeared out and replaced by phenomenological continuous functions. In certain cases the phenomenological functions can be estimated from physical models. However, generally a phenomenological approach is most useful when the physics are poorly understood, so direct experimentation is required in these cases.

It is unfortunate that the accepted state of affairs in the modern research community so greatly decouples theory from experimental investigation. That is, a combined presentation of theory with experimental validation is exceedingly rare to find in the modern literature. As noted several times in this thesis, continuum plasticity in particular is plagued with a lack of experimental techniques which can measure the constitutive parameters which are requested by the theory. The X-ray diffraction measurements in the present study suggest a possible way forward to providing constitutive information and a validation mechanism for certain theories of plasticity.

In this section we will assess the ability of synchrotron X-ray experiments to extract single crystal properties from polycrystalline materials. This was noted as a case of interest in the introduction to this chapter, since polycrystalline materials are more readily available than large single crystals for many alloys. The methods for this end goal are relatively wide open for investigation. Without a standard methodology in place, we discuss two proposed approaches.

First, we take the point of view that each grain in the polycrystal represents an independent measurement of the single crystal material properties. We track the evolving deformation in each grain throughout the loading process, and use the evolving state of lattice deformation to deduce plastic properties. For example, the concept of a yield surface can be appealed to to suppose that the strain energy of the grain remains roughly constant over a strain increment. Then the state of strain or stress in the grain represents an experimental observation of a point on the yield surface. In a second method, we use the X-ray diffraction data to generate a simulated microstructure using a grain seeding algorithm similar to that in §2.4.2.1.1. With this simulated microstructure, we can use a numerical method to predict the deformations at each macroscopic load-step. Then the numerical results can be used to refine single crystal material parameters to match the experimental estimates.

We begin by trying to extract the yield function parameters from the continuously loaded titanium alloy, initially described in §3.4.2.2.6.

3.5.1 Phenomenological constitutive analysis of continuous load scan

In this section we consider the extraction of constitutive parameters from the continuous load scan experiment presented in §3.4.2.2.6. To briefly summarize, this experiment consisted of the *in situ* measurement of lattice deformation during an uniaxial tension test. Total axial material strain and axial stress were measured by the external load frame. The total strain applied to the material was $\tilde{2}\%$. HEDM was applied to the material, and approximately 700 grains were present in the diffraction volume. The lattice strains, $\mathbf{H}$, in each of the grains were tracked throughout the deformation using X-ray diffraction scans, 18 full diffraction scans of the polycrystal were taken during the straining process. The grain averaged fitting techniques of §3.4.2.1 were used to obtain this estimate for $\mathbf{H}$.

The task of this section is to use the kinematic data, $\mathbf{H}$, in combination with the phenomenological plasticity theory developed in Chapter 2 to extract constitutive parameters. The continuous loading experiment was not executed with this end result in mind, however the attempt is worthwhile to describe.

The uncertainty associated with the estimates for $\mathbf{H}$ was presented in §3.4.2.1, with precision uncertainty on strain between $5 - 20\%$. It is not clear if this level of precision will be acceptable in yielding meaningful constitutive parameters. However obtaining even order of magnitude estimates for the parameters is a useful outcome. For the phenomenological theory of plasticity in particular, the lack of numerical constitutive parameters is glaring (Papadopoulos and Lu, 2001). In any case this attempt represents a first trial at extracting phenomenological parameters from polycrystalline bulk materials, using the high energy X-ray technique; so future experiments can be designed with the findings of this section in mind.

3.5.1.1 Overview of method

The methodology used in this section is to track the lattice deformations in each of the individual single crystal grains throughout the deformation. Based on criteria from the macroscopic change in deformation measured from the load frame, these lattice deformations may be assigned to be either representative of yielding or not. The list of all such yielding grains constitutes the input data for a least squares refinement to determine the yield function. We now describe this in more specific details. The concept of 'the set of grains determined to be yielding' is cumbersome to refer to so we formulate the problem in mathematical terms.

For the load step j, denote the data of this j^{th} scan by

$$F^j = \{\mathbf{H}_{(i)} : i = 1, 2, ..., N_{\text{grains}}\}^j,$$

where N_{grains} is the number of grains in the diffraction volume. The dataset of all lattice

deformations in each grain, denoted D, is written as

$$D = \{F^j : j = 1, 2, ..., N_{\text{meas}}\}, \tag{3.337}$$

where N_{meas} is the number of measurement scans taken during the loading. To be clear, in the continuous load scan, we had $N_{\text{grains}} \approx 700$ and $N_{\text{meas}} = 18$. It is possible that grains may not be found for certain load steps. Therefore to simplify the data analysis we only use grains which were tracked throughout the entire deformation. Enumerate the set of observed grains. The index into the full grain list is given by

$$I = \bigcap_{j=1}^{N_{\text{meas}}} \{i : \mathbf{H}_{(i)} \in F^j\}. \tag{3.338}$$

Using this the final data set is expressed by

$$D = \{\{\mathbf{H}_{(i)} : i \in I\}^j : j = 1, 2, ..., N_{\text{meas}}\}. \tag{3.339}$$

Next, assume that we have the single crystal elastic moduli, $\mathcal{C}$. Then we can obtain elastic stress in the i^{th} grain from the constitutive equation

$$\mathbf{S}_{(i)} = \mathcal{C}[\mathbf{E}_{(i)}], \tag{3.340}$$

where $\mathbf{E}_{(i)} = 1/2(\mathbf{H}_{(i)}^{\mathrm{T}}\mathbf{H}_{(i)} - \mathbf{I})$, (no sum on i). $\mathbf{S}_{(i)}$ is the symmetric Piola Kirchoff stress for the i^{th} grain. For a non hardening material we must have

$$y(\mathbf{S}; \boldsymbol{\Theta}) = 0. \tag{3.341}$$

where $y : \mathbb{R}^n \to \mathbb{R}^+$ is the yield function, n is the number of integrity basis elements in the polynomial constitutive function, and $\boldsymbol{\Theta}$ represent the model parameters, see Chapter 2 and §3.4. For example, the yield function (2.190) has $\boldsymbol{\Theta} = b_{ij}^y, c_i^y$.

Applied to experimental data, (3.341) must hold, within experimental error, when the i^{th} grain is in a state of yield. Let

$$Y = \{\mathbf{H} \in \bigcap D : \mathbf{H} \implies \text{yield}\} \tag{3.342}$$

be the set of grains at yield from the full data list. We will describe how we identify these yield points shortly. Then, using the data in Y refine the material parameters $\boldsymbol{\Theta}$ in $y(\mathbf{S}; \boldsymbol{\Theta})$ to satisfy (3.341). In terms of least squares objective functions, §3.4.1, we have

$$\Phi(\boldsymbol{\Theta}) = \sum_i^N [y(\mathbf{S}_{\hat{Y}(i)})]^2, \tag{3.343}$$

where $\hat{Y} : \mathbb{N} \to Y$ is the enumeration map for Y.

Yield point identification The identification of yield points to construct Y is an important matter do discuss. The experimental observation of yield is challenging to investigate experimentally. The sheet metal community is a good example of pursuing yield function determination. In these experiments, yield points are found by cutting elements from the sheet metal and testing them in uniaxial extension. The traditionally defined offset yield stress is then recorded as the yield stress in that direction in the plane sheet. Here, we cannot use anything like this, since we are looking for single crystal data from polycrystalline behavior. We cannot, for example, use the macroscopic yield point of the polycrystal to inform the local single crystal behavior. To identify yield points, we use the basic phenomenological observation as exploited in §2.2.2: that during plastic flow the elastic state stays roughly the same while the total material deforms. There may be slight lattice reorientation, but within some tolerance the elastic stress or strain stays on a constant yield surface in stress or strain space.

With this in mind, we looked at points where the strain energy at sequential load steps was roughly equivalent, to within a preassigned tolerance. That is

$$|W^i_{(j)} - W^{i+1}_{(j)}| < \text{tol}, \tag{3.344}$$

where $W^i_{(j)} = (1/2)\mathbf{S}^i_{(j)} \cdot \mathbf{E}^i_{(j)}$ is the strain energy at the i^{th} load step for the j^{th} grain and $\text{tol} > 0$ is the tolerance. Monitoring all points in the polycrystal where this was the case defined the input data, Y (3.342), for the objective function (3.343).

There are a few final remarks regarding the yield function. In order for a non zero stress to satisfy the functional definition (3.341), the yield function is written as

$$y(\mathbf{S}; \boldsymbol{\Theta}, y_{\max}) = y'(\mathbf{S}; \boldsymbol{\Theta}) - y_{\max}, \tag{3.345}$$

where $y_{\max} \in \mathbb{R}^+$. In the eventual application of the least squares optimization, we follow the methodology in §2.4.1.2 by scaling the yield offset parameter $y_{\max}$ to approximate strengths in uniaxial tension. Therefore to the objective function (3.343) we add the residual equation

$$r_i = y_{\max} - \frac{1}{3}(T_y)^2, \tag{3.346}$$

where T_y is obtained from the macroscopic stress strain curve, and is a constant. This parameter scaling is motivated by J_2 theory, as described in §2.4.1.2. The objective function is written

$$\Phi(\boldsymbol{\Theta}, y_{\max}) = \sum_i^N [V_i y(\mathbf{S}_{\hat{Y}(i)}; \boldsymbol{\Theta}, y_{\max})]^2 + w[y_{\max} - \frac{1}{3}(T_y)^2]^2, \tag{3.347}$$

where V_i is the volume of the grain, and w is a weight factor we can adjust to enforce the scaling property. The volume weighting is added to favor contributions to the residual from larger grains, as previous analysis found that on average smaller grains tend to be more prone

to scatter. Upon execution of the least squares algorithm to obtain $\nabla\Phi = 0$, the material parameters $\boldsymbol{\Theta}, y_{\max}$ are obtained, see Equation (3.244).

To take the analysis a step further, in the theory presented in Chapter 2, the constitutive parameters for the yield function are also of relevance to the flow function,

$$\mathbf{K}^{-1}\dot{\mathbf{K}} = -\lambda\frac{\partial y}{\partial \mathbf{S}} + \boldsymbol{\Omega}. \tag{3.348}$$

So that

$$\text{sym } \mathbf{K}^{-1}\dot{\mathbf{K}} \cong \frac{\partial y}{\partial \mathbf{S}}, \tag{3.349}$$

since $\boldsymbol{\Omega} \in$ skw. Therefore, the parameters obtained from the yield function assignment should compared favorably to measuring some of the parameters based on (3.349). It is interesting to see how compatible the parameter estimates from the yield function alone, using (3.347) will be compared to similar estimates based on the flow function.

The local plastic flow cannot be directly measured; however total material deformation can in principle be measured. In the current experiment, we do not have an ideal way to estimate this, however we can make some assumptions and see where they lead. During the continuous load scan, the total material deformation was recorded with a bonded resistance strain gage fixed to the material. In the next paragraph we show how we can use this to obtain a macroscopic estimate of the local material deformation, $\mathbf{F}$. Since we have grain level measurements of $\mathbf{H}$, we can then obtain experimental estimates of $\mathbf{K}$ from the relation

$$\mathbf{K} = \mathbf{F}^{-1}\mathbf{H}. \tag{3.350}$$

We now work out how we accomplish this.[8]

Flow function estimate. In order to estimate yield parameters based on (3.348),(3.349), we require a measurement of the direct evolution of $\mathbf{K} = \mathbf{F}^{-1}\mathbf{H}$, where $\mathbf{H}$ is given by the X-ray diffraction experiment. From the strain gage bonded to the macroscopic polycrystalline sample, we can obtain the axial material extension and stress. A reasonable deduction is that we assume that the material deformation is given by the symmetric stretching gradient

$$\mathbf{F} = \lambda_1\mathbf{e}_1 \otimes \mathbf{e}_1 + \lambda_2\mathbf{e}_2 \otimes \mathbf{e}_2 + \lambda_3\mathbf{e}_3 \otimes \mathbf{e}_3. \tag{3.351}$$

We might suppose that for plastic loading we could write

$$\mathbf{F} = \lambda\mathbf{e}_2 \otimes \mathbf{e}_2 + \frac{1}{\sqrt{\lambda}}\mathbf{e}_1 \otimes \mathbf{e}_1 + \frac{1}{\sqrt{\lambda}}\mathbf{e}_3 \otimes \mathbf{e}_3, \tag{3.352}$$

[8] As noted several times, full field digital image correlation would be better served for the task of determining local measurements of $\mathbf{F}$ at the same length scale as the X-ray diffraction. The following is clearly not the ideal methodology for this task, but it is what we have to work with.

and use λ directly the axial material strain measurement. However, due to the elastic volume change this is not strictly correct. But since we have macroscopic plasticity, Figure 3.31, we can also not use purely elastic, Hookean kinematics to obtain the total deformation from the axial stress.

The solution is to first recognize that the macroscopic polycrystalline body can be considered isotropic, with two elastic parameters E, ν the modulus and Poisson ratio. Then, note the decomposition

$$\mathbf{F} = \mathbf{F}^{\mathrm{p}}\mathbf{F}^{\mathrm{e}}. \tag{3.353}$$

This multiplicative decomposition has a much different meaning than the decomposition in §2.2.1. It conveys the classical decomposition, where $\mathbf{F}^{\mathrm{e}}$ is the strain resulting from unloading, and $\mathbf{F}^{\mathrm{p}}$ remains after the load is removed. In (3.353) $\mathbf{F}^{\mathrm{e}}$ is therefore the component of the deformation gradient due to elastic effects, e.g. from the strain obtained from Hooke's law,

$$\varepsilon^{\mathrm{e}}_{ij} = \frac{1}{2\mu}\sigma_{ij} - \frac{\lambda}{2\mu(2\mu+3\lambda)}\sigma_{kk}\delta_{ij}, \tag{3.354}$$

where λ, μ are the Lame coefficients and $\sigma = \mathrm{diag}(0, \sigma_{22}, 0)$, with σ_{22} reported from the load frame. Then basic kinematics gives

$$\mathbf{F}^{\mathrm{e}} = \mathbf{U}^{\mathrm{e}} = \sqrt{\mathbf{C}^{\mathrm{e}}} = \sqrt{2\boldsymbol{\varepsilon}^{\mathrm{e}} + \mathbf{I}}, \tag{3.355}$$

with $\mathbf{U}^{\mathrm{e}}$ the symmetric part of the polar decomposition of $\mathbf{F}^{\mathrm{e}}$, $\mathbf{C}^{\mathrm{e}} \equiv (\mathbf{U}^{\mathrm{e}})^2$, and $\boldsymbol{\varepsilon}$ is the infinitesimal elastic strain, with components given by (3.354). Since the macroscopic shear stresses are zero, we have

$$\begin{array}{lll} F^{\mathrm{e}}_{11} = \sqrt{2\varepsilon^{\mathrm{e}}_{11}+1} & F^{\mathrm{e}}_{22} = \sqrt{2\varepsilon^{\mathrm{e}}_{22}+1} & F^{\mathrm{e}}_{33} = \sqrt{2\varepsilon^{\mathrm{e}}_{33}+1} \\ F^{\mathrm{e}}_{23} = 0 & F^{\mathrm{e}}_{13} = 0 & F^{\mathrm{e}}_{12} = 0 \end{array}, \tag{3.356}$$

with $\varepsilon^{\mathrm{e}}_{ij}$ given by (3.354) with $\sigma = \mathrm{diag}(0, \sigma_{22}, 0)$. Next, $\mathbf{F}^{\mathrm{p}}$ is restricted by imposing the isochoric plastic flow condition, $\dot{J}_{\mathbf{F}^{\mathrm{p}}} = 0$ for plastic deformation, where $J_{\mathbf{F}^{\mathrm{p}}} = \det \mathbf{F}^{\mathrm{p}}$. The plastic deformation must then be of the form

$$\mathbf{F}^{\mathrm{p}} = \lambda^{\mathrm{p}}_2 \mathbf{e}_2 \otimes \mathbf{e}_2 + \frac{1}{\sqrt{\lambda^{\mathrm{p}}_2}}(\mathbf{e}_1 \otimes \mathbf{e}_1 + \mathbf{e}_3 \otimes \mathbf{e}_3), \tag{3.357}$$

where λ^{p}_2 is the plastic axial stretch.

Summary: estimate for $\mathbf{F}$. We now have enough ingredients to estimate $\mathbf{F}$ locally. For clarity we summarize the procedure. Both $\varepsilon_{22}, \sigma_{22}$, are experimentally measured, from strain gage and load frame. We compute the elastic strain, $\varepsilon^{\mathrm{e}}_{22}$ from applying the stress state $\sigma = \mathrm{diag}(0, \sigma_{22}, 0)$ in isotropic Hooke's law, (3.354). The elastic axial stretch is then given from the elastic strain by $\lambda^{\mathrm{e}}_2 = \sqrt{2\hat{\varepsilon}^{\mathrm{e}}_{22}(\sigma_{ij}) + 1}$. Next, the total material axial stretch is obtained from the total material strain gage measurement, giving

$$\lambda_2 = \sqrt{2e_{22}+1}. \tag{3.358}$$

Then the plastic stretch is obtained from using (3.357) in (3.353). With (3.358) this gives

$$\mathbf{F} = \mathbf{F}^{\mathrm{p}}\mathbf{F}^{\mathrm{e}} \implies \lambda_2 = \lambda_2^{\mathrm{p}}\lambda_2^{\mathrm{e}}, \tag{3.359}$$

giving the plastic stretch in terms of the elastic stretch and material stretch as $\lambda_2^{\mathrm{p}} = \lambda_2/\lambda_2^{\mathrm{e}}$. By the isochoric construction of (3.357), prescribing λ_2^{p} completely specifies $\mathbf{F}^{\mathrm{p}}$, hence $\mathbf{F}$ is completely determined through (3.353). For example, in a similar fashion to the $\mathbf{e}_2$ direction, considering the $\mathbf{e}_1$ direction we obtain λ_1^{e} from the isotropic Hooke's law (3.354) and (3.358), and use $\mathbf{F}_{11} = \mathbf{F}_{11}^{\mathrm{p}}\mathbf{F}_{11}^{\mathrm{e}}$ to solve for $\mathbf{F}_{11}$. This analysis works due to the diagonal structure of the matrix representations of $\mathbf{F}, \mathbf{F}^{\mathrm{e}}, \mathbf{F}^{\mathrm{p}}$. In this way we can estimate $\mathbf{F}(\lambda, E, \nu)$ when only the far field stress σ_{22} and strain ε_{22} are known. □

After obtaining the local estimate for $\mathbf{F}$, we can then compute $\mathbf{K}$ with $\mathbf{F}$ and the local diffraction measurement of $\mathbf{H}$. Then the plastic evolution $\mathbf{K}^{-1}\dot{\mathbf{K}}$ is measured from one load point to the next through

$$\mathbf{K}^{-1}\dot{\mathbf{K}}^{j}_{(i)} \approx (\mathbf{K}^{j}_{(i)})^{-1}(\mathbf{K}^{j}_{(i)} - \mathbf{K}^{j-1}_{(i)})/\Delta t, \tag{3.360}$$

where the indices $j, j-1$ denote the estimate for $\mathbf{K}_{(i)}$ from (3.350) at the $j, j-1$ load step, and where Δt is the time interval. This is related to the yield function through (3.349), where the difference between the right and left hand side comes from the scalar Lagrange multiplier λ in the flow rule (3.348). The true solution of λ requires the full integration of the flow equations, which are not feasible to solve. Furthermore the time scale between experimental observations ($\approx$ 3 minutes) is clearly of a different nature than would be computed in a numerical simulation. Therefore using this technique to obtain yield function parameters will only give an estimate of the ratios of the parameters, and not absolute numerical values. It is still informative to compare these estimates with the direct yield function estimate.

The objective function formed to estimate the flow/yield parameters is given by

$$\Phi(\boldsymbol{\Theta}) = \sum_{j}^{N_{\mathrm{grains}}} \sum_{i}^{N_{\mathrm{steps}}} V_i \left[\left\{ (\mathrm{sym}\ \ \mathbf{K}^{-1}\dot{\mathbf{K}})_i \right\}^j - \left. \frac{\partial y}{\partial \mathbf{S}} \right|_{\mathbf{S}_i} \right]^2, \tag{3.361}$$

where N_{grains} is the number of grains in the data set and N_{steps} is the number of data points taken during the continuous loading. We could attempt to more closely represent the flow rule by considering

$$\Phi(\boldsymbol{\Theta}, k) = \sum_{j}^{N_{\mathrm{grains}}} \sum_{i}^{N_{\mathrm{steps}}} V_i \left[\left\{ (\mathrm{sym}\ \ \mathbf{K}^{-1}\dot{\mathbf{K}})_i \right\}^j - k \left. \frac{\partial y}{\partial \mathbf{S}} \right|_{\mathbf{S}_i} \right]^2, \tag{3.362}$$

and optimize over $\boldsymbol{\Theta}, k$. The motivation for (3.362) would be that for the reasonably constant strain rate used in the test the plastic flow multiplier would be constant. However we get no better results from this formulation since the least squares optimization only finds where $\nabla\Phi = \mathbf{0}$ and independently varying scalar multipliers will not affect the algorithm.

Summary. In this introduction we have described the general methodology used to extract phenomenological constitutive parameters from high energy X-ray measurements of a polycrystal. The parameters we are after are the material parameters in the yield function, (3.341). We perform the parameter estimation in two ways, (1) identifying grains which appear to be in a state of plastic flow, collecting all such states of lattice strain in a large least squares objective function, and solving for the optimal parameters $\boldsymbol{\Theta}^*$, and (2): using the macroscopic stress and strain measurements to obtain estimates of the material deformation $\mathbf{F}$, and applying this deformation at the local level with the XRD measurements of $\mathbf{H}$ to enable the computation of $\mathbf{K}$. The symmetric part of the flow rule (3.348) is related to the yield function through the $\mathbf{S}$-derivatives, (3.349). These are different methods of revealing the same material parameters so results should be related to one another for consistency.

We now attempt to apply the framework to data. We will use the continuous load scan data described in §3.4.2.2.6, which was a titanium alloy. We must first develop the constitutive equations for the yield function for the dihexagonal-dipyramidal point group, characterizing this material. See Chapter 2 for other examples of constitutive function generation according to the phenomenological theory.

3.5.1.2 Constitutive equations for titanium

In this section we develop the constitutive equations for the yield function for titanium (HCP). Following the methodology in Green and Adkins (1970), we require the representation for a scalar valued function of a single symmetric tensor argument,

$$F(\mathbf{A}) = F(\mathbf{Q}\mathbf{A}\mathbf{Q}^{\mathrm{T}}), \tag{3.363}$$

where $\mathbf{Q} \in g_\kappa$, and g_κ is the symmetry group for the material. The symmetry elements in the dihexagonal-dipyramidal group are (Green and Adkins, 1970)

$$\begin{array}{l}\mathbf{I}, \mathbf{S}_1, \mathbf{S}_2, \mathbf{C}, \mathbf{C}\mathbf{S}_1, \mathbf{C}\mathbf{S}_2, \mathbf{R}_1, \mathbf{R}_1\mathbf{S}_1, \mathbf{R}_1\mathbf{S}_2, \mathbf{R}_2, \mathbf{R}_2\mathbf{S}_1, \mathbf{R}_2\mathbf{S}_2, \mathbf{R}_3, \mathbf{R}_3\mathbf{S}_1, \mathbf{R}_3\mathbf{S}_2, \\ \mathbf{D}_1, \mathbf{D}_1\mathbf{S}_1, \mathbf{D}_1\mathbf{S}_2, \mathbf{D}_2, \mathbf{D}_2\mathbf{S}_1, \mathbf{D}_2\mathbf{S}_2, \mathbf{D}_3, \mathbf{D}_3\mathbf{S}_1, \mathbf{D}_3\mathbf{S}_2\end{array} \tag{3.364}$$

where $\mathbf{S}_{1,2}$ are rotations of $2\pi/3$ about the c-axis of the unit cell, and all other rotation elements are defined after (2.140). As in §2.3.3.1 we desire a yield function of quadratic order in its argument, the stress or strain. This symmetric tensor argument is denoted by $\mathbf{A}$. The hexagonal structure is extremely difficult to generate constitutive functions for using the method applied in §2.3.3.1. However for a single symmetric tensor argument, things are more tractable; see Green and Adkins (1970, p. 24). The integrity basis for this polynomial is

$$\begin{array}{ll} x_1 = A_{11} + A_{22} & y_1 = A_{11}A_{22} - A_{12}^2 \\ x_2 = A_{33} & y_2 = A_{13}^2 + A_{23}^2, \end{array} \tag{3.365}$$

with polynomial expansion

$$F(\mathbf{A}) = \sum_{i=1}^{2}\sum_{j=1}^{2} b_{ij}x_i x_j + \sum_{i=1}^{2} c_i y_i, \tag{3.366}$$

with the symmetries $b_{ij} = b_{ji}$, for a total of 5 constants. Therefore $\mathbf{\Theta} = b_{11}, b_{12}, b_{22}, c_1, c_2$ in (3.341). We provide some visualizations of the yield surfaces obtained from (3.366) later in this section. For now, we can point out some qualitative observations of the integrity basis, motivated by information from slip planes in the HCP crystal. A few of the invariants in (3.366) have a useful interpretation. Recall that the c-axis of the crystal is aligned with $\mathbf{e}_3$ in the basis construction of (3.366). The basis element $A_{11}A_{22} - A_{12}^2$ represents the distortion energy in the basal plane. Consider the two dimensional basal stress tensor

$$\mathbf{S} = \begin{bmatrix} S_{11} & S_{12} \\ S_{12} & S_{22} \end{bmatrix}. \tag{3.367}$$

Then $I_2(\mathbf{S}) = S_{11}S_{22} - S_{12}^2$. This invariant is familiar to plasticity: the second invariant of the stress is the distortion energy in plasticity of isotropic materials. Based on the geometry of the unit cell, $\mathbf{e}_1, \mathbf{e}_2$ represent the basis for prismatic slip activity. We can therefore deduce that prismatic slip will be largely influenced by the material parameter c_1. Similarly, the terms S_{13}, S_{23} represent resolved shear stresses on the basal system. Therefore basal slip will be largely influenced by the parameter c_2. The influence of the pyramidal system will be evident in both material parameters.

The yield function must satisfy a few additional properties besides material symmetry. The maximum dissipation postulate requires the yield function to be convex, which is not guaranteed by the polynomial (3.366). (Barlat et al., 2005; Soare and Barlat, 2010) and related references constitute a segment of the literature interested in constructing convex yield function for sheet metals. For the simple form assumed in (3.366), convexity can be checked by computing the eigenvalues of the Hessian

$$J_{ijkl} = \frac{\partial^2 F}{\partial A_{ij} \partial A_{kl}}, \tag{3.368}$$

which will be constants due to the quadratic form for (3.366). To be convex, the eigenvalues of J must be non-negative, as required in Rockafellar (1972, Thm 4.5). The eigenvalues of the Voigt matrix obtained from (3.368) are solved using Mathematica. They are

$$\begin{aligned} \lambda_1 = -2c_1 \qquad \lambda_2 = -c_1 \\ \lambda_3 = \tfrac{1}{2}\left(4b_{11} + 2b_{22} + c_1 - \sqrt{16b_{11}^2 + 32b_{12}^2 + 8b_{11}\left(-2b_{22} + c_1\right) + \left(-2b_{22} + c_1\right)^2}\right) \\ \lambda_4 = \tfrac{1}{2}\left(4b_{11} + 2b_{22} + c_1 + \sqrt{16b_{11}^2 + 32b_{12}^2 + 8b_{11}\left(-2b_{22} + c_1\right) + \left(-2b_{22} + c_1\right)^2}\right) \\ \lambda_5 = 2c_2 \qquad \lambda_6 = 2c_2. \end{aligned} \tag{3.369}$$

The non-negativity of the eigenvalues can be added as a constraint in the optimization algorithm. In the application to experiment we used unconstrained optimization and were able to obtain an acceptable convex solution.

The yield function may also be required to satisfy other properties. An additional consideration is that we'd like to have isochoric plastic flow. We now compute relations between the parameters (3.366) which satisfy this constraint. Recall the flow rule is written as

$$\mathbf{K}^{-1}\dot{\mathbf{K}} = -\lambda\frac{\partial y}{\partial \mathbf{S}} + \mathbf{\Omega}.$$

The plastic volumetric flow is given by tr $(\mathbf{K}^{-1}\dot{\mathbf{K}}) \cong$ tr $\partial y/\partial \mathbf{S}$. The $\mathbf{A}$-derivative of the yield function based on (3.366) in the flow rule has components

$$\begin{aligned}
\frac{\partial y}{\partial A_{11}} &= c_1 A_{22} + 2b_{11}\left(A_{11} + A_{22}\right) + 2b_{12}A_{33} \\
\frac{\partial y}{\partial A_{22}} &= c_1 A_{11} + 2b_{11}\left(A_{11} + A_{22}\right) + 2b_{12}A_{33} \\
\frac{\partial y}{\partial A_{33}} &= 2b_{12}\left(A_{11} + A_{22}\right) + 2b_{22}A_{33} \\
\frac{\partial y}{\partial A_{23}} &= 2c_2 A_{23} \\
\frac{\partial y}{\partial A_{13}} &= 2c_2 A_{13} \\
\frac{\partial y}{\partial A_{12}} &= -2c_1 A_{12}.
\end{aligned} \tag{3.370}$$

Calculating the trace of $\partial y/\partial \mathbf{A}$ gives

$$\mathrm{tr}\frac{\partial y}{\partial \mathbf{A}} = c_1\left(A_{11} + A_{22}\right) + 4b_{11}\left(A_{11} + A_{22}\right) + 2b_{22}A_{33} + 2b_{12}\left(A_{11} + A_{22} + 2A_{33}\right). \tag{3.371}$$

After some algebra we can rewrite this as

$$\mathrm{tr}\frac{\partial y}{\partial \mathbf{A}} = \left(c_1 + 4b_{11} + 2b_{12}\right)\left(A_{11} + A_{22} + 2A_{33}\right) + \left(b_{22} - 4b_{11} - c_1\right)2A_{33}. \tag{3.372}$$

Therefore, to enforce plastic incompressibility we have the constraint equations

$$\begin{aligned}
b_{22} - 4b_{11} - c_1 &= 0 \\
c_1 + 4b_{11} + 2b_{12} &= 0.
\end{aligned} \tag{3.373}$$

This completes the required constitutive development. We now summarize this section.

Summary of constitutive development. The yield function y for dihexagonal-dipyramidal symmetry is given by (3.366). The least squares objective function for the yield point identification method is given in (3.347), with $\mathbf{S}$ being given by the single crystal elastic moduli along with the grain averaged strain measured from X-ray diffraction. The model parameters to solve for are b_{11}, c_1, c_2, with b_{12}, b_{22} given by (3.373) in order to satisfy incompressible

plastic flow. The convexity of the yield function based on the constant yield parameters is checked after an unconstrained optimization procedure. If the final solution does not give a convex result, the constraints $\lambda_i \geq 0$ with eigenvalues λ_i given by (3.369) can be added and a constrained optimization method adopted.

The same material parameters for $y(\mathbf{S})$ enter into the symmetric part of the plastic flow, Equation (3.349). Therefore, in addition to the direct yield point identification a comparative optimization will be performed using the objective function (3.361). For this step no volume incompressibility will be enforced, since we are attempting to directly measure the plastic flow rate. Therefore all model parameters in the yield function (3.366) are free. As noted previously, we cannot obtain absolute values for the yield constants using the plastic flow relation (3.361). However we can obtain qualitative assessment of the compatibility between the parameters obtained from the yield point matching and the symmetric part of the flow. For instance, by comparing the relative ratios between parameters.

3.5.1.3 Results

In this section we give the results of the least squares optimization for the yield function parameters. The far field stress at the sampled steps are shown in Figure 3.31 and Figure 3.32. The single crystal moduli are taken from Kim et al. (2001, Table 1_1). It is possible that the results we obtain for the yield point identification method may differ depending on which segments of the full load process are taken to constitute the sets D in the least squares algorithms. For example, there may be some sections of the loading which carry a heavier weight compared to the overall data set. Additionally, the modest hardening present in the macroscopic stress strain curve, Figure 3.31, suggests that we'd like the flexibility to localize the optimizations somewhat in order to determine hardening trends. In recognition of these possibilities we examine the homogeneity of the fitting algorithms at different parts of the load, given different 'bands' of data from the load sequence. That is, we analyze subsets of the loading curve to obtain parameter estimates. This is a traveling window throughout the load test, as depicted in Figure 3.57. These bands will be called slices in the figures. A slice size n indicates that n sequential image frames were used to compile the initial data set D. The local slicing also lets us compute standard statistical information on the distribution of the collective estimates for the best fit parameters. Thus we get some observation of an uncertainty in the parameters, although this uncertainty does not include the local precision uncertainty based on the lattice strain estimates described in §3.4.2.1.

In Figure 3.58 and Figure 3.59 are the results for the yield point detection and flow function objective functions, for a slice interval of 3. The values for the yield function parameters $b_{11}, b_{12}, b_{22}, c_1, c_2$ are plotted on the vertical axis, the initial slice position is plotted on the horizontal axis.

In Figure 3.58 we see in aggregate a general monotonic increase in the parameter b_{22}, c_1 as hardening commences, and monotonic decrease for c_2. c_1 is the dominant parameter, which multiplies the factor $S_{11}S_{22} - S_{12}^2$. Later on, we will see that according to crystal plasticity

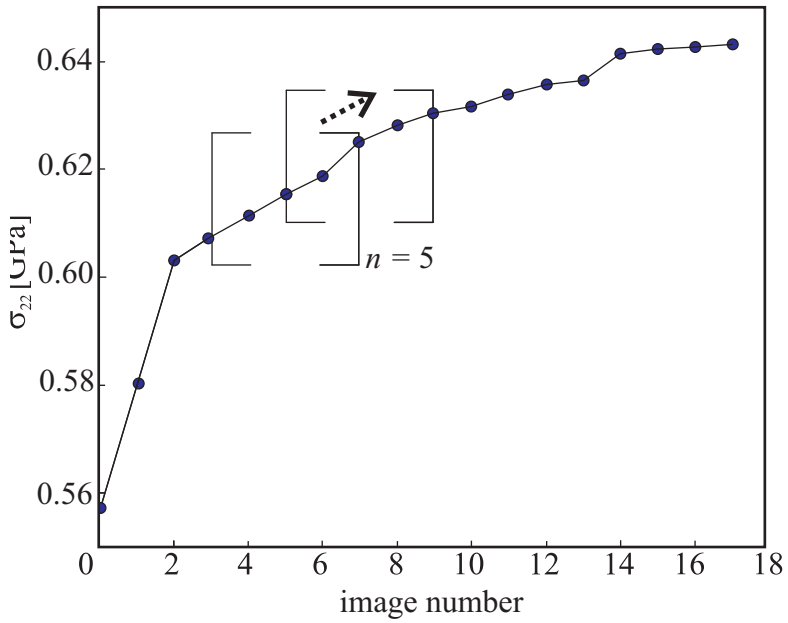

Figure 3.57: Depiction of the traveling window of data (3.342) used in the least squares refinement, such as (3.347). The data plot is the far field stress vs. diffraction image number, as in Figure 3.32.

theory, this experimental data indicates that the prismatic system is the most active. This is consistent with this integrity element being the most active due to its multiplication with S_{12}, the shear stress on prismatic planes. Figure 3.59 shows the parameters estimated from the flow function. As stated previously, this fitting is only used as a check against the yield point detection, and not for absolute parameter values since we cannot directly relate the two without integrating the full plastic evolution/boundary value problem. Qualitatively, the relative magnitude of parameters is in acceptable agreement with the data in Figure 3.58, given the large degree of assumptions that went into obtaining a local estimate for $\mathbf{K}^{-1}\dot{\mathbf{K}}$. That is, c_1 is the largest in magnitude, followed by c_2, etc. Furthermore, the numerical signs of the parameters agree with the yield point detection method. Finally, the averaged values over the entire load scan are presented in Table 3.7. Standard deviations are computed based on the local slice results.

Next, in Figure 3.60 and Figure 3.61 are plotted the results for the slice interval 5. The larger data increment smooths out the parameter estimates considerably from the slice size 3, yet still captures the monotonic trends present in Figure 3.58. The averaged numerical values are presented in Table 3.6. Relative magnitudes of the parameter estimates from the flow function method are again in agreement with the yield function detection method.

Finally, in Figure 3.62 and Figure 3.63 are shown the parameter estimates with a slice interval of 8. The parameter estimates are again smoother, but some of the monotonic

Table 3.5: Phenomenological parameters and standard deviations for yield point detection technique over the full load interval, for the slice size n =3

$\bar{b}_{11}$	$\sigma_{b_{11}}$	$\bar{b}_{12}$	$\sigma_{b_{12}}$	$\bar{b}_{22}$	$\sigma_{b_{22}}$	$\bar{c}_1$	σ_{c_1}	$\bar{c}_2$	σ_{c_2}	$\bar{y}_{\max}$ [GPa^2]
1.40	0.11	-0.25	0.13	0.50	0.25	-5.10	0.67	1.92	0.29	0.36

trend is filtered out by taking the larger set of data. Qualitative matching between the yield function and flow function is about the same as for the previous cases.

To analyze results for convexity, we take the parameters from the slice size 5 as representative. A check of the conditions (3.369) gives $\lambda_{1,2} > 0$ and $\lambda_{5,6} > 0$ automatically, and by calculation

$$\lambda_3 = 0.006, \lambda_4 = 1.26, \tag{3.374}$$

so that these parameters give a convex yield surface.

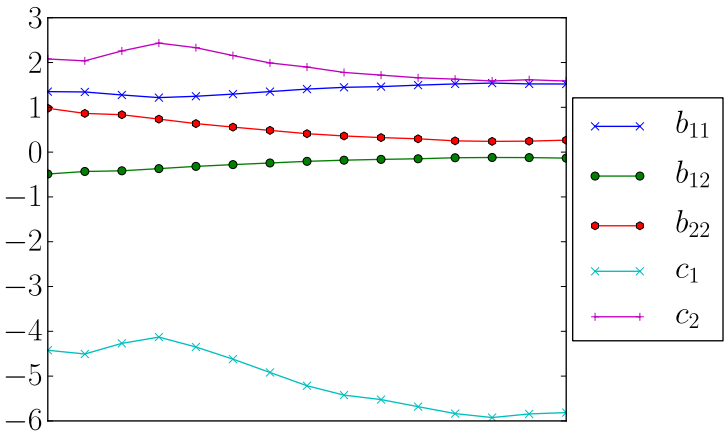

Figure 3.58: Best fit phenomenological parameters for the yield function for the Ti-7Al alloy, determined by the yield point detection technique. The load slice interval was equal to three. The monotonic trends on the parameters illustrate the hardening phenomenology as in Figure 3.31.

Visual comparison to crystal plasticity. Since crystal plasticity has been adopted by the community, the construction of yield surfaces for single crystals of the form (3.366) is

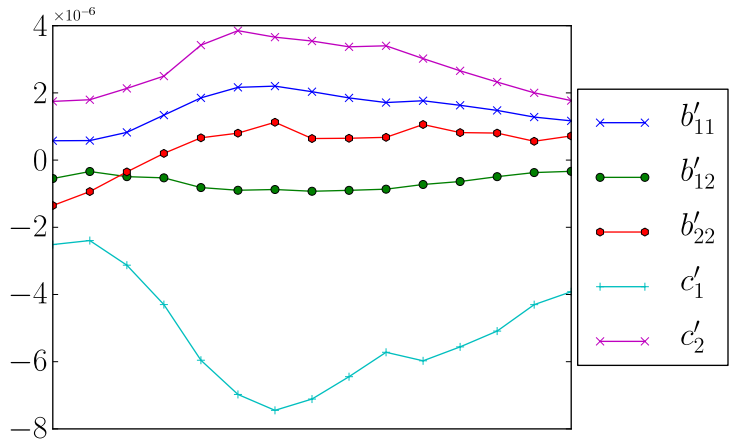

Figure 3.59: Best fit phenomenological parameters for the yield function for the Ti-7Al alloy, determined by the flow function technique. The load slice interval was equal to three. The relative values of the parameters agree with the yield point detection findings shown in Figure 3.58.

Table 3.6: Phenomenological parameters and standard deviations for yield point detection technique over the full load interval, for the slice size n =5

$\bar{b}_{11}$	$\sigma_{b_{11}}$	$\bar{b}_{12}$	$\sigma_{b_{12}}$	$\bar{b}_{22}$	$\sigma_{b_{22}}$	$\bar{c}_1$	σ_{c_1}	$\bar{c}_2$	σ_{c_2}	$\bar{y}_{\max}$ [GPa^2]
1.40	0.10	-0.23	0.10	0.47	0.20	-5.12	0.61	1.92	0.26	0.36

non-standard. Based on discussions with other researchers, it is of interest to compare the polynomial yield function with a crystal plasticity model on a visual basis.

To do this, we probe several two dimensional subspaces of $\mathbf{S}$-space and find the points $\mathbf{S}^*$ where $y(\mathbf{S}^*) = 0$. The crystal plasticity model analog to (3.366) is given by

$$y_{\text{cp}}(\mathbf{S}) = \max\left\{ \frac{|\mathbf{S}\cdot\mathbf{s}_i^j \otimes \mathbf{n}_i^j|}{(\tau_{\text{c}})_i^j} : i = 1,2,3; j = 1,2,...,N_{\text{c}}^i \right\} - 1, \tag{3.375}$$

where the index i corresponds to the slip system family, e.g. basal, prismatic, or pyramidal, and the index j corresponds to an enumeration of the slip system vectors $\mathbf{s}_j, \mathbf{n}_j$ for that particular slip system family. N_{c}^i is the number of slip systems and τ_{c}^i is the yield strength for the given slip system. Equation (3.375) could be written in the same fashion as (2.5), the double

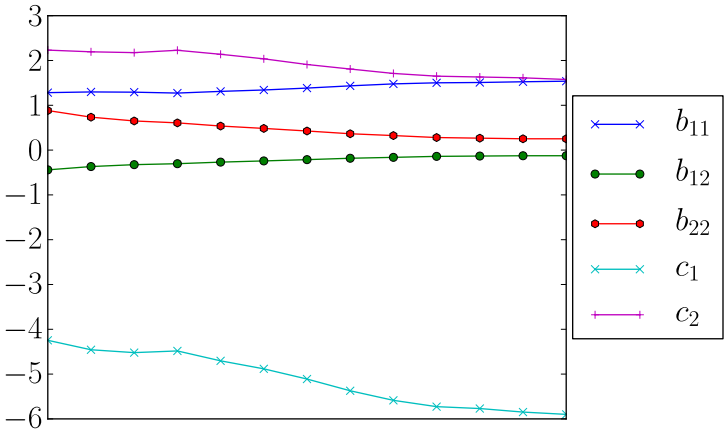

Figure 3.60: Best fit phenomenological parameters for the yield function for the Ti-7Al alloy, determined by the yield point detection technique. The load slice interval was equal to five. The monotonic trends on the parameters still illustrate the hardening phenomenology as in Figure 3.31.

Table 3.7: Phenomenological parameters and standard deviations for yield point detection technique over the full load interval, for the slice size n =8

$\bar{b}_{11}$	$\sigma_{b_{11}}$	$\bar{b}_{12}$	$\sigma_{b_{12}}$	$\bar{b}_{22}$	$\sigma_{b_{22}}$	$\bar{c}_1$	σ_{c_1}	$\bar{c}_2$	σ_{c_2}	$\bar{y}_{\max}$ [GPa^2]
1.40	0.08	-0.21	0.06	0.42	0.12	-5.19	0.43	1.88	0.18	0.36

summation simply highlights that the crystal plasticity inspired yield function is governed by three strengths, $\tau_c^i, i = 1, 2, 3$ for the basal, prismatic, and pyramidal systems. In the following figures we took $\tau_c^{\text{basal}} = 0.25$ GPa, $\tau_c^{\text{prismatic}} = 0.2$ GPa and $\tau_c^{\text{pyramidal}} = 0.55$ GPa; these values are motivated in the next section. The basal and prismatic strengths were informed from the experimental results in the next section. The pyramidal strength was informed from Barton and Dawson (2001), which lists a ratio of prismatic to pyramidal strength of 2/7. A ratio of prismatic to basal strength is given as 4/7, but since the experimental data gave a slightly different ratio we are not holding these values as strict relations.

We scanned the subspaces $(S_{11}, S_{12}), (S_{33}, S_{12}), (S_{13}, S_{23}), (S_{11}, S_{22})$ to plot the yield surfaces. For each subspace, all other stress components were set to zero. For example, for

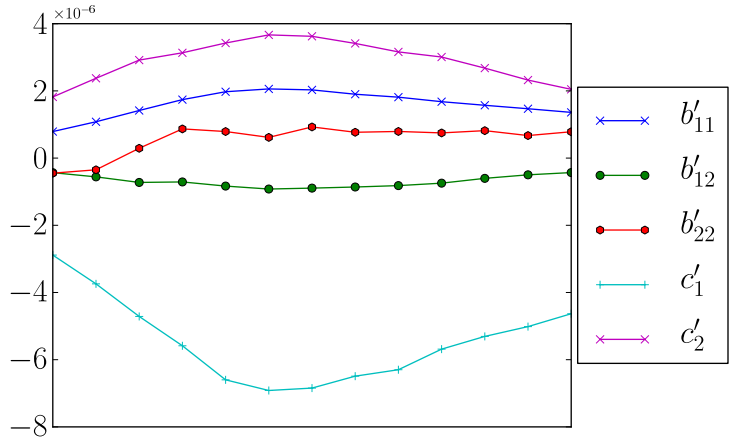

Figure 3.61: Best fit phenomenological parameters for the yield function for the Ti-7Al alloy, determined by the flow function technique. The load slice interval was equal to five. The relative values of the parameters agree with the yield point detection findings shown in Figure 3.60.

S_{11}, S_{12} the stress tensor was parametrized under one dimensional trajectories

$$\mathbf{S}(s) = \begin{bmatrix} S_{11}(s) & S_{12}(s) & 0 \\ S_{12}(s) & 0 & 0 \\ 0 & 0 & 0 \end{bmatrix}. \tag{3.376}$$

This was chosen as one among many ways to visualize the comparison between the crystal plasticity form and the polynomial. The resulting data is shown in Figure 3.64. In the figure, the polynomial fit seems to capture the general anisotropic shape of the crystal plasticity prediction, with smooth ellipses instead of facets. When placed on equal grounds, the crystal plasticity function effectively has many more material constants than the phenomenological model. While the phenomenological model has 5 constants, considering the slip system dyads $\mathbf{s}, \mathbf{n}$ to be the equivalent of 3 more constants each (two to specify a unit vector, $\mathbf{n}$, one additional to specify the unit vector orthonormal to $\mathbf{n}$), the crystal plasticity function has $18 \cdot 3 = 54$ constants from the slip dyads, plus 3 more from the τ_c^i. From this viewpoint, the polynomial function based on point group symmetry alone is appealing for further investigation.

In the next section, we use a similar method of tracking grain averaged strains, but use

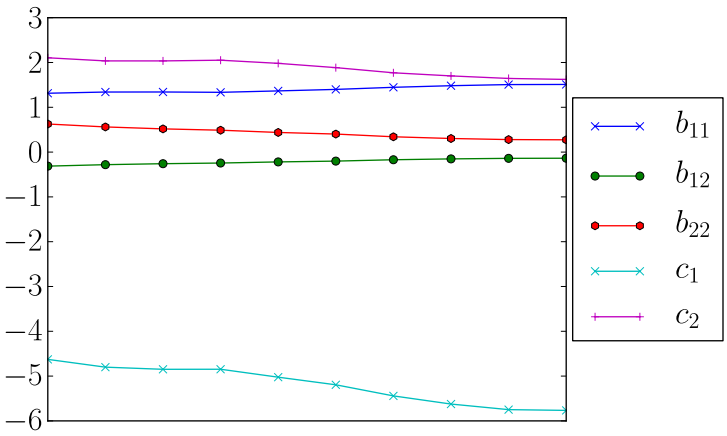

Figure 3.62: Best fit phenomenological parameters for the yield function for the Ti-7Al alloy, determined by the yield point detection technique. The load slice interval was equal to eight. The monotonic trends on the parameters don't capture the hardening phenomenology as well as the finer slice sizes.

crystal plasticity phenomenology. Restricting attention to grain averaged slip systems leads to a slightly different approach of obtaining yield parameters.

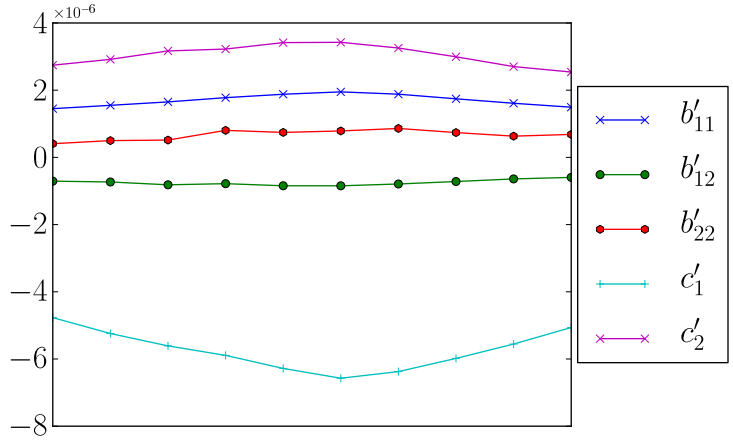

Figure 3.63: Best fit phenomenological parameters for the yield function for the Ti-7Al alloy, determined by the flow function technique. The load slice interval was equal to eight. The relative values of the parameters agree with the yield point detection findings shown in Figure 3.62.

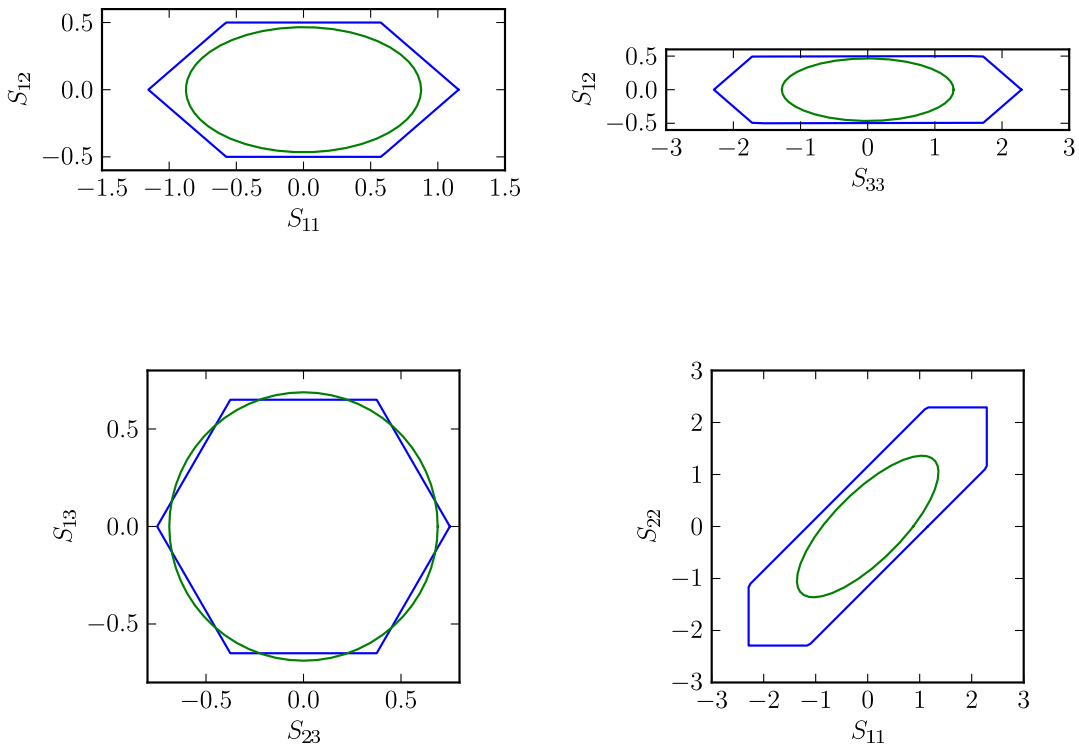

Figure 3.64: Comparison of crystal plasticity yield surface, (3.375) with polynomial fit based on experimental data.

3.5.2 Crystal plasticity constitutive analysis of continuous load scan

In this section we use the same continuous load scan data as in the previous section to determine constitutive parameters according to crystal plasticity theory. The continuous load experiment was described in §3.4.2.2.6. Recall that the crystal plasticity flow rule is of the form (2.5) and (3.5.2), rewritten here as

$$\dot{\mathbf{F}}^{\mathrm{p}} \left(\mathbf{F}^{\mathrm{p}}\right)^{-1} = \sum_{\alpha} \dot{\gamma}^{\alpha} \mathbf{m}_0^{\alpha} \otimes \mathbf{n}_0^{\alpha},$$

where the shear rate $\dot{\gamma}^{\alpha}$ is given by

$$\dot{\gamma}^{\alpha} = \dot{\gamma}_0 \left(\frac{|\tau^{\alpha}|}{s^{\alpha}} \right)^{1/m} \mathrm{sign}(\tau^{\alpha}),$$

where $\tau^{\alpha} = \mathbf{S} \cdot \mathbf{m}_0^{\alpha} \otimes \mathbf{n}_0^{\alpha}$ is the resolved shear stress on the slip system, s^{α} is the flow resistance for the slip system, $\dot{\gamma}_0$ represents a reference shear rate, and m is a rate sensitivity parameter. In the previous section, we use a yield point detection scheme to collect data points which were deemed to be in a state of yield. Then a least squares algorithm on the data set gave an estimate for the parameters in the constitutive equation for the yield function. In this section, the restricted form for yield in crystal plasticity leads to a different approach.

Plastic flow is governed by the parameter s^{α} in (3.5.2). That is for the α^{th} slip system, with associated dyad $\mathbf{m}_0^{\alpha} \otimes \mathbf{n}_0^{\alpha}$, compute the resolved shear stress $\tau^{\alpha} = \mathbf{S} \cdot \mathbf{m}_0^{\alpha} \otimes \mathbf{n}_0^{\alpha}$. Collecting all values for τ^{α}, for all grains in the crystal and all symmetrically equivalent slip systems and plotting on a histogram gives a visualization of the resolved stress magnitude on the slip system. If the resolved shear stress saturates, then this is an indirect observation that that slip system is active; hence the maximum resolved stress $\max\{\tau_i^{\alpha} : i = 1, 2, ..., N_{\mathrm{grains}} \cdot N_{\mathrm{steps}} \cdot N_{\mathrm{slipsys}}\}$ represents the experimental estimate for s^{α}. For the titanium alloy tested, there are three slip system families: prismatic, basal, and pyramidal. The prismatic system has three dyads, the basal also three, and 12 for the pyramidal system. The prismatic, basal, and pyramidal systems are illustrated in Figure 3.65.

We present these histograms in Figures 3.66, 3.67, 3.68. The prismatic projections are shown in Figure 3.66. The basal projections are shown in Figure 3.67. The pyramidal projections are shown in Figure 3.68. From Figure 3.66 we see a peak in the maximum histogram at approximately 200 MPa. From Figure 3.67 we see a peak in the maximum histogram at approximately 260 MPa. We do not see any saturation behavior in the pyramidal system, or do not have the resolution to pick up the saturation. These values are summarized in Table 3.8. It is noteworthy that according to the misorientation analysis of §3.4.2.2.6, the prismatic system was thought to be active based on the development of anisotropic texture in individual grains. That the prismatic slip system strength was observed to be weaker than the basal system is further verification of this finding.

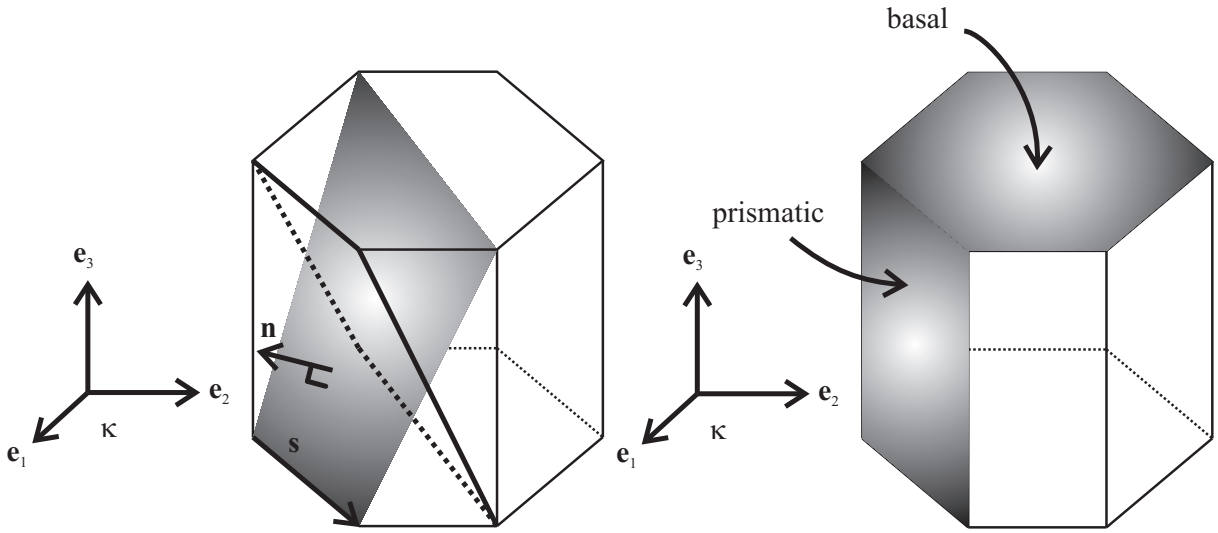

(a) Pyramidal slip plane geometry.

(b) Basal and prismatic slip planes.

Figure 3.65: Slip system geometry for titanium alloy. On the left, two slip systems are shown; there are a total of 12 slip systems in the pyramidal slip systems. Three representative slip systems from the basal and prismatic systems are also shown in Figure 3.47

Table 3.8: Estimated values for slip system strengths for HCP crystal. Uncertainties are estimated based on the spread in the histogram and uncertainty from §3.4.2.1

	Prismatic	Basal	Pyramidal
s^α	200 ± 30 MPa	260 ± 40 MPa	N/A

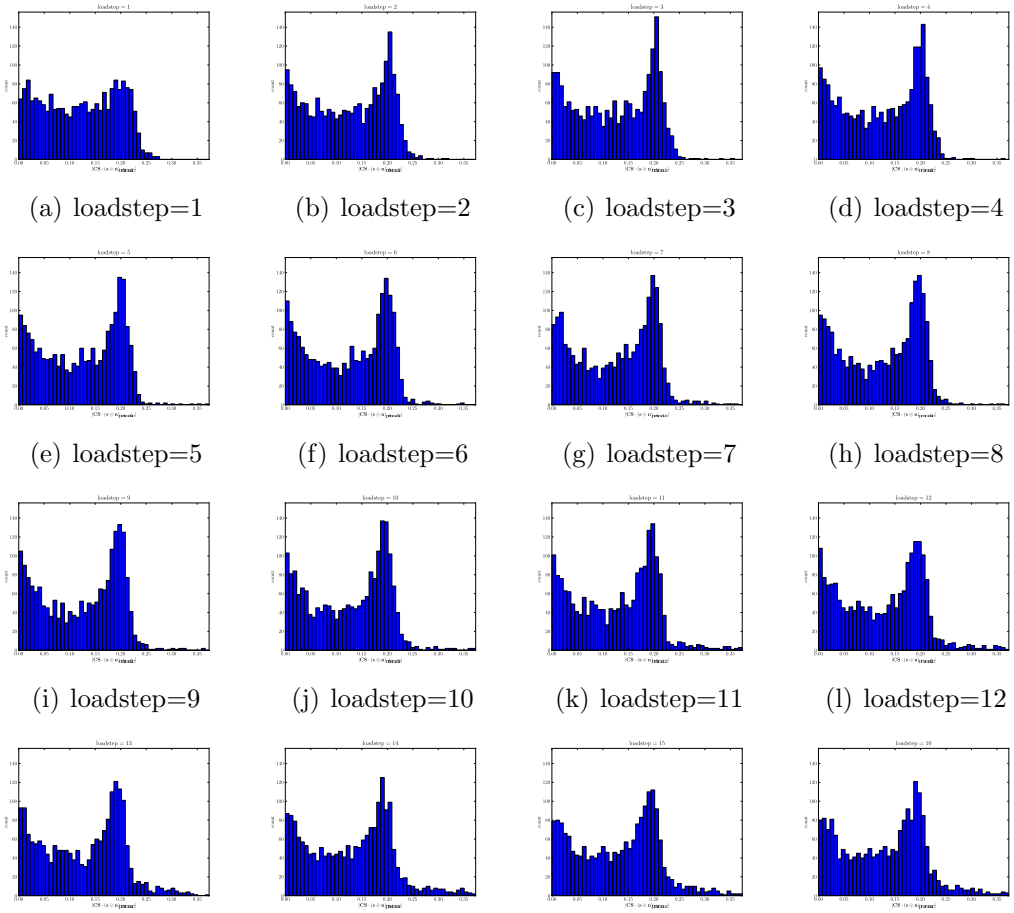

(a) loadstep=1 (b) loadstep=2 (c) loadstep=3 (d) loadstep=4

(e) loadstep=5 (f) loadstep=6 (g) loadstep=7 (h) loadstep=8

(i) loadstep=9 (j) loadstep=10 (k) loadstep=11 (l) loadstep=12

(m) loadstep=13 (n) loadstep=14 (o) loadstep=15 (p) loadstep=16

Figure 3.66: Resolved shear stresses $\tau^{\alpha} = \mathbf{S} \cdot \mathbf{s} \otimes \mathbf{n}$ for the (3) prismatic slip systems, collected for each grain in the polycrystal. Slip saturation at ≈ 200 MPa.

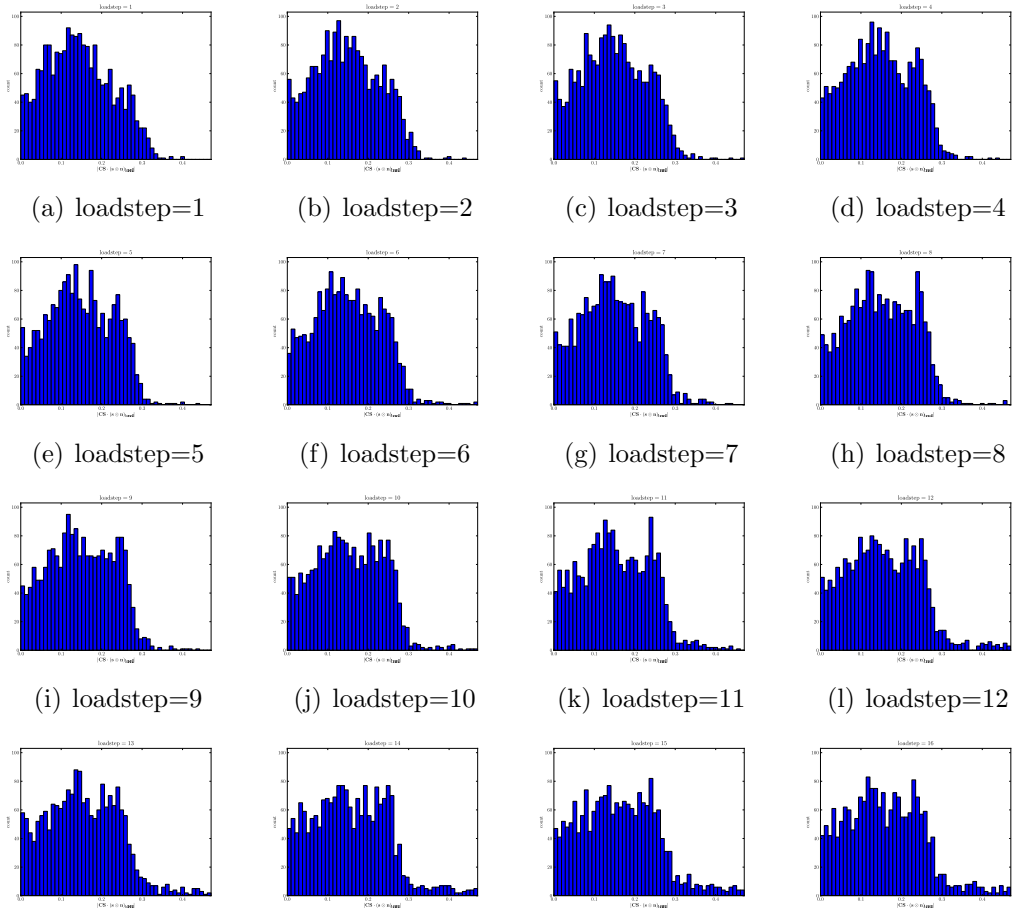

(a) loadstep=1 (b) loadstep=2 (c) loadstep=3 (d) loadstep=4

(e) loadstep=5 (f) loadstep=6 (g) loadstep=7 (h) loadstep=8

(i) loadstep=9 (j) loadstep=10 (k) loadstep=11 (l) loadstep=12

(m) loadstep=13 (n) loadstep=14 (o) loadstep=15 (p) loadstep=16

Figure 3.67: Resolved shear stresses $\tau^{\alpha} = \mathbf{S} \cdot \mathbf{s} \otimes \mathbf{n}$ for the (3) basal slip systems, collected for each grain in the polycrystal. Slip saturation at ≈ 250 MPa.

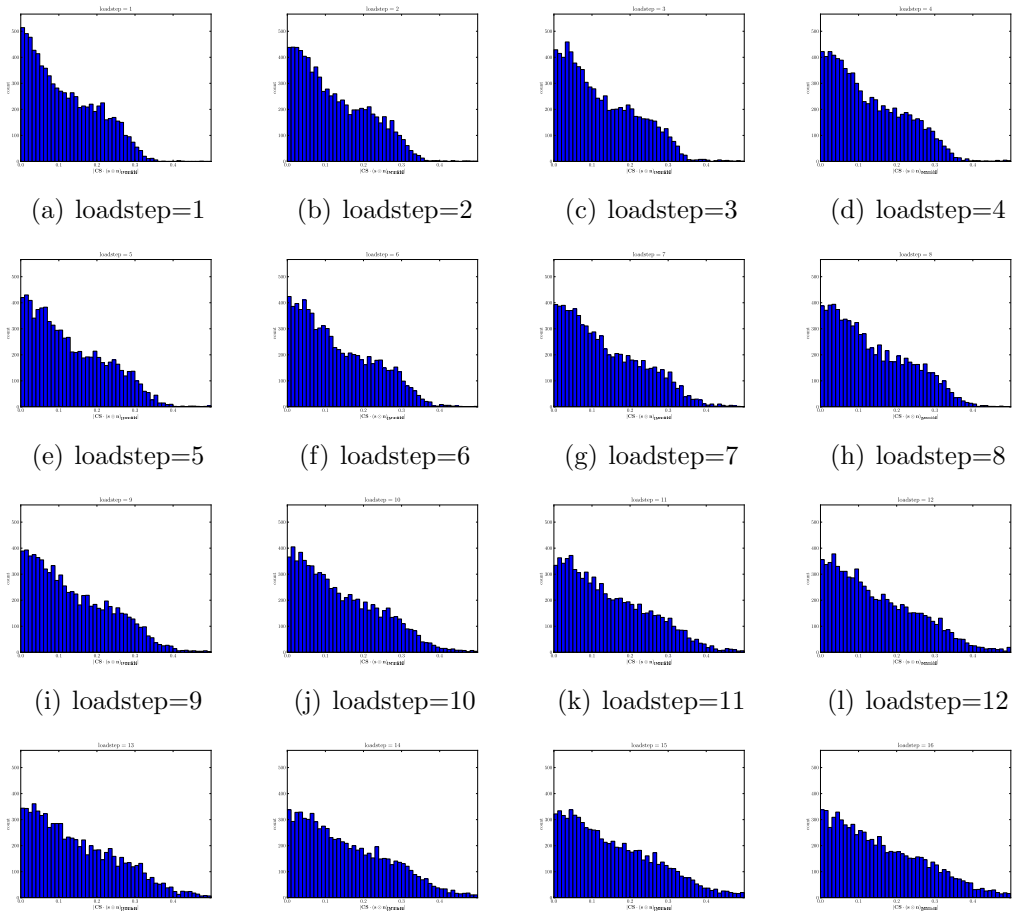

(a) loadstep=1 (b) loadstep=2 (c) loadstep=3 (d) loadstep=4

(e) loadstep=5 (f) loadstep=6 (g) loadstep=7 (h) loadstep=8

(i) loadstep=9 (j) loadstep=10 (k) loadstep=11 (l) loadstep=12

(m) loadstep=13 (n) loadstep=14 (o) loadstep=15 (p) loadstep=16

Figure 3.68: Resolved shear stresses $\tau^{\alpha} = \mathbf{S} \cdot \mathbf{s} \otimes \mathbf{n}$ for the (12) pyramidal slip systems, collected for each grain in the polycrystal. No slip saturation is observed.

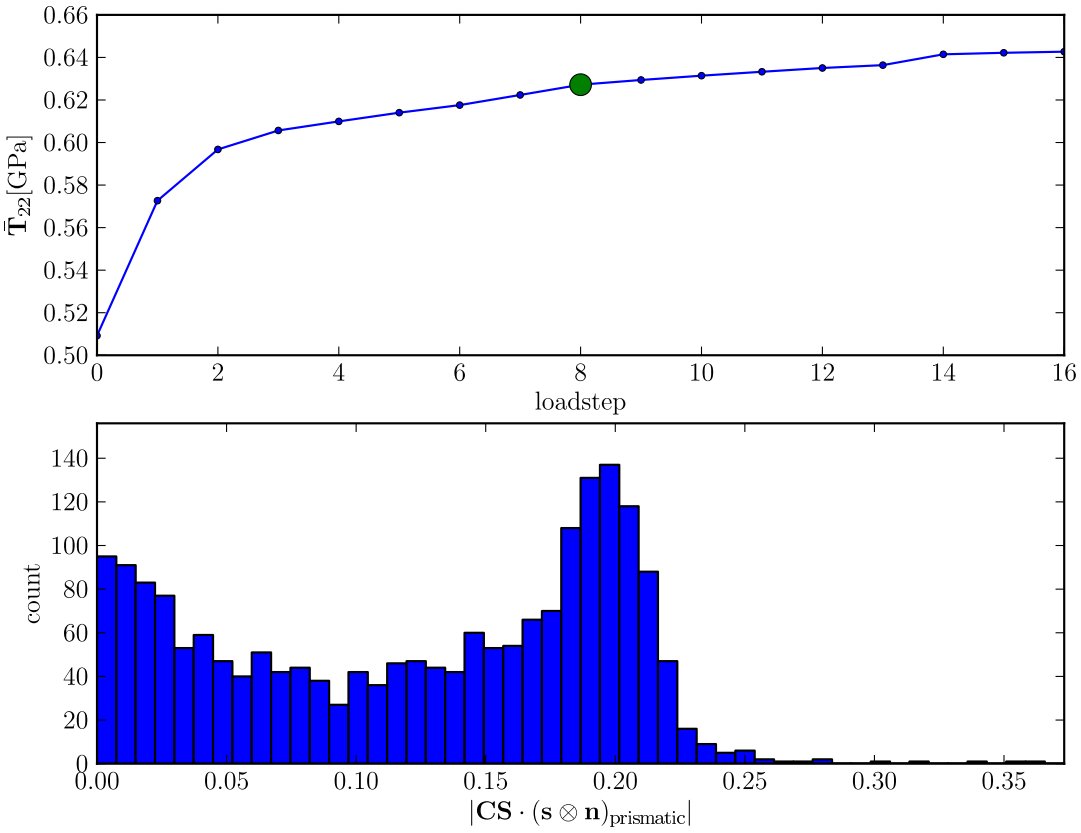

Figure 3.69: Histogram of the shear stress projection for each of the (3) prismatic systems, for each grain, along with the far field load indicated. Load step = 8.

Finally, in Figures 3.69, 3.70, and 3.71 are shown the stress projection results in higher resolution than in Figures 3.66-3.68. The far field stress level recorded by the load frame is also shown, to show that macroscopic yielding and slip system saturation occur at the same time. The resolved shear stress in the horizontal axis of the figures is the Eshelby stress of (2.48). Since the slip vector and slip normal are orthogonal, in the inner product between $\mathcal{E}' \cdot \mathbf{s} \otimes \mathbf{n}$ the term $\Psi\mathbf{I}$ gets killed off and only the term $\mathbf{H}^{\mathrm{T}}\mathbf{P} = \mathbf{CS}$ remains. Since these are small elastic strains, the figures would not change significantly by replacing $\mathbf{S} \approx \mathbf{CS}$. We do not attribute great significance to the use of the large elastic strain measure $\mathbf{CS}$. It is primarily worth pointing out the fact that the X-ray modeling approach of §3.3.5 directly captures the information required to compute such quantities. These quantities would not be available using small elastic strain X-ray kinematics of (3.228).

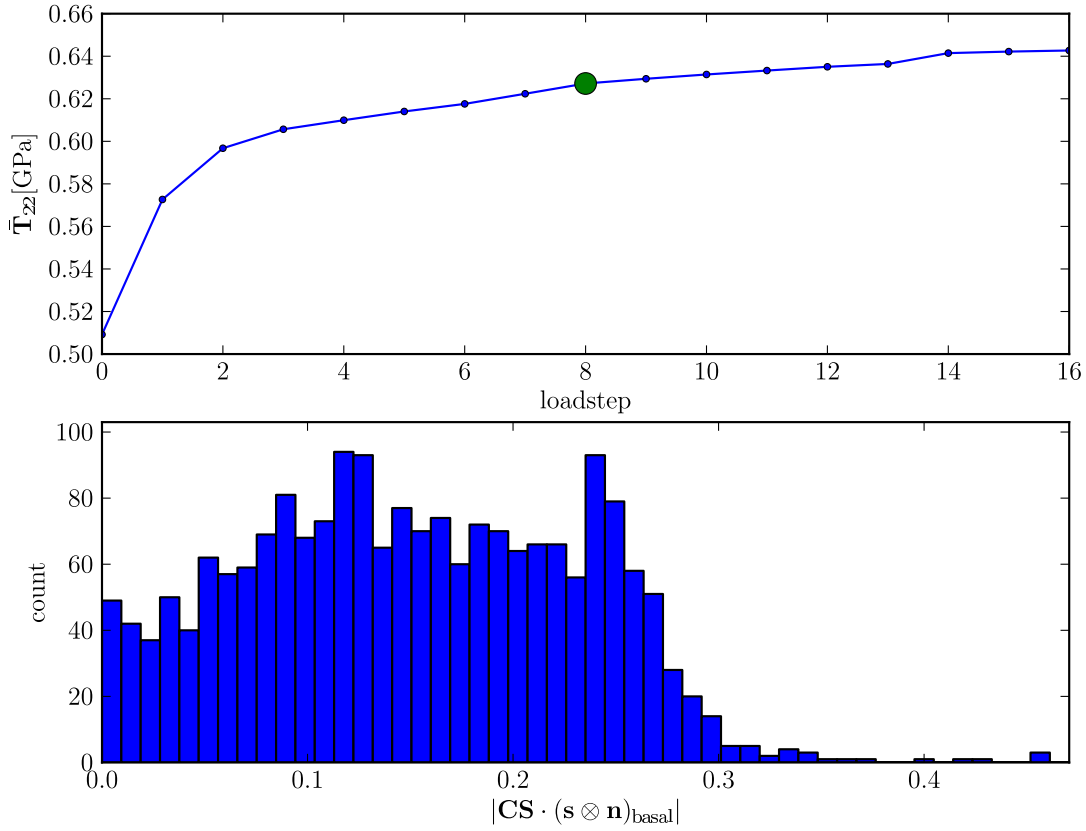

Figure 3.70: Histogram of the shear stress projection for each of the (3) basal systems, for each grain, along with the far field load indicated. Load step = 8.

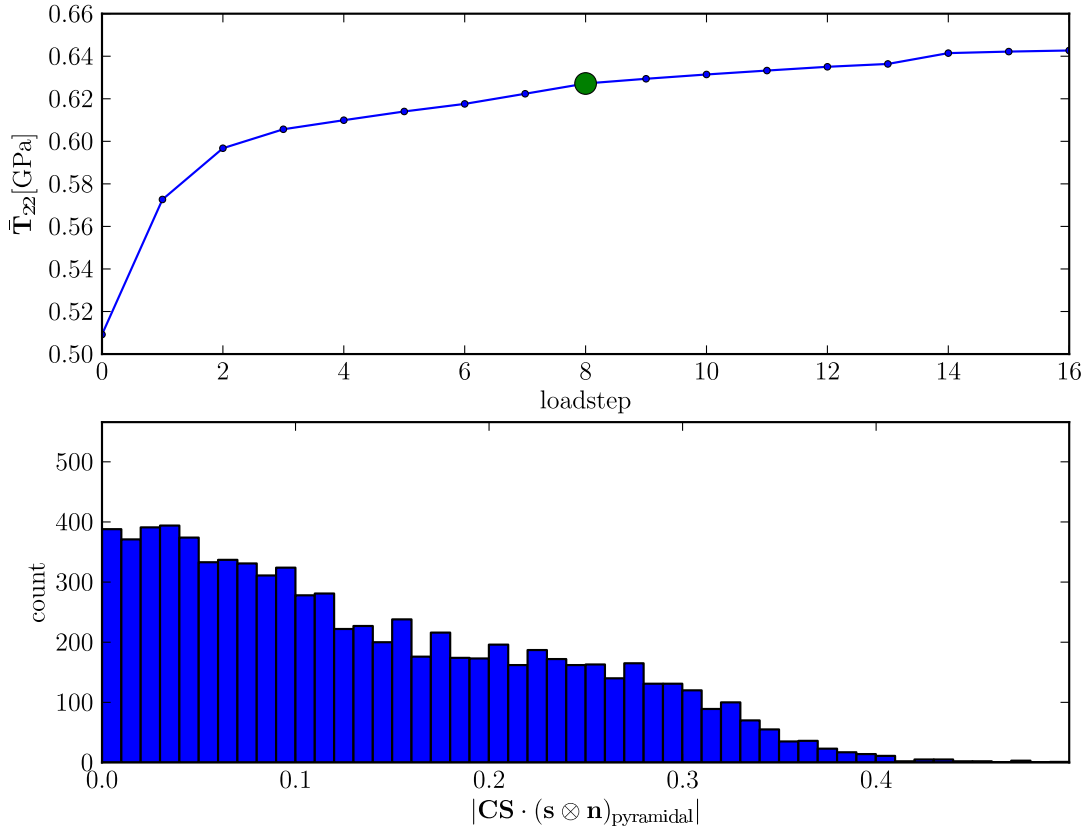

Figure 3.71: Histogram of the shear stress projection for each of the (12) pyramidal systems, for each grain, along with the far field load indicated. Load step = 8.

3.5.3 Discussion

We now discuss the further aspects of the methods and findings of this section. The phenomenological yield function based on (3.366) was found to be compatible using two different estimation methods: we used estimation methods based on (3.347), as well as based on (3.361). These methods represent different views at the same parameters, and were found to be compatible with each other, giving some degree of comfort.

The crystal plasticity function was obtained differently - not from a least squares optimization but from a histogram visualization. This was possible because of the presumed form for plastic flow, in terms of resolved shear stresses. The method was able to get good estimates for the prismatic and basal system slip system strengths.

We now discuss several topics which came up naturally in the course of this study, which are relevant to report. We also suggest methods for improvement of the parameter estimates from these two methods.

More on constitutive formulation for HCP crystals. Returning to the formulation of the phenomenological model in §3.5.1.2, it may be questioned why we didn't try the same deviatoric stress technique as for the cubic crystal in §2.3.3.1 (removing the volumetric integrity element and expressing everything in terms of deviatoric stress). We now examine this possibility.

First, recall that the integrity elements for HCP symmetry are given in (3.365). Using the relation

$$A_{11} + A_{22} + A_{33} = x_1 + x_2,$$

we can replace either of x_1 or x_2 by $A_{11} + A_{22} + A_{33}$. Then for a pressure independent yield function (pressure $\cong$ tr $\mathbf{S}$) we can remove this invariant from consideration. After this removal the integrity basis is only three elements, given by

$$x_1 = A_{33}, \qquad y_1 = A_{11}A_{22} - A_{12}^2, \qquad y_2 = A_{13}^2 + A_{23}^2, \tag{3.377}$$

with quadratic order polynomial expansion for the yield function

$$y\left(A\right) = \sum_{i=1}^{1}\sum_{j=1}^{1} b_{ij}x_i x_j + \sum_{i=1}^{2} c_i y_i. \tag{3.378}$$

But using (3.378) in (3.368), and computing the eigenvalues per the convexity condition as in (3.369) gives the results

$$\begin{array}{lll} \lambda_1 = 2b_{11} & \lambda_3 = -c_1 & \lambda_5 = 2c_2 \\ \lambda_2 = -2c_1 & \lambda_4 = c_1 & \lambda_6 = 2c_2 \end{array}. \tag{3.379}$$

For the yield function (3.378) to be convex, $\lambda_i \geq 0$, (3.379) requires that $c_1 = -c_1 \implies c_1 = 0$. Therefore we remove the integrity element y_1 from the expansion (3.378). After this

removal, we arrive at a strange looking yield function, since it is independent of many stress components at quadratic order. The integrity elements up to second order are just

$$\begin{aligned} x_1 &= A_{33} \\ y_1 &= A_{13}^2 + A_{23}^2, \end{aligned} \tag{3.380}$$

with the polynomial expansion (2 parameters)

$$y\left(A\right) = \sum_{i=1}^{1}\sum_{j=1}^{1} b_{ij} x_i x_j + \sum_{i=1}^{1} c_i y_i. \tag{3.381}$$

Equation (3.381) did not seem to be a physically valid yield function, so we retained all five integrity elements in (3.365) in developing the constitutive equations for dihexagonal-dipyramidal materials, and obtained the desired property of volume incompressibility by constraining the parameter values.

It should be noted that the five parameter yield function is pressure insensitive by virtue of the constraints (3.373). Taking a parametrized path for the stress of a pressure form,

$$\dot{\mathbf{S}} = s\mathbf{I}, \tag{3.382}$$

then for this pressure increment, the requirement that the yield function be unchanged is written as, using (3.382)

$$\begin{aligned} \dot{y} = 0 \implies 0 &= \frac{\partial y}{\partial \mathbf{S}} \cdot \dot{\mathbf{S}} \\ \implies 0 &= s\frac{\partial y}{\partial \mathbf{S}} \cdot \mathbf{I} \\ \implies 0 &= \mathrm{tr}\, \frac{\partial y}{\partial \mathbf{S}}, \end{aligned}$$

a condition which is satisfied by the parameter constraints (3.373).

Improving local estimates for F. In this study, we used macroscopic stress-strain data, along with the polycrystalline Young's modulus and Poisson ratio in order to get macroscopic estimates for $\mathbf{F}$. This was explained in §3.5.1.1. We then applied the macroscopic estimates locally, and in combination with the diffraction measurements of $\mathbf{H}$, were able to estimate $\mathbf{K}$ locally from $\mathbf{K} = \mathbf{F}^{-1}\mathbf{H}$.

Prior to this, we tried another methodology to improve the macroscopically derived estimates for $\mathbf{F}$, by attempting to estimate $\mathbf{F}$ locally from the start. Since we obtain the grain center of mass $\mathbf{x}$ during the grain averaged refinement, it was though possible to use this data to define a local measurement of $\mathbf{F}$. This would be obtained from tracking the evolution of the configuration defined by particles at each of the grain centers. But in the

end, precisions on the precessions were up to ± 75 μm, and the degree of total straining $O(2\%)$ was not high enough that any change in the grain center of mass could be attributed to material strain.

Such an approach at getting local estimates for $\mathbf{F}$ may have promise if tracer particles were present in the microstructure, perhaps at grain boundaries. If the size of the particles were small enough, the precision of the location placements would be improved over using the grains alone. However it's not clear how many particles would successfully be able to be distinguished in the data, since they would have to be processed along with the grains of interest. It may be that the beam would have to be so small to process the data that the advantages of using the efficient, wide beam illumination of the polycrystal would disappear and other X-ray techniques would be preferred. In the future, a experiment combining the use of X-ray diffraction with Digital Image Correlation on a two-dimensional material geometry (thin film) seems to be the most promising method to obtain local measurements of $\mathbf{F}$ along with the lattice measurements $\mathbf{H}$.

Moduli determination. In this section we have focused on determining plastic deformation constitutive properties of the single crystal from a simple polycrystalline test. For certain materials, particularly alloys obtained from complicated heat treatments, determining the single crystal elastic moduli is also of interest since large single crystals may not be available. We now discuss a framework for estimating single crystal moduli from the X-ray diffraction technique employed in this study. Efstathiou et al. (2010) have done something similar previously, but their approach can be criticized on many grounds, such as non-proval of initial condition dependence, so the field is still open for improvement.

In overview, we use the X-ray diffraction data from the wide beam scan to generate a numerical discretization for the microstructure in the polycrystal. Generating true microstructures from X-ray diffraction data is the field of the near field X-ray technique (Suter et al., 2006; Hefferan et al., 2010) and takes much longer than the wide beam scan, at the benefit of increased accuracy. It remains to be seen how accurate the wide beam based microstructures are compared to experimental data, however without the capability to know this we press on valiantly. After obtaining the approximate microstructure and embedding it in a numerical simulation, we can directly simulate the continuous loading experiment numerically, and compare XRD-based estimates for the grain deformation to the numerical prediction. This forms the basis for a least squares method over any set of single crystal material parameters desired, not just elastic properties. Additionally, this numerical method could be applied to refine the estimates for the plastic parameters in the previous section. We now examine the details.

In §3.2.2.4, from Equation (3.118) we obtained an expression for the intensity of a diffraction peak based on diffraction angles and physical volume of the crystal. Using this analysis of the intensity of diffraction peaks, we can determine the relative volumes of each grain measured in the polycrystal. Absolute volume could be estimated, however this would re-

quire beam intensity calibration procedures which were not used for this study. Therefore we arrive at the microstructural data

$$M = \{(\mathbf{x}, \mathbf{R}, V)_i : i = 1, 2, ..., N_{\text{grains}}\}, \tag{3.383}$$

where $\mathbf{R} \in \text{SO}(3, \mathbb{R})$ comes from the polar decomposition of the lattice deformation $\mathbf{H}$, $\mathbf{x} \in \mathbb{R}^3$ is the spatial position of the center of the grain, and V is the relative volume of the grain. Using a microstructural generation technique similar to that in §2.4.2.1.1 we can arrive at a finite element discretization of the material in the region of interest. For example, in Figure 3.5.4 we seed the image of the fixed lattice configuration (unit cell) in M under the spatial configuration placement using $\mathbf{x}, \mathbf{R}, V$. The hexagonal prisms are scaled according to the volume V. This microstructure was taking from an wide box scan of the titanium specimen in the region of interest, with a 500×1000 beam size. This scan was taken at a far field stress of $\sigma = 400$ MPa, which is not part of the continuous load scan depicted in Figure 3.31. The box scan data is given to LLNL's finite element code *ale3d* which executes the microstructural generation algorithm. Figure 3.73 is the resulting discretized material, with the 1coloring indicating material regions with the same orientation, $\mathbf{R}$. This is a different view of the same microstructure as in Figure 3.5.4.

We now consider the formulation of the least squares problem to determine single crystal moduli from this numerical capability. The load increment applied to the data is between the 400 MPa box scan level and the start of the continuous scan, at about 500 MPa, see Figure 3.31. Based on linearity, in the numerical simulation, the load increment applied is simply $\Delta\sigma = 100$ MPa, starting from an unstressed state.

Then the least squares objective function expressing the different between data and simulation is written as

$$\Phi(\boldsymbol{\Theta}) = \sum_{i=1}^{N_{\text{grains}}} \left[(\Delta\mathbf{E})_i^{\text{fem}}(\boldsymbol{\Theta}) - (\Delta\mathbf{E})_i^{\text{XRD}}\right]^2, \tag{3.384}$$

where $\boldsymbol{\Theta} \equiv \mathcal{C}$, the single crystal moduli, $(\Delta\mathbf{E})_i^{\text{XRD}} = \left[\mathbf{E}^{\text{XRD}}_{\sigma=500\ \text{MPa}} - \mathbf{E}^{\text{XRD}}_{\sigma=400\ \text{MPa}}\right]_i$, and where $(\Delta\mathbf{E})_i^{\text{fem}} = \left[\mathbf{E}^{\text{fem}}_{\sigma=100\ \text{MPa}} - \mathbf{E}^{\text{fem}}_{\sigma=0\ \text{MPa}}\right]_i = \left[\mathbf{E}^{\text{fem}}_{\sigma=100\ \text{MPa}}\right]_i$. The simulated strain is dependent on the single crystal elastic moduli, so that we can emphasize the functional dependence by writing $\mathbf{E}^{\text{fem}}_{\sigma=100\ \text{MPa}} = \hat{\mathbf{E}}^{\text{fem}}_{\sigma=100\ \text{MPa}}(\boldsymbol{\Theta})$. Least squares iterations are then performed to determine the optimal values for $\boldsymbol{\Theta}^* = \mathcal{C}^*$, see §3.4.1. In §3.4.2.1 the uncertainty in the lattice deformations from the data can be obtained. This uncertainty can be incorporated through the use of weights on the residual equations in (3.384), so that (3.384) becomes

$$\Phi(\boldsymbol{\Theta}) = \sum_{i=1}^{N_{\text{grains}}} \frac{1}{u_{\mathbf{E}}^2} \left[(\Delta\mathbf{E})_i^{\text{fem}}(\boldsymbol{\Theta}) - (\Delta\mathbf{E})_i^{\text{XRD}}\right]^2, \tag{3.385}$$

where the weight is taken as the average uncertainty between the two data points at the two stress levels, so that $u_{\mathbf{E}} = 1/2\left(u_{\mathbf{E}}^{\text{XRD}}\big|_{\sigma=500\ \text{MPa}} + u_{\mathbf{E}}^{\text{XRD}}\big|_{\sigma=400\ \text{MPa}}\right)$.

Despite the expenditure of much efforts, the results of this technique applied to the present continuous loading experiment proved unsuccessful. The optimal values from the least squares algorithm did not exhibit a strong minimum, that is, even at values where $\nabla_{\boldsymbol{\Theta}}\Phi \approx \mathbf{0}$, $\Phi(\boldsymbol{\Theta}) >> 0$ in relative terms. There are several possible reasons why the experimental data was not satisfactory for this study. First, the elastic load step was at a high state of stress (already at 80% of yield), which may have resulted in local plastic flow in the step which was presumed to be elastic. In Figure 3.31 the latter load increment at 500 MPa is very close to the knee of the stress strain curve. In fact, the data of Figures 3.66, 3.67 indicates that at the 500 MPa level at the start of the loading, saturation of slip systems is indicated in the data, indicating that plastic flow may be occurring locally in the sample before macroscopic yield at 550 MPa. Since comparing XRD data with the results of the finite element simulation relies on the lack of plastic deformation, this is probably a major problem. Further evidence of plastic flow is exhibited in Figure 3.75, where the changes in the T_{22} component of the Cauchy stress tensor are shown for the FEM and XRD data. The numerical simulation has very tight spread around 100 MPa, whereas the XRD data is centered on 100 MPa, but has grains at higher and lower increments of stress. Since the FEM data is not easily visible, it is replotted in Figure 3.75 for a higher resolution depiction. Without an independent measurement of the same microstructural data, it is not clear if the grains at very high local stress states in Figure 3.75 represent true data, or are mis-indexed grains carrying erroneous peak locations (see §3.3.4). This is a shortcoming of the full illumination technique used in this study, that there are few independent validations possible to determine if results are erroneous. In any case, removal of the grains which were deemed erroneous based on large stress increments did not improve the performance of the least squares refinement, possibly suggesting that the size of the load step, 100 MPa, is not large enough to pull elastic strain measurements for the individual grains out of the noise level.

Another point to make is the presence of possible bias in the calibration data. In Figure 3.72, the far field stress strain data is plotted against the volume weighted average Cauchy stress,

$$\bar{\mathbf{T}} = \sum_{i=1}^{N_{\text{grains}}} \phi_i \mathbf{T}_i, \tag{3.386}$$

where $\phi_i = V_i / \sum_j V_j$ is the volume fraction of the i^{th} grain. These stresses are obtained from previous studies of moduli for this alloy, so the bias in the figure may also be a result of using slightly erroneous single crystal moduli. Attempting to match the single crystal moduli to minimize a residual based on (3.386) compared to the far field stress did not give acceptable results.

Another point is that we seeded the initial microstructure with only orientation factors $\mathbf{R}$ from the XRD data, and did not take into account initial lattice strain at the initial 400 MPa level. Residual strains may also be present in the polycrystal which are not being accounted for in the finite element simulation. Residual stresses may be why we appear to have local

yielding before macroscopic yield, in Figures 3.66, 3.67. We had assumed that linearity of the stress strain response would enable direct translation of the $400-500$ MPa experimental increment to the $0-100$ MPa simulated increment. But it is possible that residual stresses in the polycrystal exacerbated the heterogeneity exhibited in Figure 3.75. Unfortunately generating the full $\mathbf{H}(\mathbf{X})$-field in the polycrystal is beyond current experimental technologies, so if the problem of residual stresses is significant the wide beam technique will prove to be ineffective in similar constitutive determinations.

Summary of suggested remedies. If this experiment were to be attempted again to measure single crystal moduli, there are several quite simple modifications which are indicated. First, measure the lattice state at an unloaded external stress level, instead of so close to the plastic region. Then the increment would be more assuredly elastic over at least some range of testing. Second, take a large enough elastic stress increment to be sure that noise will not cover up the influence of the model's residuals. From $0-50\%$ of the polycrystalline yield stress should be sufficient for most metals.

3.5.4 Summary

In this section we have suggested several methods for using the high energy X-ray diffraction technique to obtain constitutive information required for theoretical models of plasticity. This type of experiment has been successful in obtaining novel observations of material behavior, but its use in extracting constitutive data has only begun to be explored. The present contribution is among the first to investigate plastic properties using the technique.

We described different approaches to extract both elastic and plastic properties from high energy X-ray diffraction with a wide beam source. We first used an approach where each grain in the polycrystal was treated as an independent experimental test. For the model of Chapter 2 we were able to obtain reasonable estimates for the material parameters from a suggested form for the yield function. The determination of a yield event was the largest limitation on the confidence which can be assigned to the parameter values.

We performed a similar task based on crystal plasticity theory. This theory required fewer assumptions on a yield event, since attention is restricted to resolved shear stresses instead of arbitrary stress states. The crystal plasticity method of using histograms to obtain resolved shear stresses appears very efficient for getting constitutive information required for its model.

For the phenomenological theory, an accurate local measurement of $\mathbf{F}$ would go a long way to improving the deduction of constitutive parameters, by enabling more precise measurements of the plastic deformation. Then the yield point detection technique based on elastic evolution could be shelved in favor of simply monitoring the evolution of the $\mathbf{K}$ field through the use of $\mathbf{K} = \mathbf{F}^{-1}\mathbf{H}$, which would be a more accurate indication of a yield event. Based on the rate-independent theory of plastic deformation, evolution of $\mathbf{K}$ only occurs if the lattice state is on the yield surface. Local measurement of $\mathbf{F}$ could be accomplished by

simultaneous Digital Image Correlation for example, and the problem appears to be tractable in the near future.

For both cases, improvements in the experimental precision of lattice deformation measurements would be beneficial. According to §3.4.2.1, there may be gains available by reducing the pixel size or changing the distance to the detector. The closer precisions on $\mathbf{H}$ can get to the level of bonded resistance strain gauges, e.g. $5 - 20\% \rightarrow < 5\%$, the more likely these combined numerical-experimental techniques suggested in this section can be trusted to give quantitative results.

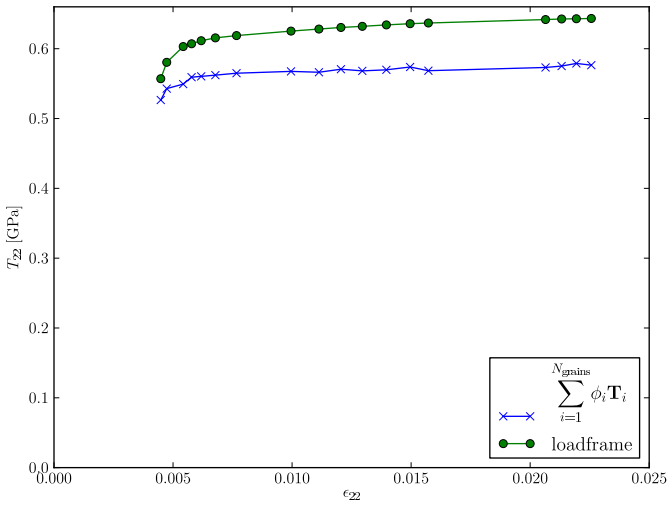

Figure 3.72: σ vs ε for the continuous load scan, along with the volume averaged Cauchy stress, computed from (3.386). Solid points indicate where diffraction measurements were taken. The discrepancy can be due to erroneous elastic moduli or to calibration bias errors.

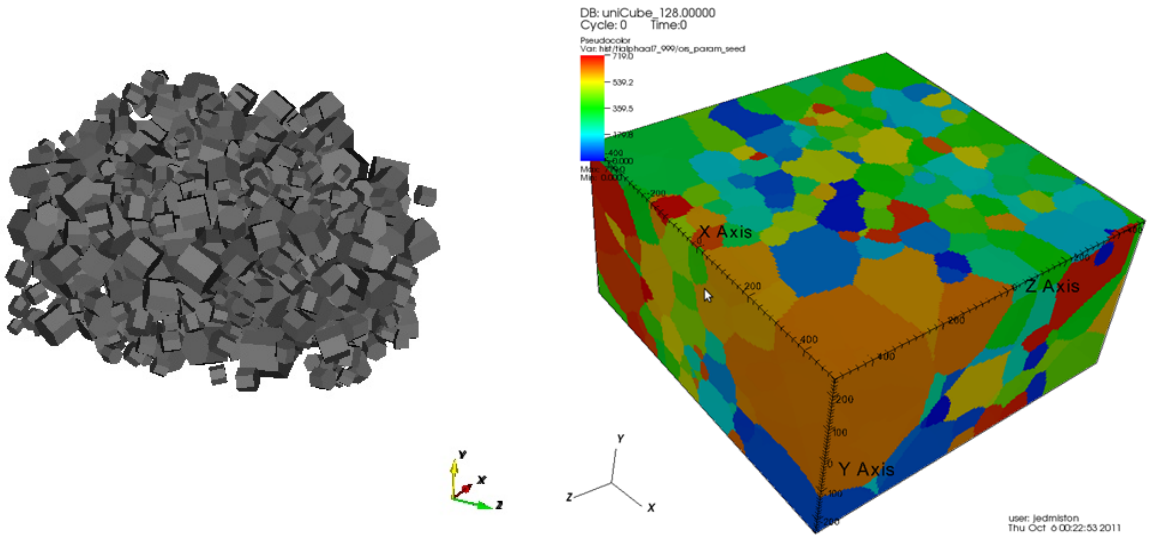

(a) Initial seed points for microstructural algorithm.

(b) Finite element mesh produced from the seed data on the left, used for the numerical discretization

Figure 3.73: The hexagonal prisms represent the images of the fixed lattice configuration under the placement $\mathbf{x}, \mathbf{R}, V$, where V is a scaling for the size of the grain.

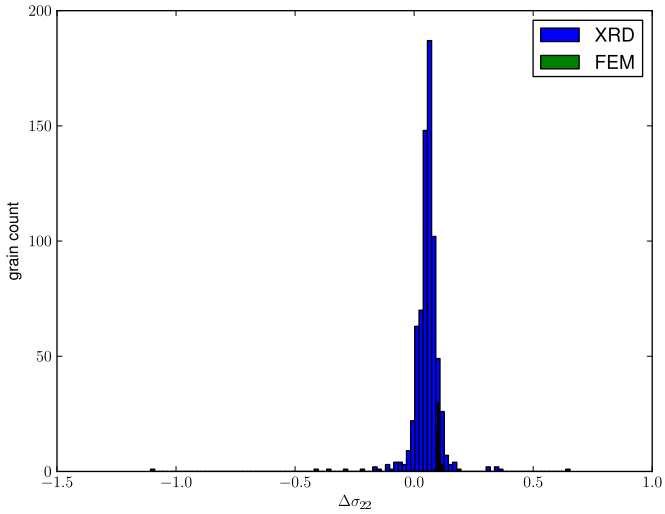

Figure 3.74: Histogram of the σ_{22} stress increment, for each individual grain after the macroscopic change $\Delta\sigma_{22} = 100$ MPa. The large spread of values in the experimental histogram suggests that plasticity has occurred. By comparison, the FEM data has a much tighter spread. This suggests that moduli determination efforts from this data set will be imprecise.

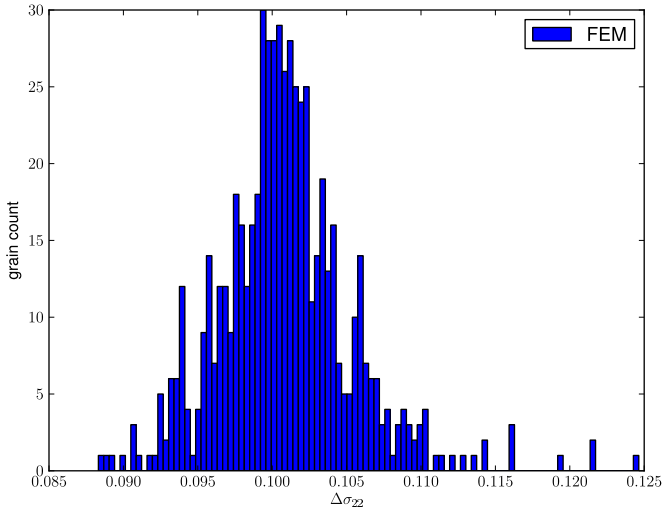

Figure 3.75: Histogram of the σ_{22} stress increment for each individual grain, from the FEM simulation after the macroscopic change $\Delta\sigma_{22} = 100$ MPa. This is the same data as Figure 3.74 on a higher resolution. This distribution of stress increment is much tighter than that observed in the X-ray data.

3.6 Conclusion

We conclude by giving a review of this chapter and some final thoughts. In this chapter we gave a thorough background for the physics of X-ray diffraction. We derived the reciprocal lattice as the Fourier transform of the physical lattice, and were able to obtain expressions for the integrated energy of a diffraction peak as it passes through the diffraction condition. This laid the foundation for rich descriptions of X-ray diffraction for spatially inhomogeneous materials.

Then we described the detailed procedures of a modern class of X-ray diffraction experiments: high energy monochromatic synchrotron measurements, with a wide beam size. This method has already shown the ability to obtain qualitative information about material behavior (Jakobsen et al., 2006), but little has been done in the way of using the technique to extract constitutive behavior. We gave a broad introduction to the method, and described two approaches to combining diffraction data with the X-ray diffraction theory to produce estimates of the lattice state and lattice inhomogeneity. Both methods represent new approaches to analyzing X-ray data for this class of diffraction experiment. The first method was a grain averaged approach, where estimates of center of volume position and lattice deformation on a volume averaged basis were obtained. The second method used a forward model to incorporate the projection of spatial inhomogeneity into the lattice deformation space.

The outcomes from these methods differ. The grain averaged method led to an estimate for the uncertainty associated with the measurements, which had not previously been explored in the literature. Such uncertainty quantification is a necessary condition for meaningful reporting of constitutive parameters from a given experiment. The forward modeling method led to the ability to track the development of intragranular misorientation. With some accepted hypotheses on slip phenomena, this led to an experimental indication of slip activity on the prismatic system of the titanium alloy tested. This purely kinematic finding was found to be consistent with subsequent constitutive analysis of the data presented in the final section.

The final section was concerned with the extraction of single crystal constitutive parameters from a continuously loaded specimen of titanium polycrystal, up to 2% total strain. The reason this attempt is worthwhile is because certain materials are difficult to obtain in the large single crystals required for an idealized experimental environment. For example, the heat treatments required to attain certain microstructures make polycrystalline samples generally easier to obtain. Therefore, if single crystal properties could be estimated from a test of a polycrystalline material, this would be a great asset to the quantitative calibration of material models in plasticity. Such calibrations are crucial to testing the predictions of theoretical models but are rare to find in modern literature. This is particularly the case for plasticity journals.

We embraced two methodologies for obtaining single crystal parameters. First, we adopted the phenomenological plasticity theory which was set up in Chapter 2. We ob-

tained best fit parameters for the yield function for dihexagonal-dipyramidal point group symmetry (HCP). These parameters also satisfied the additional requirements of constituting a convex yield surface, volume incompressibility, and pressure insensitivity. We were also able to discern qualitative hardening phenomenology through the monotonic evolution of the parameters as the test commenced, providing some encouragement for the method. The parameter estimates we obtained from the yield determination methodology were compatible with estimates we made deducing plastic flow evolution in the material, giving further credence to the numerical values we obtained. Secondly, we adopted the crystal plasticity phenomenological perspective, which considers resolved shear stresses on slip planes in the crystal as governing the yield concept. Due to the form of crystal plasticity, this approach had fewer degrees of freedom, and results were readily visualized by producing histogram plots of the resolved shear stresses on different slip systems. We obtained estimates for the critically resolved flow stress on the basal and prismatic slip systems of the crystal using this approach. The prismatic system was found to have a lower flow stress, which agrees with the kinematic observations of intragranular inhomogeneity arrived at using the forward model.

Outlook Although the data from the X-ray experiments contains scatter, the technique continues to show promise for future development. Although improvements are necessary, the method can be elevated to be used to confidently extract constitutive data, using the approaches described. For example, in a future test increasing the precision on the diffraction technique and adding direct independent measurements of the local material deformation would be a worthy addition to the experimental methodology. The former could be obtained by selecting optimum values for the geometric parameters in the experimental setup, such as the distance to the detector, pixel size, or detector area. The latter could be accomplished by coupling X-ray diffraction measurements with a technique such as Digital Image Correlation. Interestingly, this dual prescription is precisely what G.I. Taylor did in the 1920s with the tools available of the time. This underscores both the contributions of Taylor, as well as lamenting the fact that experimental techniques have evolved so slowly over the last century.

Chapter 4

Conclusion

In this thesis we have contributed to theoretical and experimental aspects of continuum plasticity. Phenomenological plasticity models for single crystals, without using the crystal plasticity formulation based on slip systems, have previously been present in the literature. However they have not been developed to the point of being able to compare predictions to experimental data. This is due to lack of proposed or validated constitutive models, which is in part due to the severe experimental challenges of plasticity. Therefore one contribution in this document was completing the constitutive framework for these models. The resulting model achieves the rate independent limit, and has a natural viscoplastic extension. We are able to attain calibration of the constitutive functions for hexoctahedral point group symmetry against crystal plasticity models for FCC and BCC materials from the literature. After calibration, we applied a variety of simple plane strain boundary value problems to exercise the model, testing the influence of various material parameters. These simulations show a rich phenomenological prediction, including a natural strain localization effect and the development of geometrically necessary dislocation networks.

We also described the experimental technique which is compatible with the theory: X-ray diffraction. The synergy between the theory and experiment is made evident in that they share the same mathematical structures when appropriately translated. We gave details of the experimental procedures for high energy synchrotron X-ray diffraction, a relatively new tool which shows promise for investigating plastic behavior which had not been previously revealed. To date this experiment has been used mostly for qualitative discoveries; we evaluated the method's ability to deliver quantitative information such as material parameters for single crystal constitutive functions. We developed two new methods of analyzing data from these experiments. The first method enabled the estimation of uncertainty in lattice deformation measurements. The quantification of experimental precision from these tests is crucial in order to properly report constitutive parameters derived from the data. The second was able to assess intragranular misorientation due to evolving spatial inhomogeneity. The misorientation information further enhances the amount of primitive data which can be derived from such experiments, in that obtaining such information is independent of any con-

stitutive function. In combination with hypotheses about plastic deformation modes, such information can lead to direct indications of plastic deformation history. This additional capability of the experimental technique makes pursuing such experiments more attractive.

Finally, we used experimental data from a continuously loaded tension test of a titanium polycrystalline alloy to determine single crystal constitutive information. This was not the original intended application of the experiment; despite this we were able to obtain quantitative estimates of the single crystal yield function parameters. The resulting estimates pass available consistency checks with theoretical aspects of the proposed plasticity model, lending credence to our reported values. Our experience with these efforts allowed us to make recommendations for future experimental programs which seek to determine similar constitutive information. For example, the independent verification of total material deformation through the use of Digital Image Correlation would allow a more precise method to detect when plastic deformation occurs, which is an important requirement of the methods we employed.

Potential application of the model. The use of crystal plasticity is widespread, and most researchers are satisfied with the model. However the proposed formulation of plasticity may be of use in the modeling of materials for which the plastic behavior is not well characterized according to slip system activity, such as $MgGeO_3$ post-perovskite, a material in the Earth's mantle. For example, the slip systems for this material are not universally agreed upon (Merkel et al., 2006). Since the point group symmetry of such a material is known (rhombic-dipyramidal in the notation of Green and Adkins (1970)), it is conceivable that using the phenomenological model proposed here would be accommodating enough to available experimental data to allow calibration. Subsequent simulations involving plastic deformation of the material could then commence. See for instance Equations (2.151) and (2.152), which characterize the yield function $y(\mathbf{S})$ and lattice reorientation function $\mathbf{\Omega}(\mathbf{S})$ for the required point group symmetry (rhombic-dipyramidal).

We should note that in our constitutive models we considered polynomial functions, which produce smoother yield surfaces than the vertex yield surfaces of crystal plasticity, see Figure 3.64. However experimental evidence indicates that for some materials, smoother yield behavior may better match experimental data. In this regard see Figure 4.1, which shows simulated and experimental deformation textures for quartz for different constitutive models of plasticity. This particular model differs from ours, but qualitative comparisons are valid. The model corresponding to the smooth yield surface matched the experimental texture (on the far right) the best.

Final remarks. Plasticity of crystals is certainly a difficult subject. The mechanisms governing the deformation of crystals are highly complex interactions between atoms. These interactions result in phenomena such as dislocations and phase transformations. In the face of all this complexity, until computational resources make continuum theories obsolete,

the flexibility of the phenomenological model to capture meso- or macro- scale observable physical effects is appealing. In the simulations of the model we observed rich phenomenological behavior such as strain localization and dislocation networks. These findings seem to discredit what was postulated in §2.1.4, item 4, which didn't think such an approach could capture microscale observations.

Although the simulations are promising, the success of a phenomenological model is determined by its ability to actually model material behavior, over a range of conditions large enough to be considered useful. For example, a phenomenological model requires the specification of constitutive formula and associated material parameters. The value of the parameters must be independent of the experiment used to obtain the parameters - as they represent an intrinsic property of the material. In other words, the calibration of the model parameters according to one experiment should result in acceptable agreement in other experimental configurations. It remains to be seen if the values obtained for the titanium yield function parameters in this work are to be borne out in subsequent experiments. In the meantime, the reported parameters can give other researchers a foothold into implementing the modeling framework for their applications.

We hope that it has been made clear that the final word in continuum plasticity theories will not be made until experimental methods advance significantly from their present state. In many fields, experiments outpace theoretical development; however this is not be the case for continuum plasticity. The high energy X-ray diffraction measurement method described in this thesis have already shown success for qualitative discoveries in plasticity. It remains to be seen how useful the method is in determining quantitative information: the sort of information which can distinguish the different predictions of various plasticity models, with sufficient precision(!). The research in this thesis suggests affirmative progress to this question.

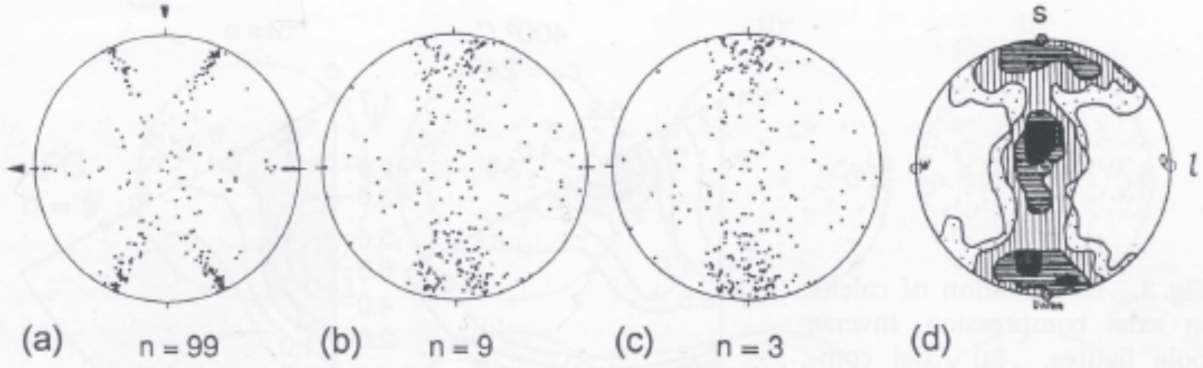

Fig. 4. (a-c) Taylor simulations for quartz in pure shear illustrating the effect of stress exponent (inverse of strain-rate sensitivity) [WENK &AL. 1989a]. The stress exponent n=3 (in $\dot{\gamma}=\tau^n$) which is applicable to quartz, gives the most realistic texture and compares well with the first measured quartz texture on the right side (d) [SCHMIDT 1925] (compression and extension directions are indicated by arrows, *s* is the normal to the schistosity and *l* the lineation).

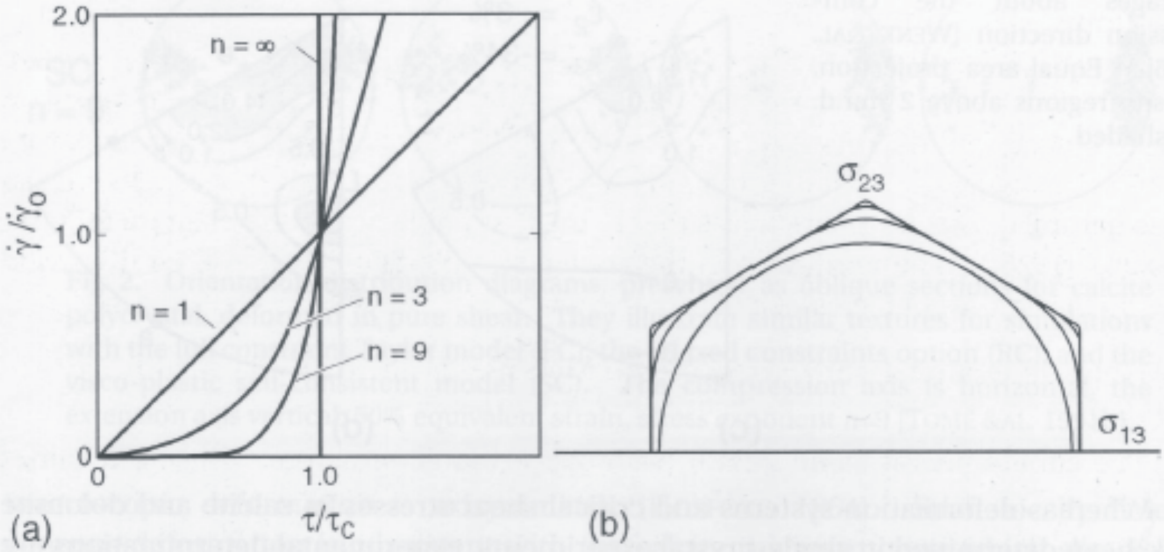

Fig. 5. Visco-plastic deformation of quartz. (a) Graph illustrating the power law to describe strain-rate sensitivity for different stress exponents. (b) Two-dimensional sections through the single-crystal yield surface of quartz according model 'α' (Table II) ,for stress exponents 3, 9 and 99. Stress coordinates σ_{23} - σ_{13} are indicated.

Figure 4.1: Deformation textures of quartz, from Kocks et al. (1998, p. 566). Copyright 1998, Cambridge University Press. Reprinted with the permission of Cambridge University Press.

Bibliography

A. Acharya and J. Bassani. Lattice incompatibility and a gradient theory of crystal plasticity. *Journal of the Mechanics and Physics of Solids*, 48:1565–1595, 2000.

L. Anand, S. Balasubramanian, and M. Kothari. Constitutive modeling of polycrystalline metals at large strains. In *Large plastic deformation of crystalline aggregates*. Springer-Verlag, 1997.

E. Andrade. The flow in metals under large constant stresses. *Proc. R. Soc. Lond. A.*, 90: 329–342, 1914.

R. Asaro. Crystal plasticity. *Journal of Applied Mechanics*, 50:921–935, 1983.

R. Asaro and A. Needleman. Texture development and strain hardening in rate dependent polycrystals. *Acta Metallurgica*, 33:923–953, 1984.

C. C. Aydiner, J. V. Bernier, B. Clausen, U. Lienert, C. N. Tomé, and D. W. Brown. Evolution of stress in individual grains and twins in a magnesium alloy aggregate. *Physical Review B*, 80:024113, 2009.

L. Azaroff, R. Kaplow, N. Kato, R. Weiss, A. Wilson, and R. Young. *X-Ray Diffraction*. McGraw-Hill Book Company, 1974.

R. Barabash, G. Ice, and F. Walker. Quantitative microdiffraction from deformed crystals with unpaired dislocations and dislocation walls. *Journal of Applied Physics*, 93:1457–1464, 2002.

Y. Bard. *Nonlinear Parameter Estimation*. Academic Press, Inc., 1974.

F. Barlat and K. Lian. Plastic behavior and stretchability of sheet metals. part 1: A yield function for orthotropic sheets under plane stress conditions. *International Journal of Plasticity*, 5:51–66, 1989.

F. Barlat, D. Lege, and J. Brem. A six-component yield function for anisotropic materials. *International Journal of Plasticity*, 7:693–712, 1991.

F. Barlat, H. Aretz, J. Yoon, M. Karabin, J. Brem, and R. Dick. Linear transformation-based anisotropic yield functions. *International Journal of Plasticity*, 21:1009–1039, 2005.

N. Barton and P. Dawson. On the spatial arrangement of lattice orientations in hot-rolled multiphase titanium. *Modelling and Simulation in Materials Science and Engineering*, 9: 433, 2001.

N. Barton, D. Benson, and R. Becker. Crystal level continuum modelling of phase transformations: the $\alpha \rightarrow \epsilon$ transformation in iron. *Modelling and Simulation in Materials Science and Engineering*, 13:707–731, 2005.

N. Barton, J. Bernier, R. Becker, A. Arsenlis, R. Cavallo, J. Marian, M. Rhee, H.-S. Park, B. Remington, and R. Olson. A multiscale strength model for extreme conditions. *Journal of Applied Physics*, 109:(073501–1)–(073501–12), 2011.

T. G. Beckwith, R. D. Marangoni, and J. H. L. V. *Mechanical Measurements*. Addison-Wesley Publishing Company, Inc., 5th edition, 1995.

J. F. Bell and R. E. Green. An experimental study of the double slip deformation hypothesis for face-centered cubic single crystals. *Philosophical Magazine*, 15:469–476, 1967.

J. V. Bernier, J.-S. Park, A. L. Pilchak, M. G. Glavicic, and M. P. Miller. Measuring stress distributions in Ti-6Al-4V using synchrotron X-ray diffraction. *Metallurgical and Materials Transactions A*, 39(13):3120–3133, 2008.

J. V. Bernier, N. R. Barton, U. Lienert, and M. P. Miller. Far-field high energy diffraction microscopy: A tool for intergranular orientation and strain analysis. *The Journal of Strain Analysis for Engineering Design*, 46(7):527–547, 2011.

T. Bohlke, G. Risy, and A. Bertram. Finite element simulation of metal forming operations with texture based material models. *Modelling and Simulation in Materials Science and Engineering*, 14:365, 2006.

J. Boumann. Theoretical principles of structural research by x-rays. In S. Flugge, editor, *Handbuch Der Physik*, volume 32, pages 97–237. Springer-Berlin, 1957.

Bunge. Texture and structure of polycrystals. In *Defect and Microstructure Analysis by Diffraction*. Oxford University Press, 1999.

J. Chaboche. Constitutive equations for cyclic plasticity and cyclic viscoplasticity. *International Journal of Plasticity*, 5:247–302, 1987.

J. Chaboche. A review of some plasticity and viscoplasticity constitutive theories. *International Journal of Plasticity*, 24:1642–1693, 2008.

P. Chadwick. *Continuum Mechanics: Concise Theory and Problems*. Dover Publications, Inc., 1999.

S. Cleja-Tigoiu and L. Iancu. Orientational anisotropy and plastic spin in finite elasto-plasticity. *International Journal of Solids and Structures*, 48:939–952, 2011.

S. Cleja-Tijoiu. Consequences of the dissipative restrictions in finite anisotropic elasto-plasticity. *International Journal of Plasticity*, 19:1917–1964, 2003.

W. Cochran. The correction of x-ray intensities for polarization and lorentz factors. *Journal of Scientific Instruments*, 25:253–254, 1948.

B. D. Coleman and M. E. Gurtin. Thermodynamics with internal state variables. *Journal of Chemical Physics*, 47, 1967.

B. D. Coleman and W. Noll. The thermodynamics of elastic materials with heat conduction and viscosity. *Archive for Rational Mechanics and Analysis*, 13:167–178, 1963.

B. Cullity. *Elements of X-ray Diffraction*. Addison-Wesley Publishing Company, Inc., 1978.

E. de Souza Neto, D. Peric, and D. Owen. *Computational Methods for Plasticity*. Wiley, 2008.

N. E. Dowling. *Mechanical Behavior of Materials*. Prentice-Hall, Inc., 1999.

V. Ebbing. *Design of Polyconvex Energy Functions For All Anisotropy Classes*. PhD thesis, Universitat Duisburg-Essen, 2010.

J. K. Edmiston, N. R. Barton, J. V. Bernier, G. C. Johnson, and D. J. Steigmann. Precision of lattice strain and orientation measurements using high-energymonochromatic x-ray diffraction. *Journal of Applied Crystallography*, 44:299–312, 2011.

J. K. Edmiston, J. V. Bernier, N. R. Barton, and G. C. Johnson. Lattice refinement strategies. *Acta Crystallographica A*, 68:181–187, 2012.

C. Efstathiou, D. Boyce, J.-S. Park, U. Lienert, P. Dawson, and M. Miller. A method for measuring single-crystal elastic moduli using high-energy x-ray diffraction and a crystal-based finite element model. *Acta Materialia*, 58:5806–5819, 2010.

Eschner. Texture analysis by means of model functions. *Textures and Microstructures*, 21: 139–146, 1993.

N. Fox. On the continuum theories of dislocations and plasticity. *Q. J. Mechanics Appl Math*, 21:67–76, 1968.

F. Frank. The conformal neo-eulerian orientation map. *Philosophical Magazine A*, 65:1141–1149, 1992.

A. Gotz, E. Knudsen, G. Suchet, G. Vaughan, H. Osholm, J. Oddershedde, J. Wright, and S. Schmidt. Fable, 2000.

A. Green and J. Adkins. *Large Elastic Deformations*. Oxford University Press, 2nd edition, 1970.

D. Greig. *Optimisation*. Longman Group Limited, 1980.

A. Guiner. *X-Ray Diffraction*. W.H. Freeman and Company, 1963.

A. Gupta, D. J. Steigmann, and J. S. Stolken. On the evolution of plasticity and incompatibility. *Mathematics and Mechanics of Solids*, 12:583–610, 2007.

A. Gupta, D. J. Steigmann, and J. Stolken. Aspects of the phenomenological theory of elastic-plastic deformation. *Journal of Elasticity*, 104:249–266, 2011.

K. Havner. *Finite Plastic Deformation of Crystalline Solids*. Cambridge University Press, 1992.

J. Hawreliak, B. El-Dasher, H. Lerenzana, G. Kimminau, A. Higginbotham, S. Vinko, W. Murphy, S. Rothman, and N. Park. In situ x-ray diffraction measurements of the c/a ratio in the high-pressure ϵ phase of shock-compressed polycrystalline iron. *Physical Review B*, 83:144144–1–144114–6, 2011.

C. Hefferan, S. Li, J. Lind, and R. Suter. Tests of microstructure reconstruction by forward modeling of high energy x-ray diffraction microscopy data. *Powder Diffraction*, 25:132–137, 2010.

W. Herrmann and L. Bertholf. Explicit lagrangian finite-difference methods. In *Computational Methods for Transient Analysis*, pages 361–413. North-Holland, 1983.

R. Hill. *The Mathematical Theory of Plasticity*. Oxford University Press, 1950.

R. Hill and K. Havner. Perspectives in the mechanics of elastoplastic crystals. *Journal of Mechanics and Physics of Solids*, 30:5–22, 1982.

R. Hill and J. Rice. Constitutive analysis of elastic-plastic crystals at arbitrary strain. *Journal of the Mechanics and Physics of Solids*, 20:401–413, 1972.

G. A. Holzapfel. *Nonlinear Solid Mechanics: A Continuum Approach For Engineeringhill*. John Wiley and Sons, LTD., 2000.

W. F. Hosford. *The Mechanics of Crystals and Textured Polycrystals*. Oxford University Press, 1993.

T. J. Hughes and K. S. Pister. Consistent linearization in mechanics of solids and structures. *Computers & Structures*, 8:391–397, 1978.

J. Hutchinson. Bounds and self-consistent estimates for creep of polycrystalline materials. *Proc. R. Soc. Lond. A.*, 348:101–127, 1976.

B. Jakobsen, H. F. Poulsen, U. Lienert, J. Almer, S. D. Shastri, H. O. Srensen, C. Gundlach, and W. Pantleon. Formation and subdivision of deformation structures during plastic deformation. *Science*, 312:889–892, 2006.

A. Jayaraman. Diamond anvil cell and high-pressure physical investigations. *Reviews of Modern Physics*, 55:65–108, 1983.

W. Kabsch. Evaluation of single-crystal x-ray diffraction data from a position-sensitive detector. *Journal of Applied Crystallography*, 21(6):916–924, December 1988.

D. Kalantar, J. Belak, G. Collins, J. Colvin, H. Davies, J. Eggert, T. Germann, J. Hawreliak, B. Holian, K. Kadau, P. Lomdahl, H. Lorenzana, M. Meyers, K. Rosolankova, M. Schneider, J. Sheppard, J. Stolken, and J. Wark. Direct observation of the - transition in shock-compressed iron via nanosecond x-ray diffraction. *Phys. Rev. Lett.*, 95:075502–1 – 075502–4, 2005.

S. Kalidindi, A. Bhattacharyya, and R. Doherty. Detailed analyses of grain-scale plastic deformation in columnar polycrystalline aluminum using orientation image mapping and crystal plasticity models. *Proc. R. Soc. Lond. A.*, 460:1935–1956, 2004.

A. Katrusiak. High-pressure crystallography. *Acta Crystallographica A*, 64:135–148, 2008.

J.-Y. Kim, V. Yakovlev, and S. I. Rokhlin. Line-focus acoustic microscopy of ti-6242 α/β single colony: determination of elastic constants. *AIP Conference Proceedings 615*, 615: 1118–1125, 2001.

U. Kocks, C. Tome, and H.-R. Wenk, editors. *Texture and Anisotropy: Preferred Orientations in Polycrystals and their Effect on Materials Properties*. Cambridge University Press, 1998.

M. Kuroda and V. Tvergaard. On the formulations of higher-order strain gradient crystal plasticity models. *Journal of the Mechanics and Physics of Solids*, 56:1591–1608, 2008.

J. W. Kysar, Y. X. Gan, T. Morse, X. Chen, and M. E. Jones. High strain gradient plasticity associated with wedge indentation into face-centered cubic single crystals: Geometrically necessary dislocation densities. *Journal of the Mechanics and Physics of Solids*, 55:1554–1573, 2007.

A. Larsen, C. Gundlach, H. Poulsen, L. Margulies, Q. Xing, and D. J. Jensen. In-situ investigation of bulk nucleation by x-ray diffraction. *Materials Science Forum*, 467-470: 81–86, 2004.

E. Lauridsen, S. Schmidt, R. M. Suter, and H. Poulsen. Tracking: a method for structural characterization of grains in powders or polycrystals. *Journal of Applied Crystallography*, 34:744–750, 2001.

S. P. Lele and L. Anand. A large-deformation strain-gradient theory for isotropic viscoplastic materials. *International Journal of Plasticity*, 25:420–453, 2009.

U. Lienert, S. Li, C. Hefferan, J. Lind, R. Suter, J. Bernier, N. Barton, M. Brandes, M. Miller, and M. Mills. High-energy diffraction microscopy at the advanced photon source. *Journal of the Minerals, Metals and Materials Society*, 63:70–77, 2011.

H. Lim, M. Lee, J. Kim, B. Adams, and R. Wagoner. Simulation of polycrystal deformation with grain and grain boundary effects. *Interational Journal of Plasticity*, 27:1328–1354, 2011.

G. Liu and X. Han. *Computational Inverse Techniques in Nondestructive Evaluation*. CRC Press, 2003.

I.-S. Liu. On representations of anisotropic invariants. *International Journal of Engineering Science*, 20:1099–1109, 1982.

I.-S. Liu. *Continuum Mechanics*. Springer-Verlag Berlin Heidelberg, 2002.

J. Lubliner. Normality rules in large-deformation plasticity. *Mechanics of Materials*, 5: 29–324, 1986.

L. E. Malvern. *Introduction to the Mechanics of a Continuous Medium*. Prentice-Hall, Inc., 1969.

L. Margulies, G. Winther, and H. Poulsen. In situ measurement of grain rotation during deformation of polycrystals. *Science*, 291:2392–2394, 2001.

K. Mathur and P. Dawson. On modeling the development of crystallographic texture in bulk forming processes. *International Journal of Plasticity*, 5:67–94, 1989.

S. Merkel, A. Kubo, L. Miyagi, S. Speziale, T. Duffy, H. Mao, and H. Wenk. Plastic deformation of $mggeo_3$ post-perovskite at lower mantle pressures. *Science*, 311:644–646, 2006.

J. R. Milch and T. C. Minor. The indexing of single-crystal x-ray rotation photographs. *Journal of Applied Crystallography*, 7(5):502–505, October 1974.

D. Mills, J. Helliwell, A. Kvick, T. Ohta, I. Robinson, and A. Authier. Report of the working group on synchrotron radiation nomenclature - brightness, spectral brightness, or brilliance? *Journal of Synchrotron Radiation*, 12:385, 2005.

P. Naghdi. A critical review of the state of finite plasticity. *Zeitschrift fur Angewandte Mathematik und Physik*, 41:315–394, 1990.

P. Naghdi and A. Srinivasa. A dynamical theory of structured solids. ii special constitutive equations and special cases of the theory. *Phil. Trans. R. Soc. Lond. A.*, 345:459–476, 1993a.

P. Naghdi and A. Srinivasa. A dynamical theory of structured solids. 1 basic developments. *Philosophical Transactions of the Royal Society A*, 345:425–458, 1993b.

M. Nakahara. *Geometry, Topology, and Physics*. Institute of Physics Publishing, 2003.

D. S. Nath. *On Finitely Deforming Elastic-Viscoplastic Materials*. PhD thesis, University of California at Berkeley, 1998.

R. Neustadt, F. W. Cagle, and J. Waser. Vector algebra and the relations between direct and reciprocal lattice quantities. *Acta Cryst. A*, 24:247–248, 1968.

J. Oddershede, S. Schmidt, H. Poulsen, H. Sörensen, J. Wright, and W. Reimers. Determining grain resolved stresses in polycrystalline materials using three-dimensional x-ray diffraction. *Journal of Applied Crystallography*, 43:539–549, 2010.

S. Offerman, N. val Dijk, J. Sietsma, E. Lauridsen, L. Margulies, S. Griguli, H. Poulsen, and S. van der Zwaag. Phase transformations in steel studied by 3dxrd microscopy. *Nuclear Instruments and Methods in Physics Research Section B: Beam Interactions with Materials and Atoms*, 246:194–200, 2006.

R. Ogden. Elastic deformations of rubberlike solids. In *Mechanics of Solids. The Rodney Hill 60th Anniversary Volume.* Pergamon Press, 1982.

P. Papadopoulos and J. Lu. On the formulation and numerical solution of problems in anisotropic finite plasticity. *Computer Methods in Applied Mechanics and Engineering*, 190:4889–4910, 2001.

Parmelee, editor. *Wind effects on high-rise buildings*. Northwestern University, 1970.

D. Peirce, R. Asaro, and A. Needleman. Material rate dependence and localized deformation in crystalline solids. *Acta Metallurgica*, 31:1951–1976, 1983.

P. Perzyna. Fundamental problems in viscoplasticity. In *Advances in Applied Mechanics*. Academic Press, 1966.

H. Poulsen, S. Garbe, T. Lorentzen, D. J. Jensen, F. Poulsen, N. Anderson, T. Frello, R. Feidenhans'l, and H. Graafsma. Applications of high-energy synchrotron radiation for structural studies of polycrystalline materials. *Journal of Synchrotron Radiation*, 4: 147–154, 1997.

H. F. Poulsen. *Three-Dimensional X-Ray Diffraction Microscopy: Mapping Polycrystals and their Dynamics*. Springer-Verlag Berlin Heidelberg, 2004.

R. Quey, D. Piot, and J. Driver. Microtexture tracking in hot-deformed polycrystalline aluminum: Comparison with simulations. *Acta Materialia*, 58:2271–2281, 2010.

E. Reusch. On a special kind of deformation in rock-salt and calcite. *Pogg. Ann.*, 132:441, 1867.

J. Rice. Inelastic constitutive relations for solids: An internal-variable theory and its application to metal plasticity. *Journal of the Mechanics and Physics of Solids*, 19:433–455, 1971.

Rockafellar. *Convex Analysis*. Princeton University Press, 1972.

E. Schmid and W. Boas. *Plasticity of Crystals*. F.A. Hughes & Co. Limited, 1950.

J. Schroeder, P. Neff, and V. Ebbing. Anisotropic polyconvex energies on the basis of crystallographic motivated structural tensors. *Journal of the Mechanics and Physics of Solids*, 56:3486–3506, 2008.

J. Schroeder, P. Neff, and V. Ebbing. Polyconvex energies for trigonal, tetragonal and cubic symmetry groups. In *IUTAM Symposium on Variational Concepts with Applications to the Mechanics of Materials*, volume 21, pages 221–232, 2010.

S. Silling. Finite different modeling of phase changes and localization in elasticity. *Computer Methods in Applied Mechanics and Engineering*, 70:251–273, 1988.

S. Soare and F. Barlat. Convex polynomial yield functions. *Journal of the Mechanics and Physics of Solids*, 58:1804–1818, 2010.

A. Spencer. Theory of invariants. In *Continuum Physics*. Academic Press, Inc., 1971.

W. Spitzig. Deformation behavior of nitrogenated fe ti mn and fe ti single crystals. *Acta Metallurgica*, 29:1359–1377, 1981.

D. J. Steigmann and A. Gupta. Mechanically equivalent elastic-plastic deformations and the problem of plastic spin. *Theoretical Applied Mechanics*, 38:397–417, 2011.

R. Suter, D. Hennessy, C. Xiao, and U. Lienert. Forward modeling method for microstructure reconstruction using x-ray diffraction microscopy: Single-crystal verification. *Review of Scientific Instruments*, 77, 2006.

M. Sutton, M. Cheng, W. Peters, Y. Chao, and S. McNeill. Application of an optimized digital correlation method to planar deformation analysis. *Image Vis. Comput*, 4:143–150, 1986.

G. Taylor. Plastic strain in metals. *J. Inst. Metals*, 62:307, 1938.

G. Taylor and C. Elam. The distortion of an aluminum crystal during a tensile test. *Proceedings of the Royal Society of London. Series A, Containing Papers of a Mathematical and Physical Character*, 102:643–667, 1923.

L. R. Treloar. The mechanics of rubber elasticity. *Journal of Polymer Science*, 48:107–123, 1974.

G. Vendroux and W. Knauss. Submicron deformation field measurements: part 2. improved digital image correlation. *Exp Mech*, 38:86–92, 1998.

B. Warren. *X-ray Diffraction*. Addison-Wesley, 1969.

G. Will. *Powder Diffraction: The Rietveld Method and the Two-Stage Method*. Springer-Berlin, 2006.

F. Winkler, C. Schutt, and S. Harrison. The oscillation method for crystals with very large unit cells. *Acta Cryst.*, A35:901–911, 1979.

G. Winther, L. Margulies, S. Schmidt, and H. Poulsen. Lattice rotations of individual bulk grains part ii: correlation with initial orientation and model comparison. *Acta Materialia*, 52:2863–2872, 2004.

W. Wong-Ng, T. Siegrist, G. T. DeTitta, L. Finger, J. H.T. Evans, E. Gabe, G. Enright, J. Armstrong, M. Levenson, L. Cook, and C. Hubbard. Standard reference material (srm 1990) for single crystal diffractometer alignment. *Journal of Research of the National Institute of Standards and Technology*, 106:1071–1094, 2001.

H. Xiao. On isotropic extension of anisotropic tensor functions. *Zeitschrift fur Angewandte Mathematik und Mechanik*, 4:205–214, 1996.

H. Xiao, O. Bruhns, and A. Meyers. Elastoplasticity beyond small deformations. *Acta Mechanica*, 182:31–111, 2006.

T. Yamanaka, T. Fukuda, T. Hattori, and H. Sumiya. New diamond anvil cell for single-crystal analysis. *Review of Scientific Instruments*, 72:1458–1462, 2001.

W. Yang and W. Lee. *Mesoplasticity and its applications*. Springer-Verlag, 1993.

Q.-S. Zheng. Theory of representations for tensor functionsa unified invariant approach to constitutive equations. *Applied Mechanics Reviews*, 47:545–588, 1994.

T. I. Zohdi. Propagation of microscale material uncertainty in a class of hyperelastic finite deformation stored energy functions. *International Journal of Fracture*, 112:13–17, 2001.

Appendix A

Appendix

A.1 Extra definitions

In this section commonly used shorthand, formula, and other similar quantities are stored for reference.

Spherical polar coordinates. The spherical polar coordinate chart is given by

$$\mathbf{e}_\rho(\alpha, \beta; \mathbf{p}, \mathbf{q}, \mathbf{r}) = \cos\alpha\mathbf{r} + \sin\alpha(\mathbf{p}\cos\beta + \mathbf{q}\sin\beta), \tag{A.1}$$

for an orthonormal basis $\mathbf{p}, \mathbf{q}, \mathbf{r}$. Regarding (A.1) as a diffeomorphism between coordinate manifolds, the metric, g_{ij}, corresponding to the map $\boldsymbol{\chi}(\rho, \alpha, \beta) = \rho\mathbf{e}_\rho(\alpha, \beta)$ is obtained from $\boldsymbol{\chi}^*\boldsymbol{\delta}$ where $\boldsymbol{\delta}$ is the Euclidean metric and $()^*$ denotes the pullback map (Nakahara, 2003):

$$g_{ij} = \begin{bmatrix} 1 & 0 & 0 \\ 0 & \rho^2 & 0 \\ 0 & 0 & \rho^2\sin^2\alpha \end{bmatrix}. \tag{A.2}$$

Euclidean norm.

$$\|\mathbf{x}\| \equiv \sqrt{\mathbf{x}\cdot\mathbf{x}}, \qquad \mathbf{x} \in \mathbb{R}^n. \tag{A.3}$$

Unitization. Given a vector $\mathbf{a}$, the unit vector associated with $\mathbf{a}$ is given by

$$\hat{\mathbf{a}} \equiv \mathbf{a}/\|\mathbf{a}\|, \tag{A.4}$$

where $\|\mathbf{a}\| = \sqrt{\mathbf{a}\cdot\mathbf{a}}$. For $\mathbf{a} \in \mathbb{R}^3, \hat{\mathbf{a}} \in \mathrm{S}^2$.

Rotation elements. Rotation tensors are conveniently parametrized as functions of an axis of rotation, $\mathbf{a} \in \mathrm{S}^2$ and angle of rotation about that axis, θ. We write this function as

$$\hat{\mathbf{R}}(\mathbf{a}, \theta) = \hat{\mathbf{R}}(\mathbf{r}) = \mathbf{I} + \mathbf{W}(\hat{\mathbf{r}}) \sin(\|\mathbf{r}\|) + \mathbf{W}^2(\hat{\mathbf{r}})(1 - \cos(\|\mathbf{r}\|), \tag{A.5}$$

where $\mathbf{r} \equiv \theta\mathbf{a}$, $\mathbf{I}$ is the identity and

$$\mathbf{W}(\hat{\mathbf{r}}) = \begin{bmatrix} 0 & -r_3 & r_2 \\ r_3 & 0 & -r_1 \\ -r_2 & r_1 & 0 \end{bmatrix}, \tag{A.6}$$

where $\hat{\mathbf{r}}$ is the unit vector associated with the angle axis parameters $\mathbf{r}$, see (A.4).

Projection. The projection operator $\mathbf{1}$ for a given vector $\mathbf{a}$ is computed by

$$\mathbf{1}[\mathbf{a}] = \mathbf{I} - \hat{\mathbf{a}} \otimes \hat{\mathbf{a}}. \tag{A.7}$$

Box product.

$$[\mathbf{a}, \mathbf{b}, \mathbf{c}] \equiv \mathbf{a} \cdot \mathbf{b} \times \mathbf{c}, \tag{A.8}$$

for vectors $\mathbf{a}, \mathbf{b}, \mathbf{c} \in \mathbb{R}^3$. See Chadwick (1999).

Fourier transform Many of the following formula can be found in Guiner (1963).

$$\mathrm{trans}[f](\mathbf{g}) \equiv \int_{-\infty}^{\infty} f(\mathbf{x}) \exp^{-2\pi i \mathbf{g}\cdot\mathbf{x}} \mathrm{d}\mathbf{x}, \tag{A.9}$$

where $f : \mathbf{x} \to \mathbb{R}$, trans[] is the Fourier transform operation, $\mathbf{g}$ is the coordinate in reciprocal space, $\mathbf{x}$ is the coordinate in the physical space, and $\mathrm{d}\mathbf{x}$ is the volume element for the coordinates $\mathbf{x}$. The integration is over all dimensions in $\mathbf{x}$.

The transform of the function 1 is given by

$$\mathrm{trans}[1](\mathbf{g}) = \delta(\mathbf{g}), \tag{A.10}$$

where δ is the Dirac-δ function.

Convolution. The convolution or Faltung between two functions $f, g : \mathbf{x} \to \mathbb{R}$ is

$$(f * g)(\mathbf{x}) \equiv \int f(\mathbf{u}) g(\mathbf{x} - \mathbf{u}) \mathrm{d}\mathbf{u}, \tag{A.11}$$

We also have the properties

$$\mathrm{trans}[f * g] = \mathrm{trans}[f]\mathrm{trans}[g], \tag{A.12}$$

$$\mathrm{trans}[fg] = \mathrm{trans}[f] * \mathrm{trans}[g]. \tag{A.13}$$

Identity matrix. When using reciprocal vectors, it is occassionally useful to express the identity in the form

$$\mathbf{I} = \mathbf{g}_i \otimes \mathbf{g}^i = \mathbf{g}^i \otimes \mathbf{g}_i. \tag{A.14}$$

Covariant/contravariant components. Given a basis $\mathbf{g}_i$, and corresponding reciprocal basis $\mathbf{g}^i$, with the property $\mathbf{g}_i \cdot \mathbf{g}^j = \delta_i^j$, any vector $\mathbf{a}$ can be resolved on this basis by

$$\mathbf{a} = (\mathbf{a} \cdot \mathbf{g}_i)\mathbf{g}^i = (\mathbf{a} \cdot \mathbf{g}^i)\mathbf{g}_i. \tag{A.15}$$

This comes from taking the identity matrix in the form (A.14) and writing out the identity $\mathbf{a} = \mathbf{I}\mathbf{a}$.

Fundamental region for crystal symmetry. Given a crystal symmetry group g_κ, the fundamental region, Q_{fund}, is defined as a distinguished element of the coset $\text{SO}(3,\mathbb{R})/g_\kappa$. For a particular $\mathbf{R} \in \text{SO}(3,\mathbb{R})$, the mapping $\text{SO}(3,\mathbb{R}) \to \text{SO}(3,\mathbb{R})/g_\kappa \to Q_{\text{fund}} : \mathbf{R}_{\text{fund}} = Q_{\text{fund}}(\mathbf{R})$ is obtained by taking the product of $\mathbf{R} \in \text{SO}(3,\mathbb{R})$ with every element in g_κ, and taking the resulting quaternion for this product with minimum first entry, say.

Axial vectors. Let $\mathbf{\Omega} \in$ skw be a skew symmetric second order tensor. Denote the associated axial vector by

$$\boldsymbol{\omega} \equiv \langle \mathbf{\Omega} \rangle, \tag{A.16}$$

where the Cartesian components of $\boldsymbol{\omega}$ are given by

$$\omega_j = \frac{1}{2}\epsilon_{ijk}\Omega_{ik}. \tag{A.17}$$

A.2 Thomson scattering

This section provides justification for the Thomson scattering factor. Here we consider a wave propagating in the $\mathbf{e}_1$ direction. According to (Guiner, 1963) we have the electric field due to an accelerated electorn as

$$\mathbf{E}(\mathbf{r}) = \left(\frac{\mu_0 e}{4\pi r}\sin\phi\right)\mathbf{a} \tag{A.18}$$

where $\mathbf{a}$ is the acceleration vector,

$$\mathbf{a} = \frac{\mathbf{E}_0 e}{m},$$

where $\mathbf{E}_0$ is the electic field vector of the propagating wave, e is the electron charge, and m is the mass of the particle, and ϕ is the angle between the position of the field test point, e.g.

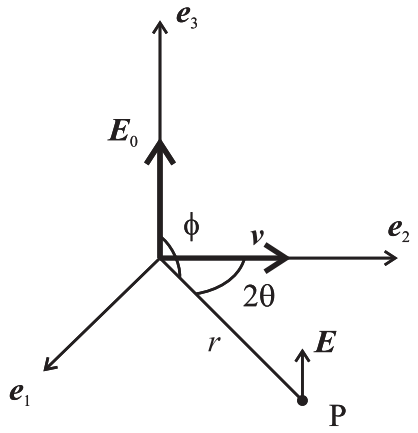

Figure A.1: Electric field vector orthogonal to the plane of the particle.

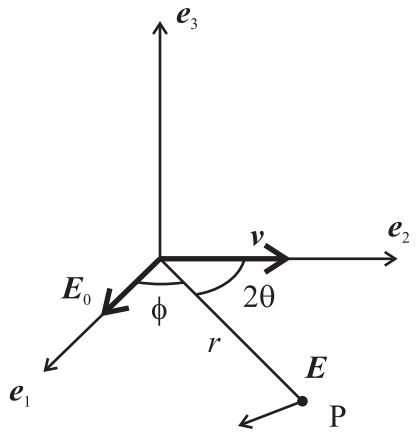

Figure A.2: Electric field vector in the plane of the particle.

$\cos\phi = \mathbf{r} \cdot \mathbf{a}$. Here $\mu_0 = 4\pi x 10^{-7}$, $e = 1.6x10^{-19}$, r is in meters and E in volts per meter. Next,

$$|\mathbf{E}| = \frac{\mu}{4\pi}\frac{e^2}{m}|\mathbf{E}_0|\frac{\sin\phi}{r}. \tag{A.19}$$

For a propagating vector with field direction $\mathbf{e}_3$, $\phi = \pi/2$ so

$$E = \frac{\mu}{4\pi}\frac{e^2}{m}\frac{|\mathbf{E}_0|}{r}. \tag{A.20}$$

The ratio of incicent to scattered intensity is equivalent to the ratio between the squared amplitutdes of the respective electic fields, so that

$$I = I_0\left(\frac{\mu_0}{4\pi}\right)^2\frac{e^4}{m^2r^2}. \tag{A.21}$$

Considering a unit surface area, the solid angle is

$$\Omega = \frac{S}{r^2} = \frac{1}{r^2},$$

so that the intensity per unit solid angle is given by

$$I = I_0 \left(\frac{\mu_0}{4\pi}\right)^2 \frac{e^4}{m^2} = r_e^2 I_0, \tag{A.22}$$

where $r_e \equiv \frac{\mu_0}{4\pi}\frac{e^2}{m}$ is called the classical radius of the electron (Guiner, 1963). For an elecric field vector in the plane of the test point, $\phi = \pi/2 - 2\theta$

$$I_{ll} = r_e^2 I_0 \cos^2 2\theta. \tag{A.23}$$

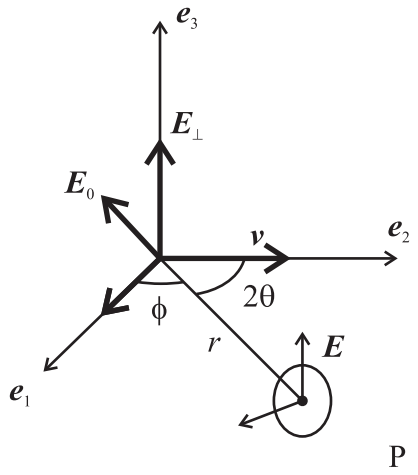

Figure A.3: Arbitrary electric field orientation.

For an arbitrary electric field, $E = E_1 e_1 + E_2 e_2$,

$$I_e = r_e^2 I_0 (E_1 + E_2 \cos^2 2\theta). \tag{A.24}$$

Then for an isotropic electric field, $E_1 = E_2 = 1/2$ so

$$I_e = r_e^2 I_0 \left(\frac{1 + \cos^2 2\theta}{2}\right). \tag{A.25}$$

So I_e is the energy per unit solid angle per second by one electron in a beam of power I_0 per square meter. The scattered beam has intensity I_e/r^2.

A.3 Derivation of Cartesian representation for crystallographic unit cell

In this section we compute the details of the derivation of the structural map reported in Equation (3.223). See also Neustadt et al. (1968) for an alternative approach. We pick up the development from Equation (3.220). Recall we adopt the convention for the mapped cell edges as

$$\mathbf{a} = a\mathbf{e}_1, \quad \mathbf{b} = b\mathbf{e}_r(\gamma; \mathbf{e}_1, \mathbf{e}_2), \quad \mathbf{c} = c\hat{\mathbf{c}}(\alpha, \beta, \gamma)$$

where from the definition of the internal angles α, β we have $\hat{\mathbf{c}} \cdot \hat{\mathbf{a}} \equiv \cos\beta$, $\hat{\mathbf{c}} \cdot \hat{\mathbf{b}} \equiv \cos\alpha$. We require an expression for $\mathbf{c}$, hence $\hat{\mathbf{c}}$, on the Cartesian basis $\mathbf{e}_1, \mathbf{e}_2, \mathbf{e}_3$. To achieve this, we find it useful to consider the intermediate step of constructing a basis which is reciprocal to that defined by

$$\mathbf{h}_1 = \mathbf{e}_1, \quad \mathbf{h}_2 = \mathbf{e}_r(\gamma; \mathbf{e}_1, \mathbf{e}_2), \quad \mathbf{h}_3 = \mathbf{e}_3. \tag{A.26}$$

Note that $\mathbf{h}_1 = \hat{\mathbf{a}}$ and $\mathbf{h}_2 = \hat{\mathbf{b}}$. Denote the corresponding reciprocal basis by $\mathbf{h}_i^*$. Next we making use of the result of Equation (A.14), we can write

$$\hat{\mathbf{c}} = \mathbf{I}\hat{\mathbf{c}} = (\hat{\mathbf{c}} \cdot \mathbf{h}_i)\, \mathbf{h}_i^* = (\hat{\mathbf{c}} \cdot \mathbf{h}_i^*)\, \mathbf{h}_i, \tag{A.27}$$

relations which hold for any vector. Expanding Equation $(A.27)_2$, we have the representation

$$\begin{aligned} \hat{\mathbf{c}} &= (\hat{\mathbf{c}} \cdot \mathbf{h}_1)\, \mathbf{h}_1^* + (\hat{\mathbf{c}} \cdot \mathbf{h}_2)\, \mathbf{h}_2^* + (\hat{\mathbf{c}} \cdot \mathbf{h}_3)\, \mathbf{h}_3^* \\ &= \cos\beta \mathbf{h}_1^* + \cos\alpha \mathbf{h}_2^* + \hat{c}_3 \mathbf{h}_3^*, \end{aligned} \tag{A.28}$$

where we have used $\mathbf{h}_1 = \hat{\mathbf{a}}$ and $\mathbf{h}_2 = \hat{\mathbf{b}}$ along with the definition of the unit cell angles β, α. The unknown component $\hat{c}_3$ can be obtained from the unit vector property, $|\hat{\mathbf{c}}| = 1$, which we now show. Using Equation (A.28) we have

$$1 = |\hat{\mathbf{c}}|^2 = \cos^2\beta\, (\mathbf{h}_1^* \cdot \mathbf{h}_1^*) + \cos^2\alpha\, (\mathbf{h}_2^* \cdot \mathbf{h}_2^*) + \hat{c}_3^2 + 2\cos\beta\cos\alpha\, (\mathbf{h}_1^* \cdot \mathbf{h}_2^*)\,. \tag{A.29}$$

where we have used $\mathbf{h}_1^* \cdot \mathbf{h}_3^* = \mathbf{h}_2^* \cdot \mathbf{h}_3^* = 0$, which will be justified shortly. After some algebra, we obtain

$$\hat{c}_3 = \left(1 - \cos^2\beta\, (\mathbf{h}_1^* \cdot \mathbf{h}_1^*) - \cos^2\alpha\, (\mathbf{h}_2^* \cdot \mathbf{h}_2^*) - 2\cos\beta\cos\alpha\, (\mathbf{h}_1^* \cdot \mathbf{h}_2^*)\right)^{1/2} \tag{A.30}$$

We now construct the reciprocal basis $\mathbf{h}_i^*$ to complete the specification of $\mathbf{c}$. Using $(A.27)_3$ applied to $\mathbf{h}_i^*$ we have

$$\mathbf{h}_i^* = \left(\mathbf{h}_i^* \cdot \mathbf{h}_j^*\right) \mathbf{h}_j = h_{ij}^* \mathbf{h}_j \tag{A.31}$$

where $h_{ij}^* = \mathbf{h}_i^* \cdot \mathbf{h}_j^*$ is the reciprocal metric tensor. It is related to the metric tensor $h_{ij} = \mathbf{h}_i \cdot \mathbf{h}_j$ by the relation $[h_{ij}^*] = [h_{ij}]^{-1}$, where the bracket notation is used to emphasize matrix representations. To see this, use the sequence $\delta_{ik} = \mathbf{h}_i^* \cdot \mathbf{h}_k = h_{ij}^* \mathbf{h}_j \cdot \mathbf{h}_k = h_{ij}^* h_{jk}$. Then by

the uniqueness of matrix inverses, $[h^*_{ij}] \equiv [h_{ij}]^{-1}$. Next we explicitly compute the metric h_{ij} in matrix form as

$$[h_{ij}] = \begin{bmatrix} \mathbf{h}_1 \cdot \mathbf{h}_1 & \mathbf{h}_1 \cdot \mathbf{h}_2 & \mathbf{h}_1 \cdot \mathbf{h}_3 \\ \mathbf{h}_2 \cdot \mathbf{h}_1 & \mathbf{h}_2 \cdot \mathbf{h}_2 & \mathbf{h}_2 \cdot \mathbf{h}_3 \\ \mathbf{h}_3 \cdot \mathbf{h}_1 & \mathbf{h}_3 \cdot \mathbf{h}_2 & \mathbf{h}_3 \cdot \mathbf{h}_3 \end{bmatrix} = \begin{bmatrix} 1 & \cos\gamma & 0 \\ \cos\gamma & 1 & 0 \\ 0 & 0 & 1 \end{bmatrix}, \tag{A.32}$$

where we have used Equations (A.26) and (3.221). The reciprocal metric h^*_{ij} is obtained by taking the matrix inverse, giving

$$[h^*_{ij}] = [h_{ij}]^{-1} = \begin{bmatrix} 1/(1-\cos^2\gamma) & -\cos\gamma/(1-\cos^2\gamma) & 0 \\ -\cos\gamma/(1-\cos^2\gamma) & 1/(1-\cos^2\gamma) & 0 \\ 0 & 0 & 1 \end{bmatrix}. \tag{A.33}$$

Use of the entries of Equation (A.33) in Equation (A.31) with Equation (A.26) gives the reciprocal bases $\{\mathbf{h}^*_i\}$ as

$$\mathbf{h}^*_1 = \left(\frac{1}{1-\cos^2\gamma}\right)\mathbf{e}_1 + \left(\frac{-\cos\gamma}{1-\cos^2\gamma}\right)\mathbf{e}_r(\gamma;\mathbf{e}_1,\mathbf{e}_2) \tag{A.34}$$

$$\mathbf{h}^*_2 = \left(\frac{-\cos\gamma}{1-\cos^2\gamma}\right)\mathbf{e}_1 + \left(\frac{1}{1-\cos^2\gamma}\right)\mathbf{e}_r(\gamma;\mathbf{e}_1,\mathbf{e}_2) \tag{A.35}$$

$$\mathbf{h}^*_3 = \mathbf{e}_3. \tag{A.36}$$

Now to complete Equation (A.30) we require

$$\mathbf{h}^*_1 \cdot \mathbf{h}^*_2 = h^*_{12} = \frac{-\cos\gamma}{1-\cos^2\gamma}, \quad \mathbf{h}^*_1 \cdot \mathbf{h}^*_1, \mathbf{h}^*_2 \cdot \mathbf{h}^*_2 = h^*_{11}, h^*_{22} = \frac{1}{1-\cos^2\gamma}. \tag{A.37}$$

where we have used Equation (A.33). These results simplify Equation (A.30) to

$$\hat{c}_3 = \frac{1}{\sin\gamma}\left(1 + 2\cos\alpha\cos\beta\cos\gamma - \cos^2\alpha - \cos^2\beta - \cos^2\gamma\right)^{1/2}. \tag{A.38}$$

Finally, we have

$$\mathbf{c} = c\hat{\mathbf{c}} = c\cos\beta\mathbf{h}^*_1 + c\cos\alpha\mathbf{h}^*_2 + c\hat{c}_3\mathbf{h}^*_3, \tag{A.39}$$

where $\hat{c}_3$ is given by Equation (A.38).

We now are able to compute $\mathbf{H}_\mathrm{s}$ from Equation (3.222). Recall that

$$\mathbf{H}_\mathrm{s} = \mathbf{a}\otimes\mathbf{e}_1 + \mathbf{b}\otimes\mathbf{e}_2 + \mathbf{c}\otimes\mathbf{e}_3.$$

We compute the matrix representation of $\mathbf{H}_\mathrm{s}$ from $H_{ij} = \mathbf{e}_i \cdot \mathbf{H}_\mathrm{s}\mathbf{e}_j$ by using Equations (A.34) - (A.36) in Equation (A.39), along with Equations (3.218),(3.219) and (3.221). We obtain

$$\mathbf{H}_\mathrm{s} = \begin{bmatrix} a & b\cos\gamma & c\cos\beta \\ 0 & b\sin\gamma & c(\cos\alpha - \cos\beta\cos\gamma)/\sin\gamma \\ 0 & 0 & c\left(1 + 2\cos\alpha\cos\beta\cos\gamma - \cos^2\alpha - \cos^2\beta - \cos^2\gamma\right)^{1/2}/\sin\gamma \end{bmatrix}$$

This matches accepted results from the literature (Bernier et al., 2011).

Table A.1: FCC Slip systems Anand1996,Anand1997

α	$[\mathbf{n}_0^\alpha]$	$[\mathbf{m}_0^\alpha]$
1	1,1,1	1,$\bar{1}$,0
2	1,1,1	$\bar{1}$,0,1
3	1,1,1	0,1,$\bar{1}$
4	$\bar{1}$,1,1	1,0,1
5	$\bar{1}$,1,1	$\bar{1}$,$\bar{1}$,0
6	$\bar{1}$,1,1	0,1,$\bar{1}$
7	1,$\bar{1}$,1	$\bar{1}$,0,1
8	1,$\bar{1}$,1	0,$\bar{1}$,$\bar{1}$
9	1,$\bar{1}$,1	1,1,0
10	$\bar{1}$,$\bar{1}$,1	$\bar{1}$,1,0
11	$\bar{1}$,$\bar{1}$,1	1,0,1
12	$\bar{1}$,$\bar{1}$,1	0,$\bar{1}$,$\bar{1}$

Table A.2: BCC Slip systems Anand1997

i	$[\mathbf{n}_0^i]$	$[\mathbf{m}_0^i]$	i	$[\mathbf{n}_0^i]$	$[\mathbf{m}_0^i]$
1	1,1,0	1,$\bar{1}$,1	13	2,1,$\bar{1}$	1,$\bar{1}$,1
2	0,1,1	1,$\bar{1}$,1	14	1,1,2	1,1,$\bar{1}$
3	1,1,0	$\bar{1}$,1,1	15	$\bar{1}$,1,2	1,$\bar{1}$,1
4	0,1,1	1,1,$\bar{1}$	16	1,$\bar{1}$,2	$\bar{1}$,1,1
5	0,1,1	1,$\bar{1}$,1	17	1,$\bar{2}$,1	1,1,1
6	1,0,1	1,1,$\bar{1}$	18	1,2,1	1,$\bar{1}$,1
7	1,0,1	$\bar{1}$,1,1	19	$\bar{1}$,2,1	1,1,$\bar{1}$
8	$\bar{1}$,1,0	1,1,1	20	1,$\bar{2}$,1	1,1,1
9	$\bar{1}$,1,0	1,1,$\bar{1}$	21	1,2,$\bar{1}$	$\bar{1}$,1,1
10	$\bar{1}$,0,1	1,1,1	22	2,1,1	$\bar{1}$,1,1
11	$\bar{1}$,0,1	1,$\bar{1}$,1	23	$\bar{2}$,1,1	1,1,1
12	0,$\bar{1}$,1	1,1,1	24	2,$\bar{1}$,1	1,1,$\bar{1}$

A.4 Integration

In this section is reviewed the technology to integrate over a discretized grid. We pick up the development from §2.4.2.1. Consider the position field $\mathbf{x}(\mathbf{X})$. We discretize the material domain with nodal points $\mathbf{X}^{(i)}$. We can regard this field as the sum of basis elements of the form

$$\mathbf{x}(\mathbf{X}) = \sum_{i=1}^{N} \mathbf{x}^{(i)} \Phi_{(i)}(\mathbf{X}), \tag{A.40}$$

where N is the number of nodes in the discretization and where the basis functions Φ have the property

$$\Phi_{(i)}(\mathbf{X}^{(j)}) = \delta_i^j. \tag{A.41}$$

This is the natural example in mechanics textbooks, but the form of (A.40) holds for any field over material coordinates, $f(\mathbf{X}) : \mathbb{R}^3 \to R$ through

$$f(\mathbf{X}) = \sum_{i=1}^{N} f^{(i)} \Phi_{(i)}(\mathbf{X}). \tag{A.42}$$

We can use this discretization method to perform numerical integrations in a convenient fashion. Consider integration on the material domain, required in §2.4.2.1. For convenience, denote this material domain by β. For each local zone in β(highlighted in Figure 2.13) we can define consider a reference region $\eta, \xi \in [-1, 1] \times [-1, 1]$, which maps to $\beta$by a function of the form (A.40), so that over a zone,

$$\mathbf{X}(\eta, \xi) = \sum_{i=0}^{3} \mathbf{X}^{(i)} \Phi_{(i)}(\eta, \xi), \tag{A.43}$$

with, to be explicit,

$$\begin{array}{llll} \Phi_0(\eta = 1, \xi = -1) & = 1 & \Phi_1(\eta = 1, \xi = -1) & = 0 \\ \Phi_0(\eta = 1, \xi = 1) & = 0 & \Phi_1(\eta = 1, \xi = 1) & = 1 \\ \Phi_0(\eta = -1, \xi = 1) & = 0 & \Phi_1(\eta = -1, \xi = 1) & = 0 \\ \Phi_0(\eta = -1, \xi = -1) & = 0 & \Phi_1(\eta = -1, \xi = -1) & = 0 \end{array} \tag{A.44}$$

$$\begin{array}{llll} \Phi_2(\eta = 1, \xi = -1) & = 0 & \Phi_3(\eta = 1, \xi = -1) & = 0 \\ \Phi_2(\eta = 1, \xi = 1) & = 0 & \Phi_3(\eta = 1, \xi = 1) & = 0 \\ \Phi_2(\eta = -1, \xi = 1) & = 1 & \Phi_3(\eta = -1, \xi = 1) & = 0 \\ \Phi_2(\eta = -1, \xi = -1) & = 0 & \Phi_3(\eta = -1, \xi = -1) & = 1 \end{array} . \tag{A.45}$$

The general form the basis functions Φ is then

$$\Phi(\eta, \xi) = c_1 + c_2\eta + c_3\xi + c_4\eta\xi. \tag{A.46}$$

Each of the set of equations in (A.44), (A.45) can be used with (A.46) in order to determine the representations for $basisfunc_{(i)}, i = 0, 1, 2, 3$.

Area computation In (2.255) the area of the material zones is required. To compute this, we need

$$\begin{aligned} A &= \int_{\Omega} \mathrm{d}\mathbf{X} \\ &= \int_{\mathbf{X}^{-1}\Omega} \mathbf{X}^{*}(\mathrm{d}\mathbf{X}) \\ &= \int_{-1}^{1}\int_{-1}^{1} (\det \nabla \mathbf{X}) \mathrm{d}\eta \wedge \mathrm{d}\xi, \end{aligned} \tag{A.47}$$

where $\mathbf{X}^*$ denotes the pullback to η, ξ of the volume element $\mathrm{d}\mathbf{X} = \mathrm{d}X_1 \wedge \mathrm{d}X_2$. Using (A.43), we can compute

$$\nabla \mathbf{X} = \sum_{i=0}^{3} \mathbf{X}^{(i)} \otimes \nabla \Phi_{(i)} \tag{A.48}$$

or in matrix form

$$\nabla \mathbf{X} = \begin{bmatrix} \partial \mathbf{X}_1/\partial\eta & \partial \mathbf{X}_1/\partial\xi \\ \partial \mathbf{X}_2/\partial\eta & \partial \mathbf{X}_2/\partial\xi \end{bmatrix}, \tag{A.49}$$

with the shorthand $\mathbf{X}_i \equiv \mathbf{X} \cdot \mathbf{e}_i$. To be explicit, again using (A.43) in (A.49) gives

$$\begin{aligned} \partial \mathbf{X}_1/\partial\eta &= \textstyle\sum_{i=0}^{3} \mathbf{X}_1^{(i)} \partial \Phi_{(i)}/\partial\eta \\ \partial \mathbf{X}_1/\partial\xi &= \textstyle\sum_{i=0}^{3} \mathbf{X}_1^{(i)} \partial \Phi_{(i)}/\partial\xi \\ \partial \mathbf{X}_2/\partial\eta &= \textstyle\sum_{i=0}^{3} \mathbf{X}_2^{(i)} \partial \Phi_{(i)}/\partial\eta \\ \partial \mathbf{X}_2/\partial\xi &= \textstyle\sum_{i=0}^{3} \mathbf{X}_2^{(i)} \partial \Phi_{(i)}/\partial\xi \end{aligned}, \tag{A.50}$$

with $\Phi_{(i)}$ given by the general form (A.46) with solution for the parameters c_1, c_2, c_3, c_4 based on the conditions (A.44), (A.45).

The integration in (A.47) is carried out using Gaussian quadrature; for the linear functions employed here we simply obtain from (A.47)

$$A = \int_{-1}^{1}\int_{-1}^{1} (\det \nabla \mathbf{X}) \mathrm{d}\eta \wedge \mathrm{d}\xi = 4 \cdot (\det \nabla \mathbf{X})(0,0), \tag{A.51}$$

where $(\det \nabla \mathbf{X})(0,0)$ denotes evaluation of the function $\det \nabla \mathbf{X}$ at $\eta, \xi = 0, 0$.

In §2.4.2.1 we arrived at nodal values of $\nabla \times \mathbf{K}^{-1}$ on the material reference grid, $\mathbf{X}^{(i)}$. We require an estimate for $\nabla \times \mathbf{K}^{-1}$ for the zones, in order to use (2.16) to get the true dislocation content. To do this we proceed as before, with the discretization

$$\nabla \times \mathbf{K}^{-1}(\mathbf{X}) = \sum_{i=0}^{3} (\nabla \times \mathbf{K}^{-1})^{(i)} \Phi_{(i)}(\mathbf{X}). \tag{A.52}$$

Then, integrating over a zone by pulling back to η, ξ and using first order Gaussian quadrature gives

$$\begin{aligned}
\nabla \times \mathbf{K}_{\text{zone}}^{-1} &= \frac{1}{A} \int_{\Omega} \nabla \times \mathbf{K}^{-1}(\mathbf{X}) \mathrm{d}\mathbf{X} \\
&= \frac{1}{A} \int_{-1}^{1} \int_{-1}^{1} \sum_{i=0}^{3} (\nabla \times \mathbf{K}^{-1})^{(i)} \Phi_{(i)}(\eta, \xi) (\det \nabla \mathbf{X}) \mathrm{d}\eta \wedge \mathrm{d}\xi \\
&= \frac{4}{A} \left(\sum_{i=0}^{3} (\nabla \times \mathbf{K}^{-1})^{(i)} \Phi_{(i)}(0,0) \right) (\det \nabla \mathbf{X})(0,0) \qquad \text{(A.53)} \\
&= \sum_{i=0}^{3} (\nabla \times \mathbf{K}^{-1})^{(i)} \Phi_{(i)}(0,0) \qquad \text{(A.54)} \\
&= \frac{1}{4} \sum_{i=0}^{3} (\nabla \times \mathbf{K}^{-1})^{(i)}. \qquad \text{(A.55)}
\end{aligned}$$

That is, the averaged zonal value is the average of the nodal values. The last result, (A.55), comes from calculation of the c_1 coefficient for each of $\Phi_{(i)}$, which turns out to evaluate to $1/4$ for each $\Phi_{(i)}, i = 0, 1, 2, 3$.

A.5 Constitutive functions for hexagonal crystals

In this section we consider similar exposition as done in §2.3.3.1, but we look at the hexagonal symmetries. These crystals are characterized by the presence of the rotations $\mathbf{S}_1, \mathbf{S}_2 \in g_\kappa$, where $\mathbf{S}_i = \hat{\mathbf{R}}(\mathbf{e}_3, 2\pi i/3), \quad i = 1, 2$. The analysis used previously in §2.3.3.1 is complicated by the incorporation of these rotations, and so deserves the special treatment made here.

From our experience, the hexagonal symmetries are the most difficult to generate polynomial constitutive functions for. For a scalar function of a single symmetric tensor argument, one can follow the examples in Green and Adkins (1970, p. 20). We found that the incorporation of more functional arguments required a slightly more careful and systematic procedure than was evident in Green and Adkins (1970). As our example, we consider constitutive functions of the form $\mathbf{\Omega} = \mathbf{\Omega}(\mathbf{A})$. Recall from Table 2.1 that this required generating a scalar valued function

$$F(\mathbf{A}, \mathbf{v}) = F\left(A_{11}, A_{22}, A_{33}, A_{23}, A_{13}, A_{12}, v_1, v_2, v_3\right), \tag{A.56}$$

where $\mathbf{A}$ is a symmetric tensor and $\mathbf{v}$ is an axial vector. The spin $\mathbf{\Omega}(\mathbf{A})$ is then obtained from

$$\mathbf{\Omega}(\mathbf{A}) = \epsilon_{ijk} \left.\frac{\partial F}{\partial v_j}\right|_{\mathbf{v}=\mathbf{0}} \mathbf{e}_i \otimes \mathbf{e}_k, \tag{A.57}$$

where F is invariant under hexagonal symmetry.

Before beginning the analysis, let us define the objectives and restate additional information. Our target symmetry group is the dihexagonal-dipyramidal group, the maximum symmetry group in the hexagonal system. The elements are

$$g_\kappa^{\text{dihexagonal-dipyramidal}} = \mathbf{I}, \mathbf{S}_1, \mathbf{S}_2, \mathbf{C}, \mathbf{C}\mathbf{S}_1, \mathbf{C}\mathbf{S}_2, \mathbf{R}_1, \mathbf{R}_1\mathbf{S}_1, \mathbf{R}_1\mathbf{S}_2, \mathbf{R}_2, \mathbf{R}_2\mathbf{S}_1, \mathbf{R}_2\mathbf{S}_2, \mathbf{R}_3, \tag{A.58}$$

$$\mathbf{R}_3\mathbf{S}_1, \mathbf{R}_3\mathbf{S}_2, \mathbf{D}_1, \mathbf{D}_1\mathbf{S}_1, \mathbf{D}_1\mathbf{S}_2, \mathbf{D}_2, \mathbf{D}_2\mathbf{S}_1, \mathbf{D}_2\mathbf{S}_2, \mathbf{D}_3, \mathbf{D}_3\mathbf{S}_1, \mathbf{D}_3\mathbf{S}_2, \tag{A.59}$$

where all rotations $\mathbf{R}_i, \mathbf{D}_i, \mathbf{C}$ were previously defined in the text after Equation (2.140). For use with (A.57) the function (A.56) is restricted to be only (up to) linear order in $\mathbf{v}$, and up to cubic order in $\mathbf{A}$, as was done for the cubic crystals.

In order to apply the technique in Green and Adkins (1970), it turns out to be useful to first restrict constitutive functions based on the elements $\mathbf{S}_1, \mathbf{S}_2$, instead of applying, for instance, (2.146) when $\mathbf{R}_1 \in g_\kappa$. Therefore the symmetry group we start with is

$$g_\kappa^{\text{trigonal-pyramidal}} = \mathbf{I}, \mathbf{S}_1, \mathbf{S}_2, \tag{A.60}$$

which defines the trigonal-pyramidal class. We now start the procedure considering (A.60) and building up to (A.59).

Constitutive reductions. By executing the rotations $\mathbf{S}_1$, $\mathbf{S}_2$, we can see profitable reformulation of (A.56) by defining

$$y_1 = A_{11} \qquad y_2 = \frac{1}{4}A_{11} - \frac{\sqrt{3}}{2}A_{12} + \frac{3}{4}A_{22} \qquad y_3 = \frac{1}{4}A_{11} + \frac{\sqrt{3}}{2}A_{12} + \frac{3}{4}A_{22} \tag{A.61}$$

and

$$z_1 = A_{13} \qquad z_2 = -\frac{1}{2}A_{13} + \frac{\sqrt{3}}{2}A_{23} \qquad z_3 = -\frac{1}{2}A_{13} - \frac{\sqrt{3}}{2}A_{23}, \tag{A.62}$$

as defined in Green and Adkins (1970, eq. 1.12.2). For the present consideration, we require the additional definitions

$$w_1 = v_1 \qquad w_2 = -\frac{1}{2}v_1 + \frac{\sqrt{3}}{2}v_2 \qquad w_3 = -\frac{1}{2}v_1 - \frac{\sqrt{3}}{2}v_1. \tag{A.63}$$

Then using (A.61)-(A.63) with (A.56) we have the equivalent reformulation

$$F = F\left(A_{11}, A_{22}, A_{33}, A_{23}, A_{13}, A_{12}, v_1, v_2, v_3\right) = F\left(y_1, y_2, y_3, z_1, z_2, z_3, w_1, w_2, w_3, A_{33}, v_3\right). \tag{A.64}$$

The benefit of these redefinitions is that under $\mathbf{S}_1, \mathbf{S}_2$ we have the transformations

$$\begin{array}{l} F = F\left(y_1, y_2, y_3, z_1, z_2, z_3, w_1, w_2, w_3, A_{33}, v_3\right) \\ = F\left(y_3, y_1, y_2, z_3, z_1, z_2, w_3, w_1, w_2, A_{33}, v_3\right) \\ = F\left(y_2, y_3, y_1, z_2, z_3, z_1, w_2, w_3, w_1, A_{33}, v_3\right) \end{array}, \tag{A.65}$$

which satisfies the requirements of Theorem 6 and Theorem 4, giving the integrity elements

$$y_1 + y_2 + y_3, y_1y_2 + y_2y_3 + y_1y_3, y_1y_2y_3, \text{etc.} \tag{A.66}$$

Therefore, we have the expression

$$\begin{array}{l} F = F(y_1 + y_2 + y_3, y_1y_2 + y_2y_3 + y_1y_3, y_1y_2y_3, \\ y_1z_1 + y_2z_2 + y_3z_3, y_1\left(z_2 - z_3\right) + y_2\left(z_3 - z_1\right) + y_3\left(z_1 - z_2\right), [...] \\ y_1z_1w_1 + y_2z_2w_2 + y_3z_3w_3, y_1z_1\left(w_2 - w_3\right) + y_2z_2\left(w_3 - w_1\right) + y_3z_3\left(w_1 - w_2\right), A_{33}, v_3), \end{array} \tag{A.67}$$

where [...] denotes all the terms not explicitly shown, but which are prescribed by Theorem 6.

Now, to get to the class (A.59) from the invariant expression (A.67), we consider the effect of each of the elements in $g_\kappa^{\text{dihexagonal-dipyramidal}}$ on the basis elements of (A.67). The main operation which will cull elements is when a basis element changes sign; for example, due to one of the reflections $\mathbf{R}_1, \mathbf{R}_2, \mathbf{R}_3 \in g_\kappa^{\text{dihexagonal-dipyramidal}}$. Then Theorem 1 applies to the terms which change sign, and this may cause the invariant to be eliminated at the order of expansion we are considering.

By using this process for each the hexagonal point groups (hexagonal-dipyramidal, ditrigonal-dipyramidal, etc.), we can get any desired constitutive equation. But here, recall we are

interested in the dihexagonal-dipyramidal point group. After checking all the elements of (A.67), the term

$$i_1 = z_1 (w_2 - w_3) + z_2 (w_3 - w_1) + z_3 (w_1 - w_2) \tag{A.68}$$

is invariant under $g_\kappa^{\text{dihexagonal-dipyramidal}}$. This is the lowest order contribution to (A.56), with linear dependence on $\mathbf{A}$. In a similar fashion we obtain the quadratic order element

$$i_2 = y_1 z_1 (w_2 - w_3) + y_2 z_2 (w_3 - w_1) + y_3 z_3 (w_1 - w_2), \tag{A.69}$$

which is found to be invariant under $g_\kappa^{\text{dihexagonal-dipyramidal}}$. For the cubic order terms consider, for instance, the action of $\mathbf{R}_1$, which gives the transformations (2.146). This operation switches the sign on the axial component

$$\bar{v}_3 = -v_3 \tag{A.70}$$

as well as the following terms from (A.67):

$$\begin{array}{l} \bar{y}_2 \bar{y}_3 (\bar{y}_2 - \bar{y}_3) + \bar{y}_3 \bar{y}_1 (\bar{y}_3 - \bar{y}_1) + \bar{y}_1 \bar{y}_2 (\bar{y}_1 - \bar{y}_2) = \\ - (y_2 y_3 (y_2 - y_3) + y_3 y_1 (y_3 - y_1) + y_1 y_2 (y_1 - y_2)), \end{array} \tag{A.71}$$

and

$$\begin{array}{l} \bar{z}_2 \bar{z}_3 (\bar{y}_2 - \bar{y}_3) + \bar{z}_3 \bar{z}_1 (\bar{y}_3 - \bar{y}_1) + \bar{z}_1 \bar{z}_2 (\bar{y}_1 - \bar{y}_2) \\ = - (z_2 z_3 (y_2 - y_3) + z_3 z_1 (y_3 - y_1) + z_1 z_2 (y_1 - y_2)). \end{array} \tag{A.72}$$

Therefore, using Theorem 1, we have the cubic order integrity elements

$$\begin{array}{l} i_3 = v_3 [y_2 y_3 (y_2 - y_3) + y_3 y_1 (y_3 - y_1) + y_1 y_2 (y_1 - y_2)] \\ i_4 = v_3 [z_2 z_3 (y_2 - y_3) + z_3 z_1 (y_3 - y_1) + z_1 z_2 (y_1 - y_2)]. \end{array} \tag{A.73}$$

As a side note, transverse isotropy is the same as hexagonal for the low order terms. Constitutive equations are easier to obtain for transverse isotropy since one considers using the structural tensor $\mathbf{e}_3$ and then following the prescription of Liu (1982) to achieve the representation. However the element i_3 of (A.73) is not picked up by considering transverse isotropy, therefore the procedure in this section is required to get a complete integrity basis for hexagonal crystals up to cubic order.

Polynomial reconstruction. We now have the necessary terms for $F(\mathbf{A}, \mathbf{v})$ which multiply $\mathbf{v}$ linearly. These terms serve as the generators of the skew tensors in the language of Liu (2002, Ch. 4). In order to get the proper cubic expansion however we need to obtain terms of $\mathbf{A}$ which do not multiply $\mathbf{v}$, up to quadratic order. After considering the action of each element of $g_\kappa^{\text{dihexagonal-dipyramidal}}$ in (A.67), we find we must retain the following elements:

$$A_{33}, \quad y_1 + y_2 + y_3, \quad y_1 y_2 + y_2 y_3 + y_3 y_1, \quad z_1 z_2 + z_2 z_3 + z_3 z_1. \tag{A.74}$$

Using (A.61), (A.62) and removing numerical factors, these elements are the familiar ones from (3.365),

$$A_{33}, A_{11}+A_{22}, A_{11}A_{22}-A_{12}^2, A_{13}^2+A_{23}^2. \tag{A.75}$$

Similarly, the other elements are rewritten as

$$i_1 = z_1\left(w_2-w_3\right)+z_2\left(w_3-w_1\right)+z_3\left(w_1-w_2\right) = A_{13}v_2 - A_{23}v_1, \tag{A.76}$$

$$\begin{aligned} i_2 = {} & y_1z_1\left(w_2-w_3\right)+y_2z_2\left(w_3-w_1\right)+y_3z_3\left(w_1-w_2\right) = \\ & -2A_{12}A_{13}v_1 - A_{11}A_{23}v_1 - 3A_{22}A_{23}v_1 + 3A_{11}A_{13}v_2 + A_{13}A_{22}v_2 + 2A_{12}A_{23}v_2, \end{aligned} \tag{A.77}$$

$$\begin{aligned} i_3 = {} & v_3\left[y_2y_3\left(y_2-y_3\right)+y_3y_1\left(y_3-y_1\right)+y_1y_2\left(y_1-y_2\right)\right] = \\ & -3A_{11}^2A_{12}v_3 + 4A_{12}^3v_3 + 6A_{11}A_{12}A_{22}v_3 - 3A_{12}A_{22}^2v_3, \end{aligned} \tag{A.78}$$

and

$$\begin{aligned} i_4 = {} & v_3\left[z_2z_3\left(y_2-y_3\right)+z_3z_1\left(y_3-y_1\right)+z_1z_2\left(y_1-y_2\right)\right] = \\ & -A_{12}A_{13}^2v_3 + A_{11}A_{13}A_{23}v_3 - A_{13}A_{22}A_{23}v_3 + A_{12}A_{23}^2v_3. \end{aligned} \tag{A.79}$$

These substitutions make the full polynomial expansion for (A.56) easier to see. Following (3.365), denote

$$\begin{array}{ll} x_1 = A_{11}+A_{22} & y_1^* = A_{11}A_{22}-A_{12}^2 \\ x_2 = A_{33} & y_2^* = A_{13}^2+A_{23}^2. \end{array} \tag{A.80}$$

Then the expansion for (A.56) for dihexagonal-dipyramidal symmetry is

$$F(\mathbf{A},\mathbf{v}) = a_1i_1 + \left(\sum_{j=1}^{2}\sum_{k=1}^{2}b_{jk}x_jx_k\right)i_1 + \left(\sum_{j=1}^{2}c_jy_j^*\right)i_1 + \left(\sum_{j=1}^{2}k_jx_j\right)i_2 + l_1i_3 + l_2i_4, \tag{A.81}$$

which has $|\{a_i\}| = 1$ constant at linear order and $|\{b_{jk}\}| + |\{c_j\}| + |\{k_j\}| + |\{l_j\}| = 3 + 2 + 2 + 2 = 9$ constants at third order, for a total of 10 constants. The linear order term, i_1, represents an axial vector in the basal plane (span $\mathbf{e}_1, \mathbf{e}_2$). Therefore in order to get lattice reorientation from prismatic slip, we need to go to the third order, and utilize the full expansion (A.81). Experimental measurements then dictate which constants can be profitably removed or retained, without affecting the predictions of the model.

A.6 Additional numerical results

A.6.1 Localization bands

This set of figures look at different mesh resolutions at fixed grain orientation, see §2.4.2.3.2 for a description of the boundary conditions and other details. The figure sequence are plots of $\|\boldsymbol{\xi}\|^2, \|\mathbf{K}\|$. This set of figures is with hardening $A_3 = 0.1$, $\theta_0 = 0$.

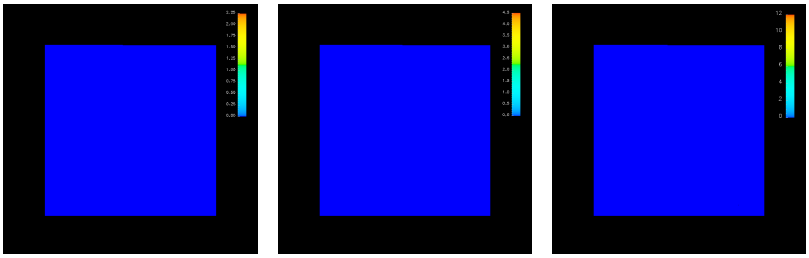

(a) 12×12 mesh (b) 24×24 mesh (c) 48×48 mesh

Figure A.4: Mesh resolution comparison for axial extension with local weakening. $\|\boldsymbol{\xi}\|^2$ $A_3 = 0.1$, $\nu = 0.0003$, hardeningmode=1, $\theta_0 = 0$, sequence number =0

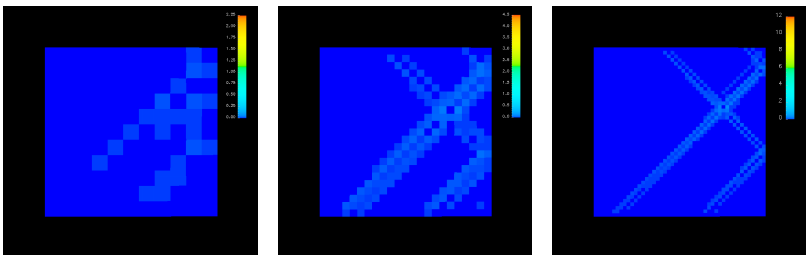

(a) 12×12 mesh (b) 24×24 mesh (c) 48×48 mesh

Figure A.5: Mesh resolution comparison for axial extension with local weakening. $\|\boldsymbol{\xi}\|^2$ $A_3 = 0.1$, $\nu = 0.0003$, hardeningmode=1, $\theta_0 = 0$, sequence number =1

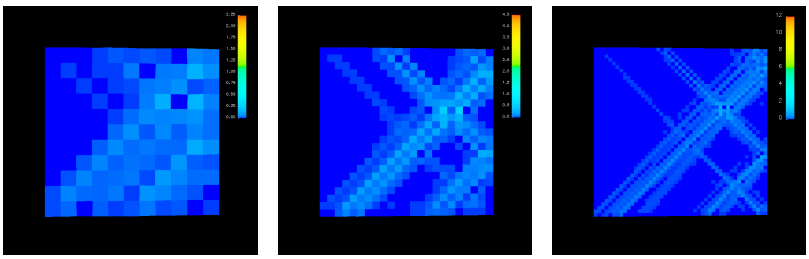

(a) 12×12 mesh (b) 24×24 mesh (c) 48×48 mesh

Figure A.6: Mesh resolution comparison for axial extension with local weakening. $\|\boldsymbol{\xi}\|^2$ $A_3 = 0.1$, $\nu = 0.0003$, hardeningmode=1, $\theta_0 = 0$, sequence number =2

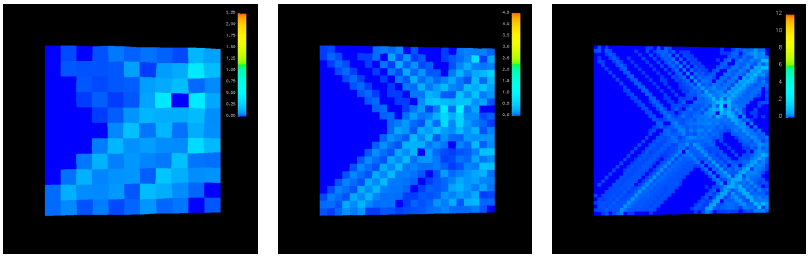

(a) 12×12 mesh (b) 24×24 mesh (c) 48×48 mesh

Figure A.7: Mesh resolution comparison for axial extension with local weakening. $\|\boldsymbol{\xi}\|^2$ $A_3 = 0.1$, $\nu = 0.0003$, hardeningmode=1, $\theta_0 = 0$, sequence number =3

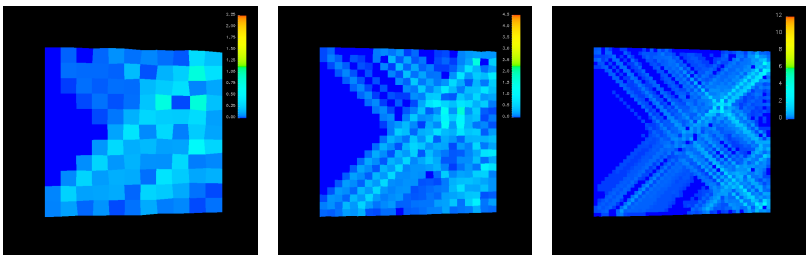

(a) 12×12 mesh (b) 24×24 mesh (c) 48×48 mesh

Figure A.8: Mesh resolution comparison for axial extension with local weakening. $\|\boldsymbol{\xi}\|^2$ $A_3 = 0.1$, $\nu = 0.0003$, hardeningmode=1, $\theta_0 = 0$, sequence number =4

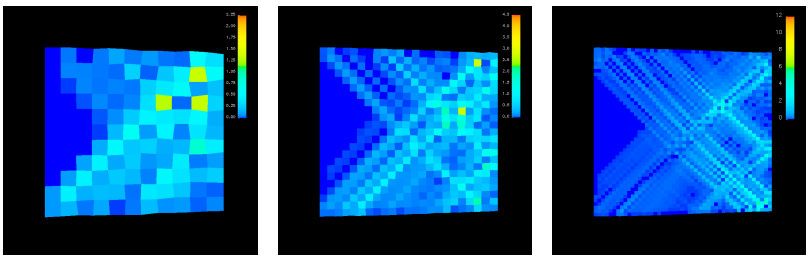

(a) 12×12 mesh (b) 24×24 mesh (c) 48×48 mesh

Figure A.9: Mesh resolution comparison for axial extension with local weakening. $\|\boldsymbol{\xi}\|^2$ $A_3 = 0.1$, $\nu = 0.0003$, hardeningmode=1, $\theta_0 = 0$, sequence number =5

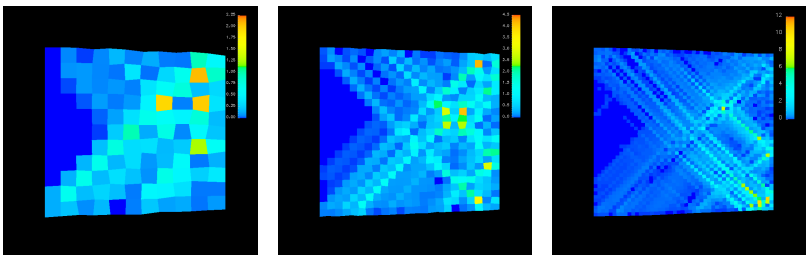

(a) 12×12 mesh (b) 24×24 mesh (c) 48×48 mesh

Figure A.10: Mesh resolution comparison for axial extension with local weakening. $\|\boldsymbol{\xi}\|^2$ $A_3 = 0.1$, $\nu = 0.0003$, hardeningmode=1, $\theta_0 = 0$, sequence number =6

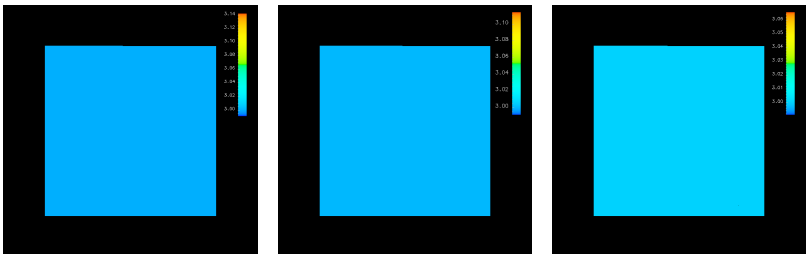

(a) 12×12 mesh (b) 24×24 mesh (c) 48×48 mesh

Figure A.11: Mesh resolution comparison for axial extension with local weakening. $\|\mathbf{K}\|$ $A_3 = 0.1$, $\nu = 0.0003$, hardeningmode=1, $\theta_0 = 0$, sequence number =0

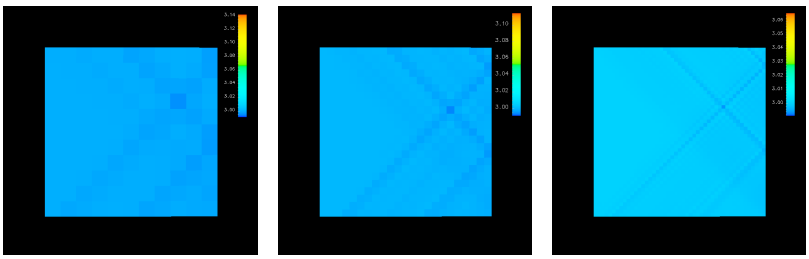

(a) 12×12 mesh (b) 24×24 mesh (c) 48×48 mesh

Figure A.12: Mesh resolution comparison for axial extension with local weakening. $\|\mathbf{K}\|$ $A_3 = 0.1$, $\nu = 0.0003$, hardeningmode=1, $\theta_0 = 0$, sequence number =1

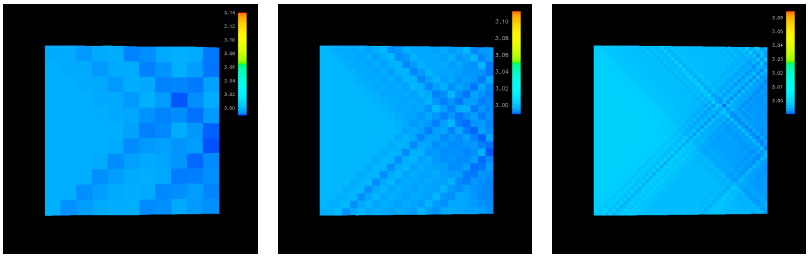

(a) 12×12 mesh (b) 24×24 mesh (c) 48×48 mesh

Figure A.13: Mesh resolution comparison for axial extension with local weakening. $\|\mathbf{K}\|$ $A_3 = 0.1$, $\nu = 0.0003$, hardeningmode=1, $\theta_0 = 0$, sequence number =2

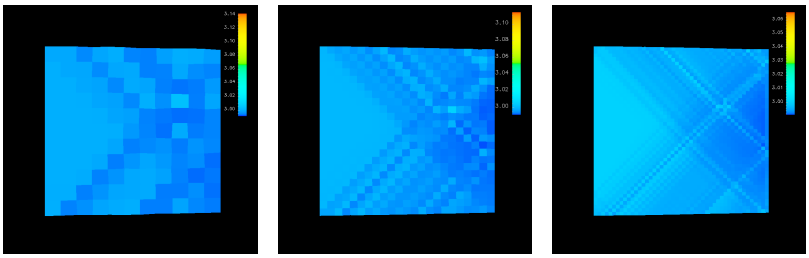

(a) 12×12 mesh (b) 24×24 mesh (c) 48×48 mesh

Figure A.14: Mesh resolution comparison for axial extension with local weakening. $\|\mathbf{K}\|$ $A_3 = 0.1$, $\nu = 0.0003$, hardeningmode=1, $\theta_0 = 0$, sequence number =3

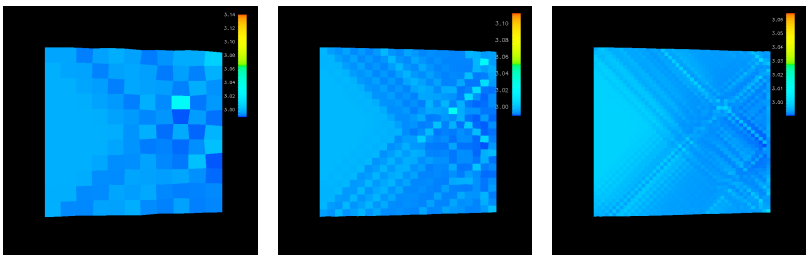

(a) 12×12 mesh (b) 24×24 mesh (c) 48×48 mesh

Figure A.15: Mesh resolution comparison for axial extension with local weakening. $\|\mathbf{K}\|$ $A_3 = 0.1$, $\nu = 0.0003$, hardeningmode=1, $\theta_0 = 0$, sequence number =4

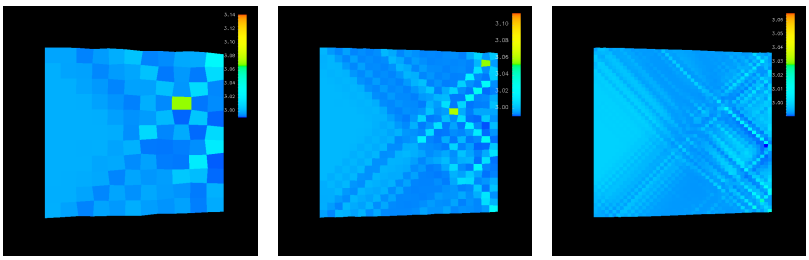

(a) 12×12 mesh (b) 24×24 mesh (c) 48×48 mesh

Figure A.16: Mesh resolution comparison for axial extension with local weakening. $\|\mathbf{K}\|$ $A_3 = 0.1$, $\nu = 0.0003$, hardeningmode=1, $\theta_0 = 0$, sequence number =5

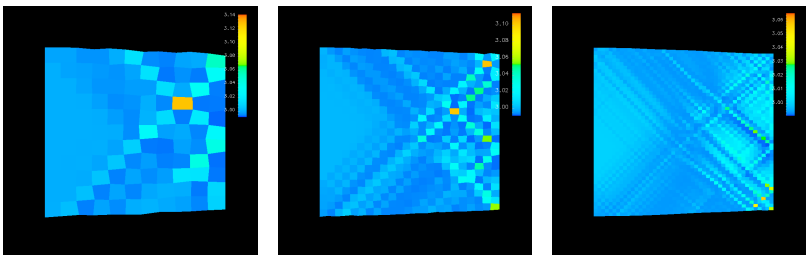

(a) 12×12 mesh (b) 24×24 mesh (c) 48×48 mesh

Figure A.17: Mesh resolution comparison for axial extension with local weakening. $\|\mathbf{K}\|$ $A_3 = 0.1$, $\nu = 0.0003$, hardeningmode=1, $\theta_0 = 0$, sequence number =6

A.6.2 Shock contraction

See §2.4.2.3.3 for information about the boundary conditions and other details. In all the following figure captions, the units of ν are $\mathrm{GPa}^{-1} \cdot s$. This first set of figures look at different grain orientations, at progressively lower plastic viscosity, ν, tending to the rate independent limit. The mesh resolution was 40×40. The figure sequence are plots of $\|\mathbf{E}\|^2, \mathrm{tr}\ \mathbf{S}, \|\boldsymbol{\xi}\|^2, \|\mathbf{K}\|$ respectively.

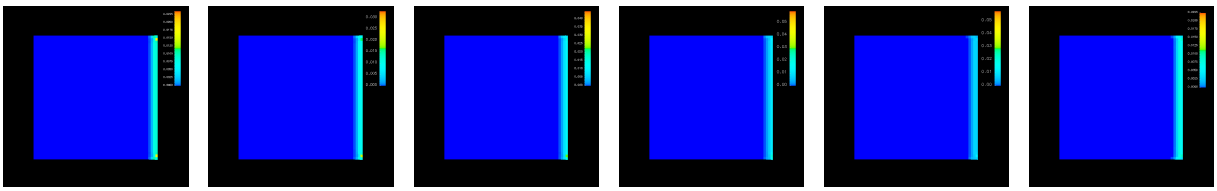

(a) θ_0 =0 (b) θ_0 =10 (c) θ_0 =20 (d) θ_0 =30 (e) θ_0 =40 (f) θ_0 =45

Figure A.18: Mesh resolution comparison for shock contraction. The colormap shows $\|\mathbf{E}\|^2$. $A_3 = 0$, $\nu = 0.1000$, hardening mode=1, sequence number = 0

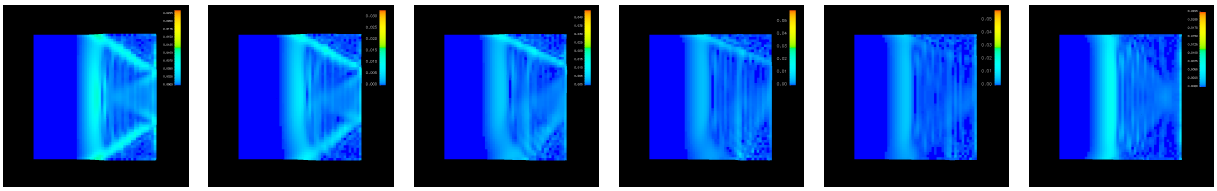

(a) θ_0 =0 (b) θ_0 =10 (c) θ_0 =20 (d) θ_0 =30 (e) θ_0 =40 (f) θ_0 =45

Figure A.19: Mesh resolution comparison for shock contraction. The colormap shows $\|\mathbf{E}\|^2$. $A_3 = 0$, $\nu = 0.1000$, hardening mode=1, sequence number = 1

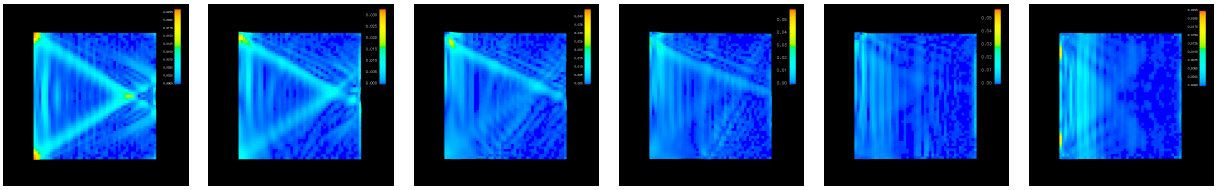

(a) θ_0 =0 (b) θ_0 =10 (c) θ_0 =20 (d) θ_0 =30 (e) θ_0 =40 (f) θ_0 =45

Figure A.20: Mesh resolution comparison for shock contraction. The colormap shows $\|\mathbf{E}\|^2$. $A_3 = 0$, $\nu = 0.1000$, hardening mode=1, sequence number = 2

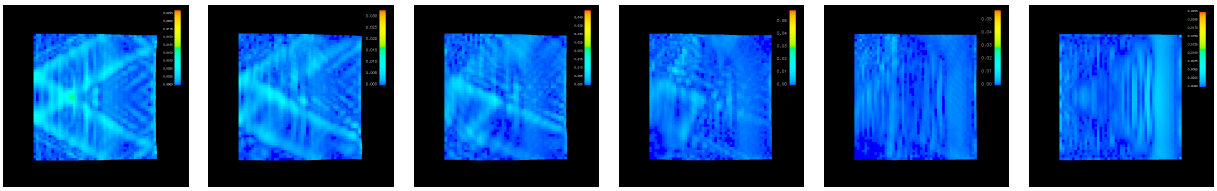

(a) θ_0 =0 (b) θ_0 =10 (c) θ_0 =20 (d) θ_0 =30 (e) θ_0 =40 (f) θ_0 =45

Figure A.21: Mesh resolution comparison for shock contraction. The colormap shows $\|\mathbf{E}\|^2$. $A_3 = 0$, $\nu = 0.1000$, hardening mode=1, sequence number = 3

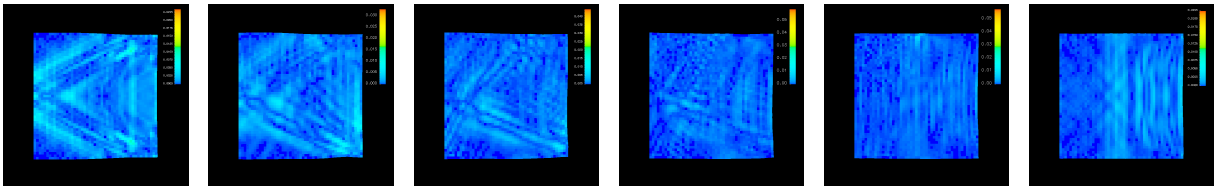

(a) θ_0 =0 (b) θ_0 =10 (c) θ_0 =20 (d) θ_0 =30 (e) θ_0 =40 (f) θ_0 =45

Figure A.22: Mesh resolution comparison for shock contraction. The colormap shows $\|\mathbf{E}\|^2$. $A_3 = 0$, $\nu = 0.1000$, hardening mode=1, sequence number = 4

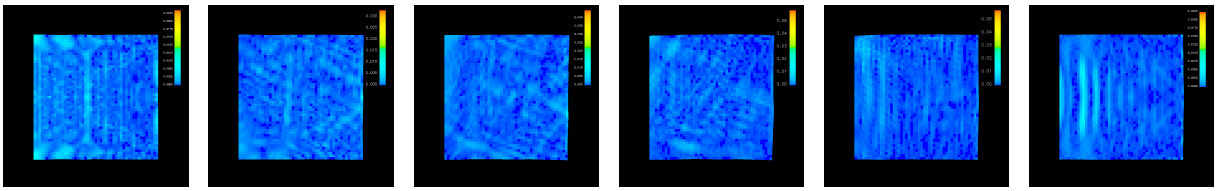

(a) θ_0 =0 (b) θ_0 =10 (c) θ_0 =20 (d) θ_0 =30 (e) θ_0 =40 (f) θ_0 =45

Figure A.23: Mesh resolution comparison for shock contraction. The colormap shows $\|\mathbf{E}\|^2$. $A_3 = 0$, $\nu = 0.1000$, hardening mode=1, sequence number = 5

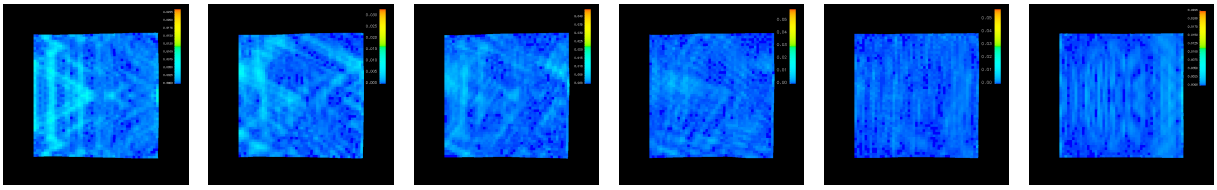

(a) θ_0 =0 (b) θ_0 =10 (c) θ_0 =20 (d) θ_0 =30 (e) θ_0 =40 (f) θ_0 =45

Figure A.24: Mesh resolution comparison for shock contraction. The colormap shows $\|\mathbf{E}\|^2$. $A_3 = 0$, $\nu = 0.1000$, hardening mode=1, sequence number = 6

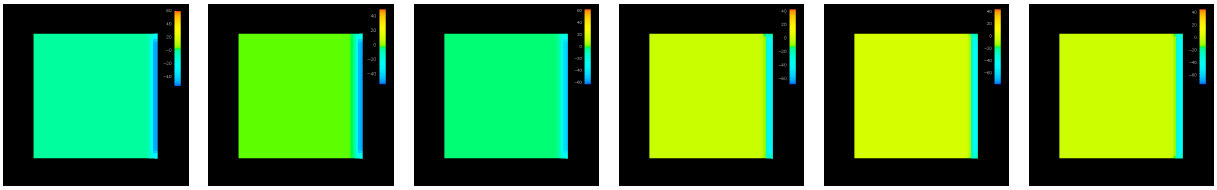

(a) θ_0 =0 (b) θ_0 =10 (c) θ_0 =20 (d) θ_0 =30 (e) θ_0 =40 (f) θ_0 =45

Figure A.25: Mesh resolution comparison for shock contraction. The colormap shows tr **S**. $A_3 = 0$, $\nu = 0.1000$, hardening mode=1, sequence number = 0

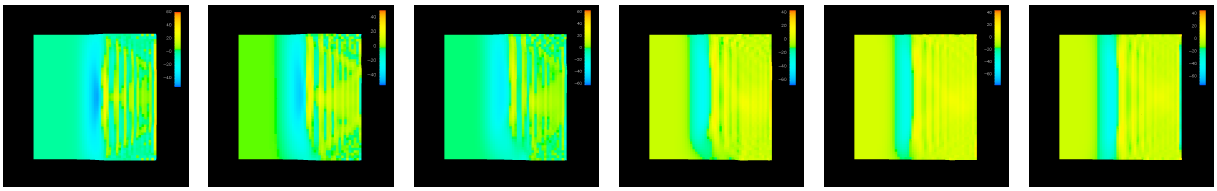

(a) θ_0 =0 (b) θ_0 =10 (c) θ_0 =20 (d) θ_0 =30 (e) θ_0 =40 (f) θ_0 =45

Figure A.26: Mesh resolution comparison for shock contraction. The colormap shows tr **S**. $A_3 = 0$, $\nu = 0.1000$, hardening mode=1, sequence number = 1

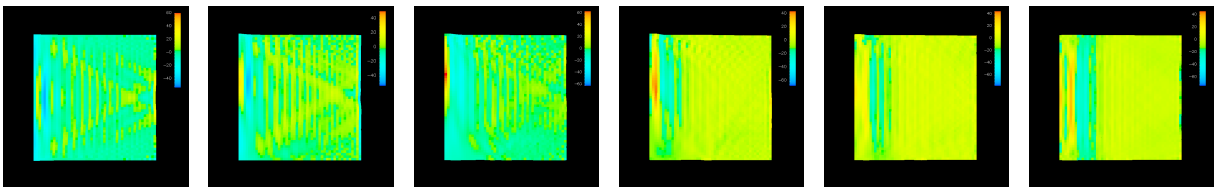

(a) θ_0 =0 (b) θ_0 =10 (c) θ_0 =20 (d) θ_0 =30 (e) θ_0 =40 (f) θ_0 =45

Figure A.27: Mesh resolution comparison for shock contraction. The colormap shows tr **S**. $A_3 = 0$, $\nu = 0.1000$, hardening mode=1, sequence number = 2

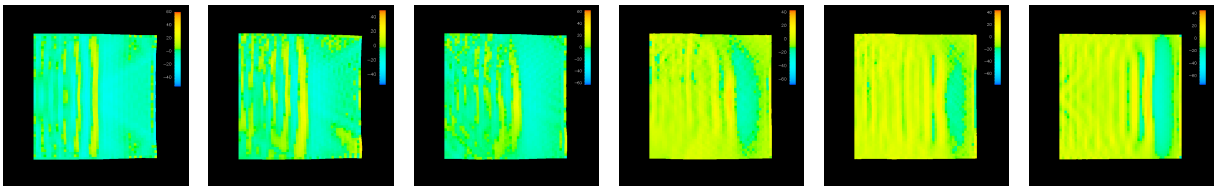

(a) θ_0 =0 (b) θ_0 =10 (c) θ_0 =20 (d) θ_0 =30 (e) θ_0 =40 (f) θ_0 =45

Figure A.28: Mesh resolution comparison for shock contraction. The colormap shows tr **S**. $A_3 = 0$, $\nu = 0.1000$, hardening mode=1, sequence number = 3

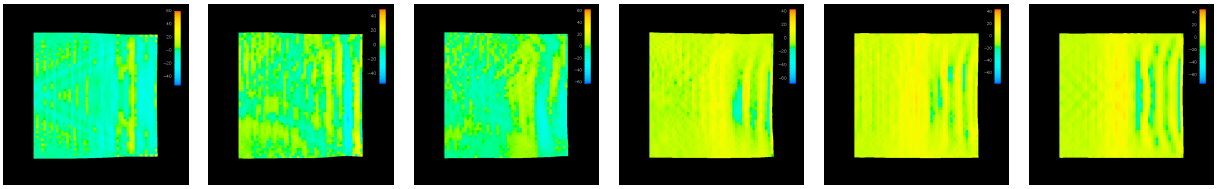

(a) θ_0 =0 (b) θ_0 =10 (c) θ_0 =20 (d) θ_0 =30 (e) θ_0 =40 (f) θ_0 =45

Figure A.29: Mesh resolution comparison for shock contraction. The colormap shows tr **S**. $A_3 = 0$, $\nu = 0.1000$, hardening mode=1, sequence number = 4

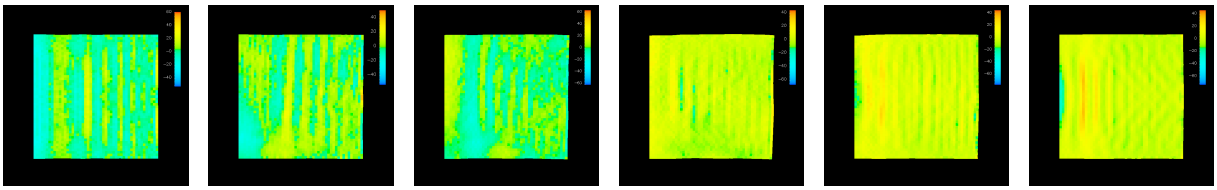

(a) θ_0 =0 (b) θ_0 =10 (c) θ_0 =20 (d) θ_0 =30 (e) θ_0 =40 (f) θ_0 =45

Figure A.30: Mesh resolution comparison for shock contraction. The colormap shows tr **S**. $A_3 = 0$, $\nu = 0.1000$, hardening mode=1, sequence number = 5

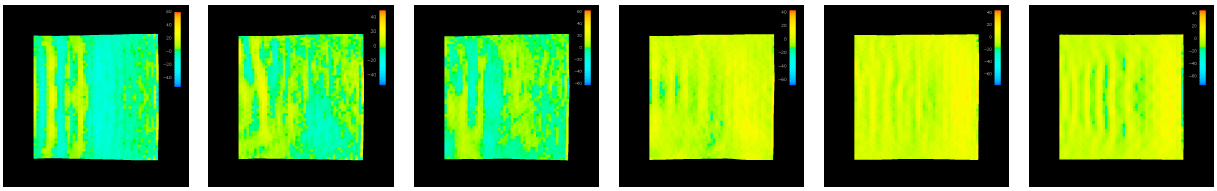

(a) θ_0 =0 (b) θ_0 =10 (c) θ_0 =20 (d) θ_0 =30 (e) θ_0 =40 (f) θ_0 =45

Figure A.31: Mesh resolution comparison for shock contraction. The colormap shows tr **S**. $A_3 = 0$, $\nu = 0.1000$, hardening mode=1, sequence number = 6

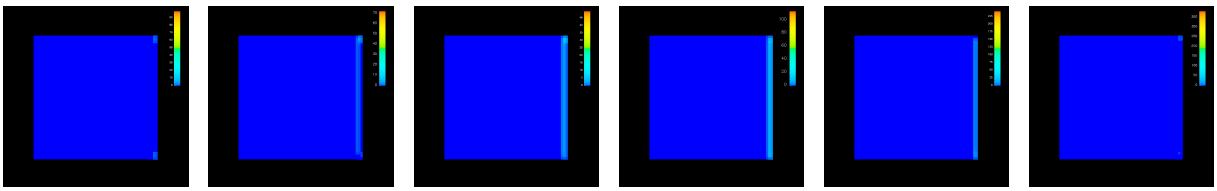

(a) θ_0 =0 (b) θ_0 =10 (c) θ_0 =20 (d) θ_0 =30 (e) θ_0 =40 (f) θ_0 =45

Figure A.32: Mesh resolution comparison for shock contraction. The colormap shows $\|\boldsymbol{\xi}\|^2$. $A_3 = 0$, $\nu = 0.1000$, hardening mode=1, sequence number = 0

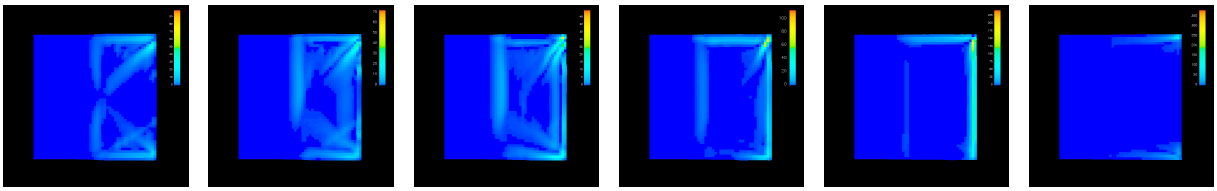

(a) θ_0 =0 (b) θ_0 =10 (c) θ_0 =20 (d) θ_0 =30 (e) θ_0 =40 (f) θ_0 =45

Figure A.33: Mesh resolution comparison for shock contraction. The colormap shows $\|\boldsymbol{\xi}\|^2$. $A_3 = 0$, $\nu = 0.1000$, hardening mode=1, sequence number = 1

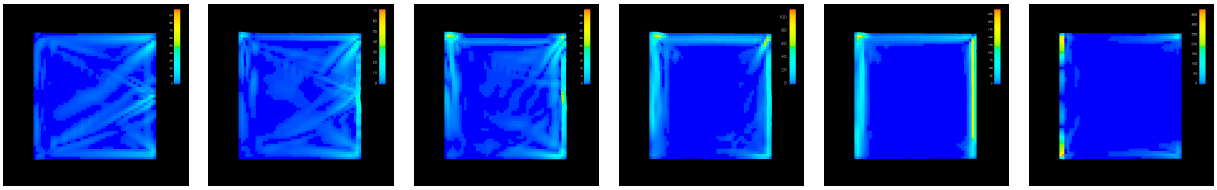

(a) θ_0 =0 (b) θ_0 =10 (c) θ_0 =20 (d) θ_0 =30 (e) θ_0 =40 (f) θ_0 =45

Figure A.34: Mesh resolution comparison for shock contraction. The colormap shows $\|\boldsymbol{\xi}\|^2$. $A_3 = 0$, $\nu = 0.1000$, hardening mode=1, sequence number = 2

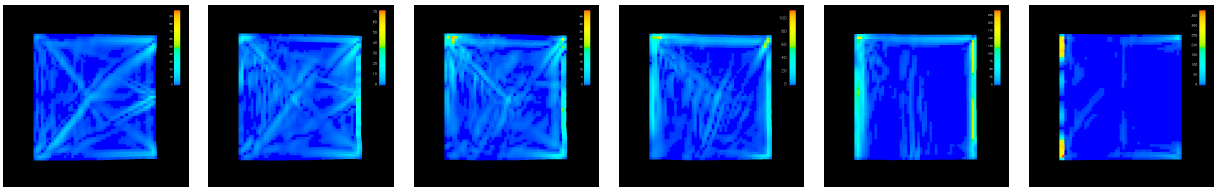

(a) θ_0 =0 (b) θ_0 =10 (c) θ_0 =20 (d) θ_0 =30 (e) θ_0 =40 (f) θ_0 =45

Figure A.35: Mesh resolution comparison for shock contraction. The colormap shows $\|\boldsymbol{\xi}\|^2$. $A_3 = 0$, $\nu = 0.1000$, hardening mode=1, sequence number = 3

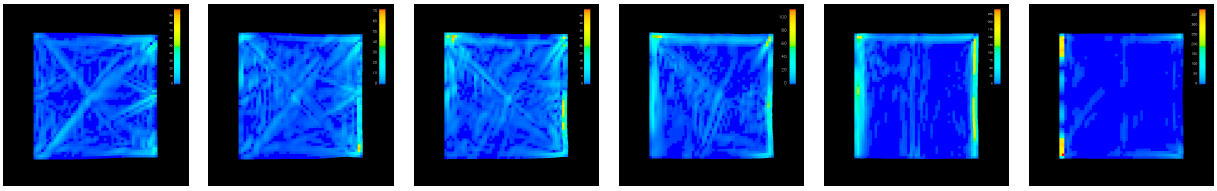

(a) θ_0 =0 (b) θ_0 =10 (c) θ_0 =20 (d) θ_0 =30 (e) θ_0 =40 (f) θ_0 =45

Figure A.36: Mesh resolution comparison for shock contraction. The colormap shows $\|\boldsymbol{\xi}\|^2$. $A_3 = 0$, $\nu = 0.1000$, hardening mode=1, sequence number = 4

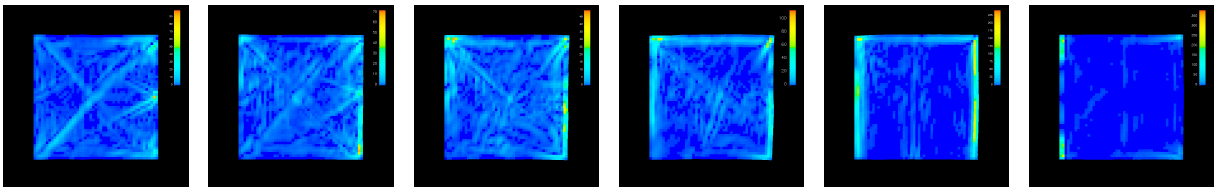

(a) θ_0 =0 (b) θ_0 =10 (c) θ_0 =20 (d) θ_0 =30 (e) θ_0 =40 (f) θ_0 =45

Figure A.37: Mesh resolution comparison for shock contraction. The colormap shows $\|\boldsymbol{\xi}\|^2$. $A_3 = 0$, $\nu = 0.1000$, hardening mode=1, sequence number = 5

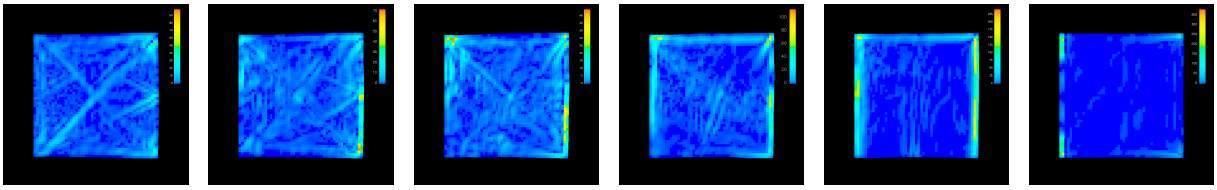

(a) θ_0 =0 (b) θ_0 =10 (c) θ_0 =20 (d) θ_0 =30 (e) θ_0 =40 (f) θ_0 =45

Figure A.38: Mesh resolution comparison for shock contraction. The colormap shows $\|\boldsymbol{\xi}\|^2$. $A_3 = 0$, $\nu = 0.1000$, hardening mode=1, sequence number = 6

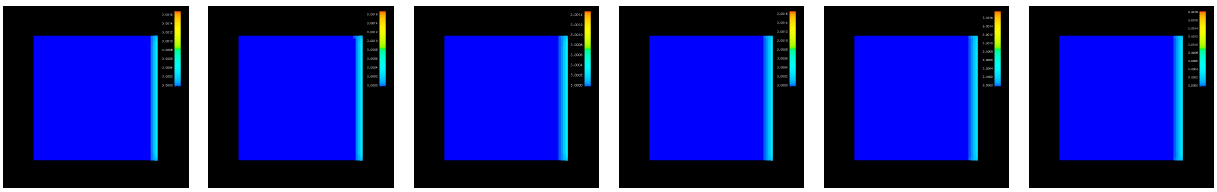

(a) θ_0 =0 (b) θ_0 =10 (c) θ_0 =20 (d) θ_0 =30 (e) θ_0 =40 (f) θ_0 =45

Figure A.39: Mesh resolution comparison for shock contraction. The colormap shows $\|\mathbf{K}\|$. $A_3 = 0$, $\nu = 0.1000$, hardening mode=1, sequence number = 0

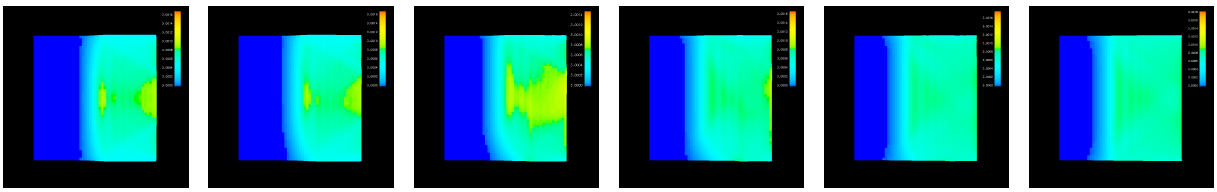

(a) θ_0 =0 (b) θ_0 =10 (c) θ_0 =20 (d) θ_0 =30 (e) θ_0 =40 (f) θ_0 =45

Figure A.40: Mesh resolution comparison for shock contraction. The colormap shows $\|\mathbf{K}\|$. $A_3 = 0$, $\nu = 0.1000$, hardening mode=1, sequence number = 1

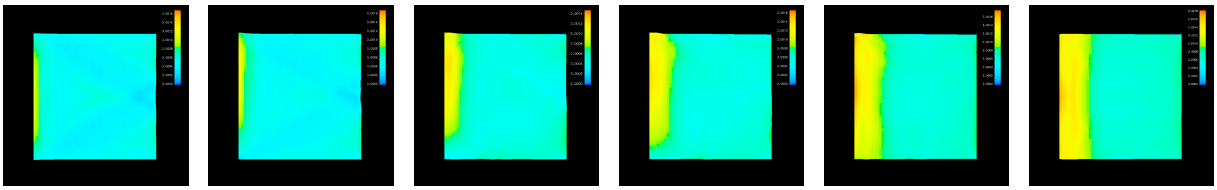

(a) θ_0 =0 (b) θ_0 =10 (c) θ_0 =20 (d) θ_0 =30 (e) θ_0 =40 (f) θ_0 =45

Figure A.41: Mesh resolution comparison for shock contraction. The colormap shows $\|\mathbf{K}\|$. $A_3 = 0$, $\nu = 0.1000$, hardening mode=1, sequence number = 2

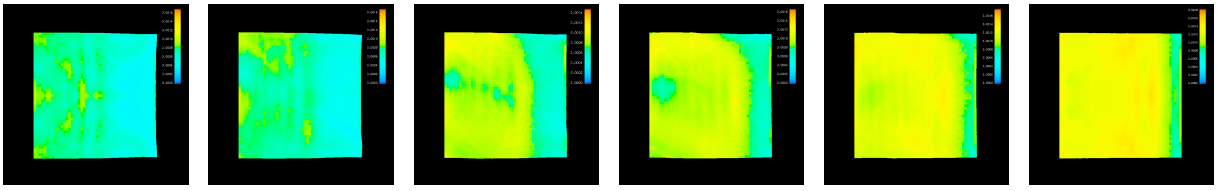

(a) θ_0 =0 (b) θ_0 =10 (c) θ_0 =20 (d) θ_0 =30 (e) θ_0 =40 (f) θ_0 =45

Figure A.42: Mesh resolution comparison for shock contraction. The colormap shows $\|\mathbf{K}\|$. $A_3 = 0$, $\nu = 0.1000$, hardening mode=1, sequence number = 3

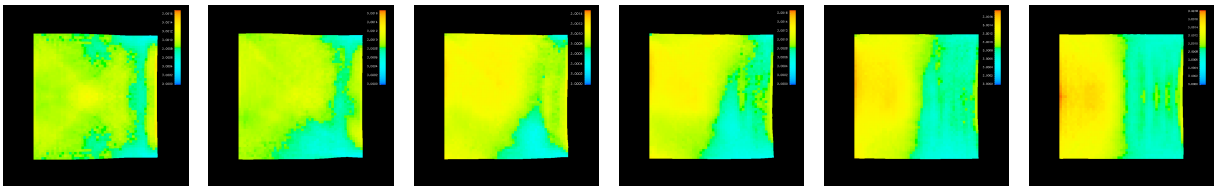

(a) θ_0 =0 (b) θ_0 =10 (c) θ_0 =20 (d) θ_0 =30 (e) θ_0 =40 (f) θ_0 =45

Figure A.43: Mesh resolution comparison for shock contraction. The colormap shows $\|\mathbf{K}\|$. $A_3 = 0$, $\nu = 0.1000$, hardening mode=1, sequence number = 4

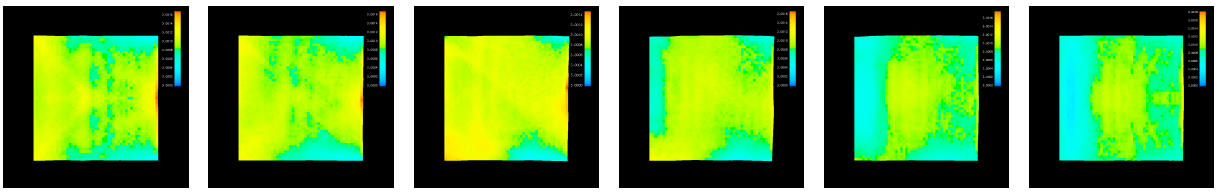

(a) θ_0 =0 (b) θ_0 =10 (c) θ_0 =20 (d) θ_0 =30 (e) θ_0 =40 (f) θ_0 =45

Figure A.44: Mesh resolution comparison for shock contraction. The colormap shows $\|\mathbf{K}\|$. $A_3 = 0$, $\nu = 0.1000$, hardening mode=1, sequence number = 5

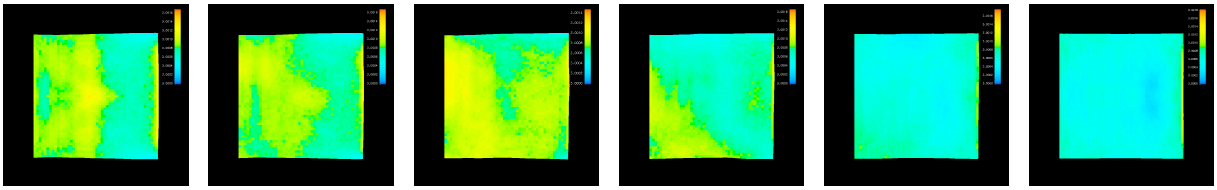

(a) θ_0 =0 (b) θ_0 =10 (c) θ_0 =20 (d) θ_0 =30 (e) θ_0 =40 (f) θ_0 =45

Figure A.45: Mesh resolution comparison for shock contraction. The colormap shows $\|\mathbf{K}\|$. $A_3 = 0$, $\nu = 0.1000$, hardening mode=1, sequence number = 6

This second set of figures look at a lower viscosity. The mesh resolution was 40×40. The figure sequence are plots of $\|\mathbf{E}\|^2, \operatorname{tr} \mathbf{S}, \|\boldsymbol{\xi}\|^2, \|\mathbf{K}\|$.

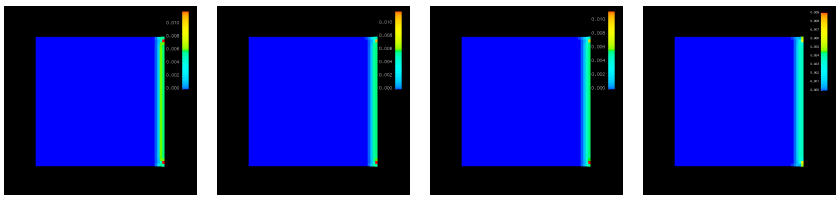

(a) theta0 = 0 (b) theta0 = 20 (c) theta0 = 30 (d) theta0 = 45

Figure A.46: Mesh resolution comparison for shock contraction. The colormap shows $\|\mathbf{E}\|^2$. $A_3 = 0$, $\nu = 0.0010$, hardening mode=1, sequence number = 0

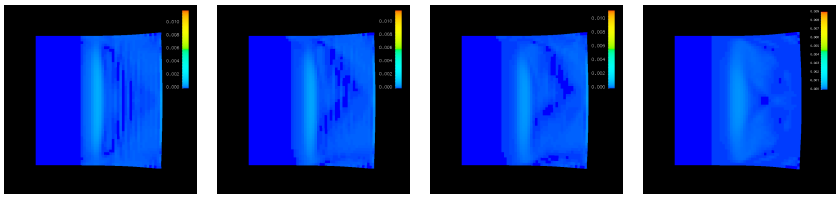

(a) theta0 = 0 (b) theta0 = 20 (c) theta0 = 30 (d) theta0 = 45

Figure A.47: Mesh resolution comparison for shock contraction. The colormap shows $\|\mathbf{E}\|^2$. $A_3 = 0$, $\nu = 0.0010$, hardening mode=1, sequence number = 1

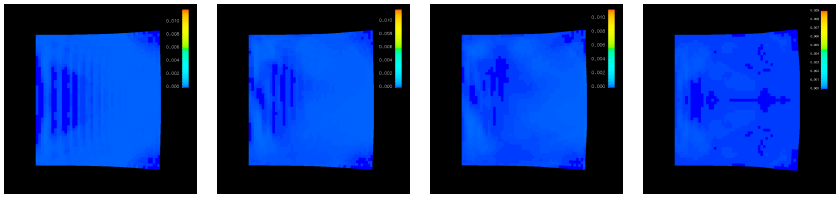

(a) theta0 = 0 (b) theta0 = 20 (c) theta0 = 30 (d) theta0 = 45

Figure A.48: Mesh resolution comparison for shock contraction. The colormap shows $\|\mathbf{E}\|^2$. $A_3 = 0$, $\nu = 0.0010$, hardening mode=1, sequence number = 2

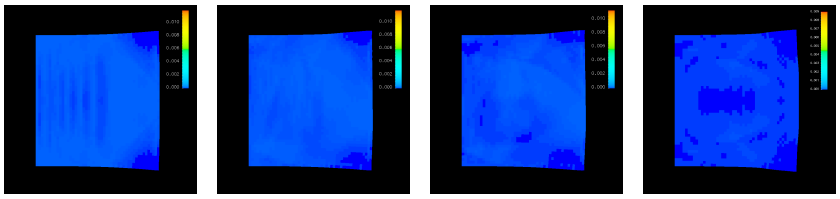

(a) theta0 = 0 (b) theta0 = 20 (c) theta0 = 30 (d) theta0 = 45

Figure A.49: Mesh resolution comparison for shock contraction. The colormap shows $\|\mathbf{E}\|^2$. $A_3 = 0$, $\nu = 0.0010$, hardening mode=1, sequence number = 3

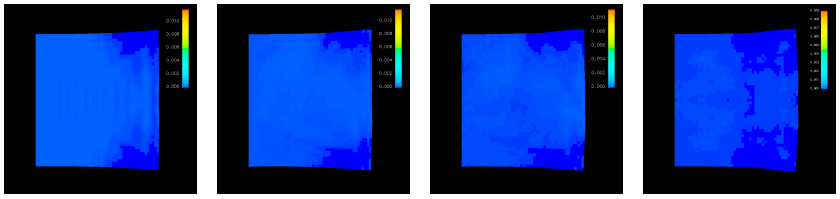

(a) theta0 = 0 (b) theta0 = 20 (c) theta0 = 30 (d) theta0 = 45

Figure A.50: Mesh resolution comparison for shock contraction. The colormap shows $\|\mathbf{E}\|^2$. $A_3 = 0$, $\nu = 0.0010$, hardening mode=1, sequence number = 4

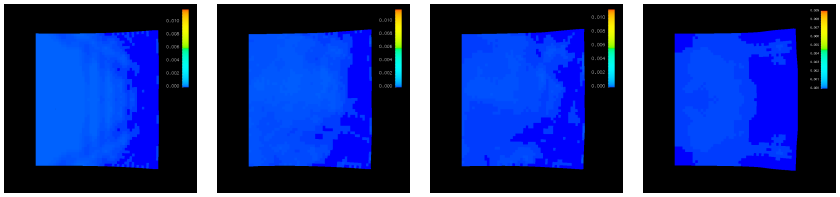

(a) theta0 = 0 (b) theta0 = 20 (c) theta0 = 30 (d) theta0 = 45

Figure A.51: Mesh resolution comparison for shock contraction. The colormap shows $\|\mathbf{E}\|^2$. $A_3 = 0$, $\nu = 0.0010$, hardening mode=1, sequence number = 5

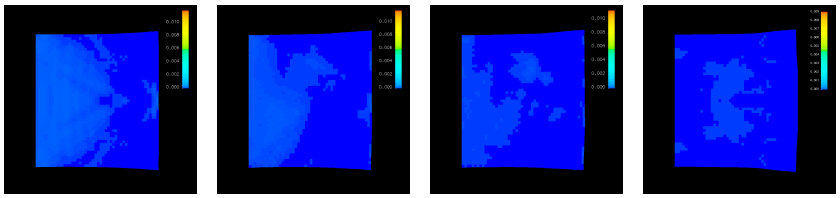

(a) theta0 = 0 (b) theta0 = 20 (c) theta0 = 30 (d) theta0 = 45

Figure A.52: Mesh resolution comparison for shock contraction. The colormap shows $\|\mathbf{E}\|^2$. $A_3 = 0$, $\nu = 0.0010$, hardening mode=1, sequence number = 6

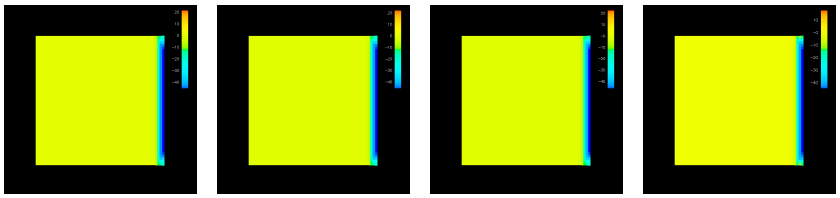

(a) theta0 = 0 (b) theta0 = 20 (c) theta0 = 30 (d) theta0 = 45

Figure A.53: Mesh resolution comparison for shock contraction. The colormap shows tr **S**. $A_3 = 0$, $\nu = 0.0010$, hardening mode=1, sequence number = 0

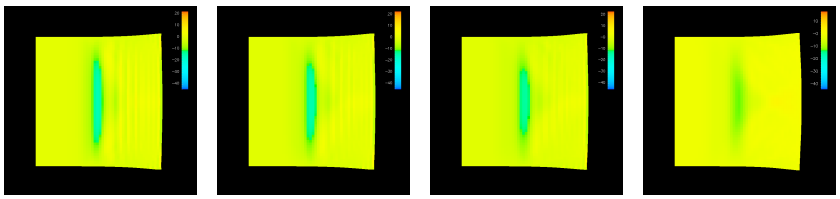

(a) theta0 = 0 (b) theta0 = 20 (c) theta0 = 30 (d) theta0 = 45

Figure A.54: Mesh resolution comparison for shock contraction. The colormap shows tr **S**. $A_3 = 0$, $\nu = 0.0010$, hardening mode=1, sequence number = 1

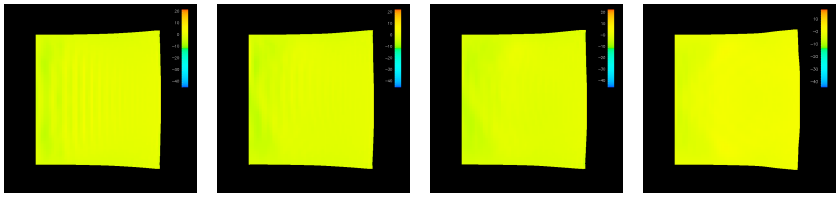

(a) theta0 = 0 (b) theta0 = 20 (c) theta0 = 30 (d) theta0 = 45

Figure A.55: Mesh resolution comparison for shock contraction. The colormap shows tr **S**. $A_3 = 0$, $\nu = 0.0010$, hardening mode=1, sequence number = 2

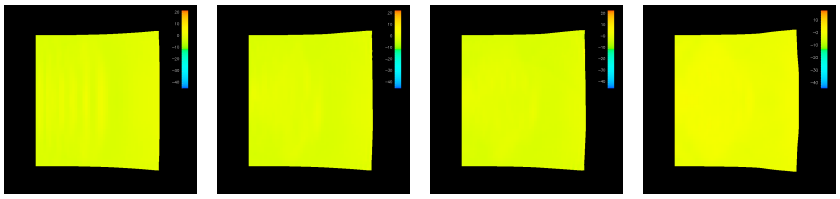

(a) theta0 = 0 (b) theta0 = 20 (c) theta0 = 30 (d) theta0 = 45

Figure A.56: Mesh resolution comparison for shock contraction. The colormap shows tr **S**. $A_3 = 0$, $\nu = 0.0010$, hardening mode=1, sequence number = 3

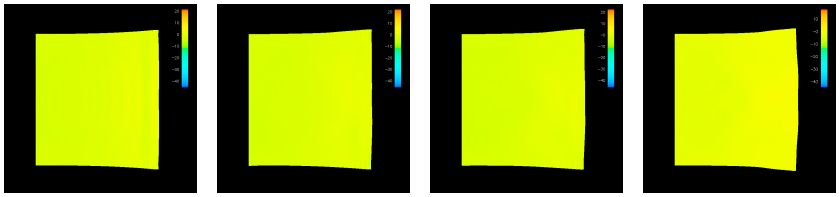

(a) theta0 = 0 (b) theta0 = 20 (c) theta0 = 30 (d) theta0 = 45

Figure A.57: Mesh resolution comparison for shock contraction. The colormap shows tr **S**. $A_3 = 0$, $\nu = 0.0010$, hardening mode=1, sequence number = 4

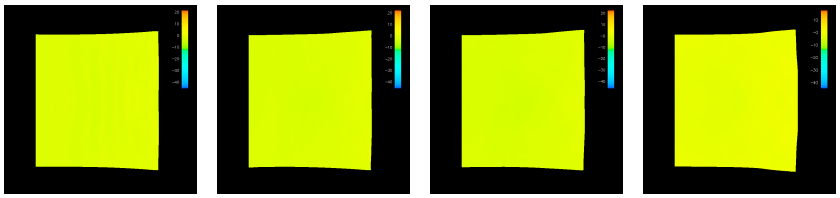

(a) theta0 = 0 (b) theta0 = 20 (c) theta0 = 30 (d) theta0 = 45

Figure A.58: Mesh resolution comparison for shock contraction. The colormap shows tr **S**. $A_3 = 0$, $\nu = 0.0010$, hardening mode=1, sequence number = 5

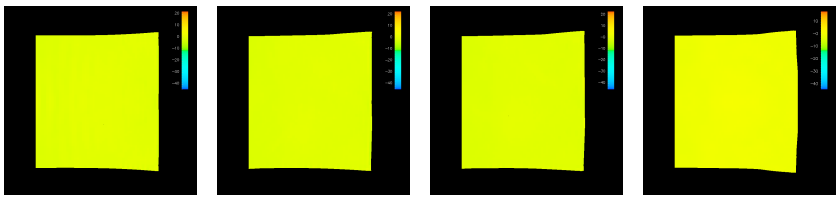

(a) theta0 = 0 (b) theta0 = 20 (c) theta0 = 30 (d) theta0 = 45

Figure A.59: Mesh resolution comparison for shock contraction. The colormap shows tr **S**. $A_3 = 0$, $\nu = 0.0010$, hardening mode=1, sequence number = 6

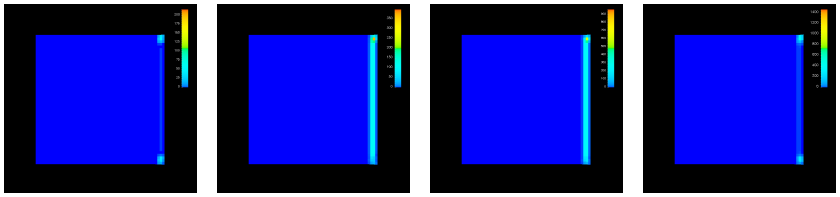

(a) theta0 = 0 (b) theta0 = 20 (c) theta0 = 30 (d) theta0 = 45

Figure A.60: Mesh resolution comparison for shock contraction. The colormap shows $\|\boldsymbol{\xi}\|^2$. $A_3 = 0$, $\nu = 0.0010$, hardening mode=1, sequence number = 0

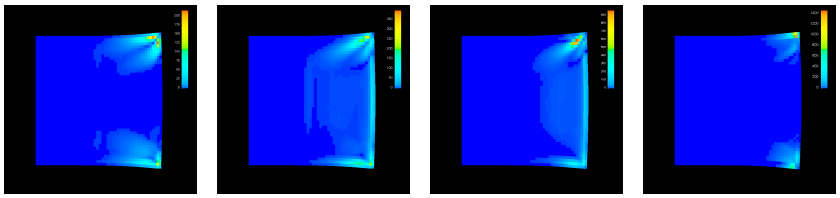

(a) theta0 = 0 (b) theta0 = 20 (c) theta0 = 30 (d) theta0 = 45

Figure A.61: Mesh resolution comparison for shock contraction. The colormap shows $\|\boldsymbol{\xi}\|^2$. $A_3 = 0$, $\nu = 0.0010$, hardening mode=1, sequence number = 1

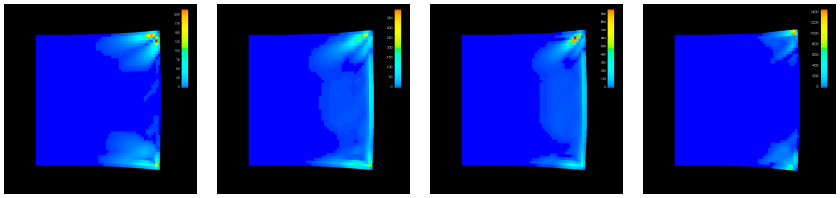

(a) theta0 = 0 (b) theta0 = 20 (c) theta0 = 30 (d) theta0 = 45

Figure A.62: Mesh resolution comparison for shock contraction. The colormap shows $\|\boldsymbol{\xi}\|^2$. $A_3 = 0$, $\nu = 0.0010$, hardening mode=1, sequence number = 2

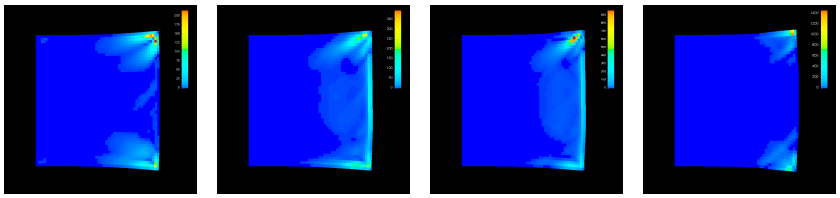

(a) theta0 = 0 (b) theta0 = 20 (c) theta0 = 30 (d) theta0 = 45

Figure A.63: Mesh resolution comparison for shock contraction. The colormap shows $\|\boldsymbol{\xi}\|^2$. $A_3 = 0$, $\nu = 0.0010$, hardening mode=1, sequence number = 3

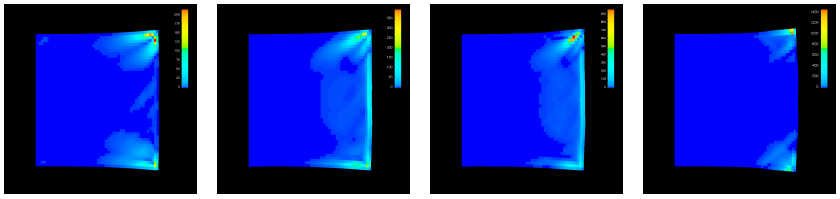

(a) theta0 = 0 (b) theta0 = 20 (c) theta0 = 30 (d) theta0 = 45

Figure A.64: Mesh resolution comparison for shock contraction. The colormap shows $\|\boldsymbol{\xi}\|^2$. $A_3 = 0$, $\nu = 0.0010$, hardening mode=1, sequence number = 4

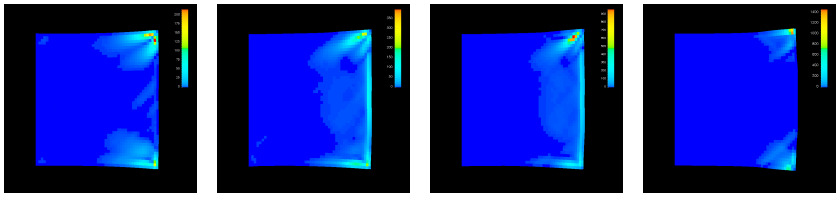

(a) theta0 = 0 (b) theta0 = 20 (c) theta0 = 30 (d) theta0 = 45

Figure A.65: Mesh resolution comparison for shock contraction. The colormap shows $\|\boldsymbol{\xi}\|^2$. $A_3 = 0$, $\nu = 0.0010$, hardening mode=1, sequence number = 5

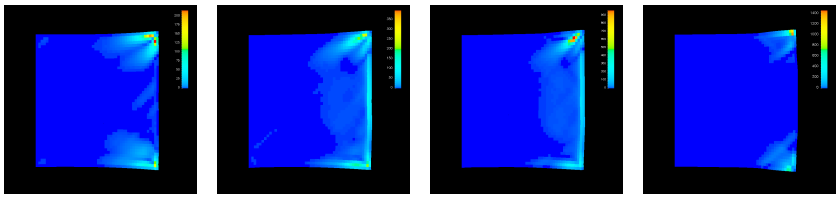

(a) theta0 = 0 (b) theta0 = 20 (c) theta0 = 30 (d) theta0 = 45

Figure A.66: Mesh resolution comparison for shock contraction. The colormap shows $\|\boldsymbol{\xi}\|^2$. $A_3 = 0$, $\nu = 0.0010$, hardening mode=1, sequence number = 6

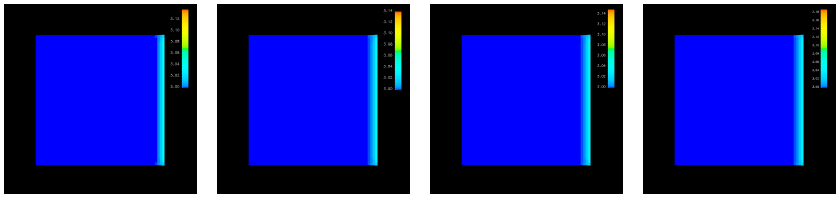

(a) theta0 = 0 (b) theta0 = 20 (c) theta0 = 30 (d) theta0 = 45

Figure A.67: Mesh resolution comparison for shock contraction. The colormap shows $\|\mathbf{K}\|$. $A_3 = 0$, $\nu = 0.0010$, hardening mode=1, sequence number = 0

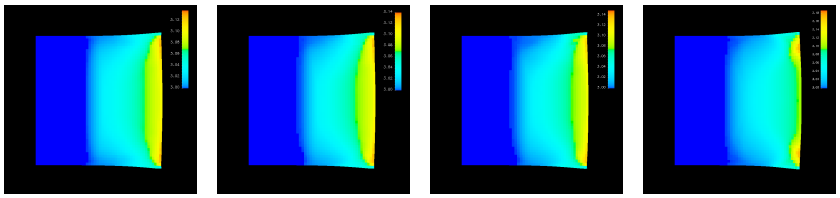

(a) theta0 = 0 (b) theta0 = 20 (c) theta0 = 30 (d) theta0 = 45

Figure A.68: Mesh resolution comparison for shock contraction. The colormap shows $\|\mathbf{K}\|$. $A_3 = 0$, $\nu = 0.0010$, hardening mode=1, sequence number = 1

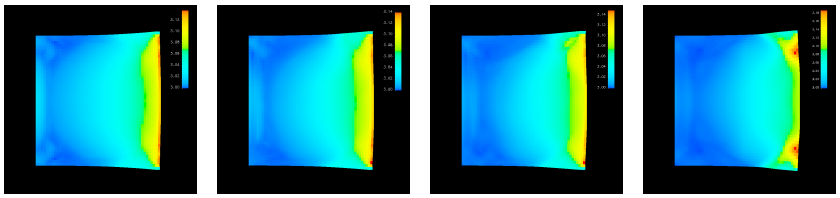

(a) theta0 = 0 (b) theta0 = 20 (c) theta0 = 30 (d) theta0 = 45

Figure A.69: Mesh resolution comparison for shock contraction. The colormap shows $\|\mathbf{K}\|$. $A_3 = 0$, $\nu = 0.0010$, hardening mode=1, sequence number = 2

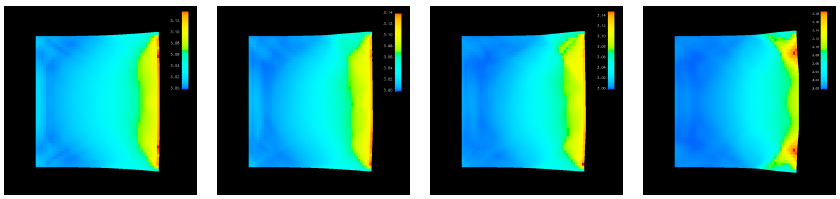

(a) theta0 = 0 (b) theta0 = 20 (c) theta0 = 30 (d) theta0 = 45

Figure A.70: Mesh resolution comparison for shock contraction. The colormap shows $\|\mathbf{K}\|$. $A_3 = 0$, $\nu = 0.0010$, hardening mode=1, sequence number = 3

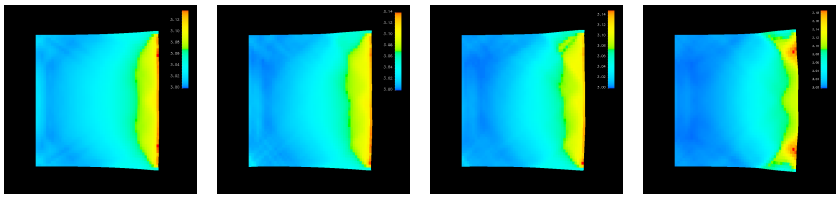

(a) theta0 = 0 (b) theta0 = 20 (c) theta0 = 30 (d) theta0 = 45

Figure A.71: Mesh resolution comparison for shock contraction. The colormap shows $\|\mathbf{K}\|$. $A_3 = 0$, $\nu = 0.0010$, hardening mode=1, sequence number = 4

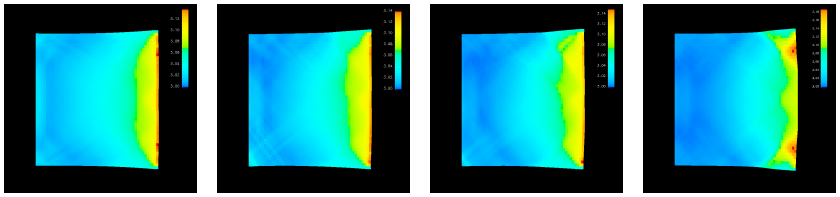

(a) theta0 = 0 (b) theta0 = 20 (c) theta0 = 30 (d) theta0 = 45

Figure A.72: Mesh resolution comparison for shock contraction. The colormap shows $\|\mathbf{K}\|$. $A_3 = 0$, $\nu = 0.0010$, hardening mode=1, sequence number = 5

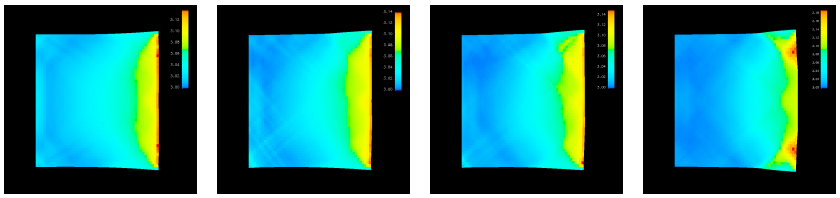

(a) theta0 = 0 (b) theta0 = 20 (c) theta0 = 30 (d) theta0 = 45

Figure A.73: Mesh resolution comparison for shock contraction. The colormap shows $\|\mathbf{K}\|$. $A_3 = 0$, $\nu = 0.0010$, hardening mode=1, sequence number = 6

This second set of figures look at a yet lower viscosity. The mesh resolution was 40×40. The figure sequence are plots of $\|\mathbf{E}\|^2, \operatorname{tr} \mathbf{S}, \|\boldsymbol{\xi}\|^2, \|\mathbf{K}\|$.

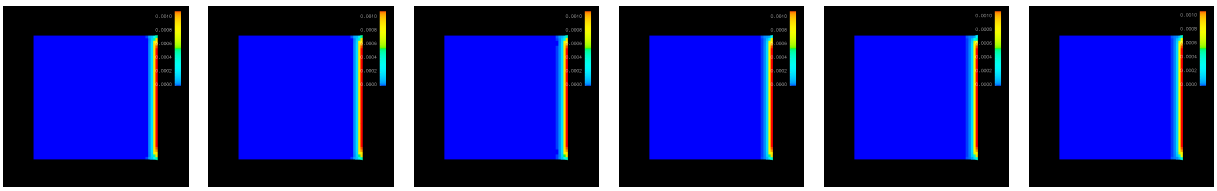

(a) theta0 = 0 (b) theta0 = 10 (c) theta0 = 20 (d) theta0 = 30 (e) theta0 = 40 (f) theta0 = 45

Figure A.74: Mesh resolution comparison for shock contraction. The colormap shows $\|\mathbf{E}\|^2$. $A_3 = 0$, $\nu = 0.0001$, hardening mode=1, sequence number = 0

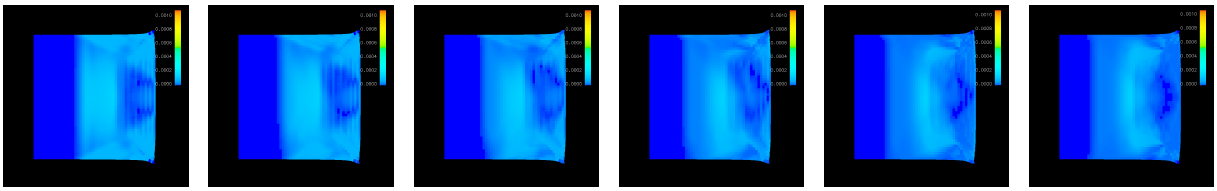

(a) theta0 = 0 (b) theta0 = 10 (c) theta0 = 20 (d) theta0 = 30 (e) theta0 = 40 (f) theta0 = 45

Figure A.75: Mesh resolution comparison for shock contraction. The colormap shows $\|\mathbf{E}\|^2$. $A_3 = 0$, $\nu = 0.0001$, hardening mode=1, sequence number = 1

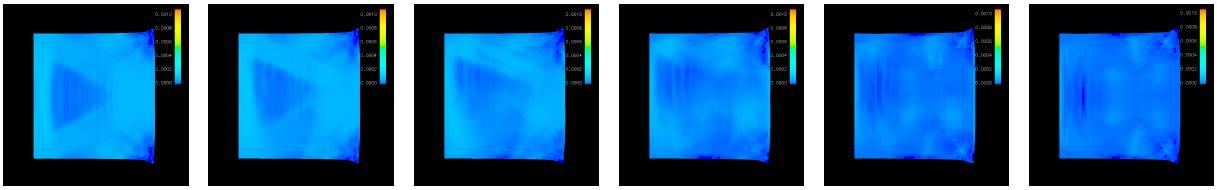

(a) theta0 = 0 (b) theta0 = 10 (c) theta0 = 20 (d) theta0 = 30 (e) theta0 = 40 (f) theta0 = 45

Figure A.76: Mesh resolution comparison for shock contraction. The colormap shows $\|\mathbf{E}\|^2$. $A_3 = 0$, $\nu = 0.0001$, hardening mode=1, sequence number = 2

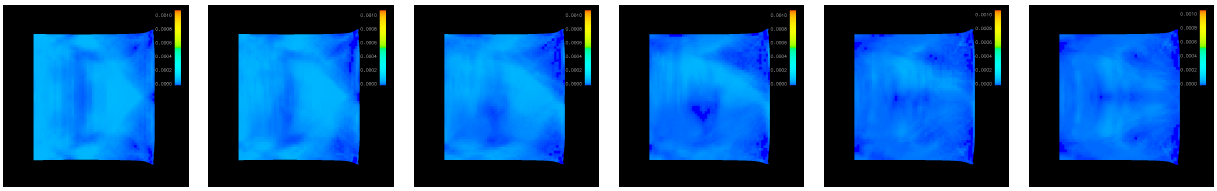

(a) theta0 = 0 (b) theta0 = 10 (c) theta0 = 20 (d) theta0 = 30 (e) theta0 = 40 (f) theta0 = 45

Figure A.77: Mesh resolution comparison for shock contraction. The colormap shows $\|\mathbf{E}\|^2$. $A_3 = 0$, $\nu = 0.0001$, hardening mode=1, sequence number = 3

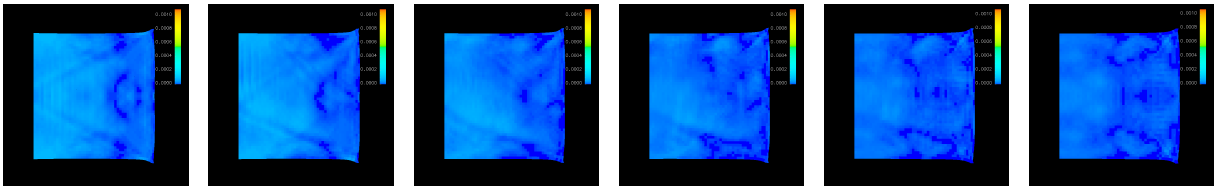

(a) theta0 = 0 (b) theta0 = 10 (c) theta0 = 20 (d) theta0 = 30 (e) theta0 = 40 (f) theta0 = 45

Figure A.78: Mesh resolution comparison for shock contraction. The colormap shows $\|\mathbf{E}\|^2$. $A_3 = 0$, $\nu = 0.0001$, hardening mode=1, sequence number = 4

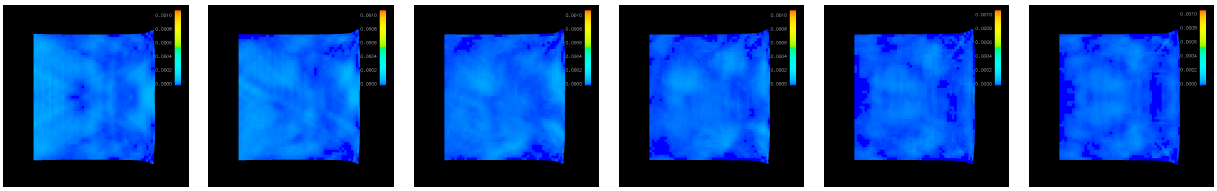

(a) theta0 = 0 (b) theta0 = 10 (c) theta0 = 20 (d) theta0 = 30 (e) theta0 = 40 (f) theta0 = 45

Figure A.79: Mesh resolution comparison for shock contraction. The colormap shows $\|\mathbf{E}\|^2$. $A_3 = 0$, $\nu = 0.0001$, hardening mode=1, sequence number = 5

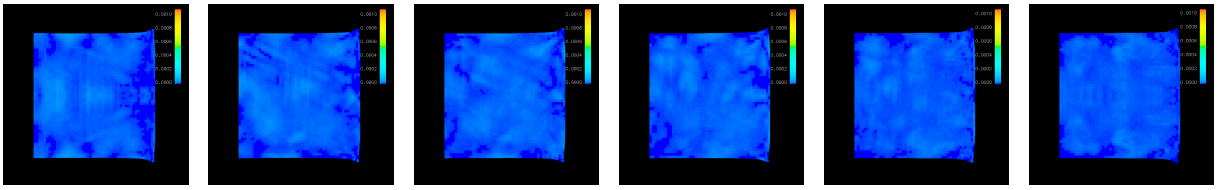

(a) theta0 = 0 (b) theta0 = 10 (c) theta0 = 20 (d) theta0 = 30 (e) theta0 = 40 (f) theta0 = 45

Figure A.80: Mesh resolution comparison for shock contraction. The colormap shows $\|\mathbf{E}\|^2$. $A_3 = 0$, $\nu = 0.0001$, hardening mode=1, sequence number = 6

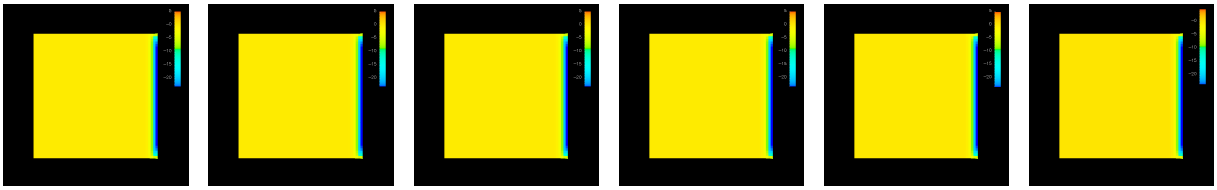

(a) theta0 = 0 (b) theta0 = 10 (c) theta0 = 20 (d) theta0 = 30 (e) theta0 = 40 (f) theta0 = 45

Figure A.81: Mesh resolution comparison for shock contraction. The colormap shows tr **S**. $A_3 = 0$, $\nu = 0.0001$, hardening mode=1, sequence number = 0

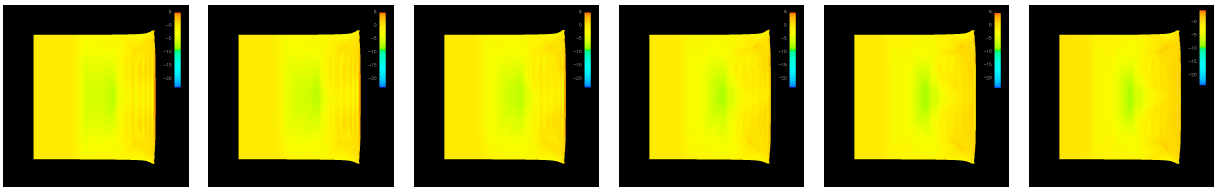

(a) theta0 = 0 (b) theta0 = 10 (c) theta0 = 20 (d) theta0 = 30 (e) theta0 = 40 (f) theta0 = 45

Figure A.82: Mesh resolution comparison for shock contraction. The colormap shows tr **S**. $A_3 = 0$, $\nu = 0.0001$, hardening mode=1, sequence number = 1

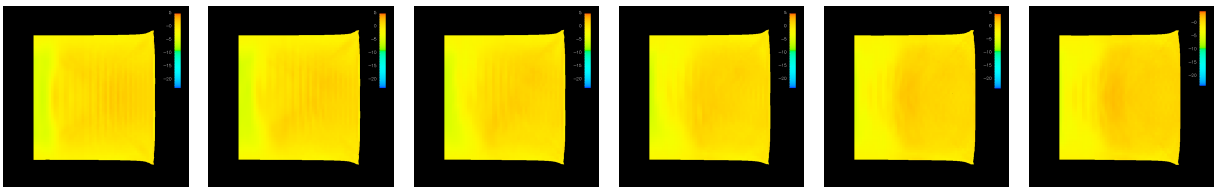

(a) theta0 = 0 (b) theta0 = 10 (c) theta0 = 20 (d) theta0 = 30 (e) theta0 = 40 (f) theta0 = 45

Figure A.83: Mesh resolution comparison for shock contraction. The colormap shows tr **S**. $A_3 = 0$, $\nu = 0.0001$, hardening mode=1, sequence number = 2

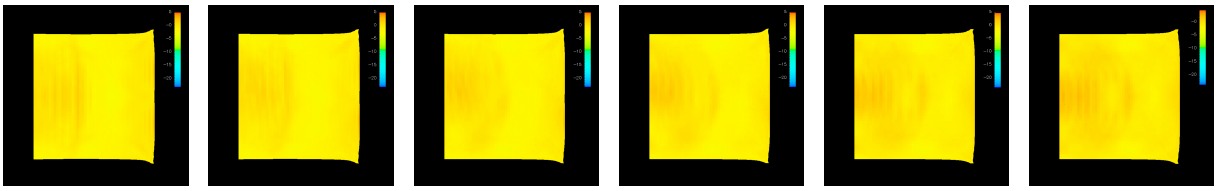

(a) theta0 = 0 (b) theta0 = 10 (c) theta0 = 20 (d) theta0 = 30 (e) theta0 = 40 (f) theta0 = 45

Figure A.84: Mesh resolution comparison for shock contraction. The colormap shows tr **S**. $A_3 = 0$, $\nu = 0.0001$, hardening mode=1, sequence number = 3

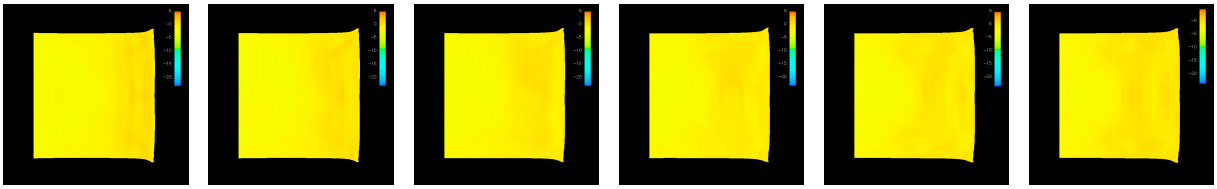

(a) theta0 = 0 (b) theta0 = 10 (c) theta0 = 20 (d) theta0 = 30 (e) theta0 = 40 (f) theta0 = 45

Figure A.85: Mesh resolution comparison for shock contraction. The colormap shows tr **S**. $A_3 = 0$, $\nu = 0.0001$, hardening mode=1, sequence number = 4

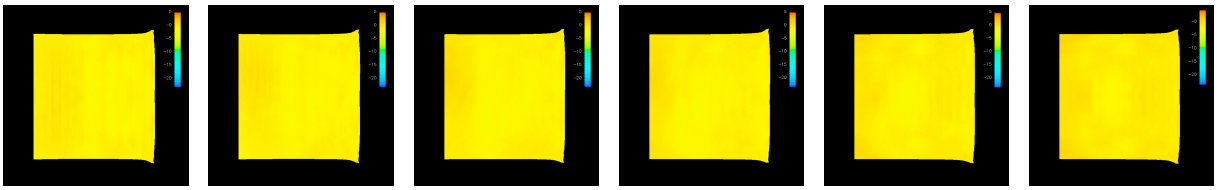

(a) theta0 = 0 (b) theta0 = 10 (c) theta0 = 20 (d) theta0 = 30 (e) theta0 = 40 (f) theta0 = 45

Figure A.86: Mesh resolution comparison for shock contraction. The colormap shows tr **S**. $A_3 = 0$, $\nu = 0.0001$, hardening mode=1, sequence number = 5

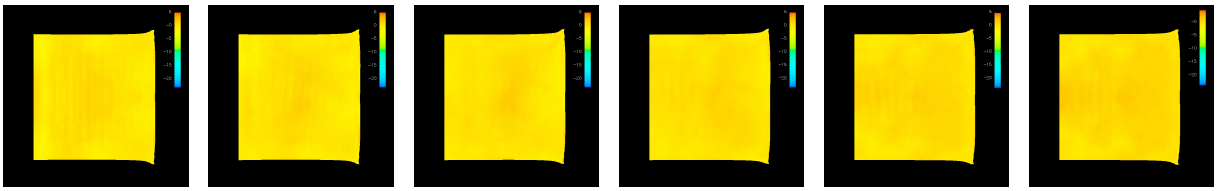

(a) theta0 = 0 (b) theta0 = 10 (c) theta0 = 20 (d) theta0 = 30 (e) theta0 = 40 (f) theta0 = 45

Figure A.87: Mesh resolution comparison for shock contraction. The colormap shows tr **S**. $A_3 = 0$, $\nu = 0.0001$, hardening mode=1, sequence number = 6

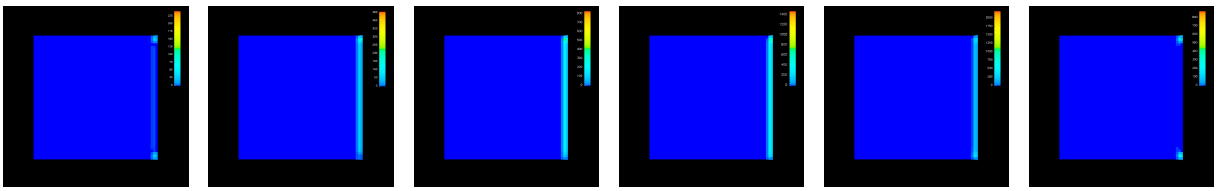

(a) theta0 = 0 (b) theta0 = 10 (c) theta0 = 20 (d) theta0 = 30 (e) theta0 = 40 (f) theta0 = 45

Figure A.88: Mesh resolution comparison for shock contraction. The colormap shows $\|\boldsymbol{\xi}\|^2$. $A_3 = 0$, $\nu = 0.0001$, hardening mode=1, sequence number = 0

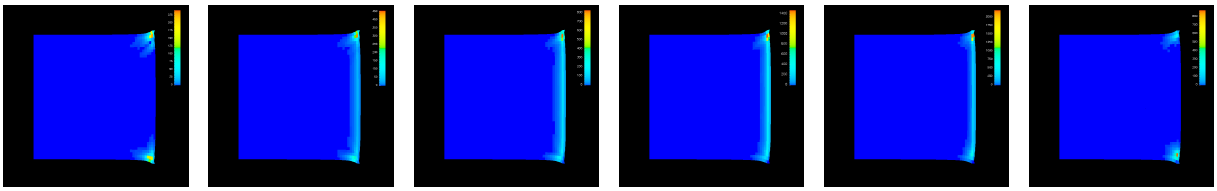

(a) theta0 = 0 (b) theta0 = 10 (c) theta0 = 20 (d) theta0 = 30 (e) theta0 = 40 (f) theta0 = 45

Figure A.89: Mesh resolution comparison for shock contraction. The colormap shows $\|\boldsymbol{\xi}\|^2$. $A_3 = 0$, $\nu = 0.0001$, hardening mode=1, sequence number = 1

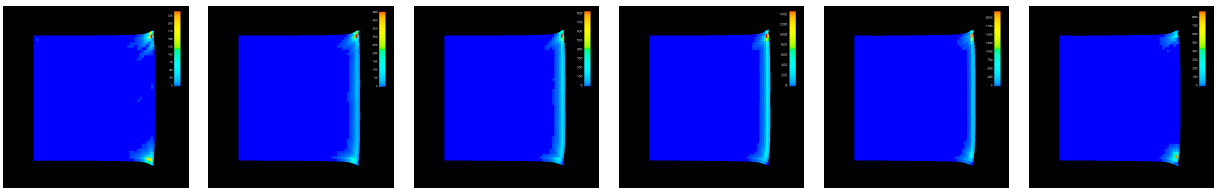

(a) theta0 = 0 (b) theta0 = 10 (c) theta0 = 20 (d) theta0 = 30 (e) theta0 = 40 (f) theta0 = 45

Figure A.90: Mesh resolution comparison for shock contraction. The colormap shows $\|\boldsymbol{\xi}\|^2$. $A_3 = 0$, $\nu = 0.0001$, hardening mode=1, sequence number = 2

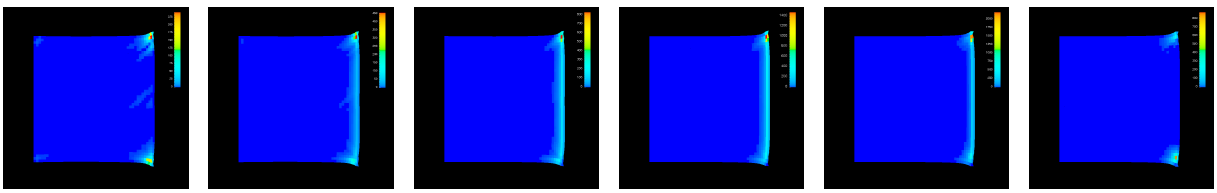

(a) theta0 = 0 (b) theta0 = 10 (c) theta0 = 20 (d) theta0 = 30 (e) theta0 = 40 (f) theta0 = 45

Figure A.91: Mesh resolution comparison for shock contraction. The colormap shows $\|\boldsymbol{\xi}\|^2$. $A_3 = 0$, $\nu = 0.0001$, hardening mode=1, sequence number = 3

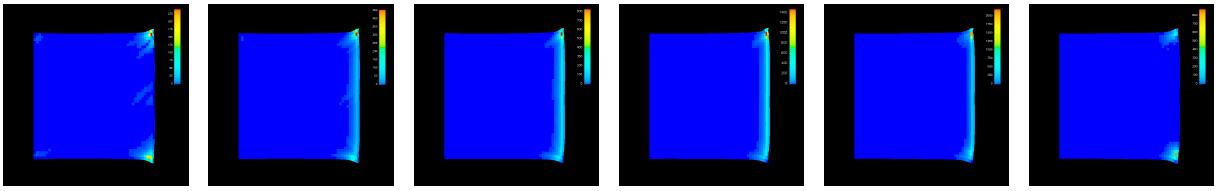

(a) theta0 = 0 (b) theta0 = 10 (c) theta0 = 20 (d) theta0 = 30 (e) theta0 = 40 (f) theta0 = 45

Figure A.92: Mesh resolution comparison for shock contraction. The colormap shows $\|\boldsymbol{\xi}\|^2$. $A_3 = 0$, $\nu = 0.0001$, hardening mode=1, sequence number = 4

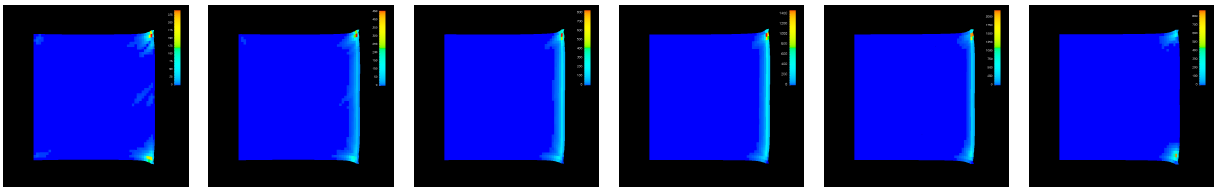

(a) theta0 = 0 (b) theta0 = 10 (c) theta0 = 20 (d) theta0 = 30 (e) theta0 = 40 (f) theta0 = 45

Figure A.93: Mesh resolution comparison for shock contraction. The colormap shows $\|\boldsymbol{\xi}\|^2$. $A_3 = 0$, $\nu = 0.0001$, hardening mode=1, sequence number = 5

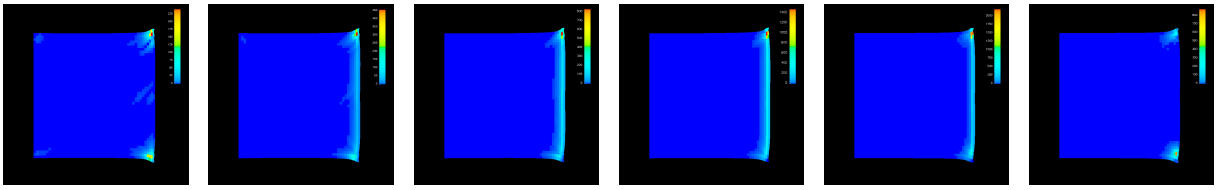

(a) theta0 = 0 (b) theta0 = 10 (c) theta0 = 20 (d) theta0 = 30 (e) theta0 = 40 (f) theta0 = 45

Figure A.94: Mesh resolution comparison for shock contraction. The colormap shows $\|\boldsymbol{\xi}\|^2$. $A_3 = 0$, $\nu = 0.0001$, hardening mode=1, sequence number = 6

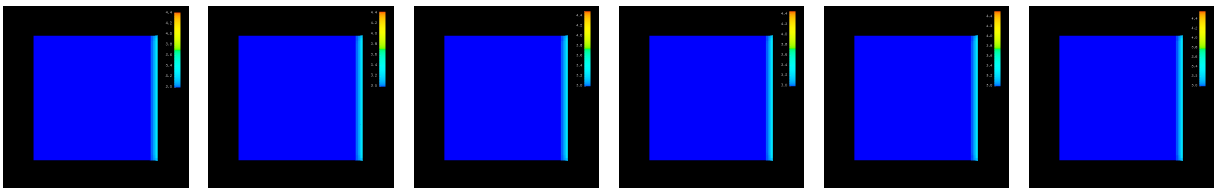

(a) theta0 = 0 (b) theta0 = 10 (c) theta0 = 20 (d) theta0 = 30 (e) theta0 = 40 (f) theta0 = 45

Figure A.95: Mesh resolution comparison for shock contraction. The colormap shows $\|\mathbf{K}\|$. $A_3 = 0$, $\nu = 0.0001$, hardening mode=1, sequence number = 0

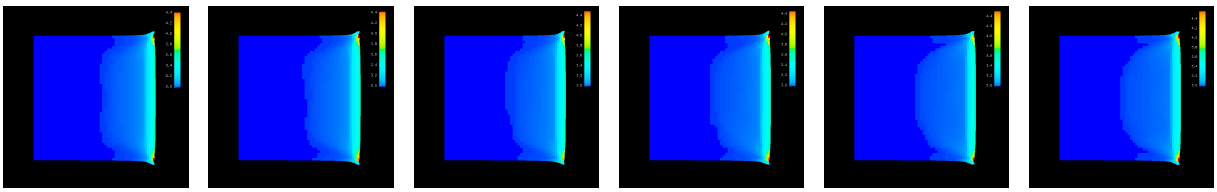

(a) theta0 = 0 (b) theta0 = 10 (c) theta0 = 20 (d) theta0 = 30 (e) theta0 = 40 (f) theta0 = 45

Figure A.96: Mesh resolution comparison for shock contraction. The colormap shows $\|\mathbf{K}\|$. $A_3 = 0$, $\nu = 0.0001$, hardening mode=1, sequence number = 1

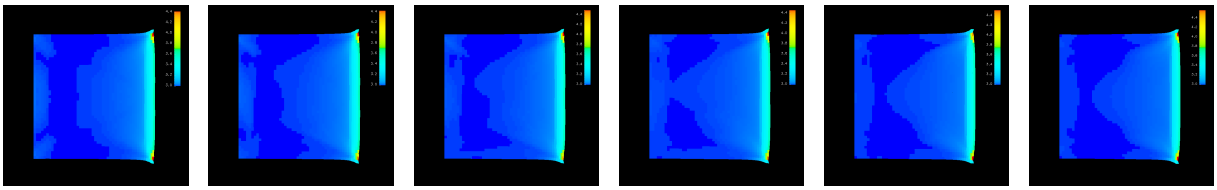

(a) theta0 = 0 (b) theta0 = 10 (c) theta0 = 20 (d) theta0 = 30 (e) theta0 = 40 (f) theta0 = 45

Figure A.97: Mesh resolution comparison for shock contraction. The colormap shows $\|\mathbf{K}\|$. $A_3 = 0$, $\nu = 0.0001$, hardening mode=1, sequence number = 2

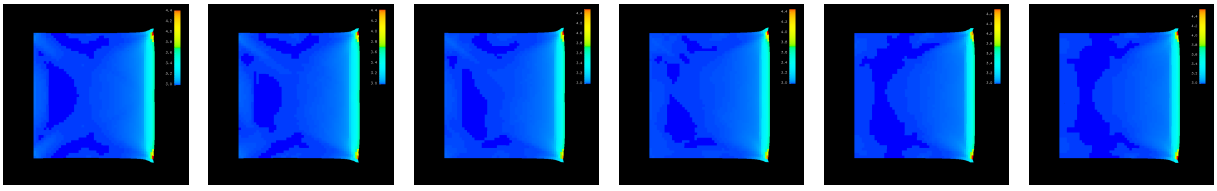

(a) theta0 = 0 (b) theta0 = 10 (c) theta0 = 20 (d) theta0 = 30 (e) theta0 = 40 (f) theta0 = 45

Figure A.98: Mesh resolution comparison for shock contraction. The colormap shows $\|\mathbf{K}\|$. $A_3 = 0$, $\nu = 0.0001$, hardening mode=1, sequence number = 3

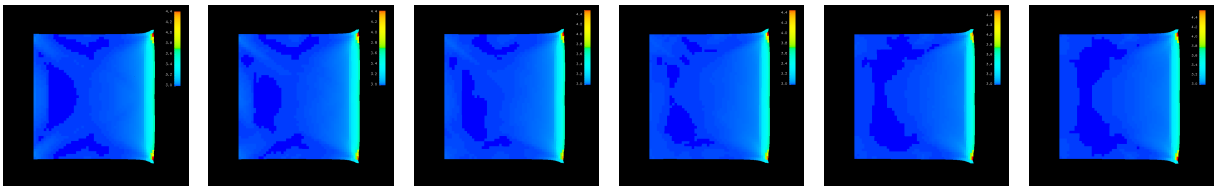

(a) theta0 = 0 (b) theta0 = 10 (c) theta0 = 20 (d) theta0 = 30 (e) theta0 = 40 (f) theta0 = 45

Figure A.99: Mesh resolution comparison for shock contraction. The colormap shows $\|\mathbf{K}\|$. $A_3 = 0$, $\nu = 0.0001$, hardening mode=1, sequence number = 4

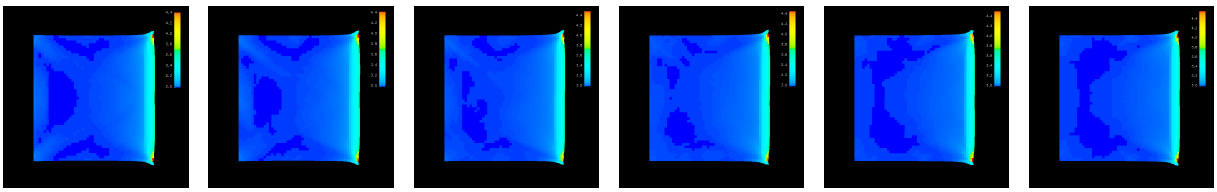

(a) theta0 = 0 (b) theta0 = 10 (c) theta0 = 20 (d) theta0 = 30 (e) theta0 = 40 (f) theta0 = 45

Figure A.100: Mesh resolution comparison for shock contraction. The colormap shows $\|\mathbf{K}\|$. $A_3 = 0$, $\nu = 0.0001$, hardening mode=1, sequence number = 5

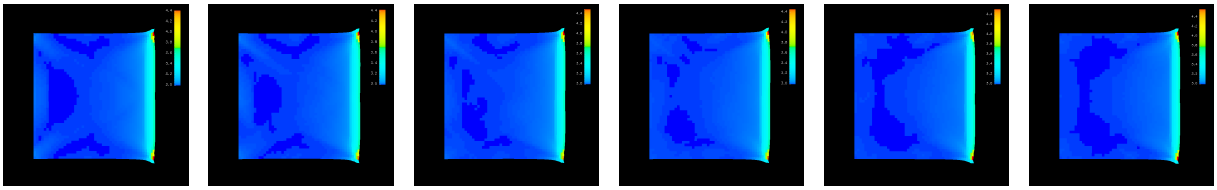

(a) theta0 = 0 (b) theta0 = 10 (c) theta0 = 20 (d) theta0 = 30 (e) theta0 = 40 (f) theta0 = 45

Figure A.101: Mesh resolution comparison for shock contraction. The colormap shows $\|\mathbf{K}\|$. $A_3 = 0$, $\nu = 0.0001$, hardening mode=1, sequence number = 6

A.6.3 Shear deformation

See §2.4.2.3.4 for information on the boundary conditions and other details. This set of figures looks at a vertical velocity on the right boundary, traction free top and bottom, with fixed left edge. The mesh resolution was 40×40. The figure sequence are plots of $\|\boldsymbol{\xi}\|^2$, $\|\mathbf{K}\|$. This set is for $A_3 = 0$.

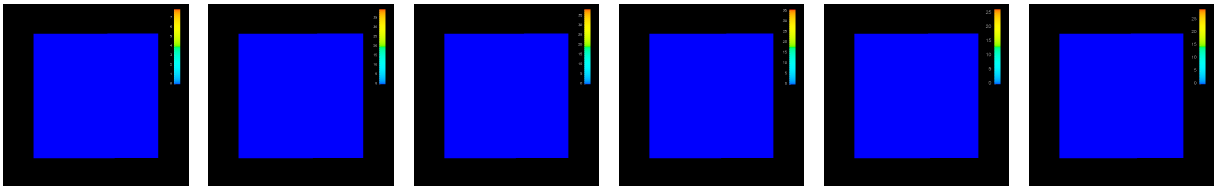

(a) $\theta = 0$ (b) $\theta = 10$ (c) $\theta = 20$ (d) $\theta = 30$ (e) $\theta = 40$ (f) $\theta = 45$

Figure A.102: Mesh resolution comparison for shear boundary condition. The colormap shows $\|\boldsymbol{\xi}\|^2$. $A_3 = 0$, $\nu = 0.0010$, hardening mode=1, sequence number = 0

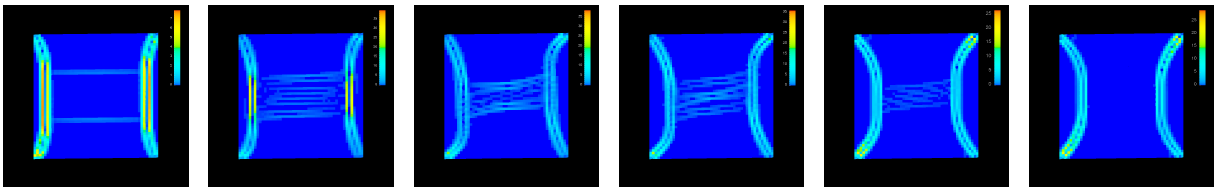

(a) $\theta = 0$ (b) $\theta = 10$ (c) $\theta = 20$ (d) $\theta = 30$ (e) $\theta = 40$ (f) $\theta = 45$

Figure A.103: Mesh resolution comparison for shear boundary condition. The colormap shows $\|\boldsymbol{\xi}\|^2$. $A_3 = 0$, $\nu = 0.0010$, hardening mode=1, sequence number = 1

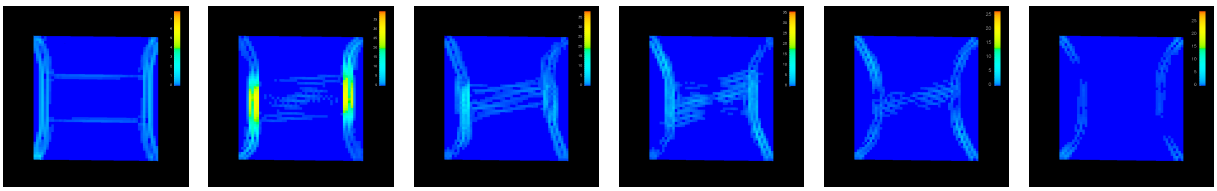

(a) $\theta = 0$ (b) $\theta = 10$ (c) $\theta = 20$ (d) $\theta = 30$ (e) $\theta = 40$ (f) $\theta = 45$

Figure A.104: Mesh resolution comparison for shear boundary condition. The colormap shows $\|\boldsymbol{\xi}\|^2$. $A_3 = 0$, $\nu = 0.0010$, hardening mode=1, sequence number = 2

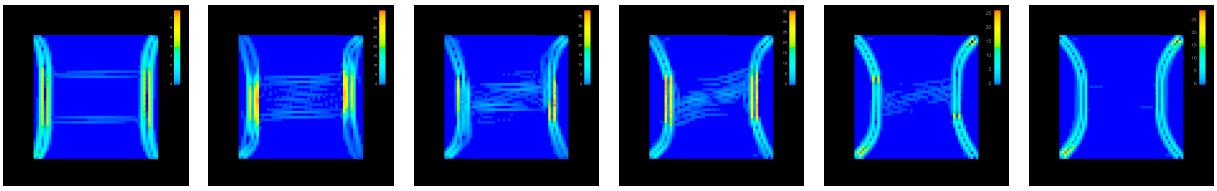

(a) $\theta = 0$ (b) $\theta = 10$ (c) $\theta = 20$ (d) $\theta = 30$ (e) $\theta = 40$ (f) $\theta = 45$

Figure A.105: Mesh resolution comparison for shear boundary condition. The colormap shows $\|\boldsymbol{\xi}\|^2$. $A_3 = 0$, $\nu = 0.0010$, hardening mode=1, sequence number = 3

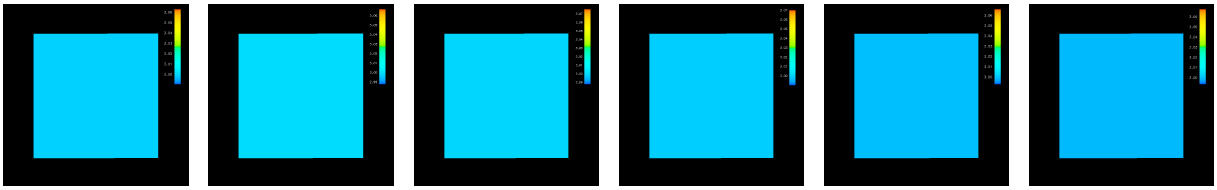

(a) $\theta = 0$ (b) $\theta = 10$ (c) $\theta = 20$ (d) $\theta = 30$ (e) $\theta = 40$ (f) $\theta = 45$

Figure A.106: Mesh resolution comparison for shear boundary condition. The colormap shows $\|\mathbf{K}\|$. $A_3 = 0$, $\nu = 0.0010$, hardening mode=1, sequence number = 0

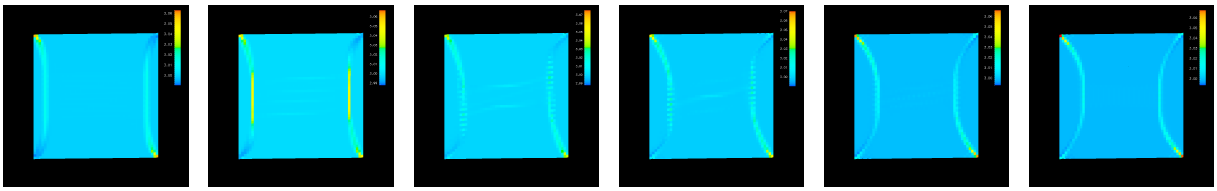

(a) $\theta = 0$ (b) $\theta = 10$ (c) $\theta = 20$ (d) $\theta = 30$ (e) $\theta = 40$ (f) $\theta = 45$

Figure A.107: Mesh resolution comparison for shear boundary condition. The colormap shows $\|\mathbf{K}\|$. $A_3 = 0$, $\nu = 0.0010$, hardening mode=1, sequence number = 1

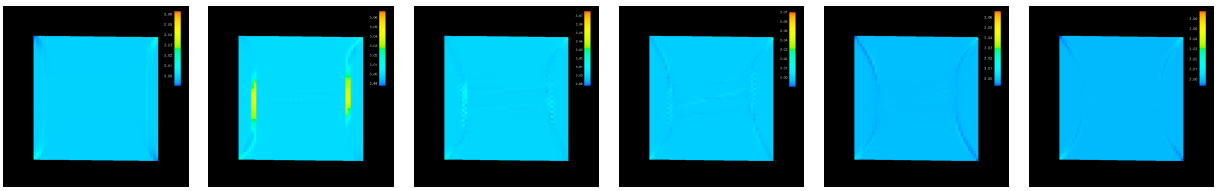

(a) $\theta = 0$ (b) $\theta = 10$ (c) $\theta = 20$ (d) $\theta = 30$ (e) $\theta = 40$ (f) $\theta = 45$

Figure A.108: Mesh resolution comparison for shear boundary condition. The colormap shows $\|\mathbf{K}\|$. $A_3 = 0$, $\nu = 0.0010$, hardening mode=1, sequence number = 2

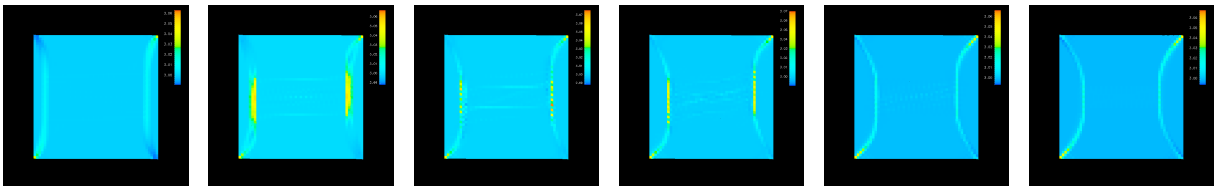

(a) $\theta = 0$ (b) $\theta = 10$ (c) $\theta = 20$ (d) $\theta = 30$ (e) $\theta = 40$ (f) $\theta = 45$

Figure A.109: Mesh resolution comparison for shear boundary condition. The colormap shows $\|\mathbf{K}\|$. $A_3 = 0$, $\nu = 0.0010$, hardening mode=1, sequence number = 3